Propagation acoustique dans le domaine temporel

Didier Dragna

Habilitation à diriger des recherches

Propagation acoustique dans le domaine temporel

Didier Dragna

Laboratoire de Mécanique des Fluides et d'Acoustique
École centrale de Lyon, Université de Lyon, CNRS

Soutenue publiquement le 12 janvier 2024 devant le jury constitué des membres suivants :

Jean-Christophe Béra	Professeur des Universités Université Claude-Bernard Lyon 1	Examinateur
Gwenaël Gabard	Professeur des universités Université du Maine	Examinateur
Benoît Gauvreau	Directeur de recherche Université Gustave Eiffel	Examinateur
Régis Marchiano	Professeur des universités Sorbonne Université	Rapporteur
Estelle Piot	Directrice de recherche ONERA Toulouse	Rapporteur
Michel Roger	Professeur des universités Ecole Centrale de Lyon	Examinateur
Victor W. Sparrow	Professeur Penn State University, États-Unis	Rapporteur

Table des matières

Résumé

Ce mémoire résume mes activités d'enseignement et de recherche depuis mon recrutement comme maître de conférences à l'École de Centrale de Lyon en 2012. Ma recherche a pour thème principal la propagation acoustique dans le domaine temporel avec une approche numérique. Elle a été développée autour de trois axes, à savoir l'acoustique environnementale, la propagation en conduit et la propagation d'ondes de choc. Dans une première partie du mémoire, je présente le bilan des activités, comprenant notamment une synthèse de mes activités d'enseignement. Dans une seconde partie, je présente les travaux réalisés en recherche, en détaillant chaque sujet d'étude avant de présenter des perspectives.

Abstract

This report summarizes my teaching and research activities since I was recruited as an assistant professor at Ecole de Centrale de Lyon in 2012. The main theme of my research is acoustic propagation in the time domain using a numerical approach. It has been developed through three topics, namely environmental acoustics, duct propagation and shock wave propagation. In the first part of the dissertation, I present a review of my activities, including a summary of my teaching activities. In the second part, I present the work carried out in research, detailing each subject of study before presenting some prospects.

Introduction générale

Depuis mon recrutement comme maître de conférences à l'École Centrale de Lyon en 2012, j'effectue ma recherche dans le groupe acoustique au sein du Laboratoire de Mécanique des Fluides et d'Acoustique et mes tâches d'enseignement dans le Département Mécanique des Fluides, Acoustique et Énergétique. Je m'implique dans des actions de formation liées à la mécanique des fluides au sens large (écoulements compressibles, biomécanique, ...) ainsi qu'à l'acoustique. Ma recherche a pour thème principal la propagation acoustique dans le domaine temporel. Pour cela, je m'appuie sur la résolution numérique des équations de la mécanique des fluides (complètes ou linéarisées).

Ma recherche s'oriente autour de trois axes. Le premier axe est l'acoustique environnementale. Les travaux se sont portés à la fois sur l'amélioration des modèles physiques et numériques pour la propagation en milieu extérieur et sur des applications pour la bioacoustique et le bruit des éoliennes. Le second axe est la propagation en conduit. Les travaux ont visé à la modélisation dans le domaine temporel des interfaces dissipatives, qu'elles soient à réaction locale ou étendue et à comportement non-linéaire. Des études spécifiques sur la suppression des instabilités au-dessus d'un liner en présence d'un écoulement ont été réalisées. Le dernier axe concerne la propagation d'ondes de chocs, avec des études sur la réflexion d'onde de choc sphérique sur une surface rugueuse et sur la propagation du bang sonique au-dessus de sols avec une topographie et en environnement urbain.

Pendant ces 11 années, j'ai co-encadré sept thèses (trois soutenues et quatre en cours), six post-doctorats et cinq stages de M2. Sur la totalité de ma carrière, je suis co-auteur de 29 publications dans des journaux internationaux avec comité de lecture et de 30 conférences internationales avec actes.

Ce mémoire est organisé en deux parties. Dans une première partie, je présente le bilan de mes activités. Après mon curriculum vitae, je détaille mes activités d'enseignement et mes responsabilités pédagogiques. J'expose ensuite mes activités de recherche, en indiquant les encadrements d'étudiants, les projets auxquels j'ai participé ainsi que mes responsabilités administratives et académiques. Je liste enfin les publications associées à ma recherche. La seconde partie du manuscrit détaille mes activités de recherche. Après avoir présenté le contexte général, je décris dans les quatre chapitres suivants les travaux réalisés autour des méthodes numériques, de l'acoustique environnementale, de la propagation en conduit et de la propagation d'ondes de choc. Un dernier chapitre vient conclure le mémoire et proposer des perspectives de recherche.

Première partie

Bilan des activités

CHAPITRE 1

Curriculum Vitae

Date et lieu de naissance : 16 Juin 1985, Marseille
Nationalité : Française

E-mail : didier.dragna@ec-lyon.fr
Page web : https://acoustique.ec-lyon.fr/didier.dragna.php

Centre Acoustique (KCA)
École Centrale de Lyon
36 avenue Guy de Collongue
69134 Ecully cedex, France

Poste actuel et formation

Depuis 2012 Maitre de conférences, Laboratoire de Mécanique de fluides et d'Acoustique (LMFA), Département de Mécanique des Fluides, Acoustique et Energetique, École Centrale de Lyon

2011 - 2012 Postdoctorat, LMFA, projet européen ACOUTRAIN, École Centrale de Lyon
Encadrement : P. Blanc-Benon et M. Jacob.

2008 - 2011 Docteur en spécialité acoustique de l'École Centrale de Lyon

Modélisation par une approche temporelle de la propagation acoustique en milieu extérieur : traitement de frontières complexes et validation sur site ferroviaire

Laboratoire de Mécanique des Fluides et d'Acoustique de l'École Centrale de Lyon.
Encadrement : P. Blanc-Benon et F. Poisson.
Soutenue le 16 novembre 2011. Mention Très Honorable.

Composition du Jury :

Dominique HABAULT	D.R. CNRS, LMA (Présidente)
Michel BÉRENGIER	Directeur de recherche, IFSTTAR (Rapporteur)
Philippe BLANC-BENON	D.R. CNRS, École Centrale de Lyon (Directeur de thèse)
Daniel JUVÉ	Professeur, École Centrale de Lyon
Philippe LAFON	Ingénieur de Recherche, EDF R&D, LaMSID (Rapporteur)
Régis MARCHIANO	Professeur, Université Pierre et Marie Curie
Franck POISSON	Ingénieur de Recherche, D.I.R. SNCF (Directeur de thèse)

2005 - 2008 Ingénieur généraliste de l'École Centrale de Lyon.

Publications et sujets de recherche

29 publications dans des revues internationales avec comité de lecture et 30 conférences internationales avec actes publiés.

Co-encadrement en cours de 4 doctorants. 3 thèses co-encadrées soutenues. Co-encadrement de 6 post-doctorants et de 5 stagiaires de M2.

Facteur h de 7 dans Web Of Science, 236 citations.

Mes travaux de recherche portent sur la propagation acoustique linéaire et non-linéaire en milieu inhomogène et en mouvement, et en particulier sur les méthodes numériques pour la propagation dans le domaine temporel. Dans une première partie de ma recherche, je m'intéresse à la propagation acoustique à grande distance dans l'atmosphère, avec plusieurs applications : bruit des transports, bruit des éoliennes et bioacoustique. Dans la seconde partie, j'étudie la propagation en conduit pour des applications en aéronautique. Dans une dernière partie, je travaille sur l'acoustique non-linéaire, plus précisément sur la propagation d'ondes de choc.

Cinq publications les plus significatives

- Dragna D., Pineau P. & Blanc-Benon P., 2015. A generalized recursive convolution method for time-domain propagation in porous media, J. Acoust. Soc. Am. 138(2), 1030-1042.
- Dragna, D., Attenborough, K. & Blanc-Benon, P., 2015, On the inadvisability of using single parameter impedance models for representing the acoustical properties of ground surfaces, J. Acoust. Soc. Am., 138(4), 2399-2413.
- Deng Y., Alomar A., Dragna D. & Galland M.-A., 2021. Characterization and suppression of the hydrodynamic instability in the time domain for acoustic propagation in a lined flow duct, J. Sound Vib. 500, 115999, 1-22.
- Lechat, T., Emmanuelli, A., Dragna, D. & Ollivier, S., 2021, Propagation of spherical weak blast waves over rough periodic surfaces, Shock Waves, 31, 379-398.
- Emmanuelli, A., Dragna, D., Ollivier, S. & Blanc-Benon, P., 2021, Characterization of topographic effects on sonic boom reflection by resolution of the Euler equations, J. Acoust. Soc. Am., 149(4), 2437-2450.

Responsabilités, sociétés savantes et récompense

Directeur du laboratoire de recherche commun LETMA (Laboratoire Études et Modélisation Acoustique) avec le CEA et Sorbonne-Université entre avril 2019 et mars 2021. Membre du comité exécutif du LETMA depuis 2019.

Membre élu du Conseil Scientifique de l'Ecole Centrale de Lyon d'avril 2017 à mars 2021.

Membre de la Société Française d'Acoustique (SFA), responsable du groupe aéro et hydroacoustique (GAHA) depuis 2022, membre élu du GAHA depuis 2016. Membre de l'Acoustical Society of America.

Prix Yves Rocard de la Société Française d'Acoustique (2015).

CHAPITRE 2

Activités d'enseignement

2.1 Présentation synthétique de l'activité d'enseignement

Mes activités d'enseignement se déroulent au sein du Département de Mécanique de Fluides, d'Acoustique et d'Energétique (DMFAE) de l'École Centrale de Lyon. Je suis impliqué dans les cours de tronc commun et de spécialité de l'École Centrale de Lyon, ainsi que dans les cours du Master international d'Acoustique de l'Université de Lyon. J'ai effectué depuis mon recrutement en 2012 entre 195 et 240 heures eqTD par an.

Pour l'enseignement de tronc commun, je réalise des TDs et des TPs pour le cours de mécanique des fluides au sein de l'Unité d'Enseignement Fluides et Energie (UE FLE) pour environ 90 heqTD par an. Je suis aussi co-responsable de l'action de formation de l'UE FLE « FLE tc 2 – Méthodes numériques et expérimentales », suivie par toute la promotion d'élèves ingénieurs de l'Ecole Centrale de Lyon (environ 350 étudiants). Outre l'aspect pédagogique, je suis en charge de l'aspect administratif. Pour l'enseignement de spécialité, j'ai repris depuis la rentrée 2019 le cours « Écoulements supersoniques » dans lequel je réalise les cours magistraux. Je suis aussi responsable du cours « Dynamique des systèmes biologiques humains » : j'y donne des cours magistraux sur la modélisation du système cardiovasculaire. Je participe aussi aux cours d'acoustique donnés à l'École Centrale de Lyon : « Acoustique Environnementale » et « Acoustique et ondes dans les fluides ». Enfin, depuis 2023, j'interviens dans le cours « The Physics and Modelling of free surface flows » sur les ondes de surface. Les effectifs pour ces cours de spécialité varient entre 20 et 40 étudiants.

Je participe aussi à l'activité de tutorat de trois élèves-ingénieurs chaque année. Je propose et j'encadre également des projets étudiants sur des sujets d'acoustique, à la hauteur d'un à deux projets par an.

Enfin, je suis fortement impliqué dans les activités de formation du Master international d'Acoustique de l'Université de Lyon. Je coorganise les projets de M1 : les étudiants ont tout le long de l'année une journée par semaine consacrée à ce projet, qui est encadré par un chercheur/enseignant-chercheur d'un laboratoire d'acoustique sur Lyon. Je suis aussi responsable du cours spécifique master « Numerical methods for acoustics », dont j'ai été à l'origine (effectif entre 10 et 20 étudiants).

2.2 Présentation des enseignements

J'interviens dans environ une dizaine d'actions de formations (AF). Je présente les enseignements ci-dessous par ordre de niveau de formation.

Cursus ingénieur généraliste Centrale Lyon – Tronc commun

Tout d'abord, j'encadre dans l'UE de tronc commun de l'Ecole Centrale de Lyon Fluide et Energie (FLE) un groupe de TD du cours « FLE – Concepts et Application », pour une vingtaine d'heures eqTD. Les TDs visent à donner une application du cours sur des aspects très généraux de mécanique des fluides.

Toujours dans l'UE FLE, je suis co-responsable de l'action de formation « FLE – Méthodes numériques et expérimentales » ; celle-ci est constitué de TP en mécaniques des fluides et énergétique sur une analyse d'un système de traitement d'air, sur une application du théorème de Bernoulli pour une conduite à section variable et enfin sur une analyse d'un écoulement de jet libre. Cette AF comprend aussi des TD de prise en main du logiciel commercial de mécanique des fluides FLUENT. Outre l'enseignement, je m'occupe pour un des deux semestres de l'organisation de l'AF, en particulier pour faire le lien avec la scolarité de Centrale Lyon et pour gérer la correction par les enseignants des rapports de TP. En tout, le volume horaire pour cette AF est de 40 heqTD.

Enfin, j'interviens aussi dans l'AF « FLE – Etudes thématiques » : cette AF, sous la forme de projet, propose aux étudiants de construire leur étude autour de thèmes prédéfinis en mécanique des fluides et d'une vingtaine de banc expérimentaux à leur disposition. Cette AF est donc moins cadrée qu'une AF classique et donne plus d'autonomie aux étudiants. Le volume pour cette AF est de 30 heqTD.

Cursus ingénieur généraliste Centrale Lyon – Cours de spécialité

J'ai repris depuis novembre 2019 le cours de spécialité « Ecoulements Supersoniques », donné au sein de l'UE Appro. Ce cours donne une vue globale sur les écoulements compressibles et la notion de choc. Il y a aussi des TDs associés ainsi qu'un mini-projet sur l'étude d'un écoulement dans une tuyère convergente-divergente organisé autour d'un TP et d'un BE sur le logiciel FLUENT. Je donne les cours magistraux pour un groupe de 24 étudiants, ce qui correspond environ à 30 heqTD. Suite à la reprise du cours, j'ai gardé globalement la même organisation pour le cours et refait les supports de cours.

Je suis aussi co-responsable du cours « Acoustique et Ondes dans les Fluides », donné lui-aussi dans l'UE Appro. Je donne les cours magistraux et les TDs pour la partie « Ondes dans les Fluides » : on rappelle la notion de relation de dispersion, d'ondes dispersives et de propagation en milieu inhomogène. J'ai repris cette partie en 2018, réalisée auparavant par Christophe Bailly ; j'ai modifié le contenu des cours et des BEs. Il y a à peu près 24 étudiants qui suivent le cours. Mes interventions correspondent à environ 20 heqTD.

Je suis aussi le référent principal du cours « Dynamique des systèmes biologiques humains » de l'UE Module Ouvert Disciplinaire. Le cours vise à donner une introduction sur la biomécanique et à présenter le fonctionnement de plusieurs systèmes biologiques humains (systèmes cardiovasculaire et musculo-squelettique). Je donne les CMs sur la partie système cardiovasculaire et les BE sur le traitement du signal appliqué à l'électrocardiogramme. Je m'occupe aussi d'animer l'équipe pédagogique du cours, les autres intervenants étant extérieurs à Centrale Lyon. Le volume horaire est d'environ 20 heqTD.

Je participe aussi au cours « Acoustique Environnementale » de l'UE Module Ouvert Disciplinaire. Le cours donne les bases en acoustique, décrit en détail l'acoustique des salles et la propagation acoustique dans l'environnement et présente les techniques de réduction du bruit passives et actives. J'interviens sur un CM sur la propagation acoustique dans l'atmosphère. Je m'implique aussi pour définir le contenu du cours : j'ai ainsi participé au renouvellement et à la création des TPs sur l'acoustique de la salle cinéma de Centrale Lyon et sur la cartographie de bruit, notamment via l'encadrement du stage de M1 d'A. Rajagopal en juillet 2018. Le volume horaire est de quelques heqTD.

Depuis 2023, je suis co-responsable avec Richard Perkins du cours « The Physics and modelling

of free surface flows » dans l'UE Electifs. Dans ce cours qui porte sur les écoulements à surface libre, je suis en charge de la partie sur les ondes de surface avec des cours magistraux et de BE. Le volume horaire est d'environ 10 heqTD.

J'interviens aussi dans deux cours de spécialité, à savoir le cours de l'UE Module Ouvert Disciplinaire « Bruits d'origine aérodynamique » et le cours de l'UE Module Ouvert Sectoriel « Bruit des transports » pour des TPs. Le volume horaire combiné est de l'ordre de 15 heures.

Master International d'Acoustique de l'Université de Lyon

Je suis responsable des projets de M1. Ceux-ci ont lieu d'octobre à mai. Chaque étudiant choisit en début d'année un projet à faire seul ou en binôme dans un laboratoire d'acoustique à Lyon. Un temps est consacré dans l'emploi du temps chaque semaine à ce projet. On demande à la fin de l'année un rapport et une présentation orale pour chaque projet. L'animation de cette AF consiste à solliciter en début d'année les chercheurs acousticiens sur Lyon pour avoir un nombre de sujets suffisant et faire le lien entre chercheur et étudiant le long de l'année, notamment pour l'organisation des soutenances. L'effectif en M1 est d'à peu près 10 étudiants par an. Le volume horaire est de 10 heqTD.

Je suis aussi responsable du cours « Numerical methods for acoustics ». Le cours vise à donner une vue globale sur les méthodes numériques employées pour des problèmes d'acoustique. Les sessions de cours sont constituées d'une partie cours magistral et d'une partie BE. Je m'occupe de la partie administrative et j'interviens sur la partie tracé de rayons. Le cours est mutualisé M1 et M2 et les effectifs sont autour de 20 étudiants. Mes interventions correspondent à environ 10 heqTD.

Autres activités pédagogiques

Je réalise aussi une activité de tutorat pour les élèves-ingénieurs en tronc commun de Centrale Lyon. Celle-ci consiste principalement en trois rendez-vous annuels pour discuter avec l'étudiant de sa scolarité à Centrale Lyon et de son projet professionnel.

Je propose et j'encadre aussi des projets étudiants, que ce soit des projets d'étude ou des projets d'application recherche en tronc commun à Centrale Lyon ou des projets du master d'Acoustique. J'encadre un à deux projets par an.

Je participe aussi à des jurys de soutenance de travaux de fin d'étude des élèves-ingénieurs ainsi que des M2 d'Acoustique (autour de cinq soutenances par an).

2.3 Responsabilités pédagogiques

Outre les responsabilités d'actions de formation, je suis responsable au sein du département MFAE de l'équipe d'enseignement acoustique (6 enseignant-chercheurs), qui vise à l'organisation des cours de spécialité en acoustique. L'animation de l'équipe reste assez informelle. Nous organisons environ une fois par an une réunion avec les enseignant-chercheurs concernés pour discuter des évolutions des cours, de propositions de cours et de projets et s'assurer de la cohérence de l'offre de cours en acoustique à l'Ecole Centrale de Lyon.

CHAPITRE 3

Activités de recherche

3.1 Encadrement d'étudiants, projets de recherche et collaborations

Les différents étudiants encadrés en thèse, post-doctorats ou stage de M1 ou M2 depuis mon recrutement sont listés dans cette section. J'indique aussi le pourcentage d'encadrement.

3.1.1 Thèses

1. Giovanni Coco (mai 2023 - , 50 %). Propagation des ondes de choc générées par une soufflante non carénée : signature acoustique sur le fuselage. Codirection avec C. Bailly. Bourse CIFRE avec SAFRAN Aircraft Engines.

2. Emanuele Sarpero (avril 2022 - , 35 %). Non-linear acoustic behaviors in a lined flow duct. Codirection avec M.-A. Galland et E. Gourdon. Bourse CeLyA.

3. Jules Colas (octobre 2021 - , 40 %). Propagation du bruit d'un parc éolien dans l'atmosphère. Codirection avec A. Emmanuelli. Directeur officiel : P. Blanc-Benon. Bourse MESR.

4. Alexis Jamois (octobre 2020 - , 25 %). Développement de « métamatériaux » pour des applications aéroacoustiques. Codirection avec M.-A. Galland. Bourse CeLyA.

5. Arthur Guibard (octobre 2019 - juillet 2023, 25 %). Analyse des contraintes de propagation sur les réseaux de communication acoustique chez les galliformes de montagne. Codirection avec S. Ollivier et F. Sèbe. Directeur officiel : M.-A. Galland. Bourse CeLyA.

6. Yuanyuan Deng (novembre 2017 - décembre 2020, 50 %). Time-domain simulation of sound propagation in a lined flow duct : characterization and suppression of hydrodynamic instabilities. Codirection avec M.-A. Galland. Bourse CSC.

7. Thomas Lechat (octobre 2016 - février 2020, 45 %). Étude de la réflexion d'ondes de choc acoustiques sur des parois rugueuses. Codirection avec S. Ollivier. Directeur officiel : C. Bailly. Bourse MESR.

3.1.2 Post-doctorats

1. Bill Kayser (octobre 2022 - septembre 2024, 60 %). Propagation du bruit avion au niveau du sol. Coencadrement avec P. Blanc-Benon. Financement par le projet DGAC MAMBO.

2. Codor Khodr (février 2021 - décembre 2022, 80 %). Coencadrement avec P. Blanc-Benon. Plateforme numérique pour la propagation des infrasons dans l'atmosphère. Financement par le CEA.

3. Daher Diab (septembre 2020 - août 2021, 50 %). Propagation acoustique non-linéaire en conduit traité sous écoulement. Coencadrement avec M.-A. Galland. Financement par le projet européen SALUTE.

4. Ariane Emmanuelli (août 2019 - novembre 2020, 45 %). Sonic boom propagation in the atmosphere : meteorological and ground effects. Coencadrement avec S. Ollivier et P. Blanc-Benon. Financement par le projet européen RUMBLE.

5. Antoni Alomar (février 2019 - mars 2020, 50 %). Sound propagation in lined flow ducts with a non-locally reacting liner. Coencadrement avec M.-A. Galland. Financement par le projet européen ARTEM.

6. Renata Troian (septembre 2014 - juillet 2016, 40 %). Modeling and numerical simulation of liners in the presence of a mean flow. Coencadrement avec M.-A. Galland et C. Bailly. Financement par le projet européen ENOVAL.

3.1.3 Stages

1. Lucas Bellaton (avril 2023 - septembre 2023, 50 %). Analyse de la propagation d'ondes de choc générées par des éclairs. Stage de M2. Coencadrement avec E. Salze.

2. Hemant Bommidala (avril 2022 - septembre 2022, 40 %). Simulation numérique de la propagation du bruit éolien dans l'environnement : prise en compte des effets 3D. Stage de M2. Coencadrement avec C. Khodr et A. Emmanuelli.

3. Jules Colas (avril 2021 - septembre 2021, 50 %). Résolution numérique des équations d'Euler linéarisées pour la propagation du bruit éolien dans l'environnement. Stage de M2. Coencadrement avec A. Emmanuelli.

4. Estelle Meziani (mars 2021 - septembre 2021, 50 %). Étude numérique de la propagation du bruit éolien dans l'environnement. Stage de M2. Coencadrement avec A. Emmanuelli.

5. Loic Berger (avril 2018 - septembre 2018, 35 %). Modélisation de la propagation des vocalisations d'oiseaux. Stage de M2. Coencadrement avec S. Ollivier et F. Sèbe.

6. Abhinav Rajagopal (juillet 2018, 50 %). Génération de cartes de bruit à l'aide d'un logiciel commercial. Stage de M1. Coencadrement avec V. Clair.

3.1.4 Collaborations

J'ai pu mené différentes collaborations nationales et internationales indiquées ci-dessous.

- Maarten Hornikx (Eindhoven University of Technology, Pays-Bas). Méthodes numériques pour la propagation acoustique dans le domaine temporel à grande distance.
- Kai Ming Li (Purdue University, États-Unis). Approches analytiques pour le bruit rayonné par des sources en mouvement.
- Keith Attenborough (Open University, Royaume-Uni). Étude comparative sur les modèles d'impédance pour les sols.
- Frédéric Sèbe (ENES, France). Propagation des vocalisations d'oiseaux dans l'atmosphère.
- Vladimir Ostashev (US Army, Etats-Unis). Equations paraxiales pour la propagation grande distance en atmosphère inhomogène.

3.1.5 Projets de recherche

J'ai participé à plusieurs projets de recherche, listés ci-dessous. Pour chaque projet, les objectifs du projet, le montant du financement ainsi que la tâche réalisée sont décrits.

- MAMBO (Méthodes Avancées pour la Modélisation du Bruit moteur et aviOn),
  projet DGAC, 258 k€, 2021-2026.

  Le projet MAMBO est un projet global autour de la modélisation des sources aéroacoustiques sur les avions ainsi que les méthodes de prédiction de bruit.

  La recherche du LMFA autour de la propagation acoustique s'intéresse au bruit avion à proximité du sol, notamment pour des problématiques de certification. L'objectif est de développer un modèle rapide de propagation acoustique de l'avion jusqu'au sol, permettant de prendre en compte les effets de sol et les effets météorologiques. Une validation du modèle est réalisée dans de nombreux cas tests avec une solution numérique des équations d'Euler linéarisées. Le modèle développé sera ensuite utilisé par les partenaires du projets pour faire une étude de sensibilité sur les niveaux de bruits prédits dans un scénario de certification de bruit avion.

  Les travaux sont effectués dans le cadre du post-doc de B. Kayser.

- RUMBLE (RegUlation and norM for low sonic Boom LEvels),
  projet européen Horizon 2020, 136 k€, 2017-2020.

  Le projet RUMBLE avait pour objectif de déterminer les niveaux de bruit acceptables générés par le bang d'avions supersoniques survolant les terres, notamment pour des raisons normatives.

  L'activité du LMFA portait sur la caractérisation des effets de sol sur la réflexion du bang sonique. Pour cela, nous avons réalisé des simulations numériques directes en résolvant les équations d'Euler. Cette approche directe permet d'éviter les limitations des approches de type rayons ou paraxiales. Nous avons réalisés deux études, la première portant sur les effets de la topographie et la seconde sur la réflexion du bang en milieu urbain.

  Les travaux ont été effectués dans le cadre du post-doc d'A. Emmanuelli. Ils ont donné lieu aux publications A20, A26, A27 et A28.

- SALUTE (Smart Acoustic Lining for UHBR Technologies Engines),
  projet européen Horizon 2020, 60 k€, 2018-2022.

  Le projet SALUTE se proposait de développer des traitements absorbants hybrides en paroi de conduit et de les tester sur le banc PHARE de l'École Centrale de Lyon.

  Parmi les différentes tâches du LMFA, j'ai été impliqué sur la modélisation du comportement des plaques perforées en présence de fort niveau. Nous avons développé une formulation d'une condition limite d'admittance non-linéaire et nous l'avons implémenté dans un code de résolution des équations d'Euler linéarisées. Nous avons pu notamment montrer que pour des forts niveaux d'excitation, des erreurs importantes sur les prédictions des performances des traitements étaient réalisées en négligeant ces effets non-linéaires.

  Les travaux ont été effectués dans le cadre du post-doc de D. Diab et ont été publiés dans l'article A24.

- ARTEM (Aircraft noise Reduction Technologies and related Environmental iMpact),
  projet européen Horizon 2020, 150 k€, 2017-2022.

  Le projet ARTEM s'intéressait à la problématique du bruit pour les nouvelles architectures d'avion, à la fois en terme de techniques de réduction de bruit, d'effets d'installation et de prédiction du bruit au sol.

Dans ce projet, nous nous sommes intéressés à la modélisation de nouveaux traitements acoustiques pour des simulations temporelles, en particulier les matériaux à réaction étendue comme les mousses métalliques ou des matériaux résonants. Pour cela, nous avons modélisé les matériaux par des fluides équivalents et avons résolu la propagation acoustique au sein des matériaux.

Les travaux ont été réalisés dans le cadre du post-doc d'A. Alomar et ont donnés lieu aux deux publications A18 et A21.

- ENOVAL (Engine Module Validators),
projet européen FP7, 150 k€, 2013-2018.

Le projet ENOVAL visait à réduire les émissions de polluant et le bruit des architectures d'avion de type UHBR.

La tâche du LMFA a consisté à développer une méthode d'identification de l'impédance de surface à partir de mesures sur un conduit traité. Nous avons proposé une méthode originale qui identifie non pas l'impédance de surface fréquence par fréquence mais qui identifie les paramètres d'un modèle d'impédance afin d'avoir une identification large bande.

Les travaux ont été réalisés dans le cadre du post-doc de R. Troian. L'article A13 est issu de ces travaux.

3.2 Autres activités académiques

3.2.1 Responsabilités administratives

J'ai été directeur du laboratoire de recherche commun (LRC) Laboratoire Études et Modélisation Acoustique (LETMA) entre avril 2019 et mars 2021. Le LRC LETMA est un laboratoire réunissant le CEA-DAM, Sorbonne Université et l'Ecole Centrale de Lyon autour de la thématique générale de la propagation d'ondes acoustiques dans l'atmosphère. Les thèmes du LRC portent principalement sur la modélisation de la propagation des ondes infrasonores et la caractérisation des sources, naturelles ou humaines (éclairs, météorites, explosions industrielles, ..). Une dizaine de chercheurs pour les trois partenaires sont impliqués au sein du LRC. En tant que directeur, je devais coordonner les activités du LETMA, notamment par la sollicitation et l'organisation des réunions semestrielles du comité exécutif et des réunions annuelles du comité directeur ainsi que par une implication forte dans l'organisation des journées annuelles du LETMA. Je suis aussi membre du comité exécutif du LRC LETMA depuis 2019.

Je suis depuis le printemps 2022 responsable du groupe aéroacoustique et hydro-acoustique (GAHA) au sein de la société française d'acoustique (SFA). Je coordonne les activités en lien avec l'aéroacoustique au sein de la SFA et je participe aux réunions trimestrielles du comité d'administration de la SFA. Je suis par ailleurs membre élu du GAHA depuis 2018.

3.2.2 Organisation de manifestations scientifiques et de sessions spécialisés

J'ai co-organisé deux conférences et deux écoles internationales :

- J'ai coorganisé avec Philippe Blanc-Benon la conférence internationale "20th International Symposium on Nonlinear Acoustics, including the 2nd International Sonic Boom Forum", qui a lieu du 29 juin au 3 juillet 2015 à l'Ecole Centrale de Lyon. Cette conférence autour de l'acoustique non-linéaire a réuni environ 180 personnes.
- J'ai coorganisé avec Philippe Blanc-Benon la conférence internationale "17th Long Range Sound Propagation Symposium" qui a eu lieu les 12 et 13 juin 2018 à l'Ecole Centrale de Lyon. Cette conférence portait sur la propagation du son dans l'atmosphère. Il y avait environ 30 participants.

- J'ai coorganisé avec Christophe Millet l'école de printemps "Waves & geosciences : Infrasound and beyond" qui a eu lieu du 28 mars au 1er avril 2022 au centre de congrès Valpré. L'école de printemps, organisée dans le cadre LRC LETMA, avait pour but de donner une description globale de l'atmosphère et des ondes qui s'y propagent et de présenter plus en détail les ondes infrasonores (physique de la propagation, sources, méthodes de détection, ...). Ella a réuni environ 80 participants.
- J'ai coorganisé avec Daniel Juvé l'école d'été "Atmospheric sound propagation", qui s'est déroulé du 13 au 15 juin 2018 au centre de congrès Valpré. Cette école d'été portait sur la propagation du son dans la couche limite atmosphérique, avec des aspects théoriques, numériques et applicatifs (bruit des transports ou des éoliennes, ...). Il y avait environ 50 participants.

J'ai coorganisé plusieurs sessions spécialisées dans des congrès nationaux et internationaux :

- 13ème Congrès Français d'Acoustique, 11-15 avril 2016, Le Mans, session "Aéroacoustique en conduit : propagation guidée et impédance de surface" avec Yves Aurégan, 10 présentations.
- 16ème Congrès Français d'Acoustique, 11-15 avril 2022, Marseille, session "Propagation longue distance" avec Benoit Gauvreau, 8 présentations.
- 10th Forum Acusticum, September 11-15 2023, Torino, Italy, sessions "Outdoor noise propagation" avec Timothy van Renterghem, 17 présentations, et "Numerical and computational acoustics" avec Manfred Kaltenbacher, 20 présentations.

3.2.3 Évaluation de la recherche

J'évalue environ une dizaine d'articles scientifiques soumis dans des journaux internationaux à comité de lecture par an, principalement pour J. Acoust. Soc. Am., AIAA J., J. Sound Vib. et J. Theor. Comput. Acoust.

J'ai été membre de quatre jurys de soutenance de thèse :

- Han Meng, soutenance le 12 mars 2018, "Acoustic properties of novel multifunctional sandwich structures and porous absorbing materials", Ecole Centrale de Lyon.
- Loris Casadei, soutenance le 23 mars 2022, "Time-domain broadband impedance model for computational aeroacoustics : application to shock-wave propagation in lined intakes", ISAE-SUPAERO.
- Annie Zelias, soutenance le 21 avril 2022, "Méthode des rayons complexes pour la propagation infrasonore. Application au bang sonique d'un météoroïde", Sorbonne Université.
- Samuel Deleu, soutenance le 6 avril 2023, "Propagation et interaction de chocs acoustiques : effets non-linéaires", ISAE-SUPAERO.

CHAPITRE 4

Liste des publications et communications

4.1 Publications internationales dans des journaux à comité de lecture

A29 Colas J., Emmanuelli A., **Dragna D.**, Cotté B., Blanc-Benon P. & Stevens R.J.A.M. (2023), Wind turbine sound propagation : Comparison of a linearized Euler equations model with parabolic equation methods, J. Acoust. Soc. Am., 154(3), 1413-1426.

A28 Emmanuelli A., **Dragna D.**, Ollivier S. & Blanc-Benon P. (2023), Sonic boom propagation over real topography, J. Acoust. Soc. Am., 154(1), 16-27.

A27 **Dragna D.**, Emmanuelli A., Ollivier S. & Blanc-Benon P. (2022), Sonic boom reflection over urban areas, J. Acoust. Soc. Am., 152(6), 3323-3339.

A26 **Dragna D.**, Emmanuelli A., Ollivier S. & Blanc-Benon P. (2022), Sonic boom reflection over an isolated building and multiple buildings, J. Acoust. Soc. Am. 151(6), 3792-3806.
Mis en avant par AIP Publishing : 'Urban Canyons' Prolong Sonic Booms in Cities.

A25 Guibard A., Sèbe F., **Dragna D.** & Ollivier S. (2022), Influence of meteorological conditions and topography on the active space of mountain birds assessed by a wave-based sound propagation model, J. Acoust. Soc. Am. 151(6), 3703-3718.
Mis en avant dans Scilight 2022, 281103 (2022).

A24 Diab D., **Dragna D.**, Salze E. & Galland M.-A. (2022), Nonlinear broadband time-domain admittance boundary condition for duct acoustics. Application to perforated plate liners, J. Sound Vib. 528, 116892, 1-26.

A23 Lechat T., Emmanuelli A., **Dragna D.** & Ollivier S. (2021), Propagation of spherical weak blast waves over rough periodic surfaces, Shock Waves 31, 379-398.

A22 Julian R., **Dragna D.**, Ollivier S. & Blanc-Benon P. (2021), Rational approximation of unsteady friction weighting functions in the Laplace domain, J. Hydraul. Eng., 147(9), 04021031, 1-9.

A21 Alomar A., **Dragna D.** & Galland M.-A. (2021), Time-domain simulations of sound propagation in a flow duct with extended-reacting liners, J. Sound Vib. 507, 116137, 1-24.

A20 Emmanuelli A., **Dragna D.**, Ollivier S. & Blanc-Benon P. (2021), Characterization of topographic effects on sonic boom reflection by resolution of the Euler equations, J. Acoust. Soc. Am. 149(4), 2437-2450.

A19 Deng Y., Alomar A., **Dragna D.** & Galland M.-A. (2021), Characterization and suppression of the hydrodynamic instability in the time domain for acoustic propagation in a lined flow duct, J. Sound Vib. 500, 115999, 1-22.

A18 Alomar A., **Dragna D.** & Galland M.-A. (2021), Pole identification method to extract the equivalent fluid characteristics of general sound-absorbing materials, Applied Acoustics 174, 107752, 1-15.

A17 Wang Y., Li K.M., **Dragna D.** & Blanc-Benon P. (2020), On the sound field from a source moving above non-locally reacting grounds, J. Sound Vib. 464, 114975, 1-20.

A16 Karzova M.M., Lechat T., Ollivier S., **Dragna D.**, Yuldashev P.V., Khokhlova V.A. & Blanc-Benon P. (2019). Effect of surface roughness on nonlinear reflection of weak shock waves, J. Acoust. Soc. Am. 146(5), EL438-433

A15 Karzova M.M., Lechat T., Ollivier S., **Dragna D.**, Yuldashev P.V., Khokhlova V.A. & Blanc-Benon P. (2019). Irregular reflection of spark-generated shock pulses from a rigid surface : Mach-Zehnder interferometry measurements in air, J. Acoust. Soc. Am. 145(1), 26-35.

A14 **Dragna D.** & Blanc-Benon P. (2017). Sound propagation above a random spatially-varying admittance plane, J. Acoust. Soc. Am. 142(4), 2058-2072.

A13 Troian R., **Dragna D .**, Bailly C. & Galland M.-A. (2017). Broadband liner impedance eduction for multimodal acoustic propagation in the presence of a mean flow, J. Sound. Vib. 392, 200-216.

A12 **Dragna D.**, Attenborough K. & Blanc-Benon P. (2015). On the inadvisability of using single parameter impedance models for representing the acoustical properties of ground surfaces, J. Acoust. Soc. Am. 138(4), 2399-2413.

A11 **Dragna D.**, Pineau P. & Blanc-Benon P. (2015). A generalized recursive convolution method for time-domain propagation in porous media, J. Acoust. Soc. Am. 138(2), 1030-1042.

A10 Hornikx M. & **Dragna D.** (2015). Application of the Fourier pseudospectral time domain method in orthogonal curvilinear coordinates for near-rigid moderately curved surfaces, J. Acoust. Soc. Am. 138(1), 425-435.

A9 **Dragna D.** & Blanc-Benon P. (2015). Sound radiation by a moving line source above an impedance plane with frequency-dependent properties, J. Sound. Vib. 349, 259-275.

A8 **Dragna D.** & Blanc-Benon P. (2014). Towards realistic simulations of sound radiation by moving sources in outdoor environments, Int. J. Aeroacoustics 13(5-6), 03-424.

A7 Jacob M.C., **Dragna D.**, Cahuzac A., Boudet J. & Blanc-Benon P. (2014). Toward hybrid CAA with ground effects, Int. J. Aeroacoustics 13(3-4), 235-260.

A6 **Dragna D.**, Blanc-Benon P. & Poisson F. (2014). Modeling of broadband moving sources for time-domain simulations of outdoor sound propagation, AIAA J. 52(9), 1928-1939.

A5 **Dragna D.** & Blanc-Benon P. (2014). Physically admissible impedance models for time-domain computations of outdoor sound propagation, Acta Acust. united Ac. 100(3), 401-410.

A4 **Dragna D.**, Blanc-Benon P. & Poisson F. (2014). Impulse propagation over a complex site : A comparison of experimental results and numerical predictions, J. Acoust. Soc. Am. 135(3), 1096-1105.

A3 **Dragna D.**, Bogey C., Hornikx M. & Blanc-Benon P. (2013). Analysis of the dissipation and dispersion properties of the Chebyshev pseudospectral method for propagation problems, J. Comp. Phys. 255, 31-47.

A2 **Dragna D.**, Blanc-Benon P. & Poisson F. (2013). Time-domain solver in curvilinear coordinates for outdoor sound propagation over complex terrain, J. Acoust. Soc. Am. 133(6), 3751-3763.

A1 **Dragna D.**, Cotté B., Blanc-Benon P. & Poisson F. (2011). Time-domain simulations of outdoor sound propagation with suitable impedance boundary conditions, AIAA J. 49(7), 1420-1428.

4.2 Publications dans des journaux nationaux

An1 **Dragna D.**, Blanc-Benon P. & Poisson F. (2012), Modélisation de la propagation acoustique en milieu extérieur par un approche temporelle : validation expérimentale sur site, Acoustique & Techniques 68, 46-51.

4.3 Conférences internationales avec actes publiés

Ci30 Ostashev V.E., Colas J., **Dragna D.** & Wilson D.K. (2023), Parabolic equations for motionless and moving inhomogeneous media and theur solution, 10th Forum Acusticum, Torino, Italy, September 11-15, 1-5.

Ci29 Colas J., **Dragna D.**, Emmanuelli A., Blanc-Benon P., Cotté B. & Stevens R.J.A.M. (2023), Investigating the impact of atmospheric boundary layer stratification on wind farm noise propagation, 10th Forum Acusticum, Torino, Italy, September 11-15, 1-4.

Ci28 Jamois A., **Dragna D.** & Galland M.-A. (2023), Acoustic modelling of material obtained by additive manufacturing placed in the wall of a duct, 10th Forum Acusticum, Torino, Italy, September 11-15, 1-5.

Ci27 Sarpero E., **Dragna D.**, Gourdon E. & Galland M.-A. (2023), Nonlinear broadband time-domain admittance boundary condition applied to a flow duct with perforated liner, 10th Forum Acusticum, Torino, Italy, September 11-15, 1-4.

Ci26 Kayser B., **Dragna D.** & Blanc-Benon P. (2023), Sound pressure radiated by a point-source in arbitrary motion above an absorbing ground : Application to aircraft noise, 10th Forum Acusticum, Torino, Italy, September 11-15, 1-4.

Ci25 Jamois A., **Dragna D.** & Galland M.-A. (2023), Impact of manufacturing uncertainties on the acoustic properties of 3D printed materials, 29th International Congress on Sound and Vibration, Prague, Czechia, July 9-13, 1-5.

Ci24 Sarpero E., **Dragna D.**, Gourdon E. & Galland M.-A. (2023), Experimental characterisation of perforated plates in a duct with flow in non-linear regime, 29th International Congress on Sound and Vibration, Prague, Czechia, July 9-13, 1-8.

Ci23 Colas J., Emmanuelli A., **Dragna D.**, Blanc-Benon P., Cotté B. & Stevens R.J.A.M. (2022), Exploring the effect of wind farm flow on wind turbine noise propagation through numerical simulations, 10th International Conference on Wind Turbine Noise, Dublin, Ireland, June 21-23, 1-11.

Ci22 **Dragna D.**, Emmanuelli A., Ollivier S. & Blanc-Benon P. (2022), Numerical simulations of sonic boom propagation over urban areas, Internoise, Glasgow, UK, August 21-24, 1-6.

Ci21 Colas J., Emmanuelli A., **Dragna D.**, Stevens R.J.A.M. & Blanc-Benon P. (2022), Effect of a 2D hill on the propagation of wind turbine noise, 28th AIAA/CEAS Aeroacoustics Conference, Southampon, UK, June 14-17, AIAA Paper 2022-2923.

Ci20 Emmanuelli A., **Dragna D.**, Ollivier S. & Blanc-Benon P. (2020), Ground elevation effects on sonic boom reflection, e-Forum Acusticum, December 7-11, Online.

Ci19 Deng Y., Alomar A., **Dragna D.** & Galland M.-A. (2020), Numerical method to remove hydrodynamic instability generated in time-domain simulation of acoustic propagation in a lined flow duct, e-Forum Acusticum, December 7-11, Online.

Ci18 Alomar A., **Dragna D.** & Galland M.-A. (2020),Time-domain simulations of a flow duct with extended-reacting liners, e-Forum Acusticum, December 7-11, Online.

Ci17 Deng Y., **Dragna D.**, Galland M.-A. & Alomar A. (2019), Comparison of three numerical methods for acoustic propagation in a lined duct with flow, 25th AIAA/CEAS Aeroacoustics Conference, Delft, The Netherlands, AIAA Paper 2019-2658.

Ci16 **Dragna D.**, Berger L., Ollivier S. & Sèbe F. (2019), Propagation of bird vocalizations in the Alpine environment, 23rd International Congress on Acoustics, 9-13 sept., Aachen, Germany, 1-6.

Ci15 Lechat T., Ollivier S., **Dragna D.** & Karzova M.M. (2019), Impact of roughness on shock wave reflection phenomena, 23rd International Congress on Acoustics, 9-13 sept., Aachen, Germany, 1-6.

Ci14 Troian R., **Dragna D.**, Bailly C. & Galland M.-A. (2016), Broadband eduction of liner impedance under multimodal acoustic propagation, 22th AIAA/CEAS Aeroacoustics Conference, Lyon, AIAA Paper 2016-2725.

Ci13 **Dragna D.**, Ollivier S., Desjouy C., Castelain T. & Blanc-Benon P. (2016), Reflection of weak shockwaves from a rough surface, 22th AIAA/CEAS Aeroacoustics Conference, Lyon, AIAA Paper 2016-3013.

Ci12 Desjouy C., Ollivier S., Marsden O., **Dragna D.** & Blanc-Benon P. (2015), Propagation of acoustic shock waves between parallel rigid boundaries and into shadow zones, 20th International Symposium on Nonlinear Acoustics including the 2nd International Sonic Boom Forum, Lyon.

Ci11 **Dragna D.**, Bontemps T. & Blanc-Benon P. (2015), Radiation of moving sources in time-domain simulations of outdoor sound propagation, Euronoise 2015, Maastricht, Pays-Bas.

Ci10 Poisson F., Margiocchi F., Bongini E. & **Dragna D.**. (2013), Global pass-by noise of high-speed train running onto slab track and ballasted track, 10th World Congress on Rail Research, Sydney, Australie.

Ci9 **Dragna D.**, Blanc-Benon P., Bongini E. & Poisson F. (2013), Outdoor sound propagation for high-speed moving sources, 21th International Congress on Acoustics, Montréal, Canada.

Ci8 **Dragna D.**, Blanc-Benon P. & Poisson F. (2012), The modeling of moving sources for time-domain simulations of outdoor sound propagation, 17th AIAA/CEAS Aeroacoustics Conference, Colorado Springs, CO, USA, AIAA Paper 2012-2613.

Ci7 **Dragna D.**, Blanc-Benon P. & Poisson F. (2012), Time-domain simulations of outdoor sound propagation : experimental validation on a complex site, Acoustics 2012, Nantes.

Ci6 **Dragna D.**, Blanc-Benon P. & Poisson F. (2011), The modelling of the topography in time-domain simulations of atmospheric sound propagation, Forum Acusticum, Aalborg, Danemark.

Ci5 **Dragna D.**, Blanc-Benon P. & Poisson F. (2011), Effects of ground surface in numerical simulations of atmospheric sound propagation, 14th Long Range Sound Propagation Symposium, Annapolis, ML, USA.

Ci4 **Dragna D.**, Hornikx M., Blanc-Benon P., Poisson F. & Waxler R. (2011), Chebyshev pseudospectral time-domain method for simulations of outdoor sound propagation, 14th Long Range Sound Propagation Symposium, Annapolis, ML, USA.

Ci3 **Dragna D.**, Blanc-Benon P. & Poisson F. (2010), Ground effects in time-domain simulations of outdoor sound propagation, 20th International Congress on Acoustics, Sydney, Australie.

Ci2 **Dragna D.**, Blanc-Benon P. & Poisson F. (2010), Effects of topography in time-domain simulations of outdoor sound propagation, 16th AIAA/CEAS Aeroacoustics Conference, Stockholm, Suède, AIAA Paper 2010-3758.

Ci1 **Dragna D.**, Cotté B., Blanc-Benon P. & Poisson F. (2009), Time-domain simulations of outdoor sound propagation with suitable impedance boundary conditions, 15th AIAA/CEAS Aeroacoustics Conference, Miami, FL, USA, AIAA Paper 2009-3306.

4.4 Conférences internationales sans actes

Cw29 Maurice S., Blanc-Benon P., Chide B., Bertrand T., Murdoch N., Lorenz R., Jacob X., **Dragna D.**, Stott A., Gillier M., de la Torre Juárez M., Rodriguez Manfredi J.A., Mimoun D. & Wiens R. (2023), Acoustic recording of near-surface turbulence on Mars, December 5-9, Jacksonville, FL, USA. Voir aussi : J. Acoust. Soc. Am. 153, A280.

Cw28 Ostashev V.E., Wilson D.K., **Dragna D.** & Colas J. (2022), Parabolic equation with arbitrary variations in the sound speed and Mach numbers of the medium velocity, 183rd Acoustical Society of America Meeting, December 5-9, Nashville, TN, USA. Voir aussi : J. Acoust. Soc. Am. 152, A81.

Cw27 Salze E., Vagnon E., Ollivier S., El-Khattabi M., Zouaghi A., **Dragna D.** & Blanc-Benon P. (2022), Laboratory-scale characterization of lightning strikes : acoustical and electrical measurements synchronized with optical visualizations, 22nd International Symposium on Nonlinear Acoustics, July 4-8, Oxford, UK. Voir aussi : Proc. Mtgs. Acoust 48, 045009, 1-11.

Cw26 Diab D., **Dragna D.**, Salze E. & Galland M.-A. (2022), Nonlinear broadband admittance boundary condition for time-domain simulation of sound propagation, 22nd International Symposium on Nonlinear Acoustics, July 4-8, Oxford, UK.

Cw25 Emmanuelli A., **Dragna D.**, Ollivier S. & Blanc-Benon P. (2022), Reflection of sonic boom over realistic urban areas, 182nd Acoustical Society of America Meeting, May 23-27, online. Voir aussi : J. Acoust. Soc. Am. 149, A75.

Cw24 Guibard A., **Dragna D.**, Ollivier S. & Sèbe F. (2021), Acoustic propagation in heterogeneous environments and its implications on the active space of rock ptarmigan, 181st Acoustical Society of America Meeting, November 29-December 3, Seattle, WA, USA. Voir aussi : J. Acoust. Soc. Am., 150, A201.

Cw23 Khodr C., **Dragna D.**, Blanc-Benon P., Marchiano R., Aubry L., Gainville O. & Millet C. (2021), PLetma — Parallel software package for intensive infrasound simulation, 181st Acoustical Society of America Meeting, November 29-December 3, Seattle, WA, USA. Voir aussi : J. Acoust. Soc. Am., 150, A201.

Cw22 Emmanuelli A., **Dragna D.**, Ollivier S. & Blanc-Benon P. (2021), Sonic boom reflection over irregular terrain, 180th Acoustical Society of America Meeting, June 8-10, Denver, CO, USA. Voir aussi : J. Acoust. Soc. Am. 151, A86.

Cw21 Emmanuelli A., Lechat T., **Dragna D.**, Ollivier S. & Blanc-Benon P. (2021), Resolution of the Euler equations in curvilinear coordinates for sonic boom propagation, 14th WCCM & ECCOMAS 2020, January 11-15, Online.

Cw20 Emmanuelli A., **Dragna D.**, Ollivier S. & Blanc-Benon P. (2020), Propagation of sonic boom reflected on irregular terrain, 18th Long Range Sound Propagation Symposium, August 3-4, Online.

Cw19 Emmanuelli A., Lechat T., **Dragna D.** & Ollivier S. (2019), Ground effects on sonic boom reflection, 178th Acoustical Society of America Meeting, December 2-7, San Diego, CA, USA. Voir aussi : J. Acoust. Soc. Am. 146, 2781.

Cw18 Alomar A., **Dragna D.** & Galland M.-A. (2019), Extended-reacting liners in time-domain simulations for broadband attenuation with flow, 178th Acoustical Society of America Meeting, December 2-7, San Diego, CA, USA. Voir aussi : J. Acoust. Soc. Am. 146, 2786.

Cw17 Karzova M.M., Lechat T., Ollivier S., **Dragna D.**, Yuldashev P.V., Khokhlova V.A. & Blanc-Benon P. (2018), Nonlinear reflection of weak shock waves from a rough surface in air, **invited paper**, 176th Acoustical Society of America Meeting, November 5–9, Victoria, BC, Canada. Voir aussi : J. Acoust. Soc. Am. 144, 1677.

Cw16 Robert L., Marchiano R., Gainville O., Millet C., Aubry L., Braeuning J.-P., **Dragna D.** & Bailly C. (2018), Inter-comparison of numerical models for propagation of infrasounds, 17th Long Range Sound Propagation Symposium, June 12-13, Lyon.

Cw15 Karzova M.M., Lechat T., **Dragna D.**, Ollivier S., Yuldashev P.V., Khokhlova V.A. & Blanc-Benon P. (2018), Modeling of nonlinear N-wave propagation in a turbulent layer : pressure field distortions and statistics, 17th Long Range Sound Propagation Symposium, June 12-13, Lyon.

Cw14 Cosnefroy M., Cheinet S., Ehrhardt L., Dagallier A., **Dragna D.** & Juvé D. (2018), Impulse sound propagation in open environments : Time-domain simulations versus measurements, Euronoise 2018, May 27-31, Hersonissos, Greece.

Cw13 **Dragna D.** & Blanc-Benon P. (2018), On the use of high-order time-domain impedance boundary conditions, invited paper, 175th Acoustical Society of America Meeting, May 7-11, Minneapolis, MN, USA. Voir aussi : J. Acoust. Soc. Am., 143, 1740.

Cw12 Cosnefroy M., Cheinet S., Ehrhardt L., **Dragna D.** & Juvé D. (2017), Efficient modeling of long range impulse sound propagation in three dimensions, 171th Meeting of the Acoustical Society of America, December 4-8, New Orleans, LA, USA. Voir aussi : J. Acoust. Soc. Am., 142, 2674.

Cw11 Yuldashev P.V., Karzova M.M., Ollivier S., **Dragna D.**, Khokhlova V.A. & Blanc-Benon P. (2017), Nonlinear propagation of N-waves through kinematic turbulence : Statistics of peak overpressure and shock front steepness, 171th Meeting of the Acoustical Society of America, December 4-8, New Orleans, LA, USA. Voir aussi : J. Acoust. Soc. Am. 142, 2674.

Cw10 **Dragna D.** & Blanc-Benon P. (2017), Sound propagation above a flat ground with random spatially varying properties, 171th Meeting of the Acoustical Society of America, December 4-8, New Orleans, LA, USA. Voir aussi : J. Acoust. Soc. Am. 142, 2673.

Cw9 **Dragna D.** & Blanc-Benon P. (2017), Sound radiation of a line source moving above an absorbing plane with a frequency-dependent admittance, **invited paper**, Acoustics'17 Boston, 173rd Meeting of the Acoustical Society of America & 8th Forum Acusticum , June 25-29, Boston, MA, USA. Voir aussi : J. Acoust. Soc. Am. 141(5), 3808.

Cw8 Blanc-Benon P., **Dragna D.**, Ollivier S., Desjouy C. & Karzova M.M. (2016), Experimental analysis and numerical simulations of the irregular reflection of weak shock waves on a plane surface, 16th Long Range Sound Propagation Symposium, Oxford, MS, USA.

Cw7 **Dragna D.** & Blanc-Benon P. (2016), Acoustic propagation above a spatially-varying impedance plane, 16th Long Range Sound Propagation Symposium, Oxford, MS, USA.

Cw6 Desjouy C., Ollivier S., Marsden O., **Dragna D.**, Karzova M.M. & Blanc-Benon P. (2016), Irregular reflection of weak acoustic shock pulses on rigid boundaries, 171st Acoustical Society of America Meeting, Salt Lake City, UT, USA. Voir aussi : J. Acoust. Soc. Am. 139, 2207.

Cw5 **Dragna D.**, Pineau P. & Blanc-Benon P. (2016), Time-domain propagation in porous media using the auxiliary differential equation method : Application for outdoor acoustics, 171st Acoustical Society of America Meeting, Salt Lake City, UT, USA. Voir aussi : J. Acoust. Soc. Am. 139, 2009.

Cw4 **Dragna D.** & Blanc-Benon P. (2014), A generalized recursive convolution method for time-domain propagation in porous media, 15th Long Range Sound Propagation Symposium, Vienne, Autriche.

Cw3 **Dragna D.** & Blanc-Benon P. (2014), Acoustic propagation over a complex site : a parametric study using a time-domain approach, 167th Acoustical Society of America Meeting, Providence, RI, USA. Voir aussi : J. Acoust. Soc. Am. 135, 2382.

Cw2 Blanc-Benon P., **Dragna D.** & Poisson F. (2011), Time-domain simulations of outdoor sound propagation in presence of a complex topography, **invited paper** to 161st Acoustical Society of America Meeting, Seattle, WA, USA. Voir aussi : J. Acoust. Soc. Am. 129(4), 2479.

Cw1 **Dragna D.**, Blanc-Benon P. & Poisson F. (2010), Ground effects in time-domain simulations of outdoor sound propagation, 159th Acoustical Society of America Meeting, Baltimore, ML, USA. Voir aussi : J. Acoust. Soc. Am. 127(3), 2037.

4.5 Conférences nationales

Cn15 Guibard A., **Dragna D.**, Ollivier S. & Sèbe F. (2022), Propagation acoustique en milieu hétérogène et variabilité de l'espace actif de la communication chez le lagopède alpin, 16ème Congrès Français d'Acoustique, 11-15 Avril, Marseille.

Cn14 Diab D., **Dragna D.**, Salze E. & Galland M.-A. (2022), Modélisation du comportement non-linéaire des plaques perforées dans des simulations temporelles de propagation acoustique en conduit, 16ème Congrès Français d'Acoustique, 11-15 Avril, Marseille.

Cn13 Colas J., Emmanuelli A., **Dragna D.**, Stevens R.J.A.M. & Blanc-Benon P. (2022), Simulation de la propagation du bruit éolien par résolution des équations d'Euler linéarisées, 16ème Congrès Français d'Acoustique, 11-15 Avril, Marseille.

Cn12 **Dragna D.**, Emmanuelli A., Ollivier S. & Blanc-Benon P. (2022), Propagation du bang sonique au-dessus d'un profil urbain, 16ème Congrès Français d'Acoustique, 11-15 Avril, Marseille.

Cn11 Khodr C., **Dragna D.**, Blanc-Benon P., Marchiano R., Aubry L., Gainville O. & Millet C. (2022), PLetma - Plateforme numérique parallèle pour la simulation des infrasons, 16ème Congrès Français d'Acoustique, 11-15 Avril, Marseille.

Cn10 Khodr C., **Dragna D.**, Emmanuelli A. & Stevens R.J.A.M. (2022), Équation parabolique 3D pour la propagation en milieu inhomogène et en mouvement : application au sillage d'une éolienne, 16ème Congrès Français d'Acoustique, 11-15 Avril, Marseille.

Cn9 Jamois A., **Dragna D.**, Zielinski T. & Galland M.-A. (2022), Modélisation acoustique d'un matériau obtenu par fabrication additive placé en paroi d'un conduit, 16ème Congrès Français d'Acoustique, 11-15 Avril, Marseille.

Cn8 Lechat T., **Dragna D.** & Ollivier S. (2018), Simulation du champ proche généré par une source impulsionnelle à arcs électriques, 14ème Congrès Français d'Acoustique, 23-27 April, Le Havre, 939-945.

Cn7 Cosnefroy M., Cheinet S., Ehrhardt L., Dagallier A., **Dragna D.** & Juvé D. (2018), Modélisation temporelle de la propagation à longue distance des sons impulsionnels en trois dimensions, 14ème Congrès Français d'Acoustique, 23-27 April, Le Havre.

Cn6 Troian R., **Dragna D.**, Bailly C. & Galland M.-A. (2016), Analyse de sensibilité d'une méthode d'identification de l'impédance large bande en écoulement, 13ème Congrès Français d'Acoustique, Le Mans.

Cn5 Ollivier S., Desjouy C., **Dragna D.**, Castelain T., Karzova M.M. & Blanc-Benon P. (2016), Interaction non-linéaire d'ondes de choc acoustiques au voisinage d'une frontière rigide, 13ème Congrès Français d'Acoustique, Le Mans.

Cn4 **Dragna D.** & Blanc-Benon P. (2016), Propagation acoustique au-dessus d'un sol d'impédance spatialement variable, 13ème Congrès Français d'Acoustique, Le Mans.

Cn3 Troian R., **Dragna D.**, Bailly C. & Galland M.-A. (2015), A broadband method for liner impedance eduction in the presence of a mean flow, Congrès Français de Mécanique 2015, Lyon.

Cn2 **Dragna D.** & Blanc-Benon P. (2014), Méthodes pseudospectrales pour la propagation acoustique en milieu extérieur, 12ème Congrès Français d'Acoustique, Poitiers.

Cn1 **Dragna D.**, Blanc-Benon P. & Poisson F. (2010), Observation d'ondes de surface dans des simulations temporelles de propagation à longue distance, 10ème Congrès Français d'Acoustique, Lyon.

4.6 Exposés présentés à des colloques et réunions de spécialistes

W20 Lechat T., Karzova M.M., Yuldashev P.V., Ollivier S., Emmanuelli A., **Dragna D.** & Blanc-Benon P. (2022), Propagation of spherical weak blast waves over rough surfaces, Spring school, Waves & geosciences : Infrasound and beyond, March 28 - April 1, Ecully.

W19 **Dragna D.** & Bailly C. (2021), Finite difference methods - Fourier analysis and optimized schemes, EAA / UKAN Computational Acoustics Summer School, online.

W18 Lechat T., Emmanuelli A., **Dragna D.**, Ollivier S. & Blanc-Benon P. (2020), Numerical investigation of acoustical shock wave propagation above non-flat surfaces, 6th Workshop on Battlefield Acoustics, 21-22 octobre, Saint-Louis.

W17 Emmanuelli A., **Dragna D.**, Ollivier S. & Blanc-Benon P. (2020), Réflexion du bang sonique sur un sol réaliste, 5ème Journée scientifique LETMA, 27 août, online.

W16 Lechat T., Ollivier S. & **Dragna D.** (2020), Propagation d'ondes de choc acoustiques au-dessus d'une surface rugueuse, 5ème Journée scientifique LETMA, 27 août, online.

W15 Deng Y., Alomar A., **Dragna D.** & Galland M.-A. (2019), Analysis of the hydrodynamic instability generated in time-domain simulations of sound propagation along a lined flow duct, Winter school, MAT& FLOW, December 4-6, Le Mans.

W14 Aubry L., **Dragna D.**, Gainville O., Marchiano R., Millet C. & Robert L. (2019), Plateforme numérique de modélisation de la propagation des infrasons dans l'atmosphère, 4ème Journée scientifique LETMA, 14 mars, Ecully.

W13 Lechat T., Ollivier S., **Dragna D.** & Karzova M.M., (2019), Réflexion d'ondes de choc acoustiques sur une surface rugueuse, 4ème Journée scientifique LETMA, 14 mars, Ecully.

W12 **Dragna D.** (2018), Numerical methods : time-domain approaches, CeLyA Summer School on Atmospheric sound propagation, 13-15 June, Ecully.

W11 Lechat T., **Dragna D.** & Ollivier S. (2018), Simulation numérique du champ acoustique généré par une source à arc électriques et application à la réflexion d'ondes de choc, 3ème Journée scientifique LETMA, 15 Mars, Bruyères-le-Chatel.

W10 Ollivier S., **Dragna D.** & Blanc-Benon P. (2016), Weak shock wave reflection on smooth and rough surfaces, 5th Workshop on Battlefield Acoustics, 11-12 octobre, Saint-Louis.

W9 **Dragna D.** & Ollivier S. (2016), Étude expérimentale et numérique de la réflexion d'ondes de choc, 2ème Journée scientifique LETMA, 30 mars, Ecully.

W8 **Dragna D.** & Blanc-Benon P. (2013), Application de méthodes pseudospectrales à la propagation acoustique en milieu extérieur, Journées GdR VISIBLE, 18 décembre, Marseille.

W7 Blanc-Benon P. & **Dragna D.** (2013), Propagation acoustique en milieu extérieur : méthodes temporelles, École d'automne "Ville & Acoustique", Journées GdR VISIBLE, 22 octobre, Nantes.

W6 **Dragna D.** & Blanc-Benon P. (2013), Long range sound propagation in an inhomogeneous atmosphere : a time-domain approach for moving sources, 17th CEAS /3rd X-Noise EV workshop, 24-25 septembre, Séville, Espagne.

W5 **Dragna D.** & Blanc-Benon P. (2013), Time-domain simulations of long-range sound propagation : topography and ground effects, Meeting on propagation challenges in battlefield acoustics, 3-4 avril, ISL, Saint-Louis.

W4 Jacob M.C., **Dragna D.**, Cahuzac A., Boudet J. & Blanc-Benon P. (2012), Towards hybrid CAA with ground effects, Computational Experiment in AeroAcoustics 2012, 19-22 septembre, Svetlogorsk, Russie.

W3 **Dragna D.**, Bellaj S., Gauvreau B., Blanc-Benon P. & Poisson F. (2011), Influence of railway track topography on acoustic propagation of railway noise : experimental setup and comparison with numerical calculations, Journées GdR VISIBLE, 11 mai, Bron.

W2 **Dragna D.**, Blanc-Benon P. & Poisson F. (2010), Time-domain impedance boundary conditions suitable for outdoor sound propagation modeling, 1st workshop Moscow State University - École Centrale de Lyon, 13-14 décembre, Écully.

W1 **Dragna D.**, Blanc-Benon P. & Poisson F. (2009), Modélisation de la propagation acoustique en milieu extérieur complexe pour des sources en mouvement : application au cas ferroviaire, Journées GDR 2493 - Bruit des transports, 14 décembre, Nantes.

Deuxième partie

Synthèse des activités de recherche

CHAPITRE 5

Contexte général

Je décris dans cette partie les activités de recherche menées depuis ma prise de fonction comme enseignant-chercheur en septembre 2012. Avant de détailler les travaux réalisés dans les chapitres suivants, je présente dans ce chapitre le contexte général de l'étude.

5.1 Thème de recherche

5.1.1 Contexte

Mes activités de recherche porte sur la propagation du son dans un milieu inhomogène et en mouvement. Le milieu de propagation peut être un milieu semi-ouvert, comme cela est le cas pour l'atmosphère, ou un guide d'onde, comme cela est le cas pour un conduit. Un schéma global représentant le problème est présenté sur la Fig. 5.1.

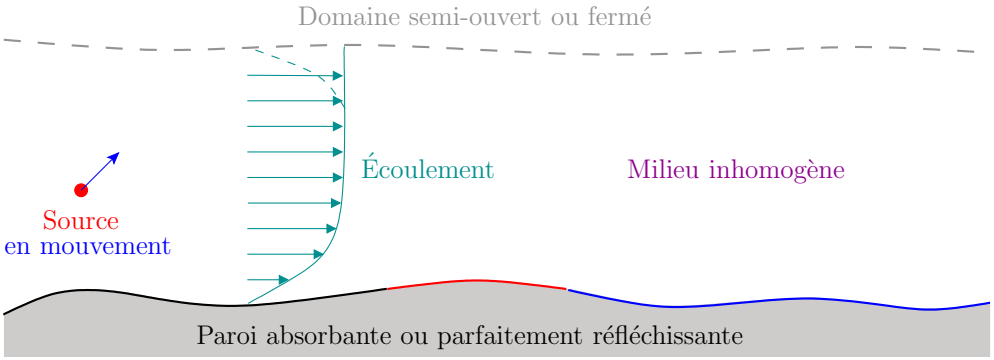

FIGURE 5.1 – Schéma du problème global considéré.

La résolution du problème passe pas une description du milieu de propagation, des frontières et des sources des ondes acoustiques. Chacun de ces trois aspects apporte une complexité importante au problème. Tout d'abord, la source peut être en mouvement avec une trajectoire quelconque. Elle peut être large bande et générer des ondes de fort niveau si bien que la propagation ne peut plus être considérée comme linéaire. Le milieu de propagation est généralement inhomogène, c'est-à-dire que ses propriétés (température, masse volumique, pression) peuvent varier spatialement, voire temporellement. Il peut aussi être en mouvement, avec un écoulement turbulent. Enfin, les frontières peuvent avoir une géométrie complexe et peuvent être absorbantes. Si on détaille ce dernier point, les phénomènes d'absorption dépendent généralement de la fréquence. De plus, la réaction de la

frontière peut être locale, c'est-à-dire que la réponse en un point de la frontière ne dépend que de l'onde incidente en ce point, ou étendue, avec la réponse en un point de la frontière qui dépend du champ incident global sur la surface. Enfin, la réponse de la frontière est généralement linéaire mais peut être dans certains cas non-linéaire.

Afin de résoudre ce problème, il est nécessaire d'utiliser une résolution numérique. Différentes approches ont été proposées dans la littérature :

- Pour la propagation atmosphérique, les méthodes géométriques restent utilisées [1], car elles permettent de prendre en compte la plupart des phénomènes physiques tout en gardant un coût de calcul extrêmement faible. Elles se basent néanmoins sur une approximation haute-fréquence, négligent la diffraction et ne sont pas valables dans les zones critiques (zones d'ombres ou à proximité des caustiques). Elles sont par contre très utiles pour identifier ces zones critiques.

- Les approches paraxiales restent encore l'état de l'art. Bien que des formulations tridimensionelles aient été proposées pour la propagation atmosphérique (par exemple Ref. [2]), la résolution de l'équation paraxiale grand angle bidimensionnelle avec une approximation axisymétrique est largement utilisée. Les équations paraxiales sont obtenues en extrayant d'une équation d'onde l'équation gouvernant la propagation selon une direction privilégiée. Elles permettent de réduire fortement le coût de résolution par rapport à l'équation d'onde. Elles ne prennent pas en compte la diffraction et ne sont valables que dans un cône autour de la direction privilégiée.

- Pour la propagation en conduit, les approches multimodales restent les plus rapides mais sont généralement limitées à des géométries simples et des écoulements uniformes ou stratifiés (voir Ref. [3] pour une approche multimodale avec un conduit lentement variable et un écoulement potentiel). Les méthodes fréquentielles qui résolvent l'équation d'onde convectée ou les équations d'Euler linéarisées (par exemple Refs. [4, 5]) sont les plus utilisées.

5.1.2 Approche globale et enjeux

Mes travaux de recherche se focalisent sur la propagation acoustique en milieu inhomogène dans le domaine temporel. Pour cela, je m'appuie sur la résolution dans le domaine temporel des équations de la mécanique des fluides (linéarisées ou complètes). Cette approche a de nombreux avantages par rapport aux méthodes existantes. Tout d'abord, elle est plus générale que les approches géométriques, paraxiales ou modales. Elle permet ainsi de fournir des solutions numériques de référence, qui peuvent servir de cas de validation de modèles numériques ou analytiques simplifiés. De plus, les approches temporelles permettent avec une seule simulation de considérer la propagation d'un bruit large bande. Elles permettent également d'étudier le rayonnement de source en mouvement avec une trajectoire quelconque. Enfin, c'est l'approche naturelle pour prendre en compte les effets non-linéaires de propagation.

Travaux antérieurs de l'équipe

Ma recherche s'appuie sur le savoir-faire développé au Centre Acoustique du LMFA. Le groupe est reconnu pour ses travaux en propagation longue distance dans l'atmosphère, en propagation non-linéaire, en méthodes numériques pour les simulations temporelles et en propagation en conduit. Ainsi, l'équipe de P. Blanc-Benon, S. Ollivier et D. Juvé a étudié la propagation longue distance dans l'atmosphère et les effets de la turbulence, aussi bien expérimentalement dans la soufflerie anéchoique du LMFA [6] que numériquement avec notamment le développement d'approches paraxiales [7]. L'équipe de C. Bailly, O. Marsden et C. Bogey a développé des schémas différences finies optimisés d'ordre élevé pour l'aéroacoustique numérique [8]. Le travail commun de ces deux équipes autour des simulations temporelles de propagation dans l'atmosphère a commencé au LMFA avec la thèse

de B. Cotté [9] et a été poursuivi pendant ma thèse. En parallèle, des travaux numériques sur la propagation infrasonore ont été menés par l'équipe de C. Bailly, O. Marsden et C. Bogey avec notamment la thèse de R. Sabatini [10]. Enfin, M.-A. Galland a une expertise reconnue sur le contrôle et l'application pour la réduction du bruit en paroi de conduit et sur les matériaux acoustiques (par exemple [11]).

Enjeux

L'utilisation de méthodes temporelles pose plusieurs enjeux :

- Tout d'abord, les simulations numériques ont un coût en mémoire et en temps de calcul importants. Ainsi, pour un domaine tridimensionnel, la demande mémoire évolue typiquement comme λ^3 où λ est la plus petite longueur d'onde d'intérêt. Le coût de calcul pour un temps de propagation équivalent évolue comme λ^4. Par exemple, si on considère une fréquence de 340 Hz correspondant à $\lambda = 1$ m pour une vitesse du son de 340 m s^{-1} et un domaine de calcul d'1 km de long, 100 m de large et 100 m de haut, le nombre de points de maillage est de l'ordre de 10 milliards en considérant une discrétisation de 10 points par longueurs d'onde. Augmenter la fréquence d'intérêt d'un facteur 2 (680 Hz au lieu de 340 Hz) conduirait à une augmentation du nombre de points d'un facteur 8 et du temps de calcul d'un facteur 16. Cet exemple montre l'importance d'utiliser d'un point de vue numérique des schémas précis pour réduire le temps de calcul et d'un point de vue informatique du parallélisme afin de réduire le temps d'exécution.

- Ensuite, la prise en compte des phénomènes d'absorption qui dépendent de la fréquence n'est pas directe dans les simulations temporelles. En effet, la translation des équations de propagation et de conditions limites dont les coefficients dépendent de la fréquence induit la présence de produits de convolution. Une discrétisation naïve du produit de convolution nécessite de stocker l'évolution temporelle des variables depuis la condition initiale et est donc extrêmement coûteuse pour un calcul à longue distance. Il est donc nécessaire de développer des méthodes numériques spécifiques pour éviter un surcoût important.

- Pour la propagation en conduit, certains modes peuvent être instables en présence d'un écoulement et d'un traitement absorbant. Les instabilités (convectives) ne sont présentes que pour quelques fréquences d'excitation. Une résolution fréquentielle évite généralement ces instabilités (à moins de choisir intentionnellement la fréquence de la source pour exciter l'instabilité). Pour une approche temporelle naturellement large bande, ces instabilités vont être générées invariablement et vont perturber l'extraction de l'information acoustique. Les enjeux sont alors de s'assurer que les instabilités observées dans les solutions numériques sont bien physiques et non pas numériques et d'extraire l'information acoustique de la solution numérique.

5.1.3 Démarche et problématiques traitées

Mon travail de recherche est axé sur deux thèmes principaux, à savoir la propagation atmosphérique et la propagation en conduit. Les différents thèmes ont été abordées à travers une approche temporelle, et plus particulièrement via des simulations numériques résolvant les équations de la mécanique des fluides (linéarisées ou complètes). Le thème autour de la propagation atmosphérique est en lien avec mon travail de thèse et de post-doctorat. Dans la suite du manuscrit, je ne présente que les travaux réalisés après ma prise de fonction en tant qu'enseignant-chercheur, soit après 2012.

Les différents points abordées pendant ma recherche sont décrits ci-dessous. Un travail important a tout d'abord été effectué sur les méthodes numériques, à la fois sur l'étude de schémas peu dissipatifs et dispersifs pour la propagation longue distance et sur le développement de méthodes numériques efficaces d'ordre élevé pour traiter les produits de convolution. A l'aide de simulations numériques dans le domaine temporel, des études spécifiques ont été ensuite réalisées en acoustique

environnementale, tout d'abord pour des applications en bruit des transports autour des sources en mouvement et des modèles d'impédance de sol. Sur la même thématique, des études ont été réalisées avec pour application la bioacoustique et le bruit des éoliennes ; des approches plus classiques, de type paraxiales dans le domaine fréquentiel, ont été utilisées pour ces applications. Les travaux en acoustique environnementale se sont aussi portés sur la propagation d'ondes de choc, plus précisément sur la réflexion d'ondes de souffle sur des paroi lisses et rugueuses et sur la propagation du bang sonique au-dessus d'un sol irrégulier et dans un environnement urbain. Ces travaux liés à l'acoustique non-linéaire seront présentés dans le manuscrit séparément des travaux mentionnés précédemment. Une seconde thématique a été ouverte sur la propagation en conduit. Différentes études ont été réalisées afin de modéliser dans les simulations temporelles des traitements absorbants en paroi à réaction locale ou étendue et avec un comportement non-linéaire. La présence d'instabilités dans les simulations de propagation en conduit traité avec écoulement a aussi été examinée.

5.1.4 Organisation du manuscrit

Cette partie du manuscrit est organisée en quatre chapitres. Dans le chapitre 6, on présente les travaux réalisées sur les méthodes numériques pour la propagation acoustique dans le domaine temporel. On décrit ensuite dans le chapitre 7 les études réalisées en acoustique environnementale autour des modèles d'impédance de surface des sols et sur les sources en mouvement. Les applications pour la bioacoustique et pour le bruit des éoliennes sont aussi présentées dans ce chapitre. Le chapitre 8 détaille les travaux en propagation en conduit, sur la modélisation de traitements absorbants à réaction locale, étendue ou avec une réponse non-linéaire dans les simulations temporelles et sur les instabilités en présence d'un écoulement moyen et d'un traitement absorbant. Le chapitre 9 traite des travaux autour de l'acoustique non-linéaire et de la propagation d'ondes de choc, sur la réflexion d'ondes de souffle sur des parois lisses et rugueuses et sur la propagation du bang sonique. Enfin, des perspectives globales sur ma recherche sont données dans le chapitre 10.

CHAPITRE 6

Méthodes numériques

Les approches temporelles sont bien adaptées pour la propagation de signaux large bande en milieu inhomogène et en mouvement. C'est en particulier le cas pour les signaux impulsionnels. Elles sont aussi pertinentes pour étudier le rayonnement de sources en mouvement. Enfin, elles sont nécessaires lorsque des effets nonlinéaires liés à des forts niveaux de pression doivent être pris en compte. Une partie importante de ma recherche s'est portée sur ces approches temporelles pour la propagation acoustique, et en particulier sur le développement ou l'application de méthodes numériques pour ces approches temporelles.

Dans ce chapitre, on détaille les travaux réalisés sur les méthodes pseudospectrales et sur les méthodes d'ordre élevé pour les produits de convolution.

6.1 Schémas numériques pour la propagation grande distance

6.1.1 Stratégie

Dans un repère cartésien tridimensionnel (x, y, z), les équations d'Euler (linéarisées ou complètes) peuvent s'écrire sous forme conservative :

$$\frac{\partial \mathbf{U}}{\partial t} + \frac{\partial \mathbf{E}}{\partial x} + \frac{\partial \mathbf{F}}{\partial y} + \frac{\partial \mathbf{G}}{\partial z} + \mathbf{H} = \mathbf{S} \tag{6.1}$$

où t est le temps, $\mathbf{U}$ est le vecteur des variables, $\mathbf{E}$, $\mathbf{F}$ et $\mathbf{G}$ sont les flux eulériens et $\mathbf{S}$ est un terme source. La résolution de l'Eq. (6.1) nécessite des schémas numériques pour calculer les dérivées spatiales et pour intégrer en temps.

Des erreurs numériques sont générées par la discrétisation des équations de propagation et l'erreur s'accumule lors de la propagation. On dissocie habituellement l'erreur de dispersion, liée à des erreurs sur la phase, qui induit une distortion du signal et l'erreur de dissipation, qui induit une diminution de l'amplitude du signal. Pour des problèmes de propagation longue distance, il est alors nécessaire d'avoir des schémas numériques pour résoudre les équations de propagation qui génèrent très peu de dispersion et de dissipation. La plupart des travaux présentés ici se sont basés sur les schémas différences finies optimisés d'ordre 4 développés par C. Bogey et C. Bailly. Plus précisément, on utilise le schéma centré sur 11 points proposé dans la Ref. [8] pour les points au centre du domaine et les schéma décentrés proposés dans la Ref. [12] pour les points aux bords du domaine. L'intégration temporelle est effectuée à l'aide de l'algorithme Runge-Kutta optimisé d'ordre 4 à stockage réduit proposé par Berland *et al.* [13]. Enfin, on utilise des filtres sélectifs [12, 14] pour enlever les composantes aux petites longueurs d'onde.

Lorsque l'amplitude des ondes acoustiques est importante, on ne peut plus considérer que le signal se propage à la célérité du son. La vitesse de propagation du signal est d'autant plus grande que son amplitude est importante. Cela amène à une déformation du signal lors de sa propagation et peut causer la formation de chocs. Numériquement, ces effets non-linéaires induisent la génération de composantes avec de petites longueurs d'ondes, qui sont mal résolues par les schémas numériques. Pour les problèmes de propagation non-linéaire, on utilise le schéma de capture de choc proposé par Bogey *et al.* [14] et modifié par Sabatini *et al.* [10]. L'idée consiste à identifier la partie du signal avec des petites longueurs d'onde et à appliquer un filtre passe-bas d'ordre faible seulement sur la partie du signal identifiée pour enlever les composantes aux petites longueur d'onde.

Différentes versions du code résolvant les équations d'Euler linéarisées ou d'Euler ont été développées suivant les applications. Les codes sont écrits en Fortran 90. Pour les applications en acoustique environnementale, les versions actuelles des codes 2D et 3D sont parallélisées en utilisant le protocole OpenMP. Les codes ont tourné sur le calculateur NEWTON de l'Ecole Centrale de Lyon ainsi que sur les calculateurs Ada et Jean-Zay de l'IDRIS. Pour les applications en propagation en conduit, les codes restent séquentiels.

6.1.2 Méthodes pseudospectrales

Dans le cadre d'une collaboration avec M. Hornikx de l'université d'Eindhoven aux Pays-Bas, nous avons étudié l'intérêt des approches pseudospectrales (PS) pour la propagation acoustique en milieu extérieur.

Les approches pseudospectrales sont une alternative aux méthodes différences finies pour évaluer les dérivées spatiales. Elles ont pour principe de chercher la variable à dériver comme une combinaison linéaire de fonctions d'une base bien choisie, typiquement des polynômes orthogonaux. La dérivée de la variable s'obtient alors à partir des dérivées des fonctions de la base. Les coefficients de la combinaison linéaire sont données par des intégrales. Leur calcul numérique est réalisé par des formules de quadrature, qui imposent la distribution des points de la grille. Hornikx *et al.* [15] ont proposé une méthode PS Fourier, basé sur des séries de Fourier. La méthode est très efficace, car la distribution des points de la grille est régulière et l'évaluation des coefficients de la série se fait à l'aide de transformées de Fourier rapide. La méthode génère des erreurs de dispersion et de dissipation négligeable jusqu'à une discrétisation de deux points par longueur d'onde. Elle impose néanmoins une périodicité dans la direction de la dérivée. Cela limite les conditions aux limites possibles et l'utilisation de la méthode PS Fourier pour la propagation en milieu extérieur.

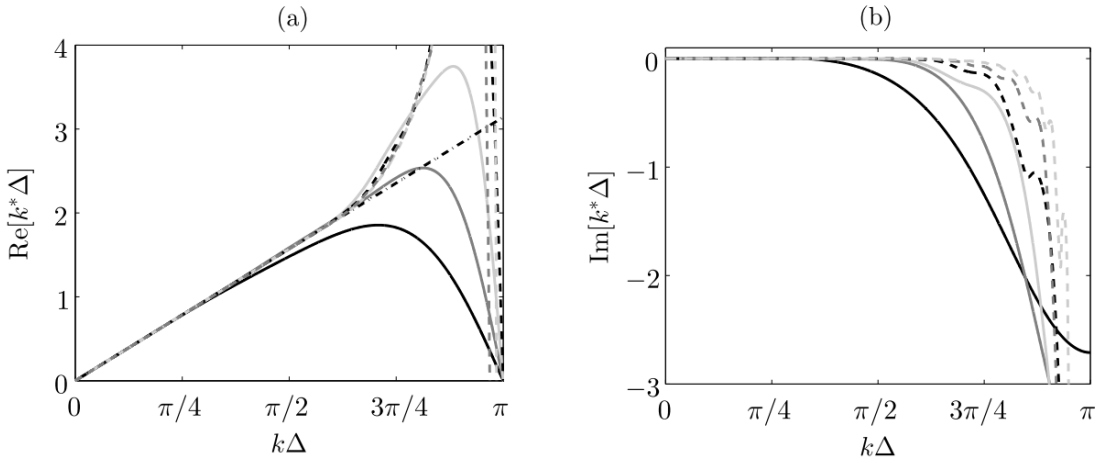

FIGURE 6.1 – Parties (a) réelle et (b) imaginaire du nombre d'onde effectif en fonction du nombre d'onde pour la méthode PS Chebyshev multidomaines avec différents nombres de points N : $N = 4$, $N = 8$, $N = 16$, $N = 32$, $N = 64$, $N = 128$ et relation de dispersion exacte. Extrait de Ref. [16].

Nous avons alors étudié l'utilisation de la méthode PS Chebyshev, qui se base sur des polynômes de Chebyshev. Celle-ci permet de passer outre la limitation sur la condition aux limites. La précision de la méthode est néanmoins réduite par rapport à la méthode PS Fourier, puisqu'elle permet une résolution jusqu'a π points par longueur d'onde. De plus, la distribution des points de la grille n'est plus uniforme ; notamment, le pas de maillage sur les bords des domaines décroît quadratiquement avec le nombre de points. En utilisant des méthodes d'intégration temporelle explicite, cela contraint grandement le pas de temps, à cause de la condition CFL, et engendre un coût de calcul supplémentaire important. Une technique employée est alors de décomposer le domaine en sous-domaines afin de relâcher la contrainte sur le pas spatial. Cette technique est appelée méthode PS Chebyshev multi-domaines. Nous avons étudié dans la Ref. [16] les propriétés de dispersion et de dissipation de cette méthode. En particulier, nous avons montré que celles-ci étaient fortement dépendantes du nombre de points dans les sous-domaines. On montre sur la figure 6.1 les parties réelles du nombre d'onde effectif k^* pour la méthode PS Chebyshev multi-domaines pour différents nombre de points en fonction du nombre d'onde k. La méthode est d'autant plus précise que le nombre d'onde effectif est proche du nombre d'onde k sur la plus grande plage de nombre d'onde. On note que lorsque le nombre de points dans les sous-domaines augmente la partie réelle de k^* se rapproche de k et la partie imaginaire tend à décroître. Des critères sur le nombre de points par longueur d'onde minimum à respecter pour avoir une bonne précision à grande distance ont été donnés. Par exemple, pour un nombre de points dans les sous-domaines choisi classiquement égal à 32, il faut environ 4 points par longueur d'onde. La résolution de π points par longueur d'onde n'est retrouvée que lorsque le nombre de points par sous-domaine dépasse la centaine. Un compromis est donc à trouver entre les erreurs de dispersion et de dissipation qui diminuent avec le nombre de points et la contrainte sur le pas de temps qui augmente avec le nombre de points.

Dans la Ref. [17], nous avons appliqué la méthode PS Fourier pour résoudre les équations d'Euler linéarisées en coordonnées curvilignes pour la propagation atmosphérique au-dessus de sols non-plans. Nous avons montré que la déformation locale du maillage induisait une réduction de la précision de la méthode, par rapport au cas plan, et avons proposé une loi simple pour estimer la précision attendue pour un maillage donné.

6.2 Méthode d'ordre élevé pour les produits de convolution

Les phénomènes d'absorption dépendent de la fréquence. Dans le domaine fréquentiel, les équations de propagation dans les milieux poreux ou les conditions aux limites d'impédance de surface font alors intervenir des paramètres qui varient avec la fréquence. Leur traduction dans le domaine temporel induit la présence de produit de convolution du type :

$$I(u(t),t) = \int_{-\infty}^{t} u(t')s(t-t')\mathrm{d}t', \tag{6.2}$$

où $s(t)$ est une fonction réelle et causale, dont la transformée de Fourier $\hat{s}(\omega)$ est connue a priori et $u(t)$ est une variable, typiquement la pression ou la vitesse acoustique.

Le calcul direct du produit de convolution est lourd car il demande notamment de stocker l'historique de la variable u. Afin de rendre le calcul du produit de convolution plus efficace, une approche consiste à approximer la fonction $\hat{s}(\omega)$ par une fraction rationnelle en $-\mathrm{i}\omega$ (convention $\mathrm{e}^{-\mathrm{i}\omega t}$) avec des pôles simples dont le numérateur et le dénominateur sont des polynômes de degré P :

$$\hat{s}(\omega) \approx \hat{s}_P(\omega) = \hat{s}_\infty + \frac{a_0 + a_1 + ... + a_{P-1}(-\mathrm{i}\omega)^{P-1}}{1 + b_1 + ... + b_P(-\mathrm{i}\omega)^P}, \tag{6.3}$$

où $\hat{s}_\infty$ est la valeur limite de $\hat{s}(\omega)$ lorsque ω tend vers l'infini. Comme $s(t)$ est une fonction à valeurs réelles, les coefficients a_i et b_i sont réels ; les pôles de $\hat{s}_P(\omega)$ sont alors soit réels, notés par la suite λ_k, soit forment une paire de pôles complexes conjugués, notés par la suite $\alpha_k \pm \mathrm{i}\beta_k$. Pour des raisons de causalité, les pôles sont situés dans le demi-plan complexe inférieur ; cela implique $\lambda_k \geq 0$ et

$\alpha_k \geq 0$. On peut alors réécrire $\hat{s}_P(\omega)$ sous la forme :

$$\hat{s}_P(\omega) = \hat{s}_\infty + \sum_{k=1}^{N} \frac{A_k}{\lambda_k - \mathrm{i}\omega} + \sum_{k=1}^{M} \frac{1}{2}\left[\frac{B_k + \mathrm{i}C_k}{\alpha_k + \mathrm{i}\beta_k - \mathrm{i}\omega} + \frac{B_k - \mathrm{i}C_k}{\alpha_k - \mathrm{i}\beta_k - \mathrm{i}\omega}\right], \tag{6.4}$$

avec $P = N + 2M$. Dans le domaine temporel, l'approximation devient :

$$s(t) \approx \hat{s}_\infty \delta(t) + \sum_{k=1}^{N} A_k \mathrm{e}^{-\lambda_k t}\mathrm{H}(t) + \sum_{k=1}^{M} \mathrm{e}^{-\alpha_k t}[B_k \cos(\beta_k t) + C_k \sin(\beta_k t)]\mathrm{H}(t), \tag{6.5}$$

où $\delta(t)$ et $H(t)$ sont respectivement la fonction de Dirac et d'Heaviside. Une interprétation physique peut être donnée à chaque terme. Le premier terme correspond à la réponse instantanée à l'excitation, car $\hat{s}_\infty$ représente la limite haute-fréquence de $\hat{s}(\omega)$. Le second terme correspond à une fonction de relaxation, qui décroît exponentiellement avec le temps ; la constante de temps est égale à $1/\lambda_k$. Enfin, le troisième terme correspond à une réponse amortie ; la période des oscillations est donnée par la partie imaginaire du pôle β_k et la décroissance avec le temps par la partie réelle α_k. L'approximation de $\hat{s}(\omega)$ par une fraction rationnelle peut être obtenue avec différentes méthodes, dont la méthode Vector Fitting [18] qui permet d'avoir une approximation précise avec un nombre de pôles faibles.

En introduisant l'approximation de $s(t)$ (voir Eq. (6.5)) dans Eq. (6.2), on obtient :

$$I(u(t), t) = \hat{s}_\infty u(t) + \sum_{k=1}^{N} A_k \phi_k(t) + \sum_{k=1}^{M} [B_k \psi_k^{(1)}(t) + C_k \psi_k^{(2)}(t)], \tag{6.6}$$

où les fonctions auxiliaires $\phi_k(t)$, $\psi_k^{(1)}(t)$ et $\psi_k^{(2)}(t)$ sont données par les produits de convolution :

$$\phi_k(t) = \int_{-\infty}^{t} u(t')\mathrm{e}^{-\lambda_k(t-t')}\mathrm{d}t', \tag{6.7}$$

$$\psi_k^{(1)}(t) = \int_{-\infty}^{t} u(t')\mathrm{e}^{-\alpha_k(t-t')}\cos[\beta_k(t-t')]\mathrm{d}t', \tag{6.8}$$

$$\psi_k^{(2)}(t) = \int_{-\infty}^{t} u(t')\mathrm{e}^{-\alpha_k(t-t')}\sin[\beta_k(t-t')]\mathrm{d}t'. \tag{6.9}$$

Différentes méthodes permettent de déterminer les fonctions auxiliaires. Les méthodes employées dans la littérature en acoustique [19] et au laboratoire [9] se basent sur des méthodes dites récursives, permettant d'exprimer l'évolution des fonctions auxiliaires entre deux pas de temps consécutifs par des relations récursives. Si on limite la présentation à ϕ_k, on obtient en discrétisant Eq. (6.7) entre deux pas de temps $n\Delta t$ et $(n+1)\Delta t$, avec n un entier et Δt le pas de temps :

$$\phi_k[(n+1)\Delta t] = \mathrm{e}^{-\lambda_k \Delta t}\phi_k[n\Delta t] + \mathrm{e}^{-\lambda_k \Delta t}\int_0^{\Delta t} \mathrm{e}^{\lambda_k t'} u[t + n\Delta t]\mathrm{d}t'. \tag{6.10}$$

En supposant ensuite que $u(t)$ est constant dans l'intervalle $[n\Delta t, (n+1)\Delta t]$ et est égal à $u[(n+1)\Delta t]$ (méthode PCRC), on obtient la relation :

$$\phi_k^{\mathrm{PCRC}}[(n+1)\Delta t] = \mathrm{e}^{-\lambda_k \Delta t}\phi_k^{\mathrm{PCRC}}[n\Delta t] + \frac{1 - \mathrm{e}^{-\lambda_k \Delta t}}{\lambda_k} u[(n+1)\Delta t]. \tag{6.11}$$

D'autres méthodes récursives existent. Ainsi, la méthode PLRC considère une évolution linéaire de $u(t)$ entre deux pas de temps. Enfin, la méthode TRC, comme la méthode PCRC, suppose que $u(t)$ est constant sur un pas de temps et égal à $(u[(n+1)\Delta t] + u[n\Delta t])/2$.

Nous avons introduit une autre méthode dans Ref. [20], qui provient de l'électromagnétisme [21]. En dérivant Eqs. (6.7)-(6.9) par rapport au temps, on montre que les fonctions auxiliaires satisfont

les équations différentielles ordinaires du premier ordre :

$$\frac{\mathrm{d}\phi_k}{\mathrm{d}t} + \lambda_k \phi_k(t) = u(t), \tag{6.12}$$

$$\frac{\mathrm{d}\psi_k^{(1)}}{\mathrm{d}t} + \alpha_k \psi_k^{(1)}(t) + \beta_k \psi_k^{(2)}(t) = u(t), \tag{6.13}$$

$$\frac{\mathrm{d}\psi_k^{(2)}}{\mathrm{d}t} + \alpha_k \psi_k^{(2)}(t) - \beta_k \psi_k^{(1)}(t) = 0. \tag{6.14}$$

Finalement, le produit de convolution s'obtient avec Eq. (6.6) et en intégrant en temps les équations différentielles Eqs. (6.12)-(6.14) en même temps que les équations de propagation. Contrairement aux méthodes récursives, aucune approximation sur u n'a été réalisée pour obtenir ces équations. Cette méthode est appelée "auxiliary differential equation" (ADE) car des équations différentielles additionnelles sont résolues pour calculer le produit de convolution.

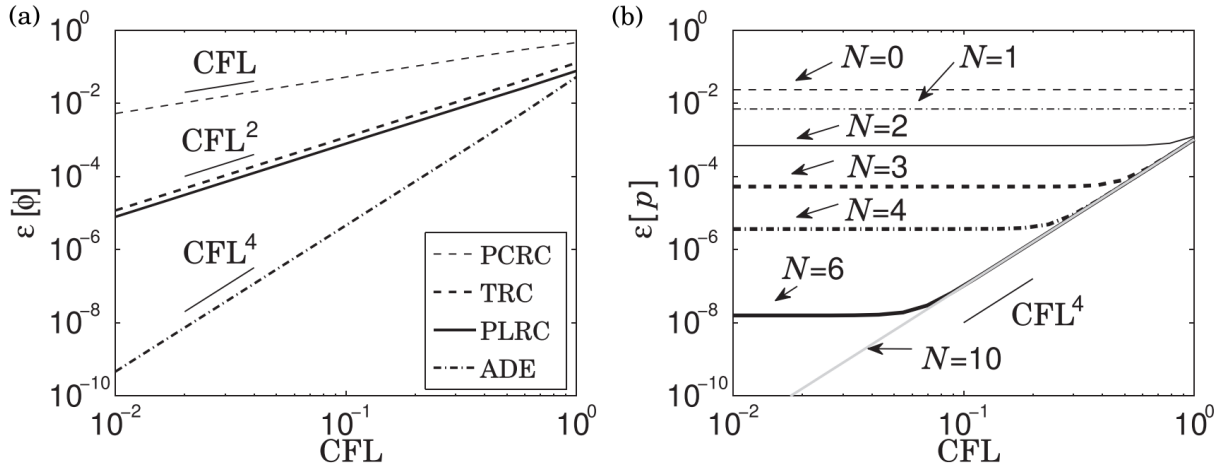

FIGURE 6.2 – Evolution de l'erreur pour deux cas-tests de propagation en milieu dissipatif : (a) pour différentes méthodes pour le calcul du produit de convolution et (b) avec la méthode ADE pour différents nombre de pôles. Extrait de Ref. [20].

Dans la Ref. [20], nous avons évalué les différentes méthodes sur différents cas de propagation dans les matériaux poreux. Nous avons montré que les méthodes récursives sont d'ordre un ou deux en temps et réduisent l'ordre de précision pour des schémas d'intégration temporelle d'ordre élevé. La méthode ADE permet, par contre, de préserver l'ordre du schéma d'intégration temporelle utilisé et est donc à préférer pour des codes d'ordre élevé. Ainsi, la figure 6.2 (a) montre un test de convergence en faisant varier le pas de temps Δt ; pour la méthode ADE, on retrouve une décroissance de l'erreur comme Δt^4, ce qui est cohérent avec l'utilisation d'un algorithme Runge-Kutta d'ordre 4 pour l'intégration temporelle, alors que l'erreur pour les méthodes récursives (PCRC, PLRC et TRC) décroit comme Δt ou Δt^2. De plus, nous utilisons des schémas Runge-Kutta à stockage réduit ; pour de tels schémas, il n'y a pas de surcoût en terme mémoire. Nous avons aussi étudié la variation de l'erreur liée à l'approximation de $\hat{s}(\omega)$ par une fraction rationnelle : l'erreur, représentée sur la figure 6.2 (b), est indépendante du pas de temps pour un nombre de pôles faible, car elle est principalement due à une mauvaise approximation de $\hat{s}(\omega)$. Lorsque le nombre de pôles devient suffisant, l'erreur décroit d'abord comme Δt^4 avant d'atteindre un plateau pour les petits Δt. Ce plateau prend des valeurs d'autant plus faibles que le nombre de pôles est important. La méthode a ensuite été appliquée à un cas de propagation extérieure avec prise en compte d'un sol à réaction étendue. Pour des simulations tridimensionnelles avec 150 millions de points, le coût supplémentaire en mémoire n'est que de 4 %.

Cette méthode a aussi été utilisée dans des travaux en propagation en conduit, détaillés dans le chapitre 8. Elle a aussi été employée dans la Ref. [22] pour prendre en compte des modèles de

frottements pariétaux dans des simulations numériques de propagation unidimensionnelle d'ondes de pression en conduite, comme par exemple les coups de bélier.

6.3 Conclusions et perspectives

Plusieurs aspects numériques ont été abordés dans mon travail de recherche. Tout d'abord, nous avons étudié l'utilisation des méthodes pseudospectrales pour la propagation à longue distance, en particulier, la méthode PS Chebyshev multi-domaines. L'étude des propriétés de dispersion et dissipation a montré que le nombre de points par longueur d'onde nécessaire pour une bonne précision était comparable à celui pour les schémas différences finis optimisés d'ordre élevé développés au laboratoire. Du fait du surcoût lié au maillage non-uniforme, nous avons préféré continuer d'employer ces schéma différences finies dans la suite des travaux.

Nous avons ensuite introduit pour l'acoustique la méthode ADE pour traiter les produits de convolution efficacement sans réduire l'ordre en temps des codes de résolution. Cette méthode est particulièrement adapté aux codes d'ordre élevé. La méthode ADE a été largement utilisé dans mes travaux de recherche pour modéliser les traitements absorbants à réaction locale ou étendue (voir ch. 8). Une extension pour prendre en compte un comportement non-linéaire des propriétés des matériaux a été récemment développée et est décrite dans le chapitre 8.

CHAPITRE 7

Acoustique environnementale

Une partie importante de mes travaux est liée à l'acoustique environnementale. Je présente dans ce chapitre les recherches effectuées sur ce thème en acoustique linéaire.

7.1 Impédance des sols

Les travaux réalisés sur la prise en compte d'interface dissipatives dans les codes de résolution dans le domaine temporel ont aussi levé des questions sur les modèles d'impédance utilisés classiquement pour représenter les sols et sur la modélisation d'un sol avec une impédance uniforme. On présente dans cette section une première étude qui examine si les modèles d'impédance de la littérature présentent une réponse temporelle physique et une seconde étude sur la propagation acoustique au-dessus de surfaces planes avec une impédance de surface aléatoire.

7.1.1 Modèles d'impédance physiquement admissibles

On utilise classiquement des modèles d'impédance de matériaux poreux pour représenter l'impédance des sols. Ceux-ci, établis dans le domaine fréquentiel, peuvent provenir d'une modélisation physique ou de lois empiriques. Dans le second cas, la validité physique de ces modèles est en question, notamment lorsqu'il faut traduire l'impédance dans le domaine temporel. Trois conditions pour avoir un modèle d'impédance physiquement admissible ont ainsi été proposées par Rienstra [23]. Ainsi, un modèle d'impédance doit être :

- passif : l'interface doit absorber l'énergie incidente quelque soit la fréquence d'excitation,
- réel : pour une onde incidente dont la pression et la vitesse ont des valeurs réelles, la réponse de l'interface doit aussi prendre des valeurs réelles,
- causal : la réponse de l'interface ne peut pas précéder l'onde incidente.

La traduction mathématique de ces conditions est précisée dans Ref. [23] et n'est pas détaillée ici.

Dans la Ref. [24], nous avons étudié les conditions proposées par Rienstra pour différents modèles d'impédance de sol de la littérature. Pour la causalité, nous avons opté pour une condition suffisante plutôt que la condition proposée par Rienstra qui n'est que nécessaire. Nous avons montré que les modèles d'impédance basés sur des modèles physiques satisfont ces conditions. Le modèle semi-empirique de Delany-Bazley ne satisfait pas ces conditions. De plus, le modèle de Miki modélisant le sol par une couche de matériau sur fond rigide n'est lui aussi pas passif à basse fréquences

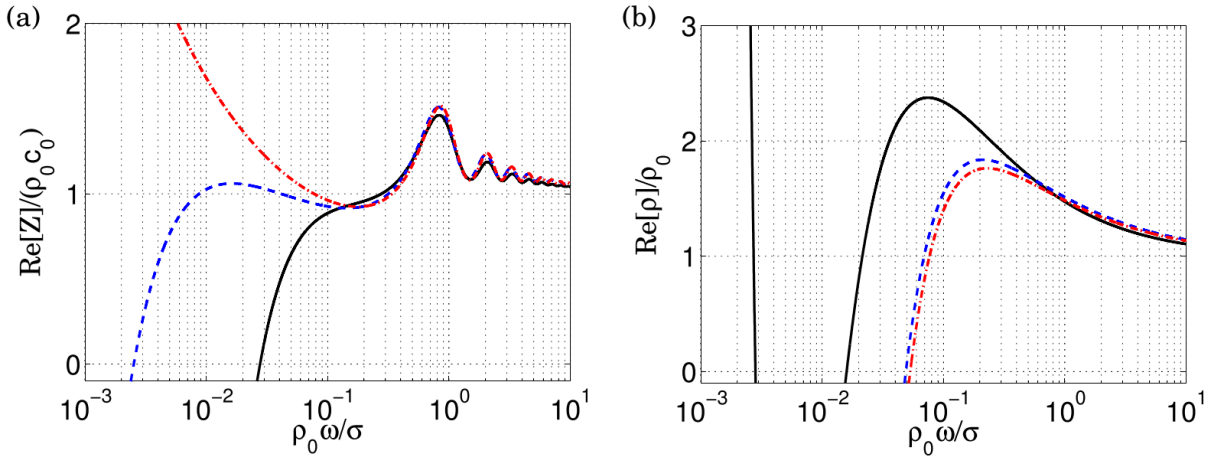

FIGURE 7.1 – (a) Partie réelle de l'impédance de surface d'une couhce de materiau poreux sur support rigide et (b) partie réelle de la masse volumique effective d'un matériau poreux pour les modèles : (noir) Delany-Bazley, (bleu) Miki et (rouge) Miki modifié. Extrait de Ref. [26].

(voir Fig. 7.1 (a)). Nous avons enfin proposé un modèle de Miki modifié pour avoir un modèle physiquement admissible.

En même temps, Kirby [25] s'est aussi intéressé à la validité physique de ces modèles semi-empiriques. Il a retrouvé que le modèle de Miki n'était pas passif à basse fréquence. Il a aussi montré que la masse volumique effective du matériau poreux prédite par le modèle de Miki avait une partie réelle négative à très basse fréquence, ce qui n'est pas physique. Une collaboration a alors été initiée par K. Attenborough afin d'étendre les résultats de la Ref. [24]. Nous avons ajouté dans la Ref. [26] une quatrième condition pour avoir un modèle d'impédance physiquement admissible, qui stipule que la partie réelle de la masse volumique doit être positive quelque soit la fréquence. Les modèles physiques satisfont cette condition ; par contre, les modèles semi-empiriques, y compris le modèle de Miki modifié, ne vérifient pas celle-ci (voir Fig. 7.1 (b)). Par ailleurs, l'impédance de surface des sols est souvent déduite indirectement de mesures de propagation. Nous avons montré que les modèles physiques permettent un accord comparable voire meilleur aux mesures par rapport aux modèles semi-empiriques. Cela justifie le choix de garder ces modèles d'impédance physiques pour la propagation extérieure et d'éviter l'utilisation de modèles semi-empiriques.

7.1.2 Variabilité spatiale de l'impédance des sols

Les propriétés acoustiques des sols ne sont connues que très partiellement. Afin de caractériser celles-ci, des mesures indirectes de l'impédance de surface ont été proposées dans la littérature (voir par exemple [27]). Cependant, comme la mesure reste lourde à mettre en place, celle-ci n'est effectuée que très ponctuellement. On suppose alors habituellement dans les simulations que l'impédance de surface est homogène pour un type de sol donné. Des mesures reportées récemment dans [27] ont néanmoins montré que les variations spatiales de l'impédance pouvaient être importantes pour un même type de sol ; les paramètres des modèles d'impédance peuvent ainsi présenter des écart-types normalisés de 30 %. L'influence de la variation spatiale de l'impédance des sols est très peu quantifiée dans la littérature. On peut citer l'étude d'Ostashev *et al.* [28] dans laquelle le cas d'un sol homogène avec des propriétés aléatoires a été étudié. Les auteurs ont montré que la pression et l'intensité moyennes étaient comparables aux valeurs obtenues en considérant les propriétés moyennes des sols.

Dans [29], nous avons généralisé les résultats de [28] en caractérisant l'influence des variations spatiales de l'impédance des sols sur le champ acoustique. Comme ces variations ne sont pas connues, nous les avons représenté par des variations aléatoires avec une fonction de corrélation donnée. Tout d'abord, une étude analytique a été menée. Nous avons en particulier déduit une admittance

effective, permettant de représenter l'effet moyen des variations spatiales sur le champ de pression. Une étude numérique a été ensuite menée en faisant des simulations numériques pour 200 réalisations des variations spatiales de l'admittance. Le champ de pression moyen déterminé à partir des 200 réalisations est en bon accord avec la solution analytique. De plus, nous avons montré que l'effet des variations spatiales était limité pour un sol semi-infini mais bien plus notable pour un sol d'épaisseur fini. Enfin, nous avons mis en évidence que l'écart entre le champ de pression obtenu pour un sol avec une impédance qui varie spatialement et celui pour un sol d'impédance homogène était d'autant plus notable que la longueur de corrélation augmentait.

7.2 Sources en mouvement

Les sources pour le bruit des transports (ferroviaire, routier ou aérien) sont en mouvement, avec des vitesses qui peuvent être importantes (nombre de Mach de l'ordre de 0.3 pour les trains à grande vitesse ou pour les avions au décollage). Pour une excitation harmonique, la fréquence du signal reçu au récepteur est différente de celle émise par la source à cause de l'effet Doppler. De même, pour une même distance source-récepteur à l'instant d'émission, l'amplitude du signal au récepteur est différente pour une source mobile et pour une source fixe, à cause de l'amplification convective.

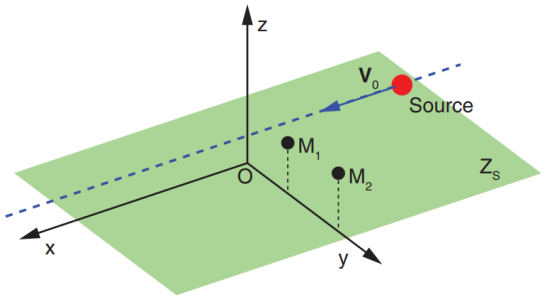

FIGURE 7.2 – Schéma pour le problème d'une source en mouvement au-dessus d'un sol absorbant. Extrait de Ref. [31].

Les approches temporelles sont bien adaptées pour l'étude de sources en mouvement. La trajectoire de la source peut être imposée et l'effet Doppler et l'amplification convective sont naturellement pris en compte. Nous avons d'abord réalisé une étude pour valider l'implémentation d'une source en mouvement dans un code de résolution des équations d'Euler linéarisées. Par ailleurs, le raisonnement dans le domaine temporel a permis aussi de remettre en cause des travaux théoriques dans la littérature sur les sources en mouvement. Des développement analytiques ont été alors réalisés sur ce thème.

7.2.1 Étude numérique

Dans la Ref. [30], nous avons étudié la prise en compte de sources en mouvement dans un code de résolution des équations d'Euler linéarisées. Pour cela, nous avons utilisé un terme source volumique dans les équations. Tout d'abord, nous avons étudié l'effet du support volumique de la source sur le champ de pression rayonné. Pour une source stationnaire harmonique et à symétrie sphérique, l'amplitude du champ de pression est modulée par la transformée de Fourier spatiale du support évaluée au nombre d'onde acoustique, ce qui peut être obtenu classiquement avec l'approximation de Fraunhofer. Dans le cas d'un support gaussien, le champ de pression peut être calculé explicitement ; cela permet de retrouver à grande distance le résultat de l'approximation de Fraunhofer. Comparé à un point source, le support gaussien agit comme un filtre passe-bas. Pour une source compacte (longueur d'onde grande devant le rayon de la gaussienne), on retrouve l'amplitude obtenue pour un point source ; l'amplitude diminue ensuite lorsque la source devient non-compacte. Pour une

source en mouvement à symétrie sphérique et harmonique, nous avons montré avec l'approximation de Fraunhofer, que l'amplitude du champ de pression était toujours modulée par la transformée de Fourier spatiale du support, mais cette fois-ci évaluée à un nombre d'onde égal au nombre d'onde acoustique divisé par le facteur Doppler. Pour un support sphérique, cela induit une directivité de la source. En particulier, pour une source à support gaussien non-compacte, cet effet s'oppose à l'amplification convective : on peut donc avoir une source qui rayonne plus dans le sens opposé au mouvement que dans le sens du mouvement. Différents cas-tests ont été réalisés, montrant que l'effet Doppler et l'effet d'amplification convective étaient bien obtenus dans les simulations. De plus, l'effet de la compacité de la source a été retrouvé dans les simulations numériques.

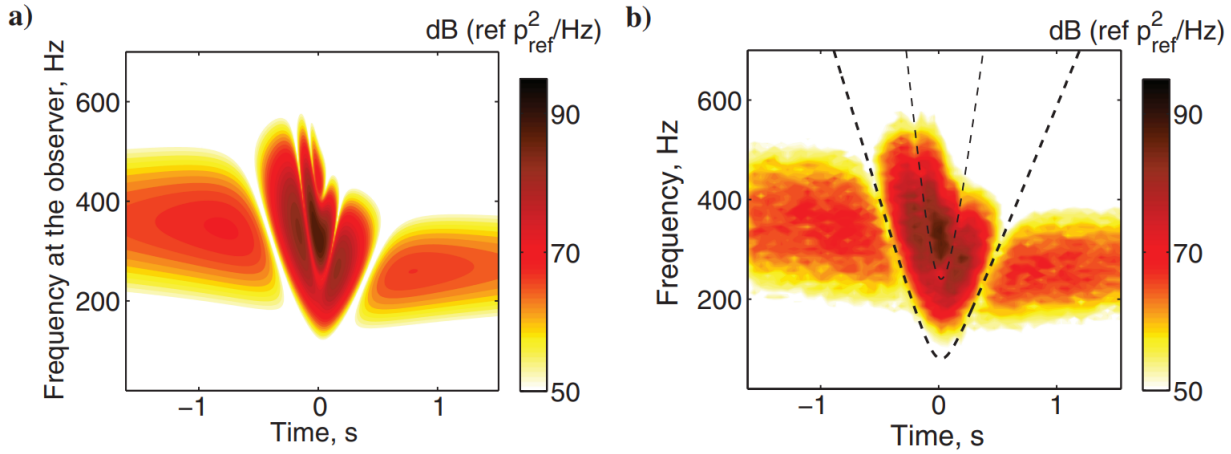

FIGURE 7.3 – Diagramme temps-fréquence à un récepteur pour une source en mouvement à hauteur et à vitesse constante au-dessus d'un sol parfaitement réfléchissant : a) solution analytique et b) solution numérique. Extrait de Ref. [30].

Nous avons ensuite montré dans la Ref. [30] l'intérêt de l'approche pour la prédiction du bruit généré par une source large bande en mouvement à vitesse constante et à hauteur constante en considérant d'abord un sol plan parfaitement réfléchissant, pour lequel une solution analytique est connue, puis un sol plan absorbant (voir le schéma sur la Fig. 7.2). Un exemple de résultat est donné sur la figure 7.3 pour un signal source de type bruit blanc filtré avec un contenu fréquentiel entre 200 et 400 Hz. Le diagramme temps-fréquence à un récepteur pour une source en mouvement large bande avec un nombre de Mach de 0.15 est représenté pour la solution analytique et pour la solution numérique. Le temps $t = 0$ correspond à l'instant où la source est au droit du récepteur. On note la différence du contenu spectral lorsque la source s'approche et s'éloigne du récepteur. On peut aussi remarquer la présence d'interférences lorsque la source est proche du récepteur représentée par des lignes pointillées sur la solution numérique. L'accord entre la solution analytique et numérique est excellent. Enfin, une illustration pour un sol mixte avec une topographie a été réalisée dans la Ref. [31].

7.2.2 Approches analytiques

Plusieurs solutions analytiques pour le cas d'une source harmonique se déplaçant à vitesse et hauteur constantes au-dessus d'un sol absorbant ont été proposés dans la littérature [32]. Cependant, celles-ci ont été obtenues en supposant une impédance de surface du sol indépendante de la fréquence, ce qui est une hypothèse forte. En effet, à cause de l'effet Doppler, la fréquence des ondes acoustiques se réfléchissant sur sol dépend de l'angle d'incidence. On doit donc prendre en compte même pour une source harmonique la dépendance avec la fréquence de l'impédance du sol.

Dans la Ref. [33], nous avons développé une solution analytique pour une ligne source harmonique se déplaçant à vitesse et hauteur constante au-dessus d'un sol absorbant avec une impédance de surface qui dépend de la fréquence. En particulier, nous avons pris soin d'écrire la condition limite

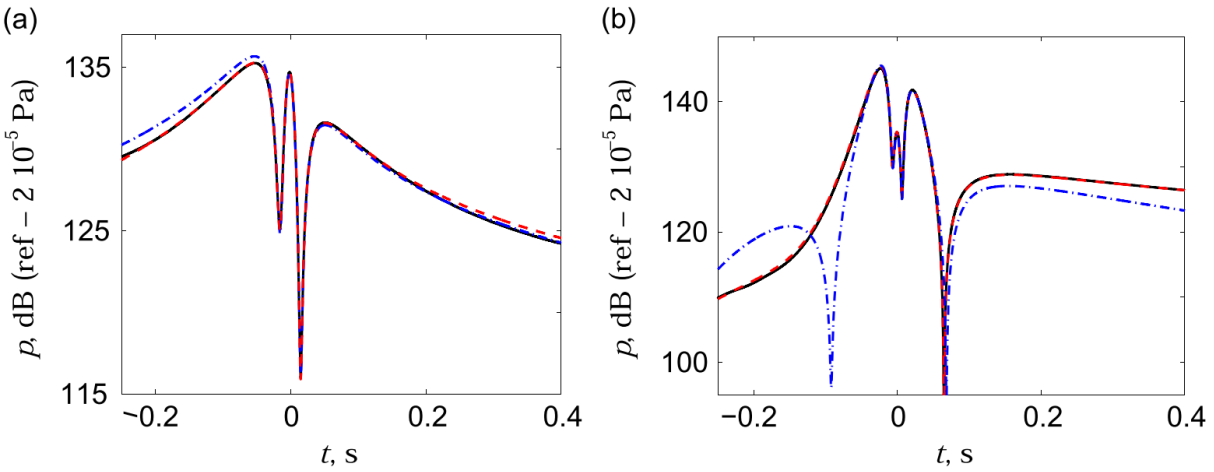

FIGURE 7.4 – Evolution du niveau sonore pour une ligne source en mouvement à hauteur constante et à une vitesse de 100 m s^{-1} émettant à une fréquence de 500 Hz pour (a) et (b) deux types de sols différents : (noir) solution numérique en résolvant les équations d'Euler linéarisées et solutions analytiques (rouge) prenant en compte l'évolution de l'impédance de surface le long de la trajectoire de la source et (bleu) la négligeant. Extrait de Ref. [33].

d'impédance dans le domaine temporel. A partir d'une formulation intégrale, une expression en champ lointain acoustique a été obtenue. Le calcul fait intervenir des notions d'analyse complexe, à savoir la méthode de descente rapide. On a montré avec des hypothèses classiques (incidence rasante, sol peu absorbant) et pour de faibles nombres de Mach, que la solution analytique correspondait à celle pour une source en mouvement avec une impédance constante, en estimant l'impédance de surface à la fréquence Doppler. Des comparaisons ont été réalisées avec succès entre la solution analytique obtenue et une solution numérique des équations d'Euler linéarisées, comme cela est montré sur la Fig. 7.4. On peut, en particulier, observer sur la Fig. 7.4 (b) la différence notable entre les niveaux de bruits prédits si on prend en compte ou si néglige la variation de l'impédance de surface lors du mouvement de la source pour le type de sol considéré.

Suite à cette étude, une collaboration a été menée avec l'équipe de K.M. Li à l'université de Purdue, États-Unis, pour étendre la solution analytique au-cas d'un sol à réaction étendue. En particulier, nous avons réalisés des simulations numériques dans le domaine temporel pour la comparaison avec les solutions analytiques développées. La collaboration a donné lieu à l'article [34].

7.3 Applications en acoustique environnementale

Les études dans le chapitre et sections précédents avaient pour objectif de développer des méthodes numériques ou d'étudier de manière générale l'influence de différents paramètres sur la propagation acoustique. J'ai participé à des applications plus spécifiques, détaillées ci-dessous.

7.3.1 Bioacoustique

Depuis 2018, nous travaillons avec F. Sèbe de l'ENES à Saint-Etienne sur des thématiques de bioacoustique. En particulier, F. Sèbe s'intéresse à une espèce d'oiseau, les lagopèdes alpins (voir Fig. 7.5), qui vivent en France dans les hautes montagnes (Alpes, Pyrénées). Le lagopède alpin est un bioindicateur, c'est-à-dire que l'évolution de la population permet de caractériser l'évolution de l'habitat. Ces oiseaux sont étudiés avec deux objectifs : le suivi de population à long terme par méthodes acoustiques et la compréhension de la communication entre oiseaux.

Dans les études de bioacoustique, les modèles de propagation acoustique sont habituellement très simples : soit des modèles analytiques qui permettent de décrire sommairement la décroissance du

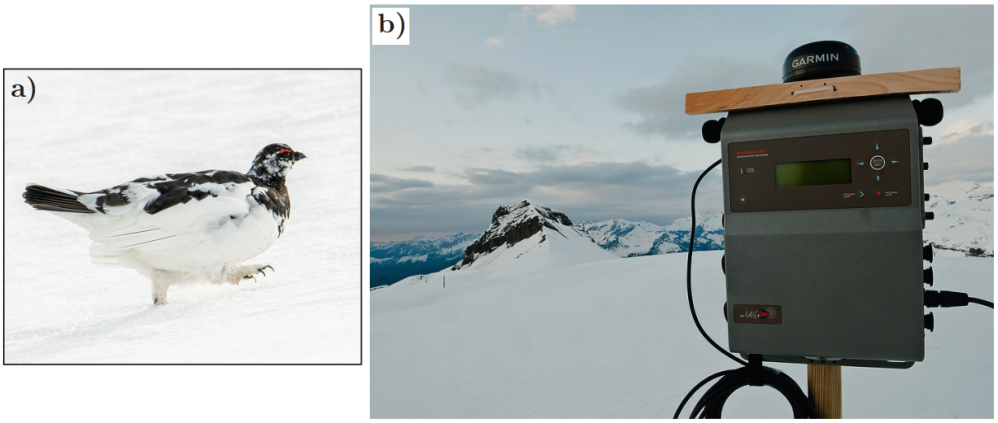

FIGURE 7.5 – Photographie (a) d'un lagopède alpin et (b) du site de Flaine avec une unité d'enregistrement autonome au premier plan. Extrait de Ref. [35].

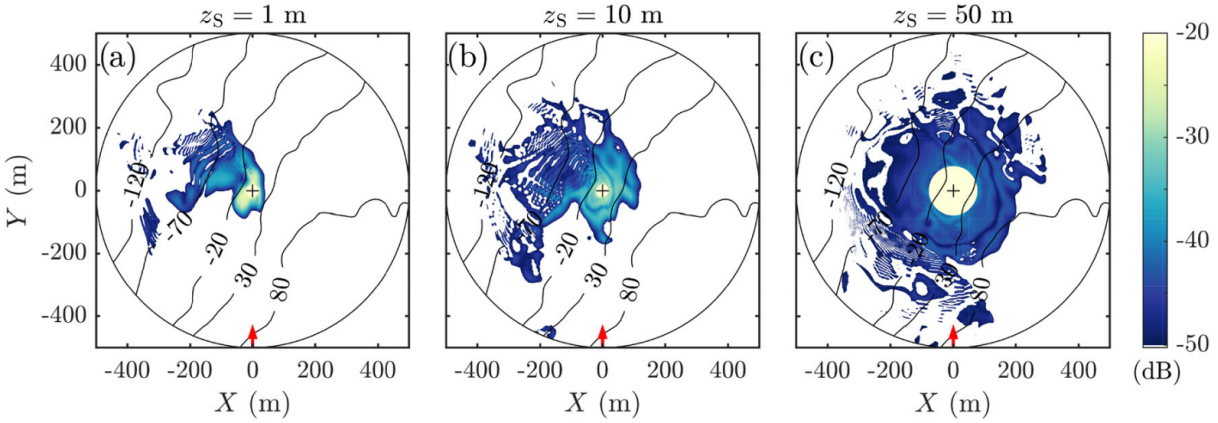

FIGURE 7.6 – Illustration de l'effet de la hauteur de la source sur l'espace actif. Cartographie de pertes par propagation pour différentes hauteurs de source sur le site de Flaine. Extrait de Ref. [36].

niveau sonore avec la distance à la source soit des modèles d'ingénierie qui ont été développés pour des sources de bruit industriels. Deux concepts-clés sont utilisés pour comprendre la communication entre oiseaux : le premier est l'espace actif, correspondant à l'espace autour de l'émetteur dans lequel celui-ci est entendu, et le second est l'espace de détection, correspond à l'espace autour du récepteur dans lequel celui-ci peut entendre un émetteur. L'objectif de la collaboration est alors de pouvoir prédire plus précisément la propagation des vocalisations d'oiseaux dans la montagne et ces espaces de communication en utilisant les approches numériques développées au laboratoire. La collaboration a donné lieu à la thèse d'A. Guibard à l'interface entre bioacoustique et acoustique physique.

Un modèle de propagation basé sur une approche paraxiale bidimensionnelle dans le domaine fréquentiel a été utilisé. Le calcul est étendu en 3D en réalisant des simulations dans des plans verticaux tout autour de la source. Des mesures de propagation acoustique sur le site du col du Lac Blanc dans les Alpes ont été réalisées par A. Guibard [36]. Des données de température, de vitesse du vent et d'humidité ont été relevées à l'aide d'un mât météorologique et des mesures d'impédance de surface de la couche neigeuse ont été effectuées pour servir de données d'entrée du modèle de propagation. Des comparaisons entre mesures et résultats de simulation ont été effectuées à différentes distances allant jusqu'à 200 m et ont montré un bon accord sur une large bande de fréquence entre 200 Hz et 3 kHz. Le modèle de propagation a ensuite été utilisé pour déterminer l'espace actif du lagopède en fonction de plusieurs paramètres environnementaux [36] : topographie, paramètres météorologiques et hauteur de source. Un exemple de la variation de l'espace actif avec la hauteur de la source est représenté sur la figure 7.6. On observe que lorsque la source est proche

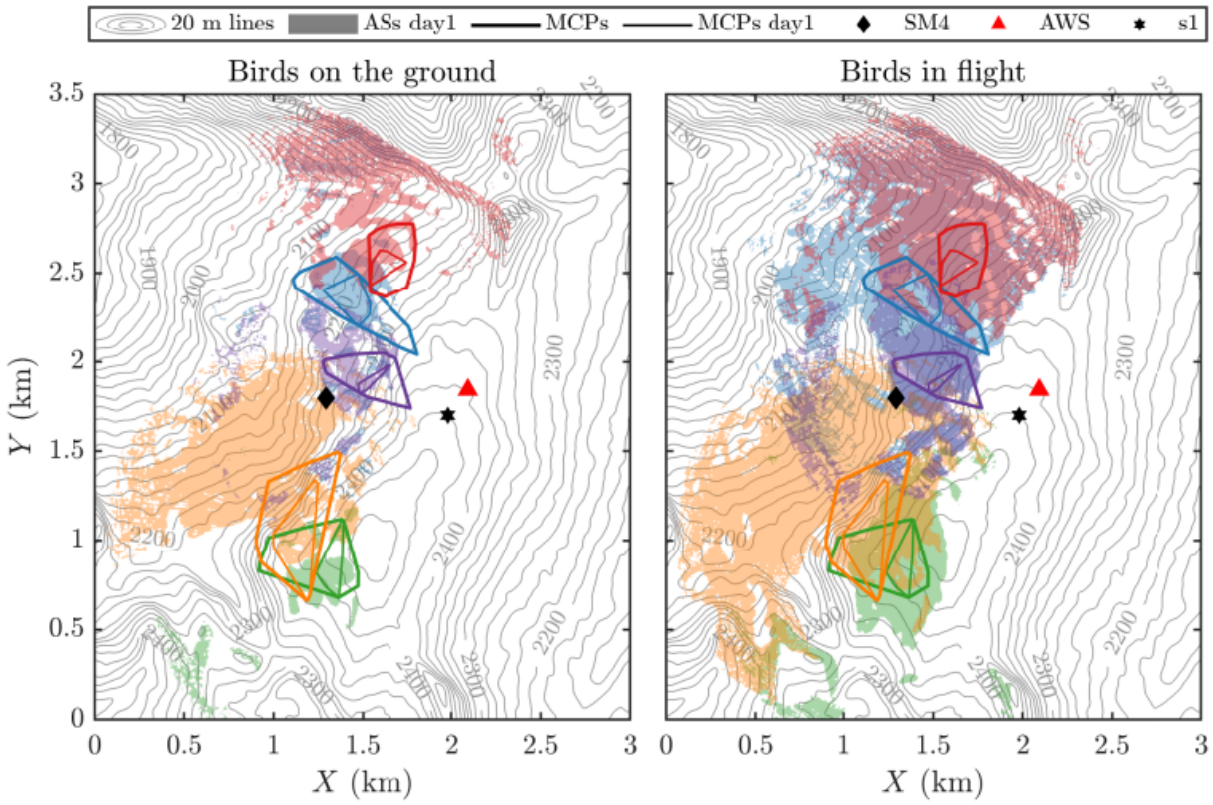

FIGURE 7.7 – Calcul d'espaces actifs sur une journée en considérant à gauche un chant des oiseaux au sol et à droite un chant des oiseaux en vol. Les polygones en ligne épaisse représentent les territoires de chaque oiseau. Chaque couleur correspond à un oiseau différent. Extrait de Ref. [35].

de la surface, l'espace actif a une forme nettement asymétrique et dépend de la topographie locale. Lorsque la hauteur de la source augmente, l'espace actif tend à s'élargir et à prendre une forme circulaire, comme cela peut l'être au-dessus d'un sol plan. Ce résultat peut être mis en relation avec le comportement du lagopède, qui effectue un vol en cloche pendant ses vocalisations lui permettant ainsi d'être entendu à plus grande distance et indépendamment de la topographie locale. L'article issu de ces travaux est joint en annexe du document.

Une seconde partie de la thèse avait pour but d'étudier l'organisation spatiale du réseau de communication des oiseaux. Pour cela, les espaces actifs de différents oiseaux munis de traceurs GPS ont été calculés sur plusieurs journées en utilisant les données d'un mât météorologique placé sur le site de Flaine et les données de sol (topographie, impédance). La figure 7.7 montre un exemple d'espaces actifs calculés pour une journée pour cinq oiseaux différents. Le calcul a été fait à la fois pour un chant réalisé au sol et en vol. Plusieurs points sont à noter. Tout d'abord, la communication acoustique est efficace pour signaler la présence de l'oiseau sur son territoire : ainsi, l'espace actif, que l'oiseau soit en vol ou au sol, permet de recouvrir son territoire. On note la forte variabilité de l'espace actif suivant la position de l'oiseau sur la topographie, par exemple, en comparant les espaces actifs représentés en bleu et en jaune. On retrouve enfin que le vol permet d'élargir considérablement l'espace actif de l'oiseau et permet aussi aux oiseaux de pouvoir communiquer avec leurs voisins. L'étude a aussi été poursuivie pour étudier un possible lien entre le chorus matinal des oiseaux et des conditions météorologiques plus favorables à la propagation à l'aube.

La dernière partie de la thèse s'est focalisée sur les espaces de détection, avec pour application le placement d'unité d'enregistrement autonome (ARU) pour l'étude de la communication des oiseaux. Les ARU sont notamment utilisés pour le suivi passif acoustique (par exemple, pour la détection des espèces, l'estimation de l'abondance, le comptage, ...). Pour calculer les espaces de détection, le principe de réciprocité a été utilisé : au lieu de faire un nombre importants de calcul en plaçant des

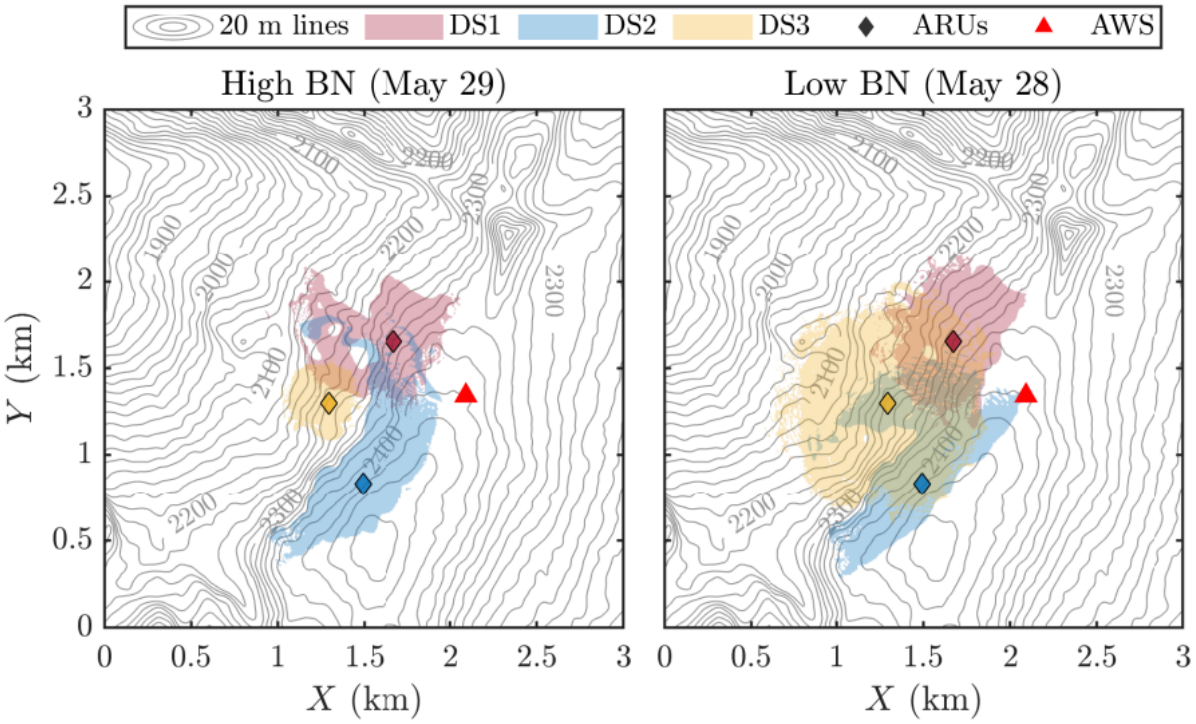

FIGURE 7.8 – Espaces de détection calculés pour trois récepteurs à différentes positions et pour deux jours différents. Extrait de Ref. [35].

sources tout autour du récepteur, l'espace de détection a été déterminé en plaçant une seule source à la place du récepteur et en inversant le sens de l'écoulement. Un exemple d'espace de détection pour trois ARUs placés sur le site de Flaine est représenté sur la Fig. 7.8 pour deux journées différentes. Les espaces de détection ont, comme les espaces actifs, une forme relativement complexe. Ils dépendent de la position du récepteur : l'espace de détection en jaune a une forme circulaire alors que celui en bleu a une forme allongée. Ils dépendent aussi fortement des conditions météorologiques et du bruit de fond : par exemple, l'espace de détection en jaune varie très grandement entre les deux journées alors que celui en bleu reste similaire. On note aussi un recouvrement entre les trois espaces de détection, notamment pour le 28 mai. Ainsi, un oiseau placé à l'intersection entre les trois espaces de détection sera entendu par les trois ARUs.

Le travail de thèse d'A. Guibard a permis de montrer l'intérêt en bioacoustique d'utiliser des outils de simulation numérique fins pour la propagation atmosphérique. La valorisation des travaux de thèse d'A. Guibard est à finaliser.

7.3.2 Propagation du bruit d'éolienne

Contexte et enjeux

L'énergie éolienne est une des clés du développement durable. Cependant, les éoliennes sont une source de bruit ; la gêne sonore induite est un des freins majeurs au développement de parcs éoliens. Les éoliennes génèrent un bruit large bande, jusqu'à quelques kHz. Le niveau sonore moyen n'est pas très élevé, notamment comparé aux sources de bruit des transports. Dans la littérature, la gêne due au bruit a été relevée jusqu'à plusieurs kilomètres des éoliennes [37]. La gêne est liée à différents facteurs (bruit de fond faible dans les zones d'implantation des éoliennes, source de bruit fluctuante liée à la rotation des pales, ...).

La prédiction du bruit des éoliennes nécessite une description précise de la source de bruit, de l'écoulement dans la couche limite atmosphérique et de la propagation acoustique dans l'atmosphère. L'état de l'art reste l'approche présentée dans Barlas *et al.* [38], à savoir une approche intégrée avec

un modèle de source aéroacoustique, des données de simulations numériques de l'écoulement atmosphérique et un modèle de propagation acoustique. Du fait des distances de propagation importantes à considérer et du contenu fréquentiel moyennes fréquences, les modèles de propagation utilisés sont limités à des approches paraxiales bidimensionelles [39] et les effets tridimensionnels de propagation n'ont été étudiés qu'avec des approches géométriques [40]. De plus, bien que plusieurs études aient été faites sur des éoliennes isolées, la littérature est peu abondante dans le cas d'un parc éolien.

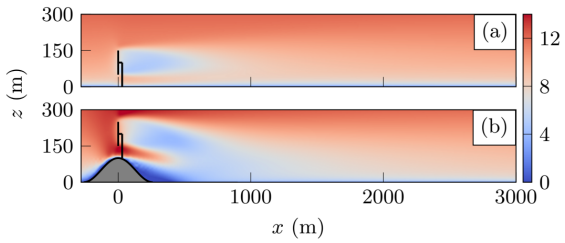

FIGURE 7.9 – Ecoulement moyen extrait de simulations LES [41] pour une éolienne (a) située sur sol plan et (b) au sommet d'une colline. Extrait de Ref. [43].

Dans le cadre du post-doctorat d'A. Emmanuelli à l'Université de Twente, une collaboration a été mise en place avec l'équipe de R.J.A.M. Stevens, qui réalise des simulations numériques de l'écoulement atmosphérique autour des éoliennes avec une approche LES [41], et avec B. Cotté (IMSIA, ENSTA), qui a développé un modèle de source étendu du bruit des éoliennes [42]. Elle a donné lieu à plusieurs stages de M2 et à la thèse de J. Colas. Les objectifs de la collaboration sont à la fois d'améliorer la prédiction du bruit des éoliennes en utilisant des méthodes de propagation avancées (résolution des équation d'Euler linéarisées en présence d'une topographie et étude des effets tridimensionnels avec une approche paraxiale) et d'étudier le bruit généré par un parc éolien.

Effet de la topographie

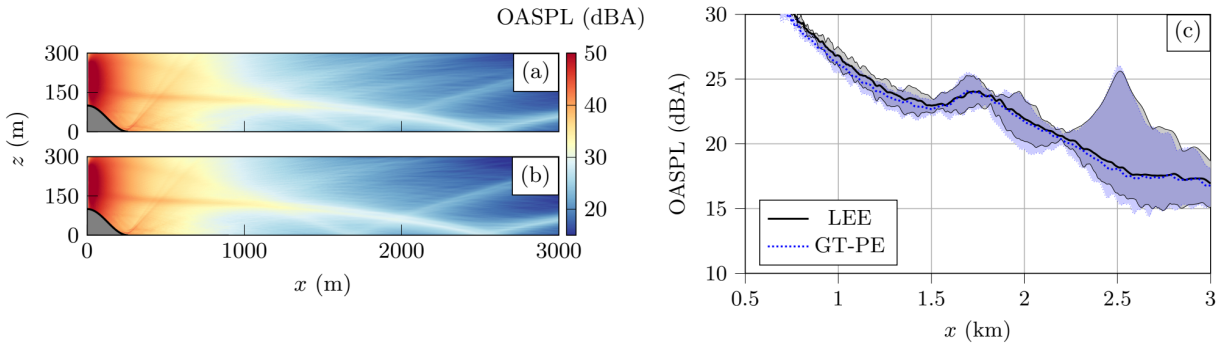

FIGURE 7.10 – Niveau de pression pour une position du rotor dans le cas de l'éolienne située sur le sommet d'une colline calculé (a) avec LEE et (b) avec l'équation parabolique. (c) Evolution du niveau sonore moyennée sur une rotation du rotor de l'éolienne avec la distance pour une hauteur de 2 m déterminé avec les deux approches. Les régions colorées délimitent les valeurs min et max sur une rotation. Extrait de Ref. [43].

Le premier axe de la thèse de J. Colas a porté sur l'effet de la topographie sur le bruit des éoliennes. Le point de départ choisi a été les simulations LES de Liu et Stevens [41] pour une éolienne isolée située sur un sol plat ou au sommet d'une colline. La figure 7.9 présente les écoulements moyens dans une atmosphère neutre pour les deux cas. On note la présence du sillage de l'éolienne pour le sol plan. Pour la colline, le sillage de l'éolienne se combine avec celui de la colline et est beaucoup plus long. Pour déterminer la propagation acoustique, les équations d'Euler linéarisées (LEE) ont été résolues dans le domaine temporel par méthode différences finies. Des coordonnées

curvilignes ont été employées pour prendre en compte la topographie. Cet approche est plus précise que l'approche paraxiale, puisqu'elle permet de considérer un écoulement moyen sans approximation et la diffraction par la topographie sans limite angulaire. Une première partie a consisté à comparer deux approches basées sur la résolution des équations d'Euler linéarisées (LEE) et sur la résolution de l'équation parabolique grand angle (PE) pour une application au bruit des éoliennes [43]. Un exemple de résultat est représenté sur la figure 7.10. On note que les cartographies de niveau sonore pour une position du rotor sur les Figs. 7.10 (a) et (b) sont très proches avec le calcul LEE et parabolique. On retrouve une décroissance globale des niveaux avec la distance ainsi que la présence de zones très localisées d'amplification du niveau sonore, liées au sillage et à la topographie. Le bon accord entre les approches LEE et PE est confirmé sur la Fig. 7.10 (c). Le niveau moyenné sur une rotation diffère entre les deux approches de moins d'1 dB. L'article issu de ces travaux est joint en annexe du document. Dans la seconde partie de l'étude, une comparaison physique des champs de niveau sonore est effectuée suivant la position de l'éolienne le long de colline. Cette partie est en cours de valorisation.

Effets tridimensionnels

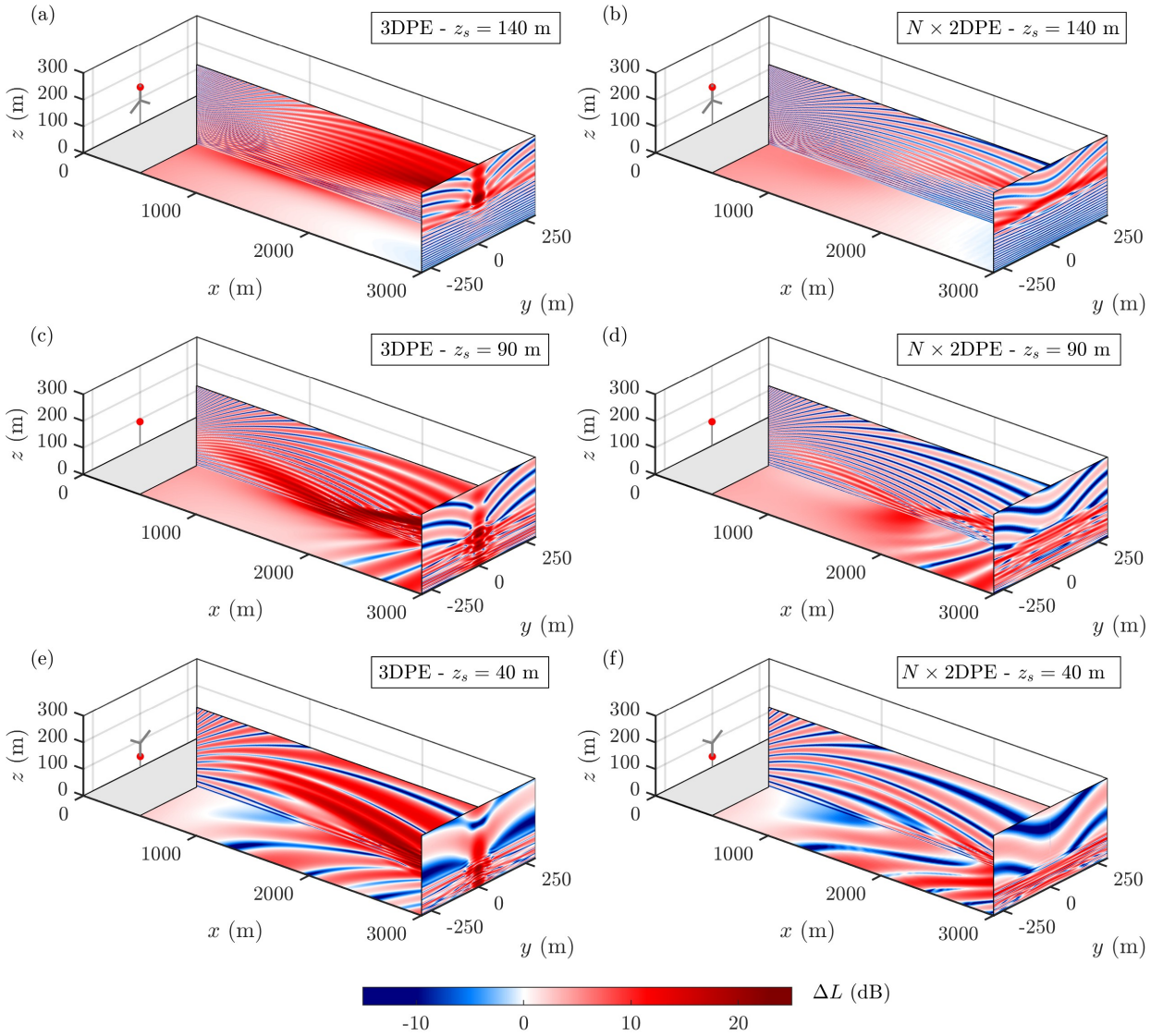

FIGURE 7.11 – Niveau de pression relatif au champ libre pour un point source situé à trois hauteurs différentes calculé (gauche) avec un code PE3D et (droite) avec un code PE2D.

Durant le stage de M2 d'H. Bommidala, nous avons analysé les effets tridimensionnels de pro-

pagation acoustique sur la prédiction du bruit des éoliennes. Pour cela, nous avons employé le code d'équation parabolique standard 3D (PE3D) développé par Khodr et al. [2] et nous avons comparé les résultats avec un code équivalent 2D (PE2D). Le cas d'une éolienne isolée sur sol plan a été étudié. Le profil moyen de vitesse du vent incluant le sillage est analytique [44]. Du fait du coût important, le calcul a été mené seulement à basse fréquence. A titre indicatif, le domaine d'une taille de 3 km de long, 150 m de hauteur et 300 m de large compte déjà 3.5 milliards de points pour une fréquence de 100 Hz. Nous avons montré que les effets de réfraction dans la direction horizontale induits par le sillage pouvaient être importants. C'est notamment le cas pour une atmosphère stable pour laquelle le sillage derrière l'éolienne est très long. Un exemple de résultat est présenté sur la figure 7.11 où sont comparés les niveaux de pression relatifs au champ libre calculés avec un code PE3D et un code PE2D pour trois hauteurs de sources différentes. Les effets de réfraction dans la direction verticale sont correctement décrits par le calcul bidimensionnel. Par contre, la prise en compte des effets tridimensionnels induit une focalisation plus importante dans le sillage, ce qui est visible avec l'augmentation forte des niveaux dans le plan vertical $y = 0$. Cet effet de focalisation est notable sur le niveau de bruit global de l'éolienne. La figure 7.12 présente le niveau de bruit pour quatre positions différentes du rotor. On peut observer sur le plan horizontal $z = 0$ et sur le plan vertical $x = 3000$ m la présence de trois zones de focalisation, chacune d'entre elles reliée à une des trois pales de l'éolienne. Lorsque les pales de l'éolienne tournent, les zones de focalisation se déplacent, ce qui conduit à une variation forte des niveaux sonores. On a montré que les modulations d'amplitude prédites avec le code PE3D étaient beaucoup plus importantes qu'avec le code PE2D mais que les niveaux sonores moyennés sur une rotation différaient peu. Ce travail reste à valoriser.

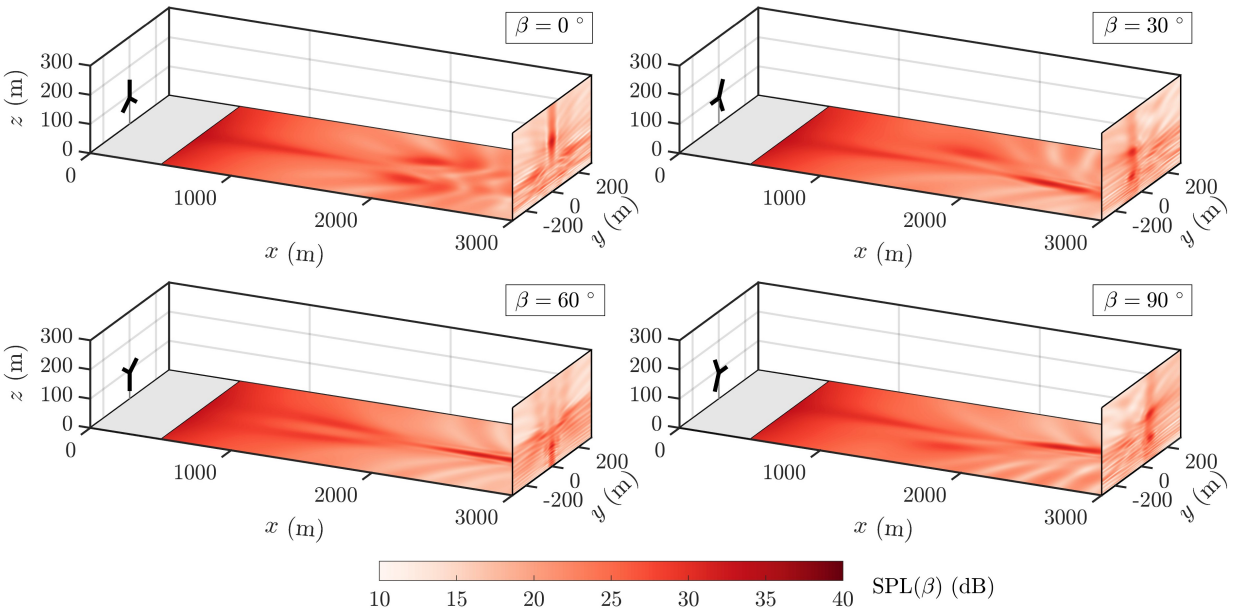

FIGURE 7.12 – Niveau de pression pour différentes positions du rotor déterminé avec le code PE3D.

7.4 Conclusions et perspectives

Les travaux autour de l'acoustique environnementale ont abordés différents sujets. La première partie liée à l'impédance de surface des sols visait à déterminer parmi les modèles d'impédance proposés dans la littérature lesquels sont physiquement admissibles ainsi qu'à quantifier les effets des variations spatiales de l'impédance de surface sur la prédiction des niveaux de pression. La deuxième partie était en lien avec les sources en mouvement, avec à la fois une étude sur leur modélisation dans les simulations temporelles ainsi que des travaux autour de l'amélioration de solutions analytiques dans des configurations simples. Ces travaux continuent avec le post-doctorat de B. Kayser dans le cadre du projet DGAC MAMBO. L'objectif est ici d'améliorer les outils de prédiction d'AIRBUS

pour le bruit avion, notamment pour des scénarios de certification. Pour cela, un modèle heuristique est développé pour prendre en compte l'effet Doppler, l'amplification convective, les effets de sol et les effets météorologiques. Des comparaisons avec une solution numérique des équations d'Euler linéarisées sont effectuées pour valider étape après étape les différents ajouts du modèle.

Une partie importante de ces travaux était à visées applicatives. Les études réalisées en bioacoustique ont permis de montrer l'intérêt d'un modèle physique de propagation acoustique dans l'environnement pour analyser les espaces de communication. L'étude pourrait être poursuivie en déterminant les espaces de communication liés à des informations individuelles contenues dans le signal et pas uniquement liés au niveau sonore. Cela demanderait de pouvoir déterminer le signal temporel après propagation, que ce soit par synthèse de Fourier ou en utilisant directement une résolution temporelle. Enfin, les premiers travaux autour du bruit des éoliennes ont mis en évidence la richesse des phénomènes physiques en jeu. En particulier, la prise en compte de profils de vitesse dans la couche limite atmosphérique réalistes est une valeur ajoutée considérable pour la prédiction du champ acoustique. L'étude s'est, pour l'instant, focalisée sur une éolienne isolée et doit être poursuivie dans la fin de la thèse de J. Colas sur un parc éolien. Les pistes d'amélioration sont nombreuses. Tout d'abord, les premiers calculs de propagation 3D ont montré que les effets 3D pouvaient être importants et que des simulations 2D pouvaient conduire à une sous-évaluation des modulations d'amplitude. Ces résultats seraient à généraliser. Ensuite, nous n'avons pas pris en compte l'effet de la turbulence sur la propagation acoustique. Celle-ci peut avoir un effet notable, en particulier dans le sillage de l'éolienne [45] et induire une diminution des modulations d'amplitude.

CHAPITRE 8

Propagation en conduit

Une autre activité importante concerne la propagation en conduit, qui était un thème déjà abordé au laboratoire mais sous un aspect expérimental. Une grande partie des travaux ont porté sur la modélisation des traitements dissipatifs en paroi de conduit dans le domaine temporel. Une application a été réalisée pour faire une identification large bande de l'impédance de surface d'un liner. Plus récemment, une première étude sur les liners réalisés par fabrication additive a été menée.

8.1 Modélisation des traitements absorbants en paroi de conduit

Les approches temporelles, décrites dans le chapitre 6 pour la propagation en milieu extérieur, sont aussi intéressantes pour la propagation en conduit. Là encore, une des difficultés est la prise en compte de traitements absorbants, placés en conduit pour la réduction de bruit, à cause de leur comportement qui dépend de la fréquence. Un travail important a été réalisé afin de pouvoir modéliser les traitements absorbants à réaction locale ou non-locale dans des simulations dans le domaine temporel.

8.1.1 Comportement linéaire des matériaux acoustiques

Une première étape, réalisée pendant le post-doctorat de R. Troian, a été de développer une condition limite d'impédance dans le domaine temporel d'ordre élevé [46] permettant de modéliser les traitements à réaction locale, en se basant sur la méthode ADE proposée dans la Ref. [20]. Nous avons montré en particulier que les modèles d'impédance usuels pour les traitements absorbants en paroi de nacelle peuvent être approximés par une fraction rationnelle sur une bande de fréquence très large avec un nombre de pôles faible. Notons que des approches comparables ont été proposées dans la littérature [47].

Une autre étape, réalisée pendant le post-doctorat d'A. Alomar, a été la prise en compte de traitements à réaction non-locale dans les simulations temporelles [48]. Pour cela, les traitements ont été modélisés par des fluides équivalents et la propagation dans le matériau a été déterminée explicitement en résolvant les équations du fluide équivalent. Comme la compressibilité et la masse volumique effectives dépendent de la fréquence, ces équations présentent dans le domaine temporel des produits de convolution. Après avoir approximé la compressibilité et la masse volumique effectives par des fractions rationnelles, le calcul des produits de convolution est réalisé en utilisant là-encore la méthode ADE. Nous avons appliqué la méthode à des matériaux poreux classiques, pour lesquels le modèle Johnson-Champoux-Allard-Lafarge (JCAL) a été utilisé pour les fonctions du fluide équivalent, ainsi qu'à des matériaux résonants. De plus, la méthode ADE a été aussi uti-

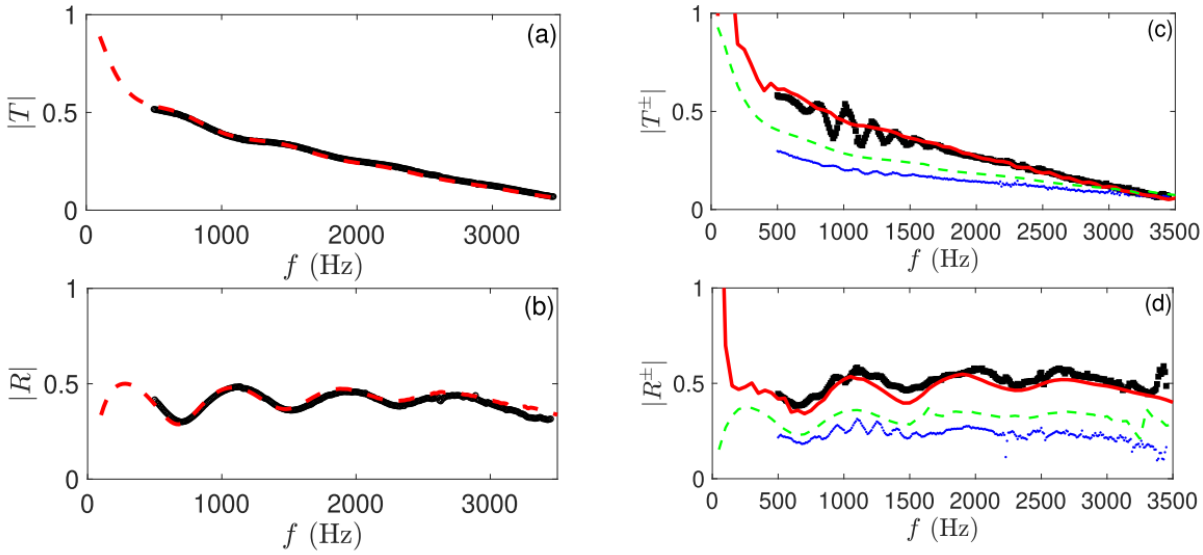

FIGURE 8.1 – Comparaison des coefficients de la matrice de diffusion pour un liner en mousse métallique calculés à partir de la simulation numérique et avec les données expérimentales d'Aurégan et Singh [49] : (gauche) sans écoulement (droite) avec un écoulement dont le nombre de Mach est de 0.2. Pour la solution numérique, T^+ et R^+ sont représentés par des lignes rouges et T^- et R^- par des lignes vertes. Pour l'expérience, T^+ et R^+ sont représentés par des points noirs et T^- et R^- par des points bleus. Extrait de Ref. [48].

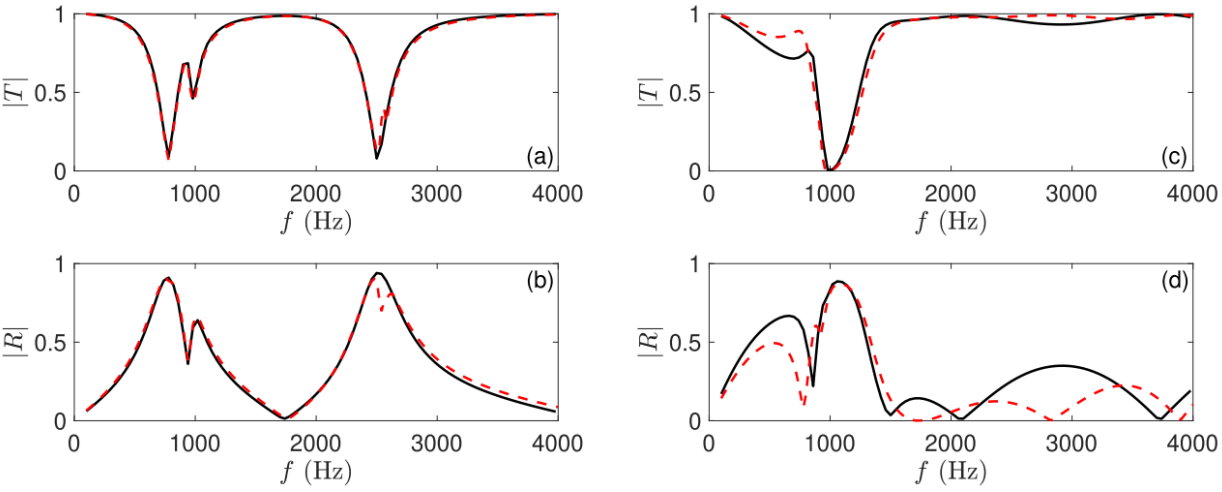

FIGURE 8.2 – Coefficients de la matrice de diffusion pour un liner constitué d'une cavité remplie d'un matériau résonant (gauche) pour une cavité courte et profonde et (droite) pour une cavité longue et peu profonde. Il n'y a pas d'écoulement. La ligne noire pleine correspond à la simulation numérique avec prise en compte de la réaction étendue et la ligne rouge en pointillés avec une modélisation de type réaction locale. Extrait de Ref. [48].

lisée pour traiter l'interface dissipative entre le fluide équivalent et l'air, comme par exemple une plaque perforée, dont la réponse dépend de la fréquence, à l'aide de la méthode des caractéristiques. Une validation a été réalisée avec les mesures reportées dans Aurégan et Singh [49] pour un liner de type mousse métallique sans et avec écoulement ; les coefficients de la matrice de diffusion dans les deux cas sont représentés sur la Fig. 8.1 et montrent un bon accord entre les résultats de la simulation et l'expérience. Un exemple de résultat obtenu pour le cas d'un liner constitué d'une cavité rempli de matériau résonant est présenté sur la figure 8.2. Les coefficients de transmission et de réflexion, calculés à partir de la simulation numérique, sont comparés pour une cavité courte et

profonde et pour une cavité longue et peu profonde en prenant en compte la réaction étendue ou en simplifiant en considérant une réaction locale. Pour la cavité courte et profonde, une approximation de type impédance est suffisant pour prédire la performance du liner alors que les coefficients de transmission et de réflexion diffèrent fortement pour la cavité longue et peu profonde. On note aussi la valeur très faible de coefficient de transmission autour de 1 kHz pour la cavité longue.

Par ailleurs, nous avons proposé dans la Ref. [50] une méthode pour extraire l'approximation par une fraction rationnelle des fonctions du fluide équivalent pour un matériau à partir de mesures avec un tube de Kundt, sans avoir à utiliser un modèle analytique. Elle se base sur la méthode de la fonction de transfert [51]. Nous avons appliqué la méthode à différents types de matériaux, pouvant être représentés par des fluides équivalents : des matériaux poreux classiques, pouvant être modélisés par le modèle JCAL, mais aussi des matériaux à double porosité, pour lesquels le modèle JCAL n'est pas adapté, ou des matériaux imprimés.

8.1.2 Comportement non-linéaire des matériaux acoustiques

Pour des niveaux d'excitation importants (supérieurs à environ 100 dB), les plaques perforées, utilisées classiquement pour les traitements absorbants de type SDOF, présentent un comportement non-linéaire, c'est-à-dire que leurs propriétés acoustiques dépendent du niveau. Cela peut-être modélisé par une impédance de surface, qui dépend des propriétés géométriques de la plaque, de la fréquence et aussi de l'amplitude de la vitesse acoustique dans les perforations (voir par exemple [52]).

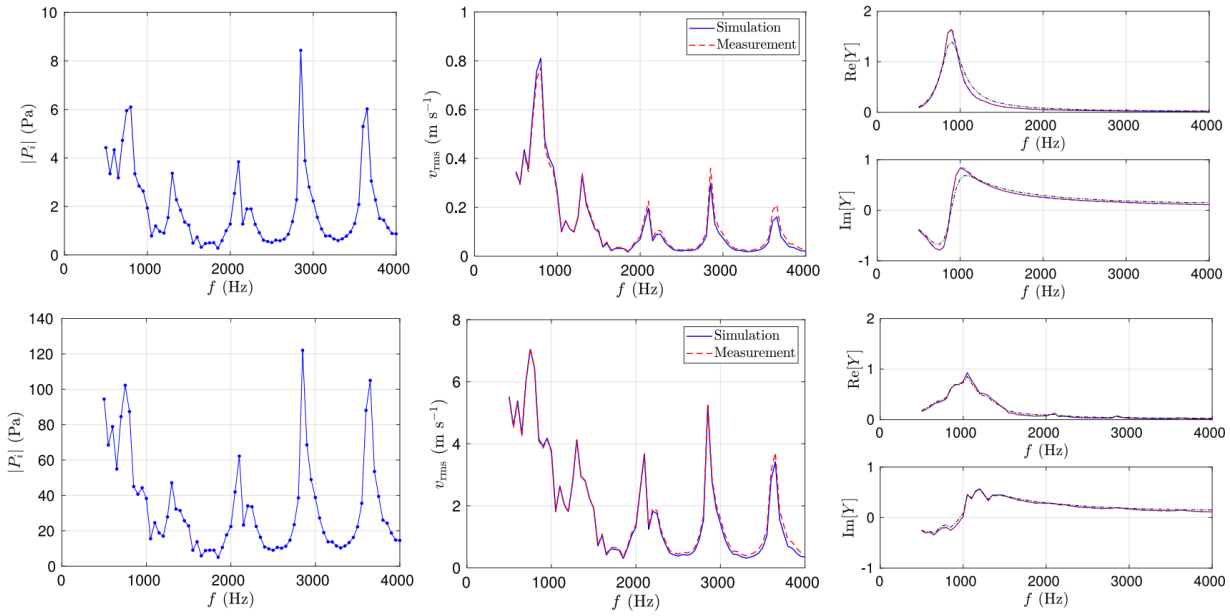

FIGURE 8.3 – Comportement d'une plaque perforée en incidence normale pour une excitation harmonique (haut) de faible amplitude et (bas) de forte amplitude. De gauche à droite : amplitude de la pression incidente déterminée expérimentalement, vitesse rms au niveau des perforations déterminée à partir des mesures et de la solution numérique et admittance de surface. Extrait de Ref. [54].

Récemment, en se basant sur les travaux de Shur *et al.* [53], nous avons étendu pendant le post-doctorat de D. Diab la condition aux limites d'impédance dans le domaine temporel au régime non-linéaire [54]. Pour cela, nous avons considéré une admittance écrite sous la forme d'une fraction rationelle, dont les coefficients dépendent de la vitesse rms dans les perforations. Cela permet à la fois de garder un calcul du produit de convolution efficace avec la méthode ADE et de pouvoir prendre en compte la variation de l'admittance avec le niveau d'excitation. Les coefficients de la fraction rationnelle ont été déterminés à partir du modèle d'impédance de Laly [52]. La vitesse rms dans les perforations est évaluée pendant le calcul, jusqu'à convergence. La condition aux limites

est ainsi seulement applicable à des excitations stationnaires. Afin de valider l'approche, nous avons d'abord fait des mesures en tube de Kundt pour différentes plaques perforées à la fois pour une excitation par un signal harmonique et par un signal aléatoire large bande. Dans les deux cas, un bon accord avec les résultats des simulations numériques est obtenu. En particulier, l'évolution des propriétés acoustiques des plaques perforées avec le niveau d'excitation est correctement reproduit avec les simulations numériques. Un exemple de résultat est montré sur la Fig. 8.3 pour une plaque microperforée sous excitation harmonique avec deux amplitudes différentes. La pression incidente est déterminée à partir des mesures en tube de Kundt et sert de donnée d'entrée de la simulation numérique. Pour les deux amplitudes d'excitation, les vitesses rms au niveau des perforations et les admittances de surface obtenues par la mesure et par la simulation numérique sont en très bon accord. On remarque aussi la variation notable de l'admittance de surface suivant la pression incidente.

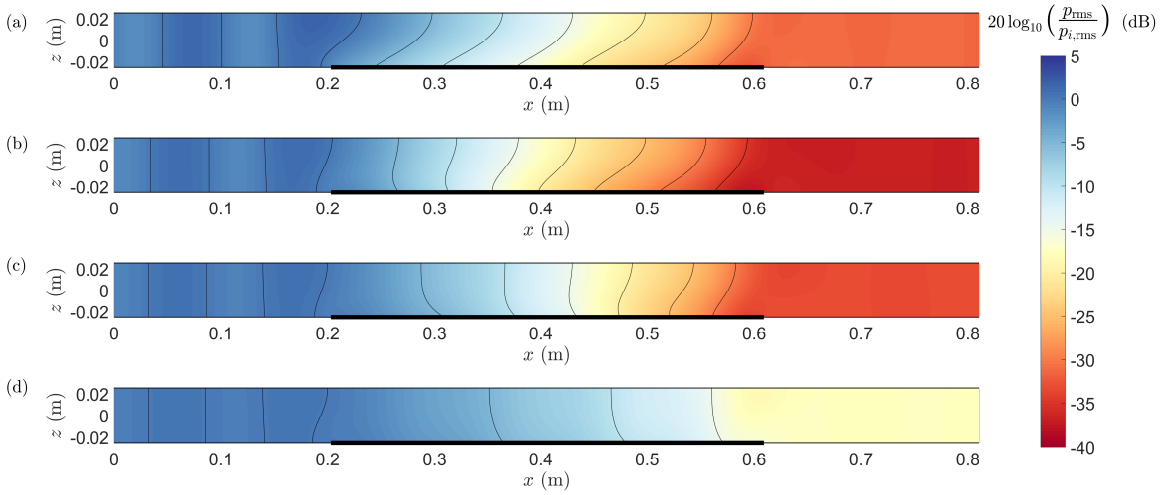

FIGURE 8.4 – Cartographies du niveau de pression (avec pour référence l'amplitude de la pression incidente) pour différents niveaux de pression incidents : (a) 80 dB, (b) 120 dB, (c) 130 dB et (d) 140 dB pour une excitation harmonique à 1600 Hz. Le traitement acoustique en paroi est représenté par une ligne noire épaisse. Les isolignes de niveaux acoustiques sont tracés tous les 5 dB. Extrait de Ref. [54].

La condition limite d'impédance non-linéaire a été utilisée ensuite pour caractériser l'évolution du champ de pression dans un conduit traité en fonction du niveau d'excitation. En particulier, la méthode permet naturellement de prendre en compte les variations de la vitesse rms, et donc de l'impédance, le long du traitement, sans avoir besoin d'un modèle décrivant l'évolution spatiale de l'impédance. Un exemple de résultat est donné sur la figure 8.4 pour un conduit partiellement traité avec une plaque micro-perforée devant une cavité et pour différents niveaux d'excitation. Le cas (a) pour un niveau d'excitation de 80 dB correspond à la solution en régime linéaire. Lorsque le niveau d'excitation augmente, on peut noter à la fois la variation des isolignes ainsi que la variation forte du niveau après le traitement ($x > 0.6$ m). Enfin, la perte par transmission a été déterminée pour différents niveaux d'excitation, ce qui a permis de montrer la variation importante de la performance du traitement avec le niveau d'excitation. L'article issu de ces travaux est joint en annexe du document.

8.2 Identification des propriétés acoustiques de matériaux en paroi

Les matériaux placés en paroi de conduit ont habituellement des propriétés acoustiques différentes de celles que l'on peut obtenir en incidence normale avec un tube à impédance. En particulier, ces propriétés peuvent dépendre du nombre de Mach de l'écoulement ou du sens de la propagation.

Il est ainsi intéressant de pouvoir évaluer l'impédance de surface de matériaux dans des conditions proches de celles d'utilisation.

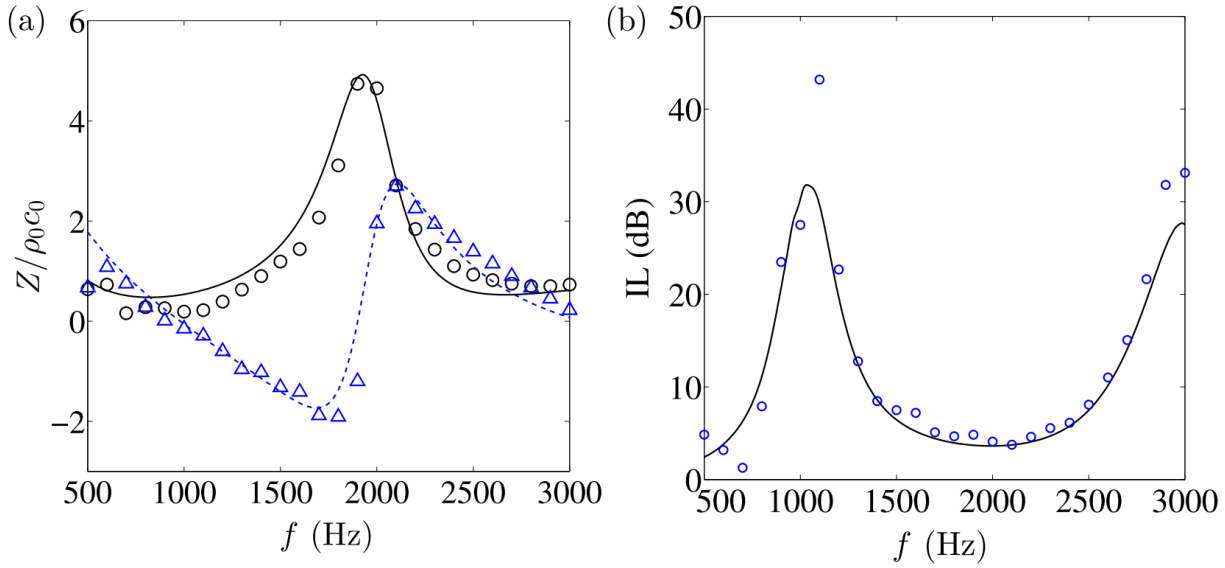

FIGURE 8.5 – (a) Parties réelle et imaginaire de l'impédance du liner identifiées (symboles) par Jones *et al.* [4] et (lignes) avec la méthode large bande proposée dans Ref. [46]. (b) Perte par insertion (symboles) déduite des mesures de Jones *et al.* [4] et (ligne) calculée à partir de l'impédance large bande. Le nombre de Mach de l'écoulement est de 0.335. Extrait de Ref. [46].

Pendant le post-doctorat de R. Troian, nous avons proposé une méthode d'identification large bande de l'impédance [46]. L'idée est de ne pas chercher directement l'impédance fréquence par fréquence mais de chercher les paramètres d'un modèle large bande de l'impédance ; nous avons choisi de chercher l'impédance sous la forme d'une fraction rationnelle, car celle-ci est générale et car cela permet d'utiliser directement la condition limite d'impédance dans le domaine temporel développée précédemment. La méthode d'identification proposée vise alors à trouver les paramètres de l'impédance minimisant à la fois l'erreur sur la perte par insertion et l'erreur sur les niveaux de pression sur la paroi en face du traitement par rapport à la mesure. Un algorithme génétique [55] est utilisé pour résoudre ce problème multi-objectifs. La méthode a été validée pour le cas d'une excitation acoustique par un mode plan avec des mesures de la littérature [4] et pour le cas d'une excitation multimodale avec des mesures synthétisées (c'est-à-dire issues d'une simulation numérique préalable). La figure 8.5 montre un exemple de résultat pour une excitation par une onde plane et un écoulement avec un nombre de Mach de 0.335. On note l'excellent accord entre l'impédance large bande identifiée et celle identifiée pour des fréquences discrètes par Jones *et al.* [4] ainsi que la bonne prédiction de la perte par insertion avec l'impédance large bande identifiée.

8.3 Étude d'instabilités en présence d'écoulement

Des expériences [56] ou des simulations numériques [57] de propagation acoustique au-dessus d'un traitement absorbant en présence d'un écoulement ont montré l'existence d'une instabilité se développant au-dessus du traitement. Cette instabilité est particulièrement problématique pour des simulations dans le domaine temporel. En effet, cette instabilité n'apparaît que pour quelques fréquences d'excitation, typiquement pour des traitements types SDOF près de la fréquence de résonance. Cependant, dans les simulations temporelles, une excitation large bande va nécessairement engendrer l'instabilité.

Durant la thèse de Y. Deng [58], nous avons mis en évidence la présence d'une instabilité au-dessus d'un liner avec un écoulement moyen dans les simulations numériques. Nous avons d'abord mené une analyse modale afin de vérifier que les propriétés de l'instabilité (type, nombre d'onde,

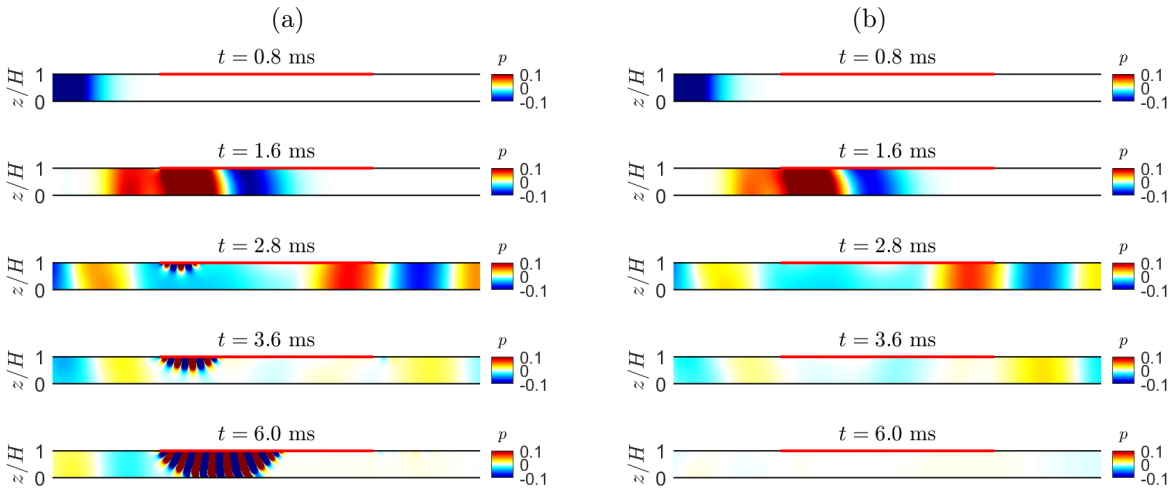

FIGURE 8.6 – Cartographies de la pression acoustique à différents instants obtenues en résolvant (a) les équations d'Euler linéarisées complètes et (b) en supprimant le terme lié au gradient de la vitesse moyenne. Le traitement acoustique en paroi est représentée par une ligne rouge. Extrait de Ref. [58].

forme modale) correspondaient à celles prédites par la théorie. Nous avons ensuite appliqué une méthode pour éliminer l'instabilité dans les simulations temporelles, proposée dans Bogey *et al.* [59] pour les instabilités se développant dans les couches de mélange. Celle-ci consiste à enlever dans l'équation de quantité de mouvement linéarisée le terme proportionnel au gradient de l'écoulement moyen. Une application a été réalisée au cas du conduit NASA GIT avec un traitement de type céramique tubulaire [4], pour lequel une instabilité a été observée dans la littérature [57]. L'analyse modale a montré que la suppression du terme de gradient permettait bien de supprimer l'instabilité. Les simulations numériques correspondantes ont aussi montré l'efficacité de l'approche. Une illustration est donnée sur la figure 8.6. Pour la résolution des équations d'Euler linéarisées complètes, on note d'abord la propagation de l'onde acoustique. Lorsqu'elle est passée au-dessus du traitement, une instabilité apparaît au bord à l'amont. Elle se propage à une vitesse plus faible que celle de l'onde acoustique tout en augmentant en amplitude. Lorsque le terme de gradient est supprimé, l'onde acoustique se propage dans le conduit sans qu'une instabilité soit générée au-dessus du traitement. Nous avons étudié l'impact de la suppression du terme de gradient sur les modes acoustiques ; nous avons montré que ceux-ci étaient aussi modifiés par la suppression du terme de gradient, comme on peut le voir sur la Fig. 8.7 (a). Néanmoins, à haute fréquence (rapport épaisseur de couche limite sur longueur d'onde grande devant le nombre de Mach), les modes acoustiques sont peu impactés par la suppression du terme de gradient (voir Fig. 8.7 (b)). L'article issu de ces travaux est joint en annexe du document.

8.4 Matériaux réalisés en fabrication additive

En liaison avec les travaux autour de la propagation en conduit, nous nous sommes intéressés aux nouvelles techniques de fabrication pour les matériaux. En effet, la fabrication additive ouvre la voie au développement de matériaux acoustiques dont les géométries n'auraient pas pu être envisagées avec les techniques traditionnelles [61, 62]. Des premières études ont montré qu'il est possible d'obtenir des pertes par transmission en conduit importantes sur une large bande de fréquence même pour un traitement de faible épaisseur [63]. Dans le cadre de la thèse d'A. Jamois, nous avons considéré des matériaux périodiques, dont un exemple est représenté sur la Fig. 8.8. L'objectif est d'étudier la pertinence des simulations numériques pour la prédiction des performances acoustiques de ces matériaux en incidence normale et en incidence rasante à partir de la géométrie de la cellule. Pour cela, les équations de Navier-Stokes linéarisées sont résolues dans le domaine fréquentiel par

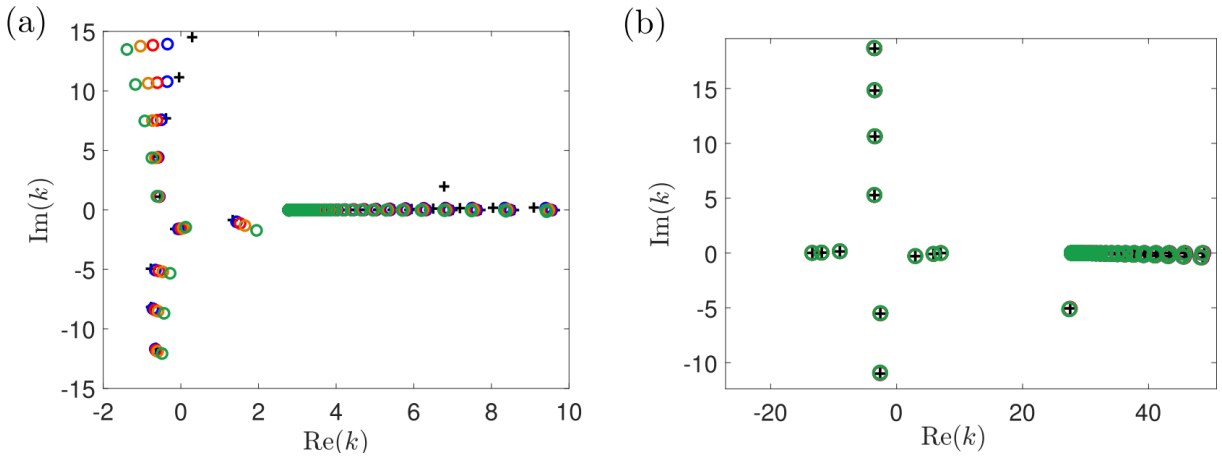

FIGURE 8.7 – Nombres d'onde des modes de conduit pour un écoulement avec un nombre de Mach de 0.3 et pour une fréquence normalisée de (a) 0.93 et (b) de 9.3, calculés à partir (+) des équations d'Euler linéarisées et (∘) avec une suppression graduelle du terme de gradient (la suppression complète correspond au vert). Extrait de Ref. [58].

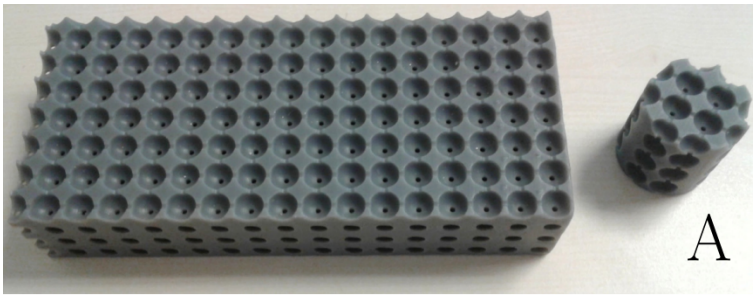

FIGURE 8.8 – Photographie d'échantillons réalisés par impression 3D pour essai en tube de Kundt et en paroi de conduit. Extrait de Ref. [64].

des méthodes éléments finis à l'aide du logiciel commercial COMSOL. Des approches simplifiées de type fluide équivalent sont aussi testées. Les premières comparaisons entre simulations et mesures montrent un bon accord ; cela demande néanmoins des précautions importantes sur la réalisation des échantillons (contrôle des paramètres d'impression) et sur les conditions expérimentales (minimisation des fuites). Ces conclusions doivent être consolidées.

8.5 Conclusions et perspectives

Les travaux sur la propagation en conduit se sont tout d'abord orientés sur la modélisation des traitements absorbants dans des simulations temporelles. L'approche ADE présentée dans le chapitre 6 s'est montrée efficace pour modéliser des interfaces dissipatives, que ce soit un traitement absorbant à réaction locale, un saut d'impédance ou un traitement absorbant à réaction étendue. Une des difficultés posées a été la développement d'instabilités au-dessus de traitements absorbants en présence d'un écoulement. Une méthode a été proposée pour supprimer l'instabilité. Elle s'est montrée efficace mais a le désavantage d'impacter aussi le champ acoustique. Ce travail pourrait être poursuivi en examinant d'autres approches pour supprimer l'instabilité. Il est, cependant, sans doute illusoire d'espérer supprimer l'instabilité sans impacter d'une façon ou d'une autre les ondes acoustiques.

L'étude sur le comportement non-linéaire de traitements absorbants ouvre de nombreuses possibilités. Tout d'abord, un effet notable du comportement non-linéaire des plaques perforées a été montré sur les performances acoustiques. L'étude a été menée numériquement, en se basant sur

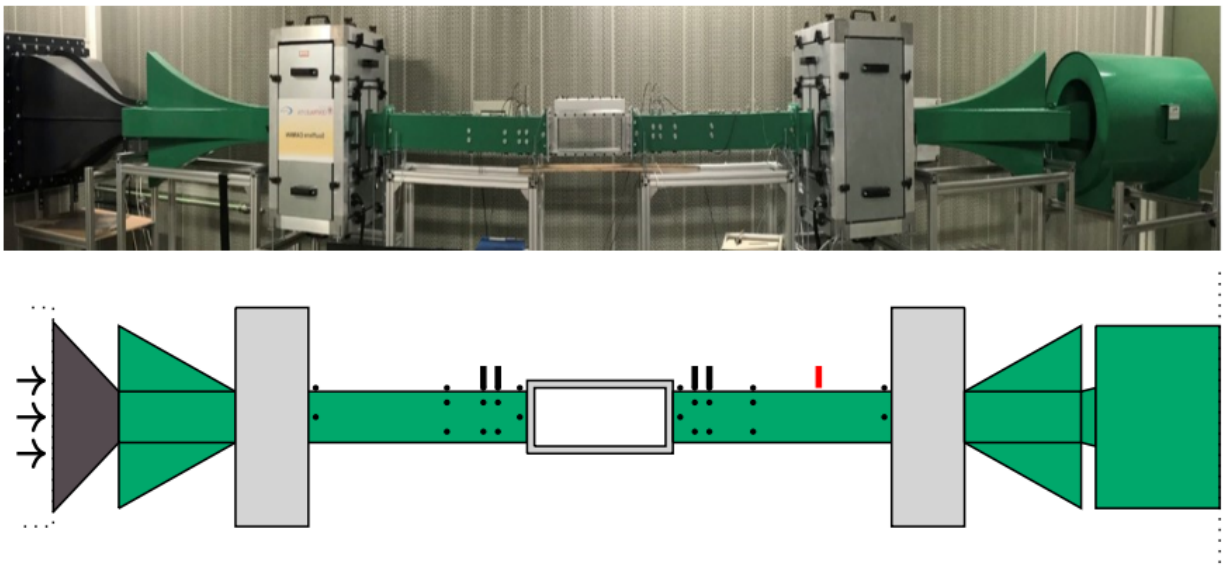

FIGURE 8.9 – Photographie et schéma du banc CAIMAN de Centrale Lyon. Extrait de Ref. [60].

un modèle d'impédance pour les plaques perforées. Il est essentiel de pouvoir confronter ces résultats issus de simulations numériques à des données expérimentales. Ce travail a commencé dans le cadre de la thèse d'E. Sarpero. Pour cela, on s'appuie sur le banc CAIMAN (voir Fig. 8.9) développé récemment au laboratoire. Par ailleurs, l'approche numérique proposée s'appuie sur la notion d'impédance, dont l'extension au régime non-linéaire est, somme toute, limitée. Il serait intéressant de considérer d'autres types de modèles du comportement non-linéaire de plaque perforée. En particulier, la description par des équations différentielles est bien adaptée à une approche temporelle [65, 66] et permettrait de considérer des signaux impulsionnels. A plus long terme, il serait aussi intéressant d'étudier les effets de propagation non-linéaire ; compte-tenu des faibles distances de propagation et des fréquences mises en jeu, les niveaux sonores devront être largement plus importants pour que les effets non-linéaires soient notables (la distance de formation de choc étant d'environ 1 m pour une onde harmonique à 2000 Hz avec une amplitude correspondant à 160 dB).

CHAPITRE 9

Propagation d'ondes de choc

Les approches temporelles sont naturelles pour la prise en compte des effets non-linéaires. Une partie importante de mes travaux de recherche a été réalisée dans ce cadre. Un premier exemple a été montré dans la section 8.1.2 sur le développement d'une condition limite d'admittance non-linéaire pour prendre en compte une réponse non-linéaire d'une interface dissipative.

Ce chapitre porte sur les recherches réalisées autour de la propagation non-linéaire, plus précisément sur la propagation d'ondes de choc. Dans une première section, je décris les études réalisées sur la réflexion d'ondes de choc sphériques sur une surface rugueuse. Je présente ensuite les travaux sur la propagation du bang sonique.

9.1 Étude de la réflexion d'ondes de choc faible

9.1.1 Contexte

Lorsqu'une onde acoustique rencontre une surface plane et lisse, une onde réfléchie est générée. En régime linéaire, les fronts d'onde des ondes incidente et réfléchi s'intersectent à la surface ; suivant la loi de Snell-Descartes, l'angle entre le front d'onde de l'onde réfléchie et la normale à la surface est égal à l'angle d'incidence. Ce n'est néanmoins plus le cas en régime non-linéaire [67], où le schéma de réflexion dépend à la fois de l'amplitude de l'onde incidente et de l'angle d'incidence (voir Fig. 9.1 (a)).

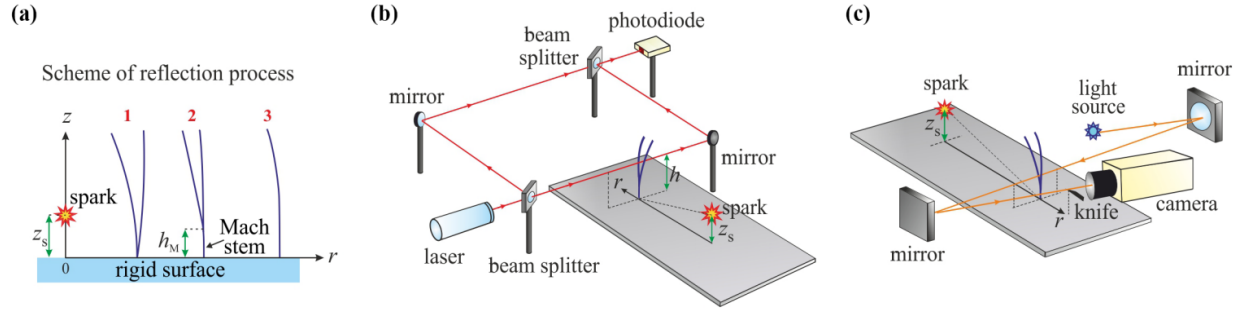

FIGURE 9.1 – (a) Réflexion d'une onde de choc sphérique sur une surface plane. (b) Méthode d'interférométrie. (c) Méthode schlieren. Extrait de Ref. [70].

Dans le cas d'une onde sphérique de forte amplitude, l'intersection des fronts d'onde incident et réfléchi a lieu à proximité de la source au niveau de la surface mais l'angle entre le front d'onde

de l'onde réfléchie et la normale à la surface est différent de l'angle d'incidence. A plus grande distance, l'intersection n'a plus lieu sur la surface mais au-dessus de la surface ; un troisième choc est généré à proximité du sol, appelé pied de Mach. Le point d'intersection des trois chocs est nommé point triple. Les pentes du pied de Mach et du front d'onde incident au point triple tout d'abord diffèrent ; le schéma de réflexion est alors appelé réflexion de Mach. Les pentes du pied de Mach et du front d'onde incident sont ensuite égales ; le schéma de réflexion est alors appelé réflexion de von Neumann.

La réflexion en régime non-linéaire a été étudiée au laboratoire pendant la thèse de M. Karzova et le post-doc de C. Desjouy. Pour cela, des expériences ont été menées à l'échelle du laboratoire en utilisant une source à arc électrique. Celle-ci génère des ondes impulsionnelles, dont la forme d'onde est comparable à celle d'ondes de souffle : elle est constituée tout d'abord d'une compression avec un choc suivi d'une détente sans choc. En champ libre, la pression maximale est d'environ 0.8 kPa, la durée de 50 µs et l'épaisseur du choc de 100 µm à une distance de 30 cm de la source. Des mesures microphoniques et optiques (schlieren et interférométrie) ont été réalisées. Les visualisations schlieren (voir Fig. 9.1 (c)) permettent d'observer le schéma de réflexion. Les mesures interférométriques (voir Fig. 9.1 (b)), sous des hypothèses de symétrie du champ de pression, permettent une mesure de la forme d'onde, avec une fréquence maximale plus élevée que la mesure microphonique.

Des premières simulations numériques ont été réalisées dans la Ref. [68] ; des comparaisons des schémas de réflexion mesurés par imagerie schlieren et déterminés à partir des résultats numériques ont été réalisés pour différentes amplitudes de la source et différents angles d'incidence. Un bon accord a été obtenu.

9.1.2 Comparaison avec l'expérience

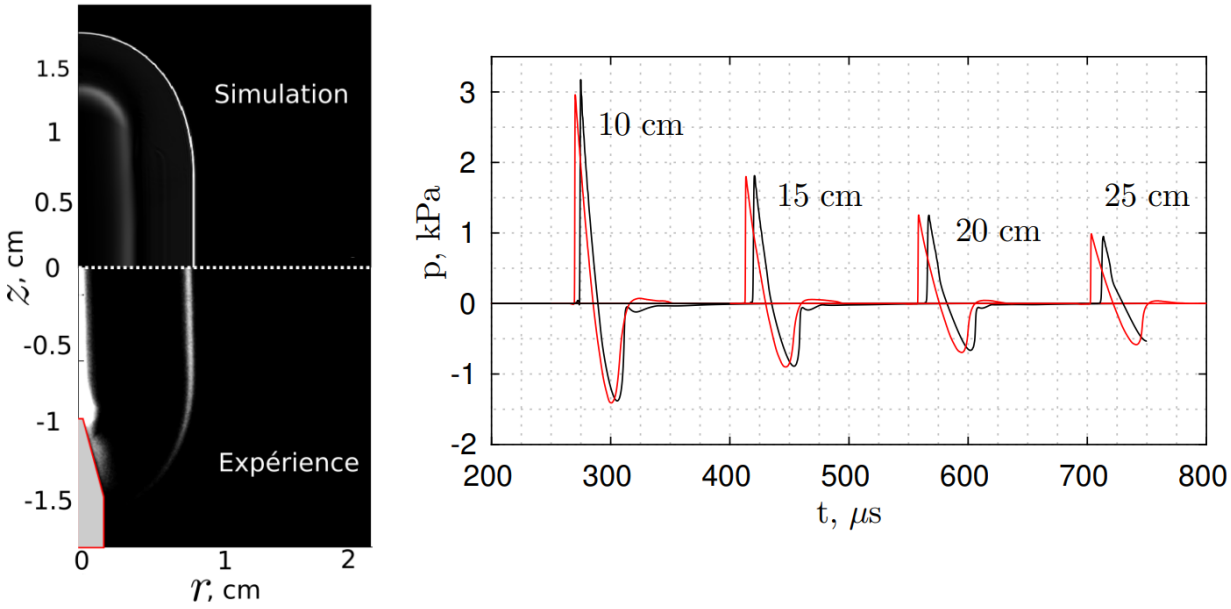

FIGURE 9.2 – (gauche) Visualisation schlieren de l'onde de choc générée par une source à arc électrique issue de l'expérience et de la simulation numérique. (droite) Formes d'ondes en champ libre à différentes distance de la source ——— mesurées par interférométrie et ——— obtenues par simulation numérique. Extrait de Ref. [69].

Les travaux sur la réflexion d'ondes de choc faible ont été poursuivis dans la thèse de Thomas Lechat. La première partie de la thèse a été consacrée à une comparaison fine entre résultats des expériences à l'échelle et des simulations numériques, basées sur la résolution des équations d'Euler en coordonnées curvilignes. Tout d'abord, une modélisation de la source à arc électriques a été réalisée. Pour cela, un modèle de source linéique a été développé. Des simulations numériques ont

d'abord été réalisées pour déterminer la largeur et l'amplitude de la source linéique permettant de reproduire en champ libre la forme d'onde mesurée par interférométrie (voir Fig. 9.2). La directivité ainsi que les effets des électrodes ont été analysés et comparés à des modèles de la littérature. Un modèle simplifié avec une source monopolaire a aussi été proposé.

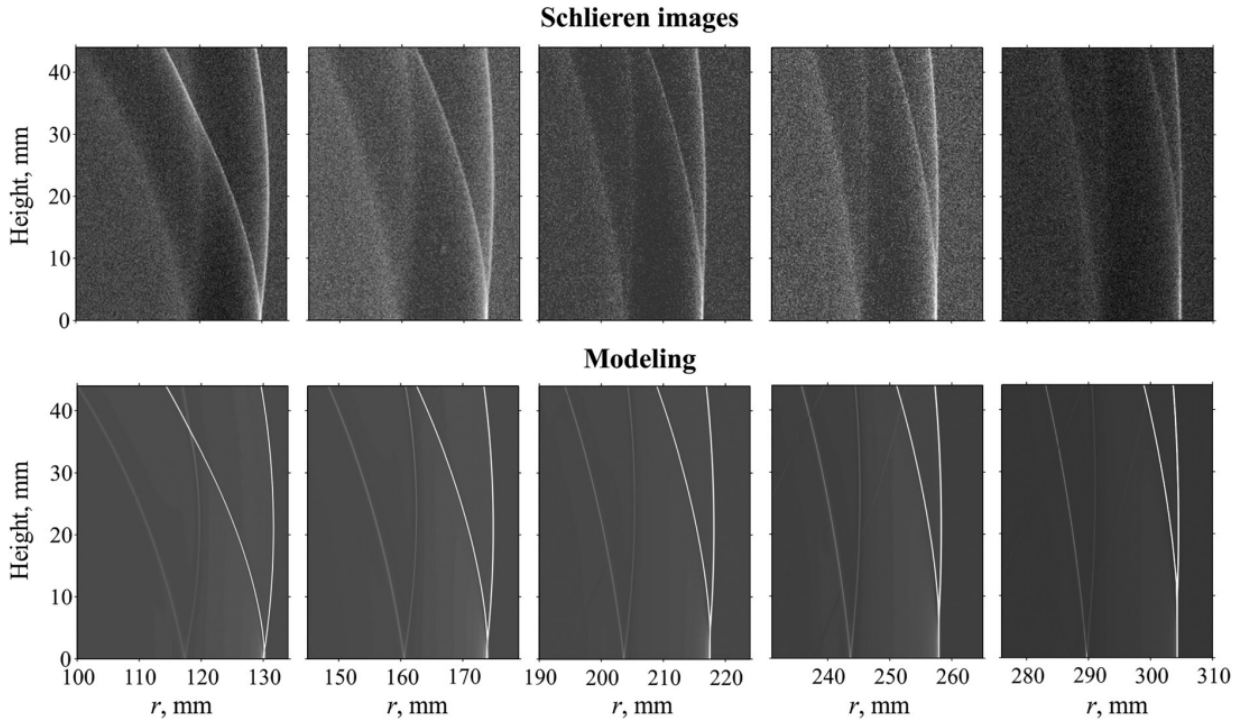

FIGURE 9.3 – Visualisation schlieren de la réflexion d'une onde de choc générée par une source à arc électrique à différentes distances (haut) issue de l'expérience et (bas) de la simulation numérique. Extrait de Ref. [70].

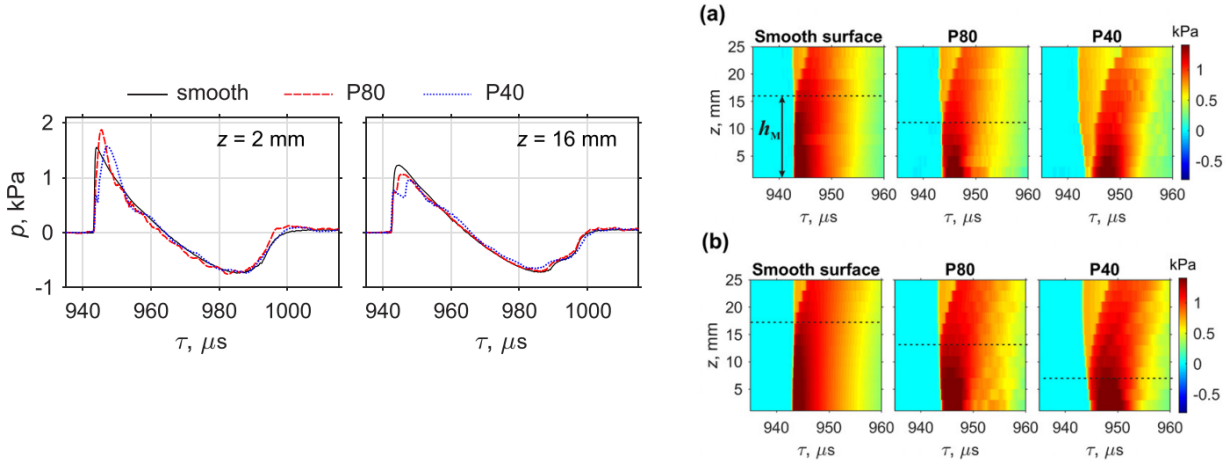

FIGURE 9.4 – Propagation d'ondes de choc sur une surface rugueuse : (gauche) formes d'onde mesurées par interférométrie au-dessus d'une surface lisse et de deux surfaces rugueuses et (droite) schéma de réflexion (haut) issue de l'expérience et (bas) de la simulation numérique. Extrait de Ref. [71].

Une première comparaison a été faite dans le cas de la réflexion sur une surface plane et lisse [70]. Pour une hauteur de source fixée, les formes d'onde mesurées par interférométrie ont été comparées avec succès à celles obtenues par simulation numérique pour différentes hauteurs de récepteur. Une comparaison a ensuite été réalisée entre les schlieren expérimentaux mesurés à différentes distances

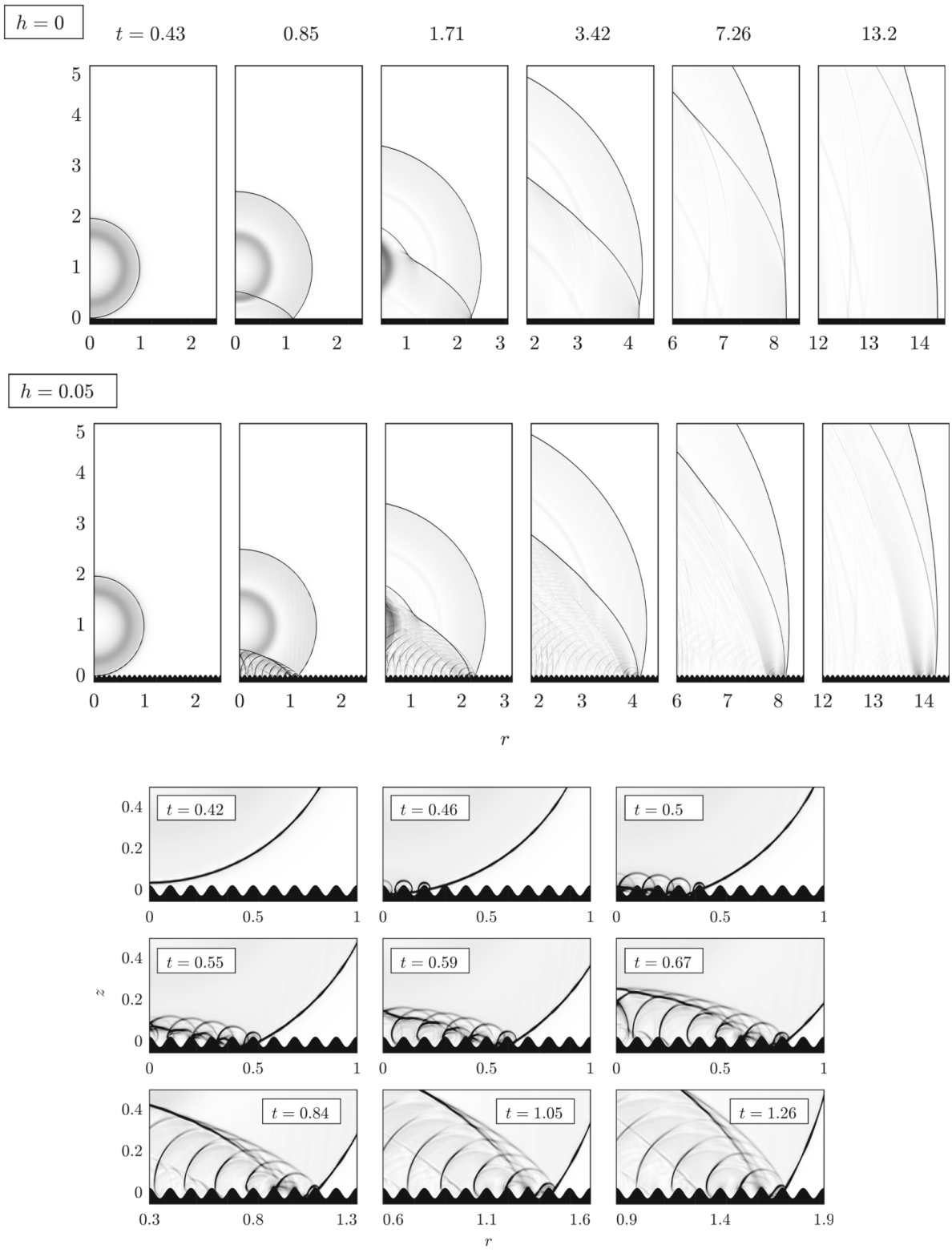

FIGURE 9.5 – (haut) Visualisation schlieren de la propagation d'une onde de choc au-dessus d'une surface lisse ($h = 0$) et d'une surface rugueuse ($h = 0.05$) à différents instants. (bas) Zoom proche de la paroi pour la surface rugueuse. Extrait de Ref. [72].

de la source et ceux déterminés à partir des solutions numériques (voir Fig. 9.3). Un accord global sur le schéma de réflexion a été obtenu. Enfin, les trajectoires du point triple déduites des mesures schlieren, des mesures interférométriques et des simulations numériques ont été comparées, montrant là aussi des trajectoires proches entre les différentes approches et similaires aux trajectoires attendues

pour les points triples pour les ondes de souffle.

Une seconde comparaison expérience/simulation numérique a été réalisée pour la réflexion sur une surface plane et rugueuse [71]. Pour cela, deux surfaces rugueuses ont été créées en collant du papier de verre avec deux tailles de grain différentes sur un support lisse. Des mesures de l'état de surface ont été réalisées à l'aide d'un microscope électronique. Les paramètres statistiques déduits (hauteur de rugosité, longueur de corrélation) ont permis de générer les profils des hauteurs de surface pour la simulation numérique. Les formes d'ondes expérimentales ont été relevées par méthode interférométrique à une distance de 33 cm et à différentes hauteurs (voir Fig. 9.4). Il en a été déduit que la rugosité induisait une réduction du pied de Mach par rapport au cas d'une surface lisse. De plus, le pied de Mach n'a pas été observé pour la taille de grain la plus grosse. Par ailleurs, la pression maximale était plus importante à proximité de la paroi pour les deux surfaces rugueuses que pour la surface lisse. La forme d'onde correspondante présentait, au lieu d'un choc net pour la surface lisse, une montée beaucoup plus lente. Les simulations numériques ont permis de retrouver qualitativement ces résultats. En particulier, les formes d'ondes obtenues étaient en bon accord avec celles déterminées expérimentalement.

9.1.3 Étude numérique

Dans une seconde partie de la thèse de T. Lechat, une étude paramétrique [72] a été réalisée afin d'analyser en détail l'effet de la rugosité sur la réflexion d'ondes de souffle. Du fait du bon accord entre mesure et simulation numérique, l'étude a été menée numériquement. Les simulations numériques ont été réalisées pour une rugosité périodique avec des échelles de rugosité correspondant à celles utilisées dans l'expérience. Tout d'abord, nous avons pu noter que la diffraction de l'onde de choc incidente par les aspérités de la surface conduisait à une onde de choc réfléchie scindée en deux parties : une issue de la diffraction sur le haut des aspérités et l'autre de la diffraction sur le bas des aspérités (voir Fig. 9.5). Cette dernière est de plus forte amplitude et peut interagir avec le choc incident pour former un pied de Mach. Ce phénomène explique la réduction de la hauteur du pied de Mach et l'absence de point triple pour les tailles de rugosité importantes.

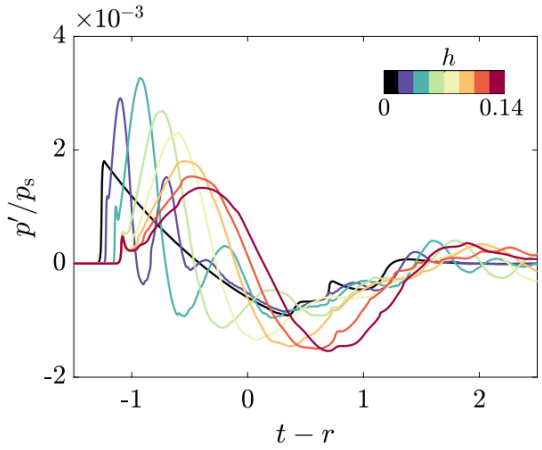

FIGURE 9.6 – Forme d'onde de la pression proche de la paroi pour une surface lisse ($h = 0$) et pour des surfaces rugueuses avec différentes échelles de rugosité. Extrait de Ref. [72].

Nous nous sommes intéressés aux formes d'ondes proches de la paroi (voir Fig. 9.6). Nous avons retrouvé comme dans l'expérience que la surpression proche de la surface était plus importante pour les rugosités faibles que pour une surface lisse. Cela n'est pas lié au choc, dont l'amplitude a tendance à diminuer avec la rugosité, mais à une oscillation qui apparaît après le choc et dont la période dépend de la rugosité. Nous avons associé ce comportement à la présence d'une onde de surface, dont l'existence au-dessus d'une surface rugueuse a été démontrée en acoustique linéaire à la fois théoriquement et expérimentalement. L'article issu de ces travaux est joint en annexe du document.

9.2 Bang sonique

9.2.1 Contexte

Les avions supersoniques génèrent une onde de choc attachée au fuselage. Le bang sonique correspond à l'onde résultante se propageant jusqu'au sol. Pour un avion supersonique standard, le signal de pression au sol correspond à un signal impulsionnel de type onde en N. Il est à noter que le bang sonique est présent tout le long du parcours de l'avion et qu'il impacte l'ensemble de la population se trouvant sous la trajectoire de l'avion. La première génération d'avions supersoniques dans les années 1960, représentée par le Concorde, causait des bang soniques de forte amplitude. Cela a motivé l'interdiction du survol supersonique des terres par les avions civils dans la plupart des pays, qui est toujours en vigueur.

Des projet industriels (Boom Overture) et des travaux de recherche [73] sont en cours afin de faire revivre des avions commerciaux supersoniques. En particulier, une conception minutieuse de la géométrie du fuselage permet de générer un bang sonique de bien plus faible amplitude, appelé low-boom. Des premières expériences [74] ont montré la faisabilité de l'approche en modifiant la géométrie d'un avion militaire. L'avion expérimental X-59 a été conçu spécifiquement pour générer un low-boom et doit permettre dans les années à venir d'évaluer l'acceptation du low-boom par la population. A terme, cela pourrait permettre la levée de l'interdiction du survol des terres par les avions supersoniques civils.

La prédiction du bang sonique au sol nécessite de calculer l'onde de choc autour de l'avion et sa propagation depuis l'avion jusqu'au sol. Habituellement, deux simulations différentes sont réalisées et la forme d'onde issue d'un calcul champ proche autour de l'avion est utilisée pour initialiser le calcul de la propagation. Récemment, des premières études [78] ont proposé une résolution simultanée de la génération du bang autour de l'avion et de sa propagation dans une atmosphère stratifiée jusqu'au sol. Le bang sonique au sol est impacté par les propriétés de l'atmosphère dans laquelle il s'est propagé ainsi que par les caractéristiques du sol (géométrie, absorption). Les études dans la littérature se sont principalement portés sur le premier point, notamment sur l'effet de la turbulence atmosphérique sur le bang. Des approches géométriques ou paraxiales (par exemple les études récentes [75, 76, 77]) sont généralement employées.

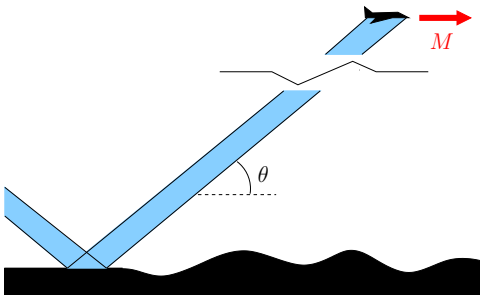

FIGURE 9.7 – Schéma de la propagation du bang au-dessus d'un sol non-plan. Extrait de Ref. [81].

Dans le cadre du projet européen RUMBLE, nous nous sommes intéressés à l'effet de la topographie et de l'environnement urbain sur le bang au sol. Pour cela, nous avons utilisé une approche originale basée sur la résolution par méthode différences finies des équations d'Euler en coordonnées curvilignes. Celle-ci permet de prendre en compte la diffraction sans approximation. En particulier, elle permet de simuler les réflexions multiples se produisant entre les bâtiments pour un environnement urbain. Une des difficultés de l'approche reste le coût numérique. Bien que l'onde du bang ait un contenu fréquentiel basse fréquence, l'estimation du niveau de bruit perçu donne un poids bien plus important aux moyennes fréquences. Pour un onde de bang présentant un choc (comme l'onde en N), il faut donc discrétiser suffisamment le choc pour éviter une dissipation numérique qui fausserait le calcul du niveau sonore.

9.2.2 Effets de la topographie

Pendant le post-doctorat d'A. Emmanuelli, nous avons examiné l'effet de la topographie sur le bang sonique (voir Fig. 9.7). La littérature est très succincte sur le sujet hormis des études expérimentales menées dans les années 1960 [79]. Une première partie du travail a été de développer des méthodes numériques spécifiques pour la propagation du bang : technique d'injection de l'onde du bang comme condition limite du domaine, mise en place d'une fenêtre glissante supersonique qui suit la propagation du bang incident pour réduire le temps de calcul et implémentation d'une condition de type PML comme condition de non-réflexion.

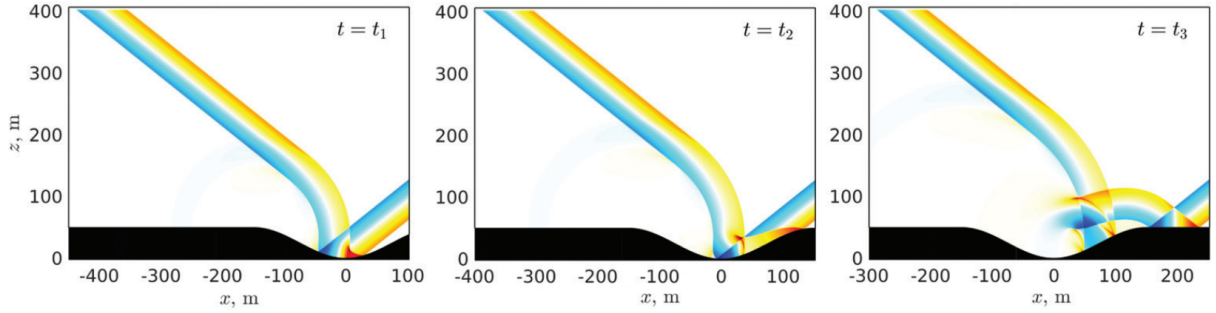

FIGURE 9.8 – Cartographies de la pression acoustique à trois instants successifs montrant la diffraction d'un bang sonique incident par une dépression de terrain. Extrait de Ref. [80].

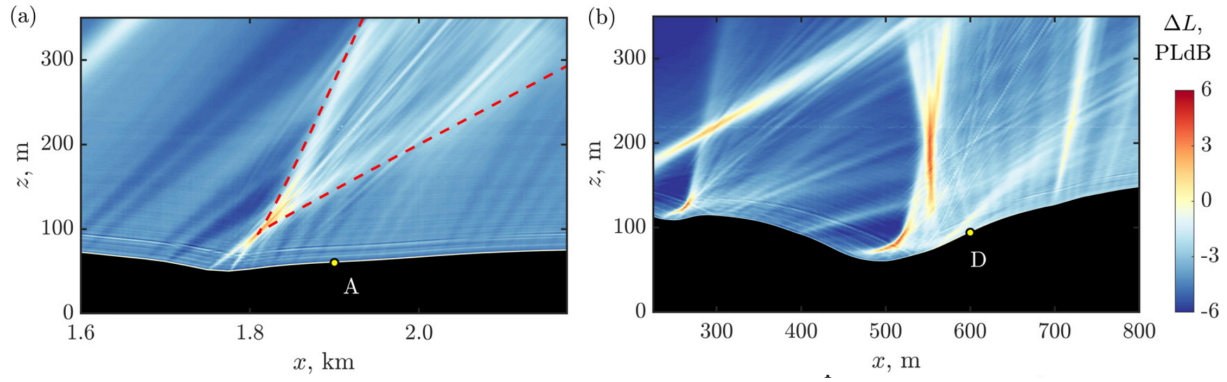

FIGURE 9.9 – Cartographies du niveau de pression normalisé pour l'onde low-boom au dessus d'une dépression de terrain avec (a) un grand rayon de courbure et (b) un rayon de courbure plus petit. Extrait de Ref. [81].

Une première étude [80] a été réalisée en définissant des profils de terrains académiques, à savoir une dépression de terrain, une colline et une succession de collines. Des simulation numériques bidimensionnelles ont été effectuées pour deux formes d'onde de bang, une onde en N et une onde de type low-boom. Nous avons montré qu'une paroi concave pouvait agir comme un miroir et induire une focalisation du bang incident. Les cartographies de pression instantanée sur la Fig. 9.8 montrent ainsi un repliement du front d'onde réfléchie induit par la focalisation. Cela se traduit pour les formes d'onde au niveau du sol par une arrivée secondaire, qui apparaît pour l'onde en N sous la forme d'une onde en U. Les champs de pression instantanée obtenus par résolution des équations d'Euler ont été comparés avec un calcul de fronts d'ondes par une méthode de lancer de rayons ; un excellent accord a été obtenu entre les deux approches. Les niveaux de bruit le long des profils ont été examinés : par rapport à un sol plan, la topographie induit une augmentation notable de 5-6 dB. Enfin, les niveaux de bruits obtenus pour l'onde en N et l'onde type low-boom ont été comparés. Nous avons montré que les variations des niveaux dues à la topographie sont similaires pour les deux ondes de bang. L'article issu de ces travaux est joint en annexe du document.

L'étude a été poursuivie dans la Ref. [81] en considérant des profils de terrain réels. Deux profils

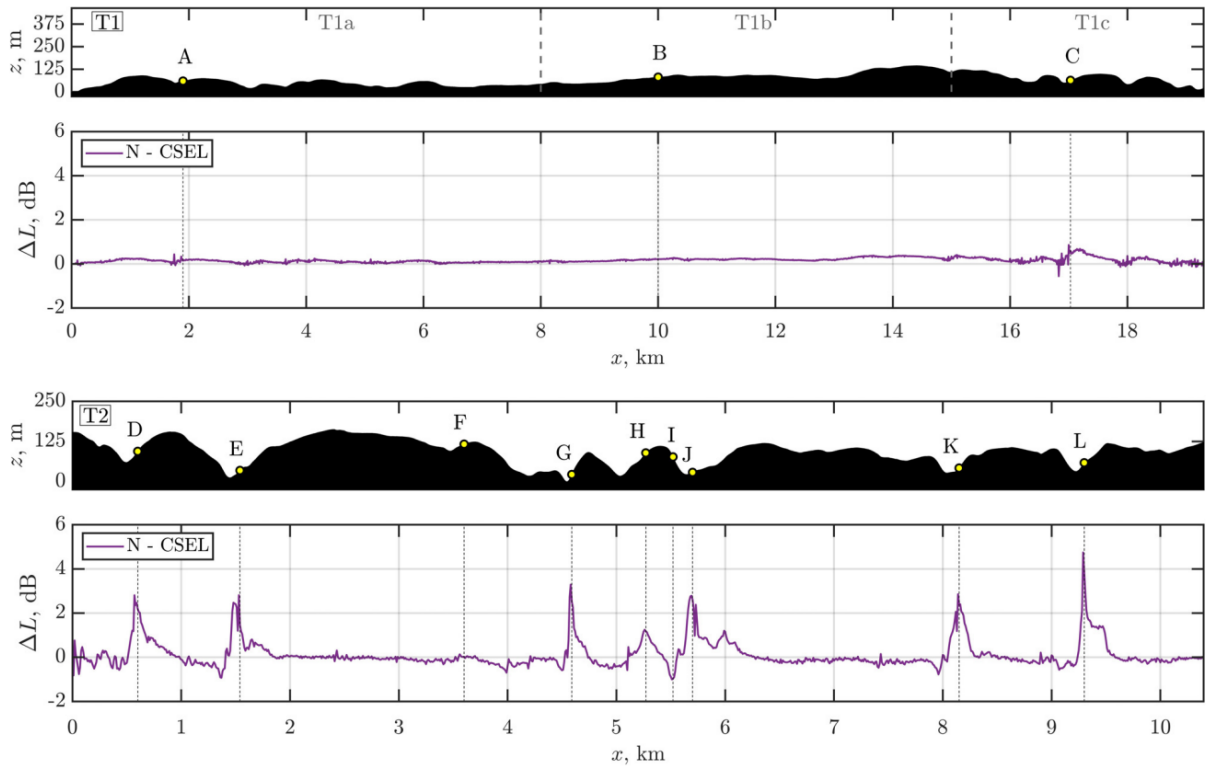

FIGURE 9.10 – Évolution du niveau de pression normalisé au sol le long de deux profils réels de sol. Extrait de Ref. [81].

de plus de 10 km de long ont été extraits de données topographiques fournies par l'IGN. Les deux profils présentent des variations de hauteurs de terrain comparables mais des variations de pente différentes. Pour le profil de terrain présentant des variations de pente douces, la focalisation par la topographie se produit près des dépressions de terrain (voir Fig. 9.9 (a)) ; cependant, la focalisation a lieu au-dessus du sol et les niveaux de bruit au sol sont très peu impactés par la topographie. Pour le profil de terrain avec des variations de pente plus importantes, la focalisation induite par la topographie se produit à proximité du sol (voir Fig. 9.9 (b)) et les niveaux sonores au sol augmentent fortement à proximité des dépressions de terrain. L'évolution des niveaux sonores normalisés par leur valeur au-dessus d'un sol plan est représentée le long des deux profils sur la figure 9.10. Pour le profil avec des variations de pente douce, le niveau sonore est très proche de celui d'un sol plan. Par contre, pour le profil avec des variations de pente plus importantes, le niveau sonore augmente à proximité des dépressions de terrain avec un rayon de courbure suffisamment petit. La variation reste néanmoins très locale : l'augmentation maximale du niveau sonore au sol est de 7 dB mais une augmentation de plus de 2 dB n'est observée que pour seulement 5 % de la surface au sol.

9.2.3 Réflexion du bang sonique en milieu urbain

L'étude sur la propagation du bang sonique a été poursuivie pour le cas d'un environnement urbain. Cela est d'un intérêt considérable pour les avions supersoniques de type low-boom, car il est espéré que ces avions pourront voler au-dessus des villes. Il est donc crucial de savoir comment l'environnement urbain modifie le bang au sol. La plupart des études expérimentales ou numériques dans la littérature se sont portés sur un bâtiment isolé [82, 84].

Dans la Ref. [85], nous avons étudié la réflexion et la propagation du bang sonique dans des configurations urbaines simples, à savoir un bâtiment isolé, deux bâtiments parallèles et un ensemble de bâtiments identiques régulièrement espacés. Pour un bâtiment isolé, on retrouve une zone illuminé à l'avant du bâtiment avec une augmentation du niveau de bruit et une zone d'ombre à l'arrière du bâtiment avec un réduction très forte des niveaux (voir Fig. 9.11). Pour le cas de deux bâtiments

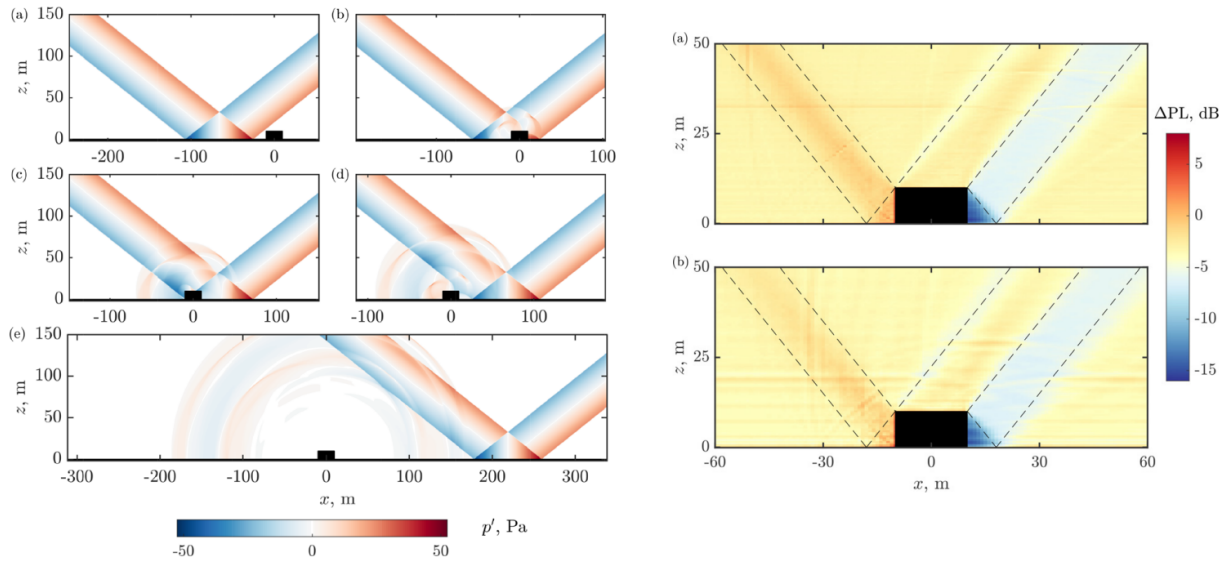

FIGURE 9.11 – (gauche) Cartographies de pression instantanée à différents instants. (droite) Niveau de pression normalisé en haut pour l'onde en N et en bas pour l'onde low-boom. Extrait de Ref. [85].

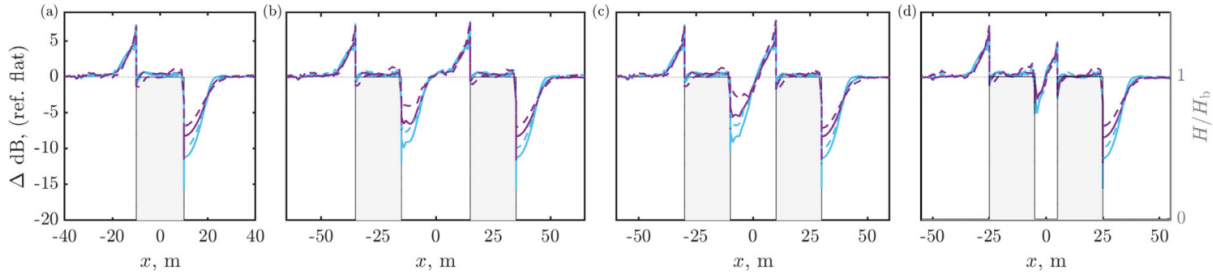

FIGURE 9.12 – Évolution du niveau de pression normalisé le long du sol et des bâtiments pour différents cas : a) bâtiment isolé et b), c) d) deux bâtiments avec différentes largeurs de rue. Les lignes pleines correspondent à l'onde en N et les lignes pointillées à l'onde low-boom. Deux métriques sont utilisées pour déterminer les niveaux sonores et sont représentées par les deux couleurs. Extrait de Ref. [85].

parallèles, des réflexions multiples sur les façades des bâtiments se produisent et induisent des arrivées supplémentaires dans le canyon entre les bâtiments. De plus, des oscillations basses fréquences peuvent être observées sur les formes d'ondes de la pression à la suite des arrivées géométriques. Les fréquences des oscillations correspondent aux fréquences de résonances d'une cavité semi-ouverte. L'amplitude des oscillations et la constante de temps associée à leur décroissance dépendent de la largeur de la rue et de la forme d'onde considérée. Les niveaux de bruit dans le canyon dépendent fortement du rapport d'aspect entre la hauteur du bâtiment et la largeur de la rue (voir Fig. 9.12). Ainsi, lorsque les bâtiments sont éloignés l'un de l'autre, les niveaux de bruit sont proches de ceux pour un bâtiment isolé. Au contraire, lorsque les bâtiments sont proches, les niveaux de bruit dans le canyon tendent à s'uniformiser. Dans tous les cas, les oscillations basse fréquence contribuent peu aux niveaux de bruit. Enfin, dans le cas de bâtiments identiques régulièrement espacés, les arrivées géométriques dans les canyons sont comparables à celles obtenues dans le cas de deux bâtiments parallèles mais les contributions basses fréquences tendent à durer plus longtemps.

Nous avons continué l'étude dans la Ref. [86] en considérant des géométries urbaines dont les caractéristiques (taille des bâtiments et largeurs des rues) correspondent à des environnements urbains réalistes. Pour cela, nous nous sommes basés sur la classification LCZ [87] pour "Local Climate Zone" qui groupe les géométries urbaines en dix catégories. Nous avons réalisé des simulations numériques pour chacune des dix classes LCZ pour l'onde en N et l'onde low boom. Pour le bang sonique,

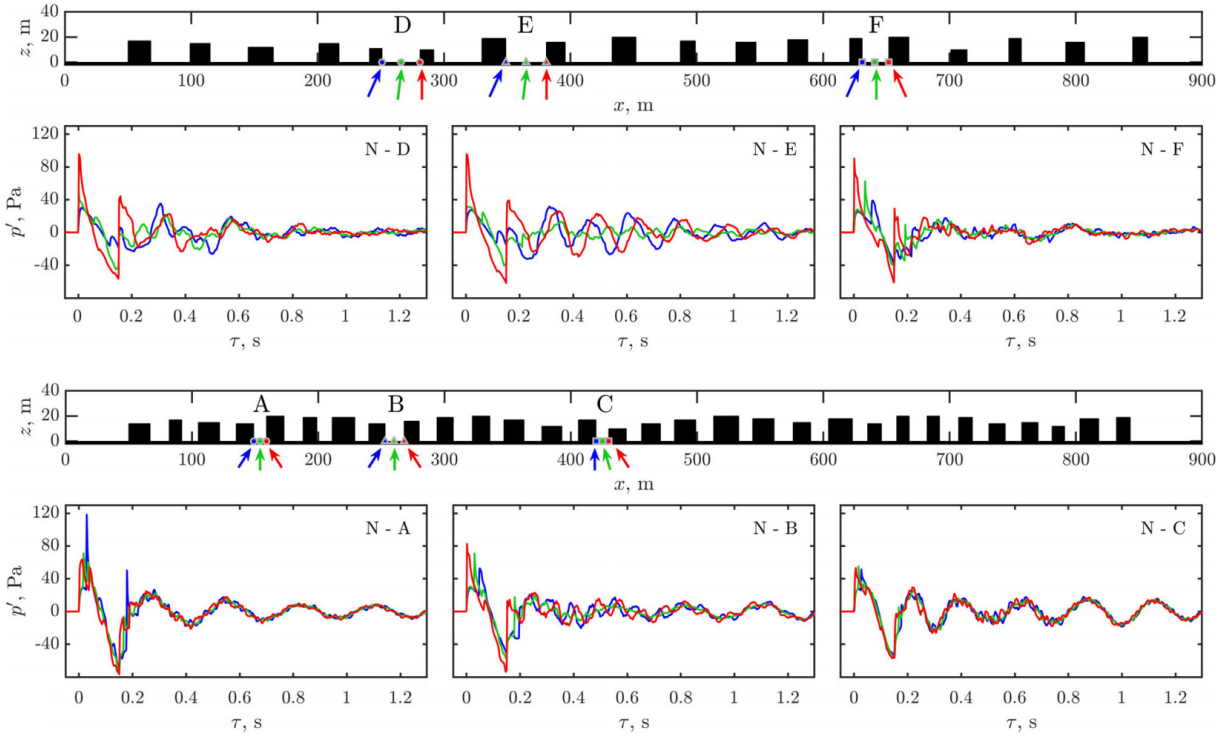

FIGURE 9.13 – Formes d'onde pour une onde en N incidente dans trois canyons pour une géométrie urbaine (haut) ouverte et (bas) compacte. Extrait de Ref. [86].

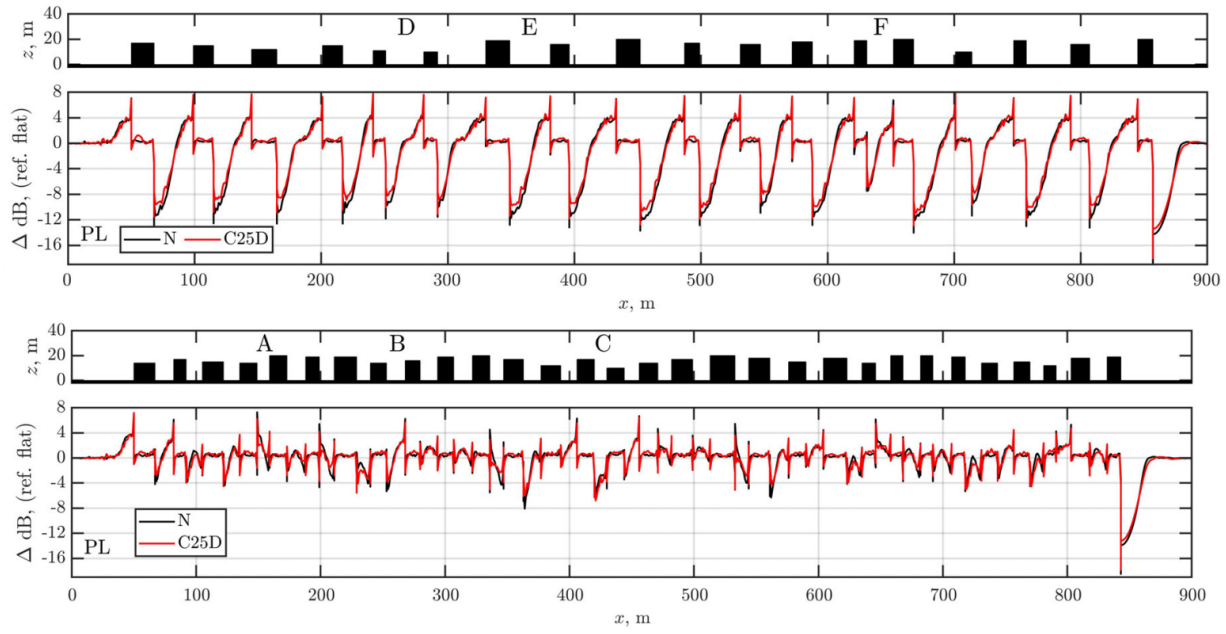

FIGURE 9.14 – Niveaux de pression normalisés pour deux profils urbain correspondant (haut) à une géométrie ouverte et (bas) une géométrie compacte et pour les deux ondes de bang soniquek. Extrait de Ref. [86].

on peut regrouper les résultats en deux grandes catégories suivant le rapport d'aspect moyen du profil urbain. Pour les géométries "ouvertes" (profils ayant un rapport d'aspect faible, avec des rues larges par rapport à la hauteur des bâtiments), les résultats (arrivées géométriques pour les formes d'ondes, niveaux sonores) sont très similaires pour les différents bâtiments du profil (voir Figs. 9.13 et 9.14) et correspondent à ceux d'un bâtiment isolé. Pour les géométries "compactes" (profils ayant

un rapport d'aspect important, avec des rues étroites), les signaux de pression varient fortement d'un canyon urbain à l'autre. Les niveaux de pression ont cependant tendance à être moins dispersés que pour les géométries ouvertes. Les oscillations basses fréquences, liées à des modes de cavité, sont observées pour tous les profils urbains. Enfin, nous avons montré que ces conclusions étaient valables pour une onde en N ou une onde low-boom.

9.3 Conclusions et perspectives

De nombreuses pistes ont été ouvertes sur l'acoustique non-linéaire. Les travaux autour de la propagation d'ondes de choc sphériques au-dessus d'une surface rugueuse pourraient avoir une suite directe en considérant des surfaces absorbantes. Les outils numériques pour réaliser une telle étude sont déjà développés. Par ailleurs, des modélisations d'une surface rugueuse par une surface plane avec une impédance de surface équivalente ont été proposées dans la littérature en acoustique linéaire [88]. Il serait intéressant de voir si ces approches sont aussi pertinentes dans le régime non-linéaire. En particulier, on peut se demander si le schéma de réflexion et l'onde de surface seraient bien reproduites avec une condition limite d'impédance équivalente.

Les différentes études autour du bang sonique ont aussi montré l'intérêt d'une résolution temporelle des équations de la mécanique des fluides pour prédire la trace du bang au sol, à la fois avec la prise en compte des caustiques produites par la topographie et de la diffraction et des réflexions multiples dans un environnement urbain. Les simulations ont été réalisées pour des configurations bidimensionnelles ; une extension directe est de considérer les effets tridimensionnels. En particulier, la poursuite de l'étude en environnement urbain pour une onde low-boom semble tout à fait envisageable d'un point de vue des contraintes de coût numérique. Ensuite, toutes les simulations ont été effectués pour une atmosphère homogène et au repos. L'inclusion de profils réalistes de vent et de température, notamment en environnement urbain, serait un ajout important. Enfin, un dernier aspect est la propagation du bang en atmosphère turbulente ; il serait aussi possible avec l'approche choisie de prendre en compte simultanément les effets de la turbulence et d'une géométrie complexe.

Les travaux autour de l'acoustique non-linéaire se poursuivent également au sein du LETMA. Bien que cela ne soit pas détaillé dans ce manuscrit, j'ai participé au développement une plate-forme numérique commune regroupant différents codes des partenaires du LETMA pour la propagation des infrasons, notamment à travers le post-doc de C. Khodr. Une activité autour de la propagation d'ondes de souffle dans l'atmosphère en conditions réalistes est envisagée et est une continuation directe des travaux présentés dans cette partie. Une autre activité concerne la propagation des ondes de choc générées par les éclairs. Cette recherche, menée avec E. Salze et le laboratoire Ampère, est en lien avec les travaux de T. Farges et F. Coulouvrat sur les éclairs naturels pour utiliser les signaux acoustiques mesurées pour caractériser l'éclair (localisation, énergie, ..) [89]. L'objectif est d'étudier via des mesures acoustiques et optiques les ondes de choc produites par un éclair d'une longueur de 1 m produite par la tour haute tension du laboratoire Ampère en environnement contrôlé [90]. Elle a donné lieu au stage de M2 de L. Bellaton. L'étude est pour l'instant expérimentale. Un volet numérique pourrait être un apport intéressant, notamment pour mieux comprendre le lien entre la géométrie de l'éclair et les ondes acoustiques générées.

Enfin, la thèse de G. Coco a récemment démarré sur la propagation d'ondes de choc avec SAFRAN Aircraft Engines dans le cadre de la chaire ARENA. On s'intéresse ici aux chocs générés en bout de pales du rotor de moteurs d'avions en régime transsonique pour les futures architectures open rotor. En effet, ces moteurs ne seront plus carénés et le choc généré en bout de pale va se propager librement jusqu'au fuselage. Il est alors nécessaire de déterminer l'excitation du fuselage par le choc afin de pouvoir prédire les niveaux de bruits en cabine de l'avion. Pour cela, a partir de champs RANS décrivant les chocs à proximité du moteur, on résoudra les équations d'Euler pour propager les chocs en prenant en compte l'écoulement moyen autour du fuselage avec la couche limite et la diffraction par le fuselage.

CHAPITRE 10

Conclusions et perspectives générales

Dans cette partie du mémoire, j'ai résumé mes activités de recherche, dont le thème central est la propagation acoustique dans le domaine temporel. Les travaux menés autour de trois axes de recherche, à savoir l'acoustique environnementale, la propagation en conduit et l'acoustique non-linéaire ont été détaillés. Des perspectives pour les années à venir ont été données à la fin de chaque chapitre. Je termine ce mémoire en récapitulant ces pistes de recherche.

Méthodes numériques

Les méthodes numériques utilisées sont efficaces pour la propagation longue distance. Une des limitations fortes des méthodes différences finies, basées sur des maillages structurées, reste la prise en compte de géométries quelconques. Les techniques de maillages curvilignes sont efficaces pour tenir compte de déformations locales de parois mais ne sont pas adaptées à la prise en compte d'objets diffractants de formes quelconques dans le domaine. Les techniques de frontières immergées semblent bien adaptées pour s'affranchir de cette difficulté. Des premières études dans la littérature ont appliqué cette méthode avec des conditions limites d'impédance pour des obstacles [91] ou des parois en mouvement [92]. Cette approche pourrait permettre d'étudier la diffraction par des obstacles de géométrie plus complexe que des pavés droits. Elle serait aussi utile pour analyser le rayonnement de structures vibrantes (immobiles ou en mouvement) dans des configurations réalistes.

Acoustique environnementale

Pour l'acoustique environnementale, le projet se poursuit à court terme autour d'application en bruit des transports. L'objectif est de développer un modèle rapide du rayonnement de sources en mouvement avec une trajectoire quelconque au-dessus d'un sol absorbant avec la prise en compte des profils de vent et de température pour des applications en aéronautique. De plus, les applications liées à l'acoustique environnementale sont sans aucun doute porteuses vis-à-vis des enjeux actuels autour du développement durable et de la biodiversité.

Les travaux en bioacoustique montrent l'intérêt d'avoir des modèles physiques fins pour améliorer l'étude des réseaux de communication. Un vaste champ d'étude est ouvert. Une suite directe des travaux peut porter sur l'étude de la propagation des signaux de vocalisations, soit avec des méthodes fréquentielles par reconstruction par synthèse de Fourier soit directement avec des méthodes temporelles. Cela permettrait d'étudier la communication avec des informations plus détaillées qu'un niveau de pression global. En particulier, les espaces de communication, associés à des informations contenues dans le signal, pourraient être déterminés. Un des enjeux de la collaboration est aussi

l'échange entre communautés scientifiques dont le langage et les pratiques sont largement différentes. Il est ainsi nécessaire d'employer des modèles adaptés et réutilisables par la communauté bioacoustique tout en gardant la complexité physique souhaitée.

L'étude sur le bruit des éoliennes ouvre de nombreuses possibilités. L'accès à des champs de vitesse et de température issus de données LES permet de s'affranchir de profils analytiques, qui restent limités à des configurations simples. Le chaînage entre données LES, modèle de source et code de propagation reste lourd, à cause du nombre de sources important à prendre en compte et donc du nombre de simulations de propagation à réaliser. Néanmoins, cela permet d'obtenir des informations détaillées sur le bruit des éoliennes, comme les modulations d'amplitude, qu'un modèle simplifié avec une source équivalente serait incapable de fournir. De nombreuses études autour des parc éoliens restent à réaliser. Tout d'abord, les premiers résultats ont montré l'importance de la stabilité atmosphérique sur la propagation du bruit pour une éolienne : on a, en particulier, mis en évidence l'augmentation des niveaux moyens et des modulations d'amplitude pour une atmosphère stable. Ces travaux sont à poursuivre pour un parc éolien. De plus, les premières simulations avec une équation parabolique 3D ont montré que les effets tridimensionnels dus au sillage sont notables. Les calculs ont pour l'instant été limités aux basses fréquences. Il serait pertinent d'étendre le calcul à des fréquences plus élevées pour quantifier les effets tridimensionnels sur des niveaux sonores globaux. Bien sûr, les effets tridimensionnels seraient aussi à étudier pour un parc éolien. Ensuite, l'agencement des éoliennes dans un parc joue un rôle important d'un point de vue aérodynamique (par exemple Ref. [93]). Il serait intéressant de réaliser une étude comparable d'un point de vue acoustique. Enfin, nous n'avons étudié pour l'instant la propagation du bruit des éoliennes que dans des écoulements moyens. De prochaines travaux pourraient prendre en compte l'effet des fluctuations turbulentes de vitesse sur la propagation du bruit des éoliennes, notamment dans le sillage des éoliennes, où l'intensité de la turbulence est importante [94]. Les données LES pourraient être mises à profit pour cela, soit en utilisant directement les champs de vitesse instantanée soit en générant des champs turbulents à partir de celles-ci.

Propagation en conduit

Les travaux en propagation en conduit vont se poursuivre en s'appuyant sur le banc CAIMAN du LMFA. Les études autour du comportement non-linéaire des plaques perforées vont pouvoir être étayées avec des mesures des performances en fonction du niveau d'excitation et de la vitesse de l'écoulement. A court terme, l'objectif est de comparer les prédictions issues de simulations numériques basées sur les équations d'Euler linéarisées avec une condition limite d'impédance non-linéaire et les mesures sur CAIMAN en présence ou non d'écoulement. A plus long terme, on pourra aussi considérer des niveaux sonores plus importants pour lesquels il sera nécessaire de prendre en compte les effets de propagation non-linéaire. Une extension vers la propagation multimodale est aussi possible avec le support du banc CAIMAN. En particulier, à fort niveau, l'interaction non-linéaire entre modes de conduit [95] serait un sujet d'étude pertinent. Enfin, les premières études avec la fabrication additive permettent d'envisager des liners dont la géométrie est conçue pour optimiser les performances en conduit. Il sera aussi intéressant d'étudier la performance de ces matériaux avec la prise en compte d'un écoulement moyen.

Propagation d'ondes de choc

Les perspectives sur la propagation d'ondes de choc sont également nombreuses.

Tout d'abord, les études sur le bang sonique ont montré l'intérêt des approches directes pour prédire la propagation en environnement complexe. Les simulations ont été restreintes à des géométries bidimensionnelles. L'extension au cas 3D est la suite directe de ces travaux. En particulier, en lien avec les études actuelles autour de l'avion expérimental X-59 et de l'acceptation du bang par la population, il serait intéressant d'étudier la propagation du bang dans un environnement urbain 3D. Pour une onde de type low-boom dont le contenu fréquentiel reste limité à quelques centaines

de Hz, cela est tout à fait envisageable. De plus, la prise en compte de conditions météorologiques permettrait aussi d'étudier la variabilité induite des niveaux sonores au sol.

Les comparaisons entre mesures et simulations numériques pour la réflexion d'ondes de chocs générées avec une source à arc électrique ont montré que les phénomènes de propagation et de réflexion nonlinéaires étaient reproduits fidèlement. Les travaux pourraient se poursuivre autour de la propagation d'ondes de souffle dans l'environnement, en lien avec le LETMA, en utilisant les outils numériques déjà développés.

Enfin, deux nouvelles études ont été lancées. La première étude porte sur la propagation d'ondes de choc générées par les éclairs, avec pour objectif de mieux comprendre le lien entre l'énergie électrique de l'éclair, la forme de l'éclair et le signal acoustique. La seconde s'intéresse à la propagation d'ondes de choc générées par la soufflante d'un moteur d'avion non-caréné et à leur impact sur le fuselage d'un avion.

Bibliographie

[1] Scott, J.F., Blanc-Benon, P. & Gainville, O. (**2017**). "Weakly nonlinear propagation of small-wavelength, impulsive acoustic waves in a general atmosphere," Wave Motion **72**, 41–61.

[2] Khodr, C., Azarpeyvand, M. & Green, D.N. (**2020**). "An iterative three-dimensional parabolic equation solver for propagation above irregular boundaries," J. Acoust. Soc. Am. **148**(2), 1089–1100.

[3] Mangin, B., Daroukh, M. & Gabard, G. (**2023**). "Propagation of acoustic waves in ducts with flow using the multimodal formulation," AIAA J. **61**(6), 2721–2733.

[4] Jones, M., Watson, W. & Parrott, T. (**2005**). "Benchmark data for evaluation of aeroacoustic propagation codes with grazing flow," 11th AIAA/CEAS Aeroacoustics Conference, Monterey, CA, USA, AIAA Paper 2005-2853, 1-18.

[5] Primus, J., Piot, E. & Simon, F. (**2013**). "An adjoint-based method for liner impedance eduction : Validation and numerical investigation," J. Sound Vib. **332**, 58-75.

[6] Salze, E., Yuldashev, P., Ollivier, S., Khokhlova, V.A. & Blanc-Benon, P. (**2014**). "Laboratory-scale experiment to study nonlinear N-wave distortion by thermal turbulence," J. Acoust. Soc. Am. **136**(2), 556-566.

[7] Blanc-Benon, P., Dallois, L. & Juvé, D. (**2001**). "Long range sound propagation in a turbulent atmosphere within the parabolic approximation," Acta Acustica **87**, 659-669.

[8] Bogey, C. & Bailly, C. (**2004**). "A family of low dispersive and low dissipative explicit schemes for flow and noise computations," J. Comput. Phys. **194**, 194–214.

[9] Cotté, B., Blanc-Benon, P., Bogey, C. & Poisson, F. (**2009**). "Time-domain impedance boundary conditions for simulations of outdoor sound propagation," AIAA J. **47**, 2391–2403.

[10] Sabatini, R., Marsden, O. Bailly, C. & Bogey, C. (**2016**). "A numerical study of nonlinear infrasound propagation in a windy atmosphere," J. Acoust. Soc. Am. **140**(1), 641-656.

[11] Betgen, B., Galland, M.A., Piot, E. & Simon, F. (**2012**). "Implementation and non-intrusive characterization of a hybrid active-passive liner with grazing flow," Applied Acoustics **73**(6-7), 624-638.

[12] Berland, J., Bogey, C., Marsden, O. & Bailly, C. (**2007**). "High-order, low dispersive and low dissipative explicit schemes for multiple-scale and boundary problems," J. Comp. Phys., **224**(2), 637-662.

[13] Berland, J., Bogey, C. & Bailly, C. (**2006**). "Low-dissipation and low-dispersion fourth-order Runge–Kutta algorithm,", Computers & Fluids **35**, 1459–1463.

[14] Bogey, C., de Cacqueray, N. & Bailly, C. (**2009**). "A shock-capturing methodology based on adaptative spatial filtering for high-order non-linear computations," J. Comp. Phys. **228**(5), 1447-1465.

[15] Hornikx, M., Waxler, R. & Forssen, J. (**2010**). "The extended Fourier pseudospectral time-domain method for atmospheric sound propagation," J. Acoust. Soc. Am. **128**, 1632-1646.

[16] Dragna, D., Bogey, C., Hornikx, M. & Blanc-Benon, P. (**2013**). "Analysis of the dissipation and dispersion properties of the multi-domain Chebyshev pseudospectral method," J. Comput. Phys. **255**, 31-47.

[17] Hornikx, M. & Dragna, D. (**2015**). "Application of the Fourier pseudospectral time-domain method in orthogonal curvilinear coordinates for near-rigid moderately curved surface," J. Acoust. Soc. Am. **138**(1), 425-435.

[18] Gustavsen, B. & Semlyen, A. (**1999**). "Rational approximation of frequency domain responses by vector fitting," IEEE Trans. Power Delivery **14**(3), 1052–1061.

[19] Reymen, Y., Baelmans, M. & Desmet, W. (**2008**). "Efficient implementation of Tam and Auriault's time-domain impedance boundary condition," AIAA J. **46**(9), 2368–2376.

[20] Dragna, D., Pineau, P. & Blanc-Benon, P. (**2015**). "A generalized recursive convolution method for time-domain propagation in porous media," J. Acoust. Soc. Am. **138**(2), 1030-1042.

[21] Joseph, R. M., Hagness, S. C. & Taflove, A. (**1991**). "Direct time integration of Maxwell's equations in linear dispersive media with absorption for scattering and propagation of femtosecond electromagnetic pulses," Opt. Lett. **16**, 1412–1414.

[22] Julian, R., Dragna, D., Ollivier, S. & Blanc-Benon, P. (**2021**). "Rational approximation of unsteady friction weighting functions in the Laplace domain," J. Hydraul. Eng., **147**(9), 04021031, 1-9.

[23] Rienstra, S. W. (**2006**). "Impedance models in time domain including the Helmholtz resonator model," 12th AIAA/CEAS Aeroacoustics Conference, Cambridge, MA, USA, AIAA Paper 2006–2686, 1-20.

[24] Dragna, D. & Blanc-Benon, P. (**2014**). "Physically admissible impedance models for time-domain computations of outdoor sound propagation," Acta Acust. united Ac., **100**(3), 401-410.

[25] Kirby, R. (**2014**). "On the modification of Delany and Bazley fomulae,", Appl. Acoust., **86**, 47–49.

[26] Dragna, D., Attenborough, K. & Blanc-Benon, P. (**2015**). "On the inadvisability of using single parameter impedance models for representing the acoustical properties of ground surfaces," J. Acoust. Soc. Am., **138**(4), 2399-2413.

[27] Guillaume, G., Faure, O., Gauvreau, B., Junker F., Bérengier, M. & L'Hermite, P. (**2015**). "Estimation of impedance model input parameters from in situ measurements : Principles and applications," Appl. Acoust., **95**, 27–36.

[28] Ostashev, V.E., Wilson, D.K. & Vecherin, S. N. (**2011**). "Effect of randomly varying impedance on the interference of the direct and ground-reflected waves," J. Acoust. Soc. Am., **130**(4), 1844–1850.

[29] Dragna, D. & Blanc-Benon, P. (**2017**). "Sound propagation over the ground with a random spatially-varying surface admittance," J. Acoust. Soc. Am., **142**(4), 2058-2072.

[30] Dragna, D., Blanc-Benon, P. & Poisson, F. (**2014**). "Modeling of broadband moving sources for time-domain simulations of outdoor sound propagation," AIAA J., **52**(9), 1928-1939.

[31] Dragna, D. & Blanc-Benon, P. (**2014**). "Towards realistic simulations of sound radiation by moving sources in outdoor environments," Int. J. Aeroacoustics, **13**(5-6), 405-426.

[32] Norum, T.D. & Liu, C.H. (**1978**). "Point source moving above a finite impedance reflecting plane-experiment and theory," J. Acoust. Soc. Am., **63**(4), 1069–1073.

[33] Dragna, D. & Blanc-Benon, P. (**2015**). "Sound radiation by a moving line source above an impedance plane with frequency-dependent properties," J. Sound Vib., **349**, 259-275.

[34] Wang, Y., Li, K.M., Dragna, D. & Blanc-Benon, P. (**2015**). "On the sound field from a source moving above non-locally reacting grounds," J. Sound Vib., **464**, 114975, 1-20.

[35] Guibard, A. (**2023**). "Acoustic propagation in heterogeneous environments and communication networks in rock ptarmigan,", thèse de doctorat 2023ECDL0027.

[36] Guibard, A., Sèbe, F., Dragna, D. & Ollivier, S. (**2022**). "Influence of meteorological conditions and topography on the active space of mountain birds assessed by a wave-based sound propagation model," J. Acoust. Soc. Am., **151**(6), 3703–3718.

[37] Hansen, K.L., Nguyen, P., Zajamsek, B., Catcheside, P. & Hansen, C.H. (**2019**). "Prevalence of wind farm amplitude modulation at long-range residential locations," J. Sound Vib. **455**, 136–149.

[38] Barlas, E., Zhu, W.J., Shen, W.Z., Dag, K.O. & Moriarty, P. (**2017**). "Consistent modelling of wind turbine noise propagation from source to receiver," J. Acoust. Soc. Am. **142**(5), 3297–3310.

[39] Kayser, B., Cotté, B., Ecotière, D. & Gauvreau, B. (**2020**). "Environmental parameters sensitivity analysis for the modeling of wind turbine noise in downwind conditions," J. Acoust. Soc. Am. **148**(6), 3623-2632.

[40] Heimann, D. & Englberger, A. (**2018**). "3D-simulation of sound propagation through the wake of a wind turbine : Impact of the diurnal variability," Applied Acoustics **141**, 393–402.

[41] Liu, L.& Stevens, R.J.A.M. (**2020**). "Effects of two-dimensional steep hills on the performance of wind turbines and wind farms," Boundary-Layer Meteorology, **176**(2), 251–269.

[42] Cotté, B. (**2019**). "Extended source models for wind turbine noise propagation,", J. Acoust. Soc. Am. **145**(3), 1363–1371.

[43] Colas, J., Emmanuelli, A., Dragna, D., Cotté, B., Blanc-Benon, P. & Stevens, R.J.A.M. (**2023**). "Wind turbine sound propagation : Comparison of a linearized Euler equations model with parabolic equation methods,", J. Acoust. Soc. Am. **154**(3), 1413-1426.

[44] Bastankhah, M. & Porté-Agel, F. (**2014**). "A new analytical model for wind-turbine wakes," Renewable Energy **70**, 116–123.

[45] Barlas, E., Zhu, W.J., Shen, W.Z., Kelly, M. & Andersen, S.J.(**2017**). "Effects of wind turbine wake on atmospheric sound propagation,", Applied Acoustics **122**, 51–61,

[46] Troian, R., Dragna, D., Bailly, C. & Galland, M.-A. (**2017**). "Broadband liner impedance eduction for multimodal acoustic propagation in the presence of a mean flow," J. Sound Vib. **392**, 200-216.

[47] Monteghetti, F., Matignon, D., Piot, E. & Pascal, L. (**2016**). "Design of broadband time-domain impedance boundary conditions using the oscillatory-diffusive representation of acoustical models," J. Acoust. Soc. Am. **140**, 1663–1674.

[48] Alomar, A., Dragna, D. & Galland, M.A. (**2021**). "Time-domain simulations of sound propagation in a flow duct with extended-reacting liners," J. Sound Vib. **507**, 116137, 1-24.

[49] Aurégan, Y. & Singh, D.K. (**2014**). "Experimental observation of a hydrodynamic mode in a flow duct with a porous material," J. Acoust. Soc. Am. **136**, 567–572.

[50] Alomar, A., Dragna, D. & Galland, M.A. (**2021**). "Pole identification method to extract the equivalent fluid characteristics of general sound-absorbing materials," Applied Acoustics **174**, 107752, 1-15.

[51] Utsuno, H., Tanaka, T. & Fujikawa, T. (**1989**). "Transfer function method for measuring characteristic impedance and propagation constant of porous materials," J. Acoust. Soc. Am. **86**, 637–43.

[52] Laly, Z., Atalla, N. & Meslioui, S.-A. (**2018**). "Acoustical modeling of micro-perforated panel at high sound pressure levels using equivalent fluid approach," J. Sound Vib. **427**, 134-158.

[53] Shur, M., Strelets, M., Travin, A., Suzuki T. & Spalart, P. (**2021**). "Unsteady simulations of sound propagation in turbulent flow inside a lined duct," AIAA J. **59**, 3054–3070.

[54] Diab, D., Dragna, D., Salze, E. & Galland, M.A. (**2022**). "Nonlinear broadband time-domain admittance boundary condition for duct acoustics. Application to perforated plate liners," J. Sound Vib. **528**, 116892, 1-26.

[55] Deb, K., Pratap, A., Agarwal, S. & Meyarivan, T. (**2002**). "A fast and elitist multiobjective genetic algorithm : NSGA-II," IEEE Trans. Evol. Comput. **6**(2), 182–197.

[56] Aurégan, Y. & Leroux, M. (**2022**). "Experimental evidence of an instability over an impedance wall in a duct with flow," J. Sound Vib. **317**(3-5), 432–439.

[57] Burak, M.O., Billson, M., Eriksson, L.E. & Baralon, S., (**2009**). "Validation of a time- and frequency-domain grazing flow acoustic liner model," AIAA J. **47**(8), 1841–1848.

[58] Deng, Y., Alomar, A., Dragna, D. & Galland, M.A. (**2021**). "Characterization and suppression of the hydrodynamic instability in the time domain for acoustic propagation in a lined flow duct," J. Sound Vib. **500**, 115999, 1-22.

[59] Bogey, C., Bailly, C. & Juvé, D. (**2002**). "Computation of flow noise using source terms in linearized Euler's equations," AIAA J. **40**(2), 235–243.

[60] Sarpero, E., Dragna, D., Gourdon, E. & Galland, M-A. (**2023**). Experimental characterisation of perforated plates in a duct with flow in non-linear regime "29th International Congress on Sound and Vibration,", 9-13 July, Prague, Czech Republic.

[61] Opiela, K.C. & Zielinsky, T.G. (**2020**), "Microstructural design, manufacturing and dual-scale modelling of an adaptable porous composite sound absorber," Composites Part B **187** 107833, 1-13.

[62] Boulvert, J., Costa-Baptista, J., Cavalieri, T., Romero-Garcia, V., Gabard, G., Fotsing, E.R., Ross, A., Perna, M., Mardjono, J. & Groby, J.-P. (**2020**), "Folded metaporous material for sub-wavelength and broadband perfect sound absorption," Appl. Phys. Lett. **117** 251902, 1-6.

[63] Boulvert, J., Humbert, T., Romero-Garcia, V., Gabard, G., Fotsing, E.R., Ross, A., Perna, M., Mardjono, J. & Groby, J.-P. (**2022**), "Perfect, broadband, and sub-wavelength absorption with asymmetric absorbers : Realization for duct acoustics with 3D printed porous resonators," J. Sound Vib. **523** 116687, 1-21.

[64] Jamois, A., Dragna, D., Zielinski, T.G. & Galland, M.-A. (**2022**). Modélisation acoustique d'un matériau obtenu par fabrication additive placé en paroi d'un conduit, "16ème Congrès Français d'Acoustique,", 11-15 Avril, Marseille.

[65] Cummings, A. (**1986**). "Transient and multiple frequency sound transmission through perforated plates at high amplitude,", J. Acoust. Soc. Am. **79**, 942-951.

[66] Monteghetti, F., Matignon, D. & Piot, E. (**2018**). "Energy analysis and discretization of nonlinear impedance boundary conditions for the time-domain linearized Euler equations," J. Comp. Phys. **375**, 393–426.

[67] Baskar, S., Coulouvrat, F. & Marchiano, R. (**2007**). "Nonlinear reflection of grazing acoustic shock waves : Unsteady transition from von Neumann to Mach to Snell-Descartes reflections,", J. Fluid. Mech. **575**, 27–55.

[68] Desjouy, C., Ollivier, S., Marsden, O., Karzova, M.M. & Blanc-Benon, P. (**2016**). "Irregular reflection of weak acoustic shock pulses on rigid boundaries : Schlieren experiments and direct numerical simulation based on a Navier-Stokes solver,", Physics of Fluids, **28** 027102, 1-14.

[69] Lechat, T. (**2020**). "Etude de la réflexion d'ondes de choc acoustiques sur des parois rugueuses,", thèse de doctorat 2020LYSEC05.

[70] Karzova, M.M., Lechat, T., Ollivier, S., Dragna, D., Yuldashev, P.V., Khokhlova, V.A. & Blanc-Benon, P. (**2019**). "Irregular reflection of spark-generated shock pulses from a rigid surface : Mach-Zehnder interferometry measurements in air,", J. Acoust. Soc. Am. **145**(1), 26-35.

[71] Karzova, M.M., Lechat, T., Ollivier, S., Dragna, D., Yuldashev, P.V., Khokhlova, V.A. & Blanc-Benon, P. (**2019**). "Effect of surface roughness on nonlinear reflection of weak shock waves,", J. Acoust. Soc. Am. **146**(5), EL438-433.

[72] Lechat, T., Emmanuelli, A., Dragna, D. & Ollivier, S. (**2021**). "Propagation of spherical weak blast waves over rough periodic surfaces,", Shock Waves **31**, 379-398.

[73] NASA's low-boom flight demonstration, https://www.nasa.gov/X59/ (vue pour la dernière fois le 12 août 2023).

[74] Pawlowski, J., Graham, D., Boccadoro, C., Coen, P. & Maglieri, D. (**2005**). "Origins and overview of the shaped sonic boom demonstration program," 43rd AIAA Aerospace Sciences Meeting and Exhibit, 10-13 January, Reno, NV, USA, AIAA-Paper 2005-5, 1–14.

[75] Stout, T. A., Sparrow, V. W. & Blanc-Benon., P. (**2021**). "Evaluation of numerical predictions of sonic boom level variability due to atmospheric turbulence," J. Acoust. Soc. Am. **149**(5), 3250–3260.

[76] Leconte, R., Chassaing, J. C., Coulouvrat, F. & Marchiano, R. (**2022**). "Propagation of classical and low booms through kinematic turbulence with uncertain parameters," J. Acoust. Soc. Am. **151**(6), 4207–4227.

[77] Carr, A. N., Lonzaga, J. B. & Miller, S.A.E. (**2022**). "Numerical prediction of loudness metrics for N-waves and shaped sonic booms in kinematic turbulence," J. Acoust. Soc. Am. **151**(6), 3580–3593.

[78] Yamashita, R. & Suzuki, K. (**2016**). "Full-field sonic boom simulation in stratified atmosphere,", AIAA J. **54**(10), 3223–3231.

[79] Bauer, A. B. & Bagley, C. J. (**1970**). "Sonic boom modeling - investigation of topographical and atmospheric effects," FAA-NO-70-10, 1–212.

[80] Emmanuelli, A., Dragna, D., Ollivier, S. & Blanc-Benon, P. (**2021**). "Characterization of topographic effects on sonic boom reflection by resolution of the Euler equations," J. Acoust. Soc. Am. **149**(4), 2437–2450.

[81] Emmanuelli, A., Dragna, D., Ollivier, S. & Blanc-Benon, P. (**2023**). " Sonic boom propagation over real topography," J. Acoust. Soc. Am. **154**(1), 16–27.

[82] Brooks, J. D., Beasley, W. D. & Barger, R. L. (**1970**). "Laboratory investigation of diffraction and reflection of sonic booms by buildings," NASA TN D-5830, 1–22.

[83] Cho, S.-L. T. & Sparrow, V. W. (**2011**). "Diffraction of sonic booms around buildings resulting in the building spiking effect," J. Acoust. Soc. Am. **129**(3), 1250–1260.

[84] Yamashita, R. & Nikiforakis, N. (**2023**). "Three-dimensional full-field simulation of sonic boom emanating from complex geometries over buildings," Shock Waves **33**, 149–167.

[85] Dragna, D., Emmanuelli, A., Ollivier, S. & Blanc-Benon, P. (**2022**). "Sonic boom reflection over an isolated building and multiple buildings," J. Acoust. Soc. Am. **151**(6), 3792–3806.

[86] Dragna, D., Emmanuelli, A., Ollivier, S.& Blanc-Benon, P. (**2022**). "Sonic boom reflection over urban areas," J. Acoust. Soc. Am. **152**(6), 3323–3339.

[87] Stewart, I. D.& Oke., T. R. (**2012**). "Local climate zones for urban temperature studies," Bulletin of the American Meteorological Society **93**(12), 1879–1900.

[88] Faure, O., Gauvreau, B., Junker, F., Lafon, P. & Bourlier, C. (**2017**). "Modelling of random ground roughness by an effective impedance and application to time-domain methods," Appl. Acoust. **119**, 1–8.

[89] Lacroix, A., Coulouvrat, F., Marchiano, R., Farges, T. & Ripoll, J. (**2019**). "Acoustical energy of return strokes : A comparison between a statistical model and measurements," Geophysical Research Letters **46**(20), 11479–11489.

[90] Salze, E., Vagnon, E., Ollivier, S., El-Khattabi, M., Zouaghi, A., Dragna, D. & Blanc-Benon, P. (**2022**), Laboratory-scale characterization of lightning strikes : acoustical and electrical measurements synchronized with optical visualizations, "22nd International Symposium on Nonlinear Acoustics,", July 4-8, Oxford, UK. Proc. Mtgs. Acoust 48, 045009, 1-11.

[91] Bilbao, S. (**2023**). "Modeling impedance boundary conditions and acoustic barriers using the immersed boundary method : The one-dimensional case," J. Acoust. Soc. Am. **153**(4), 2023–2036.

[92] Bocquet, C, Desjouy, C. & Gabard, G. (**2023**). "A high-order immersed moving boundary method using ghost points and characteristics for acoustics," J. Theor. Comput. Acoust. à paraître.

[93] Kusiak, A. & Song, Z. (**2010**). "Design of wind farm layout for maximum wind energy capture," Renewable Energy **35**(3), 685–694.

[94] Barlas, E., Zhu, W. J., Shen, W. Z., Kelly, M. & Andersen, S. J. (**2017**). "Effects of wind turbine wake on atmospheric sound propagation," Appl. Acoust. **122**, 51–61.

[95] Fernando, R., Druon, Y., Coulouvrat, F. & Marchiano, F. (**2011**). "Nonlinear waves and shocks in a rigid acoustical guide," J. Acoust. Soc. Am. **129**(2), 604–615.

Annexes

En annexe, je joins six travaux récents, dont les thèmes associés sont indiqués entre parenthèses :

- Guibard A., Sèbe F., Dragna D. & Ollivier S. (2022), Influence of meteorological conditions and topography on the active space of mountain birds assessed by a wave-based sound propagation model, J. Acoust. Soc. Am. 151(6), 3703-3718. (acoustique environnementale)
- Colas J., Emmanuelli, A., Dragna D., Cotté, B., Blanc-Benon, P. & Stevens R.J.A.M. (2023), Wind turbine sound propagation : Comparison of a linearized Euler equations model with parabolic equation methods, J. Acoust. Soc. Am., 154(3), 1413-1426. (acoustique environnementale)
- Deng Y., Alomar A., Dragna D. & Galland M.-A. (2021), Characterization and suppression of the hydrodynamic instability in the time domain for acoustic propagation in a lined flow duct, J. Sound Vib. 500, 115999, 1-22. (propagation en conduit)
- Diab D., Dragna D., Salze E. & Galland M.-A. (2022), Nonlinear broadband time-domain admittance boundary condition for duct acoustics. Application to perforated plate liners, J. Sound Vib. 528, 116892, 1-26. (propagation en conduit)
- Lechat T., Emmanuelli A., Dragna D. & Ollivier S. (2021), Propagation of spherical weak blast waves over rough periodic surfaces, Shock Waves 31, 379-398. (propagation d'ondes de choc)
- Emmanuelli A., Dragna D., Ollivier S. & Blanc-Benon P. (2021), Characterization of topographic effects on sonic boom reflection by resolution of the Euler equations, J. Acoust. Soc. Am. 149(4), 2437-2450. (propagation d'ondes de choc)

JASA ARTICLE

Influence of meteorological conditions and topography on the active space of mountain birds assessed by a wave-based sound propagation model

Arthur Guibard,[1,a] Frédéric Sèbe,[2] Didier Dragna,[1] and Sébastien Ollivier[3]

[1]*Université Lyon, École Centrale de Lyon, INSA Lyon, Université Claude Bernard Lyon I, LMFA, CNRS UMR 5509, F-69134 Écully, France*

[2]*Université de Saint-Étienne, ENES/CRNL, CNRS UMR 5292, INSERM UMRS 1028, 42023 Saint-Étienne, France*

[3]*Université Lyon, Université Claude Bernard Lyon I, École Centrale de Lyon, INSA Lyon, LMFA, CNRS UMR 5509, F-69100 Villeurbanne, France*

ABSTRACT:

The active space is a central bioacoustic concept to understand communication networks and animal behavior. Propagation of biological acoustic signals has often been studied in homogeneous environments using an idealized circular active space representation, but few studies have assessed the variations of the active space due to environment heterogeneities and transmitter position. To study these variations for mountain birds like the rock ptarmigan, we developed a sound propagation model based on the parabolic equation method that accounts for the topography, the ground effects, and the meteorological conditions. The comparison of numerical simulations with measurements performed during an experimental campaign in the French Alps confirms the capacity of the model to accurately predict sound levels. We then use this model to show how mountain conditions affect surface and shape of active spaces, with topography being the most significant factor. Our data reveal that singing during display flights is a good strategy to adopt for a transmitter to expand its active space in such an environment. Overall, our study brings new perspectives to investigate the spatiotemporal dynamics of communication networks. https://doi.org/10.1121/10.0011545

(Received 25 January 2022; revised 12 May 2022; accepted 13 May 2022; published online 3 June 2022)

[Editor: Mark A. Bee] Pages: 3703–3718

I. INTRODUCTION

In acoustic communication systems, the transmission of sound through the environment is a major source of signal degradation, caused by attenuation, absorption, and reflections. In bioacoustics and more particularly in the analysis of communication networks (Reichert *et al.*, 2021), one of the biggest challenges is the modeling of acoustic propagation to study the impact of the transmission channel on information exchange (Forrest, 1994).

Long-distance acoustic communication is used by many species of birds. Moreover, outdoor sound propagation is ruled by the influence of the habitat and environmental parameters (Dabelsteen *et al.*, 1993; Embleton, 1996). To study communication in birds, the bioacoustic notion of active space (AS) was introduced by Marten and Marler (1977) as being the "effective distance" of a signal, the distance from the source over which signal amplitude remains above the detection threshold of potential listeners. This definition was later extended to the "effective space" by McGregor and Dabelsteen, to describe communication networks (McGregor, 2005; McGregor and Dabelsteen, 1996). Considering an acoustic signal, the associated AS is determined by four factors: (1) amplitude of the signal at the source; (2) the rate at which signal energy attenuates by transmission through the environment; (3) amplitude of ambient noise in the environment; and (4) masked auditory threshold of receivers since the signal is embedded in a background noise (Brenowitz, 1982).

To the authors' knowledge, previous studies on long-distance acoustic communication have mostly considered homogeneous propagation environments and the maximum distance at which a transmitter could be heard as a criterion of AS. They were usually focused on the estimation of global excess attenuation (EA), signal-to-noise ratio (SNR), tail-to-signal ratio (TSR), or blur ratio (BR) over some frequency bands, depending on the distance to a transmitter, to estimate a radius of audibility. Many of these earlier works are based on field propagation experiments and playback experiments (Darden *et al.*, 2008; Lohr *et al.*, 2003; Loning *et al.*, 2022). The effect of transmitter and receiver heights on propagation has been investigated as well as environmental parameters (temperature, wind, humidity) (Dabelsteen *et al.*, 1993; Holland *et al.*, 1998; Jensen *et al.*, 2008; Mathevon *et al.*, 2005). The impact of diurnal

[a]Also at: Université de Saint-Étienne, ENES/CRNL, CNRS UMR 5292, INSERM UMRS 1028, 42023, Saint-Étienne, France. Electronic mail: arthur.guibard@ec-lyon.fr

variations was investigated through a similar methodology (Dabelsteen and Mathevon, 2002; Henwood and Fabrick, 1979), as was the constraint of the rain on communication (Lengagne and Slater, 2002). Although these previous works provide answers about the effects of the environment on communication, they are not as suitable as a dedicated model could be.

Modeling acoustic propagation is crucial for studying animal communication, since recordings and playback experiments require a lot of time and material and can hardly be carried out on large areas. Therefore, propagation models have been proposed in the literature to estimate ASs of communication and information degradation. Most of them are based on simplified semi-empirical approaches as proposed by Henwood and Fabrick (1979) and Parris (2002) or more recently Raynor *et al.* (2017), in which the engineering-based SPreAD-GIS model was used. These models are computationally efficient, but they do not account for all the physics, and their outputs are often restricted to global indicators. Wave-based models, i.e., models that describe the wave propagation in time or in frequency domain, are more accurate, but due to their computational cost, they have been barely used in bioacoustics. A rare example is the study of Larom *et al.* (1997) that used a fast field program (FFP) model to show that the ASs of African savanna elephants depend on wind and temperature profiles.

Actually, topography and meteorological conditions depend on the habitat. These conditions obviously have a strong effect on AS, especially in mountainous areas, which represent a noticeably heterogeneous environment as stated by Reiners and Driese (2001). Moreover, it is essential to take these parameters into account to understand the impact of habitat on communication in both space and time. The study of these effects could provide interesting clues about the features of signal propagation in communication networks and their potential adaptation to the species' habitat (Mathevon *et al.*, 2008; Wiley and Richards, 1978).

To highlight the impact of the habitat on AS, we chose to work on an iconic species of high mountains: the rock ptarmigan (*Lagopus muta*). It is a species living in the northern hemisphere, in arctic or alpine habitat. Considering the period of intense vocal activity that is the breeding season in spring between April and June, environmental conditions and species behavior are known (Bossert, 1977; Watson, 1972). During this period, male ptarmigans sing at dawn to defend their territory and indicate their location. Their songs are often made during flights, which is the main territorial demonstration (Johnsgard, 2008; MacDonald, 1970).

At altitudes above 1800 m, alpine mountain ranges are usually still largely covered with snow. The propagation distance of this type of vocalization is about a few hundred meters. The vocalizing birds may be placed either on the ground or at a height of a several dozen meters. The characteristic frequencies of ptarmigan vocalizations are in the kilohertz range. These particularities imply a large-scale problem, which must be taken up by a computational method fast enough to be applicable.

The study of ASs is carried out using numerical simulations, allowing us to test a large number of propagation conditions. With this approach, we are trying to answer two questions: How do environmental constraints affect the vocal communication of mountain birds? And how do ptarmigans adapt and optimize their communication behavior?

The objectives of this study are (1) to develop a method to estimate ASs of a bird in heterogeneous environment; (2) to compare numerical results with *in situ* measurements to evaluate the model for the intended application; (3) to assess the influence of topography, temperature, and wind on the AS; and (4) to study the potential benefit of singing during display flight for the rock ptarmigan.

This article is organized as follows. Section II describes the model used in this study and the different assumptions made. The on-site measurement campaign and the comparisons between measurements and model estimations are detailed in Sec. III. Then Sec. IV presents an application of the previously tested model on a typical mountain site where a population of ptarmigan lives. Here, we investigate the variability of the AS in such a context. Concluding remarks are given in Sec. V.

II. ACTIVE SPACE AND PROPAGATION MODEL

A. Definition of the AS

Determination of AS is based on the propagation loss (PL), defined as the sound pressure level (SPL) relative to source level (SL). It represents the attenuation of the signal energy during propagation over an area. Following Brenowitz (1982), to set the PL threshold that defines the limits of the AS, several parameters must be considered: the source level (SL), the auditory threshold in masking noise, and the background noise.

ASs are investigated for the rock ptarmigan (*L. muta helvetica*), which is considered as a model of mountain bird. The rock ptarmigan uses acoustic vocalizations to communicate, especially during display flights, when it significantly increases its altitude up to 75 m from the ground (Johnsgard, 2008). Its vocalizations are sequences of pulse trains, with a pulse rate of 21 ± 3 ms and an energy distributed in the frequency range of 900–3700 Hz (Marin-Cudraz *et al.*, 2019), the maximum amplitude being around 1000 Hz. Neither the directivity nor the nearfield sound pressure level (SPL) (in dB relative to 20 μPa) of ptarmigan vocalizations is yet well characterized. For simplicity, in the present study, the directivity is assumed to be omnidirectional. To estimate the SPL, we assume that it is comparable to that of the corncrake (*Crex crex*), which is a non-passerine bird of similar size that also produces a broadcast call with pulsed signal. Its SL has been measured in the range of 80–101 dBSPL (Aubin and Mathevon, 2020; Rek and Osiejuk, 2011). Therefore, the SL of rock ptarmigan vocalizations, defined as the SPL at 1 m from the source, is set at a median value of 90 dBSPL in the present study.

In this species, there is not much competition for vocal communication or selection pressure for encoding

https://doi.org/10.1121/10.0011545

information, because the density of birds is low with a relatively simple communication network (two to three neighbors maximum for each bird). In addition, they are the only birds that vocalize in a relatively low frequency range in this environment compared to other birds, and the latter are also scarce at this altitude. Thus, the situation is one of energetic masking due to background noise alone. For the purpose of this study, we arbitrarily set a detection threshold of 10 dB, regarded as the SNR required for comfortable communication in the sense of Dooling and Leek (2018). This value is sufficient to achieve the objectives of this article, but for a detailed study concerning the effect of ambient noise, it will be necessary to perform an estimation of the detection threshold of ptarmigan in noise. Background noise levels around 30 dBSPL or less were measured during clear daytime on the site considered in Sec. IV, where a population of ptarmigan lives. This value is kept throughout. From the last two elements, it is assumed that above a pressure level of 40 dBSPL, a receiver is able to detect and decode the information and is thus inside the AS. Below this 40 dBSPL threshold, the probability of detection decreases, and a receiver is no longer considered to be in the AS. In other words, considering a SL = 90 dBSPL and a detection threshold of 40 dBSPL, the AS is the area such that the propagation loss from the source does not exceed –50 dB. This PL threshold set to −50 dB could be corrected when the ptarmigan SL and detection threshold in noise are measured and could be different if considering other bird species.

B. Propagation model

In the context of atmospheric propagation, the choice of a model is a compromise between the computational cost, the complexity of environmental effects to be considered, and the type of results desired. For application to bird communication in mountains, the model must be able to compute vocalizations after propagation at long distances and high frequencies and include a stratified atmosphere with irregular topography.

The propagation model used here is based on the wide-angle parabolic equation (WAPE), described, e.g., by Salomons (2001), which is an efficient computational method for long-range sound propagation within the atmospheric boundary layer (ASL). It is obtained from the Helmholtz equation by considering forward propagating waves only. An $N\times$ 2D (two dimensions) approach is followed: the problem is not considered on a full three-dimensional (3D) geometry but on vertical slices, as illustrated in Fig. 1.

On each slice $(x,\ z)$, the 2D axisymmetric WAPE is solved. The source is located at $(x_s,\ z_s)$. Denoting by p_{PE} the pressure and introducing $q_{\mathrm{PE}} = \sqrt{R}\,p_{\mathrm{PE}}$, with $R = \sqrt{(x-x_s)^2 + (z-z_s)^2}$ the distance from the source, the WAPE equation can be written as

$$\left\{\frac{\partial}{\partial x} - \mathrm{i}k_0\mathcal{Q}\right\} q_{\mathrm{PE}}(x,z) = 0, \tag{1}$$

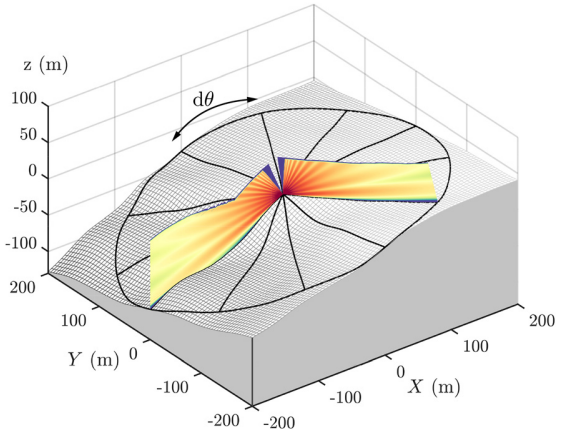

FIG. 1. (Color online) Principle of the $N \times$ 2D approach. Shown is PL on 2D domains.

where $k_0 = \omega/c_0$ is the reference wave number, c_0 is the reference sound speed chosen at the ground level, and $\omega = 2\pi f$, with f the frequency. The pseudo-differential operator $\mathcal{Q}$ is written as a Padé (1,1) approximation,

$$\mathcal{Q} = \frac{1+\eta_1\mathcal{L}}{1+\eta_2\mathcal{L}}, \tag{2}$$

with $\eta_1 = 3/4$ and $\eta_2 = 1/4$. The operator $\mathcal{L}$ is given by

$$\mathcal{L} = \epsilon_{\mathrm{eff}} + \frac{1}{k_0^2}\frac{\partial^2}{\partial_z^2}, \tag{3}$$

with $\epsilon_{\mathrm{eff}} = c_0^2/c_{\mathrm{eff}}^2 - 1$. The parameter c_{eff} is the effective sound speed, which accounts for temperature and wind variations. Its calculation is detailed in Sec. III A 2. The effective sound speed approach is a reasonable approximation in the lower ASL for low wind speed. Note that Ostashev *et al.* (2020) recently proposed a parabolic equation (PE) formulation that improves the inclusion of wind profiles. In addition, full 3D PE formulations (Khodr *et al.*, 2020) have been already proposed in the literature for atmospheric sound propagation. Although they describe 3D propagation effects, they induce a large increase in the computational cost. For application to bioacoustics, a 2D approach was deemed to be sufficient.

The topography is described by a succession of flat domains of fixed length, defined by an angle a with respect to the horizontal x axis, as suggested by Blairon *et al.* (2002) and Lihoreau *et al.* (2006). In each domain, the $(x_n,\ z_n)$ coordinate system is rotated to keep the x_n axis parallel to the ground, as shown in Fig. 2. The length of each domain is set to 5 m, which is sufficient to properly fit most real topographies. For the first domain, the calculation is initialized by the wide-angle starter, which accounts for the source image weighted with a complex reflection coefficient, derived in Salomons (2001). This reproduces a monochromatic omnidirectional point source in the acoustic far field ($k_0R \gg 1$). Note that the propagation model does not allow a precise prediction of the near field. The amplitude of the source is set so

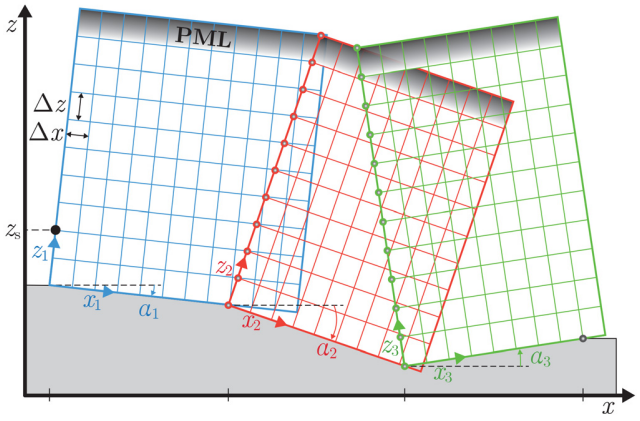

FIG. 2. (Color online) Sketch of rotated PE method: grids in the (x_n, z_n) planes, with fixed tangent grid spacing Δx and orthogonal grid spacing Δz. A PML is set at the top of each domain to ensure a reflectionless condition.

that the SPL in free field at 1 m is equal to SL. For the other domains, the starter is obtained by interpolating the pressure field of the previous domains.

In each domain, the problem is discretized using the Crank–Nicholson marching scheme in the propagating direction x_n and second-order finite-differences in the transverse direction z_n. The discretization steps are fixed to $\Delta x = \Delta z = \lambda/10$, with the wavelength $\lambda = c_0/f$. The WAPE method ensures accurate results within a propagation angle of 40° above and below the x direction (Ostashev *et al.*, 1997). This implies that the angle between two consecutive domains must remain between these limits.

At the top of each domain, a perfectly matched layer (PML), based on the work of Collino (1997), is implemented as a non-reflecting boundary condition. At the ground, a surface admittance boundary condition is applied. This assumes that the ground is locally reacting. Because of its small flow resistivity, snow is, however, usually considered as an extended-reacting ground. To mimic the effect of extended reaction at long distance, the normalized surface admittance β_s is evaluated from that of an extended-reacting hard-backed porous layer of constant effective thickness e (Li *et al.*, 1998) at grazing incidence (angle of incidence equal to $\pi/2$). This yields

$$\beta_s = \beta_c \frac{\sqrt{n^2-1}}{n} \tanh\left(-\mathrm{i}k_0 e\sqrt{n^2-1}\right), \tag{4}$$

with $n = k_c/k_0$ and β_c and k_c the characteristic admittance and the wavenumber of the snow layer. The acoustic properties of the snow (β_c, k_c) are defined according to the phenomenological model proposed by Bérengier *et al.* (1997),

$$\beta_c = \frac{\Omega}{q}\left[1-\frac{\omega_1}{\mathrm{i}\omega}\right]^{-1/2}\left[1-\frac{\omega_2}{\mathrm{i}\omega}\right]^{-1/2}\left[1-\frac{\omega_3}{\mathrm{i}\omega}\right]^{1/2}, \tag{5}$$

$$k_c = k_0 q\left[1-\frac{\omega_1}{\mathrm{i}\omega}\right]^{1/2}\left[1-\frac{\omega_2}{\mathrm{i}\omega}\right]^{-1/2}\left[1-\frac{\omega_3}{\mathrm{i}\omega}\right]^{1/2}, \tag{6}$$

with $\omega_1 = R_s\Omega/(\rho_0 q^2)$, $\omega_2 = R_s/(\rho_0 \mathrm{Pr})$, $\omega_3 = \gamma R_s/(\rho_0 \mathrm{Pr})$, ρ_0 the air density at the ground, $\gamma = 1.4$ the specific heat ratio, and $\mathrm{Pr} = 0.7$ the Prandtl number. This model uses three parameters: the airflow resistivity of the porous structure R_s, the porosity of air-filled connected pores Ω, and the tortuosity q^2. Note that other impedance models can also be used, such as the relaxation model (Wilson, 1993) or the slit-pore model (Attenborough and van Renterghem, 2021).

The PE method is a frequency-domain approach. For broadband signals, the calculation must be repeated for all frequencies of interest. In addition, it can be noted that the time signal after propagation can be determined from a broadband spectrum using an inverse Fourier transform. Several remarks can be made with regard to the limits of application of this model in mountainous areas. First, backscattering is neglected, and thereby the possible echoes are not considered. Second, three-dimensional effects relative to wind and topography are neglected by the $N\times$ 2D approach.

C. 3D pressure calculation and AS

The determination of the AS from the PE solution is detailed. Since the PE solution does not account for atmospheric absorption, a correction is then applied to the pressure,

$$p(f,x,z) = p_{\mathrm{PE}}(f,x,z)\,\exp\left[-\alpha(f)R(x,z)\right], \tag{7}$$

where the atmospheric absorption factor α is based on the ISO 9613–1 standard (ISO, 1993). From this, the SPL $L_p(x,z)$ is calculated with

$$L_p(x,z) = 10\log_{10}\left(\frac{|p(x,z)|^2}{p_{\mathrm{ref}}^2}\right), \tag{8}$$

with $p_{\mathrm{ref}} = 2\times10^{-5}$ Pa. Finally, the propagation loss is determined in each slice with $\mathrm{PL}(x,z) = L_p(x,z) - \mathrm{SL}$.

To obtain the acoustic field on the whole 3D geometry, PE calculations are repeated for each vertical slice by varying the angle θ around the z axis, with a step $\mathrm{d}\theta$, as shown in Fig. 1. The 2D topography profiles are obtained by interpolation of the 3D topography. We further consider an angular step of $\mathrm{d}\theta = 2°$. A map of PLs around the source at a given height above the ground, chosen as 1 m, is deduced as illustrated in Fig. 3.

The area of the AS, denoted by A, is then computed from the PL map. For that, the PL is determined at receivers placed at 1 m height from the ground, with a step $\mathrm{d}x = 1$ m. The receivers for which the propagation loss is above the threshold are identified. The AS area is thus the sum of elementary surface areas $x\,\mathrm{d}x\,\mathrm{d}\theta$. Because of the limitation in the propagation angle associated with the PE method, receivers placed under this angle near the source are not considered in the PE calculation and are assumed to belong to the AS.

JASA
https://doi.org/10.1121/10.0011545

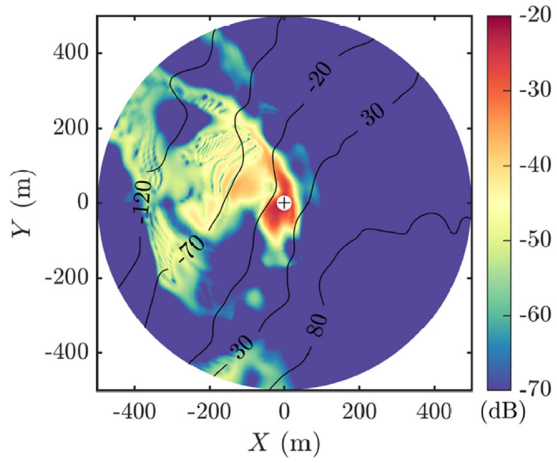

FIG. 3. (Color online) Map of the PL at 1 m height, for a frequency of 1000 Hz. Contour lines are drawn every 50 m in thin lines. Conditions: topography 1 in Fig. 13, homogeneous atmosphere, and $z_s = 1$ m.

III. COMPARISON OF WAPE MODEL WITH ON-SITE MEASUREMENTS

To validate the prediction capacity of the model, measurements were performed in a mountain environment. This section details how the environmental parameters were measured and presents the comparisons between the results of the acoustical field measurements and the corresponding numerical simulations.

A. Experiments

1. Measurement site

The measurements were conducted in October 2020 in the French Alps on the site of Col du Lac Blanc in the Massif des Grandes Rousses [45.13 N, 6.11 E, 2720 m above sea level (a.s.l.)]. This site was chosen because two research institutes [Centre d'Etudes de la Neige (CEN) and the Institut National de Recherche pour l'Agriculture, l'Alimentation et l'Environnement (INRAE)] maintain two complementary automated weather stations (AWSs) at this location. This allows us to obtain the meteorological data during the experiments. Despite the site not being dedicated to the monitoring of rock ptarmigan population, it is typical of mountain environments where the rock ptarmigan lives.

The site is a mountain pass that presents a hill shape of 15 m height in its longitudinal section (north-south direction), called hereafter the "hill." The wind is naturally channeled in this north-south direction. The weather instrumentation is installed at the top of the small hill. A digital elevation model (DEM) of the site with bare ground was determined by Guyomarc'h *et al.* (2019), using a laser scanning technique (Fig. 4). The DEM has a horizontal resolution of 1 m and a vertical resolution of 0.1 m. The chosen propagation zone is such that echoes are absent or manageable in post-processing thanks to the short duration of the source signal.

Three transects, depicted in Fig. 4, were chosen on either side of the mountain pass. Transects t1 and t2 are

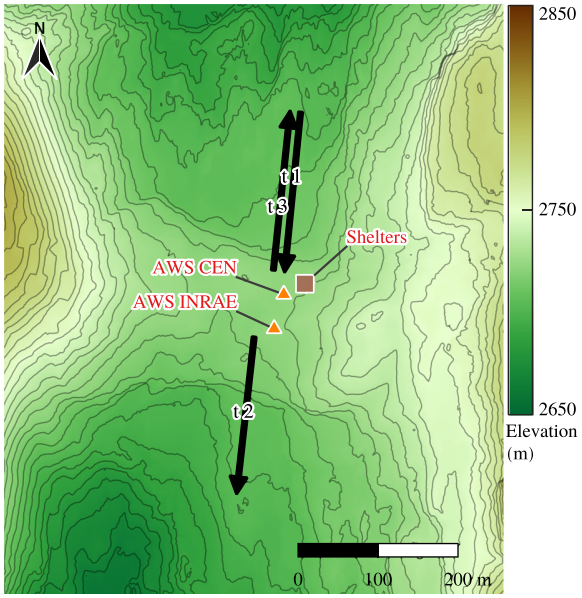

FIG. 4. (Color online) Map of the measurement field at Col du Lac Blanc (Massif des Grandes Rousses, France), with 5 m contour lines. Propagation transects (t1, t2, t3) and their direction are drawn with black arrows. AWSs (AWS CEN) and (AWS INRAE) are depicted by triangles.

directed to the south, uphill and downhill, respectively. Transect t3 is reversed with respect to t1 and thus faces north downhill. Several measurements were carried out on these different transects in various weather conditions. Among the available data, results for four representative configurations, denoted by A, B, C, and D, are presented in this paper and summarized in Table I. The configurations A and B are for similar meteorological conditions but for two different topographies, transects t1 and t2. The configurations C and D are both for the same topography, transect t3, but with different meteorological conditions.

2. Meteorological data

Atmospheric conditions during the propagation experiments were available from two AWSs, named "AWS CEN" and "AWS INRAE," which are located close to the acoustic source (Figs. 5 and 6). Temperature and humidity were measured by five sensors (HMP155A, Vaisala, Vantaa, Finland) mounted on the AWS CEN at heights of 0.8, 1.3, 3.2, 5, and 7 m above the snow surface. Wind direction and velocity were obtained from the AWS INRAE. The wind vane (W200P-01,

TABLE I. Detailed measurement configurations (A, B, C, D) with the transect concerned (t1, t2, t3), the propagation condition, and the gradient of effective sound speed near the ground Δc_{eff} ($\text{m}\cdot\text{s}^{-1}$).

Configuration	Transect	Condition	Δc_{eff} ($\text{m}\cdot\text{s}^{-1}$)
A	t1	Strong downward	4.3
B	t2	Strong downward	6.4
C	t3	Slight upward	−0.3
D	t3	Moderate upward	−1.8

Vector Instruments, Saint Asaph, UK) was mounted at a height of 11.08 m, and five anemometers (Vector Instruments A100LK) were mounted at heights of 1.76, 3.25, 4.1, 7.25, and 9.42 m. Data discussed in the following paragraphs are the average temperature and the average and standard deviation of the wind velocity, both integrated over periods of 10 min and measured during the sound propagation experiments.

The raw data of temperature and wind speed measured with the two AWSs are plotted with markers in Fig. 7 as functions of the height above the snow cover z_g. The wind speed profile presents a significant acceleration in the first 4 m above the ground. This is due to a localized Venturi effect induced by the hill in the middle of the pass.

Meteorological data were extrapolated by means of an iterative fitting procedure based on the Monin and Obukhov (1954) similarity theory (MOST). One of the assumptions of MOST is that the ground is flat and homogeneous, which is clearly not the case here. However, with no better description of the atmosphere, MOST is used as it provides representative wind and temperature profiles encountered in the ASL. Wind and temperature profiles are given by

$$U_{\mathrm{fit}}(z_g) = \frac{u_*}{\kappa}\left[\ln\left(\frac{z_g + z_0}{z_0}\right) - \psi_w\left(\frac{z_g}{L_{\mathrm{MO}}}\right)\right], \tag{9}$$

$$T_{\mathrm{fit}}(z_g) = T_0 + \frac{\theta_*}{\kappa}\left[\ln\left(\frac{z_g + z_0}{z_0}\right) - \psi_t\left(\frac{z_g}{L_{\mathrm{MO}}}\right)\right] + \alpha_0 z_g, \tag{10}$$

with $\kappa = 0.41$ the von Kármán constant, u_* the friction velocity, T_0 the air temperature near the ground, θ_* the temperature scale, L_{MO} the Monin–Obukhov length, $\alpha_0 = -0.01$ K·m^{-1} the dry adiabatic lapse rate, and z_0 the roughness length of the ground surface set to 0.01 m. The functions ψ_w and ψ_t are derived from the Businger–Dyer relations, as detailed in Salomons (2001). To get rid of the local acceleration discussed above, the fitting procedure takes into account the five measured temperature values but only the three wind speeds at the upper positions. The fitted profiles are plotted in Fig. 7 according to the four configurations. The fit with the measurements appears appropriate for the temperature $T(z_g)$. For the wind speed $U(z_g)$, noticeable discrepancies are observed: they are related to the local acceleration near the ground. The corresponding MOST parameters obtained are listed in Table II.

Typical values for u_* are indicated in Ostashev and Wilson (2016): 0.1, 0.3, and 0.6 m/s correspond to a light, moderate, and strong wind condition, respectively. Therefore, all four configurations are under light or moderate wind conditions as u_* is between 0.13 and 0.19 m/s. The angle ψ between measured wind direction and each transect remains relatively constant during each measurement period as shown by the values of its standard deviation σ_ψ, given in Table II.

The extrapolated profiles of wind speed and temperature are used to determine the effective sound speed. It is defined as the sum of the sound speed and the horizontal component of the wind speed in the direction of propagation,

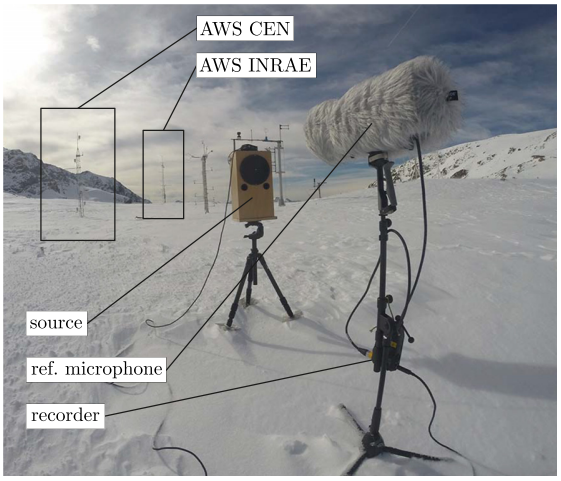

FIG. 5. (Color online) Picture of the measurement setup for acoustic propagation: source, reference microphone, and two AWSs: AWS CEN and AWS INRAE (setup of transect 3).

$$c_{\mathrm{eff}}(z_g) = \sqrt{\gamma r_{\mathrm{air}} T_{\mathrm{fit}}(z_g)} + U_{\mathrm{fit}}(z_g)\cos\psi, \tag{11}$$

with ψ the angle between the mean wind direction and the transect direction from the source and $r_{\mathrm{air}} = 287\,\mathrm{J\cdot kg^{-1}\cdot K^{-1}}$ the specific gas constant for dry air. The effective sound speed profiles are plotted in Fig. 7. It appears that configurations A and B present a predominant effect of the temperature gradient, while configurations D show a predominant effect of the wind speed gradient. Finally, configuration C is a nearly homogeneous case.

To characterize the sound speed gradient near the ground, the parameter $\Delta c_{\mathrm{eff}} = c_{\mathrm{eff}}(z_g = 20\,\mathrm{m}) - c_0$ is introduced. It determines the atmospheric refraction: upward for $\Delta c_{\mathrm{eff}} < 0$, downward for $\Delta c_{\mathrm{eff}} > 0$, or homogeneous for $\Delta c_{\mathrm{eff}} \approx 0$. Downward condition is induced by a temperature inversion and/or a downwind condition. It leads to refraction of sound waves toward the ground and to an increase in sound level at the vicinity of the ground. Conversely, upward conditions occur for negative temperature gradients and/or for headwind. Now sound waves are refracted toward the sky, inducing shadow zones at long range. The values of Δc_{eff} for the four configurations are given in Table I: A and B correspond to strong downward refracting conditions, and C and D correspond to slight and moderate upward refracting conditions, respectively.

TABLE II. Parameters of the fitted temperature and wind profiles for configurations (A, B, C, D): Monin–Obukhov length L_{MO}, air temperature near the ground T_0, temperature scale θ_*, friction velocity u_*, angle between wind direction and the transect $\psi \pm \sigma_\psi$ (σ as the standard deviation), and RH.

Configuration	L_{MO} (m)	T_0 (°C)	θ_* (K)	u_* (m·s^{-1})	$\psi \pm \sigma_\psi$ (deg)	RH (%)
A	8.4	−6.57	0.09	0.10	22 ± 12	98
B	6.4	−4.04	0.13	0.11	6 ± 13	40
C	9	−0.76	0.01	0.03	314 ± 30	90
D	205	−1.06	0.00	0.09	20 ± 19	96

https://doi.org/10.1121/10.0011545

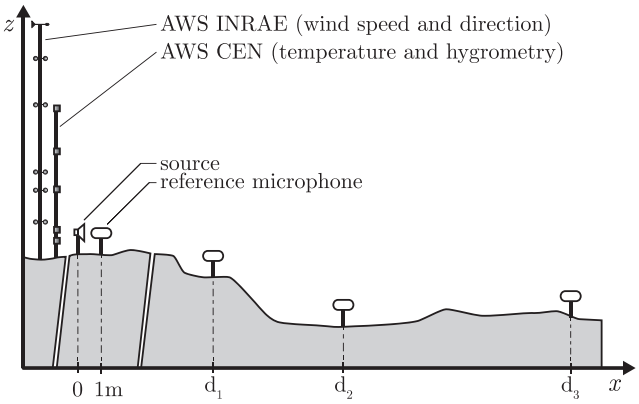

FIG. 6. Sketch of the measurement setup on a transect. Source–microphone distances are $d_1 = 50\,\text{m}$, $d_2 = 100\,\text{m}$, and $d_3 = 200\,\text{m}$.

In addition to average meteorological profiles, two other conditions are defined considering each configuration to investigate the influence of meteorological variability on sound propagation. For that, it is assumed that the temperature evolves more slowly with time than the wind speed and, as a consequence, that the meteorological variability is only due to that of the wind speed. Two other sets of temperature and wind speed profiles are thus obtained using MOST from $T(z)$ and from the reduced values $U(z) - 2\sigma_U(z)$ and increased values $U(z) + 2\sigma_U(z)$, where $\sigma_U(z)$ is the standard deviation of the wind speed given by the AWS. They are then used to determine the corresponding effective sound speed profiles.

Finally, the relative humidity (RH) (Table II), used to calculate the atmospheric absorption factor α, is determined as the time average of the values measured by the five humidity sensors.

3. Acoustic propagation measurements

The sound source was a high power portable loudspeaker, designed and built for the experiment. Its directivity was measured in an anechoic chamber. Microphones used were four Beyerdynamic (Heilbronn, Germany) MM1 audio microphones covered with a RØDE (Sydney, Australia) Blimp MkII windscreen (Fig. 5). Four H6 audio recorders (Zoom, San Jose, CA) were used. The source and the microphones were placed at 1 m above the snow cover surface. A reference microphone was first calibrated at 94 dBSPL at the frequency of 1000 Hz with a class 1 calibrator (CR517, Cirrus, Hunmanby, UK). A relative calibration of the microphone with their recorder was performed at the same time for all microphones in front of the source with a 50 dBSPL, 1000 Hz signal. This procedure allowed us to synchronize the recordings. The reference microphone was then positioned at 1 m from the loudspeaker as seen in Fig. 6, and the three other microphones were moved 50, 100, and 200 m away from the source using a GPS receiver. The relative distances were measured using a laser telemeter with an accuracy on the order of ± 1 m.

The source signal was a 1 s chirp made of a sinus sweep with frequency increasing exponentially from 100 to 3600 Hz. To ensure that the level measured at 200 m from the source is significantly higher than the background noise, the SL is set to 110 dBSPL at 1 m from the loudspeaker, which is higher than the estimated level of the vocalizations of the ptarmigan. This allows for relevant comparisons with our model in the following. The chirp was repeated every 10 s during 10 min. This led to a series of 60 measured waveforms per 10 min period that can be related to corresponding meteorological data since the weather stations provide the mean wind and temperature profiles averaged over 10 min periods.

The background noise SPL was always at least 10 dB lower than the levels measured at the microphones over the frequency band 300–3000 Hz. It is therefore reasonable to consider that the background noise had no influence on the measured pressure levels.

4. Snow impedance

Several techniques can be used to measure ground impedance (Albert, 2001; ANSI/ASA, 2010; Datt *et al.*, 2016; Guillaume *et al.*, 2015; Moore *et al.*, 1991; Nordtest, 1999). In the present study, the snow impedance was measured *in situ* using the method proposed by Guillaume *et al.* (2015), which is suited for grazing angles and has been

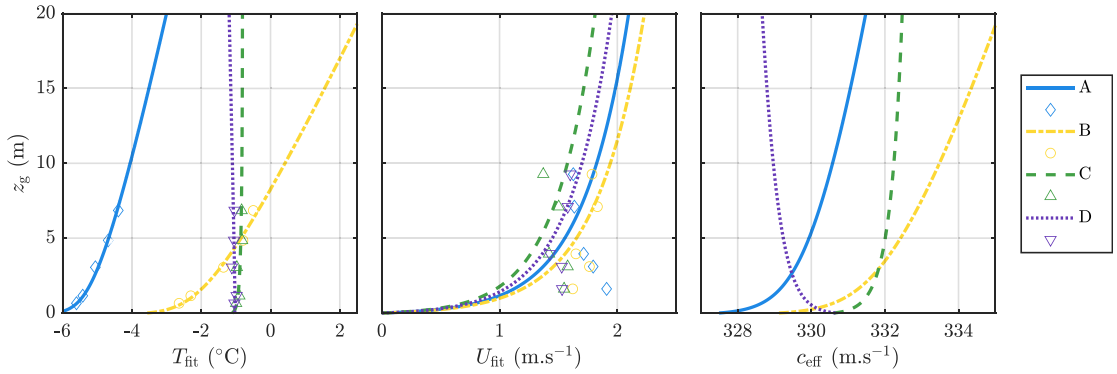

FIG. 7. (Color online) Fitted temperature T_{fit} and wind U_{fit} profiles and deduced effective sound speed profile c_{eff} from the four measurements carried out (A, B, C, D) are depicted by lines. Corresponding measured data $U(z_g)$, $T(z_g)$ are depicted by markers.

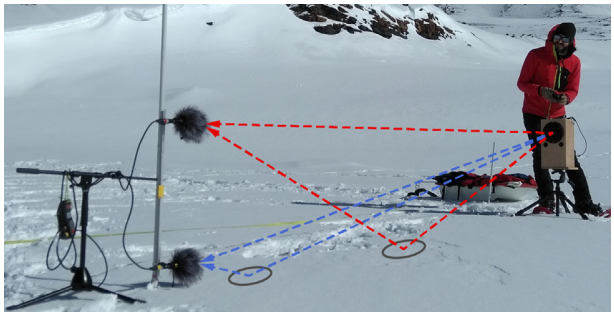

FIG. 8. (Color online) Picture of the measurement setup for snow impedance. The different wave paths are represented by dotted lines. The loudspeaker is on the right, and two microphones are on the left.

shown to provide reliable data for long-range propagation computation (Dragna *et al.*, 2014). These measurements were made just before or after the propagation experiments, at a single location representative of the snow cover along the propagation path. The method consists in carrying out a propagation experiment between a source placed at 0.7 m from the ground and two microphones 4 m apart and placed at 0.1 and 0.7 m from the ground, as shown in Fig. 8. The source signal was a 1 s exponential frequency chirp from 100 to 3000 Hz, repeated 50 times at 4 s intervals. From the measured signals, the transfer function between the two microphones is calculated and then compared to the analytical transfer function, whose impedance parameters are adjusted to adapt to the measured data. Assuming that the ground is flat and the snow cover is uniform with a constant thickness, the transfer function can be calculated analytically using the Weyl–Van der Pol equation [see, e.g., Attenborough and van Renterghem (2021)]. Note that extended reaction has been taken into account in the analytical formulation. The four parameters of the surface admittance model [see Eqs. (4)–(6)] are then manually fitted to match the analytical transfer function with the measured one. The corresponding analytical and measured transfer functions are represented in Fig. 9 for the 2 days concerned. Table III indicates the resulting parameters of the impedance model. These results are consistent with those in Moore

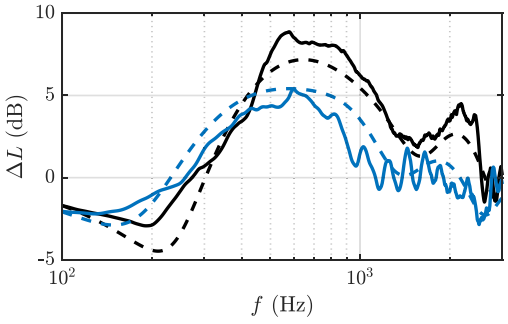

FIG. 9. (Color online) Transfer function for the determination of snow impedance ΔL for configurations A and B (black lines) and configurations C and D (blue lines): measure (solid lines) and analytical fit (dashed lines).

TABLE III. Impedance parameters obtained during the 2 days of measurement on the site of Lac du Col Blanc: the effective thickness e, the airflow resistivity R_s, the porosity Ω, and the tortuosity q^2. The corresponding configurations (A, B, C, D) are indicated.

Configuration	e (m)	R_s (Pa · s · m^{-2})	Ω	q^2
A, B	0.13	10 000	0.6	1.3
C, D	0.2	7000	0.6	1.3

et al. (1991), Albert (2001), and Datt *et al.* (2016) for the same type of snow (powder snow).

It should be noted that the method is based on assumptions that are not always valid for this type of *in situ* measurement of snow impedance. First, in the model, the snow depth is assumed to be constant, while in reality, it is not uniform over the entire propagation domain. However, specific tests carried out during the present measurement campaign in different parts of the domain showed that the surface impedance in the frequency band of interest was only slightly modified by the thickness of the snow layer, as soon as it exceeds 15 cm. This thickness value is comparable to the computed values of the effective thickness e. Second, the ground is assumed to be flat. This assumption is reasonable for the measurements presented here because the layer of fresh snow present on the site had a homogeneous structure and a smooth surface, but this may not always be the case, especially when the wind generates a wavy surface and when the surface layer is made of frozen wet snow. This could induce a rough surface, which is outside the scope of this method.

B. Comparisons with the propagation model

1. Description

To fairly compare the results of the propagation model to the measurements, the measured data were processed as explained in Sec. III A 2 for the meteorological conditions and Sec. III A 4 for the snow impedance to obtain input data of the numerical simulations. The four configurations (A, B, C, D) are described in Table I, with corresponding MOST parameters in Table II and snow impedance parameters in Table III. The position of each transect is shown in Fig. 4, and their corresponding topographic profiles are shown in Fig. 10. As the DEM of the site is given for a bare ground, it does not account for the snow cover. The DEM is then corrected by adding a snow cover estimated at 20 cm on the entire site, based on our observations.

In addition, a significant snow accumulation was noticed along the slopes of the hill: the snow cover was measured using a probe in the middle of the slopes, yielding a depth of 1 m on the north slope and of 1.4 m on the south slope. An additional correction is thus applied to the DEM along the hill slopes to account for this accumulation.

With this corrected DEM, the microphones at $x = 100$ m for configuration B and at $x = 50$ m for configurations C and D are in geometrical shadow zones, where the source has no

https://doi.org/10.1121/10.0011545

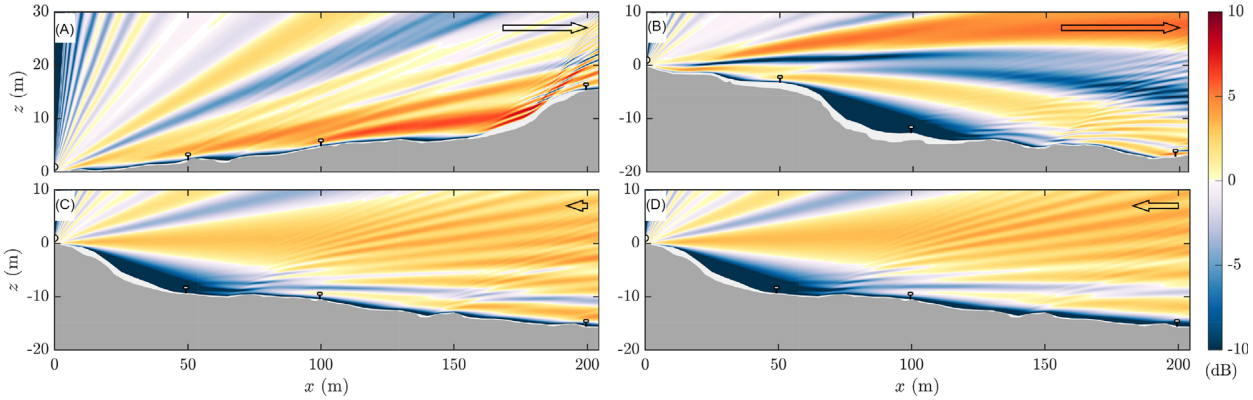

FIG. 10. (Color online) Pressure levels relative to free field ΔL simulated at 1000 Hz, for four configurations (A, B, C, D): actual terrain profile relative to source position $x_S = 0$, $z_S = 1$ m (gray surface); snow cover depth considered over the bare ground and smoothed every 5 m (white surface); microphone positions $x = 50$, 100, and 200 m (dots); and arrows of length proportional to Δc_{eff}. Scale $z/x = 1/2$.

direct view of the receivers assuming a homogeneous atmosphere with no refraction effect. Low SPLs are expected in these areas.

Computations are performed for the effective sound speed profile obtained from the average wind speed and temperature (T, U) reported in Sec. III A 2 as well as for the profiles accounting for wind speed variability $(T, U \pm 2\sigma_U)$.

2. Results

The 2D maps of the SPL relative to the free-field solution $\Delta L = \text{PL} + 20\log_{10}(R)$ computed for $f = 1000$ Hz are plotted in Fig. 10 for the four configurations. The quantity ΔL represents the deviation from SPL in free field due to atmospheric refraction and diffraction effects. The 2D maps show a strong decrease in the acoustic pressure at the vicinity of the ground caused by the snow cover. The pressure level is equivalent to or lower than that in free field in the first centimeters above the ground. In all four cases, ΔL has a variability of ± 10 dB for the majority of microphone positions except in the shadow zones. Shadow zones are noticed at $x = 100$ m for configuration B and at $x = 50$ m for configurations C and D. They are visible in Fig. 10, where ΔL approaches –10 dB or less (in dark blue).

The influence of the sound speed gradient Δc_{eff} is visible on the distribution of the acoustic field across the domain. In particular, in case B, the acoustic energy is directed to the ground beyond 150 m due to downward conditions. This refraction reduces the size of the shadow zone compared to the homogeneous case. Conversely, case D shows an upward refraction due to upwind condition.

The results of the simulations are compared to the measurements using the relative SPL ΔL_p defined as $\Delta L_p(x,z) = L_p(x,z) - L_p(x_{\text{ref}}, z_{\text{ref}})$, with the reference point located at 1 m in front of the source. The pressure obtained with the WAPE method is not accurate in the nearfield. Then the reference level $L_p(x_{\text{ref}}, z_{\text{ref}})$ is obtained from the analytical solution of the Weyl–Van der Pol equation over a flat ground of the same impedance (Attenborough and van Renterghem, 2021). To match experimental conditions, the reflected wave amplitude is corrected by the source directivity of the loudspeaker.

For each configuration, the frequency spectrum at the receivers is deduced from computations carried out on 200 frequencies logarithmically distributed over the 200–3000 Hz band. The relative pressure levels ΔL_p obtained at each receiver ($x = 50, 100, 200$ m) are plotted in Fig. 11, along with the 60 measured spectra. In this figure, we can see for all configurations that the SPL computed by the propagation model closely matches the measurements both in downward and upward condition over the frequency band 200–3000 Hz, except for some pronounced interferences. Moreover, the variability in the frequency of the destructive interference pattern is fairly well reproduced by taking into account the variability of the wind speed. The discrepancy on the absolute position of the interference patterns can be explained by the piecewise linear approximation of the topography used in the propagation model, by the uncertainty on the wind speed along the propagation path, and by the uncertainty on the position of microphones. Note that small uncertainties influence the spectra calculated by the model and in particular above a certain frequency whose wavelength approaches the size of the error on the geometry. This could also be due to the single value approximation of the snow impedance boundary condition. The level estimations in shadow zone for configuration B at 100 m show a relative agreement in variability due to wind speed. For configurations C and D in upward conditions, the measured pressure levels are also in good agreement with the propagation model in the geometrical shadow zone of transect 3 at 50 m and in the shadow zone at 200 m induced by upward refraction.

An additional comparison between measurements and numerical results is shown in Fig. 12. It presents the boxplots of ΔL_p integrated on the 1000 Hz octave band for the 60 measured waveforms at the three microphones and for the four cases. The 1 kHz octave band is chosen because the amplitude of ptarmigan vocalization is maximal in this band. For readability, the boxplots are centered on the median of the measured data. The four configurations are sorted according to the sound speed gradient Δc_{eff}.

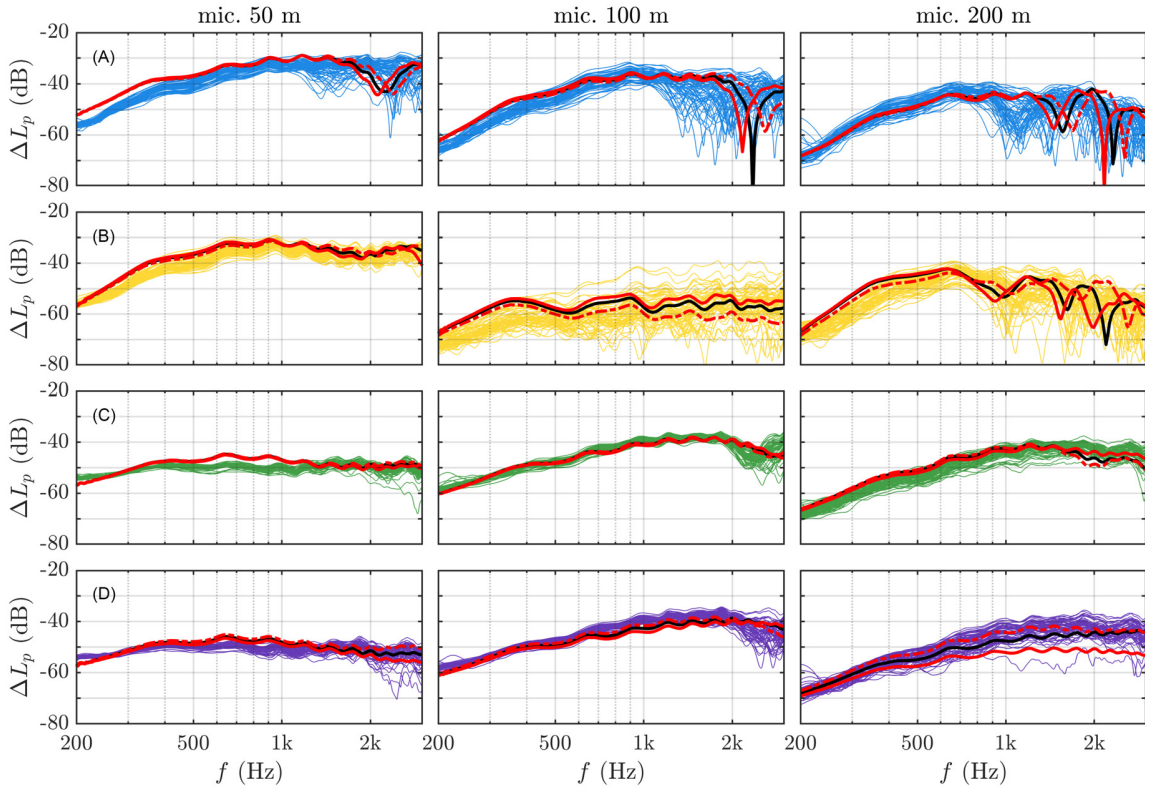

FIG. 11. (Color online) ΔL_p determined from the measurements (in thin color line) and simulated for c_{eff} deduced from (T, U) in black solid line, (T, $U-2\sigma_U$) in red dashed line, and (T, $U+2\sigma_U$) in red solid line. These results are for the four cases (A, B, C, D from top to bottom) and for the three microphone locations ($x=50$, 100, and 200 m from left to right). Same colors as in Fig. 6.

The boxplots indicate the variability of the measured SPL. The SPL calculated with the propagation model for the profiles of average temperature and wind speed (T, U) and for the profiles accounting for wind speed variability (T, $U\pm2\sigma_U$) are also plotted in Fig. 12.

The correspondence between the median of the measured SPL and the SPL predicted with the propagation model for the average meteorological conditions is first analyzed. For all conditions, the model provides an accurate estimation of the levels measured in the 1000 Hz band for receivers placed at 50, 100, and 200 m. The differences are between –3.1 and +2.9 dB, including estimate levels in geometrical shadow zones (case B at 100 m and C and at 50 m) and also in refraction-induced shadow zone (case D at 200 m). At a distance of 50 m, meteorological effects have little influence, and overestimates are more likely due to topography approximation and uncertainty in snowpack depth, which define the line of sight and therefore the geometric shadow areas. The propagation model also allows analysis of the variability of the SPL due to sound speed profiles. For that, the dispersion between the first and third quartiles in the boxplots is compared with the difference in the SPL calculated for the profiles (T, $U-2\sigma_U$) and (T, $U+2\sigma_U$). A fair agreement is obtained overall. However, in case A, the simulated variability is not accurately reproduced at 50 and 100 m. This is due to inaccurate prediction of the destructive interference frequency on the 1000 Hz octave band. In case B, the level variability matches well the measurements, except at 50 m. Cases C and D also show a good agreement for the three microphone positions. This implies in particular that the variability of the measured SPL is partly explained by the variability of the wind speed. However, we only consider the variability of wind speed at the weather station, while pressure levels may depend on local wind speed and direction fluctuations along the propagation path as well as local changes in the temperature profile.

In summary, these results show that predictions of SPLs using a wave propagation model are consistent with field measurement. Levels are correctly estimated in shadow zones, whether geometric or headwind induced, allowing the model to be used to study the AS of birds in a mountainous habitat. However, we note that partial knowledge of input parameters and approximations may induce errors in the prediction of levels. We mentioned that the approximation of terrain profiles and snowpack thickness can shift the location of geometric shadow zones. Atmospheric parameters can hardly be characterized over the entire area of interest and must be extrapolated from weather stations. In addition, the model does not account for rapid temporal or spatial variations in wind direction or for turbulence. The impedance value determined for one location was applied to the entire propagation path because the snow parameters in the chosen measurement site were nearly constant. However, in more

JASA
https://doi.org/10.1121/10.0011545

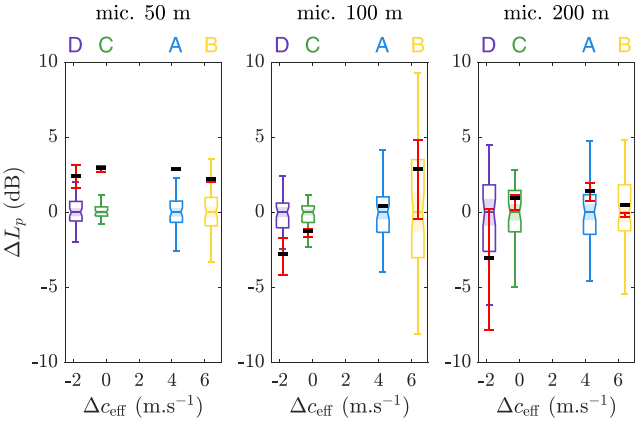

FIG. 12. (Color online) Comparison of ΔL_p of the measurements and simulations on the octave band 1000 Hz (global levels) plotted around the median of the measurements for the four configurations (A, B, C, D) and according to the three microphone distances (50, 100, and 200 m). Measurements are depicted by boxplots (without outliers), and simulations are depicted by linked dashes, with the same colors as in Fig. 11.

complex areas, the composition of the snowpack, the surface shape, and the presence of rocks may require more complex ground impedance modeling. If more complete and more complex propagation models are possible in the future, it is to the detriment of the computational cost, which is a parameter to be taken into account for parametric studies. The expected gain in terms of accuracy is also not guaranteed if one is not able to characterize the medium in more detail.

IV. VARIABILITY OF THE COMMUNICATION ACTIVE SPACE

The propagation model is now applied to investigate the influence of the topography, the meteorological conditions, and the source altitude on the AS of rock ptarmigans. Here, the source is considered static with a height above the ground defined as the typical flight altitude of the bird.

A. Description

The study is done for another site in the French Alps, which is chosen because a population of rock ptarmigans lives on this site all year round, especially during the breeding season (Canonne *et al.*, 2020; Marin-Cudraz *et al.*, 2019; Novoa *et al.*, 2019). This site is the Flaine ski resort (45.99 N, 6.73 E, 2400 m a.s.l.) and is referred to as "Flaine" in the remainder of this section. Its topography is presented in Fig. 13. DEM data of the bare ground with 5 m resolution were provided by the French National Geographic Institute (IGN: Institut national de l'information géographique et forestière). To avoid any sharp slopes, a low-pass filter has been applied to the topography. This smoothing procedure is reasonable since the actual snow layer naturally fills the depressions in the ground. The acoustic properties of the snow cover are identical in all configurations. They are chosen as $e = 0.15$ m, $R_s = 20\,000$ Pa · s · m^{-2}, $\Omega = 0.6$, $q^2 = 1.66$ to be representative of a moderately compacted snow as measured by Datt *et al.* (2016). The meteorological conditions are imposed using wind speed and temperature profiles from MOST (see Sec. III A 2) and a wind direction from south to north. The pressure field calculation is done within a 500 m radius around the point source. All the following maps are oriented with north at the top in the present section.

B. Results

1. Influence of topography

The ASs are computed for the four positions on the Flaine site presented in Fig. 13. These positions illustrate typical situations encountered in mountain environments: terrain with a steep slope (P1), gentle slope (P3), a promontory (P2), and a valley (P4). To isolate topographic effects, nearly homogeneous conditions are considered, with $u_* = 0.05$ m·s^{-1}, and $\theta_* = 0$.

Maps of the propagation loss are plotted in Fig. 14 for the four positions indicated in Fig. 13 on the Flaine site. They show that the shape of the AS depends significantly on the topography. Even in homogeneous atmospheric conditions, AS is therefore neither circular nor symmetrical over uneven landforms. In details, for P1, sound propagates preferentially toward the west, down the slope. For P2, the AS has a comparably small area and is essentially limited to the top of the promontory. For P3, the AS is discontinuous: it is made of a disk with a radius of about 200 m centered at the source and of small spots that can be seen at a large distance from the source (up to 500 m). Finally, for P4, the steep slopes of the valley prevent sound from propagating, and the AS is restricted to the bottom of the valley. In addition, the striations noticeable on P1 and P4 correspond to interference patterns due to the monochromatic calculation. Such pattern would not be visible in a broadband calculation.

2. Influence of meteorological conditions

The impact of meteorological conditions on the AS is now investigated. For that, the AS is calculated as a function

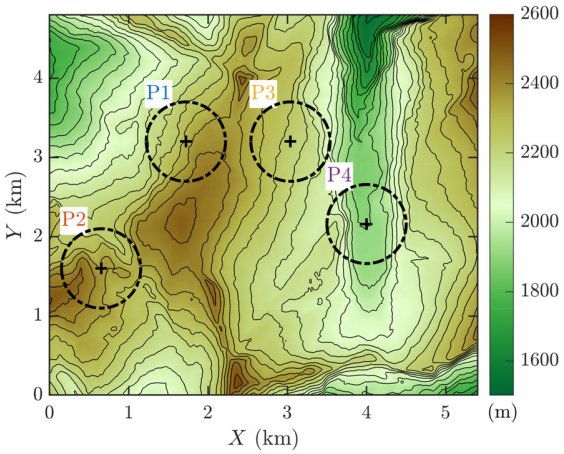

FIG. 13. (Color online) Topography of the Flaine ski resort, x, y positions of sources marked with crosses and circular computation domains for AS estimation (1, 2, 3, 4) in thick dotted lines. The map is oriented north up, and 50 m contour lines are drawn in thin black lines.

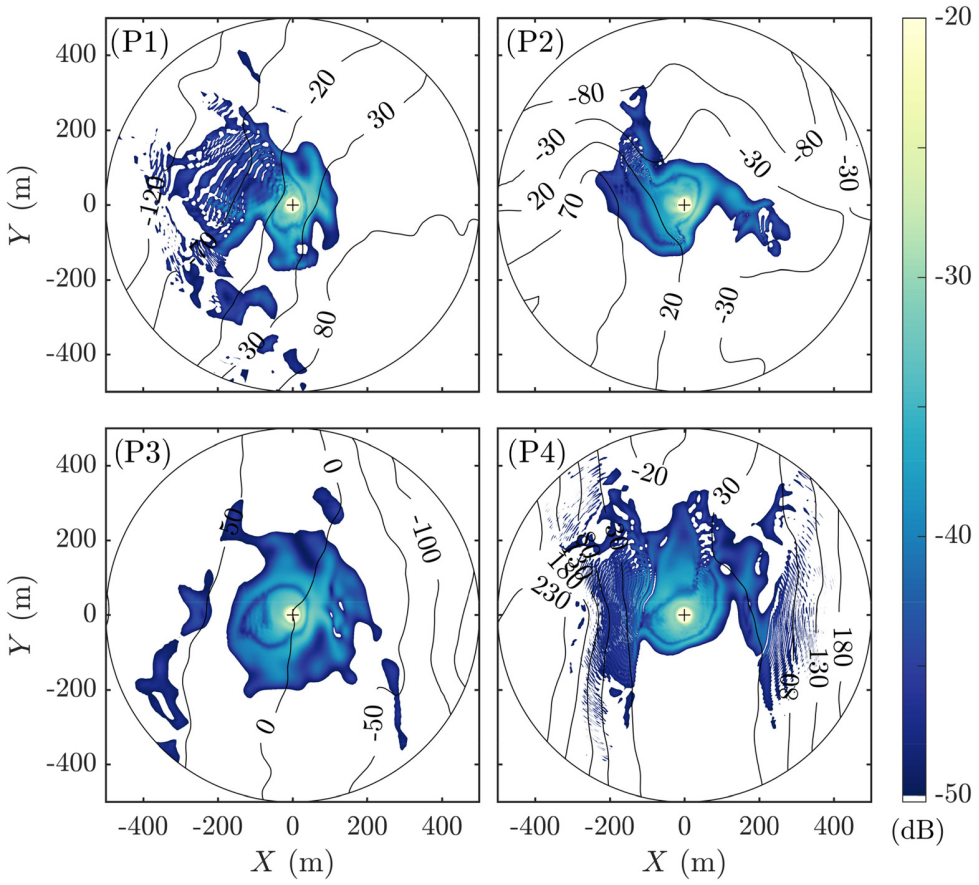

FIG. 14. (Color online) Map of the PL for the four positions (shown in Fig. 13) at 1 m height for a 1000 Hz frequency signal in nearly homogeneous atmospheric conditions: $u_* = 0.05\,\mathrm{m\cdot s^{-1}}$, $\theta^* = 0\,\mathrm{K}$, $z_S = 10$ m. Contour lines are drawn every 50 m in thin lines.

of the governing parameters for the wind and temperature profiles defined in Sec. III A 2. For the wind, the relevant parameter is still the friction velocity u_*. However, for the temperature, the sensible heat flux Q_H is now chosen instead of θ_*, because of its simpler physical interpretation. Indeed, the sensible heat flux represents the transfer of heat to the surface from the overlying air induced by the temperature difference between the ground surface and the atmosphere. It is related to u_* and θ_* by $Q_H = -\theta_* \rho_0 c_p u_*$, where c_p is the specific heat at constant pressure. The sensible heat flux depends on solar radiation and cloud cover. Thus, on a clear night, we have $Q_H < 0$, which leads to a positive temperature gradient and, hence, a positive sound speed gradient that favors sound propagation at long range. On the contrary, $Q_H > 0$ on a clear day, inducing a negative sound speed gradient that opposes sound propagation.

The AS is first computed for several values of the sensible heat flux Q_H and $u_* = 0.3\,\mathrm{m\cdot s^{-1}}$. Corresponding MOST parameters and weather conditions are given in Table IV. The values chosen for Q_H have been taken from Ostashev and Wilson (2016), and measurement data over snow were provided in Mott *et al.* (2013). They are assumed to be representative of the snow radiation behavior. Maps of PL for position 1 are shown in Fig. 15. Thus, a change from $Q_H = 400\ \mathrm{W\cdot m^{-2}}$, corresponding to a clear daytime [Fig. 15(c)], to $Q_H = -100\ \mathrm{W\cdot m^{-2}}$, corresponding to a clear nighttime over snow [Fig. 15(a)], induces an increase in the area of 30%.

Calculations of the AS are then performed for several values of u_* and for $Q_H = 0\ \mathrm{W\cdot m^{-2}}$. The chosen values of u_*, which are 0.05, 0.3, 0.7, and 1.1 m/s, induce wind speed values at 2 m height of $U_{(2m)} = 0.4$, 2.2, 5.2, and 8.2 m/s, respectively. These values imply a large scale of wind conditions, from very low to very strong wind, which slightly outstrips the proposed wind scale values of Ostashev and Wilson (2016). The corresponding maps of PL for position 1 are shown in Fig. 16. Increasing u_* tends to enlarge the shadow zone upwind and to reduce the AS accordingly.

TABLE IV. Conditions used in AS calculations, derived from the sensible heat flux: MOST parameters, wind speed 2 m above the ground, and celerity gradient in the wind direction $\Delta c^+_{\mathrm{eff}}$.

Condition	Q_H ($\mathrm{W\cdot m^{-2}}$)	u_* ($\mathrm{m\cdot s^{-1}}$)	θ_* (K)	L_{MO} (m)	$U_{(2m)}$ ($\mathrm{m\cdot s^{-1}}$)	$\Delta c^+_{\mathrm{eff}}$ ($\mathrm{m\cdot s^{-1}}$)
Clear daytime	400	0.3	−1.38	−4.6	1.7	−2.1
Daytime	200	0.3	−0.69	−9	1.9	−0.2
Mostly cloudy	0	0.3	0	$-\infty$	2.2	3.8
Nighttime	−50	0.3	0.17	36.6	2.4	7.8
Clear nighttime	−100	0.3	0.36	18.3	2.6	13.1

https://doi.org/10.1121/10.0011545

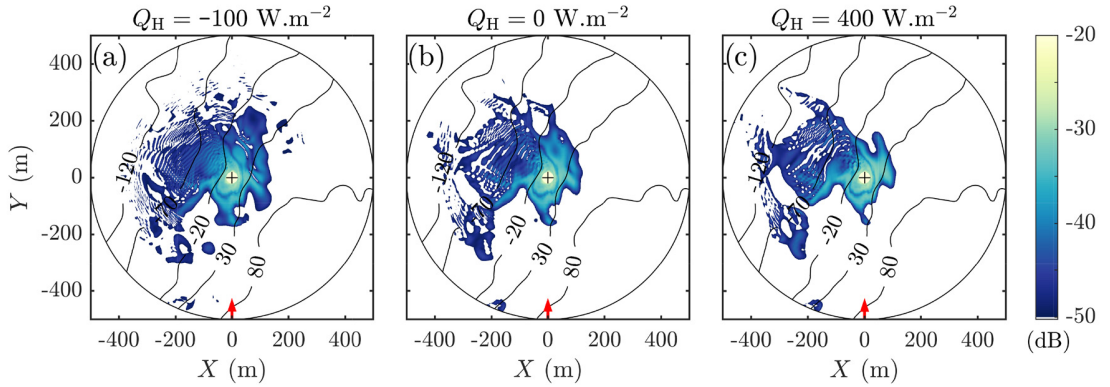

FIG. 15. (Color online) Map of the PL for different values of Q_H, at 1 m height, for a 1000 Hz frequency signal, and at P1 (shown in Fig. 13). Reference case is (b), with values $u_* = 0.3\,\mathrm{m\cdot s^{-1}}$, $Q_H = 0\,\mathrm{W\cdot m^{-2}}$, $z_S = 10\,\mathrm{m}$. Plots (a) and (c), respectively, depict the influence of sensible heat flux from $Q_H = -100$ to $400\,\mathrm{W\cdot m^{-2}}$. All other parameters are the same as the reference case. Contour lines are drawn every 50 m in thin lines. The red arrow depicts u_* and the wind direction.

In addition, a modest increase in the AS area is noticed downwind in the northeast direction for $u_* = 1.1\,\mathrm{m\cdot s^{-1}}$ [Fig. 16(c)]. Overall, the AS area is reduced by 33% when increasing u_* from 0.05 to $1.1\,\mathrm{m\cdot s^{-1}}$.

As previously shown for the plains habitat, nighttime provides a favorable condition for atmospheric propagation because of the temperature inversion (Larom *et al.*, 1997). The shape of the AS is also modified by wind speed and direction but still limited by the underlying landform.

3. Influence of source height

Finally, the influence of the source height on the AS is estimated. Calculations are performed for $Q_H = 0\ \mathrm{W\cdot m^{-2}}$, $u_* = 0.3\ \mathrm{m\cdot s^{-1}}$, and z_S between 1 and 50 m. The PL maps are plotted in Fig. 17 for position 1. The source height has a considerable influence on the AS area. When the source moves up from $z_S = 1$ m [Fig. 17(a)], the area increases by 102% for $z_S = 10$ m [Fig. 17(b)] and by +282% for $z_S = 50$ m [Fig. 17(c)]. Besides, the AS tends to be more circular as z_S increases, until it becomes a disk for a sufficiently high source, as seen for $z_S = 50$ m [Fig. 17(c)].

The results obtained here are consistent with previous studies. In forest environments, Dabelsteen *et al.* (1993), Holland *et al.* (1998), and Mathevon *et al.* (2005) showed that small changes in roost height may result in a significant increase in AS. In addition, Mathevon *et al.* (1996) highlight the importance of the singing post to limit song degradation during propagation. The crucial role of the singing height in the AS was also noticed in open areas by Jensen *et al.* (2008) in hooded crow: individuals improve their signaling condition when in flight or perched compared to the ground feeding situation. Here, the increase in the AS with source height is generalized to an uneven landform.

4. Influence of environmental parameters on different topography

Next, the influence of environmental parameters on the AS area are discussed for the four positions on the Flaine site. For comparison purposes, the area ratio (%) is introduced as A/A_{ff}, where A_{ff} is the AS area obtained in free field for the same attenuation threshold. In free field, one has $\mathrm{PL} = -20\log_{10}(R)$, and the parameter A_{ff} can then be simply calculated with $A_{ff} = \pi R_{ff}^2$, where R_{ff} is the

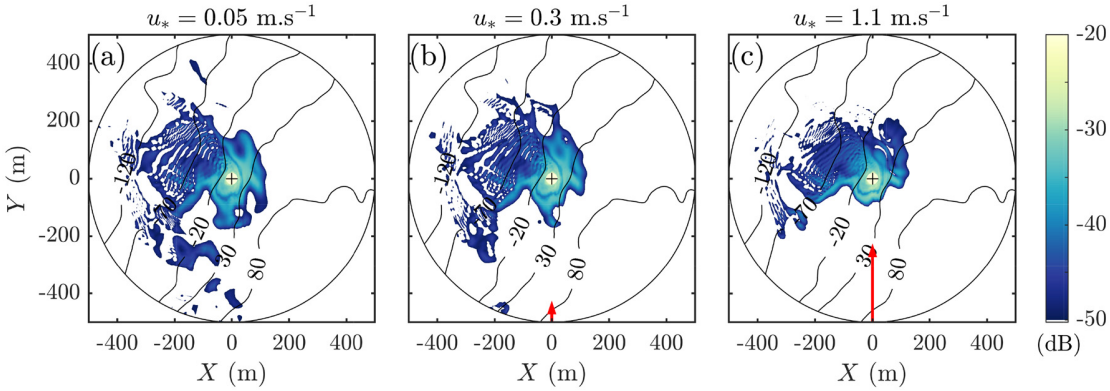

FIG. 16. (Color online) Map of the PL for different values of u_*, at 1 m height, for a 1000 Hz frequency signal, and at P1 (shown in Fig. 13). Reference case is (b), with $u_* = 0.3\,\mathrm{m\cdot s^{-1}}$, $Q_H = 0\,\mathrm{W\cdot m^{-2}}$, $z_S = 10\,\mathrm{m}$. Plots (a) and (c), respectively, depict the wind influence between $u_* = 0.05$ and $1.1\,\mathrm{m\cdot s^{-1}}$. All other parameters are the same as the reference case. Contour lines are drawn every 50 m in thin lines. The red arrow depicts u_* and the wind direction.

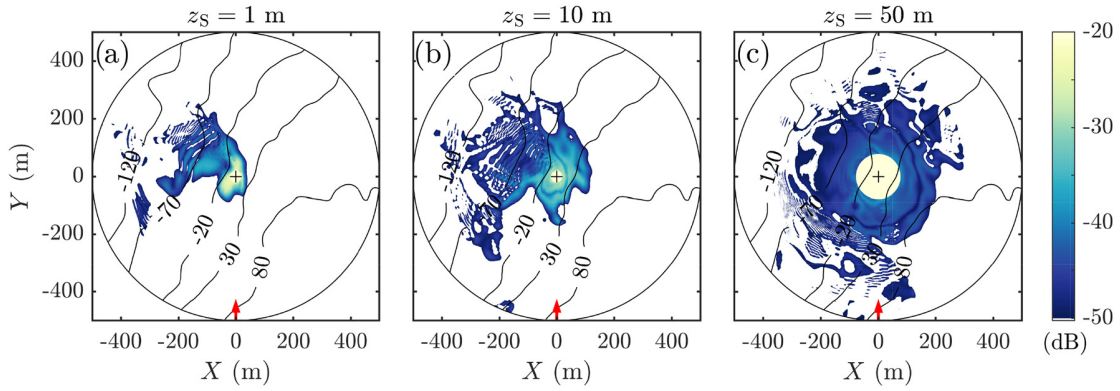

FIG. 17. (Color online) Map of the PL for different values of z_S, at 1 m height, for a 1000 Hz frequency signal, and at P1 (shown in Fig. 13). Reference case is (b), with values of $u_* = 0.3\,\mathrm{m \cdot s^{-1}}$, $Q_H = 0\,\mathrm{W \cdot m^{-2}}$, $z_S = 10$ m. Plots (a) and (c), respectively, show the influence of the source height above ground from $z_S = 1$ to 50 m. All other parameters are the same as the reference case. Contour lines are drawn every 50 m in thin lines. The red arrow depicts u_* and the wind direction.

maximum distance of detection in free field, which is equal to $R_{ff} = 10^{50/20} \approx 316$ m for a threshold of –50 dB.

Figure 18 shows the variation of the area ratio as a function of u_*, Q_H, and z_S for the four positions. The increase in the friction velocity from $u_* = 0.05$ to $1.1\,\mathrm{m \cdot s^{-1}}$ induces for all positions a reduction of the area, which varies between –4% and –23% depending on the topography. A similar reduction of the area in a range between –11% and –38% is estimated for the first three positions with the increase in Q_H from –100 to $400\,\mathrm{W \cdot m^{-2}}$. A slight augmentation of 7% is, however, noticed for position 4. This is due to its location in a valley: upward refraction leads to increased SPLs higher up in the valley. Regarding the source height, its increase from 1 to 50 m implies in all cases a large increase in the AS area, by +37% for position 4 in a valley and up to +75% for position 3 on a gentle slope.

In conclusion, the AS is dependent on the topography, the wind and temperature profiles, and the source position. Both area and shape of the AS are changed by the modification of one of these conditions. We have shed light on two predominant factors: first the topography, which constrains the spatial limits of the AS whatever the atmospheric conditions are, and second the source height. Particularly, it can be deduced that performing a display flight while singing allows the rock ptarmigan to augment its AS but also to overcome the constraint of the topographic heterogeneity.

V. CONCLUSION

The variability of the AS was investigated for the rock ptarmigan in mountain environment using numerical simulations. A model for atmospheric sound propagation based on the PE was proposed to calculate the AS. It accounts for the topography, the ground impedance, the wind and temperature profiles, and the atmospheric absorption. An experimental campaign was carried out in the French Alps to evaluate the model against long-range sound propagation measurements. Despite some uncertainties regarding weather conditions and snow impedance, a good agreement was obtained between calculations and measurements.

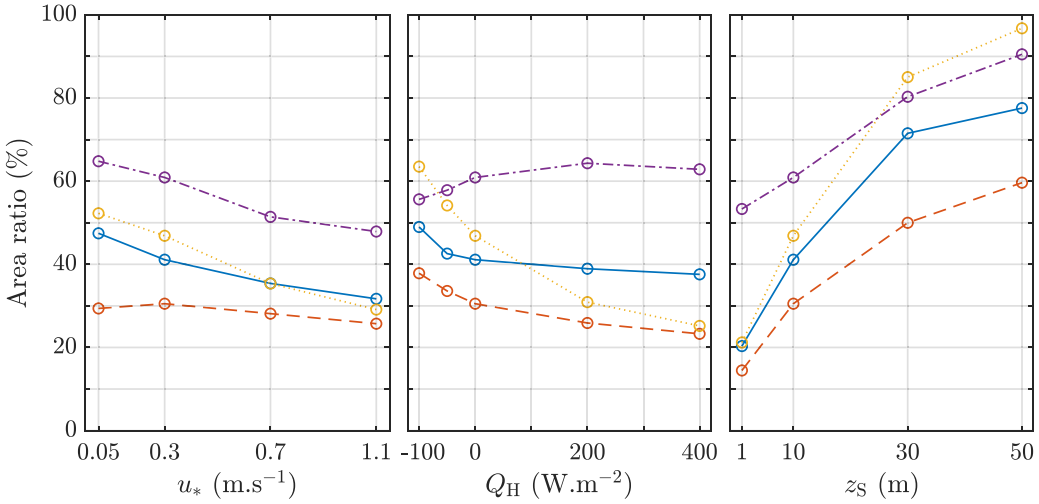

FIG. 18. (Color online) Variations of the area ratio with the friction velocity u_*, the sensible heat flux Q_H, and the source height z_S for the four positions shown in Fig. 13: 1 (blue solid), 2 (orange dashed), 3 (yellow dotted), 4 (violet dashed-dotted).

The variability was also correctly reproduced by the propagation model under most conditions.

The propagation model was then applied to calculate the AS. The influence of the topography, the meteorological conditions, and the source altitude on the AS was examined. It was shown that the AS is clearly asymmetric. Therefore, considering an effective distance is not relevant for such a heterogeneous environment since the AS shape is mostly driven by the underlying topography. Moreover, the source height was shown to be also a decisive parameter impacting the size and the shape of the AS. Especially, it was concluded that the display flight allows the rock ptarmigan to increase its AS and to overcome the landform heterogeneity encountered in mountain ranges. AS also depends to a lesser extent on weather conditions. The AS variability can be expected both in space, according to the movements of the birds on their territories, and in time, from day to day and even from hour to hour.

The propagation model proposed in the paper can be used to estimate AS in various habitat and weather conditions. It can be used to study communication networks and their spatial and temporal dynamics. In addition, the ability to deduce temporal signal after its propagation is likely to provide interesting clues concerning the degradation of information carried by the vocalization (Mouterde *et al.*, 2014). However, it should be noted that the generalization and application of such a model to other species will require the knowledge of several parameters: SL, hearing threshold, and background noise. An appropriate estimation of acoustic communication networks could provide insights into species behaviors, like territory defense and mating strategy. It also opens up new possibilities for automated counting techniques using audio recorders.

ACKNOWLEDGMENTS

This research is supported by the Labex CeLyA of Université de Lyon (ANR-10-LABX-0060). A collaboration with the Centre d'Etudes de la Neige (UMR 3589), Grenoble, France, allowed us to conduct experiments on a maintained instrumented alpine site. Isabelle Gouttevin made this collaboration possible. Yannick Deliot provided meteorological data and helped with site logistics at Col du Lac Blanc. Hugo Merzisen provided the topographic data at Col du Lac Blanc. Hervé Bellot provided additional meteorological data. Léo Papet took part in the propagation experiments and impedance measurements. Simulations were made possible by access to the high-performance computing resources of PMCS2I (Pôle de Modélisation et de Calcul en Sciences de l'Ingénieur et de l'Information) of Ecole Centrale de Lyon. We would like to thank Codor Khodr and Michael Greenfield for their helpful comments on the manuscript.

Albert, D. G. (**2001**). "Acoustic waveform inversion with application to seasonal snow covers," J. Acoust. Soc. Am. **109**(1), 91–101.

ANSI/ASA (**2010**). S1.18, *Method for Determining the Acoustic Impedance of Ground Surfaces, Accredited Standards Committee S1, Acoustics*, American National Standard (revision of ANSI S1.18-1999) (Acoustical Society of America, New York).

Attenborough, K., and van Renterghem, T. (**2021**). *Predicting Outdoor Sound*, 2nd ed. (CRC, Boca Raton, FL).

Aubin, T., and Mathevon, N. (**2020**). *Coding Strategies in Vertebrate Acoustic Communication* (Springer, Cham, Switzerland).

Bérengier, M. C., Stinson, M. R., Daigle, G. A., and Hamet, J. F. (**1997**). "Porous road pavements: Acoustical characterization and propagation effects," J. Acoust. Soc. Am. **101**(1), 155–162.

Blairon, N., Blanc-Benon, P., Bérengier, M., and Juvé, D. (**2002**). "Outdoor sound propagation in complex environment: Experimental validation of a PE approach," in *Proceedings of the 10th International Symposium on Long Range Sound Propagation*, September 12–13, Grenoble, France, pp. 114–128.

Bossert, A. (**1977**). "Bestandesaufnahmen am Alpenschneehuhn (*Lagopus mutus*) im Aletchgebiet" ["Inventory of the rock ptarmigan population (Lagopus mutus) in the Aletsch region (Swiss Alps)]," Der Ornithologische Beobachter **74**, 95–98.

Brenowitz, E. A. (**1982**). "The active space of red-winged blackbird song," J. Comp. Physiol. **147**(4), 511–522.

Canonne, C., Novoa, C., Muffat-Joly, B., Resseguier, J., Desmet, J.-F., Casadesus, J. B., Arvin-Berod, M., and Besnard, A. (**2020**). "Life on the edge: Common slow pace of life but contrasted trajectories of alpine rock ptarmigan populations at their southern margin," Wildl. Biol. **2020**(2), 1–11.

Collino, F. (**1997**). "Perfectly matched absorbing layers for the paraxial equations," J. Comput. Phys. **131**(1), 164–180.

Dabelsteen, T., Larsen, O. N., and Pedersen, S. B. (**1993**). "Habitat-induced degradation of sound signals: Quantifying the effects of communication sounds and bird location on blur ratio, excess attenuation, and signal-to-noise ratio in blackbird song," J. Acoust. Soc. Am. **93**(4), 2206–2220.

Dabelsteen, T., and Mathevon, N. (**2002**). "Why do songbirds sing intensively at dawn? A test of the acoustic transmission hypothesis," Acta Ethologica **4**(2), 65–72.

Darden, S. K., Pedersen, S. B., Larsen, O. N., and Dabelsteen, T. (**2008**). "Sound transmission at ground level in a short-grass prairie habitat and its implications for long-range communication in the swift fox *Vulpes velox*," J. Acoust. Soc. Am. **124**(2), 758–766.

Datt, P., Kapil, J. C., Kumar, A., and Srivastava, P. K. (**2016**). "Experimental measurements of acoustical properties of snow and inverse characterization of its geometrical parameters," Appl. Acoust. **101**, 15–23.

Dooling, R. J., and Leek, M. R. (**2018**). "Communication masking by man-made noise," in *Effects of Anthropogenic Noise on Animals*, edited by H. Slabbekoorn, R. J. Dooling, A. N. Popper, and R. R. Fay (Springer, New York), pp. 23–46.

Dragna, D., Blanc-Benon, P., and Poisson, F. (**2014**). "Impulse propagation over a complex site: A comparison of experimental results and numerical predictions," J. Acoust. Soc. Am. **135**(3), 1096–1105.

Embleton, T. F. W. (**1996**). "Tutorial on sound propagation outdoors," J. Acoust. Soc. Am. **100**(1), 31–48.

Forrest, T. G. (**1994**). "From sender to receiver: Propagation and environmental effects on acoustic signals," Am. Zool. **34**(6), 644–654.

Guillaume, G., Faure, O., Gauvreau, B., Junker, F., Bérengier, M., and L'Hermite, P. (**2015**). "Estimation of impedance model input parameters from *in situ* measurements," Appl. Acoust. **95**, 27–36.

Guyomarc'h, G., Bellot, H., Vionnet, V., Naaim-Bouvet, F., Déliot, Y., Fontaine, F., Puglièse, P., Nishimura, K., Durand, Y., and Naaim, M. (**2019**). "A meteorological and blowing snow data set (2000–2016) from a high-elevation alpine site (Col du Lac Blanc, France, 2720 m a.s.l.)," Earth Syst. Sci. Data **11**(1), 57–69.

Henwood, K., and Fabrick, A. (**1979**). "A quantitative analysis of the dawn chorus: Temporal selection for communicatory optimization," Am. Naturalist **114**(2), 260–274.

Holland, J., Dabelsteen, T., Pedersen, S. B., and Larsen, O. N. (**1998**). "Degradation of wren *Troglodytes troglodytes* song: Implications for information transfer and ranging," J. Acoust. Soc. Am. **103**(4), 2154–2166.

ISO (**1993**). ISO 9613-1:1993(E), "Acoustics—Attenuation of sound during propagation outdoors—Part 1: Calculation of the absorption of sound by the atmosphere," (International Organization for Standardization, Geneva, Switzerland).

Jensen, K. K., Larsen, O. N., and Attenborough, K. (**2008**). "Measurements and predictions of hooded crow (*Corvus corone cornix*) call propagation over open field habitats," J. Acoust. Soc. Am. **123**(1), 507–518.
Johnsgard, P. A. (**2008**). "14 Rock ptarmigan," in *Grouse and Quails of North America* (University of Nebraska, Lincoln, NE), pp. 225–239.
Khodr, C., Azarpeyvand, M., and Green, D. N. (**2020**). "An iterative three-dimensional parabolic equation solver for propagation above irregular boundaries," J. Acoust. Soc. Am. **148**(2), 1089–1100.
Larom, D., Garstang, M., Payne, K., Raspet, R., and Lindeque, M. (**1997**). "The influence of surface atmospheric conditions on the range and area reached by animal vocalizations," J. Exp. Biol. **200**(3), 421–431.
Lengagne, T., and Slater, P. J. B. (**2002**). "The effects of rain on acoustic communication: Tawny owls have good reason for calling less in wet weather," Proc. R. Soc. Lond. B **269**(1505), 2121–2125.
Li, K. M., Waters-Fuller, T., and Attenborough, K. (**1998**). "Sound propagation from a point source over extended-reaction ground," J. Acoust. Soc. Am. **104**(2), 679–685.
Lihoreau, B., Gauvreau, B., Bérengier, M., Blanc-Benon, P., and Calmet, I. (**2006**). "Outdoor sound propagation modeling in realistic environments: Application of coupled parabolic and atmospheric models," J. Acoust. Soc. Am. **120**(1), 110–119.
Lohr, B., Wright, T. F., and Dooling, R. J. (**2003**). "Detection and discrimination of natural calls in masking noise by birds: Estimating the active space of a signal," Anim. Behav. **65**(4), 763–777.
Loning, H., Griffith, S. C., and Naguib, M. (**2022**). "Zebra finch song is a very short-range signal in the wild: Evidence from an integrated approach," Behav. Ecol. **33**(1), 37–46.
MacDonald, S. (**1970**). "The breeding behavior of the rock ptarmigan," Living Bird **9**, 195–238.
Marin-Cudraz, T., Muffat-Joly, B., Novoa, C., Aubry, P., Desmet, J.-F., Mahamoud-Issa, M., Nicolè, F., Van Niekerk, M. H., Mathevon, N., and Sèbe, F. (**2019**). "Acoustic monitoring of rock ptarmigan: A multi-year comparison with point-count protocol," Ecol. Indic. **101**, 710–719.
Marten, K., and Marler, P. (**1977**). "Sound transmission and its significance for animal vocalization," Behav. Ecol. Sociobiol. **2**, 271–290.
Mathevon, N., Aubin, T., and Dabelsteen, T. (**1996**). "Song degradation during propagation: Importance of song post for the wren *Troglodytes troglodytes*," Ethology **102**(3), 397–412.
Mathevon, N., Aubin, T., Vielliard, J., da Silva, M.-L., Sebe, F., and Boscolo, D. (**2008**). "Singing in the rain forest: How a tropical bird song transfers information," PLoS ONE **3**(2), e1580.
Mathevon, N., Dabelsteen, T., and Blumenrath, S. H. (**2005**). "Are high perches in the blackcap *Sylvia atricapilla* song or listening posts? A sound transmission study," J. Acoust. Soc. Am. **117**(1), 442–449.
McGregor, P. K. (**2005**). *Animal Communication Networks* (Cambridge University, Cambridge, MA).
McGregor, P. K., and Dabelsteen, T. (**1996**). "Communication networks," in *Ecology and Evolution of Acoustic Communication in Birds*, edited by D. E. Kroodsma and E. H. Miller (Cornell University, Ithaca, NY), pp. 409–425.
Monin, A. S., and Obukhov, A. M. (**1954**). "Basic laws of turbulent mixing in the surface layer of the atmosphere," Contrib. Geophys. Inst. Acad. Sci. USSR **151**, 163–187.
Moore, H. M., Attenborough, K., Rogers, J., and Lee, S. (**1991**). "*In-situ* acoustical investigations of deep snow," Appl. Acoust. **33**, 281–301.
Mott, R., Gromke, C., Grünewald, T., and Lehning, M. (**2013**). "Relative importance of advective heat transport and boundary layer decoupling in the melt dynamics of a patchy snow cover," Adv. Water Resources **55**, 88–97.
Mouterde, S. C., Theunissen, F. E., Elie, J. E., Vignal, C., and Mathevon, N. (**2014**). "Acoustic communication and sound degradation: How do the individual signatures of male and female zebra finch calls transmit over distance?," PLoS ONE **9**(7), e102842.
Nordtest (**1999**). "Ground surfaces: Determination of the acoustic impedance," NT ACOU 104, Project 1365-97 (Nordtest, Taastrup, Denmark).
Novoa, C., Desmet, J.-F., Brenot, J.-F., Muffat-Joly, B., Arvin-Bérod, M., Resseguier, J., and Tran, B. (**2019**). "Demographic traits of two alpine populations of rock ptarmigan," in *Ecology, Conservation, and Management of Grouse*, edited by B. K. Sandercock, K. Martin, and G. Segelbacher (University of California, Oakland, CA), pp. 267–280.
Ostashev, V. E., Juvé, D., and Blanc-Benon, P. (**1997**). "Derivation of a wide-angle parabolic equation for sound waves in inhomogeneous moving media," Acta Acust. united Acust. **83**, 455–460.
Ostashev, V. E., and Wilson, D. K. (**2016**). *Acoustics in Moving Inhomogeneous Media* (CRC, London).
Ostashev, V. E., Wilson, D. K., and Muhlestein, M. B. (**2020**). "Wave and extra-wide-angle parabolic equations for sound propagation in a moving atmosphere," J. Acoust. Soc. Am. **147**(6), 3969–3984.
Parris, K. M. (**2002**). "More bang for your buck: The effect of caller position, habitat and chorus noise on the efficiency of calling in the spring peeper," Ecol. Modell. **156**(2), 213–224.
Raynor, E. J., Whalen, C. E., Bomberger Brown, M., and Powell, L. A. (**2017**). "Location matters: Evaluating Greater Prairie-Chicken (*Tympanuchus cupido*) boom chorus propagation," Avian Conserv. Ecol. **12**(2), art 17.
Reichert, M. S., Enriquez, M. S., and Carlson, N. V. (**2021**). "New dimensions for animal communication networks: Space and time," Integr. Comp. Biol. **61**(3), 814–824.
Reiners, W. A., and Driese, K. L. (**2001**). "The propagation of ecological influences through heterogeneous environmental space," BioScience **51**(11), 939–950.
Ręk, P., and Osiejuk, T. S. (**2011**). "Nonpasserine bird produces soft calls and pays retaliation cost," Behav. Ecol. **22**(3), 657–662.
Salomons, E. M. (**2001**). *Computational Atmospheric Acoustics* (Springer, Dordrecht, Netherlands).
Watson, A. (**1972**). "The behaviour of ptarmigan," Br. Birds **65**(1), 6–26.
Wiley, R. H., and Richards, D. G. (**1978**). "Physical constraints on acoustic communication in the atmosphere: Implications for the evolution of animal vocalizations," Behav. Ecol. Sociobiol. **3**(1), 69–94.
Wilson, D. K. (**1993**). "Relaxation-matched modeling of propagation through porous media, including fractal pore structure," J. Acoust. Soc. Am. **94**(2), 1136–1145.

JASA ARTICLE

Wind turbine sound propagation: Comparison of a linearized Euler equations model with parabolic equation methods

Jules Colas,[1,a)] Ariane Emmanuelli,[1] Didier Dragna,[1] Philippe Blanc-Benon,[2] Benjamin Cotté,[3] and Richard J. A. M. Stevens[4]

[1]*Université de Lyon, Ecole Centrale de Lyon, CNRS, Université Claude Bernard Lyon 1, Institut National des Sciences Appliquées de Lyon (INSA Lyon), Laboratoire de Mécanique des Fluides et d'Acoustique (LMFA), UMR5509, 69134 Ecully Cedex, France*

[2]*Université de Lyon, CNRS, Ecole Centrale de Lyon, INSA Lyon, Université Claude Bernard Lyon 1, LMFA, UMR5509, 69134 Ecully Cedex, France*

[3]*Institute of Mechanical Sciences and Industrial Applications (IMSIA), ENSTA Paris, CNRS, Commissariat a l'Energie Atomique, Électricité de France, Institut Polytechnique de Paris, Paris, France*

[4]*Physics of Fluids Group, Max Planck Center Twente for Complex Fluid Dynamics, J. M. Burgers Center for Fluid Dynamics, University of Twente, P.O. Box 217, 7500 AE Enschede, The Netherlands*

ABSTRACT:

Noise generated by wind turbines is significantly impacted by its propagation in the atmosphere. Hence, for annoyance issues, an accurate prediction of sound propagation is critical to determine noise levels around wind turbines. This study presents a method to predict wind turbine sound propagation based on linearized Euler equations. We compare this approach to the parabolic equation method, which is widely used since it captures the influence of atmospheric refraction, ground reflection, and sound scattering at a low computational cost. Using the linearized Euler equations is more computationally demanding but can reproduce more physical effects as fewer assumptions are made. An additional benefit of the linearized Euler equations is that they provide a time-domain solution. To compare both approaches, we simulate sound propagation in two distinct scenarios. In the first scenario, a wind turbine is situated on flat terrain; in the second, a turbine is situated on a hilltop. The results show that both methods provide similar noise predictions in the two scenarios. We find that while some differences in the propagation results are observed in the second case, the final predictions for a broadband extended source are similar between the two methods. https://doi.org/10.1121/10.0020834

(Received 13 April 2023; revised 26 July 2023; accepted 14 August 2023; published online 6 September 2023)

[Editor: Vladimir E. Ostashev] Pages: 1413–1426

I. INTRODUCTION

The noise produced by wind turbines is one of the main constraints for the installation of new wind farms. It can also entail curtailment plans when annoyance issues emerge after the construction of the farm, leading to energy production loss of up to 70% during the night (Dumortier *et al.*, 2015). Therefore, accurate prediction tools are needed to assess the wind farm noise during the development and operational phases. The modeling of the aerodynamic noise sources and the propagation of sound in the atmosphere are two critical fields of study for the prediction of wind turbine noise. Several models for the noise emitted by a wind turbine have been developed in recent years (Barlas *et al.*, 2017a; Cotté, 2019). These models aim at capturing both the mean sound pressure level (SPL) emitted by the source and the amplitude modulation (AM) induced by the rotation of the blades. The unsteady nature of the source is considered to be one of the main annoyance causes as the global SPL is usually quite low (Hansen *et al.*, 2019). To predict the SPL field around the turbine, outdoor sound propagation models need to consider ground effects, atmospheric absorption, and refraction induced by the variability of wind and temperature within the atmospheric boundary layer (ABL). The effect of the ABL flow on wind turbine sound propagation has been extensively studied (Barlas *et al.*, 2018; Heimann and Englberger, 2018). The evolution of the temperature and wind speed gradients during the day modifies the sound propagation and, hence, the SPL around the wind turbine. Furthermore, the presence of the wind turbine creates a wake that acts as a waveguide and tends to increase the SPL at a specific location downwind of the turbine (Barlas *et al.*, 2017b). Finally, topography was also shown to play a significant role in wind turbine sound propagation (Heimann *et al.*, 2018; Sessarego and Shen, 2020; Shen *et al.*, 2019).

Various numerical methods have been used to calculate wind turbine sound propagation. Engineering tools based on simple empirical models are more suited for operational purposes. Methods based on ray acoustics can consider atmospheric refraction (Heimann and Englberger, 2018; Prospathopoulos and Voutsinas, 2007). However, they are usually less precise in terms of SPL and rely on a high-frequency approximation. The parabolic equation (PE) methods have been used extensively both for their good

a)Email: jules.colas@ec-lyon.fr

accuracy at long range and for their low computational cost (Gilbert and White, 1989). They consist in solving a one-way-wave equation in the frequency domain usually in a two-dimensional (2D) geometry, although the formulation holds in three dimensions (3D). PE methods have, thus, become the state of the art for wind turbine noise propagation (Barlas *et al.*, 2017b; Kayser *et al.*, 2020). Nevertheless, they suffer from several limitations. First, the solution is only valid for propagation angles close to the main propagation direction. Second, the one-way wave equation neglects backscattering. This could lead to inaccuracies in the presence of topography with steep slopes. Finally, approximations are usually made in order to consider propagation in an inhomogeneous moving medium. The most common approach is to consider an atmosphere at rest with an effective sound speed that includes the effect of both the temperature and the wind velocity gradient. This approach can be inaccurate if the wind speed is too high or if its vertical component is not negligible (Dallois *et al.*, 2001). Improved PE methods consider the effect of the ABL on sound propagation by including the mean flow terms when deriving the one-way wave equation (Dallois *et al.*, 2001; Ostashev *et al.*, 2020). The range of application of PE methods for wind turbine noise has already been investigated in several studies, by comparing PE results to analytical solutions or measurements (Kayser *et al.*, 2023; Lee *et al.*, 2016; Nyborg *et al.*, 2022). However, validation against analytical solutions is restricted to simple cases. In addition, outdoor experiments are not perfectly controlled, as, for instance, the wind field is only known partially, or the wind turbine noise sources have to be modeled. Comparison against measurements remains, thus, overall limited.

A more advanced sound propagation method is to solve the linearized Euler equations (LEE) directly. This method is also widely used for outdoor propagation (Blumrich and Heimann, 2002; Dragna and Blanc-Benon, 2014; Salomons *et al.*, 2002; Van Renterghem, 2014). It takes the effect of the mean flow on sound propagation accurately into account. In particular, it considers the vertical component of the wind speed, which is neglected in the effective sound speed approach. The LEE method overcomes the PE limitations, which include restricted angular validity and restrictions on backscattering. In addition, as a time-domain method, it provides a broadband solution and can be used to consider unsteady effects. The main drawback is the higher computational cost of the LEE compared to the PE method, which explains why it has not yet been considered for wind turbine noise propagation.

The objectives of this paper are to introduce a LEE model for wind turbine noise propagation and to assess the advantages of using a LEE model with respect to state-of-the-art PE methods. The LEE model can account for topography, ground impedance, and inhomogeneous mean flow. For comparison, two different PE implementations are considered: a vector PE able to handle strong wind variation but limited to flat terrain and a PE formulation able to consider topography and wind gradients through an effective sound speed approach. We compare the results of the LEE and PE approaches for two realistic cases: first a wind turbine on flat ground and second a wind turbine located on top of a steep hill. For both cases, the mean flow in which the sound propagates is obtained from previously computed large eddy simulations (LES) by Liu and Stevens (2020), and an extended moving source model based on Amiet's theory (Cotté, 2019) is used.

The paper is organized as follows. In Sec. II, the complete methodology for the wind turbine noise prediction is described, including the LEE and PE methods. Then Sec. III details the two cases studied. In Sec. IV, the SPL and AM obtained with both methods are compared for the two cases. Finally, concluding remarks are given in Sec. V.

II. METHOD

A. General methodology

The general framework used to compute wind turbine noise at a receiver location is summarized in Fig. 1. It is based on the coupling of three different models: a LES code used to obtain the mean wind velocity in the ABL, a source model based on Amiet's theory, and a propagation model. The propagation models studied in this work are then detailed in Sec. II B.

First, the LES code is used to compute a realistic ABL. The interaction between the flow and the wind turbine is modeled with an actuator disk method. This code has been extensively tested both for the computation of realistic atmospheric boundary layers (Gadde *et al.*, 2021) and for the simulation of wind farm flow, with or without topography (Gadde and Stevens, 2021; Liu and Stevens, 2020). Although the simulations are unsteady, only the mean velocity fields are used in the following. By doing so, the turbulence scattering is not considered in this study, although it is known to have an impact on the propagation of wind turbine noise (Barlas *et al.*, 2017b). The flow data are then fed into

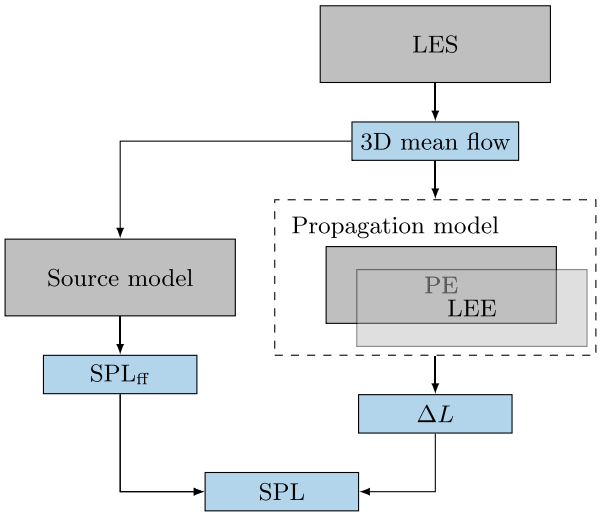

FIG. 1. (Color online) Diagram of the complete prediction methodology.

https://doi.org/10.1121/10.0020834

an extended source model and a propagation model based on either the LEE or the PE.

The source model derives from Amiet's strip theory: Each blade is divided into several segments, considered as uncorrelated sources. For each segment, the turbulent inflow and trailing edge noise are computed using the model developed by Tian and Cotté (2016). The resulting SPL in free field, denoted $\mathrm{SPL}_{\mathrm{ff}}$, depends on the wind turbine geometry (chord length and type of the blade segment) and on the incoming velocity profile and turbulent spectrum. Additionally, to determine the propagation effects, such as ground reflection or atmospheric refraction, the SPL relative to the free field, denoted ΔL, must be computed for each source-receiver pair.

Finally, source and propagation effects are considered by computing the SPL at a receiver produced by one segment i at a given angular position of the blades β such that

$$\mathrm{SPL}^i(\mathbf{x},\omega,\beta) = \mathrm{SPL}^i_{\mathrm{ff}}(\mathbf{x},\omega,\beta) + \Delta L^i(\mathbf{x},\omega,\beta) - \alpha(\omega)R, \tag{1}$$

where $\mathbf{x}$ is the receiver coordinates, ω the angular frequency, α the atmospheric absorption coefficient, and R the distance from source to receiver. The contributions of each segment are combined to obtain the total SPL at the receiver,

$$\mathrm{SPL}(\mathbf{x},\omega,\beta) = 10\log_{10}\left(\sum_{i=1}^{N_s} 10^{\,\mathrm{SPL}^i(\mathbf{x},\omega,\beta)/10}\right), \tag{2}$$

where N_s is the number of segments used to discretize the three blades. The overall sound pressure levels (OASPLs) are then computed by summing the SPL over ω for a given angular position of the blades. In addition, amplitude modulation can be quantified by measuring the difference between the minimum and maximum OASPL values during one rotation of the blades. This method can become very expensive as the number of propagation simulations is proportional to the number of receivers, angular positions, and blade segments.

To limit the computational cost, the method proposed by Cotté (2019) considers a number of fictive source heights distributed over a vertical line in the rotor plane, as depicted in Fig. 2(a). The propagation simulations are performed only for these fictive sources. Subsequently, the SPL^i in Eq. (1) is computed using the value of ΔL corresponding to the closest fictive source [see Fig. 2(b)]. Note that the number of propagation simulations is reduced by considering a small number of source positions and by positioning all fictive sources in the same propagation plane. Hence, the same ΔL results are utilized to compute SPL for all receivers in this plane. This method is based on the assumption that the dimension of the wind turbine rotor is relatively small in relation to the propagation distances. To use this method, it is also important to ensure that the number of fictive source heights is sufficient to obtain convergence of the results, i.e., that the average SPL and AM during a rotation do not depend on the number of sources used. In Cotté (2019), it was shown that a minimum of seven source heights is necessary to obtain this convergence in the downwind direction.

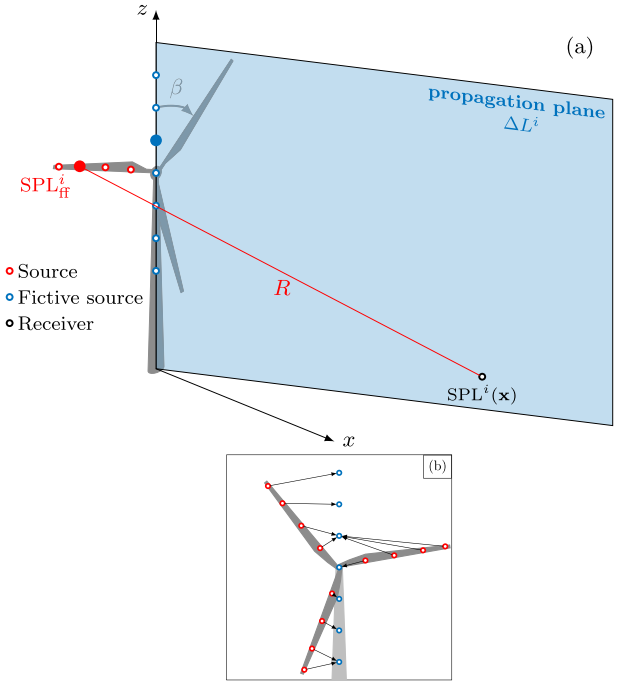

FIG. 2. (Color online) (a) Calculation of the SPL at a receiver due to one blade segment. (b) Total SPL from all segments is determined using the closest fictive source to compute the ΔL.

B. Acoustic propagation simulation

In this section, the models used to predict the sound propagation in the ABL are introduced. First, the LEE model developed for this study is presented, and then the PE implementations are described.

1. LEE

a. Acoustic model. This propagation model is based on the finite-difference solution of the LEE in a curvilinear mesh (Dragna and Blanc-Benon, 2014). Thus, the acoustic field is solved separately from the mean flow field and does not affect it. The LEE are derived from the conservation of mass, momentum, and energy for atmospheric propagation by neglecting terms of order $(|\mathbf{V_0}|/c_0)^2$ (Ostashev *et al.*, 2005),

$$\begin{aligned} &\frac{\partial p}{\partial t} + (\mathbf{V_0}\cdot\nabla)p + \rho_0 c_0^2 \nabla\cdot\mathbf{v} = 0\,,\\ &\frac{\partial \mathbf{v}}{\partial t} + (\mathbf{V_0}\cdot\nabla)\mathbf{v} + (\mathbf{v}\cdot\nabla)\mathbf{V_0} + \frac{\nabla p}{\rho_0} = 0, \end{aligned} \tag{3}$$

where t is the time; p and $\mathbf{v} = (u, w)$ are the acoustic pressure and velocity; and ρ_0, c_0, and $\mathbf{V_0} = (u_0, w_0)$ are the mean density, sound speed, and velocity. The 2D LEE in the (x, z) plane can be written in conservative form as

$$\mathbf{U}_t + \mathbf{E}_x + \mathbf{F}_z + \mathbf{H} = 0, \tag{4}$$

where $\mathbf{U} = [p, \rho_0 u, \rho_0 w]^T$ is the vector of unknowns; the partial derivatives are denoted $i_j = \partial i/\partial j$; and $\mathbf{E}$, $\mathbf{F}$, and $\mathbf{H}$ are the Eulerian fluxes defined as

$$\begin{aligned}\mathbf{E} &= \left[u_0 p + \rho_0 c_0^2 u, u_0 \rho_0 u + p, u_0 \rho_0 w\right]^T,\\ \mathbf{F} &= \left[w_0 p + \rho_0 c_0^2 w, w_0 \rho_0 u, w_0 \rho_0 w + p\right]^T,\\ \mathbf{H} &= \left[-p(\nabla \cdot \mathbf{V_0}), \rho_0(\mathbf{v}.\nabla)u_0, \rho_0(\mathbf{v}.\nabla)v_0\right]^T.\end{aligned} \tag{5}$$

The acoustic source is a pulse with a Gaussian spatial distribution, introduced via the initial conditions of Eq. (4),

$$\mathbf{U}(x, z, t = 0) = \left[S_0 \exp\left(-\frac{R^2}{B^2}\right), 0, 0\right]^T, \tag{6}$$

where $R = \sqrt{x^2 + (z - z_S)^2}$, $B^2 = (3\Delta x)^2/\log(2)$, z_S is the height of the center of the pulse, $S_0 = 1$ Pa is the amplitude of the source, and Δx is the streamwise grid spacing. This source aims to represent a broadband monopole, with frequency content up to $f = 0.6c_0/B$; see Eq. (A22).

b. Curvilinear transformation. To take into account a ground profile h, a transformation of the coordinate system is applied from Cartesian coordinates (x, z) to curvilinear coordinates (ξ, η) such that

$$\begin{aligned}x(\xi, \eta) &= \xi,\\ z(\xi, \eta) &= h(\xi) + \frac{\eta}{z_{\max}}[z_{\max} - h(\xi)],\end{aligned} \tag{7}$$

where $h(x)$ is the terrain elevation, and $z_{\max}$ is the maximum height of the domain. Hence, Eq. (4) becomes

$$\left(\frac{\mathbf{U}}{J}\right)_t + \left(\frac{\xi_x \mathbf{E} + \xi_z \mathbf{F}}{J}\right)_\xi + \left(\frac{\eta_x \mathbf{E} + \eta_z \mathbf{F}}{J}\right)_\eta + \frac{\mathbf{H}}{J} = 0, \tag{8}$$

where $J = |\xi_x \eta_z - \xi_z \eta_x|$ is the Jacobian of the transformation. This transformation was proposed by Gal-Chen and Somerville (1975) to recover a flat top boundary.

c. Numerical scheme. The formulation in Eq. (8) can be written as

$$\mathbf{U}_t = \mathcal{F}(\mathbf{U}), \tag{9}$$

where $\mathcal{F}$ is a function of $\mathbf{U}$ and its spatial derivatives. A fourth-order six-step Runge–Kutta (RK) algorithm (Berland *et al.*, 2006) is used to integrate the solution from $\mathbf{U}(t_n)$ to $\mathbf{U}(t_{n+1})$ with t_n the discrete time. The spatial derivatives needed at each step of the RK algorithm are computed using a fourth-order 11-point stencil finite-difference centered scheme (Bogey and Bailly, 2004) whose coefficients are optimized to minimize the dispersion error over a large range of wavenumbers. For the points near the boundary, non-centered 11-point stencil schemes are used (Berland *et al.*, 2007). Selective filters are also applied to remove grid-to-grid oscillations.

d. Moving frame. A moving frame method (Dragna and Blanc-Benon, 2014) is used to keep an affordable computational cost for long range propagation. In this method, the distance between the wavefront and the right boundary of the domain is computed at each iteration, and the acoustic variables are shifted to maintain this distance constant throughout the simulation (see Fig. 3). This approach allows for a large reduction of the computational domain size. Thus, in the simulations, a 300 m × 300 m moving frame is used to calculate the sound propagation in a 3000 m × 300 m domain, which reduces the computational cost by one order of magnitude.

e. Boundary conditions. A broadband impedance condition is used at the bottom boundary of the domain to model realistic ground absorption. The impedance condition is developed in the time domain (Rienstra, 2006) such that it writes as a convolution. By taking the surface impedance as a rational function of the frequency, it is possible to substitute this convolution by additional differential equations that can be solved along the RK scheme (Troian *et al.*, 2017). This saves computational resources while preserving high-order accuracy. In this work, the method was not implemented on the impedance but on the reflection coefficient for stability reasons.

At the top of the domain, a perfectly matched layer (PML) is implemented to simulate unbounded atmosphere. Inside this layer, the derivative in z in Eq. (4) is modified such that

$$\frac{\partial}{\partial z} \to \frac{1}{\kappa + \sigma/i\omega}\frac{\partial}{\partial z}, \tag{10}$$

with

$$\begin{aligned}\sigma(z) &= \sigma_0\left[(z - z_{\mathrm{PML}})/L\right]^3,\\ \kappa(z) &= 1 + (\kappa_0 - 1)\left[(z - z_{\mathrm{PML}})/L\right]^3,\end{aligned} \tag{11}$$

where z_{PML} is the coordinate at the bottom of the layer, and L is its thickness. As for the impedance condition, this transformation can be written in the time domain as a convolution that is integrated along the RK scheme with additional

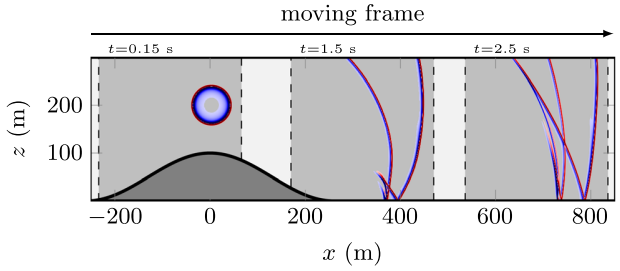

FIG. 3. (Color online) Snapshots of the moving frame at three different instants in time as the wave propagates inside the domain.

https://doi.org/10.1121/10.0020834

differential equations (Cosnefroy, 2019; Komatitsch and Martin, 2007).

Finally, on the left side of the domain, the waves must also leave the computational domain without producing any reflections. To achieve this, the sound speed is gradually reduced in a thin layer to ensure that potentially reflected waves move slower than the domain, which is moving at the speed of sound. Hence, they cannot re-enter the domain (Cosnefroy, 2019).

f. Post-processing. During the computation, pressure time signals $p(t)$ are recorded at several receiver locations. Then the Fourier transform $\hat{p}(\omega)$ of each signal is computed, and the relative sound pressure is retrieved by dividing $\hat{p}(\omega)$ by the solution for a Gaussian pulse in free field,

$$\Delta L(\mathbf{x},\omega) = 10\log_{10}\left(\frac{|\hat{p}(\mathbf{x},\omega)|^2}{|\hat{p}_{\mathrm{ff}}(\mathbf{x},\omega)|^2}\right), \tag{12}$$

where $\hat{p}_{\mathrm{ff}}$ is given by

$$\hat{p}_{\mathrm{ff}}(\mathbf{x},\omega) = \frac{\pi k_0 B^2 S_0}{4c_0}\exp\left(\frac{-k_{\mathrm{eff}}^2 B^2}{4}\right)H_0^{(1)}(k_0 R), \tag{13}$$

$H_0^{(1)}$ is the zeroth order Hankel function of the first kind, k_0 is the wave number, and $k_{\mathrm{eff}} = k_0/(1+M)$ with $M = u_0/c_0$ the Mach number at the wind turbine hub's height. The term k_{eff} accounts for the effect of the flow on the source which induces a shift in frequency. The derivation of this correction term can be found in the Appendix.

Once ΔL is computed, it can be used in the SPL prediction methodology explained in Sec. II A.

2. PE method

a. PE formulations. Two 2D PE formulations are implemented. The first one is a curvilinear formulation of the wide-angle PE with the effective sound speed approximation ($\mathrm{WAPE}_{\mathrm{topo}}$). It is derived from the methodology described by Sack and West (1995) for the generalized terrain parabolic equation (GT-PE), but with the coordinate transformation shown in Eq. (7). The $\mathrm{WAPE}_{\mathrm{topo}}$ allows us to consider topography with slope that does not exceed around 30° (Salomons, 2001). The moving atmosphere is modeled by defining an effective sound speed profile such that

$$c_{\mathrm{eff}}(x,z) = c_0(T_0(x,z)) + u_0(x,z), \tag{14}$$

where c_0 is the sound speed that depends on the mean temperature T_0. It is worth mentioning that the $\mathrm{WAPE}_{\mathrm{topo}}$ is equivalent to the classical effective sound speed WAPE formulation for flat ground. The accuracy of the $\mathrm{WAPE}_{\mathrm{topo}}$ strongly depends on quantities computed at the ground (ground profile and its derivatives, ground surface impedance, etc.), where small numerical errors can appear and accumulate (Sack and West, 1995). Errors can also arise from the effective sound speed approach with phase errors accumulating over the distance.

The second PE is a wide-angle vector PE formulation ($\mathrm{WAPE}_{\mathrm{vec}}$), that incorporates a vector wind field and is valid for arbitrary high Mach numbers. It is presented in Sec. VI A of Ostashev *et al.* (2020). Here, the velocity field is considered with fewer assumptions. However, it was not derived in curvilinear coordinates and, hence, cannot consider topography. While $\mathrm{WAPE}_{\mathrm{vec}}$ can consider both the vertical and horizontal components, only the horizontal component of the wind velocity u_0 is considered in our implementation.

The two methods employ second-order finite-difference schemes in the z-direction and a Crank–Nicolson algorithm to advance the solution to $x+\Delta x$ from the solution at x. Numerically, this involves inverting a tridiagonal matrix at each step of the resolution, which is done efficiently using the Thomas algorithm. The starting field is the second-order starter presented in Salomons (2001), which represents a monopole source.

b. Boundary condition. At the top of the domain, a PML is implemented (Collino, 1997) by modifying the partial derivative along the vertical coordinate as for the LEE method [see Eq. (10)]. At the bottom of the domain, an impedance boundary condition is used. The implementation of the boundary conditions leads to modifications of the matrix coefficients, while conserving the tridiagonal shape. The boundary conditions are similar for the two PE formulations, but, because of the differences in the equations, the resulting modifications of the matrix coefficients are not identical.

III. CASES STUDIED

The study examines two scenarios: one with a wind turbine on a flat surface and one with a wind turbine positioned on a hilltop. The latter scenario is particularly relevant, as wind turbines are often installed on hills to maximize energy output. Therefore, it is crucial to accurately model sound propagation in such complex settings. For both cases, LES results from Liu and Stevens (2020) for a truly neutral ABL are used. The mean flow fields from these simulations are normalized by the friction velocity u_* and by the diameter of the wind turbine. In this work, the wind turbine hub height and diameter are both set to 100 m. The friction velocity is set to $u_* = 0.512\,\mathrm{m\,s^{-1}}$ to get a wind velocity equal to $10\ \mathrm{m\ s^{-1}}$ at the hub height. For simplicity, the temperature and the sound speed are assumed constant, which is a valid assumption when considering a neutral atmosphere but would not be for a stable or unstable one. For the second case, the hill is defined such that

$$h(x) = h_{\max}\cos^2\left(\frac{\pi x}{2l}\right) \quad \text{for } -l < x < l, \tag{15}$$

where $h(x)$ is the terrain elevation, $h_{\max} = 100$ m, and $l = 260$ m is the half-width of the hill. The mean axial velocity component is plotted for both cases in Figs. 4(a) and 4(b). A velocity deficit can be observed just after the

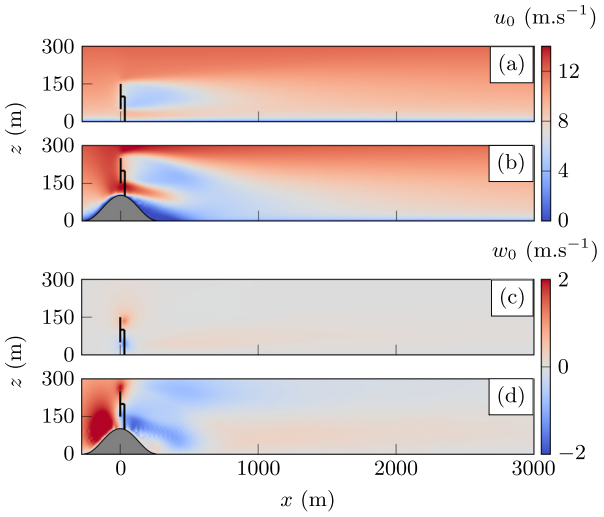

FIG. 4. (Color online) Mean axial velocity field u_0 for the two cases of interest: (a) a wind turbine over flat ground and (b) on top of a hill. Mean vertical velocity field w_0 for (c) a wind turbine over flat ground and (d) on top of a hill.

turbine in both cases. In the first case, a ducting effect is expected due to the wind turbine wake (Barlas *et al.*, 2017b). The acoustic waves are trapped inside the wake and then redirected toward the ground when the unperturbed ABL is recovered. This generates a focusing zone at the ground with high SPL. Ducting in the presence of the hill is expected to be stronger as the wake is more pronounced and more directed toward the ground. The vertical component of the wind speed, plotted in Fig. 4(c), is small in the flat case (less than 4% of u_0), so that the vector PE and the LEE are expected to produce similar results. In the case with topography, the hill induces a vertical component of the wind speed just before the wind turbine of a few meters per second, shown in Fig. 4(d), which is not taken into account by the WAPE$_{\text{topo}}$. This difference of a few meters per second upstream of the hill could introduce some discrepancies between the LEE and WAPE$_{\text{topo}}$ methods in the final OASPL. In addition, errors could arise for both cases due to the one-way approximation and the angular validity of the two PE methods.

The variable porosity model (Attenborough *et al.*, 2011) is used with a flow resistivity of 50 kN s m^{-4} and a porosity change rate of 100 m^{-1} to model a grassy ground. The PE simulations are performed for a set of frequencies used to compute third octave band spectrum between 50 Hz and 1 kHz. Values of ΔL for the same frequencies are extracted from the broadband results of the LEE simulation for comparison. These frequencies are gathered in Table I. For all simulations, the numerical parameters are set to obtain accurate results up to 1 kHz and 3 km downwind of the turbine. For the LEE, this implies setting a grid size of 0.05 m and a CFL of 0.5, which corresponds to 127 000 time iterations to complete the simulation with a computational moving domain of 36×10^6 points. The computational time for one simulation is approximately 1200 central processing unit (CPU) hours, which is equivalent to 3 days on a 16-core machine. For WAPE$_{\text{vec}}$ and WAPE$_{\text{topo}}$, the grid size depends on the computed frequency. For the flat case, convergence was reached for $\Delta x = \Delta z = \lambda/10$, which requires 1 CPU hour to compute the results at all frequencies. The hill case requires a higher resolution to capture sharp gradients, and convergence is reached for $\Delta x = \Delta z = \lambda/50$, which leads to an increased computational time of 30 CPU hours.

The source model used for the wind turbine is the same as described in Tian and Cotté (2016). The only difference is that the wind turbine is scaled up to be 100 m in diameter instead of 93 m. The blade is decomposed into eight segments, and 36 angular positions are considered for one rotation of the blades. Finally, it was found by Cotté (2019) that seven fictive source heights are sufficient to obtain a convergence on SPL and AM for the flat case at ground level using the approach described in Sec. II A. However, for the case with a hill, 30 source heights are required for convergence. This significant increase in the number of sources needed to achieve convergence can be explained by the strong dependence between the focusing pattern and the source height in the presence of the hill. Thus, changing the source height by a few meters can affect the position of the focusing zone at the ground of more than 100 m. Therefore, it is necessary to reduce the step between the simulated source heights.

IV. COMPARISON

A. Over flat ground

1. Relative SPL

The value of ΔL represents the effect of the ground absorption and the mean flow on the propagation with respect to the solution in the free field. The ΔL fields are depicted in Fig. 5 for LEE and WAPE$_{\text{vec}}$ at 100 Hz for three source heights corresponding to the highest (142 m) and lowest (58 m) fictive sources and to the fictive source at hub height (100 m). The results for the WAPE$_{\text{topo}}$ are not plotted as they are almost identical with those of the WAPE$_{\text{vec}}$.

TABLE I. Frequencies f used to compute the third octave band spectrum with the PE methods. f_c is the central frequency of each band.

f_c (Hz)	50	63	80	100	125	160	200	250	315	400	500	630	800	1000
f (Hz)	50	63	80	100	125	160	192	241	297	373	467	588	741	926
							208	260	315	391	489	616	770	962
									334	409	512	645	800	1000
										429	536	675	831	1039
													864	1080

JASA
https://doi.org/10.1121/10.0020834

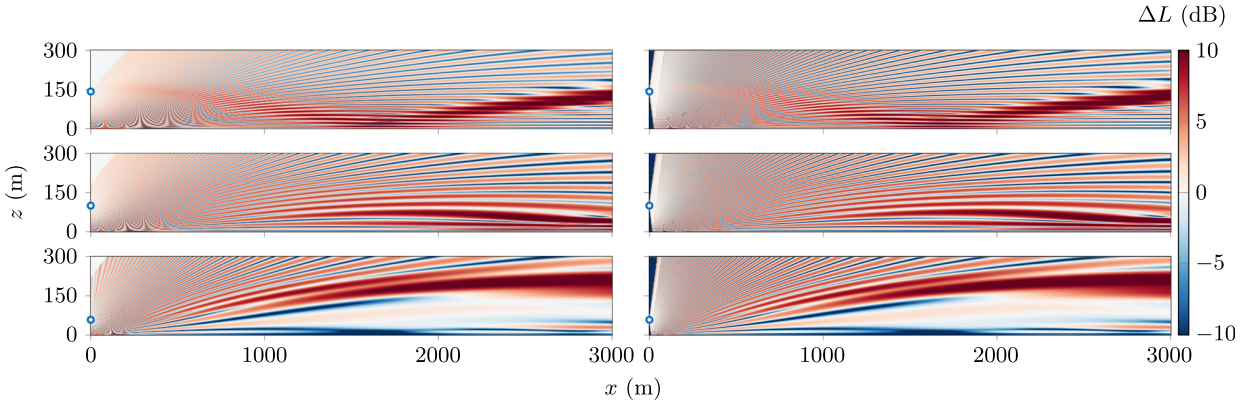

FIG. 5. (Color online) ΔL computed with LEE (left) and WAPE_{vec} (right) at 100 Hz for several source heights (circles): 142 m (top), 100 m (middle), and 58 m (bottom).

In this case, the two main effects are the occurrence of constructive and destructive interference patterns due to ground reflection and the ducting of acoustic waves by the wake of the wind turbine. In particular, note the large increase in ΔL at $x = 1.7$ km at the ground for the source at 142 m height. It is clear that the same interference patterns and the same ducting are obtained in the WAPE_{vec} and LEE results. The influence of the wind speed gradient and of the wake length and intensity on the propagation for different source heights is well captured with both methods as the ΔL levels are similar. Still, a small difference between the two methods can be observed at the very beginning of the domain ($x < 100$ m). For the LEE method, the moving frame does not allow the reflected wave to reach the top of the domain close to the source, leading to a zone without any interferences and a value of ΔL close to 0. In the case of PE, the classic cone due to the angle of validity of the method can be seen at the very beginning of the domain. Hence, the two methods do not produce the same results in the near field.

The relative SPL is plotted for a line of receivers 2 m above the ground in Fig. 6 for three different frequencies. At all frequencies, a strong peak is visible at 1.7 km, which corresponds to the distance where the focused wave hits the ground. The values of ΔL obtained with $\text{WAPE}_{\text{topo}}$ and WAPE_{vec} methods are compared with the LEE results. The curves are almost identical for the three methods. The difference between the ΔL obtained with the three methods does not exceed 0.5 dB for $x > 1$ km. At 512 and 1000 Hz, a small shift is found between the position of the peaks in the $\text{WAPE}_{\text{topo}}$ and WAPE_{vec} results. The latter seems, as expected, to better account for the wind field, and the results are closer to those of the LEE. For other source or receiver heights (not plotted here), it was observed that the difference between $\text{WAPE}_{\text{topo}}$ and LEE results tends to increase with distance. It was also seen that as the interference pattern gets more complex, the difference is more visible.

The average difference of ΔL is plotted in Fig. 7 to quantify the error made with PE formulations. This difference is defined with

$$\epsilon = \frac{1}{N_f}\sum_{i=1}^{N_f} |\Delta L_{\text{LEE}}(f_i) - \Delta L_{\text{PE}}(f_i)|, \tag{16}$$

with N_f the total number of frequencies computed. To assess the effect of the mean flow on the results, an additional simulation for an atmosphere at rest is performed for all three methods. The difference for the atmosphere at rest is shown in Figs. 7(a) and 7(c). Note that the error is almost identical for the WAPE_{vec} and the $\text{WAPE}_{\text{topo}}$. The error is very large close to source due to the angle of validity of the PE and can

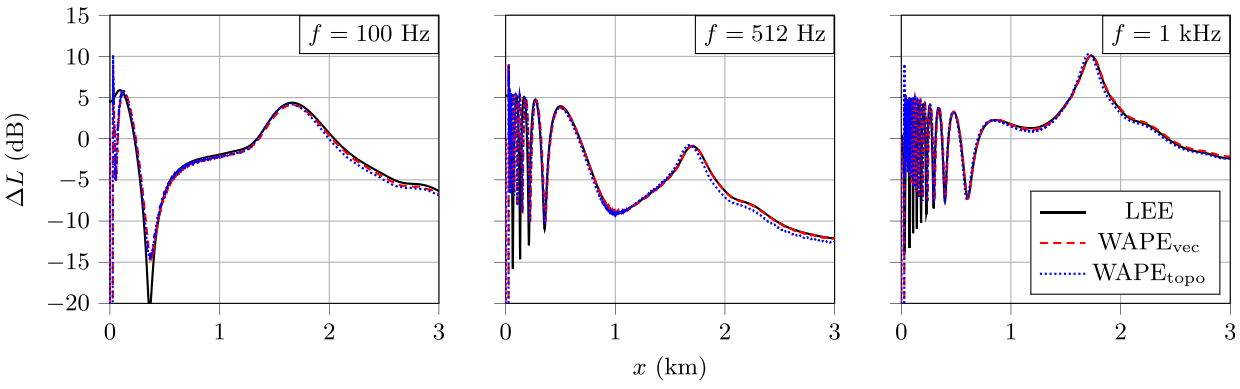

FIG. 6. (Color online) ΔL computed for a source at 142 m and a receiver at 2 m for three different frequencies.

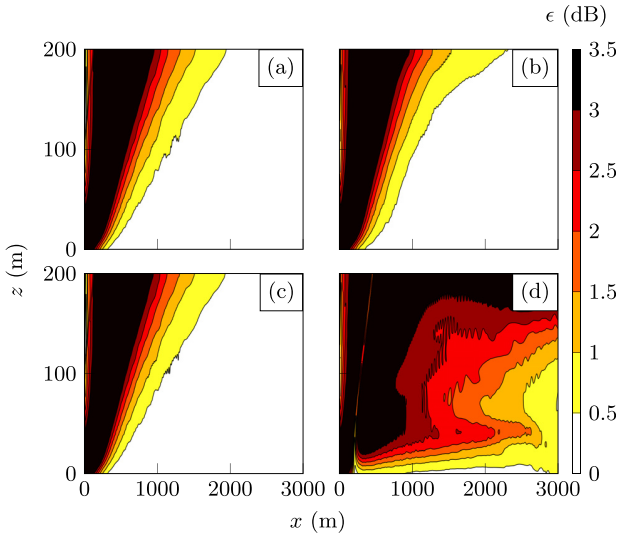

FIG. 7. (Color online) ΔL difference computed between the LEE and [(a) and (b)] $\mathrm{WAPE_{vec}}$ and [(c) and (d)] $\mathrm{WAPE_{topo}}$ for [(a) and (c)] an atmosphere at rest and [(b) and (d)] an ABL profile with 10 m s^{-1} at hub height. The results are averaged over $N_f = 35$ frequencies (see Table I) and are computed for flat terrain.

even go above 3 dB. Further away, the propagation angle lies within the angle of validity of the $\mathrm{WAPE_{topo}}$, and the error reduces to less than 0.5 dB. The introduction of a mean flow does not significantly modify the error for the $\mathrm{WAPE_{vec}}$ [Fig. 7(b)]. The effect of the flow is very well accounted for in this method, as expected. On the contrary, for $\mathrm{WAPE_{topo}}$, the addition of a mean flow [Fig. 7(d)] greatly increases the error. The difference is not only significant in the near field but in the entire domain with differences going above 3 dB. It can be observed that close to the ground, the error is still relatively small, which corresponds to the case presented in Fig. 6. It is worth noting that, because we are considering a flat ground, the error in the $\mathrm{WAPE_{topo}}$ method is only due to the effective sound speed approach.

2. SPL

In this section, the SPLs obtained by combining ΔL with the source model described in Sec. II A are compared for the LEE and the two PE methods. The OASPL field for one angular position of the blades obtained from the LEE and $\mathrm{WAPE_{topo}}$ methods is presented in Fig. 8. It corresponds to the contribution of all blade segments for one angular position (here $\beta = 0°$, i.e., for one of the three blades pointing upward) summed over the frequency bands between 50 Hz and 1 kHz. The results from $\mathrm{WAPE_{vec}}$ are omitted as they are again almost identical with those of $\mathrm{WAPE_{topo}}$. Several zones of large OASPL produced by the different sources distributed along the blades can be observed in both cases. The OASPL obtained from the $\mathrm{WAPE_{topo}}$ and the LEE methods for several positions of the blades is available in Mm. 1. As the position of the blades changes, different ΔL calculations are activated, leading to distinct focusing

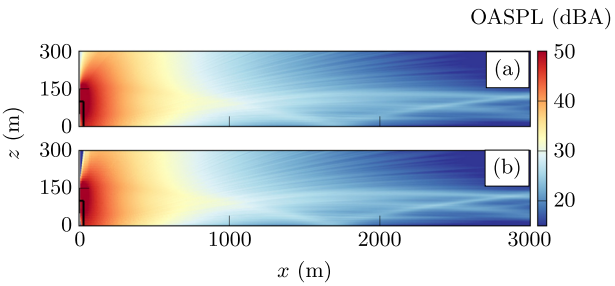

FIG. 8. (Color online) OASPL at $\beta = 0°$ for the flat case computed using (a) LEE and (b) $\mathrm{WAPE_{topo}}$.

zones on the ground. This mechanism is responsible for the amplitude modulation in the far field (Barlas *et al.*, 2018). Hence, it is not expected that strong discrepancies would appear as the error observed in Fig. 7 would tend to average out with an extended broadband source.

Mm. 1. Evolution of the OASPL with the angle β, in the flat case for the $\mathrm{WAPE_{topo}}$ and the LEE methods.

The mean OASPL over one rotation for receivers located 2 m above the ground is shown in Fig. 9(a). The minimum and maximum values reached during the rotation are also delimited by color patches. The mean OASPL obtained with the three methods is very similar. The peak

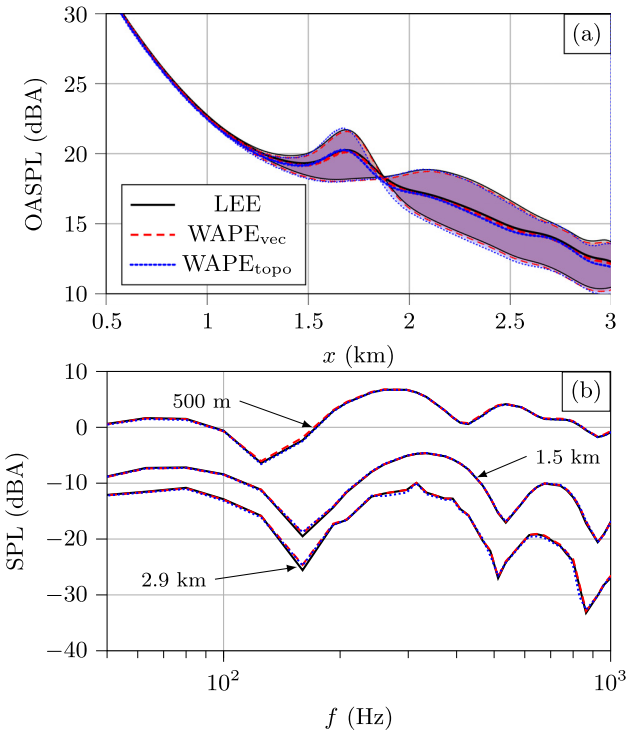

FIG. 9. (Color online) (a) Averaged OASPL over one rotation computed with the three propagation methods, minimum and maximum delimited with color patches. (b) Averaged spectrum obtained over a full rotation of the turbine blades for receivers at a height of 2 m, positioned at distances of $x = 500$ m, $x = 1.5$ km, and $x = 2.9$ km downstream of the turbine (listed from top to bottom).

https://doi.org/10.1121/10.0020834

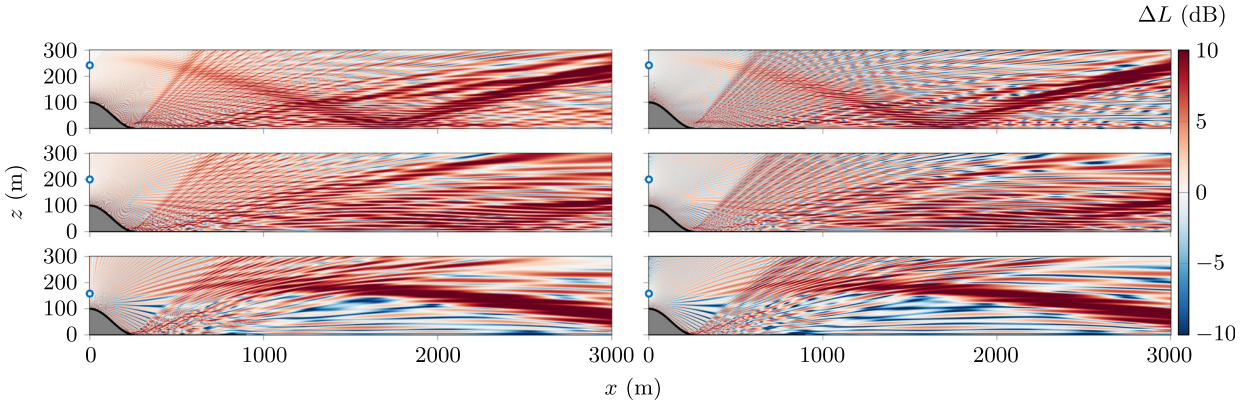

FIG. 10. (Color online) ΔL computed with LEE (left) and $\text{WAPE}_{\text{topo}}$ (right) at 100 Hz for several source heights (circles) 242 m (top), 200 m (middle), and 158 m (bottom).

observed 1.7 km from the source is well captured by both PE methods. The small phase shift in ΔL observed for the $\text{WAPE}_{\text{topo}}$ is still present in the OASPL prediction but is less pronounced. The two amplitude modulation zones from 1.25 to 1.9 km and from 1.9 to 3 km are similar with all methods. They correspond to the areas where the SPL varies due to the motion of the blades.

The narrowband spectrum at three downstream locations is shown in Fig. 9(b) for the LEE and the two PE formulations. Spectra are nearly identical over the considered frequency range. The dips induced by ground absorption are equally captured. The error does not increase with frequency or distance, which shows the good convergence of the three methods for this frequency range and domain length.

B. On top of a hill

1. Relative SPL

The presence of the hill influences sound propagation by its geometry and by inducing a more complex mean flow, which changes the refraction of acoustic waves in the ABL. This refraction pattern is shown in Fig. 10 for the LEE and the $\text{WAPE}_{\text{topo}}$ methods and for three source heights. As for the flat case, different focusing zones can be identified depending on the source height. The presence of a caustic at the bottom of the hill can also be observed. The interference dips look more pronounced for the $\text{WAPE}_{\text{topo}}$, and the levels are slightly higher for the LEE. Furthermore, important differences can be seen in the results, especially at 100 Hz, for a line of receivers at 2 m height and for a source at 242 m (Fig. 11). These large discrepancies are due to a combined effect of the hill and of the mean flow. In fact, the steep slope of the hill is the main cause of the error in this case as discrepancies were already visible without any mean flow (not shown here). The maximum slope of the hill (reached at $x = 130$ m) is equal to 31°, which is at the limit of the $\text{WAPE}_{\text{topo}}$ validity range (Salomons, 2001). It is worth noting that the regularity of the ground profile and the precision with which its derivatives are calculated are not issues here as they are analytical. The mean error in the whole domain for all frequencies is between 3 and 4 dB for all heights, which is 2 dB higher than for the flat case. Still, it can be observed that the effect of the hill and the mean flow is the same for the LEE and $\text{WAPE}_{\text{topo}}$. Thus, the shape of the peak at 1.8 km is similar for both methods at 512 and 1000 Hz. Even if the $\text{WAPE}_{\text{topo}}$ introduces errors in this case, the effects of the ABL and the hill remain well captured in terms of both amplitude and position of the focusing.

2. SPL

As for the flat terrain case, the OASPL map depicted in Fig. 12 corresponds to the superposition of SPL from the

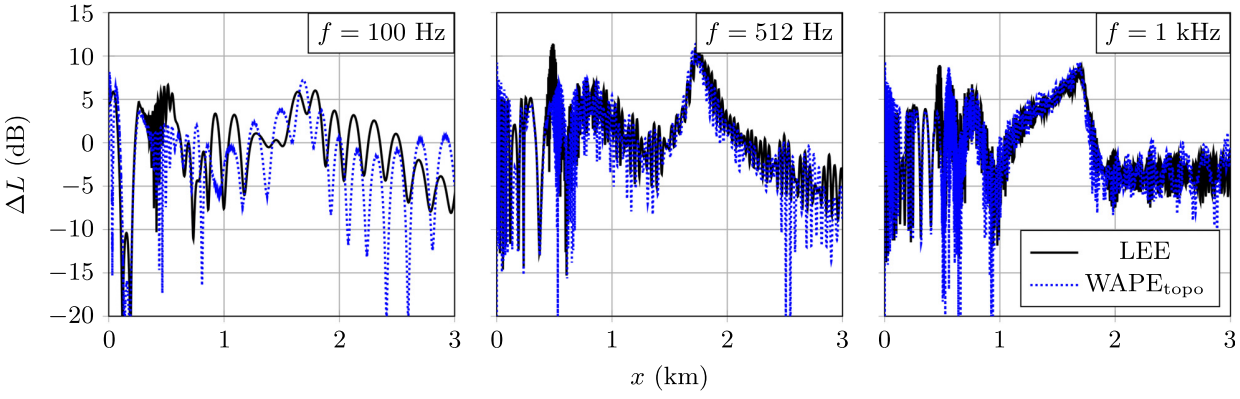

FIG. 11. (Color online) ΔL computed for a source at 242 m and a receiver at 2 m for three different frequencies.

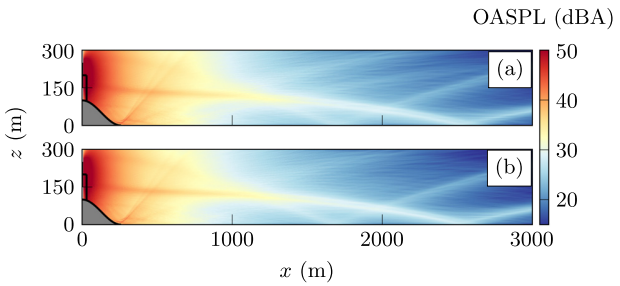

FIG. 12. (Color online) OASPL at $\beta = 0°$ for the hill case computed using (a) LEE and (b) $\text{WAPE}_{\text{topo}}$.

different sources distributed along the blades. The caustic observed at the bottom of the hill in Fig. 10 is still present, as well as several sound focusing zones. A notable difference from the flat terrain case is that the focusing is significantly stronger. Additionally, as discussed in Sec. III, the presence of the hill results in greater amplitude modulation due to blade movement. This can be observed in Mm. 2, and it is clear that both methods capture this phenomenon.

Mm. 2. Evolution in the hill case of the OASPL with the angle β for the $\text{WAPE}_{\text{topo}}$ and the LEE method.

To further investigate the discrepancies between the LEE and $\text{WAPE}_{\text{topo}}$ methods, the mean OASPL over one rotation is plotted in Fig. 13(a) along with the minimum and maximum OASPL for a line of receivers at 2 m height. The burst in mean OASPL at 1.8 km is similar for the two methods as well as the maximum of amplitude modulation with a strong peak at 2.5 km. Hence, it is clear that the same propagation effects are captured with both methods. However, the OASPLs computed with LEE are slightly higher than those computed with the $\text{WAPE}_{\text{topo}}$ (less than 1 dB). Finally, SPL spectra at three receiver positions are presented in Fig. 13(b). The figure demonstrates that $\text{WAPE}_{\text{topo}}$ and LEE exhibit excellent agreement over the entire frequency range at $x = 1.5$ km and $x = 2.5$ km downstream of the turbine. However, for the receiver situated close to the turbine (at 500 m downstream), $\text{WAPE}_{\text{topo}}$ slightly underpredicts the SPL compared to LEE.

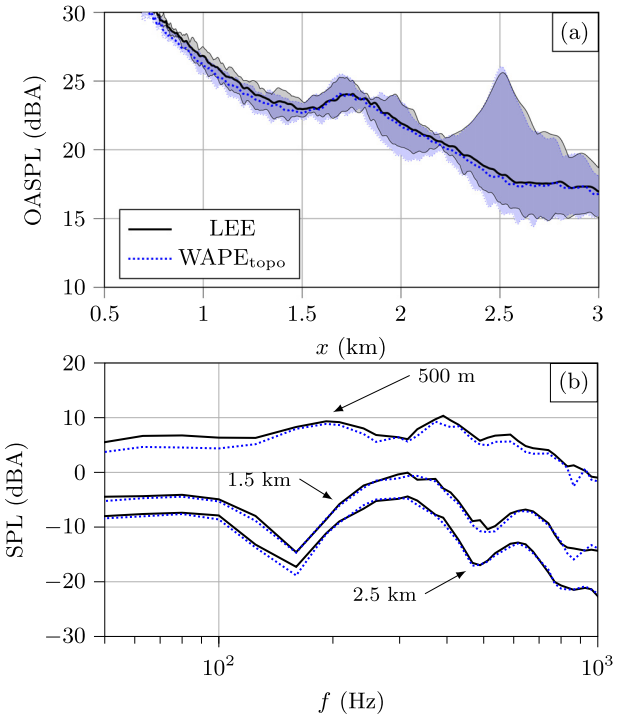

FIG. 13. (Color online) (a) Averaged OASPL over one rotation computed with the LEE and $\text{WAPE}_{\text{topo}}$ methods, minimum and maximum delimited with color patches. (b) Averaged spectrum obtained over a full rotation of the turbine blades for receivers at a height of 2 m, positioned at distances of $x = 500$ m, $x = 1.5$ km, and $x = 2.5$ km downstream of the turbine (listed from top to bottom).

V. CONCLUSION

The use of a new method based on the LEE for predicting wind turbine noise propagation was investigated. The method includes a flow model based on LES and an extended source model based on Amiet's theory. Comparison with the state-of-the-art PE methods (WAPE_{vec} and $\text{WAPE}_{\text{topo}}$) was performed for two cases: a baseline case with a wind turbine over flat ground and a more complex case where the wind turbine is positioned at the top of a hill. For the baseline case, the SPLs relative to the free field and the OASPL are almost identical when using LEE and the WAPE_{vec}. It was noticed that, as expected, the $\text{WAPE}_{\text{topo}}$ introduces phase errors due to the effective sound speed approach. However, this has a minor impact on the prediction of the SPLs at the ground and of OASPL. It is worth noting that the WAPE_{vec} is still preferable as it is derived with fewer assumptions and that it could be improved further by considering the vertical component of the wind speed. In the case with topography, the $\text{WAPE}_{\text{topo}}$ generates a noticeable error in the relative SPL computed for a given frequency (on the order of 3 dB). This is due to the steep slope of the hill. Nevertheless, the OASPL and AM obtained with the $\text{WAPE}_{\text{topo}}$ remain very close to those obtained with the LEE method. The main effects of the flow on the propagation are still well simulated by the $\text{WAPE}_{\text{topo}}$, and the shifts in the interference pattern observed at each frequency tend to average out for the prediction of overall levels.

Hence, we find that for situations with topography, PE methods in general and $\text{WAPE}_{\text{topo}}$ in particular provide a suitable first approach to determine sound propagation from wind turbines. It is still worth noting the advantages of using LEE. First, a time-domain solution is obtained, which allows one to compute a broadband SPL spectrum. The flow is taken into account with fewer assumptions, and higher wind speed can be considered without introducing errors due to the effective sound speed approach. The main drawback of this method is its computation cost, especially when numerous source heights must be considered.

ACKNOWLEDGMENTS

The authors thank Luoqin Liu for providing access to the LES data of Liu and Stevens (2020). This work was

https://doi.org/10.1121/10.0020834

performed within the framework of the LABEX CeLyA (ANR-10-LABX-0060) of Université de Lyon, within the program "Investissements d'Avenir" (ANR-16-IDEX-0005) operated by the French National Research Agency (ANR). The authors were granted access to the HPC resources of PMCS2I (Pôle de Modélisation et de Calcul en Sciences de l'Ingénieur et de l'Information) of Ecole Centrale de Lyon, PSMN (Pôle Scientifique de Modélisation Numérique) of ENS de Lyon, and P2CHPD (Pôle de Calcul Hautes Performances Dédiés) of Université Lyon I and members of FLMSN (Fédération Lyonnaise de Modélisation et Sciences Numériques), partner of EQUIPEX EQUIP@MESO. This work was supported by the Franco-Dutch Hubert Curien partnership (Van Gogh Programme No. 49310UM). For the purpose of Open Access, a CC-BY public copyright license has been applied by the authors to the present document and will be applied to all subsequent versions up to the author accepted manuscript arising from this submission. The authors declare no conflicts of interest. Data from numerical simulations are available from the authors on reasonable request.

APPENDIX: CALCULATION OF THE NOISE LEVEL RELATIVE TO THE FREE FIELD FOR THE LEE

This appendix details the derivation of the formula in Eq. (12) for calculating the noise levels relative to the free field from the LEE solution.

A. Analytical derivation

We first derive the analytical solution in the frequency domain and in far field for an impulsive source in a 2D homogeneous uniformly moving medium and in free-field, as sketched in Fig. 14. The derivation closely follows that presented in Ostashev *et al.* (2005) for the case of a monochromatic point source.

1. Solution as a convolution

A Cartesian system of coordinates $\mathbf{x} = (x, z)$ is used. A moving homogeneous atmosphere with a constant mean flow $\mathbf{V_0} = (u_0, 0)$ is considered. The initial conditions are $p(\mathbf{x}, t = 0) = S(\mathbf{x})$ and $\mathbf{v}(\mathbf{x}, t = 0) = \mathbf{0}$, and the source spatial distribution $S(\mathbf{x})$ is centered at the origin. Incorporating the initial conditions as source terms, the LEEs in Eq. (3) are written as

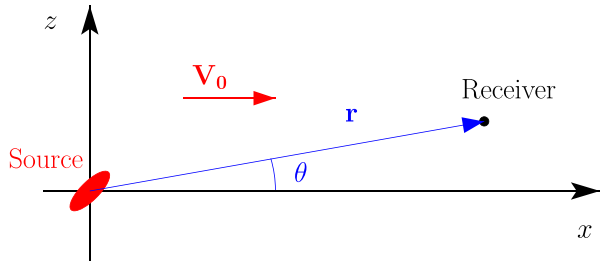

FIG. 14. (Color online) Sound propagation from a spatially distributed source in a 2D homogeneous uniformly moving medium.

$$\frac{\partial p}{\partial t} + u_0 \frac{\partial p}{\partial x} + \rho_0 c_0^2 \nabla \cdot \mathbf{v} = S(\mathbf{x})\delta(t), \tag{A1}$$

$$\frac{\partial \mathbf{v}}{\partial t} + u_0 \frac{\partial \mathbf{v}}{\partial x} + \frac{1}{\rho_0} \nabla p = 0, \tag{A2}$$

with δ the Dirac delta function. Combining Eqs. (A1) and (A2) leads to

$$\left(\frac{\partial}{\partial t} + u_0 \frac{\partial}{\partial x}\right)^2 p - c_0^2 \Delta p = \left(\frac{\partial}{\partial t} + u_0 \frac{\partial}{\partial x}\right) S(\mathbf{x})\delta(t). \tag{A3}$$

To translate the problem into the frequency domain, we employ the Fourier transform,

$$\hat{p}(\mathbf{x}, \omega) = \int_{-\infty}^{\infty} p(\mathbf{x}, t)\, \mathrm{e}^{\mathrm{i}\omega t}\, \mathrm{d}t. \tag{A4}$$

Taking the Fourier transform of Eq. (A3) and dividing by c_0^2 gives

$$\Delta \hat{p} - \left(-\mathrm{i}k_0 + M\frac{\partial}{\partial x}\right)^2 \hat{p} = -\frac{1}{c_0}\left(-\mathrm{i}k_0 + M\frac{\partial}{\partial x}\right) S(\mathbf{x}), \tag{A5}$$

with $k_0 = \omega/c_0$ and $M = u_0/c_0$. Substituting in Eq. (A5) the function $\hat{\phi}$ defined by

$$\hat{p} = -\frac{1}{c_0}\left(-\mathrm{i}k_0 + M\frac{\partial}{\partial x}\right)\hat{\phi} \tag{A6}$$

leads to

$$\Delta \hat{\phi} - \left(-\mathrm{i}k_0 + M\frac{\partial}{\partial x}\right)^2 \hat{\phi} = S(\mathbf{x}). \tag{A7}$$

For simplifying the previous equation, we use the transformation of coordinates $\mathbf{X} = (X, Z)$, with $x = X/\gamma$, $z = Z$, and $\gamma = 1/\sqrt{1 - M^2}$. Finally, introducing the function $\hat{\psi}$ defined by $\hat{\phi} = \exp(-\mathrm{i}K_0 M X)\hat{\psi}$ with $k_0 = K_0/\gamma$ in Eq. (A7) yields

$$\left(\frac{\partial^2}{\partial X^2} + \frac{\partial^2}{\partial Z^2} + K_0^2\right)\hat{\psi} = Q(\mathbf{X}), \tag{A8}$$

with $Q(\mathbf{X}) = \exp(\mathrm{i}K_0 M X) S(\mathbf{X})$. Eq. (A8) corresponds to the 2D inhomogeneous Helmholtz equation. Its solution is written as a convolution of the source term $Q(\mathbf{X})$ and the Green's function, which gives

$$\hat{\psi}(\mathbf{X}) = -\frac{\mathrm{i}}{4}\int H_0^{(1)}(K_0|\mathbf{X} - \mathbf{X}'|) Q(\mathbf{X}')\, \mathrm{d}\mathbf{X}', \tag{A9}$$

with $H_0^{(1)}$ the zeroth order Hankel function of the first kind.

2. Far-field approximation

To evaluate the convolution in Eq. (A9), a far-field approximation, known as the Fraunhofer approximation, is performed. It is assumed that the source-receiver distance is

large compared to the characteristic size of the source B, i.e., $|\mathbf{X}| \gg B$. As a consequence, the source-receiver distance is approximated at the zeroth order in the amplitude of the integrand, i.e., $|\mathbf{X}-\mathbf{X}'| = |\mathbf{X}|$, and at the first order in its phase, i.e., $|\mathbf{X}-\mathbf{X}'| = |\mathbf{X}| - (\mathbf{X}\cdot\mathbf{X}')/|\mathbf{X}|$. Under the Fraunhofer approximation, one has

$$H_0^{(1)}(K_0|\mathbf{X}-\mathbf{X}'|) = H_0^{(1)}(K_0|\mathbf{X}|)\exp(-\mathrm{i}K_0|\mathbf{X}|) \times \exp\left[\mathrm{i}K_0\left(|\mathbf{X}| - \frac{\mathbf{X}\cdot\mathbf{X}'}{|\mathbf{X}|}\right)\right], \tag{A10}$$

which allows us to express the function $\hat{\psi}$ in Eq. (A9) as

$$\hat{\psi}(\mathbf{X}) = \frac{-\mathrm{i}}{4}H_0^{(1)}(K_0|\mathbf{X}|)\int S(\mathbf{X}') \times \exp\left(\mathrm{i}K_0 MX' - \mathrm{i}K_0\frac{\mathbf{X}\cdot\mathbf{X}'}{|\mathbf{X}|}\right)\mathrm{d}\mathbf{X}'. \tag{A11}$$

Returning in the physical space, we get

$$\hat{\psi}(\mathbf{x}) = \frac{-\mathrm{i}\gamma}{4}H_0^{(1)}\left(k_0\gamma\sqrt{\gamma^2x^2+z^2}\right)\int S(x',z') \times \exp\left[-\mathrm{i}k_0\gamma^2(\cos\Theta - M)x'\right] \times \exp\left(-\mathrm{i}k_0\gamma\sin\Theta z'\right)\mathrm{d}x'\mathrm{d}z', \tag{A12}$$

where $\cos\Theta = X/|\mathbf{X}|$ and $\sin\Theta = Z/|\mathbf{X}|$ are related to $\cos\theta = x/|\mathbf{x}|$ and $\sin\theta = z/|\mathbf{x}|$ by

$$\cos\Theta = \frac{\cos\theta}{\sqrt{1-M^2\sin^2\theta}}, \quad \sin\Theta = \frac{\sin\theta}{\gamma\sqrt{1-M^2\sin^2\theta}}. \tag{A13}$$

Using Eq. (A12), we can write an expression for the function $\hat{\phi}$ in compact form as

$$\hat{\phi}(\mathbf{x}) = \frac{-\mathrm{i}\gamma}{4}\mathrm{e}^{\mathrm{i}k_0\gamma^2Mx}H_0^{(1)}\left(k_0\gamma\sqrt{\gamma^2x^2+z^2}\right) \times \tilde{S}(k_0\gamma^2(\cos\Theta - M), k_0\gamma\sin\Theta), \tag{A14}$$

with $\tilde{S}$ the spatial Fourier transform of $S(\mathbf{x})$,

$$\tilde{S}(k_x,k_z) = \int S(x,z)\,\mathrm{e}^{-\mathrm{i}k_xx-\mathrm{i}k_zz}\,\mathrm{d}x\,\mathrm{d}z. \tag{A15}$$

Finally, the pressure in the frequency domain is obtained from Eqs. (A6) and (A14),

$$\hat{p}(\mathbf{x}) = A(\omega,M,\theta)\frac{-\mathrm{i}\gamma^3}{4}\mathrm{e}^{\mathrm{i}k_0\gamma^2Mx}\left(H_0^{(1)}\left(k_0\gamma\sqrt{\gamma^2x^2+z^2}\right) - \frac{\mathrm{i}\gamma xM}{\sqrt{\gamma^2x^2+z^2}}H_1^{(1)}\left(k_0\gamma\sqrt{\gamma^2x^2+z^2}\right)\right), \tag{A16}$$

where $A(\omega,M,\theta)$ represents the equivalent amplitude of the impulsive source,

$$A(\omega,M,\theta) = \frac{\mathrm{i}k_0}{c_0}\tilde{S}(k_0\gamma^2(\cos\Theta - M), k_0\gamma\sin\Theta). \tag{A17}$$

B. Source correction

At long range, we can assume that the acoustic waves have been launched at small angles, corresponding to $\theta \approx 0$. Denoting $A_M(\omega) \equiv A(\omega,M,\theta\approx 0)$, the source amplitude becomes

$$A_M(\omega) = \frac{\mathrm{i}k_0}{c_0}\tilde{S}\left(\frac{k_0}{1+M},0\right). \tag{A18}$$

1. Case of a Gaussian spatial distribution

In this work, the impulsive source has a Gaussian spatial distribution

$$S(x,z) = S_0\exp\left(-\frac{x^2+z^2}{B^2}\right), \tag{A19}$$

whose Fourier transform is

$$\tilde{S}(k_x,k_z) = \pi B^2S_0\exp\left(-\frac{(k_x^2+k_z^2)B^2}{4}\right). \tag{A20}$$

The source amplitude in Eq. (A18) is then given by

$$A_M(\omega) = \frac{\mathrm{i}k_0}{c_0}\pi B^2S_0\exp\left(-\frac{k_0^2B^2}{4(1+M)^2}\right). \tag{A21}$$

Note that for $M=0$, the amplitude for the Gaussian impulse source in Eq. (A21) leads to the same expression as given in Eq. (23) in Dragna *et al.* (2011) for the case of a homogeneous atmosphere at rest. From this expression, we can also assess the frequency content of the Gaussian pulse. The maximum is reached for $f = c_0/(\sqrt{2}\pi B)$, and a cut-off frequency f_{10} can be defined such that the amplitude is equal to 10% of this maximum,

$$f_{10} \approx 0.6c_0/B. \tag{A22}$$

The amplitude of the Gaussian impulsive source, thus, depends on the surrounding mean velocity. As an illustration, Fig. 15 shows the source amplitude A_M for $M=0$ and for $M=0.03$, which corresponds to the Mach number at the height of the wind turbine hub. The source amplitude tends to be shifted toward higher frequencies. The difference in dB is negligible at low frequencies. However, it becomes noticeable at high frequencies, even for this small Mach number. Thus, the difference reaches around 1.5 dB at 1 kHz.

2. Evaluation of noise levels relative to the free field

The calculation of the noise levels relative to the free field from the LEE has to account for the modification of the source amplitude by the presence of the mean flow. For that, we estimate the free-field solution as

$$\hat{p}_{\mathrm{ff}}(\mathbf{x},\omega) = -\frac{\mathrm{i}}{4}A_M(\omega)H_0^{(1)}(k_0R), \tag{A23}$$

https://doi.org/10.1121/10.0020834

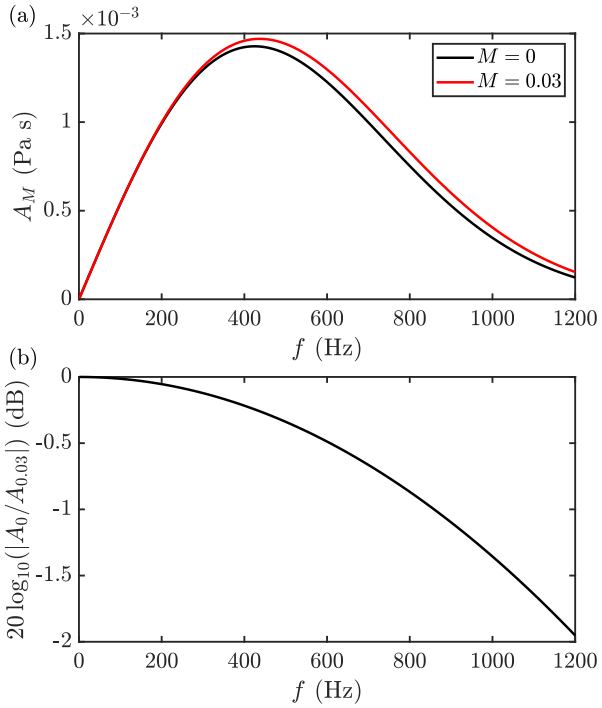

FIG. 15. (Color online) (a) Amplitude of the Gaussian impulsive source without mean flow and with a mean flow of Mach number equal to 0.03 and (b) difference in dB.

where the amplitude of the source is determined with Eq. (A18) considering the Mach number at the source height instead of $M = 0$. Eq. (A23) is equivalent to Eq. (13).

Attenborough, K., Bashir, I., and Taherzadeh, S. (**2011**). "Outdoor ground impedance models," J. Acoust. Soc. Am. **129**(5), 2806–2819.

Barlas, E., Wu, K. L., Zhu, W. J., Porté-Agel, F., and Shen, W. Z. (**2018**). "Variability of wind turbine noise over a diurnal cycle," Renew. Energy **126**, 791–800.

Barlas, E., Zhu, W. J., Shen, W. Z., Dag, K. O., and Moriarty, P. (**2017a**). "Consistent modelling of wind turbine noise propagation from source to receiver," J. Acoust. Soc. Am. **142**(5), 3297–3310.

Barlas, E., Zhu, W. J., Shen, W. Z., Kelly, M., and Andersen, S. J. (**2017b**). "Effects of wind turbine wake on atmospheric sound propagation," Appl. Acoust. **122**, 51–61.

Berland, J., Bogey, C., and Bailly, C. (**2006**). "Low-dissipation and low-dispersion fourth-order Runge–Kutta algorithm," Comput. Fluids **35**(10), 1459–1463.

Berland, J., Bogey, C., Marsden, O., and Bailly, C. (**2007**). "High-order, low dispersive and low dissipative explicit schemes for multiple-scale and boundary problems," J. Comput. Phys. **224**(2), 637–662.

Blumrich, R., and Heimann, D. (**2002**). "A linearized Eulerian sound propagation model for studies of complex meteorological effects," J. Acoust. Soc. Am. **112**(2), 446–455.

Bogey, C., and Bailly, C. (**2004**). "A family of low dispersive and low dissipative explicit schemes for flow and noise computations," J. Comput. Phys. **194**(1), 194–214.

Collino, F. (**1997**). "Perfectly matched absorbing layers for the paraxial equations," J. Comput. Phys. **131**(1), 164–180.

Cosnefroy, M. (**2019**). "Simulation numérique de la propagation dans l'atmosphère de sons impulsionnels et confrontations exp érimentales" ("Numerical simulation of atmospheric propagation of impulse sound and experimental comparisons"), Ph.D. thesis, Ecole Centrale de Lyon, Lyon, France.

Cotté, B. (**2019**). "Extended source models for wind turbine noise propagation," J. Acoust. Soc. Am. **145**(3), 1363–1371.

Dallois, L., Blanc-Benon, P., and Juvé, D. (**2001**). "A wide-angle parabolic equation for acoustic waves in inhomogeneous moving media: Applications to atmospheric sound propagation," J. Comp. Acoust. **09**(02), 477–494.

Dragna, D., and Blanc-Benon, P. (**2014**). "Towards realistic simulations of sound radiation by moving sources in outdoor environments," Int. J. Aeroacoust. **13**(5–6), 405–426.

Dragna, D., Cotté, B., Blanc-Benon, P., and Poisson, F. (**2011**). "Time-domain simulations of outdoor sound propagation with suitable impedance boundary conditions," AIAA J. **49**(7), 1420–1428.

Dumortier, B., Vincent, E., and Deaconu, M. (**2015**). "Acoustic control of wind farms," in *Proceedings of the European Wind Energy Association Conference*, *EWEA*, Paris, France, November 17–20, pp. 1–8.

Gadde, S. N., and Stevens, R. J. A. M. (**2021**). "Interaction between low-level jets and wind farms in a stable atmospheric boundary layer," Phys. Rev. Fluids **6**(1), 014603.

Gadde, S. N., Stieren, A., and Stevens, R. J. A. M. (**2021**). "Large-eddy simulations of stratified atmospheric boundary layers: Comparison of different subgrid models," Boundary Layer Meteorol. **178**(3), 363–382.

Gal-Chen, T., and Somerville, R. C. (**1975**). "On the use of a coordinate transformation for the solution of the Navier–Stokes equations," J. Comput. Phys. **17**(2), 209–228.

Gilbert, K. E., and White, M. J. (**1989**). "Application of the parabolic equation to sound propagation in a refracting atmosphere," J. Acoust. Soc. Am. **85**(2), 630–637.

Hansen, K. L., Nguyen, P., Zajamšek, B., Catcheside, P., and Hansen, C. H. (**2019**). "Prevalence of wind farm amplitude modulation at long-range residential locations," J. Sound Vib. **455**, 136–149.

Heimann, D., and Englberger, A. (**2018**). "3D-simulation of sound propagation through the wake of a wind turbine: Impact of the diurnal variability," Appl. Acoust. **141**, 393–402.

Heimann, D., Englberger, A., and Schady, A. (**2018**). "Sound propagation through the wake flow of a hilltop wind turbine—A numerical study," Wind Energy **21**(8), 650–662.

Kayser, B., Cotté, B., Ecotière, D., and Gauvreau, B. (**2020**). "Environmental parameters sensitivity analysis for the modeling of wind turbine noise in downwind conditions," J. Acoust. Soc. Am. **148**(6), 3623–3632.

Kayser, B., Mascarenhas, D., Cotté, B., Ecotière, D., and Gauvreau, B. (**2023**). "Validity of the effective sound speed approximation in parabolic equation models for wind turbine noise propagation," J. Acoust. Soc. Am. **153**(3), 1846–1854.

Komatitsch, D., and Martin, R. (**2007**). "An unsplit convolutional perfectly matched layer improved at grazing incidence for the seismic wave equation," Geophys. J. Int. **72**(1), 333–344.

Lee, S., Lee, D., and Honhoff, S. (**2016**). "Prediction of far-field wind turbine noise propagation with parabolic equation," J. Acoust. Soc. Am. **140**(2), 767–778.

Liu, L., and Stevens, R. J. A. M. (**2020**). "Effects of two-dimensional steep hills on the performance of wind turbines and wind farms," Boundary Layer Meteorol. **176**(2), 251–269.

Nyborg, C. M., Fischer, A., Thysell, E., Feng, J., Søndergaard, L. S., Hansen, T. R., Hansen, K. S., and Bertagnolio, F. (**2022**). "Propagation of wind turbine noise: Measurements and model evaluation," J. Phys. Conf. Ser. **2265**, 032041.

Ostashev, V. E., Wilson, D. K., Liu, L., Aldridge, D. F., Symons, N. P., and Marlin, D. (**2005**). "Equations for finite-difference, time-domain simulation of sound propagation in moving inhomogeneous media and numerical implementation," J. Acoust. Soc. Am. **117**(2), 503–517.

Ostashev, V. E., Wilson, D. K., and Muhlestein, M. B. (**2020**). "Wave and extra-wide-angle parabolic equations for sound propagation in a moving atmosphere," J. Acoust. Soc. Am. **147**(6), 3969–3984.

Prospathopoulos, J. M., and Voutsinas, S. G. (**2007**). "Application of a ray theory model to the prediction of noise emissions from isolated wind turbines and wind parks," Wind Energy **10**(2), 103–119.

Rienstra, S. (**2006**). "Impedance models in time domain, including the extended Helmoltz resonator model," in *Proceedings of the 12th AIAA/CEAS Aeroacoustics Conference (27th AIAA Aeroacoustics Conference)*, May 8–10, Cambridge, MA (American Institute of Aeronautics and Astronautics, Reston, VA).

Sack, R. A., and West, M. (**1995**). "A parabolic equation for sound propagation in two dimensions over any smooth terrain profile: The generalised terrain parabolic equation (GT-PE)," Appl. Acoust. **45**(2), 113–129.

Salomons, E. M. (**2001**). *Computational Atmospheric Acoustics* (Springer, Dordrecht, Netherlands).

Salomons, E. M., Blumrich, R., and Heimann, D. (**2002**). "Eulerian time-domain model for sound propagation over a finite-impedance ground surface: Comparison with frequency-domain models," Acta Acust. united Acust. **88**(4), 483–492.

Sessarego, M., and Shen, W. Z. (**2020**). "Noise propagation calculation of a wind turbine in complex terrain," J. Phys: Conf. Ser. **1452**(1), 012063.

Shen, W. Z., Zhu, W. J., Barlas, E., and Li, Y. (**2019**). "Advanced flow and noise simulation method for wind farm assessment in complex terrain," Renew. Energy **143**, 1812–1825.

Tian, Y., and Cotté, B. (**2016**). "Wind turbine noise modeling based on Amiet's theory: Effects of wind shear and atmospheric turbulence," Acta Acust. united Acust. **102**(4), 626–639.

Troian, R., Dragna, D., Bailly, C., and Galland, M.-A. (**2017**). "Broadband liner impedance eduction for multimodal acoustic propagation in the presence of a mean flow," J. Sound Vib. **392**, 200–216.

Van Renterghem, T. (**2014**). "Efficient outdoor sound propagation modeling with the finite-difference time-domain FDTD method: A review," Int. J. Aeroacoust. **13**(5–6), 385–404.

Journal of Sound and Vibration 500 (2021) 115999

Contents lists available at ScienceDirect

Journal of Sound and Vibration

journal homepage: www.elsevier.com/locate/jsv

Characterization and suppression of the hydrodynamic instability in the time domain for acoustic propagation in a lined flow duct

Yuanyuan Deng*, Antoni Alomar, Didier Dragna, Marie-Annick Galland

Universite de Lyon, Ecole Centrale de Lyon, INSA Lyon, UCB Lyon 1, CNRS LMFA UMR 5509, 36 Av Guy de Collongue, Ecully 69134, France

ARTICLE INFO

Article history:
Received 15 April 2020
Revised 15 January 2021
Accepted 30 January 2021
Available online 8 February 2021

Keywords:
Lined flow duct
Hydrodynamic instability
Instability suppression
Time domain

ABSTRACT

The gradient term suppression (GTS) method for removing the hydrodynamic instability appearing in the time-domain solutions of the linearized Euler equations (LEE) along a lined flow duct is assessed. For this, the characterization of a convective instability in the time domain, with the aid of a complementary modal analysis, is first presented. The effect of the mesh size and spatial filtering on the instability is investigated. In particular, a convergence of the instability in the time domain is achieved for a small enough grid size. The consequence of suppressing the mean flow gradient term on the modes is then investigated. It is shown that the unstable modes are indeed removed, but also that acoustic modes are significantly modified, especially for low Helmholtz numbers. The GTS method is finally applied to the NASA grazing impedance tube benchmark. It is found that tuning the weight of the mean flow gradient term within the LEE can be effective for suppressing the instability while conserving a reasonable accuracy of the acoustic component.

1. Introduction

Acoustic liners are widely used in the intake or bypass of the aero-engines to attenuate the noise generated by airplanes. To study their interaction with acoustic waves in the presence of a mean flow, time-domain approaches, based on the linearized Euler equations (LEE), are well-suited, as broadband results can be obtained with a single simulation [1–3]. In addition, extension to account for nonlinear effects due to large sound pressure levels can be considered. Time-domain approaches are however especially sensitive to instabilities, which can contaminate the pressure field and complicate the extraction of the acoustic component.

The presence of an instability over acoustic liners was first detected experimentally through the transmission coefficient [4–7]. The transmission coefficient became larger than 1 around the liner resonance at sufficiently high Mach numbers, implying a source of acoustic energy. The source was rightfully attributed to an instability. Optical flow measurements [8,9] led to a full spatial characterization of the instability, and revealed its convective nature.

* Corresponding author.
E-mail addresses: yuanyuan.deng@ec-lyon.fr (Y. Deng), tonignasi@gmail.com (A. Alomar), didier.dragna@ec-lyon.fr (D. Dragna), marie-annick.galland@ec-lyon.fr (M.-A. Galland).

https://doi.org/10.1016/j.jsv.2021.115999
0022-460X/

The use of the Ingard-Myers boundary condition [10,11], which describes how acoustic perturbations interact with an impedance wall for a vanishingly-thin inviscid boundary layer, was the usual approach from the early numerical and theoretical works on the subject. By doing so, instabilities were observed in many studies [1,12–16]. Later, Brambley [17] showed that the Ingard-Myers boundary condition is mathematically ill-posed in the time domain because the model supports unstable modes of unlimited exponential growth at arbitrarily short wavelengths. He [18] has shown later theoretically that accounting for a boundary layer thickness in the boundary condition (modified Ingard-Myers boundary condition) regularizes the problem. Since many studies have questioned the validity of the Ingard-Myers boundary condition [19,20], the use of a finite boundary layer thickness has been explored to improve the modeling of the instabilities [21–26]. Detailed numerical analysis with a mass-spring-damper impedance model showed that the use of a mean velocity profile instead of the Ingard-Myers boundary condition with a uniform flow transformed the unstable mode from absolute to convective [27]. However, even with a full velocity profile, absolute instabilities seems to be present in time-domain simulations for liners with a more realistic broadband impedance [28].

The thermoviscous effects [29] or turbulent dissipation through an eddy viscosity profile [30–32] are capable of attenuating the instability. It can even lead the nature of instability to change from absolute to convective [29,30]. Including turbulent dissipation, the properties of the instability appear to be close to the experimental results. More recently, numerical simulations of a channel flow with an acoustic liner using implicit large eddy simulations [33] were performed. Surface waves with characteristics similar to the instability predicted by linear stability analysis were exhibited. However, very fine grids, and even tremendous computational resources for direct numerical simulations, are needed in those studies to properly capture the instability, which is a strong disadvantage if the goal of the simulations is the computation of the acoustic field.

Various strategies to attenuate the instability numerically in time-domain simulations have been explored in the past. Since it is observed that the instability often appears in fine grids, the use of coarse grids and artificial damping has been recommended to attain a stable simulation by some authors. In particular, the studies of Gabard and Brambley [27,34] suggest that the origin of the absolute instability lies in the dispersion properties of the finite-difference schemes, and they proved the effectiveness of numerical filtering at the boundary to avoid spurious numerical instabilities. Marx [25] examined the case of a convective instability in the timedomain, and assessed the impact of selective filtering and grid size. He considers that if the instability is physical, increasing the grid size or strengthening the selective filters do not necessarily attenuate the instability.

Another approach, widely used in flows reminiscent of shear instabilities, is the substitution of the underlying LEE by a new set of equations which are inherently stable. Among them we can mention the gradient term suppression method (GTS) [35–39], the acoustic perturbation equations [40], the linearized perturbed compressible equations [41,42], or the gradient term filtering method [43,44]. These methods have been applied to deal with Kelvin-Helmholtz (KH) instabilities in various cases with shear flows, such as sound radiation through two-dimensional shear layers and sound radiation from a bypass duct [36,44]. It has been shown that most of them are similarly effective for these particular flows [44].

To the authors' knowledge, such methods have not been employed yet for the suppression of instabilities generated in a lined flow duct. It is worth mentioning that the mechanism for these instabilities, while related to KH instabilities, is different. Specifically, the instabilities in a lined flow duct are related to the presence of acoustic liners and not only due to the shear flow. Among the methods existing in the literature for KH instabilities, we have opted to restrict ourselves to GTS in this study, as a first approach to the case of acoustic liners. However, other methods might perform similarly or even better in certain cases, so a future comparative study would certainly be useful.

The objective of the paper is to analyze the effectiveness of the GTS method in suppressing the hydrodynamic instability that appears in the time-domain simulations of acoustic propagation along a lined duct. For this, it is beforehand verified that the instability is not of numerical origin and is a part of the LEE solution and that its characteristics are in good agreement with the predictions of a reference modal analysis, following Marx [25]. In particular, the impact of the grid resolution and the amount of selective filtering on instabilities are analyzed.

The paper is organized as follows. The configuration of the model, the governing equations and the numerical schemes are presented in Section 2. An example of an instability in the time-domain approach is shown and is characterized in Section 3. In Section 4, the effect of the selective filter and mesh size on the instability is assessed. Finally, in Section 5, the performance of the partial GTS method to suppress the instability is analyzed, and is applied on the NASA GIT benchmark problem.

2. Numerical models

A two-dimensional partially lined duct, of size $H \times L$, is considered, as shown in Fig. 1. The acoustic liner is installed on the upper wall, while the lower wall is rigid. A point source is fixed in the center of the duct. The source is impulsive, unless stated otherwise. A parallel shear flow of velocity profile u_0 goes from left to right, and vanishes on the walls. ρ_0 is the mean density, and c_0 is the sound speed. The physical quantities with dimensions of length, time, velocity, and pressure are nondimensionalized using H, H/c_0, c_0 and $\rho_0 c_0^2$, respectively.

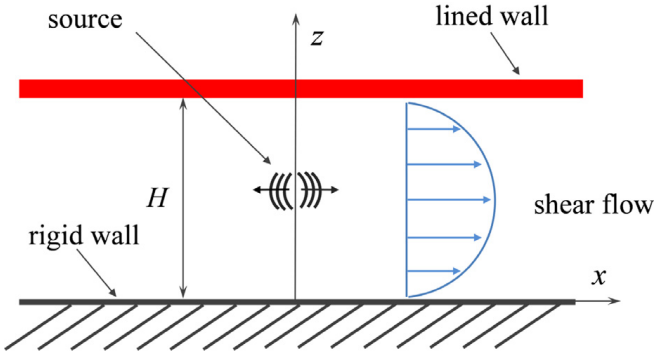

Fig. 1. Numerical configuration.

2.1. Governing equations

Acoustic propagation in a lined flow duct is governed by the LEE. Assuming the mean flow is homentropic and neglecting the gradient of mean pressure, the LEE in dimensionless form are written as:

$$\frac{\partial p}{\partial t} + u_0 \frac{\partial p}{\partial x} + \frac{\partial u}{\partial x} + \frac{\partial v}{\partial z} = Q \tag{1a}$$

$$\frac{\partial u}{\partial t} + u_0 \frac{\partial u}{\partial x} + v \frac{\mathrm{d}u_0}{\mathrm{d}z} + \frac{\partial p}{\partial x} = 0 \tag{1b}$$

$$\frac{\partial v}{\partial t} + u_0 \frac{\partial v}{\partial x} + \frac{\partial p}{\partial z} = 0 \tag{1c}$$

where p, u and v are the acoustic pressure and components of the acoustic velocity along the x and z-direction, respectively.

The mean flow velocity profile is given by:

$$u_0(z) = M \frac{n_t + 1}{n_t} \left(1 - |1 - 2z|^{n_t}\right), \tag{2}$$

where M is the Mach number corresponding to the mean velocity. The parameter n_t specifies the flow profile and can be related to the boundary layer thickness. The displacement thickness, defined by:

$$\delta = \int_0^{1/2} \left(1 - \frac{u_0(z)}{u_0(1/2)}\right) \mathrm{d}z \tag{3}$$

is equal to $\delta = 1/[2(n_t + 1)]$. Unless stated otherwise, the flow profile parameter is set to $n_t = 9$, corresponding to $\delta = 5$ %. Note the 2D velocity profile in Eq. (2) does not have an inflection point and should not support any KH instability. While not shown for conciseness, it has been verified that the time-domain simulations in a rigid duct with this sheared flow profile do not present any instability.

2.2. Time-domain solver

The LEE are solved using high order finite-difference time-domain methods. The spatial derivatives are calculated by optimized 4th-order finite-difference schemes over 11 points. Namely, the centered scheme of Bogey and Bailly [45] and the non-centered schemes of Berland et al. [46] are employed for the interior and boundary points, respectively. The optimized 4th-order 6-stage Runge-Kutta algorithm of Berland et al. [47] is employed for time integration. The time step is $\Delta t = 0.0014$.

Selective filters are used to remove grid-to-grid oscillations. For the interior points, the centered 11-point 6th-order selective filter of Bogey et al. [48] is adopted. For the boundary points, the selective filters of Berland et al. [46] are used. A parameter, denoted by σ and referred to as the filtering strength, allows one to adjust the effect of the selective filters. It ranges from 0 to 1, 0 meaning that no filtering is applied and 1 meaning that grid-to-grid oscillations are totally removed. As the filtering is applied at every iteration, a filtering strength of 1 is usually not necessary and can even deteriorate longer, well-resolved wavelengths. The default value is $\sigma = 0.5$.

The mesh is uniform in the x-direction with a size of $\Delta x = 0.02$. This ensures that the number of points per acoustic wavelength $\lambda = 2\pi/\omega$ is larger than 10 up to $\omega = 10\pi$. It can be noticed that the duct cut-off frequency in the no-flow case corresponds to $\omega = \pi$. Damping zones with a length of 20, are implemented upstream and downstream to prevent reflections. In these zones, the mesh spacing gradually increases with a stretching factor of 3% and a Laplacian filter is

applied to add artificial dissipation [49]. Along the z-direction, the mesh size decreases gradually towards the walls with a shrinking factor of 1%. The number of grid points along the duct height is n_z, with default value 175.

For the rigid wall, the boundary condition $v(x, z = 0) = 0$ is imposed. The lined wall is modelled through the impedance boundary condition:

$$p(x, z = 1, t) = [\tilde{z} * v_n](x, t), \tag{4}$$

where $*$ denotes the convolution operator, $v_n(x, t) = v(x, z = 1, t)$ and $\tilde{z}(t)$ is the impedance model in the time domain. To avoid computing the convolution integral, the time-domain boundary condition proposed in Troian et al. [50] is employed. For this, the admittance in the frequency domain $\beta(\omega)$, related to the time-domain impedance model by

$$\beta(\omega)^{-1} = \int_{-\infty}^{+\infty} \tilde{z}(t) \mathrm{e}^{-\mathrm{i}\omega t} \mathrm{d}t, \tag{5}$$

is approximated by a rational function:

$$\beta(\omega) = Y_\infty + \sum_{i=1}^{P} \frac{A_i}{\lambda_i + \mathrm{i}\omega} + \sum_{i=1}^{S} \left(\frac{B_i - \mathrm{i}C_i}{\alpha_i - \mathrm{i}\beta_i + \mathrm{i}\omega} + \frac{B_i + \mathrm{i}C_i}{\alpha_i + \mathrm{i}\beta_i + \mathrm{i}\omega} \right), \tag{6}$$

where λ_i and $\alpha_i \pm \mathrm{i}\beta_i$ are respectively the real poles and complex-conjugate pole pairs of $\beta(\omega)$, P and S denote their number and Y_∞, A_i, B_i and C_i are real coefficients. For a given broadband impedance model, the admittance parameters in Eq. (6) are determined using the vector fitting algorithm [51] in the frequency band of interest. The implementation of the time-domain impedance boundary condition is not further described here but interested readers can refer to Troian et al. [50] for details.

The source term Q in Eq. (1a) is chosen as

$$Q(x, z, t) = \lambda(t) \exp\left(-\frac{x^2 + (z - 0.5)^2}{B_s^2} \ln 2 \right), \tag{7}$$

where B_s is the Gaussian half-width of the source, with a value of 0.104. Both impulsive and harmonic sources are used in this study. For impulsive sources, $\lambda(t)$ is defined as:

$$\lambda(t) = \frac{t - t_s}{t_c} \exp\left(-\frac{(t - t_s)^2}{t_c^2} \ln 2 \right) H(t) \tag{8}$$

where $t_s = 5.42$ is a time shift, $t_c = 0.95$ specifies the frequency content of the source signal and $H(t)$ is the Heaviside function. In the case of a harmonic source, $\lambda(t)$ is defined as:

$$\lambda(t) = \exp(\mathrm{i}\omega t) H(t) \tag{9}$$

with ω the angular frequency. A complex-valued harmonic source is chosen for an easier extraction of instability characteristics. It can be noticed that acoustic pressure and velocity fields in the time-domain numerical simulations are also complex-valued when this harmonic source is employed.

2.3. Modal analysis approach

A modal analysis is also performed to determine the stability properties of the lined section, from which the wavenumbers and the mode shapes of all modes can be determined, including the unstable modes. Monochromatic waves propagating in an infinite, homogeneous duct are considered:

$$\begin{aligned} u &= U(z) \mathrm{e}^{\mathrm{i}(\omega t - kx)}, \\ v &= V(z) \mathrm{e}^{\mathrm{i}(\omega t - kx)}, \\ p &= P(z) \mathrm{e}^{\mathrm{i}(\omega t - kx)}, \end{aligned} \tag{10}$$

where U, V and P are the mode shapes, which depend only on z, and k is the mode wavenumber. Note that ω and k can be complex-valued.

In order to obtain this information, the next step is to introduce Eq. (10) into Eqs. (1) to obtain an eigenvalue problem. The eigenvalue problem is not directly formulated using the physical variables; instead, the characteristic variables, i.e., U, $P - V$ and $P + V$, are used. Specifically, $P - V$ and $P + V$ are the characteristic waves travelling along the $-z$ and $+z$-direction, respectively. The motivation for using the characteristic variables is described below. The discretization of the LEE on a grid with N points leads to a system of $3N$ equations for $3N$ unknowns. The boundary conditions however bring two additional equations. In order to avoid having an overdetermined system, it is thus necessary to choose two equations to eliminate, which is not trivial and somewhat arbitrary. The characteristic variables allow for a suitable choice (see Appendix A).

Doing so, the LEE in the frequency domain are written as:

$$\begin{pmatrix} 1 & \frac{-1}{2\mathrm{i}\omega} \frac{\mathrm{d}u_0}{\mathrm{d}z} & \frac{1}{2\mathrm{i}\omega} \frac{\mathrm{d}u_0}{\mathrm{d}z} \\ 0 & 1 - \frac{1}{\mathrm{i}\omega} \frac{\mathrm{d}}{\mathrm{d}z} & 0 \\ 0 & 0 & 1 + \frac{1}{\mathrm{i}\omega} \frac{\mathrm{d}}{\mathrm{d}z} \end{pmatrix} \begin{pmatrix} U \\ P - V \\ P + V \end{pmatrix} = \frac{k}{\omega} \begin{pmatrix} u_0 & \frac{1}{2} & \frac{1}{2} \\ 1 & u_0 & 0 \\ 1 & 0 & u_0 \end{pmatrix} \begin{pmatrix} U \\ P - V \\ P + V \end{pmatrix}. \tag{11}$$

This matrix system has to be completed with appropriate boundary conditions. On the rigid wall, the boundary condition becomes $[P+V](z=0)=[P-V](z=0)$. On the lined wall, the impedance boundary condition is written as:

$$[P-V](z=1)=\frac{1-\beta}{1+\beta}[P+V](z=1) \tag{12}$$

Note that the admittance in Eq. (12) depends on the frequency. In the stability analysis performed in Section 3, the frequency can be complex-valued and the admittance has to be calculated accordingly. To be noticed, admittance models given by a rational function in Eq. (6) are used in the paper.

The eigenvalue problem in Eq. (11) is solved numerically. The spatial derivatives are discretized using the Chebyshev spectral method [52], which is able to generate smaller numerical errors than finite-difference schemes for a given number of grid points. The gradient of the mean flow $\mathrm{d}u_0/\mathrm{d}z$ is also calculated numerically using the Chebyshev spectral method. The default value of the number of grid points N used in the modal analysis is 150. The discretized LEE are then recast into a generalized eigenvalue problem, which is solved by the \verb|eig| function of *MATLAB*. Details on the discretization and on the implementation of boundary conditions are provided in Appendix A.

3. Stability analysis

As described in the previous section, both methods will be applied to study hydrodynamic instabilities. The occurrence of a hydrodynamic instability depends on the characteristics of the liner, the mean flow profile and the source frequency. Two cases with Mach numbers of $M=0.1$ and $M=0.3$ are considered. The corresponding flow profiles are shown in Fig. 2. For simplicity, a mass-spring-damper (MSD) liner is used, with impedance

$$Z(\omega)=R+\mathrm{i}\omega m+\frac{K}{\mathrm{i}\omega}, \tag{13}$$

where R, m and K are respectively the damping, mass and spring stiffness. The impedance spectrum of the liner used in our case is shown in Fig. 3, with $R=0.2$, $m=5.4\times10^{-3}$ and $K=0$.

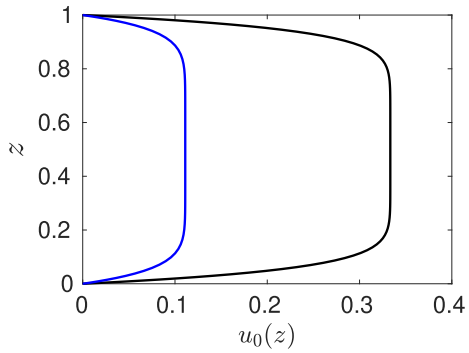

Fig. 2. Mean flow profile for: $M=0.1$ and $M=0.3$.

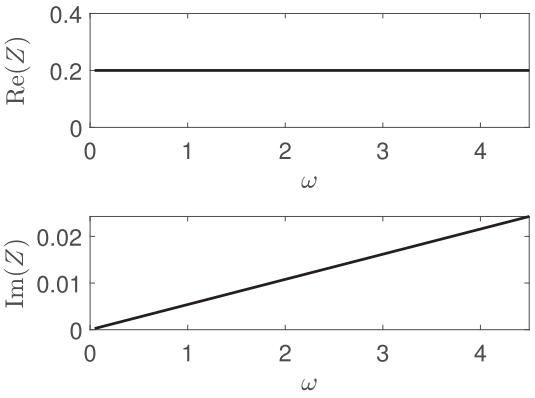

Fig. 3. Impedance of the MSD liner.

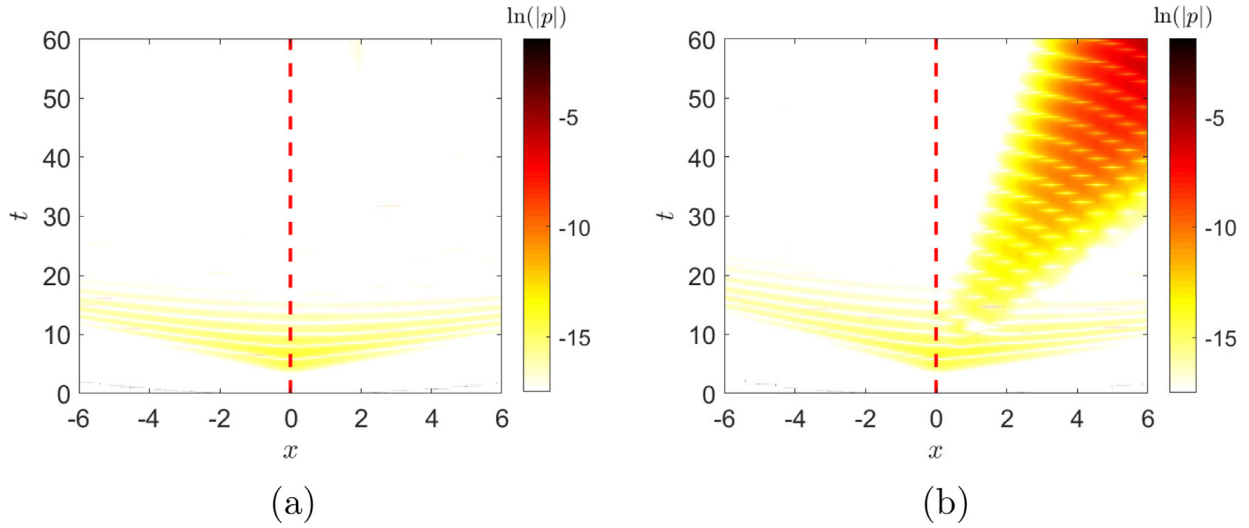

Fig. 4. Pressure response $\ln|p(x, z = 1, t)|$ to an impulsive source on the lined wall for (a) $M = 0.1$ and (b) $M = 0.3$. The source position is indicated by the vertical dashed line.

3.1. Example of time-domain simulation

Time-domain simulations are first performed using an impulsive source to illustrate the acoustic propagation along the lined duct. Fig. 4 shows the pressure response varying with time and position along the x-axis on the lined wall. For $M = 0.1$, two branches originating from $t = t_s$ are observed, corresponding to upstream and downstream propagating waves. These acoustic waves are attenuated along the lined wall. After $t \approx 18$, they have left the computational domain and the remaining fluctuating pressure is almost null. For $M = 0.3$, these two branches are retrieved. Their orientation is modified due to the difference in the Mach number. Another contribution is however observed in the downstream direction. Its magnitude and its spatial extent increase as it propagates away from the source, indicating it is an instability. Moreover, since the pressure response is given as a function of the distance and time, the velocity of acoustic waves and instabilities can be deduced from the slopes of the different branches. It can then be estimated that the propagation velocity of the instability is smaller than that of the acoustic waves.

3.2. Characterization of the instability from modal analysis

This section aims at correlating the instability observed in the time-domain simulations with the modal analysis. Therefore, a harmonic source is imposed on both approaches. For predicting the response to a harmonic excitation, a spatial stability analysis is performed: the frequency is real-valued and the mode wavenumbers can be complex. Fig. 5 displays the wavenumbers of all modes at $\omega = 0.9271$ for both $M = 0.1$ and $M = 0.3$. This particular frequency is chosen because it corresponds to a dimensional frequency $f = 1000$ Hz for the benchmark data of the NASA GIT duct (sound speed

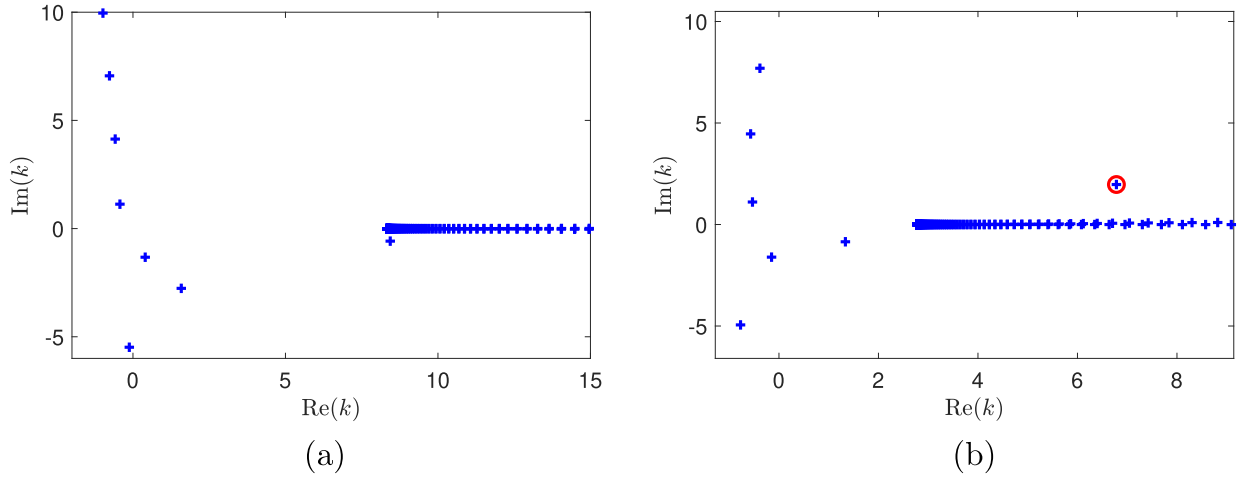

Fig. 5. Wavenumber obtained from modal analysis for $\omega = 0.9271$ and for (a) $M = 0.1$ and (b) $M = 0.3$. The encircled wavenumber indicates a possible unstable hydrodynamic mode.

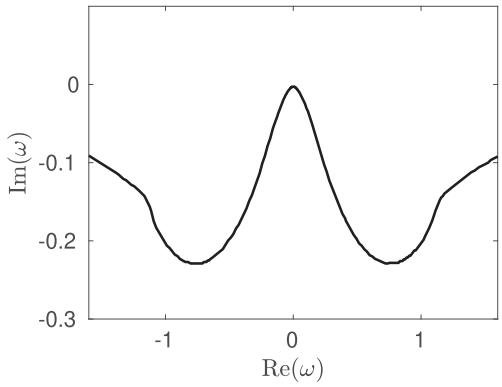

Fig. 6. Growth rate of the unstable mode for a real wavenumber and for $M = 0.3$.

$c_0 = 344.28$ m s^{-1} and duct height $H = 0.0508$ m), which is considered in Section 5.3. It is also close to the frequency $\omega = 0.8344$ where the maximal spatial growth rate is observed (not shown). For $M = 0.1$, there is no mode in the upper-right complex k-plane and therefore no possible instability. For $M = 0.3$, the wavenumber of one mode ($k = 6.78 + 1.97$i) has both positive real and imaginary parts. This is possibly an unstable mode, and its stability depends on the propagation direction. If the mode is an upstream decaying mode, the propagation is stable. On the other hand, if it propagates in the downstream direction, it corresponds to an instability. The propagation direction of this mode therefore needs to be determined.

In Fig. 5, noticeable modes other than the acoustic modes and the instability are convected modes which satisfy the dispersion relation $ku_0(z) = \omega$. For a sheared mean flow, they come as a continuous spectrum, located in the k-plane along the horizontal half-line starting at $k = \omega/\max(u_0)$. In solving numerically the eigenvalue problem, this continuous spectrum turns into individual modes, which are greatly dependent on the discretization. In particular, the wavenumbers of these modes may have small positive imaginary parts and thus be weakly unstable. As shown in the study of Brambley et al. [53], the contributions of the continuous spectrum are negligible when the point source is located at the duct centerline, where the mean flow is relatively unsheared. Note that the use of selective filters, as employed in the time-domain simulations, tends to move the convected modes towards the lower right quadrant of the k-plane [25] and thus to make all these modes stable. As we are primarily interested in the instability, no specific method is employed to have an accurate prediction of convective modes. Such a method has been for instance described in Vilenski and Rienstra [54].

The Briggs-Bers criterion [55,56] is used to determine the propagation direction of the modes, and, if an unstable mode is present, whether it is convective or absolute. This criterion has been introduced to study the plasma instability and has been later considered for the stability analysis of acoustic propagation in a lined flow duct [17]. However, before using the Briggs-Bers criterion, it must be checked that it is applicable. For instance, as discussed by Brambley [17], the acoustic propagation in a lined duct with a plug flow and the Myers impedance boundary condition is mathematically ill-posed, implying that Briggs-Bers criterion can not be used. In order to apply the Briggs-Bers criterion, one must first check that the growth rates of all modes, and in particular the unstable modes, are bounded. To do so, a temporal stability analysis is conducted. The wavenumber here remains real, and the frequency ω, possibly complex-valued, satisfying the dispersion relation is sought. If for a particular value of the wavenumber, one has $\mathrm{Im}(\omega) < 0$, the system is then unstable. Fig. 6 shows the growth rate of the possible unstable mode for $M = 0.3$ as a function of $\mathrm{Re}(\omega)$. It is observed that the growth rate is bounded at $\mathrm{Im}(\omega) \approx -0.23$, meaning that the instability will not be amplified at an arbitrarily large growth rate for any given real frequency. The Briggs-Bers criterion can thus be applied in this case.

To determinate if a possible unstable mode is an instability, the trajectory of its wavenumber in the complex k-plane is recorded as $\omega = \mathrm{Re}(\omega) + \mathrm{i}\,\mathrm{Im}(\omega)$ is varied. More specifically, $\mathrm{Re}(\omega)$ is fixed while $\mathrm{Im}(\omega)$ is varied from $-\infty$ to 0. Fig. 7 shows this process for $\mathrm{Re}(\omega) = 0.9271$, while the imaginary part $\mathrm{Im}(\omega)$ goes from -1.4 to 0. The wavenumber of the possible unstable mode crosses the real k-axis from the lower k-plane when $\mathrm{Im}(\omega)$ is approaching 0. The crossing of the real k-axis from the lower half k-plane indicates that this mode is indeed a downstream propagating mode and is thus an instability.

In addition, in order to discard the existence of an absolute instability, it should be verified, that the trajectories of the wavenumbers in the k-plane for any $\mathrm{Re}(\omega)$ do not show any saddle point, which corresponds to merging roots of k from different halves of the k-plane. This has been carefully checked on a large range of values of $\mathrm{Re}(\omega)$. To sum up, for $\omega = 0.9271$, there is only one hydrodynamic instability, and it is a convective instability.

3.3. Characterization of the instability from time-domain simulation

3.3.1. Instability type

The type of the instability observed in the time-domain simulations can also be investigated by considering acoustic propagation driven by a harmonic source with $\omega = 0.9271$. The logarithm of $|p|$ on the lined wall $z = 1$ varying with t and

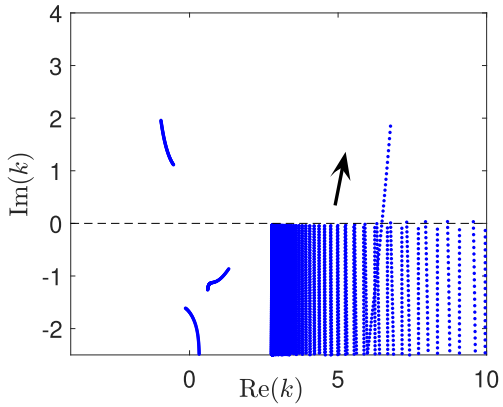

Fig. 7. Trajectories of the wavenumbers for $\mathrm{Re}(\omega) = 0.9271$ as $\mathrm{Im}(\omega)$ varies from -1.4 to 0. The arrow indicates the direction of increasing $\mathrm{Im}(\omega)$.

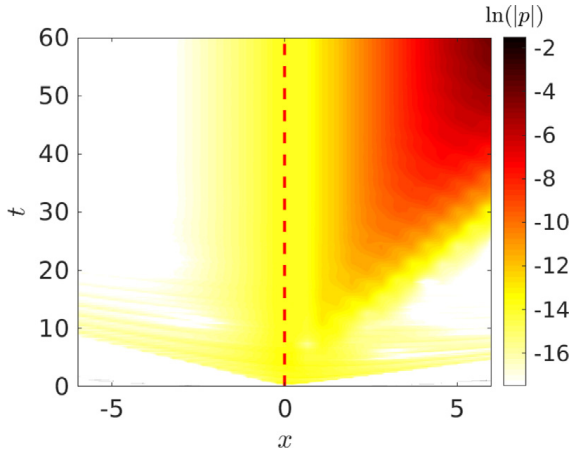

Fig. 8. Pressure response $\ln|p(x, z = 1, t)|$ to a harmonic source at $\omega = 0.9271$ obtained from the time-domain simulation for $M = 0.3$. The source position is indicated by the vertical dashed line.

x is shown in Fig. 8. With a harmonic source, the response of pressure has a constant value at $x = 0$. The attenuation by the liner can be noticed along the upstream direction, and the hydrodynamic instability is observed in the downstream direction. Once a steady-state is attained, the magnitude of the instability at a given location is not increasing over time. It thus appears that the instability observed in the time-domain simulation is also a convective one.

3.3.2. Wavenumber

If the instability is convective and is the main contribution to the pressure field, the fluctuating pressure will have the form:

$$p(x, z, t) = P_{\mathrm{HI}}(z)\mathrm{e}^{\mathrm{i}\omega t}\mathrm{e}^{-\mathrm{iRe}(k_{\mathrm{HI}})x}\mathrm{e}^{\mathrm{Im}(k_{\mathrm{HI}})x}, \tag{14}$$

where P_{HI} is the mode shape of the instability and k_{HI} is its wavenumber.

In this case, the phase of the complex pressure, denoted by arg is given by:

$$\arg[p(x, z, t)] = -\mathrm{Re}(k_{\mathrm{HI}})x + \omega t + \arg[P_{\mathrm{HI}}(z)]. \tag{15}$$

The real part of the instability wavenumber can then be estimated from the time-domain solution through the axial evolution of the phase for the complex pressure. Fig. 9 shows $\arg(p)$ along the liner ($z = 1$) at $t = 90$, for which it has been checked that the instability is well developed. The phase has been unwrapped to ensure that $\arg(p)$ is continuous. The estimated slope for $2 \leq x \leq 6$ of the phase is -6.89, which is very close to the prediction of modal analysis $\mathrm{Re}(k_{\mathrm{HI}}) = 6.78$.

Similarly, the growth rate of the convective instability $\mathrm{Im}(k_{\mathrm{HI}})$ in Eq. (14) can be calculated from the logarithm of $|p(x, z, t)|$:

$$\ln|p(x, z, t)| = \mathrm{Im}(k_{\mathrm{HI}})x + \ln|P_{\mathrm{HI}}(z)|. \tag{16}$$

A snapshot of $\ln|p|$ at $t = 90$ from the time-domain simulation is depicted in Fig. 10(a). The instability is seen growing from the source at the vicinity of the liner. Fig. 10(b) shows the spatial variation of $\ln|p(x, z = 1, t = 90)|$. A linear growth is observed downstream, where the instability is the dominant contribution to the pressure field. The estimated slope for $2 \leq x \leq 6$ is 1.99, which is again in close agreement with the spatial growth rate predicted by modal analysis $\mathrm{Im}(k_{\mathrm{HI}}) = 1.97$.

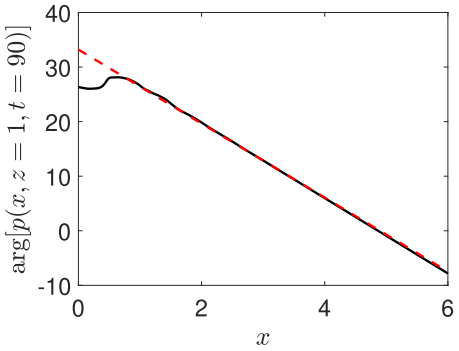

Fig. 9. Comparison of the phase of the pressure on the lined wall from the time-domain solution at $t = 90$ ——— and from the analytical solution in Eq. (15) ($\arg(p) \propto -6.78x$) - - - -.

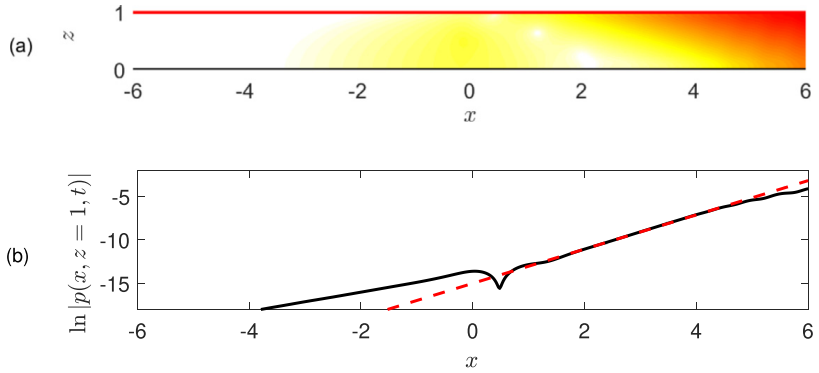

Fig. 10. (a) Snapshot of $\ln|p|$ at $t = 90$ and (b) comparison of the amplitude of the pressure on the lined wall from the time-domain solution ——— and from the analytical solution in Eq. (16) ($\ln|p| \propto 1.97x$) - - - -.

Another example for a different frequency $\omega = 0.4636$ can be found in Appendix B. This shows the viability of the time-domain method in simulating the instability.

3.3.3. Mode shapes

The mode shapes P, U and V of the instability determined from modal analysis are compared with the vertical profiles of p, u and v calculated from the time-domain solution in Fig. 11. The results of the time-domain solution correspond to the section $x = 4$ at $t = 90$, for which it has been checked that the solution is not changing after additional time iterations. When the time-domain solution is in a steady-state, the vertical profiles of p, u and v should hold similar shapes regardless of x-position and time iteration. For comparison, the mode shapes of the instability and the vertical profiles of p, u and v are normalized by the maximum of the pressure modulus. The peaks of the amplitudes are observed near the lined wall. Then they gradually decrease to a small value on the rigid wall. The match between modal analysis and the time-domain solution is remarkable.

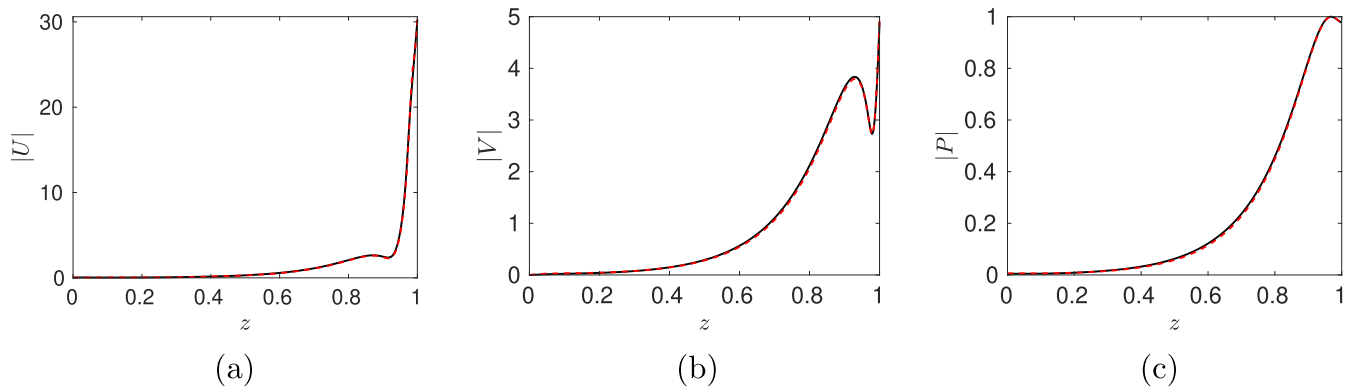

Fig. 11. Comparison of the mode shape of the instability for (a) $U(z)$, (b) $V(z)$ and (c) $P(z)$ ——— determined from the time-domain solution at $x = 4$ and $t = 90$ and - - - - calculated by modal analysis.

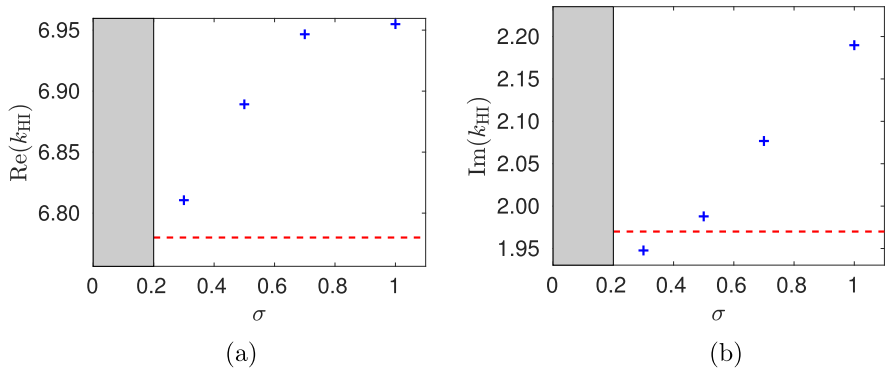

Fig. 12. (a) Real and (b) imaginary parts of the instability wavenumber + estimated from the time-domain solution as a function of the filtering strength σ and - - - predicted by modal analysis. The grey region indicates unstable simulations.

4. Convergence of instability

Previous studies on the same topic, i.e., instabilities appearing during sound propagation in a lined flow duct, have investigated the impact of spatial filters and grid resolution on the instabilities. It was concluded that selective filtering is effective to remove or partly remove the instability [3,34] and that the use of fine grids can reinforce the instability [2,27], in particular when using the Myers impedance boundary condition instead of resolving the boundary layer as done here. Therefore, the effects of both factors on the hydrodynamic instabilities are studied.

4.1. Effect of the filtering strength

In the time-domain simulations, a selective filter of strength σ is applied on the whole domain to remove the grid-to-grid oscillations. In the previous sections, σ was set to 0.5. Simulations are now performed with different values of σ in order to study how the properties of the hydrodynamic instability are modified.

Fig. 12 shows the real and imaginary parts of the instability wavenumber obtained with the time-domain solutions as a function of σ. The results are compared with the reference wavenumber obtained by modal analysis. When the strength of selective filter is between 0.7 and 1, the strong dissipation of the selective filter results in a noticeable deviation between the reference result and the time-domain prediction. In particular, the growth rate of the instability is overestimated. As σ decreases, Re(k_{HI}) and Im(k_{HI}) start to approach the reference wavenumber. The value of σ does not make a significant difference to Re(k_{HI}) and Im(k_{HI}), when it is in the range between 0.2 and 0.5. For σ below 0.2, spurious numerical waves with a short wavelength are rapidly growing near the duct walls and the simulations become unstable instantly. Therefore, for accurately predicting the hydrodynamic instability, the filtering strength should be chosen as small as possible while sufficiently large to stabilize the numerical calculation. A value of σ between 0.2 and 0.5 seems to be a good compromise considering the time step used in the time-domain simulations.

4.2. Effect of the mesh size along the duct height

Along the x-direction, centered high-order finite-difference schemes, with dispersion-relation preserving properties, are employed. It is assumed that the mesh size Δx is small enough so that the dispersion properties of the instability are well-reproduced. In particular, it has been checked that $k^*(k_{HI})$ is very close to k_{HI}, where k^* is the effective wavenumber of the centered finite-difference scheme employed here. No particular effect in reducing Δx is thus expected. The grid along the z-direction is anticipated to have more impact on the instability. Indeed, non-centered schemes are used near the walls, which enhance dispersion. They can amplify or dissipate even constant-amplitude waves, contrary to centered schemes. In addition, the instability is directly related to the mean flow profile through u_0 and $\mathrm{d}u_0/\mathrm{d}z$. The discretization of the mean flow profile, in particular within the boundary layer, is expected to play a role in the results.

Fig. 13 shows the impact of the number of grid points along the z-direction n_z on the real and imaginary parts of the instability wavenumber. For $n_z \leq 155$, the deviations of Re(k_{HI}) and Im(k_{HI}) estimated from the time-domain simulations and the modal analysis are noticeable. Note that the mesh is already fine enough for $n_z = 55$ to precisely calculate the acoustic propagation. As shown in [57], the pressure of instabilities should decay exponentially away from the lining as $\exp[-\mathrm{Re}(\mu)(1-z)]$ with $\mu^2 = k^2 - (\omega - Mk)^2$. In the present case, $\mathrm{Re}(\mu) = 6.69$ so that the number of points per wavelength is about $2\pi n_z/\mathrm{Re}(\mu) \approx 52$, which is very large. However, that is still not sufficient to precisely calculate the hydrodynamic instability. As n_z increases, the features of hydrodynamic instability can be captured and the wavenumber gradually approaches the prediction of modal analysis. With $n_z \geq 175$ the time-domain solution is deemed converged.

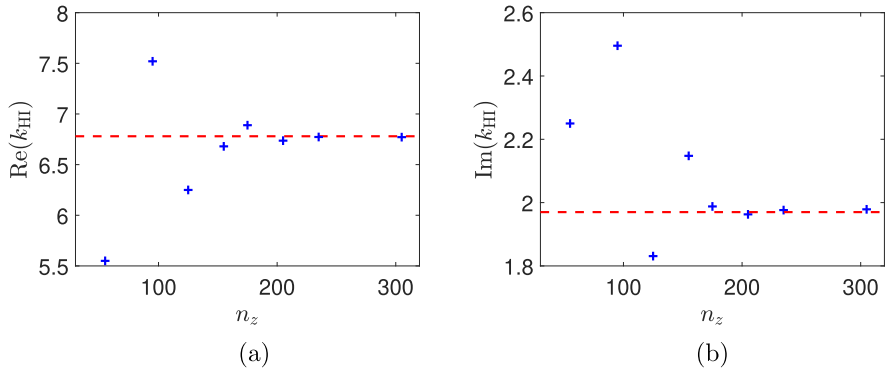

Fig. 13. (a) Real and (b) imaginary parts of the instability wavenumber + estimated from the time-domain solution as a function of the number of grid points along the duct height n_z and - - - predicted by modal analysis.

5. Suppression of the hydrodynamic instability

In all cases tested with realistic Mach numbers, it was not possible to prevent the appearance of the instability using coarse grids and increased selective filter strength. We turned therefore to the methods based on the stabilization via modification of the underlying equations. Given the similar performance of many of these methods in turbulent jets [44], we opted for the gradient term suppression (GTS) method due to its simplicity and performance.

In the case that the acoustic field is generated by an impulsive source, as in the present case, it may be possible to separate the acoustic and instability components in time through a temporal window. This would allow to account for the full LEE, but it is of use only when the instability is weak enough. In general, a robust suppression strategy is needed with a minimal impact on acoustic propagation.

5.1. Partial GTS

A natural generalization of the original GTS method is used here to suppress the instability, consisting of a partial suppression of the gradient term instead of a complete suppression. Eqs. (1) are modified by adding a coefficient ϵ in front of the term of $\mathrm{d}u_0/\mathrm{d}z$. Therefore, Eq. (1b) turns to

$$\frac{\partial u}{\partial t} + u_0 \frac{\partial u}{\partial x} + \epsilon \frac{\mathrm{d}u_0}{\mathrm{d}z} v + \frac{\partial p}{\partial x} = 0 \tag{17}$$

where ϵ adjusts the strength of the mean flow gradient term and ranges from 1 to 0.

Combining Eqs. (1a), (17) and (1c) leads to the wave equation:

$$\frac{\mathrm{D}}{\mathrm{D}t}\left(\frac{\mathrm{D}^2 p}{\mathrm{D}t^2} - \nabla^2 p\right) + (\epsilon + 1)\frac{\mathrm{d}u_0}{\mathrm{d}z}\frac{\partial^2 p}{\partial x \partial z} = \frac{\mathrm{D}^2 Q}{\mathrm{D}t^2} \tag{18}$$

where $\mathrm{D}/\mathrm{D}t = \partial/\partial t + u_0\,\partial/\partial x$ is the material derivative. In particular, the Lilley's equation is recovered for $\epsilon = 1$. The decrease of ϵ from 1 to 0 is thus equivalent to transforming the original Lilley's equation, which sustains unstable modes, to a simplified form of Lilley's equation which appears to be inherently stable [35]. In addition, decreasing ϵ from 1 to 0 diminishes the refraction term proportional to $\mathrm{d}u_0/\mathrm{d}z$ in the original Lilley's equation by a factor of two. A gradual suppression of the instability is then expected when diminishing the value of ϵ.

Another remarkable value is $\epsilon = -1$ for which Eq. (18) corresponds to the material derivative of the convected wave equation. However, Eq. (18) is already stable for $\epsilon = 0$. In addition, it will be shown that the prediction of the acoustic propagation tends to be deteriorated with the decrease of ϵ. Therefore, the study is hereafter restricted to $\epsilon \in [0, 1]$.

The GTS method is expected to provide an accurate prediction of acoustic propagation at high frequencies [35]. This can be explained by conducting an order of magnitude analysis. The order of the magnitude of each term in Eq. (1b) is as follows:

$$\frac{\mathrm{D}u}{\mathrm{D}t} \sim (\omega - Mk)\hat{u}, \qquad \frac{\mathrm{d}u_0}{\mathrm{d}z} v \sim \frac{M}{\delta}\hat{v}, \qquad \frac{\partial p}{\partial x} \sim k\hat{p},$$

where for acoustic modes the wavenumber is in the order of the frequency $k \sim \omega$ and the acoustic variables are in the same order of magnitude $\hat{u} \sim \hat{v} \sim \hat{p}$. The mean flow gradient term in Eq. (1b) can be neglected if

$$\left|v\frac{\mathrm{d}u_0}{\mathrm{d}z}\right| \ll \left|\frac{\partial p}{\partial x}\right|, \left|\frac{\mathrm{D}u}{\mathrm{D}t}\right|. \tag{19}$$

which, considering the orders of magnitude above, shows that the mean flow gradient term is expected to have a negligible effect on the acoustic propagation for $\omega\delta \gg M$. This explains why the high frequency components are less impacted by the partial GTS method.

5.2. Effect on the wavenumber and the mode shape

The wavenumbers are studied when ϵ varies from 1 to 0. Fig. 14 shows the wavenumbers in the k-plane determined by modal analysis for different values of ϵ for the rigid and partially lined duct. It is first noticed that modifying ϵ tends to move all the modes in the complex k-plane. The instability for the lined duct, observed for $\epsilon = 1$, is not seen for the smaller values of ϵ, which shows that a small decrease of ϵ is sufficient to suppress the instability. Also, the wavenumbers for the rigid duct are less sensitive to ϵ than for the lined duct.

To analyze more finely the effect of ϵ on the instability, the variations of the instability wavenumber are plotted as a function of ϵ in Fig. 15. The results are shown for three different grid sizes ($N = 100$, 200 and 300). The growth rate of the unstable mode $\mathrm{Im}(k_{\mathrm{HI}})$ decreases gradually with ϵ which proves the stabilizing effect of decreasing ϵ. It is interesting to note that for $\epsilon \leq 0.94$, the wavenumber of the unstable mode starts depending on the grid size. There, the unstable mode merges into the continuous spectrum of convected modes near the real k-axis.

Acoustic modes are also affected by reducing the parameter ϵ. To quantify the impact of the partial GTS method on the wavenumbers of the acoustic modes, the attenuation rate of the propagative acoustic mode is provided in Fig. 16(a). The attenuation rate α, defined as $\alpha = 20\log_{10} \mathrm{e}^{-\mathrm{Im}(k)}$, expresses the decrease per unit distance (H) of the signal amplitude during the propagation along the axial direction. For $\omega = 0.9271$, the attenuation rate of the plane wave mode increases from 7.39 to 14.95 dB/H when ϵ decreases from 1 to 0.

In addition, Fig. 17 depicts the mode shapes of the acoustic velocity components and pressure for the plane wave mode and for the leading upstream and downstream evanescent modes for different values of ϵ. The modulus of all three variables are normalized by the maximum of $|P|$. Modifying ϵ has an evident impact on $|U|$ and $|V|$, noticeably near the lined wall. This effect is particularly dramatic for $|U|$, whose peak on the lined wall decreases by a factor of 10 from $\epsilon = 1$ to $\epsilon = 0$. Also, a noticeable increase of $|V|$ near the lined wall is observed as ϵ decreases. Concerning the pressure, the mode shape does not vary too much with ϵ. For the plane wave mode, a decrease of the amplitude is noticed near the rigid wall, while for the evanescent modes, the amplitude grows gradually near the lined wall as ϵ decreases.

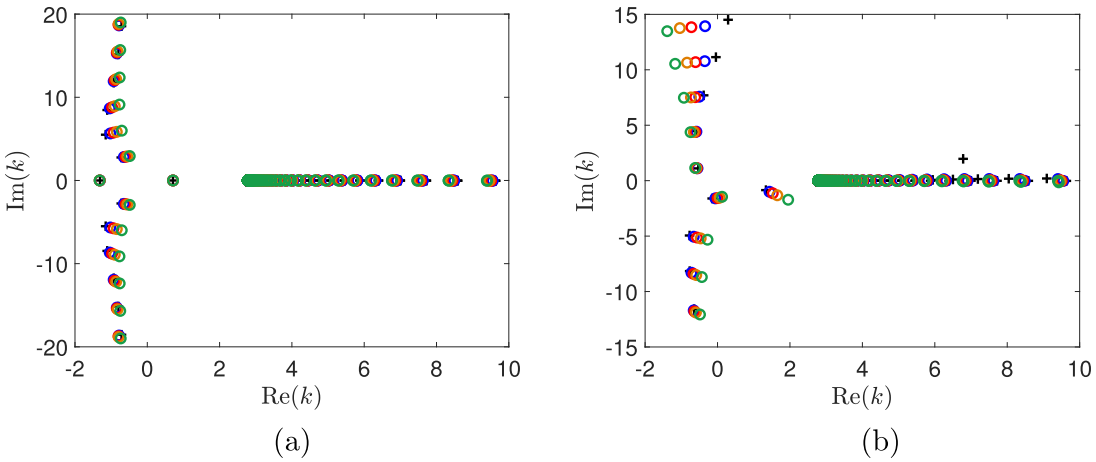

Fig. 14. Wavenumbers in the k-plane at $\omega = 0.9271$ for a duct (a) with two rigid walls, (b) with one rigid wall and for different strengths of gradient term: + $\epsilon = 1$, ○ $\epsilon = 0.7$, ○ $\epsilon = 0.5$, ○ $\epsilon = 0.3$ and ○ $\epsilon = 0$.

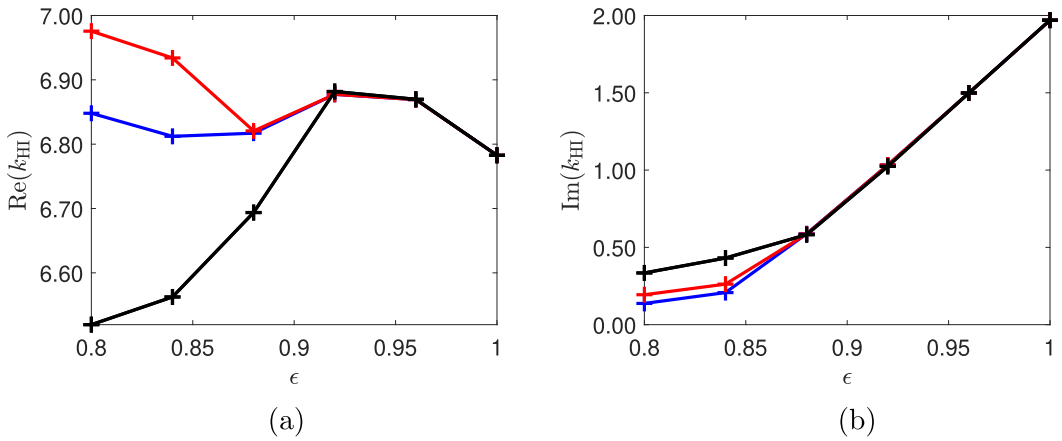

Fig. 15. Variations of the (a) real and (b) imaginary parts of the instability wavenumber k_{HI} as a function of ϵ for different numbers of grid points: $N = 100$, $N = 200$ and $N = 300$.

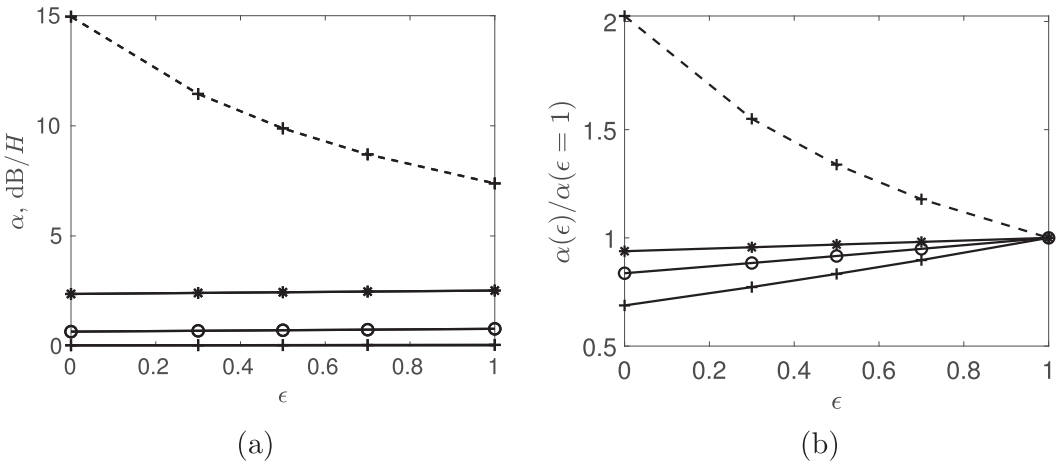

Fig. 16. (a) Attenuation rate of acoustic modes and (b) ratio of the attenuation rate determined for the partial GTS method to that for the original LEE for (dashed) $\omega = 0.9271$ and (full) $\omega = 9.271$: + plane wave mode, ∘ second downstream propagative mode and ∗ third downstream propagative mode.

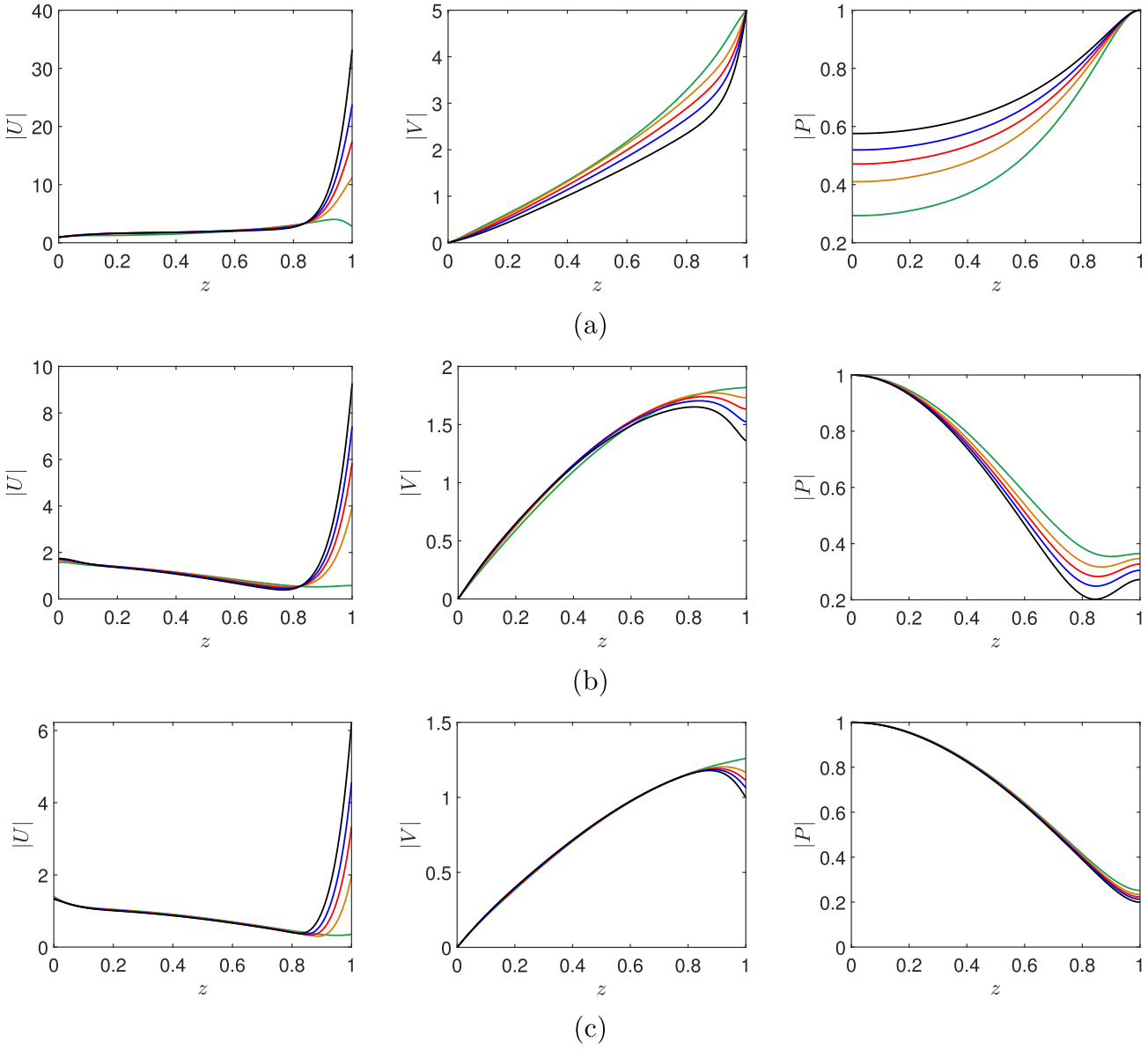

Fig. 17. Mode shapes for the MSD liner at $\omega = 0.9271$ and for several values of ϵ: (a) plane wave mode and leading (b) downstream and (c) upstream evanescent modes for, from left to right, velocity components along x and z-direction and pressure: $\epsilon = 1$, $\epsilon = 0.7$, $\epsilon = 0.5$, $\epsilon = 0.3$ and $\epsilon = 0$.

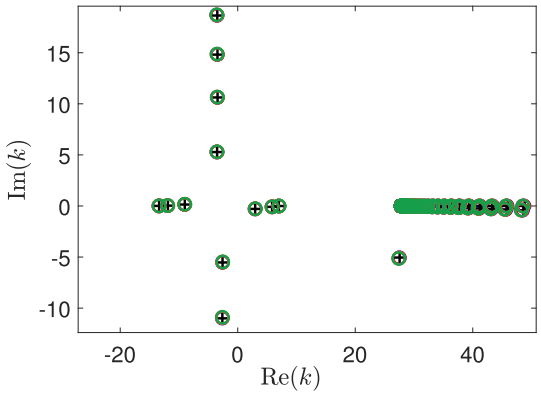

Fig. 18. Wavenumbers in the k-plane at $\omega = 9.271$ for a lined duct and for several values of ϵ: + $\epsilon = 1$, ○ $\epsilon = 0.7$, ○ $\epsilon = 0.5$, ○ $\epsilon = 0.3$ and ○ $\epsilon = 0$.

The impact of the partial GTS method on the acoustic propagation at high Helmholtz numbers is here studied. Fig. 18 provides the mode wavenumbers for $\omega = 9.271$, while keeping the same impedance and boundary layer thickness as for $\omega = 0.9271$. Three downstream propagative modes are noticed and no unstable mode is observed. The mode wavenumbers are less changed due to the partial GTS method compared with Fig. 14. The attenuation rates for the three downstream propagative modes are also plotted in Fig. 16(a). The deviation caused by the gradient term suppression are respectively 0.017, 0.13 and 0.16 dB/H for the three modes. The ratio of the attenuation rate obtained with the partial GTS method to that determined with the original LEE is also shown in Fig. 16(b). It is seen that the largest changes of attenuation rate occur for low Helmholtz numbers.

5.3. NASA GIT benchmark

The GTS method is now applied to the GIT benchmark problem [58], which is widely used for validation of aeroacoustic solvers of lined ducts under plane wave propagation. A number of numerical studies have reported the existence of an instability at 1 kHz for this problem [16,28,59]. The tube has a dimension of $0.8128 \times 0.0508 \times 0.0508$ m. The upper wall is lined with a ceramic tubular liner (CT57) with a length of 0.406 m. The sound pressure level (SPL) and phase of acoustic waves have been measured at various Mach numbers and for frequencies from 500 Hz to 3 kHz.

The source is installed ahead of the section $x = 0$ at a distance of 0.05 m. The mean velocity profile is given by Eq. (2), with a Mach number of 0.335 and a boundary layer thickness equal to 2 % of the duct height. A grid of 55 points is used along the z-direction, while the grid size along the x-direction is $\Delta x = 0.0011$ m. The time step has been set to 2×10^{-6} s. The broadband admittance of the liner (see. Eq. (6)) is obtained by a fit of the educed values provided by Jones et al. [58] for $M = 0.335$. In this case, two pairs of complex-conjugate poles are sufficient to have a good match from 500 Hz up to 3 kHz, as shown in Fig. 19. The coefficients of the obtained admittance model are given in Table 1.

Fig. 20 shows a series of successive snapshots of the pressure. The left and right columns correspond to the results without GTS ($\epsilon = 1$) and full GTS ($\epsilon = 0$), respectively. We focus first on the case without GTS. Once the incoming pulse encounters the liner leading edge, it splits into two wave fronts, a first one that is transmitted downstream and is progressively attenuated by the liner, and a second one that is reflected upstream. At the same time, the instability is generated at

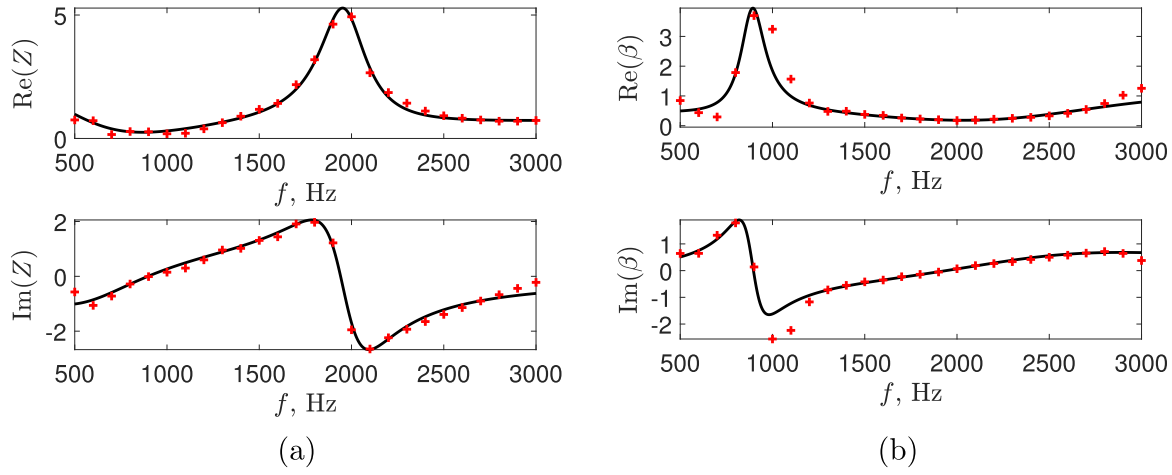

Fig. 19. (a) Impedance and (b) admittance of the CT57 liner: + NASA educed values and ——— fit obtained with the vector fitting algorithm.

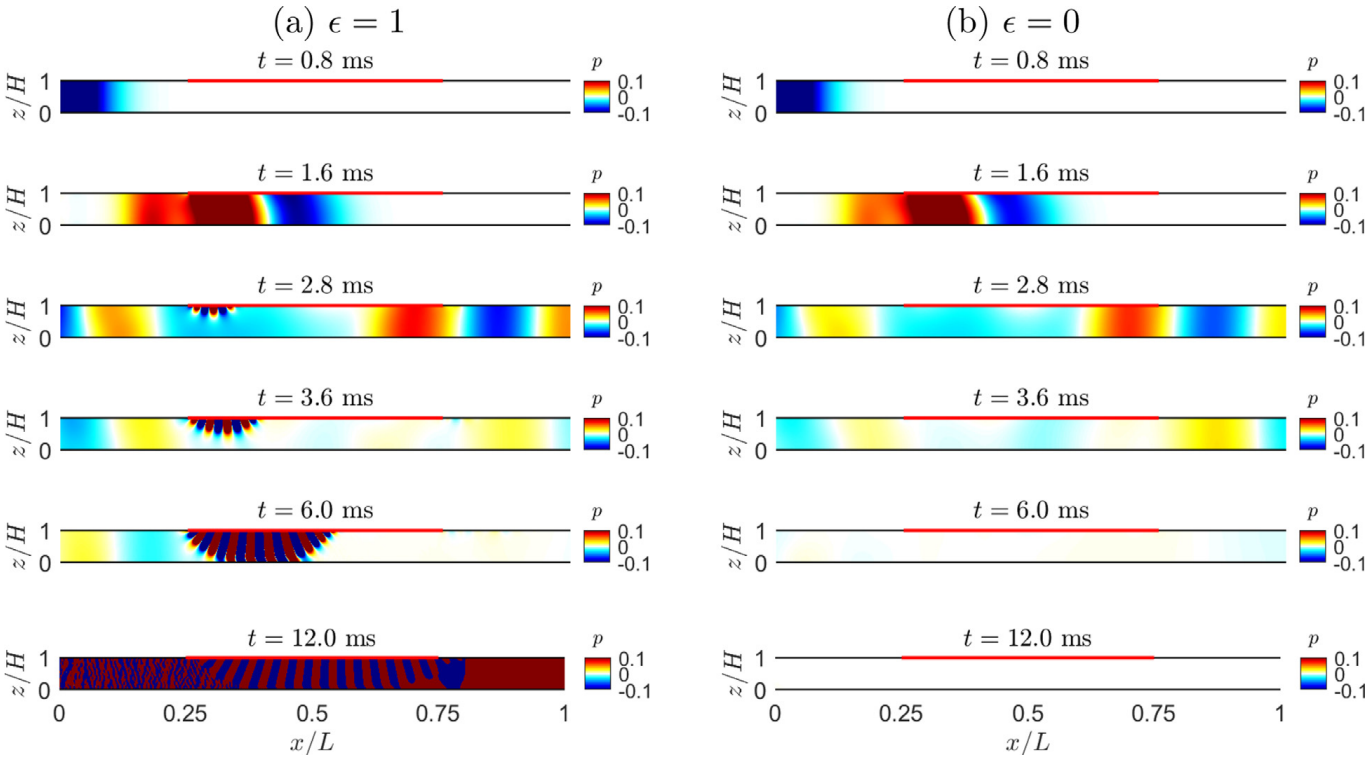

Fig. 20. Pressure map (Pa) along the duct at different times for (a) $\epsilon = 1$ and (b) $\epsilon = 0$.

the leading edge of the liner. Briefly afterwards, when most of the transmitted and reflected acoustic pulses have left the computational domain, the instability takes over in the entire lined section, leading to a divergent pressure field. In the case of full GTS, the same overall behavior is observed for the acoustic component. However, no instability is generated and the acoustic energy falls to zero at increasing times.

Even though the full GTS method shows encouraging results for suppressing instabilities, it should be applied carefully. Indeed, it may not be always physically valid to ignore the instability. Alomar et al. [9] showed experimentally a feedback mechanism between the instability and the acoustic waves for a liner of finite length. The instabilities generated at the leading edge of the liner are scattered into acoustic waves at the trailing edge; these acoustic waves propagate upstream and trigger another instabilities once they are scattered at the leading edge. This feedback mechanism can not be reproduced when the full GTS method is employed.

The time series of the pressure at three virtual microphones located on the rigid wall, at different axial locations, are shown in Fig. 21 for several values of ϵ. The successive appearance of the initial acoustic pulse and the instability is observed at all three locations. The impact of ϵ is mainly on the instability component: decreasing values of ϵ induces a delay in the emergence of the instability. This is the expected behavior, as decreasing ϵ causes a decrease of the amplification of the unstable mode, and thus it takes more time for the instability to leverage the acoustic pressure levels. For $\epsilon = 0.3$ and 0, no instability appears within the simulation time.

In order to obtain the frequency spectrum of the pressure field, a tapered cosine window is applied to the pressure signals to discard the instability component, as shown in Fig. 22. The Fourier transform of the filtered signals is then computed. Note that for the cases for which the partial GTS method induces a delay in the appearance of the instability, the window could have be chosen longer; moreover, for the cases for which the partial GTS allows a suppression of the instability, the window is not necessary. However, for consistency, the same window is applied on all the pressure signals and for all the cases considered.

The resulting SPL and phase of the acoustic pressure along the duct wall opposite to the liner are shown in Fig. 23, at different frequencies and for different values of ϵ. For comparison with the NASA measurements, the curves are adjusted

Table 1
Coefficients of the rational function for the normalized broadband admittance model of CT57.

	α_i	β_i	B_i	C_i	Y_∞
$i = 1$	6135	−14886	−4584	3729	1.16
$i = 2$	507	5577	1788	−290	

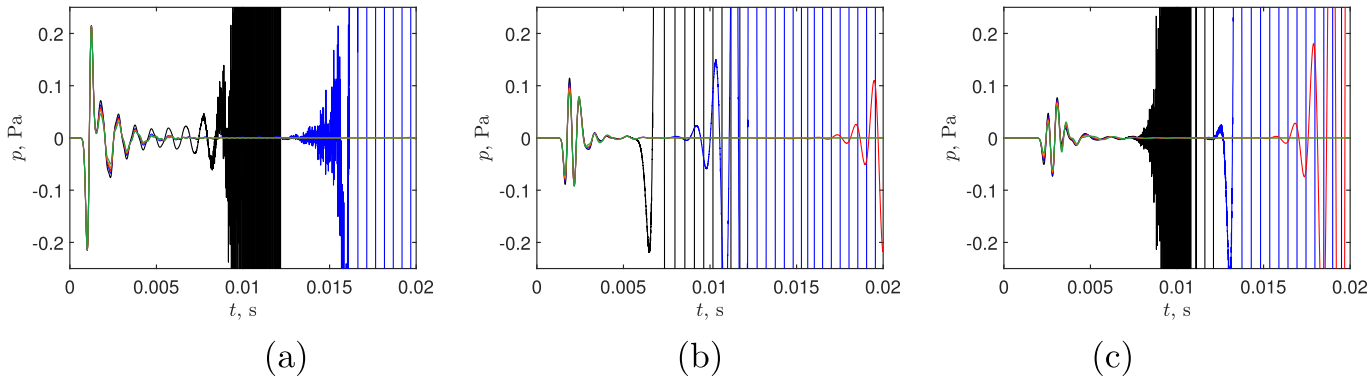

Fig. 21. Time series of pressure on the rigid wall at (a) $x = 0.12L$, (b) $x = 0.5L$ and (c) $x = 0.86L$ for: $\epsilon = 1$, $\epsilon = 0.7$, $\epsilon = 0.5$, $\epsilon = 0.3$ and $\epsilon = 0$.

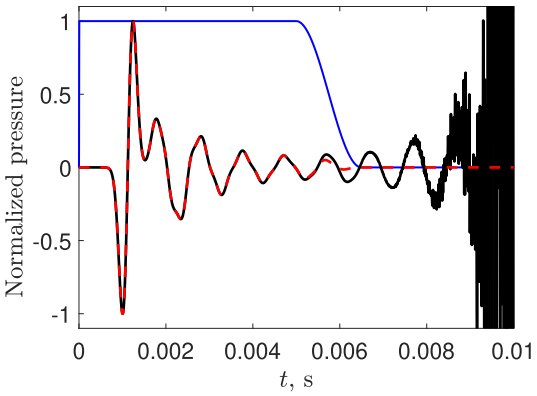

Fig. 22. Window function used for signal processing and example of (normalized) pressure signal at $x = 0.12L$ before and after windowing.

so that the SPL and the phase are 130 dB and 0°, respectively, at $x = 0$. Without GTS ($\epsilon = 1$), some oscillations on the SPL and on the phase are observed at 500, 1000 and 1500 Hz in the lined section. These are due to the difficulty in isolating the acoustic contribution by simple windowing. Indeed, as seen in Fig. 21(a) and (b), there is an overlap near $t = 0.005$ s between the acoustic pulse and the instability. An obvious deviation between the simulations and the experimental results is noticed at 3 kHz. One of the reasons is that the window function applied for calculating the Fourier transform does not account for the full acoustic signal. It can also be partly explained by the proximity of the cut-off frequency of the rigid duct, which induced a significant error in the impedance eduction of the liner in the GIT experiment. Overall, the trends of both the SPL and the phase are insensitive to ϵ. Decreasing ϵ tends to underestimate the pressure levels, especially downstream of the liner. The largest discrepancies are observed at $f = 1$ and 3 kHz. For the other frequencies, the SPL predictions are within a few dBs from the measured values.

To assess the effectiveness of the GTS, another quantity of interest, namely the insertion loss (IL), is considered. It is defined as the difference in acoustic power at the exit section $x = L$ with and without liner. Details on the calculation of the acoustic power from the time-domain numerical solution can be found in Troian et al. [50]. Fig. 24 shows the frequency variations of IL calculated for different values of ϵ, as well as estimated from the NASA measurements. A peak is observed close to the liner resonance (1.1 kHz) for $\epsilon = 1$ and 0.7, in good agreement with the experimental values. The impact of ϵ on the IL is weak except in the immediate vicinity of the resonance and also for $f > 2.5$ kHz. Note that even if a significant increase of IL is observed for $f > 2.5$ kHz when decreasing ϵ, a good match is achieved for $\epsilon = 0.5$. Figs. 21 and 23 show that, for this particular case, $\epsilon = 0.5$ seems to be the optimal value ensuring a good compromise between a stable simulation and an accurate prediction. However, this is not a general conclusion, as the optimal value of ϵ may depend on the flow profile, the Mach number and the liner, among others, and may thus be different from case to case.

The NASA GIT benchmark deals with small Helmholtz numbers ($\omega \leq 2.8$). To examine the performance of the partial GTS method for high Helmholtz numbers, an additional set of time-domain simulations are conducted for a duct whose height $H = 0.508$ m is 10 times larger than the one of the NASA GIT duct. The lengths of the duct and of the liner are also increased, with respective values of 4.06 m and 2.03 m. The boundary layer thickness of the mean flow remains equal to 2 % of the duct height. The numerical parameters are the same as before except the number of grid points along the z-direction, set to $n_z = 175$.

The time series of the pressure at $x = 0.5L$ on the rigid wall of the large duct are presented for several values of ϵ in Fig. 25. Compared with the waveforms for the smaller duct in Fig. 21, the signals are more complex because of the

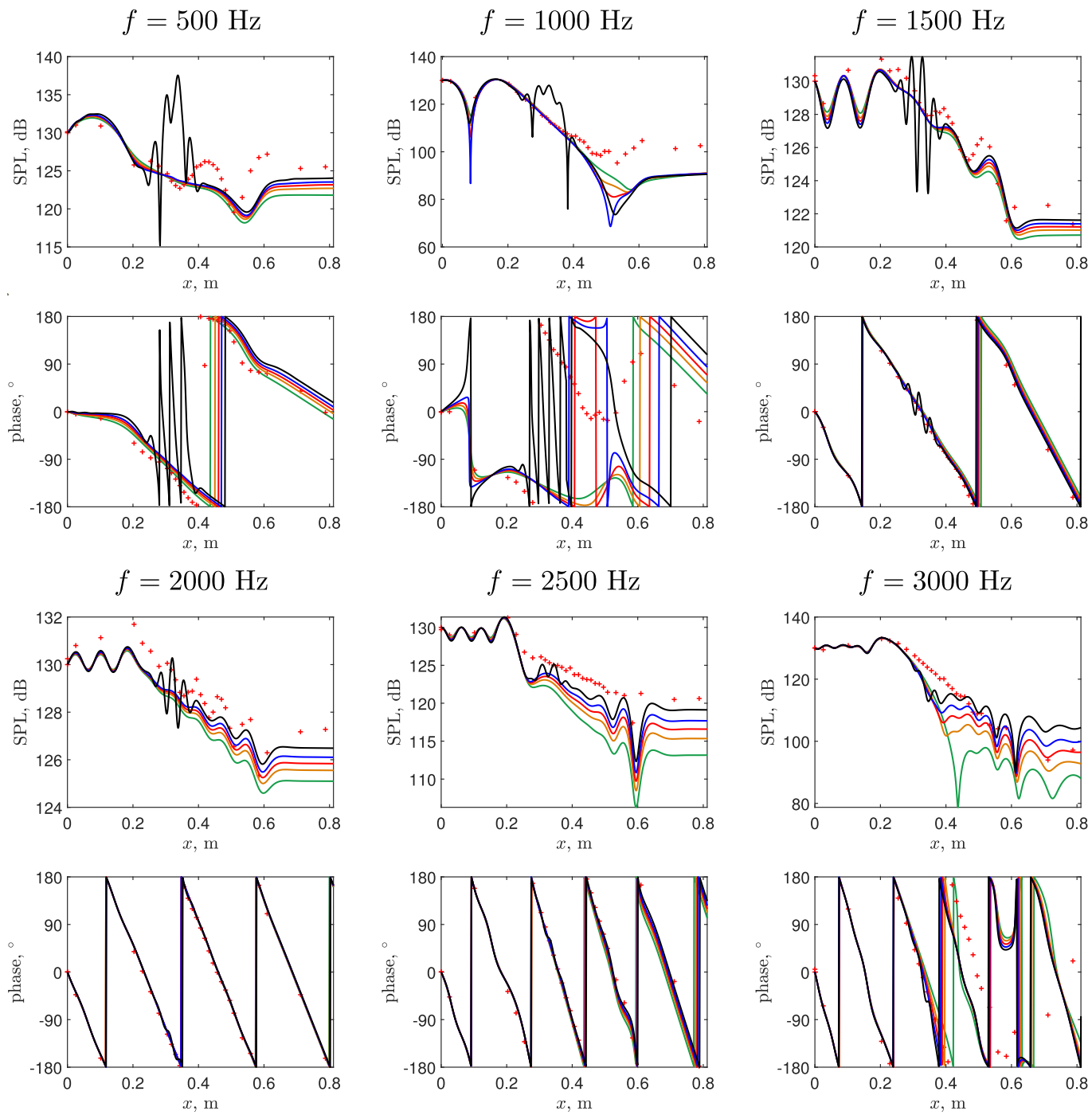

Fig. 23. SPL and phase of the acoustic pressure along the duct for $M = 0.335$ and for different values of ϵ: $\epsilon = 1$, $\epsilon = 0.7$, $\epsilon = 0.5$, $\epsilon = 0.3$, $\epsilon = 0$, NASA experiments.

multimodal propagation. Instabilities are only observed for $\epsilon = 1$ and do not appear when the partial GTS method is applied. A view on the pressure response for 0.004 s $< t <$ 0.01 s is shown in Fig. 25(b). The signals for the several values of ϵ are almost superimposed even if the amplitude of the waveform is slightly reduced as ϵ decreases.

The SPL and phase along the large duct on the wall opposite to the liner are provided for three frequencies and for several values of ϵ in Fig. 26. A window function, shown in Fig. 25(a) is also applied to avoid the influence of instabilities and is wider than the one shown in Fig. 22. Compared with the results for the NASA GIT duct shown in Fig. 23, the differences due to the suppression of the gradient term are relatively small.

Finally, the powers W at the exit plane $x = L$ are compared for several values of ϵ and for both ducts. Fig. 27 shows the power difference ΔW, which is defined as $\Delta W = 10 \log_{10}[W(\epsilon)/W(\epsilon = 1)]$, where $W(\epsilon)$ is the power when the partial GTS method is applied and $W(\epsilon = 1)$ is the power calculated from the original LEE solution. For the NASA GIT case, ΔW has a large peak near $f = 1.1$ kHz due to the suppression of the instability and has largest variations near $f = 3$ kHz. For the

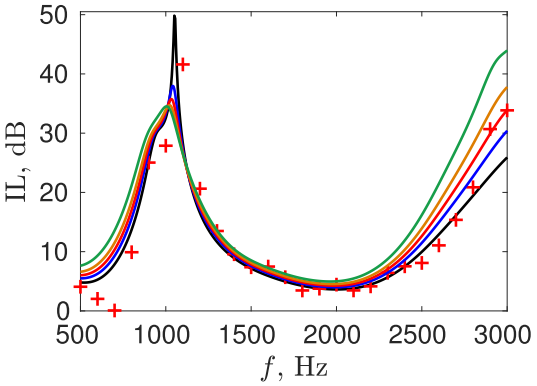

Fig. 24. Insertion loss for $M = 0.335$ and for: $\epsilon = 1$, $\epsilon = 0.7$, $\epsilon = 0.5$, $\epsilon = 0.3$, $\epsilon = 0$, + NASA experiments.

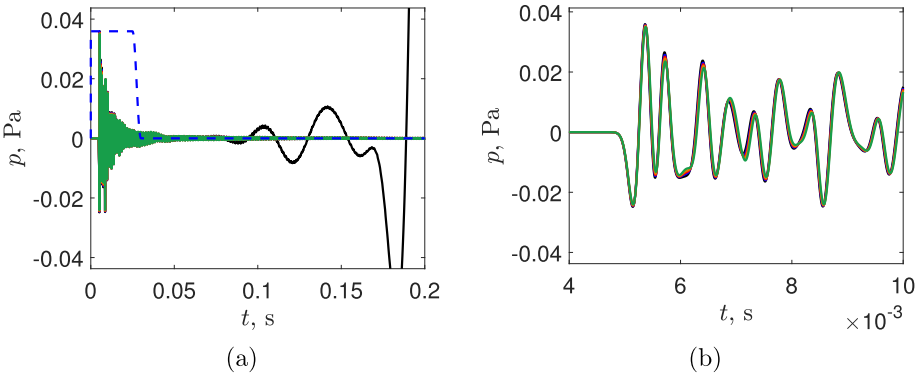

Fig. 25. (a) Time series of pressure on the rigid wall of the large duct at $x = 0.5\,L$ and (b) view for 0.004 s $\leq t \leq$ 0.01 s for $\epsilon = 1$, $\epsilon = 0.7$, $\epsilon = 0.5$, $\epsilon = 0.3$ and $\epsilon = 0$. The dashed line shows the shape of the window function used in signal processing.

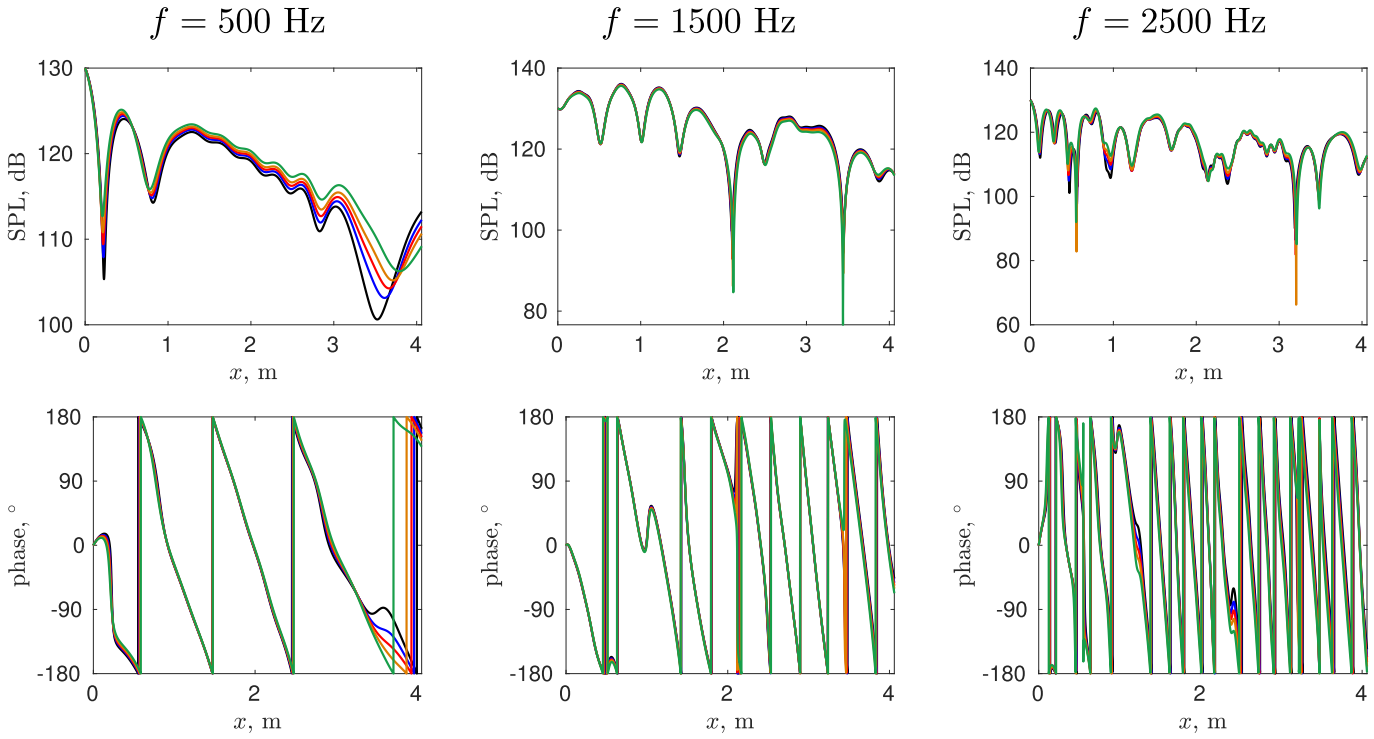

Fig. 26. SPL and phase of the acoustic pressure along the large cross-section duct for $M = 0.335$ and for different values of ϵ: $\epsilon = 1$, $\epsilon = 0.7$, $\epsilon = 0.5$, $\epsilon = 0.3$, $\epsilon = 0$.

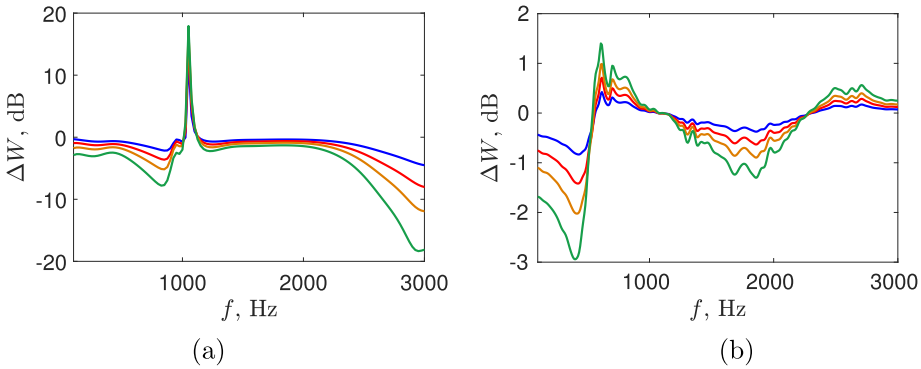

Fig. 27. Power difference $W(\epsilon)/W(\epsilon = 1)$ as a function of the frequency (a) for the NASA GIT duct and (b) for the large duct and for different values of ϵ: $\epsilon = 0.7$, $\epsilon = 0.5$, $\epsilon = 0.3$, $\epsilon = 0$.

large duct, ΔW takes much smaller values. Over the entire frequency band of interest, it is smaller than 3 dB for the full GTS method and than 1 dB for the partial GTS method and for $\epsilon = 0.7$. The results shown in this section confirm that the partial GTS method noticeably impacts the acoustic propagation for low Helmholtz numbers but should be acceptable for large Helmholtz numbers.

6. Conclusion

An analysis of the partial GTS method for suppressing hydrodynamic instabilities in a lined flow duct has been performed. The case of a convective instability generated in a lined flow duct was first illustrated. The instability was calculated by solving the linearized Euler equations with a finite-difference time-domain approach. The characteristics of the instability were compared with the predictions of modal analysis. It was shown that both methods indicate that the instability is convective. Perfect matches of wavenumber and mode shapes were also obtained. The effect of the grid resolution and selective filter, which have been reported in the literature to have a significant impact on the instabilities, was investigated. It turns out that very fine grids, compared with what is required for acoustic waves, are needed for precisely calculating the instability.

The partial GTS method for suppressing the instability was then assessed. The impact of diminishing the mean flow gradient term on the modes has been investigated. The unstable mode turns to be highly sensitive to the mean flow gradient term. The acoustic modes are also greatly altered for small Helmholtz numbers, but are less affected for high Helmholtz numbers. The partial GTS method was finally applied on the NASA GIT benchmark. The effectiveness of this method has been shown for removing the instabilities in time-domain simulations. The SPL was however underestimated by several dBs for certain frequencies. In particular, a total suppression of the mean flow gradient term seems too severe to accurately predict sound propagation in a lined flow duct, while a partial suppression of this term seems to provide an acceptable prediction, especially in the high frequency range.

In addition, even if removing instabilities allows for a stable numerical calculation, it may be, in particular cases, not physically valid: as an example, the feedback mechanism between the instability and acoustic waves for a liner of finite length discussed in Alomar and Aurégan [9] could not be reproduced when the instability is suppressed.

Future works can be conducted to study an absolute instability in the time-domain approach. Since the effectiveness of the partial GTS method has been proved, other techniques proposed for dealing with shear instabilities [40–44] can also be considered.

Declaration of Competing Interest

The authors declare that they have no known competing financial interests or personal relationships that could have appeared to influence the work reported in this paper.

CRediT authorship contribution statement

Yuanyuan Deng: Investigation, Writing - original draft, Formal analysis, Validation. **Antoni Alomar:** Conceptualization, Writing - review & editing. **Didier Dragna:** Conceptualization, Methodology, Writing - review & editing. **Marie-Annick Galland:** Supervision, Project administration.

Acknowledgments

Y. Deng is sponsored by China Scholarship Council as a Ph.D. student in Ecole Centrale de Lyon. This work was performed within the framework of the Labex CeLyA of the Université de Lyon, within the programme “Investissements d’Avenir” (ANR-

10-LABX-0060/ANR-16-IDEX-0005) operated by the French National Research Agency (ANR). The authors would like to thank Dr. Michael Jones (NASA) for providing the data for the NASA GIT benchmark.

Appendix A. Matrices of the discretized eigenvalue problem

This appendix details the discretization of the eigenvalue problem to obtain the mode wavenumber and mode shapes. The number of grid points is denoted by N. Eq. (11) could be rewritten as: $\mathbf{AX} = \frac{k}{\omega}\mathbf{BX}$ with $\mathbf{X}$ being the column vector of unknowns at the grid points:

$$\mathbf{X} = [U(z_1)\cdots U(z_N)\ \ (P-V)(z_1)\cdots(P-V)(z_N)\ \ (P+V)(z_1)\cdots(P+V)(z_N)]^T \tag{A.1}$$

where $(z_i)_{1\le i\le N}$, with $z_1 = 0$ and $z_N = 1$, are the grid points. At the boundary points, the variables should satisfy both the LEE equations and the boundary conditions. To avoid having an over-constrained system, some information must be discarded. The use of characteristic variables allows one to make a suitable choice. Thus, at $z = 0$, the incident wave on the boundary is $P - V$ and the reflected wave is $P + V$. Therefore, $P + V$ is determined with the boundary condition and not from the LEE. Similarly, at $z = 1$, the incident and reflected wave are $P + V$ and $P - V$, respectively and, hence, $P - V$ is determined with the boundary condition.

Bringing the LEE equations and the boundary conditions together lead to the $3N \times 3N$ matrices:

$$\boldsymbol{A} = \left[\begin{array}{c|c|c} \boldsymbol{I}_{(1:N),(1:N)} & -\frac{\epsilon}{2i\omega}(\boldsymbol{D}\boldsymbol{U}_0)_{(1:N),(1:N)} & \frac{\epsilon}{2i\omega}(\boldsymbol{D}\boldsymbol{U}_0)_{(1:N),(1:N)} \\ \hline \mathbf{0}_{N,N} & \left(\boldsymbol{I} - \frac{1}{i\omega}\boldsymbol{D}\right)_{(1:N-1),(1:N)} & \mathbf{0}_{N-1,N} \\ & 0\ \ \ldots\ \ 0\ \ -1-\beta & 0\ \ \ldots\ \ 0\ \ 1-\beta \\ \hline \mathbf{0}_{N,N} & 1\ \ 0\ \ \ldots\ \ 0 & -1\ \ 0\ \ \ldots\ \ 0 \\ & \mathbf{0}_{N-1,N} & \left(\boldsymbol{I} + \frac{1}{i\omega}\boldsymbol{D}\right)_{(2:N),(1:N)} \end{array}\right] \tag{A.2}$$

$$\boldsymbol{B} = \left[\begin{array}{c|c|c} \boldsymbol{U}_{0(1:N),(1:N)} & \frac{1}{2}\boldsymbol{I}_{(1:N),(1:N)} & \frac{1}{2}\boldsymbol{I}_{(1:N),(1:N)} \\ \hline \boldsymbol{I}_{(1:N-1,N)} & \boldsymbol{U}_{0(1:N-1),(1:N)} & \mathbf{0}_{N,N} \\ \hline \mathbf{0}_{1,N} & \mathbf{0}_{1,N} & \\ \hline \mathbf{0}_{1,N} & \mathbf{0}_{N,N} & \mathbf{0}_{1,N} \\ \hline \boldsymbol{I}_{(2:N,N)} & & \boldsymbol{U}_{0(2:N),(1:N)} \end{array}\right] \tag{A.3}$$

where $\mathbf{0}_{I,J}$ is the zero matrix with I rows and J columns and $\mathbf{D}$ and $\mathbf{I}$ are the differentiation and identity matrix, respectively, both square matrices of size N. The matrix $\mathbf{U_0}$ is a diagonal matrix of size N with diagonal elements $\mathbf{U_0}_{i,i} = u_0(z_i)$. In addition, the notation $\mathbf{M}_{(I:J),(K:L)}$ indicates the submatrix of $\mathbf{M}$ formed by rows I to J and columns K to L. Finally, the parameter ϵ in matrix $\mathbf{A}$ controls the mean flow gradient term and is equal to $\epsilon = 1$ for the LEE equations and to $\epsilon = 0$ for the full GTS method.

Appendix B. Comparison of the instability characteristics for another frequency

In this appendix, the comparison of the instability characteristics determined from the time-domain numerical solution with those predicted by the modal analysis approach, done in Section 3 for $\omega = 0.9271$, is performed for another frequency, namely $\omega = 0.4636$. The objective is to confirm the viability of the time-domain method in simulating the instability.

Fig. B1 displays the wavenumbers of the modes determined by modal analysis for $\omega = 0.4636$. The reference result $\omega = 0.9271$ is also indicated. Note that the MSD liner model is still used and the liner impedance at these two frequencies is different. The wavenumbers of the acoustic propagating mode ($k = 0.79 - 0.33\mathrm{i}$) and the unstable mode ($k_{\mathrm{HI}} = 2.57 + 1.31\mathrm{i}$) show the most evident change. Compared with $\omega = 0.9271$, the spatial growth rate of the unstable mode decreases only slightly. On the other hand, the wavelength becomes three times longer. Fig. B2 shows the evolution of $\arg(p)$ and $\ln|p|$ along the lined wall for $\omega = 0.4636$ obtained from the time-domain solution at $t = 90$ and predicted with the analytical solution in Eq. (14), where the value of k_{HI} obtained from modal analysis has been used. Here again, an excellent match is observed.

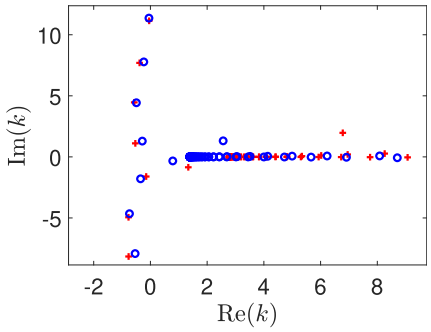

Fig. B1. Wavenumber obtained by modal analysis for ○ $\omega = 0.4636$ and + $\omega = 0.9271$.

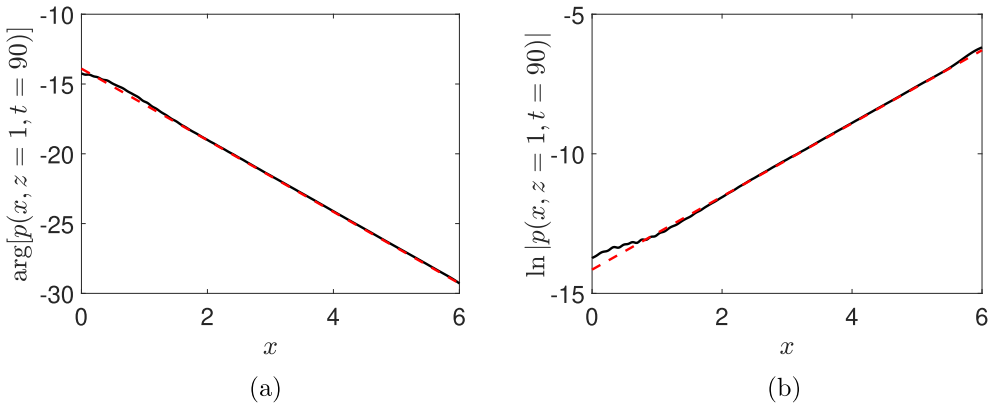

Fig. B2. Comparison of (a) the phase and (b) amplitude of the pressure on the lined wall for $\omega = 0.4636$ from the time-domain solution at $t = 90$ ——— and from the analytical solution ———.

Supplementary material

Supplementary material associated with this article can be found, in the online version, at doi:10.1016/j.jsv.2021.115999.

References

[1] Y. Özyörük, L.N. Long, M.G. Jones, Time-domain numerical simulation of a flow-impedance tube, J. Comput. Phys. 146 (1) (1998) 29–57.
[2] H. Ju, K.-Y. Fung, Time-domain impedance boundary conditions with mean flow effects, AIAA J. 39 (9) (2001) 1683–1690.
[3] C. Richter, F.H. Thiele, X.D. Li, M. Zhuang, Comparison of time-domain impedance boundary conditions for lined duct flows, AIAA J. 45 (6) (2007) 1333–1345.
[4] E. Meyer, F. Mechel, G. Kurtze, Experiments on the influence of flow on sound attenuation in absorbing ducts, J. Acoust. Soc. Am. 30 (3) (1958) 165–174.
[5] M. Brandes, D. Ronneberger, Sound amplification in flow ducts lined with a periodic sequence of resonators, 1995, pp. 893–901. Munich, Germany
[6] Y. Aurégan, M. Leroux, Experimental evidence of an instability over an impedance wall in a duct with flow, J. Sound Vib. 317 (3-5) (2008) 432–439.
[7] Y. Aurégan, D. Kumar Singh, Experimental observation of a hydrodynamic mode in a flow duct with a porous material, J. Acoust. Soc. Am. 136 (2) (2014) 567–572.
[8] D. Marx, Y. Aurégan, H. Bailliet, J.-C. Valiére, PIV and LDV evidence of hydrodynamic instability over a liner in a duct with flow, J. Sound Vib. 329 (18) (2010) 3798–3812.
[9] A. Alomar, Y. Aurégan, Particle image velocimetry measurement of an instability wave over a porous wall in a duct with flow, J. Sound Vib. 386 (2017) 208–224.
[10] U. Ingard, Influence of fluid motion past a plane boundary on sound reflection, absorption, and transmission, J. Acoust. Soc. Am. 31 (7) (1959) 1035–1036.
[11] M. Myers, On the acoustic boundary condition in the presence of flow, J. Sound Vib. 71 (3) (1980) 429–434.
[12] B.J. Tester, The propagation and attenuation of sound in lined ducts containing uniform or “plug” flow, J. Sound Vib. 28 (2) (1973) 151–203.
[13] C.K. Tam, L. Auriault, Time-domain impedance boundary conditions for computational aeroacoustics, AIAA J. 34 (5) (1996) 917–923.
[14] S.W. Rienstra, A classification of duct modes based on surface waves, Wave Motion. 37 (2) (2003) 119–135.
[15] S.W. Rienstra, B.J. Tester, An analytic Green’s function for a lined circular duct containing uniform mean flow, J. Sound Vib. 317 (3-5) (2008) 994–1016.
[16] X.D. Li, C. Richter, F. Thiele, Time-domain impedance boundary conditions for surfaces with subsonic mean flows, J. Acoust. Soc. Am. 119 (5) (2006) 2665–2676.
[17] E.J. Brambley, Fundamental problems with the model of uniform flow over acoustic linings, J. Sound Vib. 322 (4-5) (2009) 1026–1037.
[18] E.J. Brambley, Well posed boundary condition for acoustic liners in straight ducts with flow, AIAA J. 49 (6) (2011) 1272–1282.
[19] S. Rienstra, G. Vilenski, Spatial instability of boundary layer along impedance wall, in: 14th AIAA/CEAS Aeroacoustics Conference, AIAA Paper 2008-2932, Vancouver, BC, Canada, 2008, pp. 1–13.
[20] Y. Renou, Y. Aurégan, Failure of the Ingard-Myers boundary condition for a lined duct: an experimental investigation, J. Acoust. Soc. Am. 130 (1) (2011) 52–60.
[21] S. Rienstra, Impedance models in time domain, including the extended Helmholtz resonator model, in: 12th AIAA/CEAS Aeroacoustics Conference, AIAA Paper 2006-2686, Cambridge, MA, USA, 2006.
[22] S.W. Rienstra, M. Darau, Boundary-layer thickness effects of the hydrodynamic instability along an impedance wall, J. Fluid Mech. 671 (2011) 559–573.
[23] G. Boyer, E. Piot, J.-P. Brazier, Theoretical investigation of hydrodynamic surface mode in a lined duct with sheared flow and comparison with experiment, J. Sound Vib. 330 (8) (2011) 1793–1809.
[24] D. Marx, A piecewise linear mean flow model for studying stability in a lined channel, J. Sound Vib. 331 (16) (2012) 3809–3823.
[25] D. Marx, Numerical computation of a lined duct instability using the linearized Euler equations, AIAA J. 53 (8) (2015) 2379–2388.
[26] L. Pascal, E. Piot, G. Casalis, Global linear stability analysis of flow in a lined duct, J. Sound Vib. 410 (2017) 19–34.
[27] G. Gabard, E. Brambley, A full discrete dispersion analysis of time-domain simulations of acoustic liners with flow, J. Comput. Phys. 273 (2014) 310–326.
[28] Y. Deng, D. Dragna, M.-A. Galland, A. Alomar, Comparison of three numerical methods for acoustic propagation in a lined duct with flow, in: 25th AIAA/CEAS Aeroacoustics Conference, AIAA Paper 2019-2658, Delft, The Netherlands, 2019, pp. 1–15.
[29] D. Khamis, E.J. Brambley, Viscous effects on the acoustics and stability of a shear layer over an impedance wall, J. Fluid Mech. 810 (2017) 489–534.
[30] D. Marx, Y. Aurégan, Effect of turbulent eddy viscosity on the unstable surface mode above an acoustic liner, J. Sound Vib. 332 (15) (2013) 3803–3820.
[31] J. Rodríguezánchez, Étude théorique et numérique des modes propres acoustiques dans un conduit avec é coulement et parois absorbantes, Toulouse, ISAE, 2016 PhD thesis.
[32] B. Xin, D. Sun, X. Jing, X. Sun, Numerical study of acoustic instability in a partly lined flow duct using the full linearized Navier-Stokes equations, J. Sound Vib. 373 (2016) 132–146.
[33] R. Sebastian, D. Marx, V. Fortuné, Numerical simulation of a turbulent channel flow with an acoustic liner, J. Sound Vib. 456 (2019) 306–330.
[34] E. Brambley, G. Gabard, Time-domain implementation of an impedance boundary condition with boundary layer correction, J. Comput. Phys. 321 (2016) 755–775.
[35] C. Bogey, C. Bailly, D. Juvé, Computation of flow noise using source terms in linearized Euler’s equations, AIAA J. 40 (2) (2002) 235–243.

[36] C. Richter, H. Lueck, L. Panek, F. Thiele, Methods for suppressing shear layer instabilities for CAA, J. Comput. Acoust. 19 (02) (2011) 181–203.
[37] Y. Özyörük, B.J. Tester, Application of frequency-domain linearized Euler solutions to the prediction of aft fan tones and comparison with experimental measurements on model scale turbofan exhaust nozzles, J. Sound Vib. 330 (16) (2011) 3846–3858.
[38] A. Iob, R. Arina, C. Schipani, Frequency-domain linearized Euler model for turbomachinery noise radiation through engine exhaust, AIAA J. 48 (4) (2010) 848–858.
[39] X. Li, C. Schemel, U. Michel, F. Thiele, Azimuthal sound mode propagation in axisymmetric flow ducts, AIAA J. 42 (10) (2004) 2019–2027.
[40] R. Ewert, W. Schröder, Acoustic perturbation equations based on flow decomposition via source filtering, J. Comput. Phys. 188 (2) (2003) 365–398.
[41] J.-H. Seo, Y.J. Moon, Perturbed compressible equations for aeroacoustic noise prediction at low Mach numbers, AIAA J. 43 (8) (2005) 1716–1724.
[42] J.H. Seo, Y.J. Moon, Linearized perturbed compressible equations for low Mach number aeroacoustics, J. Comput. Phys. 218 (2) (2006) 702–719.
[43] X. Zhang, X. Chen, J. Gill, Gradient term filtering for stable sound propagation with linearized Euler equations, in: 20th AIAA/CEAS Aeroacoustics Conference, AIAA Paper 2014-3306, Atlanta, GA, 2014, pp. 1–14.
[44] Y. Sun, R. Fattah, S. Zhong, X. Zhang, Stable time-domain CAA simulations with linearised governing equations, Comput. Fluids. 167 (2018) 187–195.
[45] C. Bogey, C. Bailly, A family of low dispersive and low dissipative explicit schemes for flow and noise computations, J. Comput. Phys. 194 (1) (2004) 194–214.
[46] J. Berland, C. Bogey, O. Marsden, C. Bailly, High-order, low dispersive and low dissipative explicit schemes for multiple-scale and boundary problems, J. Comput. Phys. 224 (2) (2007) 637–662.
[47] J. Berland, C. Bogey, C. Bailly, Low-dissipation and low-dispersion fourth-order Runge Kutta algorithm, Comput. Fluids. 35 (10) (2006) 1459–1463.
[48] C. Bogey, N. de Cacqueray, C. Bailly, A shock-capturing methodology based on adaptative spatial filtering for high-order non-linear computations, J. Comput. Phys. 228 (5) (2009) 1447–1465.
[49] C. Bogey, C. Bailly, Three-dimensional non-reflective boundary conditions for acoustic simulations: far field formulation and validation test cases, Acta Acust. united Ac. 88 (2002) 463–471.
[50] R. Troian, D. Dragna, C. Bailly, M.-A. Galland, Broadband liner impedance eduction for multimodal acoustic propagation in the presence of a mean flow, J. Sound Vib. 392 (2017) 200–216.
[51] B. Gustavsen, A. Semlyen, Rational approximation of frequency domain responses by vector fitting, IEEE Trans. Power Deliv. 14 (3) (1999) 1052–1061.
[52] L.N. Trefethen, Spectral Methods in MATLAB, vol. 10, Siam, 2000.
[53] E.J. Brambley, M. Darau, S.W. Rienstra, The critical layer in linear-shear boundary layers over acoustic linings, J. Fluid Mech. 710 (2012) 545–568.
[54] G.G. Vilenski, S.W. Rienstra, Numerical study of acoustic modes in ducted shear flow, J. Sound Vib. 307 (3-5) (2007) 610–626.
[55] R. Briggs, Electron-Stream interaction with Plasmas, MIT Press, Cambridge, 1964.
[56] P. Huerre, P.A. Monkewitz, Local and global instabilities in spatially developing flows, Annu. Rev. Fluid Mech. 22 (1) (1990) 473–537.
[57] E.J. Brambley, N. Peake, Classification of aeroacoustically relevant surface modes in cylindrical lined ducts, Wave Motion. 43 (4) (2006) 301–310.
[58] M. Jones, W. Watson, T. Parrott, Benchmark data for evaluation of aeroacoustic propagation codes with grazing flow, in: 11th AIAA/CEAS Aeroacoustics Conference, AIAA Paper 2005-2853, Monterey, CA, USA, 2005, pp. 1–18.
[59] M.O. Burak, M. Billson, L.-E. Eriksson, S. Baralon, Validation of a time- and frequency-domain grazing flow acoustic liner model, AIAA J. 47 (8) (2009) 1841–1848.

Journal of Sound and Vibration 528 (2022) 116892

Contents lists available at ScienceDirect

Journal of Sound and Vibration

journal homepage: www.elsevier.com/locate/jsvi

Nonlinear broadband time-domain admittance boundary condition for duct acoustics. Application to perforated plate liners

Daher Diab *, Didier Dragna, Edouard Salze, Marie-Annick Galland

Univ Lyon, Ecole Centrale de Lyon, CNRS, Univ Claude Bernard Lyon 1, INSA Lyon, LMFA, UMR5509, 69130, Ecully, France

ARTICLE INFO

Keywords:
Nonlinear admittance
Perforated plate
Time-domain simulation
Time-domain admittance boundary condition
Spatially-varying admittance

ABSTRACT

The behavior of perforated plates at high excitation level is generally modeled by a surface impedance that depends on the rms velocity in the perforations. A time-domain admittance boundary condition (TDABC) is developed to account for this variation using a multipole model. Two formulations are considered, based on the interpolation either of the admittance or of the multipole coefficients from a data set of reference values. These TDABC are implemented in a finite-difference time-domain solver of the linearized Euler equations and are validated by comparison with experimental results on an impedance tube. Application to a two-dimensional lined duct corresponding to the reference geometry of the NASA Grazing Incidence Tube is then performed. The spatial variation of the perforated plate liner impedance is highlighted and it is shown that assuming a uniform impedance can lead to an unacceptable prediction of the liner attenuation. These results are confirmed both for a harmonic or broadband excitation.

1. Introduction

Acoustic liners are widely used for noise reduction in several industrial applications such as nacelles of aircraft engines, exhaust ducts or air ventilation systems. Among them, the perforated plate (PP) liner is probably the most employed, because of its simplicity, its efficiency and its applicability to extreme environmental conditions (temperature and pressure) where porous materials cannot be used. It is made of a perforated plate, mounted on a honeycomb cavity attached to the system frame. This liner behaves as a resonator. As such, PP liners provide a significant acoustic attenuation, but only near the resonant frequencies that depend mainly on the cavity depth.

Starting from Sivian [1], it has been noted that the perforated plate excited by an acoustic wave with a large amplitude exhibits a nonlinear behavior. More precisely, the measured acoustic impedance was shown to depend on the rms velocity in the perforation. This behavior is associated to the flow separation that occurs at the perforation edges for a sufficiently large amplitude of the velocity in the perforation. This induces generation of vortices and conversion of acoustic energy into vortical energy, which results in an increase of the plate resistance. Even for moderate SPL (around 110–120 dB), at which sound propagation remains a linear process, perforated plates can exhibit a nonlinear behavior. In ducted systems, such as engine nacelles, the sound pressure level (SPL) can be much higher. In such conditions, the nonlinear response of PP liners must be accounted for.

Detailed direct numerical simulations of the flow in a perforated liner excited by an acoustic wave with a large amplitude have been already performed [2,3]. Due to their high computational cost, they are however limited to simple configurations. For predicting the sound attenuation brought by a whole panel, it is more suitable to rely on numerical simulations in which the acoustic behavior of the perforated liner is modeled.

* Corresponding author.
E-mail addresses: daher.diab@ec-lyon.fr (D. Diab), didier.dragna@ec-lyon.fr (D. Dragna), edouard.salze@ec-lyon.fr (E. Salze), marie-annick.galland@ec-lyon.fr (M.-A. Galland).

https://doi.org/10.1016/j.jsv.2022.116892
Received 30 August 2021; Received in revised form 16 February 2022; Accepted 6 March 2022
Available online 14 March 2022

To do so, the most common approach is to employ a surface impedance model of the perforated plate liner, that includes nonlinear effects. It should be noted that the concept of surface impedance is strictly valid in the linear regime. It can be extended for a sinusoidal excitation in the nonlinear regime without difficulty, as long as the harmonic distortion remains limited. In the other cases, especially for a broadband excitation, the surface impedance in the nonlinear regime has to be used carefully. Several semi-empirical models for surface impedance of perforated plate liners [4–9] have been proposed. In most of them, based on measurements reported in the literature (among others Refs. [10,11]), the nonlinear correction consists in an increase of the resistance and a decrease of the orifice end correction, with the amplitude of the acoustic velocity in the orifice. Recently, Laly et al. [12] have extended in the nonlinear regime the model developed by Atalla and Sgard [13] based on an equivalent fluid approach to represent perforated panels: the resistivity and the tortuosity of the equivalent fluid depends on the geometrical properties of the perforated plate as well as the amplitude of the acoustic velocity in the perforation. An other approach proposed by Cummings [14] is to directly relate the pressure jump at the perforated plate and the velocity in the perforation through a nonlinear differential equation in the time-domain.

Nevertheless, there are few attempts to account for nonlinear models of PP liners in numerical simulations of sound propagation in lined ducts. One can refer to Eversman [15] or, more recently, to Roncen et al. [16], that use frequency-domain approaches to investigate the effect of nonlinearity on liner performance in a flow duct. While frequency-domain methods can still be used for a high-level harmonic excitation, time-domain methods are the natural approach to account for nonlinear effects. In the time-domain, the impedance boundary condition translates into a convolution, whose direct numerical evaluation is time-consuming [17]. A vast literature thus aimed at proposing time-domain impedance or admittance boundary conditions (TDIBC or TDABC) in the linear regime (e.g. [17–21]). Among the proposed approaches, TDIBC based on the multipole model has attracted lot of attention [19,22–24], as it can be used to represent surface impedance models of generic liners and as it allows for an efficient numerical implementation. In particular, Dragna et al. [25] and Troian et al. [24] proposed the auxiliary differential equation (ADE) method, in which the calculation of the convolution is reduced to the time integration of additional first-order partial differential equations. This is especially well-suited for high-order methods. Recently, Shur et al. [26] extended this TDIBC based on the multipole model in the nonlinear regime.

The objectives of the paper are to propose and evaluate formulations of the TDABC for the multipole model in the nonlinear regime and to exemplify sound propagation along a lined duct in high sound pressure environment. The impedance model proposed by Laly et al. [12] is used as the reference model for the perforated panel. Two approaches for the TDABC in the nonlinear regime are considered. In the first one, based on Shur et al. [26], the admittance is interpolated as a function of the rms velocity in the orifice. In the second one, the poles and coefficients of the multipole model are directly interpolated as a function of the rms velocity in the orifice. The two approaches are validated against a one-dimensional (1D) impedance tube configuration, first for numerical experiments and then for measurements performed for three perforated plates. Application to a two-dimensional (2D) lined duct is then performed. The evolution of the liner attenuation with the excitation level is studied. The spatial variation of the surface impedance along the liner is analyzed. Finally, it is investigated whether or not accounting for the spatial variations of the impedance is important for accurately predicting the liner attenuation.

This paper is organized as follows. Section 2 presents the acoustic impedance model of Laly et al. [12] for predicting the response of perforated panels at high level of excitation. In Section 3, the numerical model that solves the linearized Euler equations in the time-domain using finite difference techniques is described. The time domain admittance boundary condition based on the multipole model is first presented in the linear regime. The two extensions of the TDABC in the nonlinear regime are then introduced. The validation of the proposed approach is performed in Section 4. Application to a 2D lined duct is then investigated in Section 5. Concluding remarks are finally given in Section 6.

2. Impedance model of perforated plates in the nonlinear regime

Throughout the paper, the time-dependence convention $\mathrm{e}^{-\mathrm{j}\omega t}$ is used, where ω denotes the angular frequency, j the imaginary complex number ($\mathrm{j}^2 = -1$) and t the time. The air is characterized by its density ($\rho_0 = 1.211$ kg m^{-3}), its dynamic viscosity ($\eta = 1.84\times10^{-5}$ kg m^{-1} s^{-1}) and the corresponding sound speed ($c_0 = 340$ m s^{-1}). The geometry of the perforated plate is described by its thickness h, the perforation radius r and the percentage open area (POA) φ.

Atalla and Sgard [13] modeled the perforated panel in the linear regime by an equivalent fluid model following the Johnson-Allard approach [27]. The normalized acoustic impedance of a perforated panel backed by an air cavity of depth D is

$$Z_{\mathrm{L}} = \frac{-\mathrm{j}\omega\alpha_\infty h}{c_0\varphi}\left(1-\frac{\sigma\varphi}{\mathrm{j}\omega\rho_0\alpha_\infty}\sqrt{1-\frac{4\mathrm{j}\omega\rho_0\eta\alpha_\infty^2}{\varphi^2\sigma^2\Lambda^2}}\right)-\coth(\mathrm{j}k_0D), \tag{1}$$

where $k_0 = \omega/c_0$ is the wave number in air. The parameters of the equivalent fluid are related to the PP geometry. Thus, the viscous characteristic length Λ is equal to the perforation radius ($\Lambda = r$). The flow resistivity σ is given by $\sigma = \frac{8\eta}{\varphi r^2}$ in the case of cylindrical orifices. The tortuosity α_∞ is a function of the correction length ε, that accounts for sound radiation effects at the end of the perforations through $\alpha_\infty = 1+\frac{2\varepsilon}{h}$. The correction length is related to the POA and the radius of perforation. Following Laly et al. [12], it can be written:

$$\varepsilon = \Psi 0.48\sqrt{\pi r^2}\left[\sum_{n=0}^{8} a_n\left(\sqrt{\varphi}\right)^n\right], \tag{2}$$

Table 1
Geometric parameters of the PPs absorber.

	PP#1	PP#2	PP#3
Plate thickness (mm)	1	1	1
Perforation radius (mm)	0.25	0.25	1
Perforation ratio (%)	1.5	1	1.5

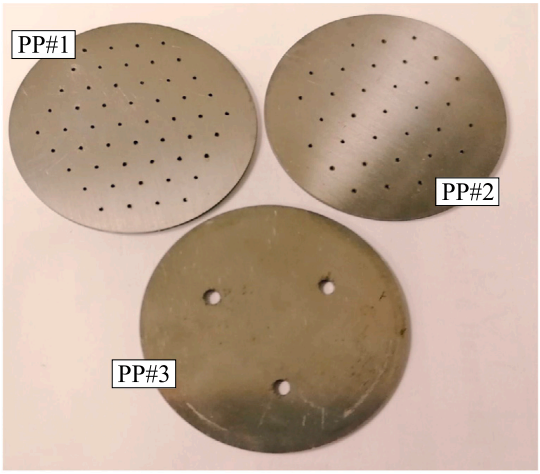

Fig. 1. Photo of the three perforated plates considered.

where $0.48\sqrt{\pi r^2}$ is the correction length for a single circular orifice, the sum over the coefficients a_n is an approximation of the Fok function that accounts for orifice interaction effects [11] and Ψ is a constant. The coefficients a_n are given by $a_0 = 1$, $a_1 = -1.4092$, $a_2 = 0$, $a_3 = 0.33818$, $a_4 = 0$, $a_5 = 0.06793$, $a_6 = -0.02287$, $a_7 = 0.003015$ and $a_8 = -0.01614$ [11] and Ψ is set to 4/3. Note that the Fok function and the empirical constant Ψ are not present in the original model proposed by Atalla and Sgard [13], but are introduced here for coherence with the nonlinear model.

Laly et al. [12] proposed an extension of the model in Eq. (1) to characterize the acoustic response of perforated plates in the nonlinear regime. The impedance model of a PP backed by an air layer has the same form as in the linear regime:

$$Z_{\mathrm{NL}} = \frac{-\mathrm{j}\omega h}{c_0 \varphi} \alpha_{\infty\,\mathrm{NL}} \left(1 - \frac{\sigma_{\mathrm{NL}} \varphi}{\mathrm{j}\omega \rho_0 \alpha_{\infty\,\mathrm{NL}}} \sqrt{1 - \frac{4\mathrm{j}\omega \rho_0 \eta \alpha_{\infty\,\mathrm{NL}}^2}{\varphi^2 \sigma_{\mathrm{NL}}^2 \Lambda^2}} \right) - \coth(\mathrm{j}k_0 D), \tag{3}$$

except that the flow resistivity σ_{NL} and the tortuosity $\alpha_{\infty\,\mathrm{NL}}$ now depend on the rms velocity in the orifice v_{rms}. The flow resistivity of the PP in the nonlinear regime is modeled via a Forchheimer-type law. It is thus equal to its value in the linear regime plus a nonlinear correction:

$$\sigma_{\mathrm{NL}} = \sigma + \frac{\beta \rho_0 (1 - \varphi^2)}{\pi h \varphi C_D^2} \sqrt{2} v_{\mathrm{rms}}, \tag{4}$$

where C_D is the discharge coefficient, that depends on the perforation geometry, the edge sharpness among others and that vary between 0.6 and 0.8 and β is a coefficient. Thereafter, the values used in Laly et al. [12], i.e. $C_D = 0.76$ and $\beta = 1.6$, are employed. The tortuosity $\alpha_{\infty\,\mathrm{NL}}$ in the nonlinear regime is defined as in the linear regime by

$$\alpha_{\infty\,\mathrm{NL}} = 1 + \frac{2\varepsilon_{\mathrm{NL}}}{h}. \tag{5}$$

Following Maa [5], the correction length $\varepsilon_{\mathrm{NL}}$ is modified to account for the nonlinear effects with

$$\varepsilon_{\mathrm{NL}} = \varepsilon \left(1 + \frac{\sqrt{2} v_{\mathrm{rms}}}{\varphi c_0} \right)^{-1}. \tag{6}$$

The tortuosity thus decreases with the increase of the acoustic velocity in the perforation.

The model proposed by Laly et al. [12] is more accurate for micro-perforated liners ($r \leq 0.5$ mm) than for macro-perforated liners and for a POA range from 1% to 5% [28].

In this work, results are exemplified for three PP absorbers, whose photo is shown in Fig. 1. Their geometrical characteristics are given in Table 1. The PPs #1 and #2 correspond to micro-perforated plates, with perforation radius below 0.5 mm and POA in the order of 1%. PP#3 has a larger perforation radius and is in between a micro- and macro-perforated plate.

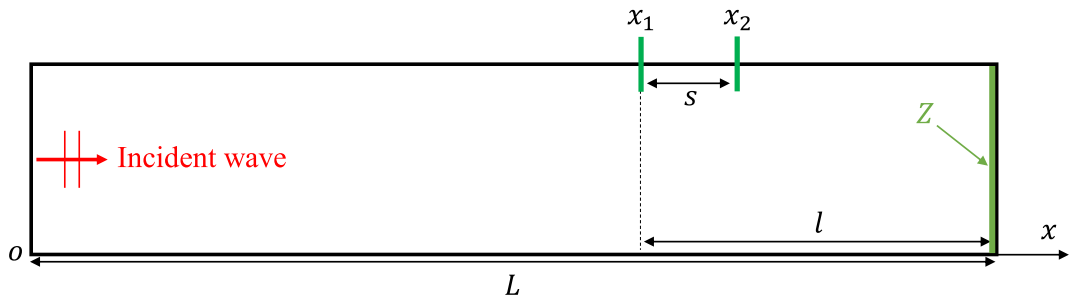

Fig. 2. Schematic for the one-dimensional configuration, corresponding to an impedance tube.

3. Time-domain numerical model

3.1. Geometrical configuration

An impedance tube, schematized in Fig. 2, is considered as a canonical problem to evaluate time-domain impedance boundary conditions in the nonlinear regime. It is treated as a one-dimensional problem. Denoting by x the spatial variable, the domain of interest is limited to $0 \leq x \leq L$. The PP liner is located at $x = L$ and an incident wave $p_i(t)$ is traveling towards the liner.

3.2. Equations and numerical methods

For acoustic perturbations of sufficiently small amplitude, sound propagation is governed by the linearized Euler equations (LEE). For a homogeneous medium at rest, they write:

$$\begin{cases} \dfrac{\partial u}{\partial t} + \dfrac{1}{\rho_0}\dfrac{\partial p}{\partial x} = 0 \\ \dfrac{\partial p}{\partial t} + \rho_0 c_0^2 \dfrac{\partial u}{\partial x} = 0, \end{cases} \tag{7}$$

where u and p are the acoustic velocity and pressure, respectively.

The LEE are solved using high-order finite-difference time-domain methods. The spatial derivatives are calculated using optimized 4th-order finite differences schemes over 11 points [29,30]. Time integration is performed using an optimized 6-stage 4th-order Runge–Kutta algorithm [31]. In order to avoid numerical instabilities and to remove grid-to-grid oscillations, optimized selective filters [30,32] are applied after each time iteration.

The incident wave $p_i(t)$ is prescribed using the method of characteristics. The incoming and outgoing characteristics in the computational domain at the boundary $x = 0$, denoted by q_i and q_o, respectively, are given by:

$$q_i(t) = \frac{1}{2}(p(x=0,t) + Z_0 u(x=0,t)) \qquad q_o(t) = \frac{1}{2}(p(x=0,t) - Z_0 u(x=0,t)), \tag{8}$$

with $Z_0 = \rho_0 c_0$. To force the incident wave and avoid reflections at the boundary, the method consists in determining the outgoing characteristic from the numerical solution and imposing the incoming characteristic to $q_i(t) = p_i(t)$, after each stage of the Runge–Kutta algorithm. The pressure and the velocity at the boundary are then corrected with the relations:

$$p(x=0,t) = q_i(t) + q_o(t) \qquad u(x=0,t) = \frac{q_i(t) - q_o(t)}{Z_0} \tag{9}$$

Finally, all variables are initialized to zero at time $t = 0$.

3.3. Time-domain admittance boundary condition (TDABC) in the linear regime

Before discussing its extension for the nonlinear regime, the time-domain admittance boundary condition proposed by Troian et al. [24] for the linear regime is briefly summarized. Implementation on the admittance rather than on the impedance was preferred, as numerical instabilities were observed for some liners in the latter case. Note that implementations based on the reflection coefficient have been also proposed [19] and seem to offer better stability properties [33]. Denoting by $Y(\omega)$ the normalized surface admittance, the admittance boundary condition is defined in the frequency domain by $Z_0 U_n(\omega) = Y(\omega)P(\omega)$, with $U_n = \mathbf{U}\cdot\mathbf{n}$ where $P(\omega)$ and $\mathbf{U}(\omega)$ are the Fourier transforms of the acoustic pressure and velocity on the PP surface, respectively, and $\mathbf{n}$ is the normal unit vector pointing into the liner surface.

The time domain admittance boundary condition (TDABC) is obtained from the translation of the frequency domain boundary condition, yielding the convolution $Z_0 u_n(t) = [y * p](t)$, where $y(t)$ is the surface admittance in the time domain. To avoid the tedious

calculation of the convolution integral, Troian et al. [24] proposed to express the broadband admittance model $Y(\omega)$ as a multipole model:

$$Y(\omega) = Y_\infty + \sum_{k=1}^{P} \frac{A_k}{\lambda_k - \mathrm{j}\omega}, \tag{10}$$

where λ_k are the poles of the admittance and P denotes their number. Note that the poles and the associated coefficients A_k are either real or come as complex conjugate pairs. Finally, the coefficient Y_∞ is real-valued.

The analytical surface admittance of the PP is obtained from Eq. (1) with $Y(\omega) = [Z_\mathrm{L}(\omega)]^{-1}$ and is approximated by a multipole model in the form of Eq. (10). To do so, the poles and the coefficients of the broadband admittance are determined using the vector fitting (VF) algorithm [34] in the frequency band of interest. The VF algorithm allows the multipole model to have stable poles. The passivity of the multipole model ($\mathrm{Re}[Y(\omega)] \geq 0$ for $\omega > 0$) is however not guaranteed and has to be checked for all frequencies and for each set of coefficients obtained with the VF algorithm. In particular, it was observed that the real part of the multipole model can be negative at very low frequencies for PP liners. Generally, this issue can be overcome by increasing the number of poles. This solution might however not be worthwhile because we usually want to keep the number of poles as small as possible to reduce the computational cost. As the minimum of $\mathrm{Re}[Y]$ denoted by $Y_\_$ generally remains small ($Y_\_$ in the order of -10^{-3}), an alternative to enforce passivity is to add $-Y_\_$ to Y_∞ so that $\mathrm{Re}[Y] \geq 0$ over the frequency band of interest.

With the multipole form, the surface admittance in the time domain has a closed-form expression, that greatly simplifies the expression of the convolution. After some calculation detailed in Ref. [24], the time-domain admittance boundary condition (TDABC) finally relates the acoustic velocity and pressure on the liner surface with the expression:

$$Z_0 u_n(t) = Y_\infty p(t) + \sum_{k=1}^{P} A_k \phi_k(t), \tag{11}$$

where the new temporal functions $\phi_k(t)$, called accumulator in Reymen et al. [22], verify the system of ordinary differential equations (ODE):

$$\frac{\mathrm{d}\phi_k}{\mathrm{d}t} + \lambda_k \phi_k(t) = p(t) \tag{12}$$

This system is numerically solved using the same time scheme as for the LEE presented in Eq. (7). Eqs. (11) and (12) constitute the TDABC.

Note that the formulation of the TDABC presented in this section is an alternative to that proposed in Ref. [24], as there is no explicit distinction between the real poles and the pairs of complex conjugate poles. As a consequence, the accumulators ϕ_k are complex-valued.

3.4. Extension of the TDABC in the nonlinear regime

Some remarks are first made on nonlinear impedance models. Surface impedance is rigorously defined in the linear regime. For a harmonic excitation, a surface impedance that depends on the excitation amplitude seems relevant, as long as the harmonic distortion is negligible. For other types of excitation, the concept of nonlinear surface impedance is somewhat empirical. A straightforward extension of the impedance model proposed by Laly et al. [12] for broadband stationary signal is to consider that the main information on the velocity in the perforations governing the nonlinear effects remains its overall amplitude rather than any specific frequency-dependent information. Such approach has been employed by Eversman [15] for propagation of multiple tones inside a lined duct using a frequency-domain finite element method. Therefore, the impedance model in Eq. (3) can be used as is for a broadband stationary excitation.[1] Despite its simplicity, recent comparisons [35] have shown an excellent agreement between predictions using this approach and measurements with an impedance tube for a white noise excitation.

The rest of the study is thus limited to stationary signals. For non-stationary signals, such as transient signals, other models than frequency-based surface impedance models might be better suited to represent the acoustic response of perforated plates in the nonlinear regime. Thus, Cummings [14] propose nonlinear differential equations in the time-domain, that directly relate the velocity in the perforation and the pressure jump through the perforated plate. These equations are obtained from simplification of the fluid mechanics equations and do not include all physical effects considered in the surface impedance model, such as the effects of the interaction between holes of the perforates on the end correction length or the reduction of the end correction length with the increase of the orifice velocity. Comparisons were however performed for a transmitted pulse through a perforated plate between measurements in an impedance tube and numerical predictions and were promising. Implementation of such nonlinear models of perforated plates for time-domain simulations in a lined duct has been done in Monteghetti et al. [33].

The implementation of the nonlinear TDABC in the time-domain numerical model is now presented. It is based on the recent work of Shur et al. [26] that has extended the TDABC of Troian et al. [24] in the nonlinear regime. To do so, a quasi-steady approach is employed. The idea is that the rms velocity on the liner has to be determined from the numerical solution. As the solution is however advanced in time starting from some initial conditions, a transient period is necessarily present. Thus, a time-varying evaluation of v_rms, denoted by $\tilde{v}_\mathrm{rms}(t)$, is determined and the surface admittance is dynamically modified to $Y(\omega, \tilde{v}_\mathrm{rms})$, until steady-state is reached.

[1] Other nonlinear surface impedance models are based on the rms acoustic pressure on the liner rather than the rms velocity in the perforations, as considered by Shur et al. [26]. The numerical methods presented subsequently can be also employed similarly.

Second, to account for the variation of the admittance with both ω and v_{rms}, two approaches are investigated. They are both based on the approximation of the admittance by a multipole model for some reference values of v_{rms}, that allows for the use of the ADE method. In the first approach proposed by Shur et al. [26], the admittance is determined for a given v_{rms} by interpolation. This method was shown to be accurate and efficient. One of its drawback is that compared to the linear regime, the number of poles significantly increases and is globally proportional to the number of reference values of v_{rms} chosen for the interpolation. This first approach, referred to as the interpolation of the admittance (IA) method is detailed in Section 3.4.1. We propose a second approach, in which, the multipole coefficients, rather than directly the admittance, are calculated for a given v_{rms} by interpolation. Once the coefficients are known, the admittance is easily deduced. This approach, referred to as the interpolation of the admittance parameters (IAP) method is presented in Section 3.4.2.

3.4.1. Interpolation of the admittance (IA)

The method based on the interpolation of the admittance is first presented. Following Shur et al. [26], we define a set of reference values for the rms velocity $v_{\mathrm{rms}}^{(l)}$, $l = 1, 2, \dots, N$. This set covers the expected range of variation of v_{rms} and has to be adapted according to the problem under consideration. At each of these reference values $v_{\mathrm{rms}}^{(l)}$, the frequency-dependent admittance $Y(\omega, v_{\mathrm{rms}}^{(l)}) = [Z_{\mathrm{NL}}(\omega, v_{\mathrm{rms}}^{(l)})]^{-1}$ (see Eq. (3)) is approximated by a multipole model

$$Y^{(l)}(\omega) = Y(\omega, v_{\mathrm{rms}}^{(l)}) = Y_{\infty}^{(l)} + \sum_{k=1}^{P^{(l)}} \frac{A_k^{(l)}}{\lambda_k^{(l)} - \mathrm{j}\omega}, \tag{13}$$

where the same notation than in Eq. (10) is employed. The poles and coefficients of the admittances ($Y_{\infty}^{(l)}$, $A_k^{(l)}$ and $\lambda_k^{(l)}$) are determined for the reference values $v_{\mathrm{rms}}^{(l)}$ using the VF algorithm. Note that the number of real poles and pairs of complex conjugate poles can vary depending on the rms velocity. Then, for any v_{rms} value in the range $[v_{\mathrm{rms}}^{(1)}, v_{\mathrm{rms}}^{(N)}]$, the admittance of the perforated panel ($Y(\omega, v_{\mathrm{rms}})$) is calculated using a linear combination of the individual admittances at each of these reference values $v_{\mathrm{rms}}^{(l)}$

$$Y(\omega, v_{\mathrm{rms}}) = \sum_{l=1}^{N} \sigma_l(v_{\mathrm{rms}}) Y^{(l)}(\omega) \qquad \sum_{l=1}^{N} \sigma_l = 1, \tag{14}$$

where σ_l are the weights, that provide information about the rms velocity in the perforation.

As done by Shur et al. [26], the weights are obtained by linear interpolation between the defined reference values $v_{\mathrm{rms}}^{(l)}$. Thus, for v_{rms} belonging into the range $v_{\mathrm{rms}}^{(l-1)} \leq v_{\mathrm{rms}} \leq v_{\mathrm{rms}}^{(l)}$, the weights are calculated as follows:

$$\begin{cases} \sigma_l = \dfrac{v_{\mathrm{rms}} - v_{\mathrm{rms}}^{(l-1)}}{v_{\mathrm{rms}}^{(l)} - v_{\mathrm{rms}}^{(l-1)}} \\ \sigma_{l-1} = 1 - \sigma_l \\ \sigma_k = 0 \text{ for } k < (l-1) \text{ and } k > l \end{cases} \tag{15}$$

In the case where v_{rms} is outside the range of the reference values ($v_{\mathrm{rms}} \leq v_{\mathrm{rms}}^{(1)}$ or $v_{\mathrm{rms}} \geq v_{\mathrm{rms}}^{(N)}$), the admittance is set to the admittance at the corresponding end value of the velocity range, i.e. all the weights are equal to zero, except the weight of the end value which is equal to 1. Note that the linear interpolation is not a requirement of the method and that higher-order interpolation could be used.

It remains to evaluate v_{rms} from the numerical solution. To do so, the rms velocity is estimated at a given time t with the relation

$$\tilde{v}_{\mathrm{rms}}^2(t) = \frac{1}{t} \int_0^t v^2(t') \mathrm{d}t', \tag{16}$$

where $v(t)$ is the velocity fluctuation in the orifice. Due to the conservation of the acoustic flow rate, it is equal to the ratio of the acoustic normal velocity on the liner to the POA, i.e. $v(t) = u_n(t)/\varphi$. Taking the time derivative of the above equation leads to the differential equation:

$$\frac{\mathrm{d}(t\tilde{v}_{\mathrm{rms}}^2)}{\mathrm{d}t} = \frac{u_n^2(t)}{\varphi^2}, \tag{17}$$

that is integrated in time with the time-marching scheme to obtain $\tilde{v}_{\mathrm{rms}}(t)$. In practice, a simpler approach is employed. The value of $\tilde{v}_{\mathrm{rms}}$ at the time iteration n is calculated from its value at iteration $n-1$ using the recursive expression:

$$\tilde{v}_{\mathrm{rms}}^2(n\Delta t) = \left(1 - \frac{1}{n}\right) \tilde{v}_{\mathrm{rms}}^2[(n-1)\Delta t] + \frac{1}{n} \frac{u_n^2(n\Delta t)}{\varphi^2}, \tag{18}$$

with Δt the time step. This expression can be obtained by integrating Eq. (17) between two consecutive time steps and by assuming that u_n is constant over a time step.

Therefore, the nonlinear extension of the TDABC in Eq. (11) with the IA method is rewritten as follows

$$Z_0 u_n(t) = \sum_{l=1}^{N} \sigma_l(\tilde{v}_{\mathrm{rms}}) \left(Y_{\infty}^{(l)} p(t) + \sum_{k=1}^{P^{(l)}} A_k^{(l)} \phi_k^{(l)}(t) \right), \tag{19}$$

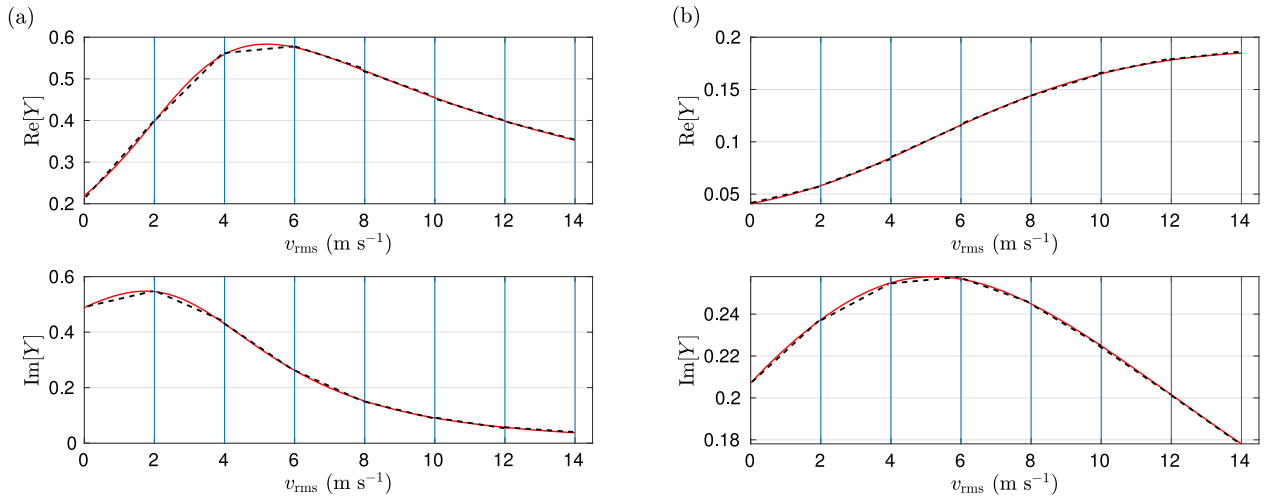

Fig. 3. Real and imaginary parts of the admittance for a frequency of (a) $f = 2000$ Hz and (b) $f = 3000$ Hz as a function of the rms velocity in the perforation for PP#1 absorber with a cavity depth of 10 mm calculated with Eq. (3) (solid line) and by linear interpolation (dotted line). The vertical lines at $v_{\mathrm{rms}} = 0$, 2, 4, 6, 8, 10, 12 and 14 m s^{-1} show the reference values used for the interpolation.

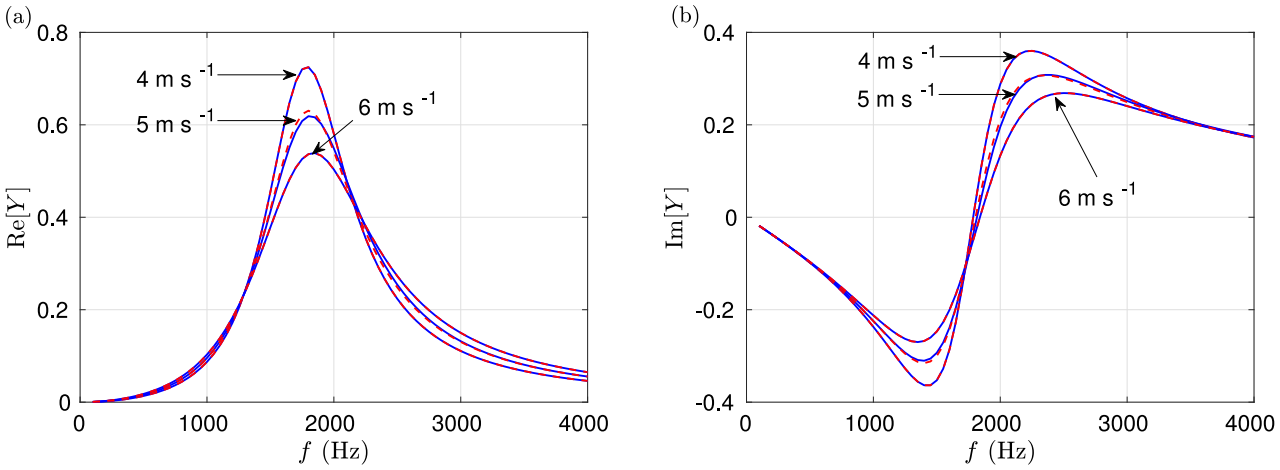

Fig. 4. (a) Real and (b) imaginary parts of the admittance of PP#1 absorber with a cavity depth of 10 mm as a function of the frequency for three rms velocities: exact calculation (solid blue line) and approximation with the IA method (dotted red line).

where the accumulators $\phi_k(t)$ are obtained by integrating the ODE:

$$\frac{\mathrm{d}\phi_k^{(l)}}{\mathrm{d}t} + \lambda_k^{(l)}\phi_k^{(l)}(t) = p(t) \tag{20}$$

and $\tilde{v}_{\mathrm{rms}}$ by integrating Eq. (17).

In order to choose the set of reference values $v_{\mathrm{rms}}^{(l)}$, the evolution of the admittance with the rms velocity in the perforation is investigated. Fig. 3 shows the normalized admittance (solid line) as a function of v_{rms} for PP#1 with a cavity depth of 10 mm and for two frequencies (2000 and 3000 Hz). It is seen that the nonlinear behavior is strongly dependent on the frequency: the variation with v_{rms} is significant for 2000 Hz, which is close to the resonant frequency of the PP liner, but limited for 3000 Hz. In addition, the admittance is not varying simply with v_{rms}. In order to use linear interpolation, it is necessary to choose a sufficiently small step between two consecutive reference values to represent correctly the variations of Y with v_{rms}. The dotted line thus corresponds to a linear interpolation using a step of 2 m s^{-1}. With this step, the interpolated admittance shows a good agreement with the exact admittance.

Fig. 4 shows the comparison between the exact admittance model and its approximation with the IA method for three rms velocities (4, 5, and 6 m s^{-1}). This velocity range is chosen because the error in Fig. 3 is maximum in this range. Note that $v_{\mathrm{rms}} = 4$ and 6 m s^{-1} are considered as reference values in the IA method: for these two rms velocities, the exact admittance is approximated by a multipole model using the VF algorithm. The approximation is performed for 200 Hz $< f <$ 4000 Hz using two poles, which is seen to be sufficient to accurately represent the variation of Y over the entire frequency range of interest. For the intermediate rms velocity $v_{\mathrm{rms}} = 5$ m s^{-1}, the admittance in the IA method is obtained by linear interpolation from the multipole models at $v_{\mathrm{rms}} = 4$ and 6 m s^{-1}. Here also, a close agreement with the exact admittance is observed.

Table 2
Number of real poles and pairs of complex conjugate poles for the reference values $v_{\mathrm{rms}}^{(l)}$ and for the three PPs absorbers.

PP#1, PP#3													
Cavity depth (mm)		10						30					
Reference rms velocity (m s^{-1})		2	4	6	8	10	12	2	4	6	8	10	12
Incident SPL (dB)		114	122	128	132	135	138	114	122	128	132	135	138
Poles number	Real	0	0	0	0	0	0	0	0	0	0	0	0
	Complex conjugate pair	1	1	1	1	1	1	1	1	1	1	1	1
PP#2													
Cavity depth (mm)		10						30					
Reference rms velocity (m s^{-1})		2	4	6	8	10	12	2	4	6	8	10	12
Incident SPL (dB)		112	121	127	131	134.5	137.5	112	121	127	131	134.5	137.5
Poles number	Real	0	0	0	0	0	0	0	0	0	0	2	2
	Complex conjugate pair	1	1	1	1	1	1	1	1	1	1	0	0

In accordance with the discussion around Fig. 3, we have chosen the set of reference values for the rms velocity $v_{\mathrm{rms}}^{(l)}$ = 2, 4, 6, 8, 10 and 12 m s^{-1} with $N = 6$. For each reference value, the admittance is fitted over the frequency range 200–4000 Hz by a multipole model using the VF algorithm with two poles. The number of real poles and of pairs of complex conjugate poles for the reference values is indicated in Table 2 for the three PPs absorber. The related incident sound pressure levels (SPL) is also indicated. It represents the SPL of the incident wave, that generates the corresponding rms velocity in the perforation. It is estimated from the relation derived by Ingard [36] that expresses the rms incident pressure $p_{i,\mathrm{rms}}$ as a function of v_{rms}:

$$p_{i,\mathrm{rms}} = \frac{\rho_0 c_0^2}{2} \frac{\varphi v_{\mathrm{rms}}}{c_0} \left(1 + \frac{1-\varphi^2}{\varphi} \frac{\sqrt{2}\, v_{\mathrm{rms}}}{c_0} \right) \tag{21}$$

This expression is valid only at the resonant frequency of the PP, for which the velocity in the perforation is maximum for a given incident SPL. To reach the same value of v_{rms} at frequencies different from the resonant frequency, a larger incident SPL is necessary. Therefore, the SPL indicated in Table 2 has to be interpreted as the minimum incident SPL generating the corresponding value of the velocity in the perforation. For information, the poles and coefficients of the multipole model used for the IA method are indicated in Table A.4 in Appendix A for PP#1 with the cavity depths of 10 and 30 mm.

The main disadvantage of this method can be brought to light. For v_{rms} outside the range of the reference values, it is not possible to evaluate correctly the admittance. The range covered by the reference values has thus to be broadened considerably to avoid such cases. In addition, to represent accurately the variation of the admittance with v_{rms}, the step between two successive reference values should be sufficiently small. Therefore, the number of reference values and, hence, of poles can be significant with the IA method, which can lead to an increase in the computational cost. For PP liners, the admittance can be approximated over a broad range of frequencies using few poles: the cost of the IA method is thus moderate. For other types of liner, this can become a shortcoming of the IA method.

3.4.2. Interpolation of the admittance parameters (IAP)

In this section, a new approach to account for the nonlinear effects on the admittance is proposed. To do so, the admittance is still written as a multipole model, as in Eq. (10), but the coefficients and the poles are allowed to vary with v_{rms}. This gives:

$$Y(\omega, v_{\mathrm{rms}}) = Y_\infty(v_{\mathrm{rms}}) + \sum_{k=1}^{P} \frac{A_k(v_{\mathrm{rms}})}{\lambda_k(v_{\mathrm{rms}}) - \mathrm{j}\omega}. \tag{22}$$

It is then necessary to calculate the poles and coefficients of the multipole model as a function of v_{rms}. To do so, one idea could be to couple the VF algorithm and the time-domain numerical model, so that the poles and the coefficients of the admittance are determined dynamically as the value of $\tilde{v}_{\mathrm{rms}}$ changes. This would however require to run the VF algorithm after each iteration (or after each step of the Runge–Kutta algorithm). Even if the VF algorithm usually takes few tenths of a second to run, this would add complexity and computational cost to the approach. Especially for multi-dimensional problems, it would be necessary to run the VF algorithm for each grid point on the liner. A more efficient strategy is to have an approximate analytical expression giving the evolution of the poles and coefficients of Y with v_{rms}. In this work, the multipole coefficients (real and imaginary parts, separately) are approximated by a rational function with quadratic polynomials. For example, one has:

$$Y_\infty(v_{\mathrm{rms}}) = \frac{Y_\infty^{n,0} + Y_\infty^{n,1} v_{\mathrm{rms}} + Y_\infty^{n,2} v_{\mathrm{rms}}^2}{1 + Y_\infty^{d,1} v_{\mathrm{rms}} + Y_\infty^{d,2} v_{\mathrm{rms}}^2}, \tag{23}$$

where $Y_\infty^{n,0}$, $Y_\infty^{n,1}$, $Y_\infty^{n,2}$, $Y_\infty^{d,1}$ and $Y_\infty^{d,2}$ are constants. A similar expression holds for $\mathrm{Re}[A_k(v_{\mathrm{rms}})]$, $\mathrm{Im}[A_k(v_{\mathrm{rms}})]$, $\mathrm{Re}[\lambda_k(v_{\mathrm{rms}})]$, and $\mathrm{Im}[\lambda_k(v_{\mathrm{rms}})]$. The rational function approximation is determined using the curve fitting toolbox of MATLAB (with data points obtained with the VF algorithm for $0 \leq v_{\mathrm{rms}} \leq 12$ m s^{-1} with a step of 1 m s^{-1}). Other approaches, such as the VF algorithm, could also have been employed. As an example, the poles and coefficients of the multipole function are plotted as a function of v_{rms}

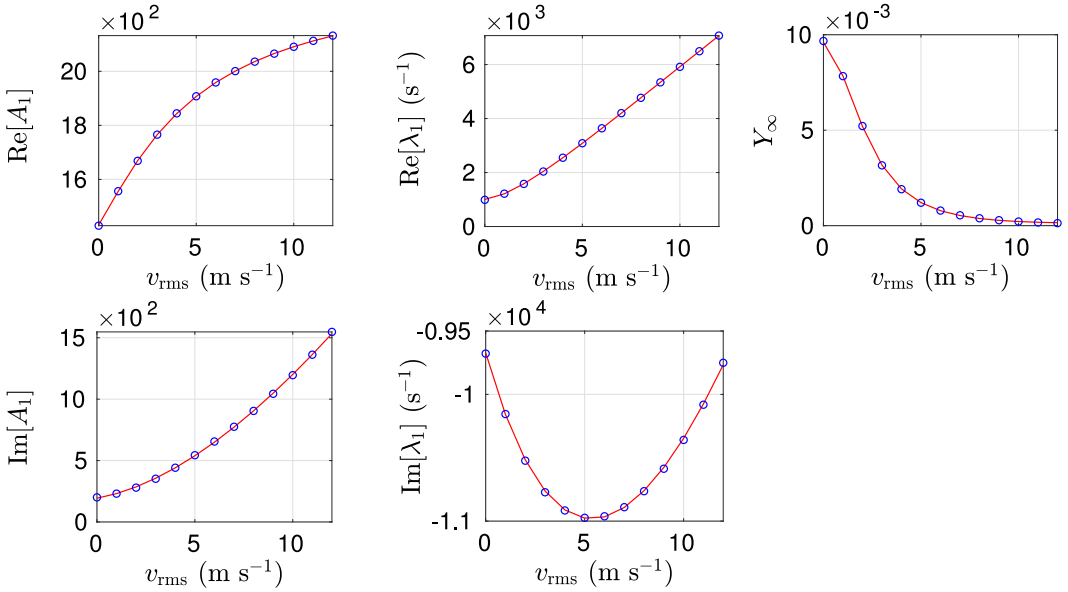

Fig. 5. Coefficients of the multipole model as a function of the rms velocity v_{rms} (blue circle symbols) and their approximation (red solid lines) using a rational function (PP#1 for a cavity depth of 10 mm).

in Fig. 5 along with their rational function approximation for PP#1 with a cavity depth of 10 mm. The constants of the rational function approximation for the multipole coefficients are given in Appendix A in Table A.5 for PP#1 liner with the two cavity depths of 10 and 30 mm.

With the expression of the admittance in Eq. (22), the nonlinear extension of the TDABC in Eq. (11) with the IAP method is defined as follows:

$$Z_0 u_n(t) = Y_\infty(\tilde{v}_{\text{rms}})p(t) + \sum_{k=1}^{P} A_k(\tilde{v}_{\text{rms}})\phi_k(t), \tag{24}$$

where the function ϕ_k is governed by the ODE:

$$\frac{\mathrm{d}\phi_k}{\mathrm{d}t} + \lambda_k(\tilde{v}_{\text{rms}})\phi_k(t) = p(t) \tag{25}$$

and $\tilde{v}_{\text{rms}}$ is determined from Eq. (17).

The IAP method is simpler to implement than the IA method. One difficulty is that, while in the VF algorithm, the total number of poles can be chosen, it is not possible to set their type (real poles or pair of complex conjugate poles). Therefore, a pair of complex conjugate poles can switch to two real poles for a given value of v_{rms} and inversely. Thus, the number of each type of poles is constant in all cases considered for rms velocities in the perforations between 0 and 12 m s^{-1}, except for PP#2 with a cavity depth of 30 mm for which it changes from 10 m s^{-1} (see Table 2). As a consequence, the variation of the poles and coefficients A_k and λ_k with v_{rms} is discontinuous when the poles type changes. A simple method to handle this issue with the IAP method is to define the poles and coefficients A_k and λ_k as piecewise rational functions of v_{rms} with a different set of coefficients for velocities for which the poles are real and for velocities for which the poles come as complex conjugate pairs. This approach has been tested for the impedance tube configuration, detailed in Section 4. It was shown to be effective but induced a longer transient before convergence. Results are not shown for conciseness. Because this issue was only noticed for PP#2 with a cavity depth of 30 mm and for a large velocity in the perforations, further investigation is left for future work.

4. 1D validation

The present section aims to verify that the proposed methods in Section 3.4 allow for an accurate representation of the surface impedance in the nonlinear regime. For that, the one-dimensional configuration corresponding to an impedance tube is considered, as shown in Fig. 2. Numerical experiments are first presented in Section 4.2 and comparisons to measurements are then performed in Section 4.3. The MATLAB codes employed for the numerical experiments with the IAP method are available in the supplementary material.

4.1. Numerical parameters

The computational domain ($0 \leq x \leq L$) is discretized by 101 points with a uniform spatial step $\Delta x = 0.0085$ m. The total simulation time is $t_{\text{max}} = 0.3$ s. The CFL (Courant–Fridrichs–Lewy) number is set to 0.5, which gives a time step $\Delta t = 1.25 \times 10^{-5}$ s.

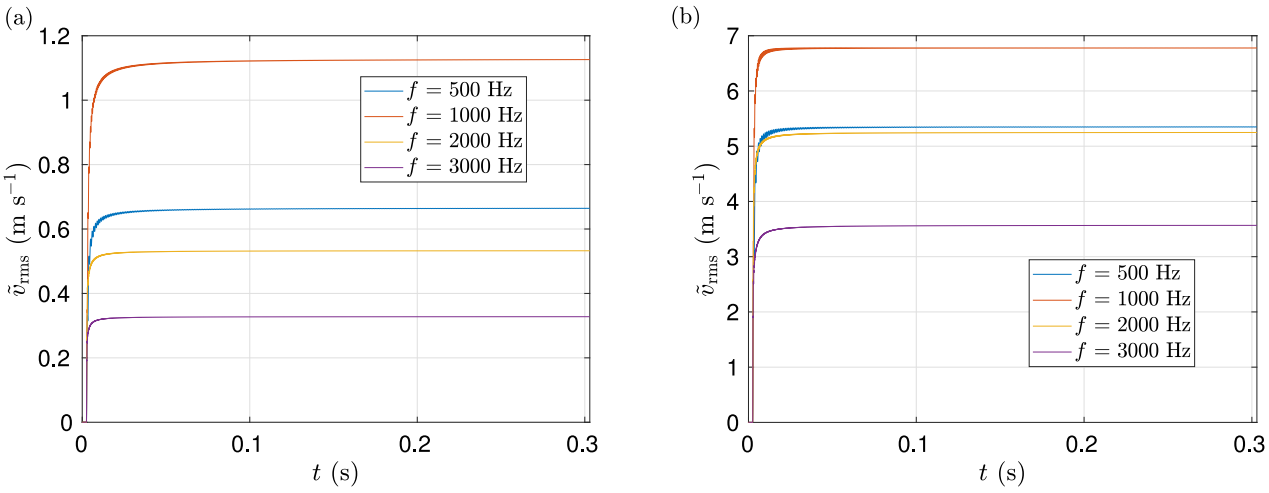

Fig. 6. Time-variation of the estimated rms velocity in the perforation $\tilde{v}_{\mathrm{rms}}$ for PP#1 absorber with a cavity depth of 30 mm and for two incident SPL: (a) $\mathrm{SPL}_i = 110$ dB and (b) $\mathrm{SPL}_i = 130$ dB.

Numerical simulations are carried out for two types of incident waves, namely a harmonic and a broadband wave. For the former case, the incident wave is $p_i(t) = \sqrt{2}\, p_{i,\mathrm{rms}} \sin(2\pi f t)$, where $p_{i,\mathrm{rms}}$ is the rms value. For the latter case, the incident wave is $p_i(t) = p_{i,\mathrm{rms}}\, s(t)$, where $s(t)$ is a broadband stationary signal of unitary rms value. The incident SPL is also used thereafter to characterize the excitation and is defined by:

$$\mathrm{SPL}_i = 20 \log_{10} \left(\frac{p_{i,\mathrm{rms}}}{p_{\mathrm{ref}}} \right) \tag{26}$$

with the reference pressure set to $p_{\mathrm{ref}} = 2 \times 10^{-5}$ Pa.

The two-microphone method is employed to estimate the surface impedance of the PP liner (Z) for both the numerical simulations and the experiments. The normalized surface impedance is determined from the frequency response function H_{12} between two microphones at positions x_1 and x_2

$$Z = -\mathrm{j} \frac{\sin[k_0(l-s)] - H_{12} \sin(k_0 l)}{H_{12} \cos(k_0 l) - \cos[k_0(l-s)]}, \tag{27}$$

where $l = L - x_1$ and $s = |x_1 - x_2|$. For the numerical simulations, the frequency response function H_{12} is obtained directly by the ratio of the Fourier transforms of the time pressure signals at positions x_1 and x_2, in the case of harmonic excitation and by the ratio of the cross power spectral density of the time pressure signals at positions x_1 and x_2 to the power spectral density at x_2, in the case of broadband excitation.

4.2. Numerical experiment

4.2.1. Harmonic excitation

The case of a harmonic excitation is first treated. Simulations are performed for incident waves with the same SPL and with frequencies between 200 and 4000 Hz, in steps of 100 Hz. At the initial time $t = 0$, all variables are set to zero, including $\tilde{v}_{\mathrm{rms}}$. Once the incident wave impinges on the liner, $\tilde{v}_{\mathrm{rms}}$ increases. This modifies the surface impedance which in turn induces a variation of the acoustic field and of $\tilde{v}_{\mathrm{rms}}$. This process repeats itself until a steady-state is obtained. This can be checked by looking at the convergence of $\tilde{v}_{\mathrm{rms}}$, i.e. when the difference between the values of $\tilde{v}_{\mathrm{rms}}$ at two successive iterations becomes sufficiently small ($\approx 10^{-3}$ m s^{-1}). Fig. 6 shows the time-variation of the estimated rms velocity for four frequencies (500, 1000, 2000, 3000 Hz) at two incident SPL (110 and 130 dB) using PP#1. It is seen that $\tilde{v}_{\mathrm{rms}}$ monotonously increases with time and that convergence is reached from $t = 0.2$ s for all cases. In addition, it can be noted that the rms velocity strongly depends on the frequency.

Fig. 7 shows the rms velocity as a function of the frequency for PP#1 absorber for two cavity depths and for several incident SPL. The maximum of velocity is obtained near the resonant frequency and the latter is slightly shifted towards the high frequencies with the increase of the incident SPL. The variations of the rms velocity with the frequency for the two other absorbers PP#2 and PP#3 are similar but they are not shown for conciseness.

The real and imaginary parts of the admittance estimated from the numerical simulation with the IA and IAP methods are shown in Figs. 8 and 9 for PP#1 and PP#3 with two cavity depths and for several incident SPL. It is seen that the surface admittance is significantly different depending on the incident SPL: in particular, increasing the incident SPL tends to flatten the curves. The corresponding analytical admittances calculated from Eq. (3) are also plotted in Figs. 8 and 9. Note that the rms velocity in the perforations determined from the numerical solution is used as input data for the analytical admittance model. For both IA and IAP methods, the numerical results are in good agreement with the analytical results over the entire frequency range for the reference values as well as for the intermediate values of the velocity. This shows that both methods allow for an accurate representation of the nonlinear admittance in the time domain.

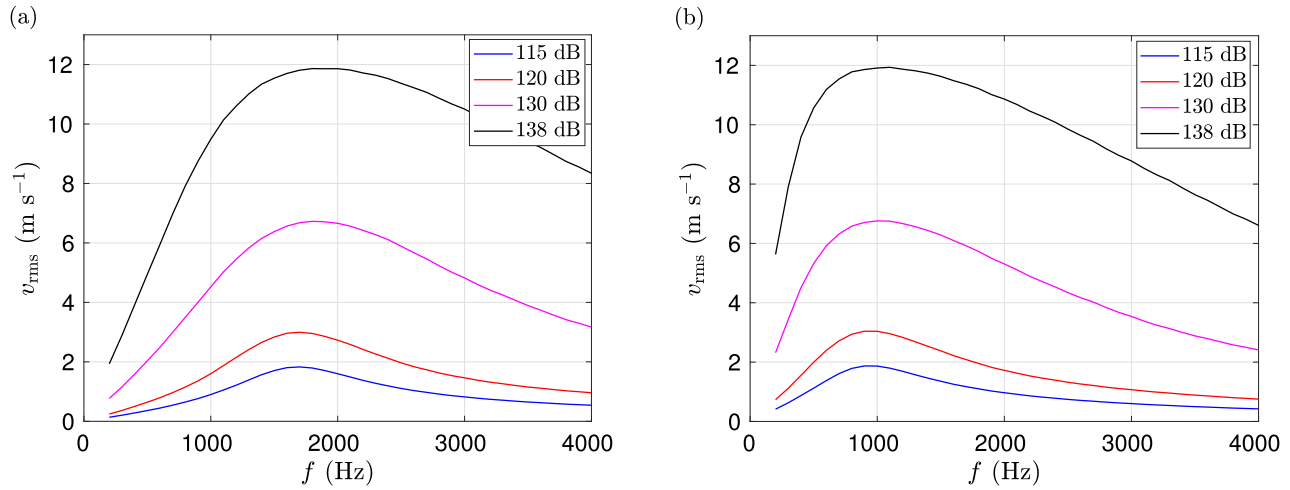

Fig. 7. Variation of the rms velocity in the perforation with the frequency for several incident SPL and for PP#1 with two cavity depths: (a) $D = 10$ mm and (b) $D = 30$ mm.

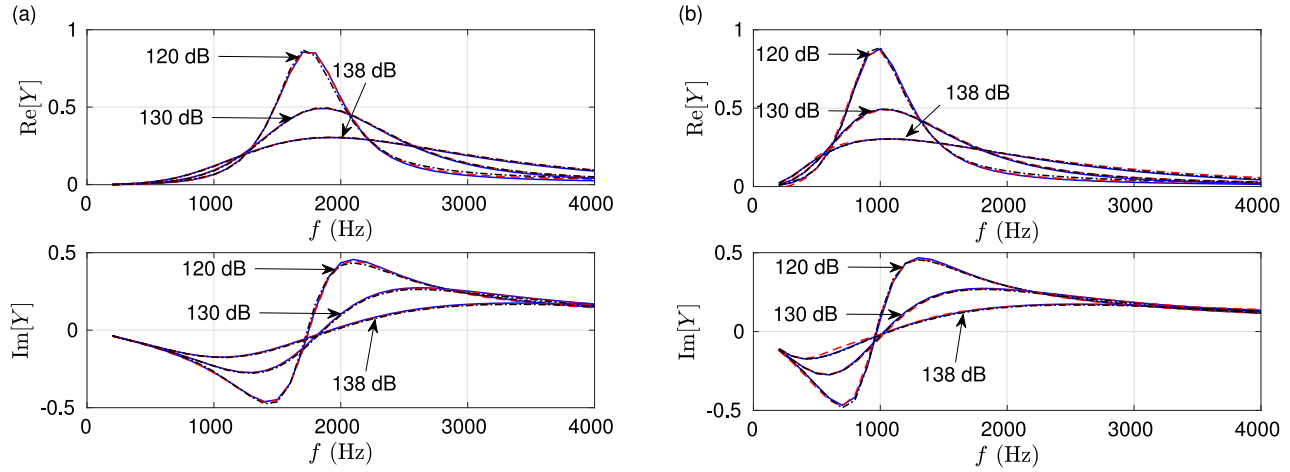

Fig. 8. Admittance for PP#1 absorber with a cavity depth of (a) $D = 10$ mm and (b) $D = 30$ mm: calculated with the analytical model in Eq. (3) (blue solid) and determined from the numerical solution using the IAP (red dashed) and the IA (black dash-dotted) methods. A harmonic excitation is used.

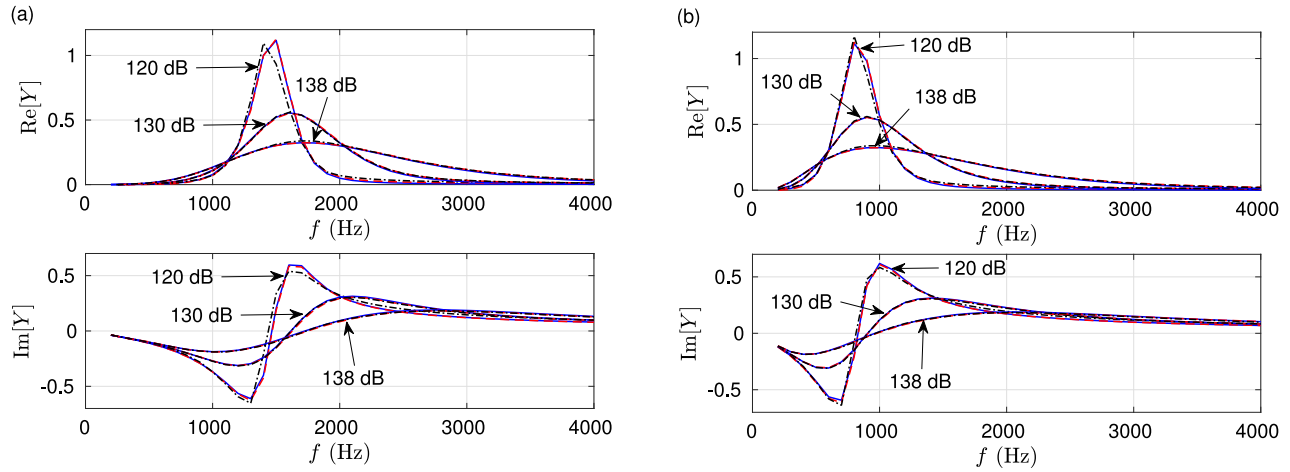

Fig. 9. Admittance for PP#3 absorber with a cavity depth of (a) $D = 10$ mm and (b) $D = 30$ mm: calculated with the analytical model in Eq. (3) (blue solid) and determined from the numerical solution using the IAP (red dashed) and the IA (black dash-dotted) methods. A harmonic excitation is used.

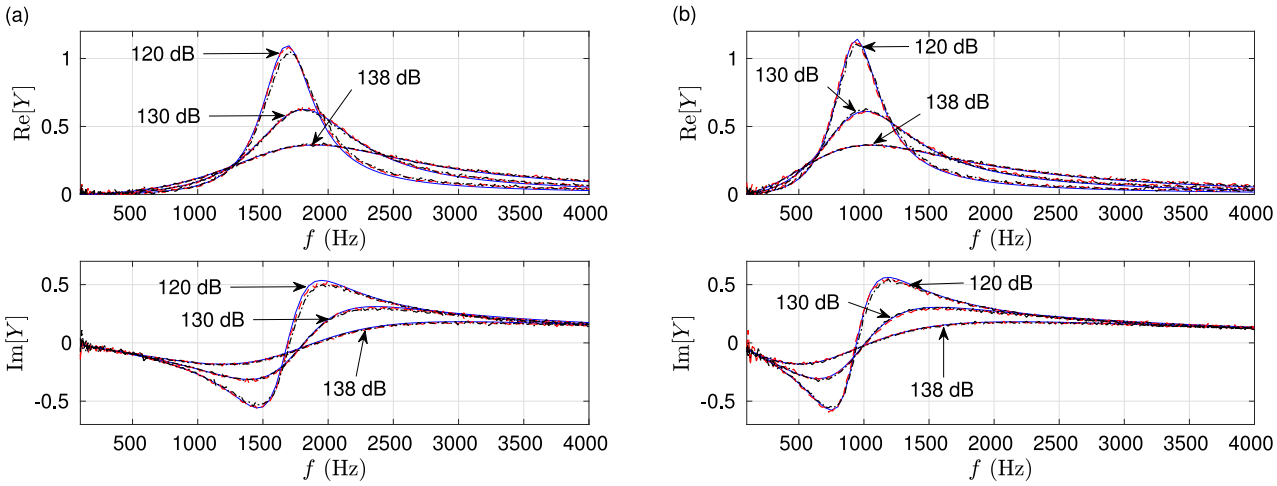

Fig. 10. Admittance for PP#1 absorber with a cavity depth of (a) $D = 10$ mm and (b) $D = 30$ mm: calculated with the analytical model in Eq. (3) (blue solid) and determined from the numerical solution using the IAP (red dashed) and the IA (black dash-dotted) methods. A broadband excitation is used.

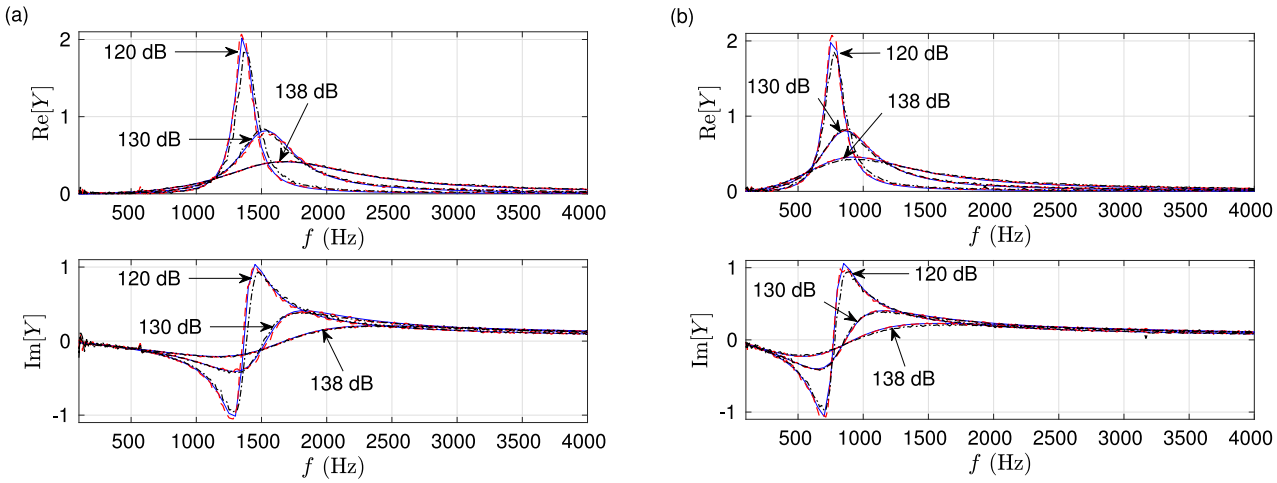

Fig. 11. Admittance for PP#3 absorber with a cavity depth of (a) $D = 10$ mm and (b) $D = 30$ mm: calculated with the analytical model in Eq. (3) (blue solid) and determined from the numerical solution using the IAP (red dashed) and the IA (black dash-dotted) methods. A broadband excitation is used.

4.2.2. Broadband excitation

In this section, the case of a broadband excitation is studied. A white noise filtered using a Butterworth bandpass filter with lower and upper cutoff frequencies of 200 Hz and 4000 Hz, respectively, is employed.

The admittance determined from the numerical solution using the two methods IA and IAP is shown in Figs. 10 and 11 for PP#1 and #3 with two cavity depths and for three incident SPL. The dependence of the surface admittance in the nonlinear regime with the characteristics of the incident signal can be first noticed by comparing these two figures with Figs. 8 and 9. Indeed, the surface admittance for the harmonic excitation is significantly different from that for the broadband excitation, despite that the incident SPL on the liner is the same. In particular, for PP#3 (Figs. 9 and 11), the admittance amplitude for the broadband excitation is almost two times larger than for the harmonic excitation.

Second, the analytical admittance in Eq. (3) is also plotted in Figs. 10 and 11. Here as well, the rms velocity in the perforations deduced from the numerical simulation is used for the calculation of the analytical admittance. As a reminder, v_{rms} is a single value for the broadband admittance spectrum. As an example, for PP#1 absorber with a cavity depth of 10 mm, v_{rms} is equal to 1.8, 5 and 9.6 m s^{-1} for incident SPL of 120, 130 and 138 dB, respectively. For the three incident sound pressure levels of 120, 130 and 138 dB, the predicted real and imaginary parts of the admittance are in good agreement with the analytical results for both PPs absorber with two cavity depths of 10 and 30 mm. The comparison is more favorable to the IAP method than to the IA method, which may be due to the low-order interpolation used in the IA method.

4.3. Experimental validation

As a last check, numerical results with the nonlinear TDABC are compared to experimental results.

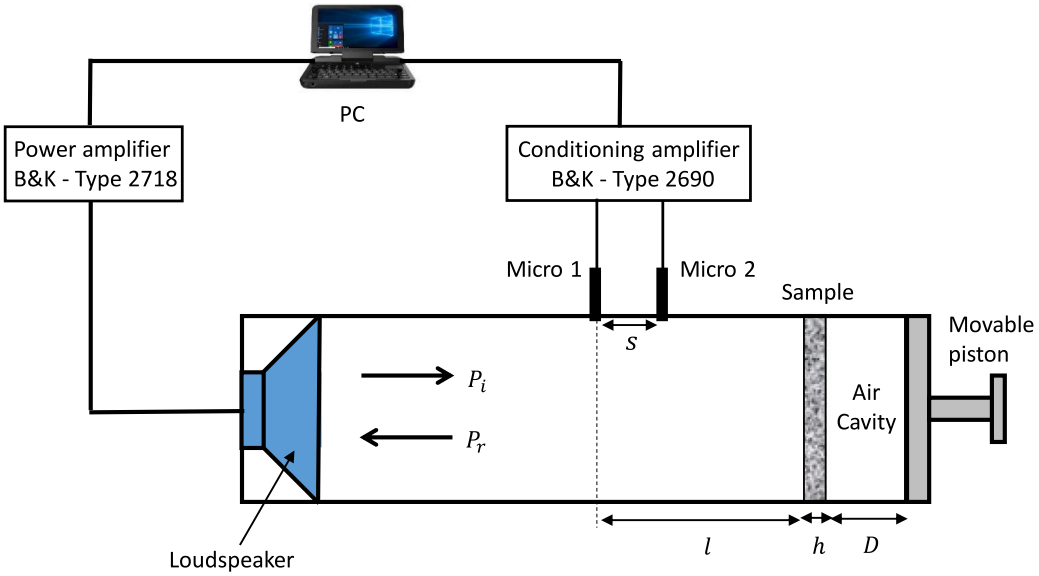

Fig. 12. Schematic diagram of the impedance tube for measuring the surface admittance of a sample by using the two-microphone transfer-function method.

The measurements were performed using a B&K Type 4206 impedance tube kit, as illustrated in Fig. 12. The tube has a circular cross-section, with an inner diameter of 3 cm, yielding a cut-off frequency around 6400 Hz. The sample plate is located at the right hand side of the tube. An air cavity of depth D is created behind the plate by a movable piston which is used as a rigid backing wall. Two sets of measurements were made, considering a harmonic excitation and a broadband excitation. For harmonic excitation, acoustic waves were generated by a loudspeaker mounted at the left hand side of the tube. For broadband excitation, the loudpspeaker of the impedance tube kit was replaced by a JBL 2447H compression driver. The acoustic sources were powered by a B&K power amplifier type 2718. Pressure signals were measured using two flush-mounted 1/4″ microphones (B&K type 4187), associated to two B&K type 2670 preamplifiers, a conditioning amplifier type 2690, and National Instrument 9250 front-end. An amplitude and phase calibration method was used to correct the transfer function between the two measurement channels.

The two-microphone method [37], as described in Section 4.1, was used to determine the surface impedance of the PP sample. The distance between the sample and the microphone 1 is $l = 55$ mm and the two microphones were separated by a distance $s = 20$ mm.

4.3.1. Harmonic excitation

The measurements were carried out for the three PP absorbers described in Section 2 using a harmonic excitation over a frequency range between 500 and 4000 Hz in steps of 50 Hz. Two levels of excitation, corresponding to two different gains of the power amplifier, were considered. In the first case, denoted as the low SPL case, the amplifier gain was set to ensure that the SPL inside the tube was sufficiently small to be in the linear regime, while maintaining a good signal-to-noise ratio for all frequencies. In the second case, denoted as the high SPL case, the amplifier gain was increased to its maximum, while ensuring negligible harmonic distortion.

In the literature, measurements to characterize perforated plates at high SPL are rather performed by keeping the same level of the incident wave on the plate (see, e.g., Refs. [12,38]), as done in the numerical experiments in Section 4.2.1. As we are mostly interested in validating the numerical model proposed in Section 3, this was not deemed necessary in this study.

A quantitative information on the acoustic excitation of the PP plate can be determined from the measurements. To do so, the acoustic pressure and velocity in the tube are expressed under the plane wave hypothesis as

$$P(x,\omega) = P_i(\omega)\mathrm{e}^{\mathrm{j}k_0 x} + P_r(\omega)\mathrm{e}^{-\mathrm{j}k_0 x} \qquad U(x,\omega) = \frac{1}{Z_0}\left[P_i(\omega)\mathrm{e}^{\mathrm{j}k_0 x} - P_r(\omega)\mathrm{e}^{-\mathrm{j}k_0 x}\right] \tag{28}$$

where P_i and P_r represent the amplitude of the incident and reflected pressure waves in the tube, respectively. They can be determined thanks to the two-microphone method, with the relations:

$$P_i = \mathrm{j}P(x_1)\frac{\mathrm{e}^{-\mathrm{j}k_0 x_2} - H_{12}\,\mathrm{e}^{-\mathrm{j}k_0 x_1}}{2\,\sin(k_0 s)} \qquad P_r = -\mathrm{j}P(x_1)\frac{\mathrm{e}^{\mathrm{j}k_0 x_2} - H_{12}\,\mathrm{e}^{\mathrm{j}k_0 x_1}}{2\,\sin(k_0 s)}. \tag{29}$$

Fig. 13 shows the amplitude of the incident wave $|P_i|$ for PP#1 absorber with a cavity depth of 30 mm as a function of the driving frequency for the low and the high SPL cases. Although it can be expected that the amplitude of the acoustic wave generated by the loudspeaker is constant over the entire frequency range, the amplitude of the incident wave greatly varies with the frequency. The incident pressure is maximal for some frequencies; this could be related to the resonant frequencies of the tube. For the low SPL case, $|P_i|$ is below 9 Pa for all frequencies corresponding to incident SPL below 110 dB. For the high SPL case, $|P_i|$ reaches a maximum of 122 Pa for $f = 2850$ Hz, corresponding to an incident SPL of about 133 dB.

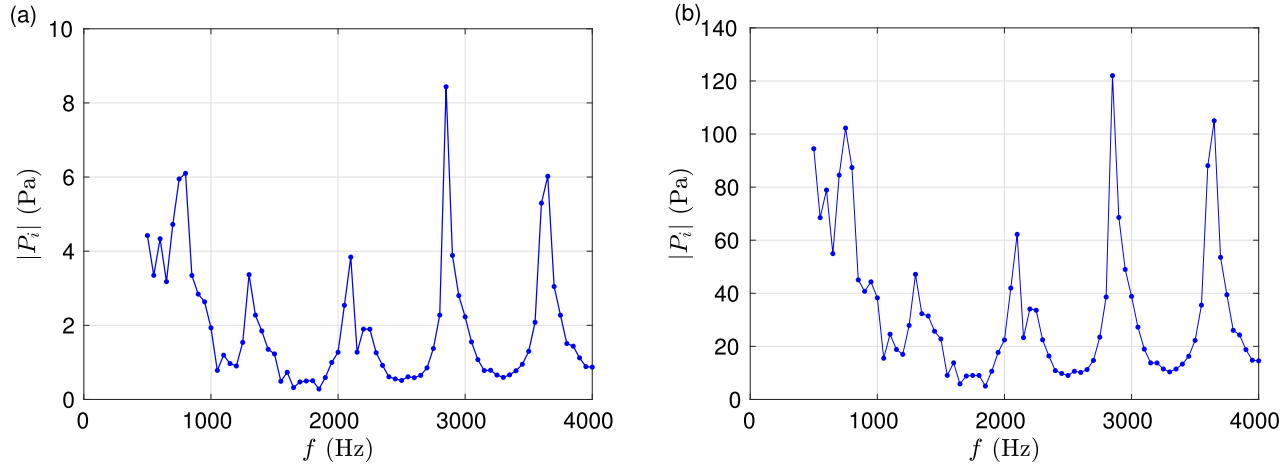

Fig. 13. Measured amplitude of the incident acoustic pressure for PP#1 absorber with a cavity depth of 30 mm for (a) low and (b) high SPL cases.

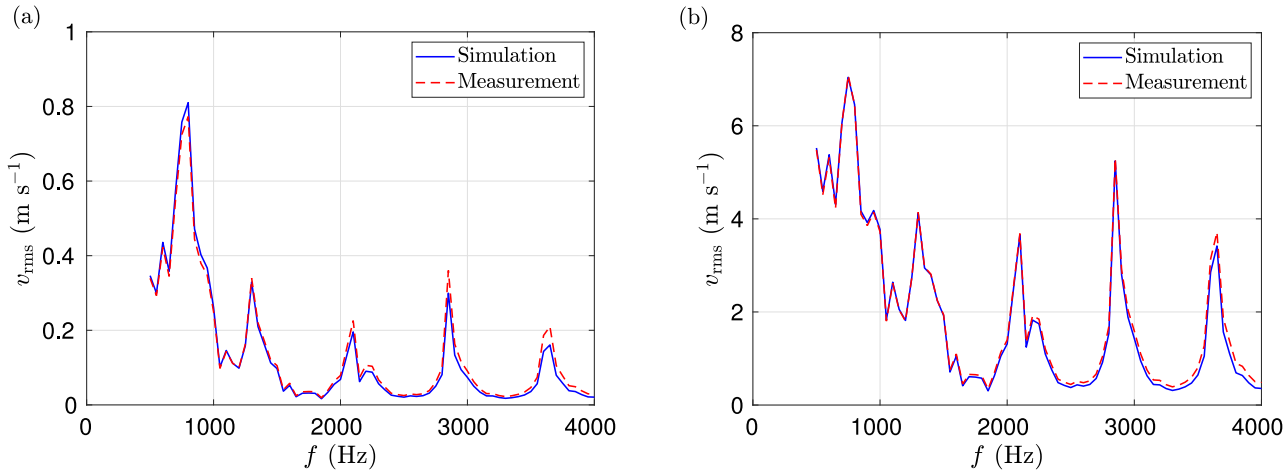

Fig. 14. Rms amplitude of the velocity in the perforations for a harmonic excitation determined from the experiments and from the numerical simulation for PP#1 absorber with a cavity depth of 30 mm for the (a) low and (b) high SPL cases.

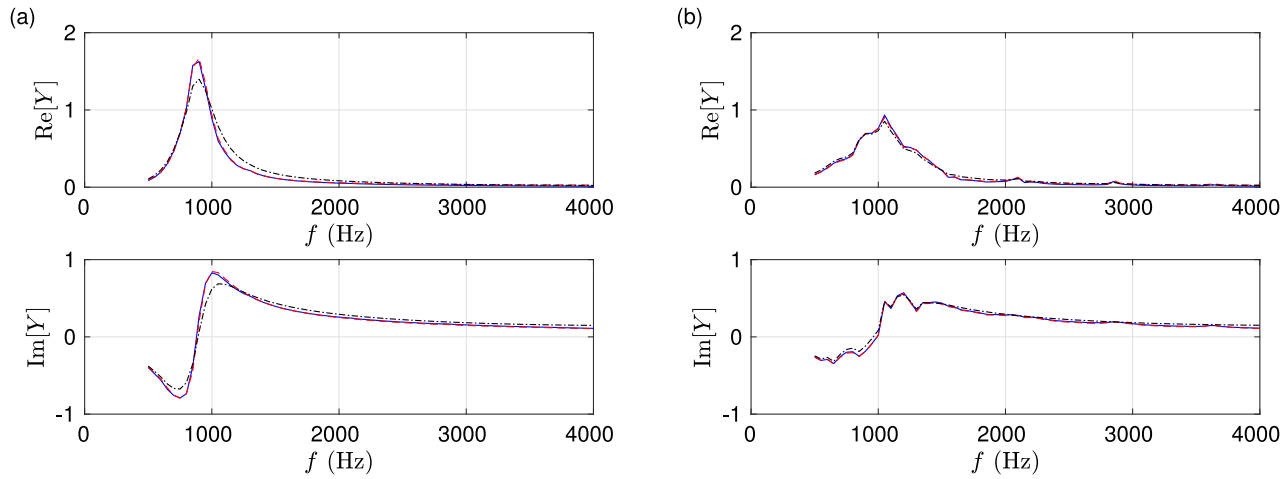

Fig. 15. Surface admittance of PP#1 absorber with a cavity depth of 30 mm for a harmonic excitation for the (a) low and (b) high SPL cases: measured (black dash-dotted) and determined from the analytical model in Eq. (3) (blue solid) and from the numerical solution (red dashed).

The numerical simulations are performed using the IAP method for the TDABC. In addition to the nonlinear surface admittance model of the PP liner, the amplitude of the incident wave has to be prescribed. It is set to the value determined in the experiments, i.e. $p_{i,\mathrm{rms}} = |P_i|/\sqrt{2}$.

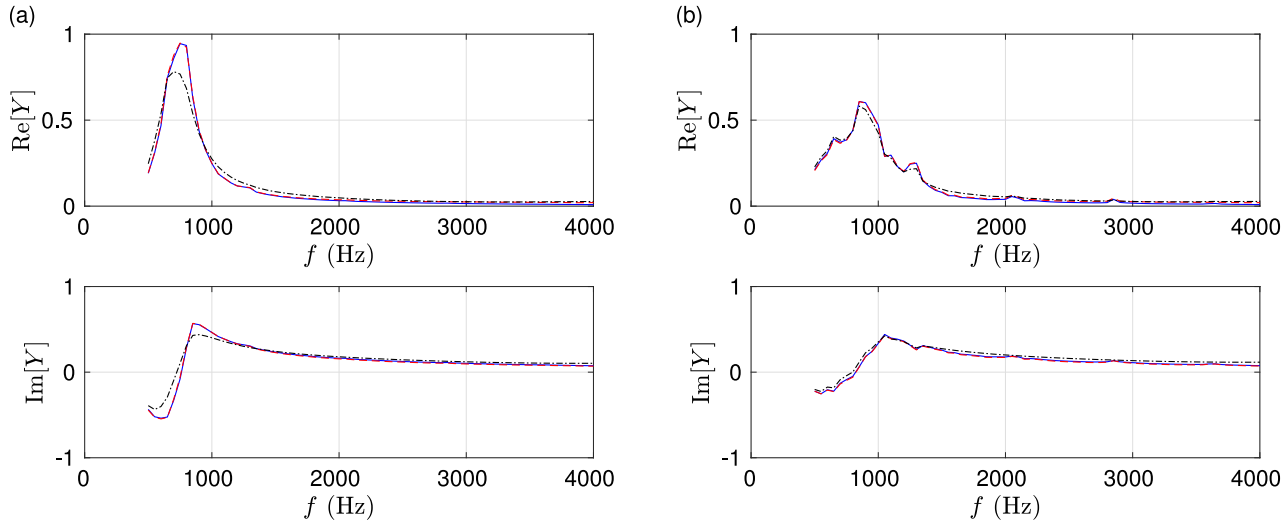

Fig. 16. Surface admittance of PP#2 absorber with a cavity depth of 30 mm for a harmonic excitation for the (a) low and (b) high SPL cases: measured (black dash-dotted) and determined from the analytical model in Eq. (3) (blue solid) and from the numerical solution (red dashed).

The comparison between the experimental and numerical results is now presented. The rms amplitude of the velocity in the perforations is shown in Fig. 14 both for the experiments and for the numerical solution and for PP#1 with a cavity depth of 30 mm. Note that the experimental value of v_{rms} is determined from the pressure measurements with the two microphones using Eq. (28), which yields $v_{\text{rms}} = |U(x = L)|/(\sqrt{2}\varphi)$. An excellent agreement is seen at both low and high SPL. In addition, the frequency of the peaks observed in Fig. 14 is in accordance with those of the incident pressure amplitude in Fig. 13.

The experimental admittances obtained for PP#1 and #2 are shown in Figs. 15 and 16, respectively, along with those determined from the numerical models for the two levels of excitation. Both are determined with the two-microphone method using Eq. (27). The analytical admittance obtained with the Laly model using the rms velocity in the perforations determined from the measurements is also plotted. A good agreement is obtained between the measurements and the numerical and analytical models, especially for the high SPL case. We can also note the difference in the real and imaginary parts of the admittance between the low and the high SPL cases, due to the nonlinear effect. In addition, the abrupt variations of the surface admittance observed for the high SPL case are due to the corresponding variations of the incident pressure with the frequency.

4.3.2. *Broadband excitation*

The measurements were repeated for the three PPs absorbers using a white noise signal as the excitation signal and for several levels of excitation. Results are exemplified below for PP#1 absorber with a cavity depth of 30 mm. The comparisons for PP#2 and PP#3 both with a cavity depth of 30 mm are shown in Appendix B.

Information on the incident pressure has to be obtained from the experiments for the numerical simulations. With this aim, the power spectral density of the incident pressure S_{ii} is calculated from those of the pressure at the two microphones based on Eq. (29). For comparison purpose, the power spectral density of the velocity in the perforations S_{vv} iss also calculated on the basis of Eq. (28). Only the part of the spectra below the tube cutoff frequency, i.e. for $f < 6400$ Hz, is considered. The power spectral densities are shown in Fig. 17. The spectrum of the incident pressure is not flat in the experiments, probably due to the resonances of the impedance tube, as already noticed for the harmonic excitation in Section 4.3.1. This is also the case for the spectrum of the velocity in the perforations. Note that the variations of S_{vv} with the frequency is slightly different from that of S_{ii}. The rms values of the incident pressure and velocity in the perforations are then estimated by integrating the corresponding power spectral density from 100 Hz up to 6400 Hz.

The numerical simulations are carried out using the IAP method for the TDABC. The incident pressure signal is a random signal, built so that its power spectral density is equal to the one measured. It induces in particular that the rms value of the incident pressure is the same in the simulations and in the experiments.

Fig. 18 shows the surface admittance determined from the measurements for three incident SPL: 76.4 dB in (a), corresponding to the linear regime, and 126.4 dB and 133.1 dB in (b) and (c), respectively, corresponding to the nonlinear regime. The variations of the surface admittance with the incident SPL are similar to those observed in Section 4.2.2: the amplitude of the real and imaginary parts of Y decreases and the peak of Re[Y] widens with the increase of the incident SPL. The surface admittance deduced from the numerical simulations is also plotted in Fig. 18. While the match is not perfect with the measurements, a close agreement is noted. In particular, the evolution of the admittance with the incident SPL is well reproduced. Finally, the analytical model in Eq. (3) is also represented using the rms velocity in the perforations determined from the numerical simulations as input.

As an additional comparison, the corresponding absorption coefficients α are plotted in Fig. 19 for the three incident SPL. The impact of the incident SPL on the measured absorption coefficient is noticeable: the absorption bandwidth broadens and the maximum of α reduces with the increase of the incident SPL. Some ripples are seen in Figs. 19(b) and (c) near 1800 Hz in the

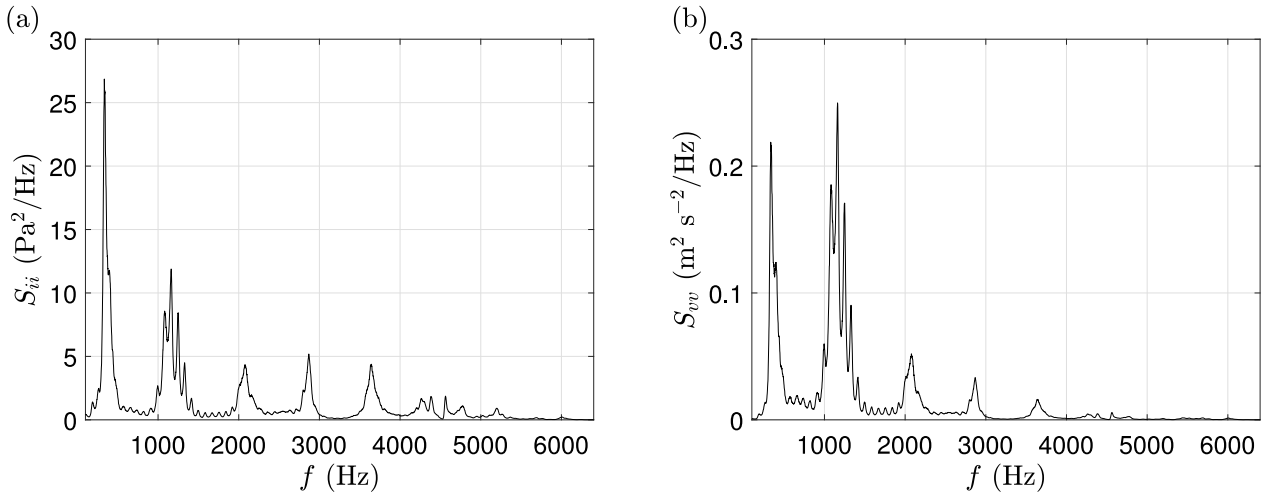

Fig. 17. One-sided power spectral densities of (a) the incident pressure and (b) the velocity in the perforations for PP#1 absorber with a cavity depth of 30 mm. A broadband excitation is used.

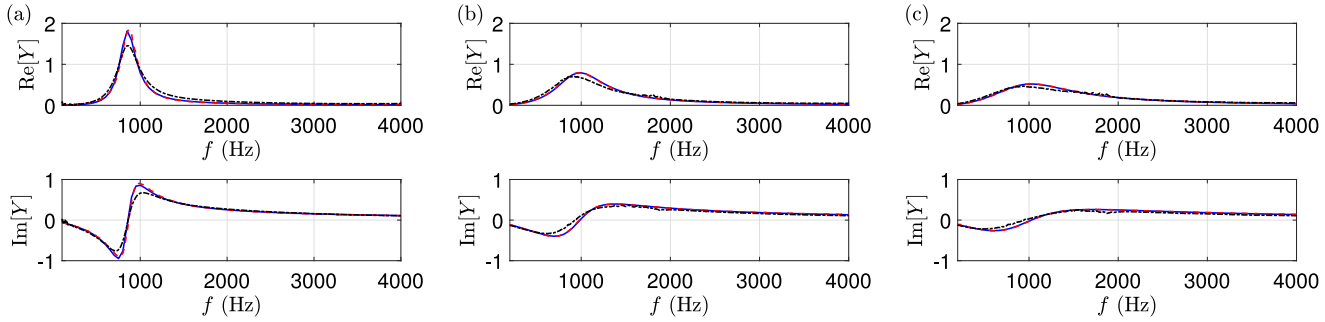

Fig. 18. Surface admittance of PP#1 absorber with a cavity depth of 30 mm for a broadband excitation and for three incident SPL (a) 76.4 dB, (b) 126.4 dB and (c) 133.1 dB: measured (black dash-dotted) and determined from the analytical model in Eq. (3) (blue solid) and from the numerical solution (red dashed).

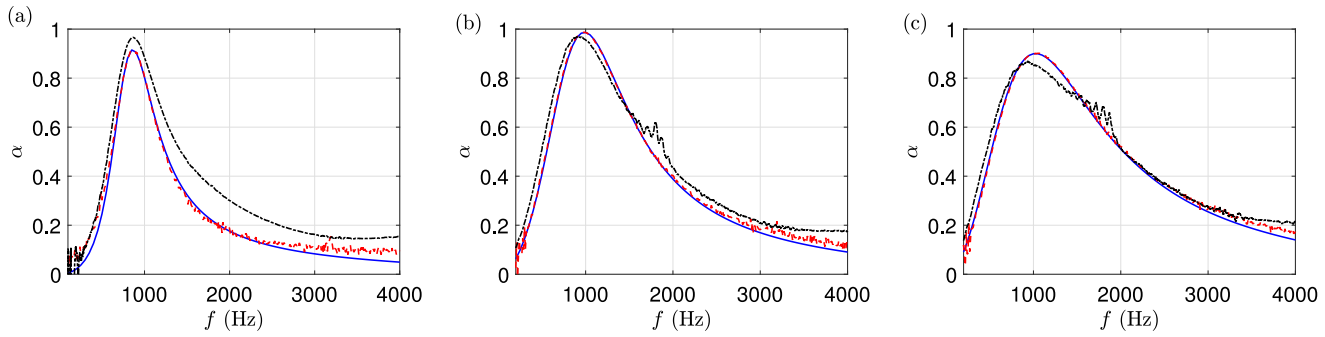

Fig. 19. Absorption coefficient of PP#1 absorber with a cavity depth of 30 mm for a broadband excitation and for three incident SPL (a) 76.4 dB, (b) 126.4 dB and (c) 133.1 dB: measured (black dash-dotted) and determined from the analytical model in Eq. (3) (blue solid) and from the numerical solution (red dashed).

Table 3
Rms amplitude of the velocity in the perforations for PP#1 absorber with a cavity depth of 30 mm for a broadband excitation: values deduced from the experiments and from the numerical simulations.

Incident SPL (dB)		76.4	86.2	96.7	106.0	116.2	126.4	133.1
v_{rms} (m s^{-1})	exp.	1.24×10^{-2}	3.69×10^{-2}	1.21×10^{-1}	3.56×10^{-1}	1.14	3.37	6.44
	num.	1.49×10^{-2}	4.86×10^{-2}	1.60×10^{-1}	4.54×10^{-1}	1.35	3.56	6.36

experimental curves; they are related to a lack of coherence due to low values of pressure at the microphones in this frequency range. The absorption coefficient determined from the numerical and analytical models are in good agreement with the measured one. While the curves of α are not superimposed, the numerical simulations capture especially the evolution of the absorption coefficient with the increase of the incident SPL.

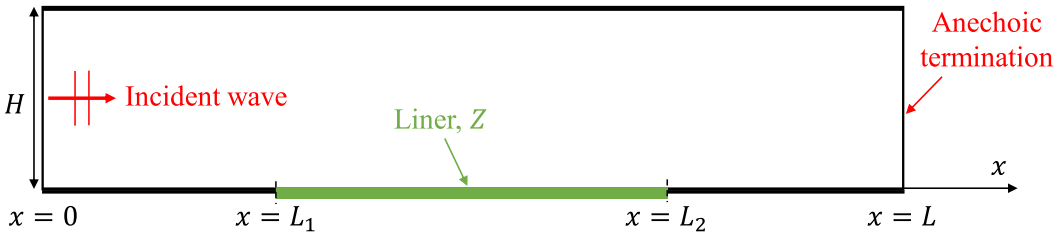

Fig. 20. Schematic of the 2D lined duct.

Finally, the rms amplitude of the velocity in the perforations deduced from the experiments and from the numerical simulations is reported in Table 3 for several incident SPL. It is observed that v_{rms} is noticeably well predicted from the numerical simulations.

5. Application to a 2D lined duct

This section is concerned with a two-dimensional (2D) lined duct, which is representative of industrial applications. The objectives are to evaluate the numerical model including the nonlinear TDABC in this situation as well as to analyze the impact of nonlinear TDABC on sound propagation and attenuation in a 2D lined duct. In particular, the nonlinear admittance model of PP liners depends on the velocity in the perforations. It is expected that this quantity varies significantly along the treatment and, as a consequence, that it is also the case for the surface admittance. Most of the existing methods for predicting sound propagation in a duct however consider a treatment with a uniform admittance. It is therefore worthwhile to investigate whether accounting for the spatial variations of the admittance at high excitation level is important for predicting the transmission loss in a lined duct.

5.1. Numerical configuration

A 2D lined duct of size $L \times H = 0.812$ m$\times$ 0.0508 m is considered, as shown in Fig. 20. The liner of length 0.406 m is located on the duct lower wall from $x = L_1 = 0.203$ m to $x = L_2 = 0.609$ m. The other duct walls are rigid. This geometry corresponds to that of the Grazing Incidence Tube of NASA (see, e.g., Ref. [39]), which is one of the well-known duct facility for evaluating liner efficiency. There is no flow and the sound speed and air density are constant.

All the results presented in this section are obtained for the PP#1 absorber with a cavity depth of 10 mm. The frequency range of interest is between 200 Hz and 3000 Hz, which respects the cut-off frequency (around 3.35 kHz) of the duct. Two types of incident pressure waveforms, i.e. harmonic and broadband, are considered. The broadband signal is obtained by filtering a white noise signal using a Butterworth bandpass filter with lower and upper cutoff frequencies set to 200 Hz and 3000 Hz, respectively.

The 2D LEEs are solved using the numerical methods presented for the 1D case in Section 3.2. At the boundary $x = 0$, an incident plane wave propagating along the x-direction is generated using the method of characteristics, as described in Section 3.2. At $x = L$, a non-reflecting boundary condition is applied, using also the method of characteristics: the idea is the same, except that the incoming characteristic variable into the computational domain at the interface is set to zero so that no reflected waves are generated at the boundary. Finally, the normal velocity is set to zero on the duct rigid walls and the TDABC is applied along the lined section using the interpolation of the admittance parameters (IAP) approach presented in Section 3.4.2.

The mesh is uniform in the x-direction with a size $\Delta x = 1.1\times10^{-3}$ m. Along the z-direction, the mesh size is progressively reduced towards the liner walls with a stretching factor of 0.99. It is equal to $\Delta z = 1.1\times10^{-3}$ m at the duct axis and $\Delta z = 8.19\times10^{-4}$ m on the walls. The time step is set to $\Delta t = 2\times10^{-6}$ s, which yields a CFL number of 0.84. The total simulation time is 0.02 s for the harmonic excitation. It is increased to 0.35 s for the broadband excitation to get a longer signal in order to improve spectral resolution.

5.2. Harmonic excitation

5.2.1. Effect of the incident SPL

Results are first considered for several incident SPL and for a driving frequency of 1600 Hz, which is close to the resonant frequency of the liner. The contours of the SPL are depicted in Fig. 21 for four incident SPL. The reference for the SPL calculation is chosen here as the rms amplitude of the incident wave to ease the comparison between the results. The SPL maps are globally similar in the rigid section for $x < L_1$. For the incident SPL of 120 and 130 dB, differences from the case of an incident SPL equal to 80 dB can already be seen. The isolines above the liner are noticeably modified, especially the slope on the liner. The SPL in the exit section ($x > L_2$) also depends on the incident SPL. Finally, for the largest incident SPL of 140 dB, strong alteration of the SPL map is observed.

In order to analyze the evolution of the acoustic field with the incident SPL, the properties of the liner are investigated. Fig. 22 shows the variation of the rms velocity in the perforations along the liner for three incident SPL of 120, 130 and 140 dB. The effect of the liner is reflected by the reduction of v_{rms} along the liner. It decreases almost linearly for the incident SPL of 130 and 140 dB. For 120 dB, it decreases also linearly at the beginning of the liner but less rapidly from $x = 0.4$ m.

The corresponding spatial variation of the surface impedance is depicted in Fig. 23 for four incident SPL. For the smallest incident SPL (80 dB), the real and imaginary parts of the impedance are constant along the liner and equal to the values in the linear regime.

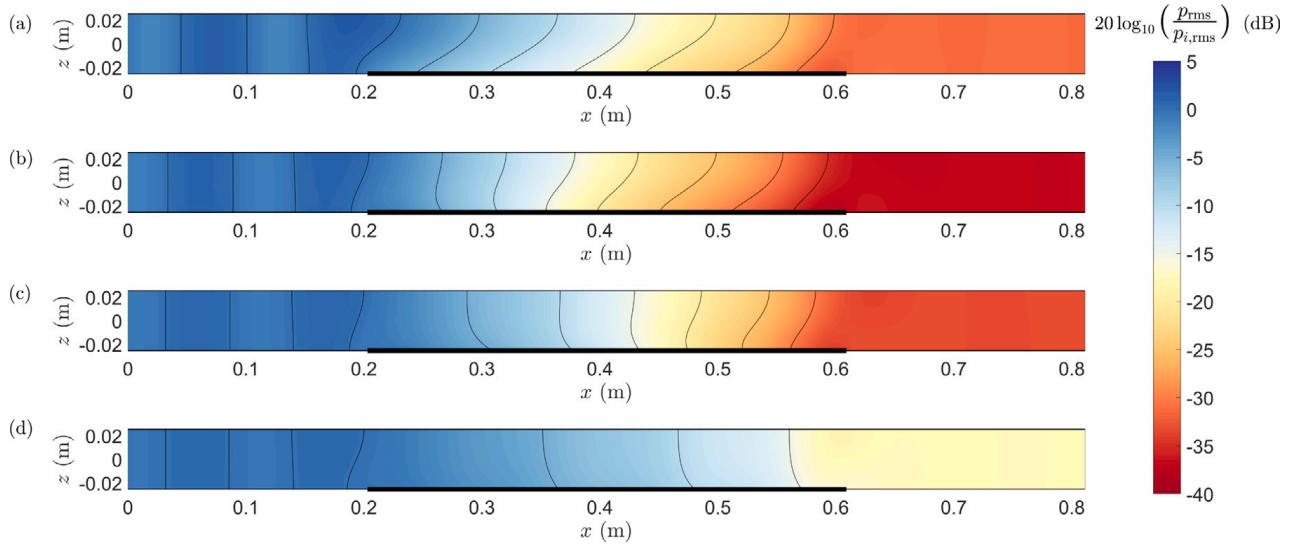

Fig. 21. SPL ($20\log_{10}(p_{\mathrm{rms}}/p_{i,\mathrm{rms}})$) in dB for an incident SPL of: (a) 80 dB, (b) 120 dB, (c) 130 dB and (d) 140 dB with a harmonic excitation at $f = 1600$ Hz. The liner location is indicated by the black thick horizontal line. Isolines are plotted every 5 dB in black lines.

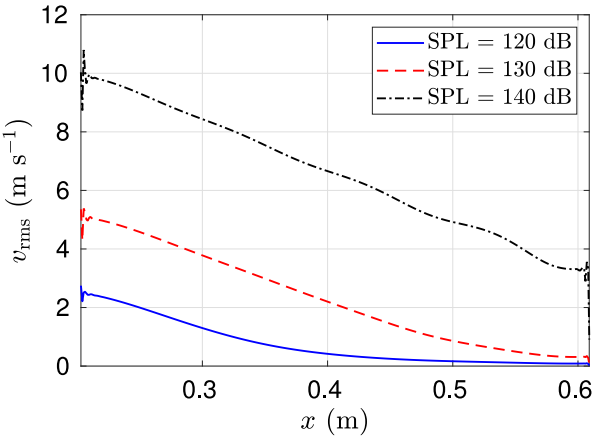

Fig. 22. Variation along the liner of the rms velocity for three incident SPL of 120, 130 and 140 dB with a harmonic excitation at $f = 1600$ Hz.

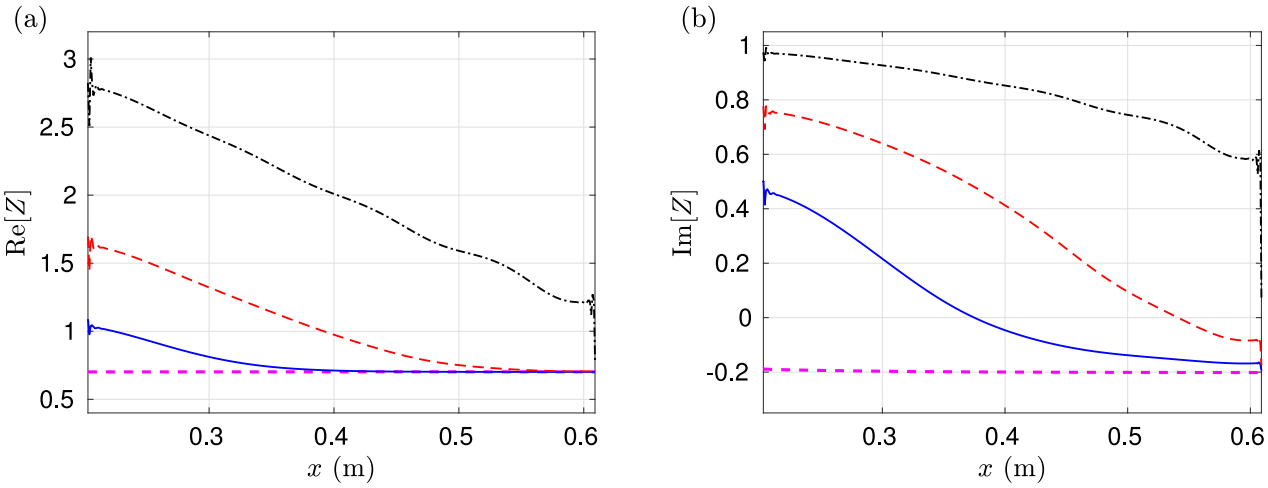

Fig. 23. Variation along the liner of the real (a) and imaginary (b) parts of the impedance for four incident SPL of 80 dB (magenta dashed lines), 120 dB (blue solid lines), 130 dB (red dashed lines) and 140 dB (black dashed–dotted lines) with a harmonic excitation at $f = 1600$ Hz. (For interpretation of the references to color in this figure legend, the reader is referred to the web version of this article.)

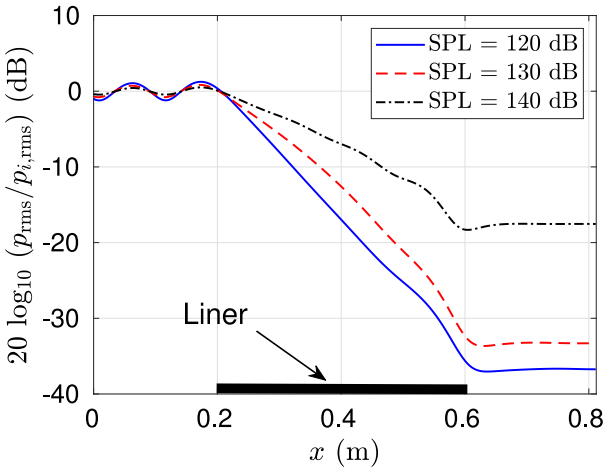

Fig. 24. Variation along the wall opposite to the liner of the SPL for three incident SPL of 120, 130 and 140 dB with a harmonic excitation at $f = 1600$ Hz.

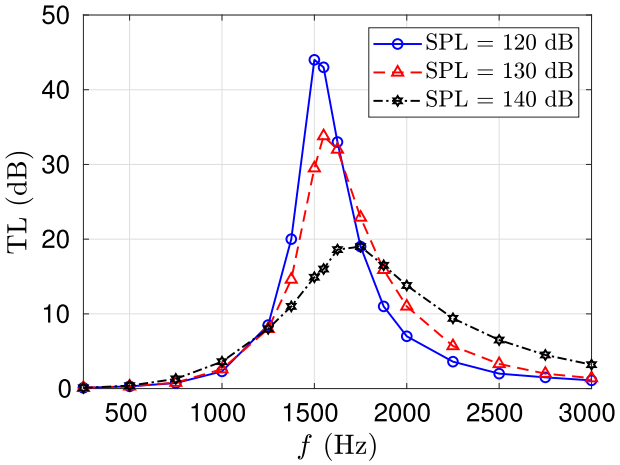

Fig. 25. Transmission loss versus frequency for a harmonic excitation with incident SPL of 120, 130 and 140 dB.

As the SPL increases, large spatial variations of the impedance are noticed. In more details, the impedance is seen to vary at the beginning of the liner before reaching almost the impedance value in the linear regime. Thus, the resistance is almost equal to that in the linear regime from $x = 0.4$ m for an incident SPL of 120 dB and from $x = 0.55$ m for an incident SPL of 130 dB. For the largest SPL (140 dB), this is however not the case and the impedance remains different from that in the linear regime along the whole liner. The spatial variations of the impedance echo the recent studies of Lafont et al. [40] and Chen et al. [41], in which impedance eduction of PP liners in high SPL environments was performed from measurements or numerical simulations. In order to improve comparisons with the reference results, a spatially-varying impedance function (linear or piecewise linear) was used. This was also discussed in detail by Roncen et al. [16]. The authors proposed an iterative strategy based on a frequency-domain solver of the linearized Euler equations for two objectives: first, for prediction of the acoustic field in a duct lined with a perforate plane liner accounting for the spatial variations of the surface impedance and second, for eduction of a spatially-varying surface impedance at high excitation level from measurements.

The evolution of the SPL along the wall opposite to the liner is plotted in Fig. 24 for three incident SPL. It is seen that the SPL varies in a similar manner for the three incident SPL: it is approximately constant in the rigid sections and decreases almost linearly in the lined section. The attenuation due to the liner however depends significantly on the incident SPL: it is quite similar for incident SPL of 120 dB and 130 dB, with a value of 36 dB and 33 dB, respectively, but suffers a dramatic reduction to 18 dB for an incident SPL of 140 dB.

In order to characterize the variation of the attenuation with the driving frequency, the transmission loss (TL) is determined from the numerical solution. The plane wave mode is the only propagating mode in the rigid sections, as the driving frequencies are below the duct cutoff frequency. Thus, the transmission loss can be calculated with:

$$\mathrm{TL} = 20 \log_{10} \left(\frac{p_{i,\mathrm{rms}}}{p_{t,\mathrm{rms}}} \right) \tag{30}$$

where $p_{t,\mathrm{rms}}$ is the rms value of the transmitted wave amplitude in the exit section. As an anechoic termination is considered, $p_{t,\mathrm{rms}}$ is simply calculated from the acoustic pressure at a point sufficiently far from the liner. The transmission loss is shown for three

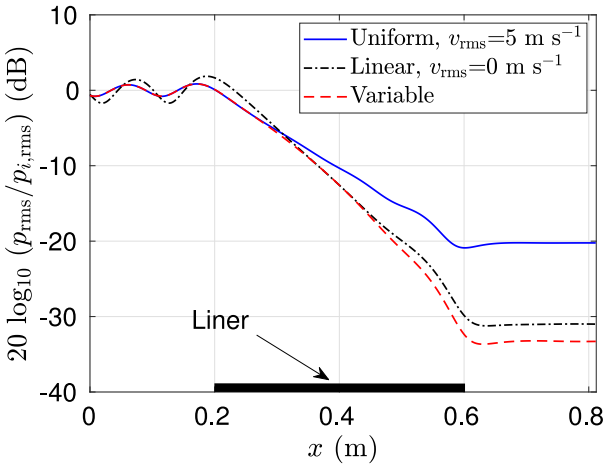

Fig. 26. Variation along the wall opposite to the liner of the SPL for an incident SPL of 130 dB with a harmonic excitation at $f = 1600$ Hz: spatially variable admittance (red dashed line), linear admittance (black dashed–dotted line) and spatially uniform admittance with $v_{\rm rms} = 5$ m s^{-1} (blue solid line).

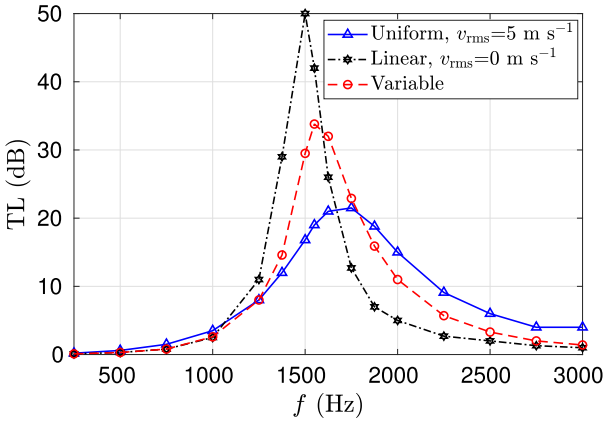

Fig. 27. Comparison of the transmission loss for an incident SPL of 130 dB between three cases: spatially variable admittance (red), linear admittance (black) and spatially uniform admittance with $v_{\rm rms} = 5$ m s^{-1} (blue).

incident SPL in Fig. 25. It is seen that increasing the incident SPL tends to widen the TL peak and reduce its amplitude. The TL peak is observed near the resonant frequency of the liner and is shifted towards higher frequencies with the increase of the incident SPL. Note that the TL peak is not at the resonant frequency of the liner because the optimal impedance at grazing incidence and for a liner of finite length is not equal to that at normal incidence.

5.2.2. Influence of the impedance spatial variation

An additional study is performed to investigate more precisely the influence of the impedance modeling on the prediction of sound propagation and attenuation in a lined duct under high level of excitation. To do so, three models of the liner are considered: first, the reference model with a spatially-varying nonlinear impedance model that accounts for the variation of $v_{\rm rms}$ along the liner, i.e. $Z_{\rm NL}[\omega, v_{\rm rms}(x)]$, second, a uniform impedance model using the nonlinear impedance model but for a constant and representative value of $v_{\rm rms}$ and third, the linear impedance model. Simulations are performed for an incident SPL of 130 dB.

The SPL variation along the wall opposite to the liner is depicted in Fig. 26 for a frequency of 1600 Hz and for the three liner models. Note that as the rms velocity in the perforations is about 5 m s^{-1} at the beginning in the liner for this frequency and for the incident SPL of 130 dB using the nonlinear impedance model (see Fig. 22), this value was chosen to determine the impedance in the uniform case. It is seen that the SPL prediction is significantly different for the three liner models. In particular, the SPL for a uniform impedance with $v_{\rm rms} = 5$ m s^{-1} is superimposed with that for a spatially-varying impedance for $x < 0.3$ m but is then substantially smaller. The results for the linear model differ from those with the nonlinear model but a better estimation is obtained in the exit section than with the uniform case for this particular frequency and incident SPL.

Fig. 27 shows the transmission loss as a function of the frequency for the three liner models. The effect of the SPL on the transmission loss, shown in Fig. 25 discussed in Section 5.2.1, is here observed by comparing the TL between the linear and nonlinear impedance model: the TL peak is wider and shifted towards high frequencies and its amplitude is reduced for the nonlinear impedance model compared to the linear one. In addition, the TL determined for the spatially-varying impedance model and for the uniform impedance model dramatically differs; assuming a uniform impedance leads to an under-prediction of the TL peak amplitude and an over-prediction of the peak width and of the frequency at the peak.

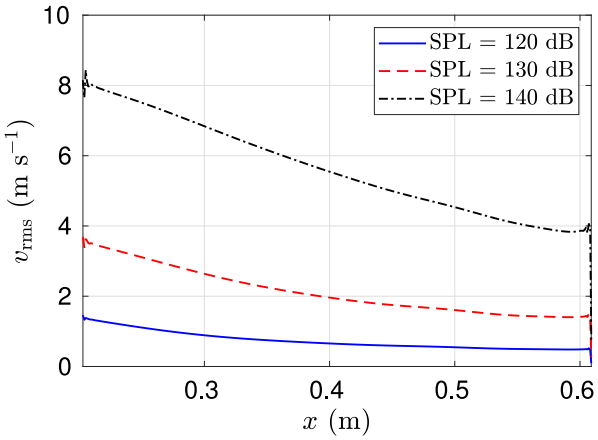

Fig. 28. Variation along the liner of the rms velocity for three incident SPL of 120, 130 and 140 dB with a broadband excitation.

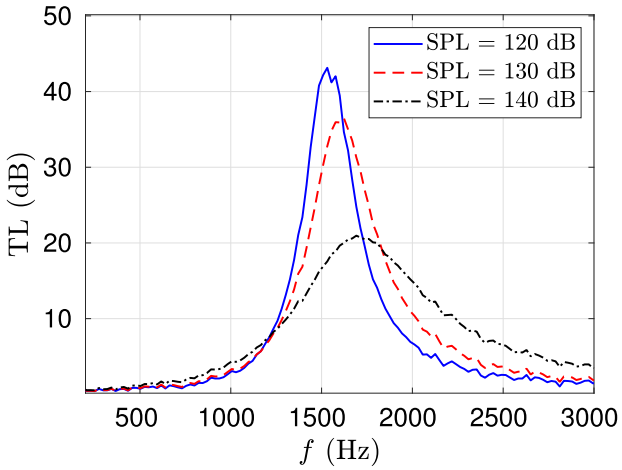

Fig. 29. Transmission loss versus frequency for a broadband excitation with incident SPL of 120, 130 and 140 dB.

Two conclusions can be drawn from this example. First, neglecting nonlinear effects on the response of a perforated plate can lead to a dramatic error on the prediction of the liner attenuation. Second, the spatial variations of the parameter governing the nonlinear effect on the liner impedance (here v_{rms}) should be taken into account for an accurate modeling of the liner acoustic properties and that assuming a constant value for the impedance at high SPL might be a rough approximation.

5.3. Broadband excitation

Finally, the case of an incident broadband signal is considered for different incident SPL.

The rms amplitude of the velocity in the perforations is plotted along the liner in Fig. 28. Compared to the harmonic excitation at $f = 1600$ Hz for the same incident SPL in Fig. 22, v_{rms} is in the same order of magnitude and similarly reduces along the liner. However, it decreases at a lower rate and its value at the beginning of the liner is smaller. For this given liner length, v_{rms} for the broadband excitation is thus smaller than that for the harmonic excitation in the first part of the lined section and larger in the second part.

Fig. 29 shows the transmission loss in the case of the broadband signal. It is determined with:

$$\mathrm{TL} = 10 \log_{10} \left(\frac{S_{ii}}{S_{tt}} \right) \tag{31}$$

where S_{ii} and S_{tt} are the power spectral densities of the incident and transmitted pressure signal, respectively. The evolution of the TL for the broadband excitation is similar to that observed for the harmonic excitation in Fig. 25. Actually, the TL for PP#1 and for the three incident SPL are, remarkably, almost identical for both types of excitation: thus, the width and amplitude of the TL peak is similar and it is observed near the same frequencies. While this should be the case in the linear regime, it is seen that, for this particular liner, the liner attenuation does not depend significantly on the type of excitation. Some differences in the TL can however be noticed. For example, the TL at $f = 1600$ Hz for an incident SPL of 130 dB is equal to 32 dB for a harmonic excitation but to 36 dB for the broadband excitation. In addition, the maximum of TL is observed near a frequency of 1600 Hz for the broadband excitation but near 1550 Hz for a harmonic excitation.

A thorough analysis of the difference in the acoustic propagation along a lined duct depending on the type of excitation remains to be done and can be the subject of future research.

6. Conclusion

Time-domain admittance boundary conditions in the nonlinear regime were investigated to model the acoustic behavior of liners under a high excitation level. A particular focus was brought on perforated plate liners. The nonlinear model of Laly et al. [12] was employed for that. It accounts for the variation of the surface admittance with the frequency and the rms velocity in the perforation.

Two extensions of the TDABC proposed by Troian et al. [24] in the linear regime were considered. They are both based on a multipole model, so that the TDABC can be evaluated by integrating ODEs. The variation of the surface admittance with the rms velocity is dealt with by interpolation from a set of reference values. They however differ on the interpolation process. The first nonlinear TDABC, referred to as the IA method and proposed by Shur et al. [26], is based on the direct interpolation of the admittance. The IA method thus requires to determine a multipole approximation of the surface admittance model for each reference value; the number of poles of the corresponding nonlinear multipole model is therefore considerably larger than the linear counterpart. In the second nonlinear TDABC, called the IAP method, interpolation of the multipole function coefficients is preferred. This allows for a large reduction in the number of poles compared to the IA method.

The two methods were implemented in a finite-difference time-domain solver of the linearized Euler equations. Numerical experiments and comparisons with measurements on an impedance tube configuration were performed for validation and evaluation purposes. Three PP liners were considered for a harmonic and a broadband excitation. It was shown that the IA and IAP methods allow both for an accurate and efficient representation of the surface admittance in the nonlinear regime. Depending on the situation, one of the two methods is preferable. When considering analytical models for which the admittance varies smoothly with the frequency, a multipole function with only two poles is sufficient to accurately represent the admittance. Since the IAP has the smallest computational cost (because of the smallest number of poles), it may be preferred over the IA method in this case. When considering experimental admittance data, the multipole representation may require a significantly larger (5 to 8) number of poles in order to achieve acceptable accuracy. With such number of poles, the IAP approach may well become inaccurate because of the high sensitivity of the multipole function to the location of the poles and may lead to non-physical results, such a negative resistance over a given frequency band. Furthermore, the admittance approximation with a decent accuracy may require using different number of poles for different reference values of v_{rms}; this is not possible with the current formulation of the IAP method. For such cases, the IA method may be superior.

Finally, the proposed TDABC was applied to sound propagation along a 2D lined duct under high level of excitation. It was exemplified that the spatial variations of the surface impedance are significant near the resonant frequency of the liner and has to be taken into account for an accurate prediction of liner attenuation at high SPL.

There are several ways to pursue this study. The simulations have been restricted to a medium at rest. Future work will consider the effect of a mean flow. Besides, along impedance tube measurements, it will be interesting to have a detailed acoustic database on a duct lined with a PP absorber for benchmarking. In addition, the concept of optimal impedance has been developed for a lined duct with a uniform impedance. It should be extended to the case of a spatially-varying impedance to be applicable to perforated liners at high level of excitation. Finally, a methodology to account for extended-reacting liners in time-domain simulations has been recently proposed in Alomar et al. [42]. In particular, perforated liners with a back cavity were considered by modeling the perforated plate by an impedance jump. Following the nonlinear TDABC investigated in this paper, it would be also possible to extend this methodology for perforated liners in the nonlinear regime.

CRediT authorship contribution statement

Daher Diab: Conceptualization, Methodology, Validation, Experiments, Investigation, Writing – original draft, Writing – review & editing. **Didier Dragna:** Conceptualization, Methodology, Writing – original draft, Formal analysis. **Edouard Salze:** Conceptualization, Methodology, Validation, Experiments, Investigation. **Marie-Annick Galland:** Conceptualization, Methodology, Writing – review & editing, Supervision, Funding acquisition.

Declaration of competing interest

The authors declare that they have no known competing financial interests or personal relationships that could have appeared to influence the work reported in this paper.

Acknowledgments

This work was performed within the framework of the Labex CeLyA of the University of Lyon, within the program "Investissements d'Avenir" (ANR-10-LABX-0060/ANR-16-IDEX-0005) operated by the French National Research Agency. This project has received funding from the Clean Sky 2 Joint Undertaking under the European Union's Horizon 2020 research and innovation program under grant agreement N° 821093 (SALUTE). This publication reflects only the author's view and the JU is not responsible for any use that may be made of the information it contains.

Table A.4
Poles and coefficients of the multipole model for the interpolation of the admittance (IA) method.

PP#1, Cavity depth of 10 mm						
Reference rms velocity (m s^{-1})	2	4	6	8	10	12
Re[A_1]	1.680e+03	1.840e+03	1.962e+03	2.035e+03	2.085e+03	2.129e+03
Im[A_1]	2.827e+02	4.331e+02	6.624e+02	9.044e+02	1.162e+03	1.532e+03
Re[λ_1] (s^{-1})	1.609e+03	2.504e+03	3.675e+03	4.770e+03	5.795e+03	7.029e+03
Im[λ_1] (s^{-1})	−1.054e+04	−1.091e+04	−1.096e+04	−1.076e+04	−1.041e+04	−9.776e+03
Y_∞	4.0492e−03	1.7636e−03	7.288e−04	3.7514e−04	2.231e−04	1.315e−04
PP#1, Cavity depth of 30 mm						
Reference rms velocity (m s^{-1})	2	4	6	8	10	12
Re[A_1]	1.552e+03	1.700e+03	1.803e+03	1.861e+03	1.900e+03	1.933e+03
Im[A_1]	3.983e+02	6.782e+02	1.115e+03	1.675e+03	2.547e+03	6.661e+03
Re[λ_1] (s^{-1})	1.418e+03	2.290e+03	3.369e+03	4.359e+03	5.280e+03	6.382e+03
Im[λ_1] (s^{-1})	−5.771e+03	−5.792e+03	−5.460e+03	−4.849e+03	−3.940e+03	−1.852e+03
Y_∞	4.949e−03	1.723e−03	6.431e−04	3.223e−04	1.921e−04	1.154e−04

Table A.5
Constants of the rational functions used for the coefficients of the multipole model with the interpolation of the admittance parameters (IAP) method.

PP#1, Cavity depth of 10 mm					
X	Re[A_1]	Im[A_1]	Re[λ_1] (s^{-1})	Im[λ_1] (s^{-1})	Y_∞
a	1.430e+03	1.965e+02	9.911e+02	−9.678e+03	2.379e−04
b	5.176e+02	3.294e+01	3.717e+02	−1.054e+03	−5.229e−03
c	1.033e+02	9.665e+00	1.853e+02	4.519e+01	4.199e−02
d	2.746e−01	2.404e−02	2.785e−01	5.174e−02	5.924e−01
e	4.354e−02	9.060e−08	1.431e−03	3.785e−08	3.499e+00
PP#1, Cavity depth of 30 mm					
X	Re[A_1]	Im[A_1]	Re[λ_1] (s^{-1})	Im[λ_1] (s^{-1})	Y_∞
a	1.308e+03	1.738e+02	7.187e+02	−5.398e+03	1.310e−02
b	8.897e+02	8.252e+01	4.897e+02	1.402e+01	−1.615e−03
c	3.224e+02	−6.832e+00	2.652e+02	2.951e+01	7.271e−05
d	6.127e−01	−1.235e−01	4.883e−01	−3.844e−02	5.355e−02
e	1.517e−01	3.524e−03	8.734e−04	3.995e−09	2.183e−01

Appendix A. Coefficients of the nonlinear TDABC

This appendix provides the coefficients of the nonlinear TDABC for the PP#1 absorber with two cavity depths 10 and 30 mm. The Laly model for this liner is approximated by a single pair of complex conjugate poles λ_1 and $\lambda_2 = \lambda_1^*$, with $A_2 = A_1^*$ over the range of velocities in the perforations considered in this paper.

For the interpolation of the admittance (IA) method, the poles and the coefficients of the multipole model (see Eq. (13)) are given for the different reference values of the rms velocity in the perforations in Table A.4.

For the interpolation of the admittance parameters (IAP) method, the poles and the coefficients (see Eq. (22)) are approximated by a rational function with quadratic polynomials, that can be written as follows:

$$X(v_{\text{rms}}) = \frac{a + b\, v_{\text{rms}} + c\, v_{\text{rms}}^2}{1 + d\, v_{\text{rms}} + e\, v_{\text{rms}}^2}. \tag{A.1}$$

The constants a, b, c, d and e are given for each coefficient of the multipole model in Table A.5.

Appendix B. Additional comparisons with impedance tube experiments for broadband excitation

In this appendix, additional comparisons between the impedance tube measurements for a broadband excitation and corresponding numerical results are presented. The experimental set-up is described in Section 4.3 and the procedure used for the numerical simulations is detailed in Section 4.3.2.

Fig. B.30 shows the surface admittance and the absorption coefficient for PP#2 with a cavity depth of 30 mm and for three incident sound pressure levels. The experimental results are qualitatively similar to those obtained for PP#1 in Figs. 18 and 19. The increase of the incident sound pressure level leads to a flattening of the admittance curves and a reduction and a broadening of the absorption peak. The results obtained with the numerical simulations do not match exactly the experimental curves, but the evolution of the admittance and the absorption coefficient with the incident SPL is correctly reproduced. Note also that the numerical results provide a close agreement with the analytical model.

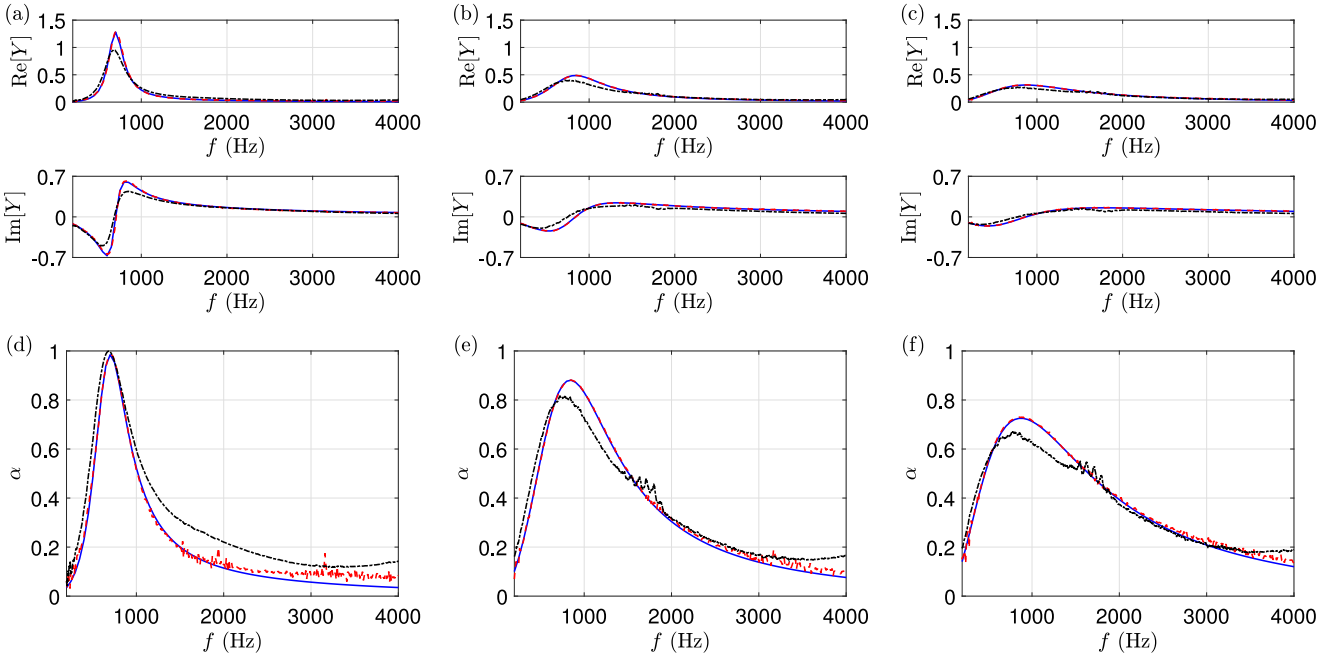

Fig. B.30. (top) Surface admittance and (bottom) absorption coefficient of PP#2 absorber with a cavity depth of 30 mm for a broadband excitation and for three incident SPL (a)–(d) 76.8 dB, (b)–(e) 126.5 dB and (c)–(f) 133.4 dB: measured (black dash-dotted) and determined from the analytical model in Eq. (3) (blue solid) and from the numerical solution (red dashed).

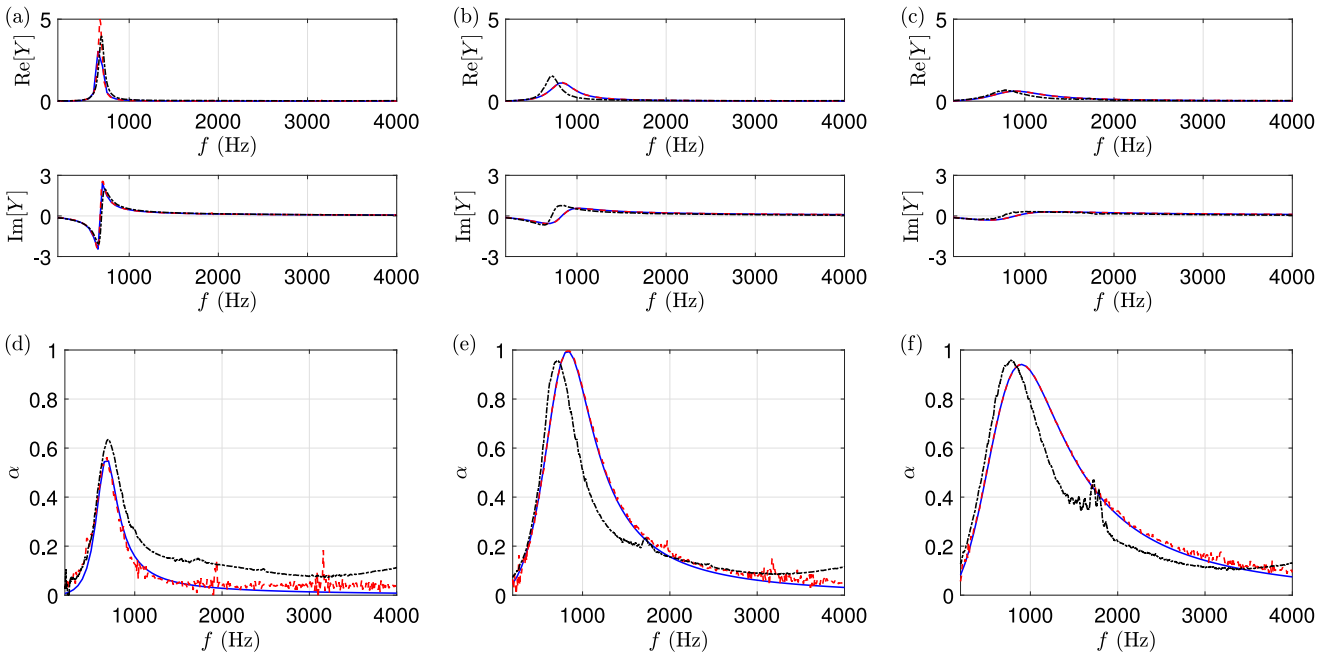

Fig. B.31. (top) Surface admittance and (bottom) absorption coefficient of PP#3 absorber with a cavity depth of 30 mm for a broadband excitation and for three incident SPL (a)–(d) 76.6 dB, (b)–(e) 125.3 dB and (c)–(f) 133.5 dB: measured (black dash-dotted) and determined from the analytical model in Eq. (3) (blue solid) and from the numerical solution (red dashed).

Corresponding results for PP#3 with a cavity depth of 30 mm are plotted in Fig. B.31. In this case also, the experimental admittance curves tends to flatten with the increase of the incident SPL. Nevertheless, the absorption coefficient behaves differently. The absorption coefficient significantly rises with the increase of the incident SPL from 76.6 dB to 125.3 dB. Then, the peak value decreases and the absorption peak broadens with a further increase of the incident SPL up to 133.5 dB. The numerical simulations predict the overall evolution of the admittance and the absorption coefficient with the increase of the incident SPL. Discrepancies are however noticeable for this PP absorber. For the incident SPL of 125.3 dB, the peak in Re[Y] is thus predicted at a higher frequency. The absorption peak is also shifted towards high frequencies with the increase of the SPL, while it is centered around

Table B.6
Rms amplitude of the velocity in the perforations for PP#2 and PP#3 absorbers with a cavity depth of 30 mm for a broadband excitation: values deduced from the experiments and from the numerical simulations.

PP#2, Cavity depth of 30 mm								
Incident SPL (dB)		76.8	86.5	97.2	106.7	116.5	126.5	133.4
v_{rms} (m s^{-1})	exp.	1.59×10^{-2}	4.59×10^{-2}	1.56×10^{-1}	4.58×10^{-1}	1.35	3.78	7.13
	num.	1.93×10^{-2}	6.17×10^{-2}	2.16×10^{-1}	6.02×10^{-1}	1.60	4.03	7.16
PP#3, Cavity depth of 30 mm								
Incident SPL (dB)		76.6	86.6	96.4	106.2	116.1	125.3	133.5
v_{rms} (m s^{-1})	exp.	1.24×10^{-2}	3.73×10^{-2}	1.15×10^{-1}	3.55×10^{-1}	1.07	2.84	6.43
	num.	2.23×10^{-2}	7.34×10^{-2}	2.17×10^{-1}	6.19×10^{-1}	1.70	3.52	6.61

a frequency independent of the incident SPL in the experiments. In addition, the results from the analytical model and from the numerical simulations show a close agreement.

Finally, Table B.6 indicates the rms amplitude of the velocity in the perforations for PP#2 and PP#3 with a cavity depth of 30 mm determined from the measurements and from the numerical simulations. While a decent prediction is noticed, the value of v_{rms} tends to be overestimated in the numerical simulations, in particular in the linear regime. In the nonlinear regime, the differences between the values determined from the experiments and the numerical simulations reduce. Thus, v_{rms} is accurately predicted with an error smaller than 5% for the largest incident SPL.

Appendix C. Supplementary data

Supplementary material related to this article can be found online at https://doi.org/10.1016/j.jsv.2022.116892.

References

[1] L. Sivian, Acoustic impedance of small orifices, J. Acoust. Soc. Am. 7 (1935) 94–101.
[2] C.K.W. Tam, H. Ju, M.G. Jones, W.R. Watson, T.L. Parrott, A computational and experimental study of resonators in three dimensions, J. Sound Vib. 329 (2010) 5164–5193.
[3] Q. Zhang, D.J. Bodony, Numerical investigation and modelling of acoustically excited flow through a circular orifice backed by a hexagonal cavity, J. Fluid Mech. 693 (2012) 367–401.
[4] A.W. Guess, Calculation of perforated plate liner parameters from specified acoustic resistance and reactance, J. Sound Vib. 40 (1975) 119–137.
[5] D.-Y. Maa, Potential of microperforated panel absorber, J. Acoust. Soc. Am. 104 (1998) 2861–2866.
[6] A. Hersh, B. Walker, J. Celano, Helmholtz resonator impedance model, part 1: Nonlinear behavior, AIAA J. 41 (2003) 795–808.
[7] H. Bodén, Y. Guo, H.B. Tözün, Experimental investigation of nonlinear acoustic properties for perforates, in: 12th AIAA/CEAS Aeroacoustics Conference, 27th AIAA Aeroacoustics Conference, Cambridge, MA, USA, 8–10 May, 2006, AIAA Paper 2006–2404, 2020, pp. 1–8.
[8] R. Tayong, T. Dupont, P. Leclaire, On the variations of acoustic absorption peak with particle velocity in micro-perforated panels at high level of excitation, J. Acoust. Soc. Am. 127 (2010) 2875–2882.
[9] S.-H. Park, A design method of micro-perforated panel absorber at high sound pressure environment in launcher fairings, J. Sound Vib. 332 (2013) 521–535.
[10] U. Ingard, H. Ising, Acoustic nonlinearity of an orifice, J. Acoust. Soc. Am. 42 (1967) 6–17.
[11] T.H. Melling, The acoustic impendance of perforates at medium and high sound pressure levels, J. Sound Vib. 29 (1973) 1–65.
[12] Z. Laly, N. Atalla, S.-A. Meslioui, Acoustical modeling of micro-perforated panel at high sound pressure levels using equivalent fluid approach, J. Sound Vib. 427 (2018) 134–158.
[13] N. Atalla, F. Sgard, Modeling of perforated plates and screens using rigid frame porous models, J. Sound Vib. 303 (2007) 195–208.
[14] A. Cummings, Transient and multiple frequency sound transmission through perforated plates at high amplitude, J. Acoust. Soc. Am. 74 (1986) 942–951.
[15] W. Eversman, Effect of local impedance variation and non-linearity on multiple tone attenuation, Int. J. Aeroacoustics 14 (2015) 281–303.
[16] R. Roncen, F. Méry, E. Piot, P. Klotz, Spatially-varying impedance model for locally reacting acoustic liners at a high sound intensity, J. Sound Vib. 524 (116741) (2022) 1–19.
[17] Y. Özyörük, L. Long, A time-domain implementation of surface acoustic impedance condition with and without flow, J. Comput. Acoust. 5 (1997) 277–296.
[18] C.K.W. Tam, L. Auriault, Time-domain impedance boundary conditions for computational aeroacoustics, AIAA J. 34 (1996) 917–923.
[19] K.Y. Fung, H. Ju, Broadband time-domain impedance models, AIAA J. 39 (2001) 1449–1454.
[20] C. Richter, F.H. Thiele, X.D. Li, M. Zhuang, Comparison of time-domain impedance boundary conditions for lined duct flows, AIAA J. 45 (2007) 1933–1945.
[21] F. Monteghetti, D. Matignon, E. Piot, L. Pascal, Design of broadband time-domain impedance boundary conditions using the oscillatory-diffusive representation of acoustical models, J. Acoust. Soc. Am. 140 (2016) 1663–1674.
[22] Y. Reymen, M. Baelmans, W. Desmet, Efficient implementation of Tam and Auriault's time-domain impedance boundary condition, AIAA J. 46 (2008) 2368–2376.
[23] X.Y. Li, X.D. Li, C.K.W. Tam, Improved multipole broadband time-domain impedance boundary condition, AIAA J. 50 (2012) 980–984.
[24] R. Troian, D. Dragna, C. Bailly, M.-A. Galland, Broadband liner impedance eduction for multimodal acoustic propagation in the presence of a mean flow, J. Sound Vib. 392 (2017) 200–216.
[25] D. Dragna, P. Pineau, P. Blanc-Benon, A generalized recursive convolution method for time-domain propagation in porous media, J. Acoust. Soc. Am. 138 (2015) 1030–1042.
[26] M. Shur, M. Strelets, A. Travin, T. Suzuki, P. Spalart, Unsteady simulations of sound propagation in turbulent flow inside a lined duct, AIAA J. 59 (2021) 3054–3070.
[27] J. Allard, N. Atalla, Propagation of Sound in Porous Media: Modelling Sound Absorbing Materials, second ed., John Wiley & Sons, 2009.
[28] Z. Laly, N. Atalla, S.-A. Meslioui, K. El Bikri, Sensitivity analysis of micro-perforated panel absorber models at high sound pressure levels, Appl. Acoust. 156 (2019) 7–20.

[29] C. Bogey, C. Bailly, A family of low dispersive and low dissipative explicit schemes for flow and noise computations, J. Comput. Phys. 194 (2004) 194–214.
[30] J. Berland, C. Bogey, O. Marsden, C. Bailly, High-order, low dispersive and low dissipative explicit schemes for multiple-scale and boundary problems, J. Comput. Phys. 224 (2007) 637–662.
[31] J. Berland, C. Bogey, C. Bailly, Low-dissipation and low-dispersion fourth-order Runge–Kutta algorithm, Comput. & Fluids 35 (2006) 1459–1463.
[32] C. Bogey, N. De Cacqueray, C. Bailly, A shock-capturing methodology based on adaptative spatial filtering for high-order non-linear computations, J. Comput. Phys. 228 (2009) 1447–1465.
[33] F. Monteghetti, D. Matignon, E. Piot, Energy analysis and discretization of nonlinear impedance boundary conditions for the time-domain linearized Euler equations, J. Comput. Phys. 375 (2018) 393–426.
[34] B. Gustavsen, A. Semlyen, Rational approximation of frequency domain responses by vector fitting, IEEE Trans. Power Deliv. 14 (1999) 1052–1061.
[35] R. Billard, Study of Perforated Liners for Aeronautics (Ph.D. thesis), Le Mans Université, 2021.
[36] K.U. Ingard, Theoretical Acoustics, McGraw Hill, 1968.
[37] J. Chung, D. Blaser, Transfer function method of measuring in-duct acoustic properties. I. Theory, J. Acoust. Soc. Am. 68 (1980) 907–913.
[38] B.S. Beck, N.H. Schiller, M.G. Jones, Impedance assessment of a dual-resonance acoustic liner, Appl. Acoust. 93 (2015) 15–22.
[39] M.G. Jones, W.R. Watson, T.L. Parrott, Benchmark data for evaluation of aeroacoustic propagation codes with grazing flow, in: 11th AIAA/CEAS Aeroacoustics Conference, Monterey, CA, USA, 23–25 May, 2005, AIAA Paper 2005–2853, pp. 1–18.
[40] V. Lafont, F. Méry, R. Roncen, F. Simon, E. Piot, Liner impedance eduction under shear grazing flow at a high sound pressure level, AIAA J. 58 (2020) 1107–1117.
[41] C. Chen, X. Li, F. Hu, On spatially varying acoustic impedance due to high sound intensity decay in a lined duct, J. Sound Vib. 483 (115430) (2020) 1–28.
[42] A. Alomar, D. Dragna, M.-A. Galland, Time-domain simulations of sound propagation in a flow duct with extended-reacting liners, J. Sound Vib. 507 (116137) (2021) 1–24.

Shock Waves (2021) 31:379–398
https://doi.org/10.1007/s00193-021-01024-8

ORIGINAL ARTICLE

Propagation of spherical weak blast waves over rough periodic surfaces

T. Lechat[1] · A. Emmanuelli[1] · D. Dragna[1] · S. Ollivier[1]

Received: 17 November 2020 / Revised: 31 May 2021 / Accepted: 21 June 2021 / Published online: 12 July 2021

Abstract
Spherical weak blast propagation above a rough periodic surface is investigated by performing numerical simulations of the Euler equations. The study of the reflection pattern shows that waves diffracted by the surface asperities merge to form an effective reflected shock. It is initially detached from the incident shock but gradually catches up with it. If the source energy is sufficient, the reflected shock interacts with the incident one and Mach reflection occurs. Thus, the triple point has a similar trajectory to that over a smooth surface. In addition, the maximal overpressure is shown to be greater for small roughness scales in a layer near the surface. Far from the surface, it is close to that of a smooth surface for small roughness scales and to the free field for the highest ones. The increase in the maximal overpressure is related to oscillations on the waveforms that appear behind the shock. These properties are associated with the existence of a surface wave that propagates along the surface. Comparison of results in the linear regime with an analytic solution confirms this explanation.

Keywords Shock wave · Rough surface · Blast wave · Surface wave · Triple point

1 Introduction

When spherical blast waves propagate in outdoor environments, they interact with the inhomogeneities of the atmosphere as well as with the ground. The reflection of a spherical shock wave over a flat smooth impermeable and rigid ground surface is well documented in the literature (for instance, [1,2]). The reflection pattern is at first a regular reflection: The incident and reflected shocks intersect on the ground and the angle of reflection usually differs from the angle of incidence. At larger distances, the reflected shock catches up with the incident shock; the point of intersection is no longer on the surface but above and a third shock, named the Mach stem, is formed near the surface. The Mach stem then grows with the shock wave propagation. The slopes of the three shocks at the triple point are first different, and the reflection pattern is referred to as Mach reflection. The slopes of the Mach stem and the incident shock then become equal, corresponding to the von Neumann reflection.

However, actual outdoor surfaces are neither flat nor impermeable, nor rigid, nor smooth. Among the surface properties, roughness was shown to have a significant effect on the reflection of spherical blast waves. Dewey and colleagues [3,4] have investigated the characteristics of spherical blast wave reflection over an ideal surface and two real surfaces. For this, they use two identical explosive charges of approximately 500 kg of pentolite and consider the plane midway of the two charges as a plane of symmetry. The shock along this plane thus corresponds to a shock that would be reflected over an ideal surface. With the help of a painted backdrop or smoke puffs, a high-speed camera was used to determine the shock trajectories, and Rankine–Hugoniot relations were employed to deduce the pressure jump from the measurements of the shock speed. The shock characteristics for the ideal surface were compared to those measured for two ground surfaces: a smooth one and a rough one that was obtained by furrowing in a circular pattern the smooth surface. It was observed that the peak pressure along the ground and the length of the Mach stem were reduced for real surfaces compared to the ideal one, especially for the rough ground.

The characteristics of real ground in terms of roughness or absorption can hardly be measured with precision, in

Communicated by A. Hadjadj.

D. Dragna
didier.dragna@ec-lyon.fr

[1] Laboratoire de Mécanique des Fluides et d'Acoustique, UMR5509, Univ Lyon, Ecole Centrale de Lyon, CNRS, Univ Claude Bernard Lyon 1, INSA Lyon, 69130 Ecully, France

particular over a large surface area. Consequently, outdoor experiments provide valuable information but it is mostly qualitative. An alternative to study the roughness effects of spherical blast wave reflection is to perform controlled experiments, in which the roughness can be known precisely. The first study at laboratory scale was carried out by Huber and McFarland [5]. Blast waves were generated by a small explosive charge, and measurements were taken along a propagation line using flush-mounted surface microphones and schlieren optical systems. Both a smooth surface and a rough surface made of pyramid-shaped elements of 3.2-mm height and 6.4-by-6.4-mm base were considered. It was found that with the rough surface, the peak overpressure at the surface was slightly reduced, the formation of the Mach stem was delayed, and the Mach stem height was reduced compared to the smooth surface case, in agreement with Dewey et al. [3]. These are the main conclusions reported in Needham [6] on the effects of roughness on blast wave propagation.

Experiments on the reflection of spherical shock waves on a flat plane at laboratory scale have been recently reported [7,8]. ln Karzova et al. [7], an electric spark source was used to generate weak shock waves, with characteristics typical of blast waves. The waveform duration was about 50 μs corresponding to a wavelength of 20 mm. A significant contribution of the study was the measurement of the pressure waveforms thanks to a Mach–Zehnder optical interferometry method. Three different surface conditions were considered: a smooth surface and two rough surfaces made of sandpaper with correlation lengths of 0.18 and 0.34 mm. In accordance with previous studies, it was noted that roughness induces a reduction in the Mach stem height. For the largest roughness scale, the Mach stem did not appear. In addition, close to the surface, the waveforms for a rough surface exhibit oscillations, whose pattern depends on the roughness scale. Interestingly, these oscillations lead to an increase in peak overpressure compared to a smooth surface, which seems to contradict the previously mentioned experiments. Numerical simulations were also performed using a solver of the axisymmetric Euler equations. For the three surface conditions, close agreement between the measured and numerical waveforms was obtained, which shows that numerical simulations based on the Euler equations can accurately reproduce the effects of roughness on weak shock wave propagation.

In Qin and Attenborough [8], weak spherical shock waves were generated by focusing of a high-power laser beam. Their characteristics were similar to those obtained with a spark source. Several roughness values were considered with length scales between 0.2 and 5 mm. Microphones were used for the measurements of pressure waveforms, limiting their validity to the low-frequency range. Compared to the waveform for a smooth surface, a low-frequency component was noticed for the largest roughness scales and was identified as a surface wave. Surface waves above rough surfaces have been widely studied in the linear regime. Their existence is related to the property that a rough surface can be effectively replaced by a smooth surface with a frequency-dependent surface impedance [9,10]. The roughness causes an increase in, or creation of, the imaginary part of the effective impedance, thereby meeting one of the important conditions for the formation of a surface wave [9]. The amplitude of surface waves decays exponentially with height, but they undergo cylindrical spreading, rather than spherical spreading, with increasing distance from the source. At long range and grazing incidence, they can become a significant contribution to the pressure field. Since the 1970s, several experiments have been carried out to bring surface waves to light using as rough surfaces, either a lattice of rectangular cavities [11,12] or rectangular strips and cylinder arrays on a smooth surface [13,14], among others.

Experimental studies have been also performed using a shock tube and, consequently, for plane wave shocks. Though not directly applicable to spherical blast waves, they can give a hint as to the local reflection pattern [15]. In a series of papers, Ben-Dor, Takayama, and colleagues [16–18] considered the diffraction at a rough wedge and the transition from Mach reflection to regular reflection as the angle of the wedge increases. They observed that the transition angle was reduced due to roughness. For spherical blast waves, this implies that the Mach reflection should appear at a larger incidence angle for rough surfaces than for a smooth surface and, consequently, at a larger distance. Following Reichenbach [19], a detailed experiment on the diffraction of a shock with a Mach number of 1.425 at a crenellated wedge was performed by Adachi et al. [20]. Three angles of incidence, namely 20°, 30°, and 40°, were investigated. The crenellation had equal width and height, and six sizes (0.25, 0.5, 1, 2, 4, and 8 mm) were tested. A Mach stem was observed in all configurations, and two mechanisms for its formation were highlighted. The first mechanism was only observed for small angles of incidence (20° and 30°). As the plane shock impinges on the wedge, Mach reflection appears and a Mach stem grows as the plane shock propagates on the top of the first crenellation. The Mach stem then leaves it and continues growing in the crenellation cavity. As it impinges on the top of the second crenellation, a second reflected shock and Mach stem are observed at the foot of the first Mach stem. This pattern is repeated each time the plane shock impacts a new crenellation. A succession of triple points can thus be seen at the shock foot. At long distance, the reflected shocks merge into a single reflected shock, noted C_e. The second mechanism was observed for all the angles of incidence. As the plane shock propagates above the crenellation cavities, diffracted shock waves are generated. At a long distance, they also tend to merge into a single shock, noted C_{se}, which can be of sufficient amplitude to interact with the incident shock and form a Mach stem. In addition, in the cases for

which the two mechanisms were at play, the shock C_{se} was of larger amplitude than C_e and overtook it. Further analysis [21] revealed that the triple-point trajectory was discontinuous.

This paper aims at further studying the reflection of spherical weak blast waves over rough surfaces by performing a detailed numerical study. The objectives are to discuss the reflection pattern for rough surfaces and (if existing) to investigate some characteristics of the Mach stem observed experimentally, namely the reduction in its length, the delay in its formation compared to a smooth surface, and its absence for large roughness scales. In addition, the evolution of the peak pressure with the roughness scale is analyzed, with the aim of explaining the increase in peak pressure, observed in Karzova et al. [7].

The paper is structured as follows. In Sect. 2, the configuration, the numerical methods, and the source model are described. The reflection pattern for spherical weak shocks above a rough surface and its modification with source amplitude and roughness scale is examined in Sect. 3. The variations of the peak pressure along the surface, as well as the presence of a surface wave, are discussed in Sect. 4. Concluding remarks are given in Sect. 5.

2 Configuration and numerical model

2.1 Configuration

The propagation of a spherical blast wave above a rough surface is investigated. For simplicity, axisymmetric rough and flat surfaces are considered and the source is located on the axis of symmetry of the surface. The study can therefore be restricted to a two-dimensional (axisymmetric) problem. The cylindrical coordinates are denoted by (r, z). Similarly, for ease of analysis, the surface profile is chosen as sinusoidal:

$$\sigma(r) = \frac{h}{2}\cos\left(\pi\frac{r}{h}\right), \tag{1}$$

where h is the only roughness parameter. It can be interpreted as both the height and half-width of the asperities. In addition, the atmosphere is homogeneous and at rest and the air is assumed to be a perfect gas with the ratio of specific heats $\gamma = 1.4$. The geometry of the problem is sketched in Fig. 1.

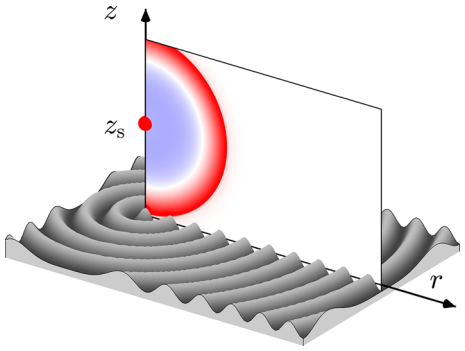

Fig. 1 Propagation of a spherical shock wave over a flat surface with axisymmetric roughness. An example of overpressure contours is shown

2.2 Equations and numerical methods

2.2.1 Equations

In what follows, ρ denotes the density, p the pressure, ρe the total energy density, u and w the radial and axial velocity components, respectively, and t the time. The variables are non-dimensionalized using the height of the source z_s as the length scale, the ambient density ρ_0 as the density scale, the ambient pressure p_0 as the pressure scale, the ambient sound speed $c_0 = \sqrt{\gamma p_0/\rho_0}$ as the velocity scale, and z_s/c_0 as the time scale.

The axisymmetric Euler equations are solved using high-order finite-difference techniques. To account for the rough surface, a body-fitted grid is used. A curvilinear coordinate transformation is then defined between the physical domain (r, z) and its computational counterpart (ξ, η). Using the notation $i_j = \partial i/\partial j$ for the metrics, the dimensionless equations are written in quasi-conservative form as:

$$\frac{\partial}{\partial t}\left(\frac{\mathbf{U}}{J}\right) + \frac{\partial}{\partial \xi}\left(\frac{\xi_r\mathbf{F} + \eta_r\mathbf{G}}{J}\right) + \frac{\partial}{\partial \eta}\left(\frac{\xi_z\mathbf{F} + \eta_z\mathbf{G}}{J}\right) + \frac{\mathbf{H}}{J} = 0, \tag{2}$$

where $\mathbf{U} = [\rho\ \rho u\ \rho w\ \rho e]^{\mathrm{T}}$ is the vector of the unknown variables, $J = \xi_r\eta_z - \xi_z\eta_r$ is the Jacobian of the transformation, and $\mathbf{F}$, $\mathbf{G}$, and $\mathbf{H}$ are vectors given by:

$$\mathbf{F} = \begin{bmatrix} \rho u \\ \rho u^2 + \frac{1}{\gamma}p \\ \rho u w \\ u(\rho e + p) \end{bmatrix} \quad \mathbf{G} = \begin{bmatrix} \rho w \\ \rho u w \\ \rho w^2 + \frac{1}{\gamma}p \\ w(\rho e + p) \end{bmatrix}$$

$$\mathbf{H} = \frac{1}{r}\begin{bmatrix} \rho u \\ \rho u^2 \\ \rho u w \\ u(\rho e + p) \end{bmatrix}. \tag{3}$$

These equations are complemented by the definition of the total energy density, which for a perfect gas writes:

$$\rho e = \frac{p}{\gamma - 1} + \frac{\gamma\rho}{2}\left(u^2 + w^2\right). \tag{4}$$

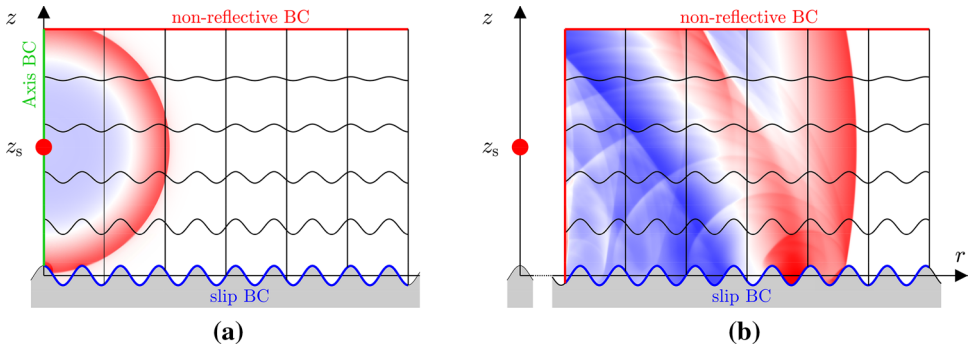

Fig. 2 Illustration of the computational domain with the boundary conditions **a** for a static frame and **b** for a moving frame. Examples of overpressure contours are shown

Note that the presence of the extra coefficient γ in (3) and (4) compared to the standard formulation of the Euler equations is due to the set of scales used.

The coordinate transformation proposed by Gal-Chen and Sommerville [22] is employed:

$$r(\xi, \eta) = \xi, \tag{5}$$

$$z(\xi, \eta) = \sigma(\xi) + \frac{\eta}{z_{\max}}[z_{\max} - \sigma(\xi)], \tag{6}$$

where $z_{\max}$ is the maximum height of the computational domain.

2.2.2 Numerical methods

As we consider the propagation of a signal of finite duration and thus of finite spatial extent, the useful information is contained near the incident and reflected shocks. It is thus not necessary to compute the shock propagation for a large domain in which the variables are mainly equal to their constant ambient values. To reduce the computational cost, the domain is thus restricted to a narrow domain that follows the propagation of the shocks. In detail, at each time step, we determine the last position along the r-direction at which the fluctuating pressure at the source height is greater than a threshold value (set to $p_s/10^4$). If this position is too close to the right boundary, the mesh is shifted along the r-direction by an integer number of mesh steps. This methodology, referred to as the moving frame [23], is illustrated in Fig. 2. It should be noted the moving frame usually employed for Cartesian grids can also be used for curvilinear grids, provided that a suitable coordinate transformation is adopted.

At the surface, a slip boundary condition is imposed by setting the normal wall velocity to zero. At the top boundary, the non-reflective boundary condition proposed by Bogey and Bailly [24] is used. At the left boundary, as long as the computational domain is static, axisymmetric boundary conditions as presented in Mohseni and Colonius [25] are used. More precisely, the symmetry of the variables is exploited to compute the spatial derivatives and to apply selective filtering using centered schemes along the ξ-direction. Note also that the $1/r$ singularity in the equations is treated by shifting the mesh in the ξ-direction by a half mesh size to avoid placing grid points at $r = 0$. Once the computational domain starts to move, non-reflective boundary conditions are applied at the left boundary instead of the axisymmetric boundary conditions.

Equation (2) is discretized by low-dispersion and low-dissipation explicit numerical schemes, developed in computational aeroacoustics. For the interior points, separated by at least five points from the boundary, and for the boundary points near the axis of symmetry, the centered fourth-order finite-difference scheme of Bogey and Bailly [26] and the centered sixth-order selective filter of Bogey et al. [27] are used. For the other boundary points, the 11-point non-centered finite-difference schemes and selective filters of Berland et al. [28] are implemented. To handle shock discontinuities, the shock-capturing methodology presented in Bogey et al. [27] with the detector proposed in Sabatini et al. [29] is applied. Time integration is carried out using a fourth-order six-stage Runge–Kutta algorithm [30].

The simulations are performed using an OpenMP-based in-house solver. The solver has been already used in two studies related to reflection of spherical weak shock waves over flat or rough surfaces [7,31]. An excellent agreement was obtained between the measured and simulated characteristics of the weak shocks, and in particular the overpressure waveforms. In addition, results of two test cases are presented in Supplementary Material of this article. The first test case deals with diffraction of a spherical pulse of small amplitude by a sphere. It aims to verify that diffraction by a curved surface is accurately simulated. The second test case considers plane-wave propagation of an N-wave. It aims to verify that nonlinear propagation of weak shocks is accurately simulated and does not generate spurious waves on a distorted mesh. Moreover, this solver was also employed in a related study to characterize the topographic effects on sonic boom reflection [32].

2.2.3 Computational parameters

The computational domain is $0 \leq \xi \leq 4.5$ and $0 \leq \eta \leq z_{\max} = 5$. The mesh is uniform, with a mesh size equal to 4×10^{-3} in the η-direction and to 1.5×10^{-3} for $0.01 \leq h \leq 0.045$ and 2.5×10^{-3} for $h = 0$ and $h \geq 0.05$ in the ξ-direction. This ensures that there are at least 13 points per period of the sinusoidal surface profile. A grid convergence study presented in Appendix 1 confirms that this choice of grid sizes allows for an accurate prediction of weak shock propagation over a rough surface. The mesh thus contains 2.25 or 3.75 million points, depending on the roughness. The time step is set to $\Delta t = 4.27 \times 10^{-4}$ and the corresponding CFL number is below 0.3 for all cases. The simulations are run using eight processors for 85,000 iterations, which allows for propagation distances up to $r = 36$.

2.3 Source and initial conditions

The source is set as an instantaneous release of energy with a Gaussian spatial envelope via the initial conditions:

$$p(r, z, t = 0) = 1 + p_s \exp\left(-\log(2)\frac{r^2 + (z-1)^2}{B^2}\right), \tag{7}$$

$$\rho(r, z, t = 0) = 1, \tag{8}$$

$$\rho u(r, z, t = 0) = 0, \tag{9}$$

$$\rho w(r, z, t = 0) = 0. \tag{10}$$

This source model has previously been employed for the study of spherical weak shock wave propagation above a flat and smooth surface [31] and was shown to produce pressure waveforms similar to those measured for an electric spark source. The source is characterized by its width B and its maximal overpressure p_s. Unless otherwise stated, they are set to $B = 0.25$ and $p_s = 7.5$. An important parameter for spherical shock wave is the source energy E_s, which is the main factor for the positive phase of the pressure waveform. It is obtained by integrating the energy density over the source volume, which relates E_s, $B_s = B/\sqrt{\log(2)}$, and p_s with:

$$E_s = \frac{p_s}{\gamma - 1}\pi^{3/2} B_s^3. \tag{11}$$

A preliminary simulation is performed in free field to get the characteristics of the incident shock wave on the surface. Figure 3a shows the evolution of the Mach number along the surface. The shock velocity was determined from the pressure jump at the shock and the Rankine–Hugoniot relation. The Mach number of the incident spherical shock does not exceed 1.3, it is smaller than 1.05 from $r > 3.3$, and it reaches 1.003 at $r = 35$. As an example, the time series of the overpressure $p' = p - 1$ in free field at $r = 10$ is depicted in Fig. 3b. Notice that the shape of the waveform generated by the source is typical of a blast wave.

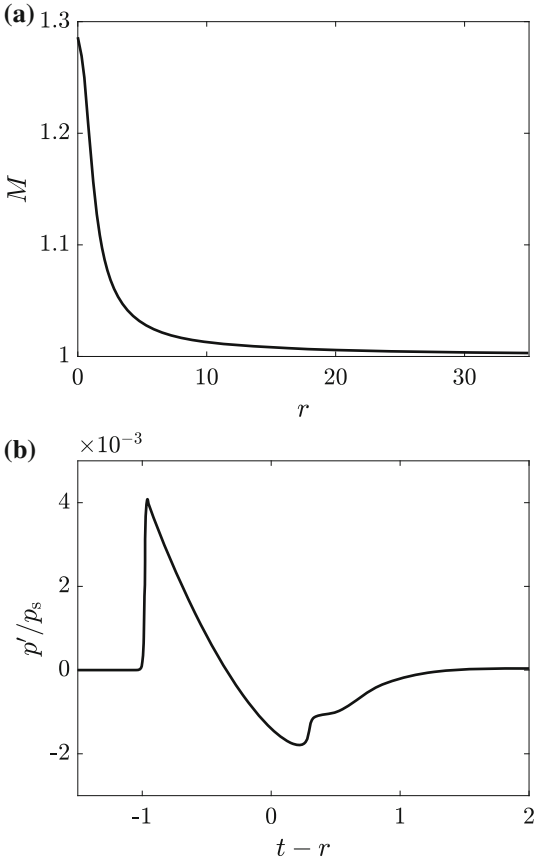

Fig. 3 **a** Mach number of the incident shock wave on the surface as a function of the radial coordinate. **b** Example of an overpressure waveform in free field at $r = 10$

2.4 Discussion of the non-dimensionalization

The parameters of the source and of the rough surface have been chosen to correspond to the measurements at laboratory scale of Karzova et al. [7]. The height of the spark source was about $z_s = 1$ cm with propagation distances up to $r = 33$ cm. In the model for the spark source [31], the maximal overpressure is $p_s = 7.5 \times 10^5$ Pa and the source characteristic length is $B = 0.25$ cm, which yields a source energy of $E_s = 0.28$ J. Assuming that a gram of TNT represents 4610 J [1], this source is equivalent to a mass of 61.3 µg of TNT. The roughness scales considered in the paper are between 100 and 1500 µm, which are in the order of the roughness correlation lengths for the sandpapers used in Karzova et al. [7].

For a source height of $z_s = 1$ m with the same ratio B/z_s and the same source amplitude, the results shown in the paper correspond to a source with an energy of 283.7 kJ or to an

equivalent mass of TNT of 61.3 g and to roughness scales between 1 and 15 cm.

3 Reflection pattern

3.1 General comments

In order to investigate the effect of roughness on the reflection pattern, schlieren pictures are shown at several instants in time in Fig. 4 for three different surface conditions. They are obtained by calculating the norm of the density gradient $|\nabla\rho|$ and allow for a clear visualization of the shocks. At $t = 0.43$, the spherical incident shock impinges the surface. At $t = 0.85$, a single reflected shock, which intersects the incident shock on the surface, is observed for the smooth surface, while additional diffracted shocks at the surface asperities can be seen for the rough surfaces. At $t = 1.71$, the reflection pattern for the smooth surface is of Mach type: There are three shocks with different slopes at the triple point. For the rough surfaces, a contribution is predominant over all the diffracted shocks and can be interpreted as an effective reflected shock. At following times, the Mach stem grows for the smooth surface and the reflection pattern progressively switches from Mach reflection to von Neumann reflection, as the shock front of the incident shock and of the Mach stem becomes continuous along the triple point. For the rough surface $h = 0.02$, the effective reflected shock has caught up and merged with the incident shock by $t = 3.42$. As for a smooth surface, the Mach stem then grows at following times. For $h = 0.05$, the effective reflected shock progressively catches up with the incident shock at $t = 3.42$ and 7.26 before merging at $t = 13.2$.

Additional close-up schlieren pictures near the surface for $h = 0.05$ are shown in Fig. 5 to clarify the reflection pattern for the rough surface. A schematic drawing is depicted in Fig. 6 to facilitate the discussion. The incident spherical shock (I) is observed at $t = 0.42$. Once it has impinged on the surface, diffracted waves are generated first, at the top of the asperities, at $t = 0.46$. The majority of the energy is diffracted leftward, and the amplitude of diffracted waves propagating along with the incident shock wave is comparatively small. As the incident shock continues to propagate in the surface cavities, a reflection pattern similar to a triple-shock pattern is observed at its foot (at $t = 0.55$, 0.59, 0.67, or 1.05). However, the amplitude of the diffracted wave is expected to be too small to interact nonlinearly with the incident shock. Once the incident shock reaches the bottom of the cavity, other diffracted waves are generated and propagate upward, as seen for $t = 0.5$. As they propagate, the different diffracted waves progressively coalesce into two wavefronts ($t > 0.55$). The first one (R_t), corresponding to the waves diffracted at the top of the asperities, is attached to the incident shock. The second one (R_b), of larger amplitude, corresponding to the waves diffracted at the bottom of the asperities, is detached from the incident shock. At long range, the latter becomes the effective reflected wave, shown in Fig. 4, that may interact with the incident shock. From the schlieren picture at $t = 1.26$, it is noted that the space between the incident and reflected shocks near the surface and close to the source is of the order of the roughness period $2h$. In addition, a fourth wavefront (D) can be seen at $t = 0.84$, 1.05, and 1.26 and is due to diffracted waves that are diffracted a second time at the surface asperities.

3.2 Effect of the source amplitude

Figure 7 shows schlieren pictures at time $t = 19.1$ for three surface conditions and five source amplitudes. For $p_s = 0.01$, the source amplitude is sufficiently small for the propagation to be essentially linear and there is no shock. The pictures for the smooth surface and the rough surface with $h = 0.02$ have similar patterns. For $h = 0.05$, additional contributions can be distinguished near the surface for $r < 18.5$. For the smooth surface, the Mach reflection is observed from $p_s = 1$. As the source amplitude increases, the Mach stem grows. With the rough surfaces, the incident and reflected shocks first appear separated. The space between them reduces with increasing p_s, and the Mach stem is formed starting from $p_s = 4$ for $h = 0.02$ and $p_s = 8$ for $h = 0.05$. Moreover, the contributions observed near the surface for $h = 0.05$ and $p_s = 0.01$ are observed for $p_s \geq 1$ just behind the reflected shock. A similar pattern can also be identified for $h = 0.02$ and $p_s \geq 1$.

The trajectory of the triple point for these three surface conditions is now investigated for different source amplitudes. It is determined graphically from the schlieren pictures. The triple-point location is accurately estimated when the slopes of the three shocks at the triple point differ significantly. However, at long range, these slopes have comparable values, which makes the determination of the triple-point location imprecise. In this case, the estimated precision for the triple-point location is ± 0.1. In addition, for a rough surface, the merging of the incident and reflected shocks can occur at a long distance from the source, at which point the propagation direction and the speed of the incident and reflected shock fronts are almost identical. The incident and reflected shocks thus appear on the schlieren pictures as two parallel lines that slowly come closer, and the exact instant at which the Mach stem appears is then difficult to determine. In the following, only the location of triple points that can be clearly distinguished in the schlieren pictures is reported, so that the starting point of the triple-point trajectory for rough surfaces can not only be on the surface but above.

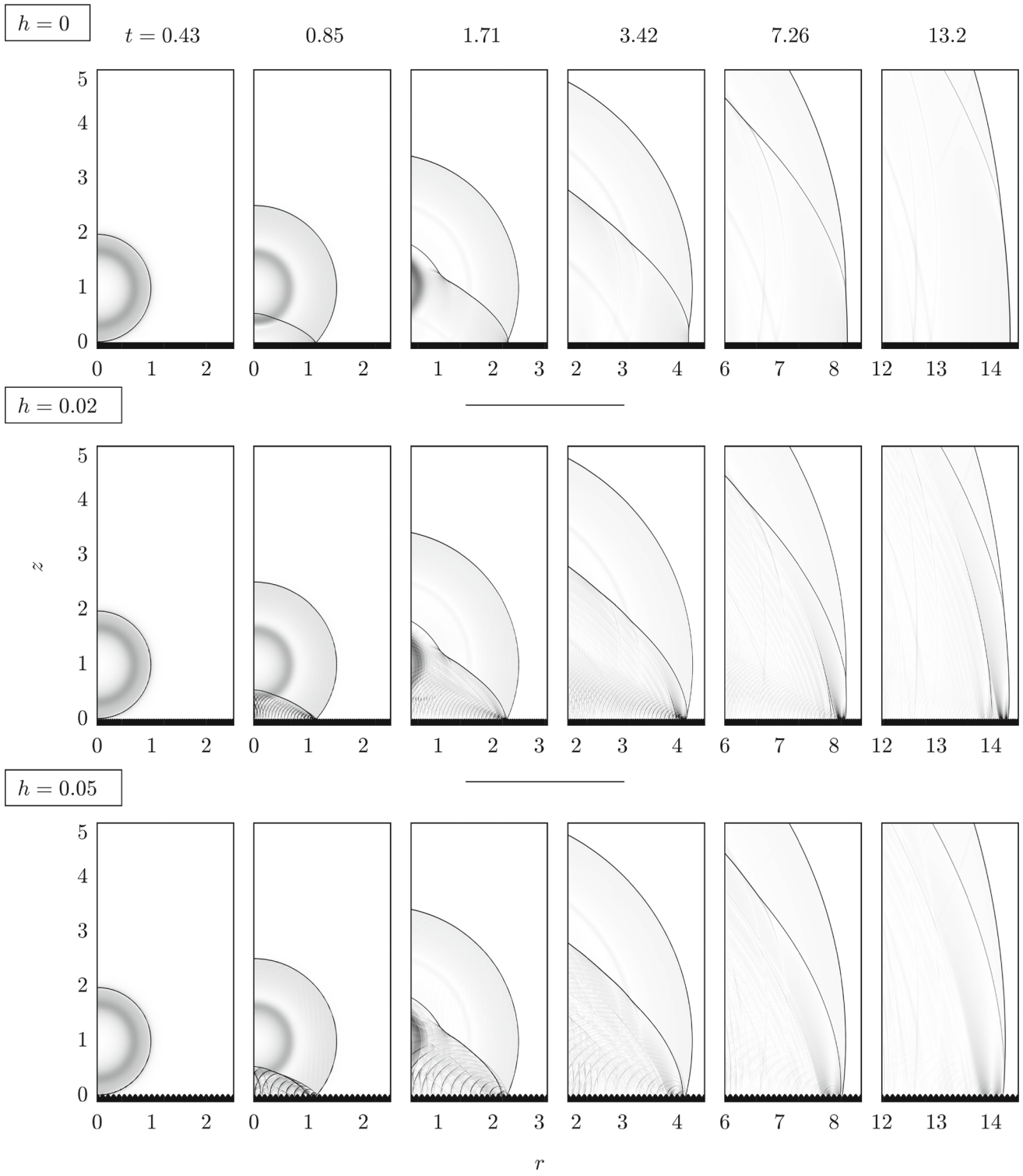

Fig. 4 Schlieren pictures showing the time evolution of the reflection pattern at $t = 0.43$, 0.85, 1.71, 3.42, 7.26, and 13.2 and for surfaces with (top) $h = 0$, (middle) 0.02, and (bottom) 0.05. The source amplitude is $p_s = 7.5$

The triple-point trajectory for the smooth surface and for several source amplitudes is shown in Fig. 8a. As reported for blast waves [1,6,33] and noticed previously for similar simulations [31], the trajectory has a parabolic shape. The source amplitude is a key parameter to estimate this trajectory. As it increases, the triple point leaves the wall closer

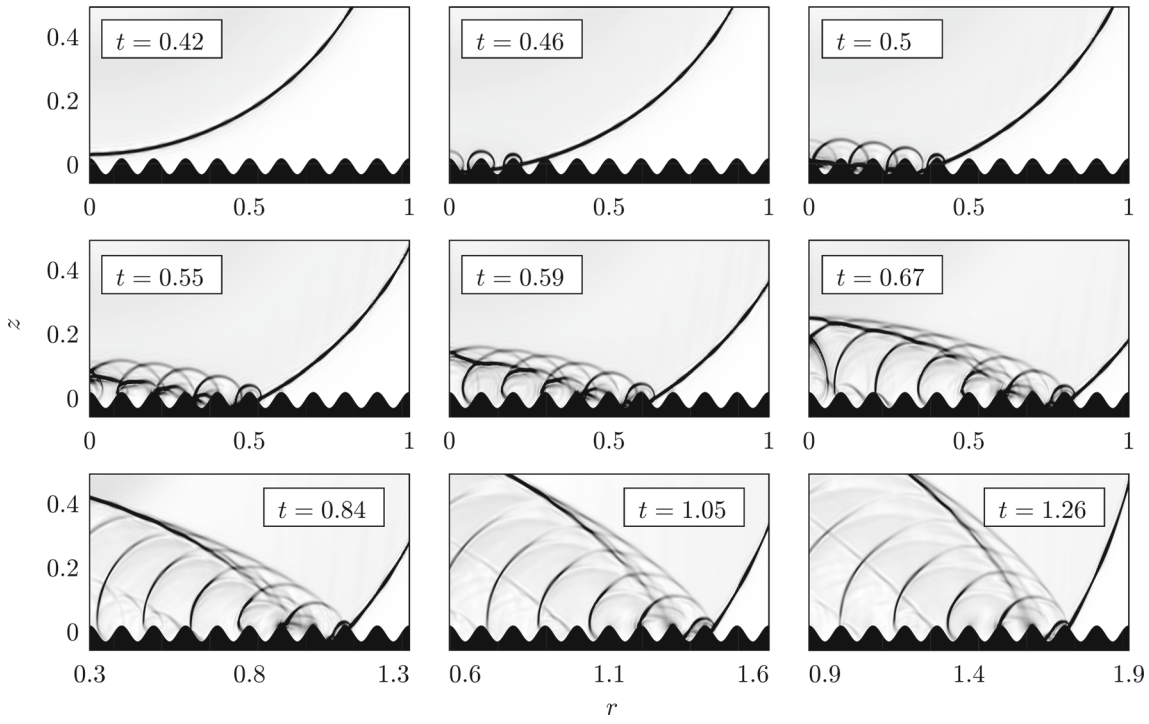

Fig. 5 Close-up schlieren pictures for $h = 0.05$ and for $t = 0.42$, 0.46, 0.5, 0.55, 0.59, 0.67, 0.84, 1.05, and 1.26

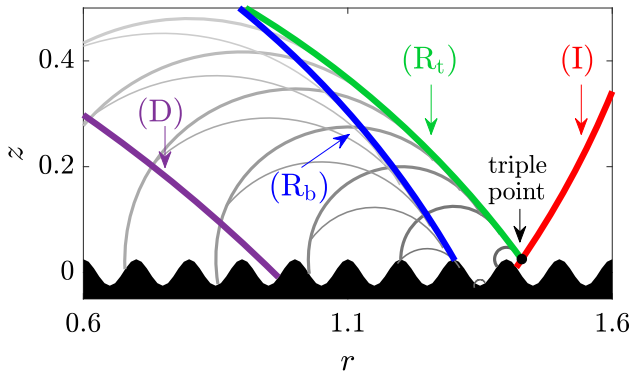

Fig. 6 Schematic diagram representing the reflection pattern for a rough periodic surface observed in Fig. 5

to the source and its vertical velocity increases as well. For comparison purposes, Fig. 8b, c shows the trajectory of the triple point for the two rough surfaces with $h = 0.02$ and $h = 0.05$, respectively. Contrary to the smooth surface, there is no Mach stem for $p_s = 1$ and $h = 0.02$. For $h = 0.05$, the Mach reflection is only observed for $p_s = 6$, 7, and 8. It is also noticed that the roughness induces a delay in the formation of the Mach stem. Thus, for $p_s = 4$, the triple point can be observed from $r = 3.1$ for the smooth surface but from $r = 6.2$ for the rough surface $h = 0.02$. Once formed, the growth of the Mach stem follows a similar evolution than for a smooth surface. As discussed by Dewey et al. [3], the reflection pattern for a rough surface at long range is equivalent to the one with a smooth surface and a smaller energy source at a closer distance. For instance, the trajectory of the triple point for a smooth surface and for a source amplitude $p_s = 3$ is comparable to the one for a rough surface $h = 0.02$ with a source that is more energetic, $p_s = 5$, and a delay in the apparition of the Mach stem $\Delta r = 1$. For the larger roughness scale $h = 0.05$, the source amplitude should be increased to $p_s = 8$ and the delay to $\Delta r = 5.5$.

3.3 Effect of the roughness scale

Figure 9 shows schlieren pictures at $t = 19.1$ for several roughness scales and for a source amplitude $p_s = 7.5$. Mach reflection is observed for $h \leq 0.05$. The Mach stem gradually shortens with h. For the largest roughness scales $h = 0.1$ and 0.15, the incident and reflected shocks are detached. This echoes the measurements of Karzova et al. [7] using sandpapers in which the Mach stem was observed for the smaller grain and was absent for the larger one. For h between 0.015 and 0.04, a fourth shock is observed behind the triple-shock pattern. It is related to the double-diffracted waves noticed in Fig. 5 and referred to as (D) in Fig. 6. Finally, for all the roughness cases, the contribution located near the surface and attached to the incident shock is observed. Its wavelength appears to vary with the roughness scale.

The triple-point trajectories for the smooth surface and rough surfaces for which $h \leq 0.06$ are shown in Fig. 10. As observed in outdoor or laboratory experiments [3,5,7], it is

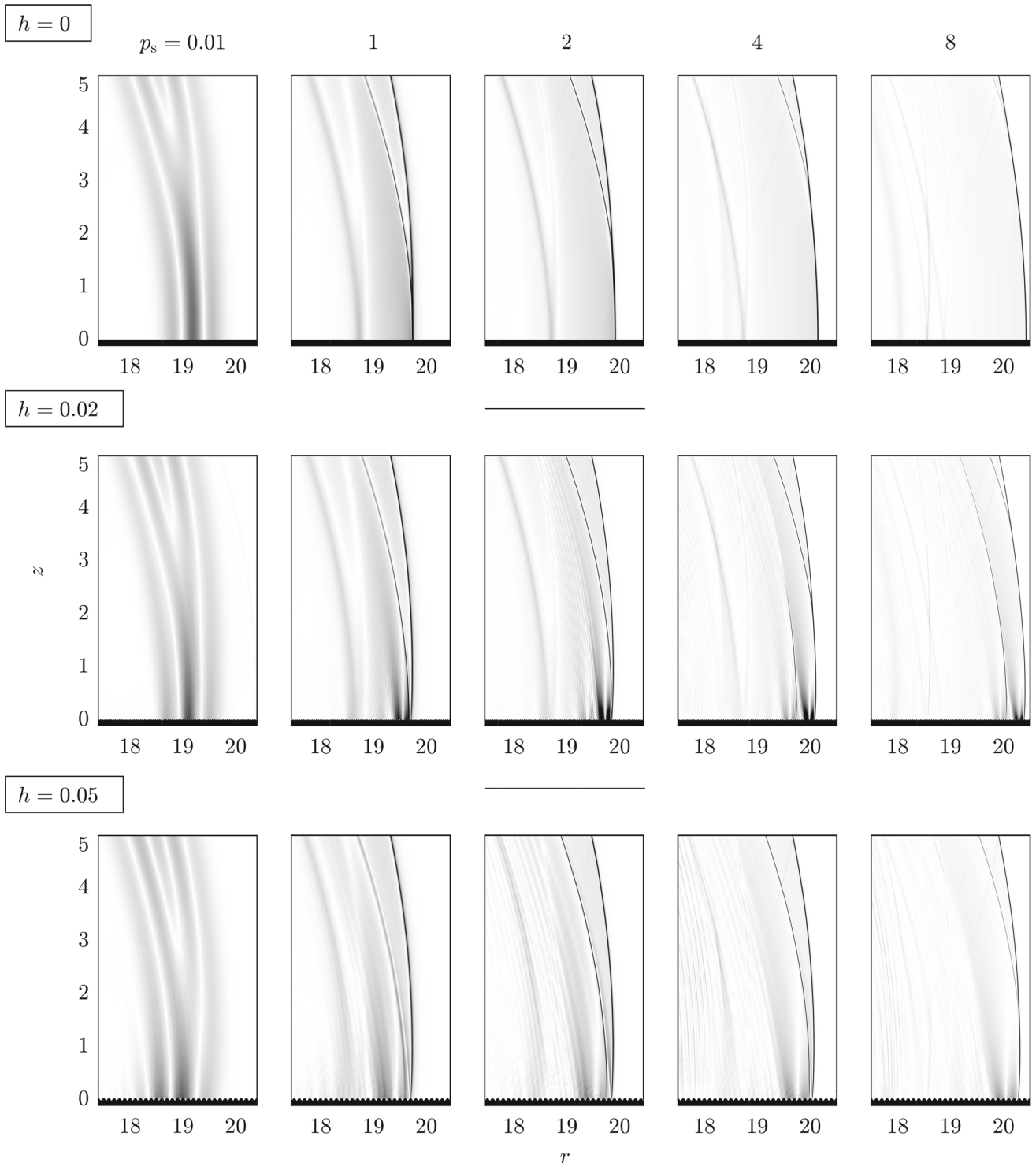

Fig. 7 Schlieren pictures at $t = 19.1$ for (top) $h = 0$, (middle) 0.02, and (bottom) 0.05 and for five source amplitudes $p_s = 0.01$, 1, 2, 4, and 8

found that, for a given distance, the length of the Mach stem reduces with the roughness scale. In addition, the delay in the formation of the triple point is seen to increase with h. Finally, once formed, the height of the Mach stem increases less rapidly with the roughness scale. For instance, it grows from $z_M = 1$ to 2 over a distance of $\Delta r = 4$ for $h = 0$ but over a distance of $\Delta r = 4.4$ for $h = 0.02$ and $\Delta r = 6$ for $h = 0.05$.

This delay in the formation of the triple point for a rough surface can be attributed to two factors. First, the roughness

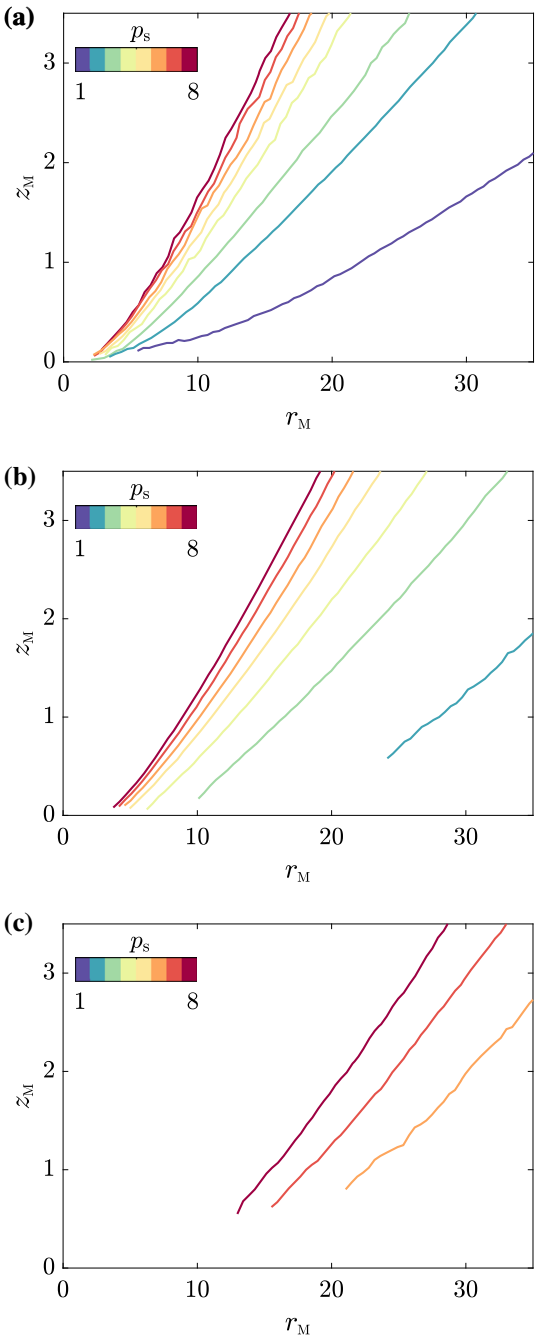

Fig. 8 Trajectory of the triple point **a** for a smooth surface and for a rough surface with **b** $h = 0.02$ and **c** $h = 0.05$ and for different source amplitudes

induces a delay in the formation of the effective reflected shock, because it originates from the merging of the waves diffracted at the bottom of the surface asperities as seen from the close-up schlieren pictures in Fig. 5. Second, the amplitude of the effective reflected shock decreases with the roughness, which tends to reduce the nonlinear interaction between the direct and reflected shocks. These two points are illustrated in Fig. 11, which shows the overpressure waveforms at $r = 5$ and $z = 1$ for $h \leq 0.1$. At this location, the Mach stem is not yet formed for any of the surfaces considered, and the direct and reflected shocks are separated. The direct shock is first observed at the reduced time $t - r = -0.9$ and is the same for all the surfaces. The reflected shock is then seen, starting from $t - r = -0.7$ for the smooth surface. It is noticed that the arrival time of the effective reflected shock increases with the roughness, while its amplitude reduces.

4 Overpressure

4.1 Profiles of peak overpressure

The evolution of the maximum value of the pressure along the surface is now considered. For the rough surfaces, it presents a periodic behavior associated with roughness periodicity, with local minima and maxima, as suggested in Fig. 5, for instance. For better readability, a moving average is applied over three periods of the rough profile to smooth the curves.

The evolution of the peak pressure along the surface for both the smooth and rough surfaces is shown in Fig. 12a. As expected, the peak pressure diminishes with range for the smooth surface. A slower decrease is observed near $r = 5$, where the Mach stem is forming. The peak pressure on the surface decreases with roughness scale. However, for $h \leq 0.1$, it is greater than with the smooth surface over the entire range considered. The opposite behavior is only observed for the largest roughness scales and at long range ($r \geq 10$). In order to extrapolate the overpressure decay at larger distances, the curves are fitted by the power law $\max(p') \propto r^{\alpha}$ over the range $20 \leq r \leq 35$. The resulting values of α are plotted as a function of h in Fig. 12b. For the smooth surface, it is equal to $\alpha = -1.23$, which is close to the expected value for spherical shock waves in free field [34]. For rough surfaces, α is smaller than with the smooth surface for $h < 0.04$, which means that at longer range the peak pressure for the smooth surface will be greater. The opposite behavior is observed for $h \geq 0.04$, implying that, in particular, the peak pressure for $0.05 \leq h \leq 0.1$ will remain larger for rough surfaces at increased distances.

Figure 13 shows the vertical profile of the peak overpressure at $r = 30$. In accordance with Fig. 12, the peak overpressure at the surface ($z = 0$) is greater for rough surfaces with $h < 0.1$ than for the smooth surface. Near the surface, the peak overpressure decreases exponentially with height for rough surfaces. In contrast, it is almost constant along the Mach stem for a smooth surface. Above the surface ($z \geq 2$), the peak overpressure is comparable to that of a smooth surface for the smallest roughness scales ($h < 0.04$) and then gradually decreases with h to attain a constant value, which corresponds to the peak overpressure value in free field.

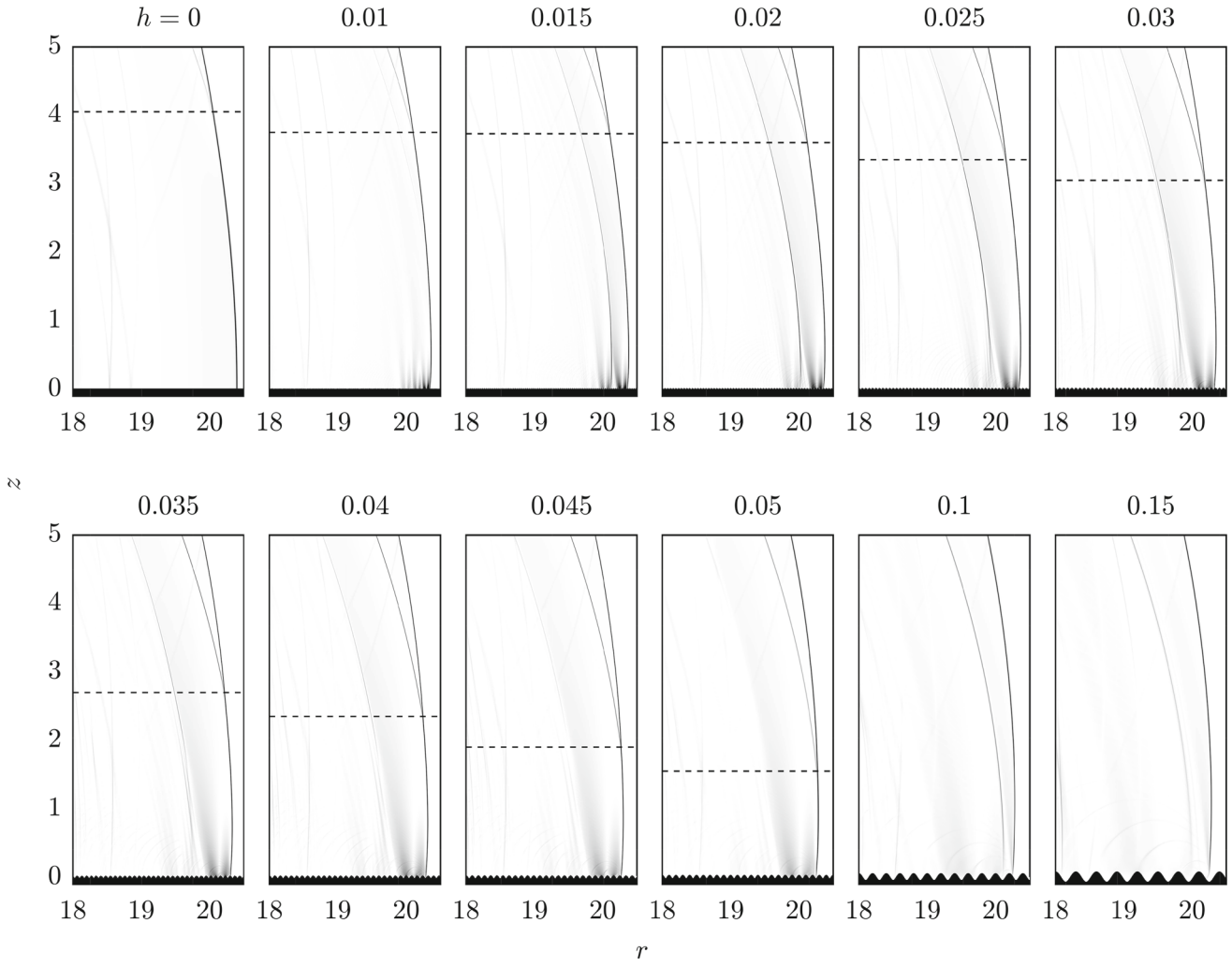

Fig. 9 Schlieren pictures showing the reflection pattern at $t = 19.1$ for several roughness scales with the same source amplitude, $p_s = 7.5$. The height of the triple point is indicated by a dashed line

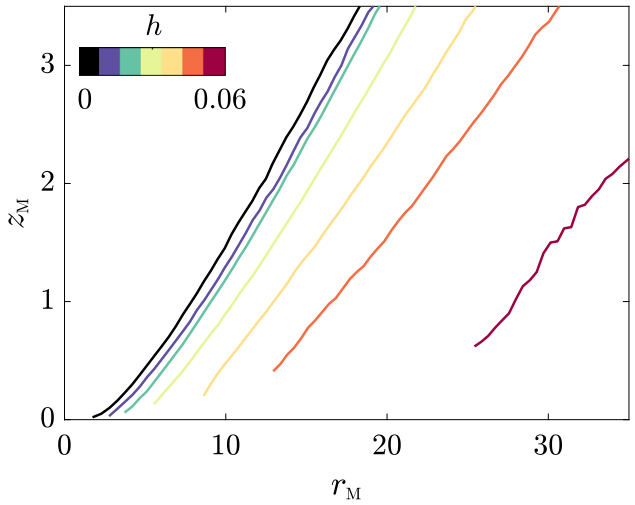

Fig. 10 Trajectory of the triple point for different surface conditions with the same source amplitude, $p_s = 7.5$

The overpressure waveforms for the smooth surface and some rough surfaces at long range $r = 30$ and just above the surface at $z = 0.2$ are depicted in Fig. 14. The waveform for a smooth surface looks like a blast wave in free field, with the peak overpressure at the shock discontinuity (see also Fig. 3b). Roughness has a dramatic effect on the waveform. First, the shock strength decreases with roughness scale. Second, an oscillation appears after the shock. Its period is related to the roughness scale, as it tends to increase with h. In addition, its maximum value is greater than the pressure at the shock front. For small roughness scales, it is even greater than the peak overpressure for a smooth surface. In addition, note that the waveforms for the large roughness scales are similar to the one reported in Fig. 11 in Qin and Attenborough [8]. In particular, the low-frequency oscillation was associated with the presence of a surface wave.

Figure 15 shows the peak overpressure and the shock pressure jump determined from the waveforms in Fig. 14 as a

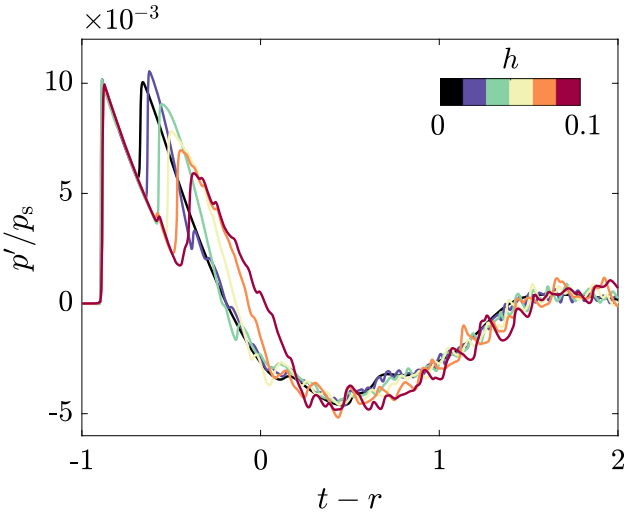

Fig. 11 Overpressure waveforms at $r = 5$ and $z = 1$ for different surface conditions

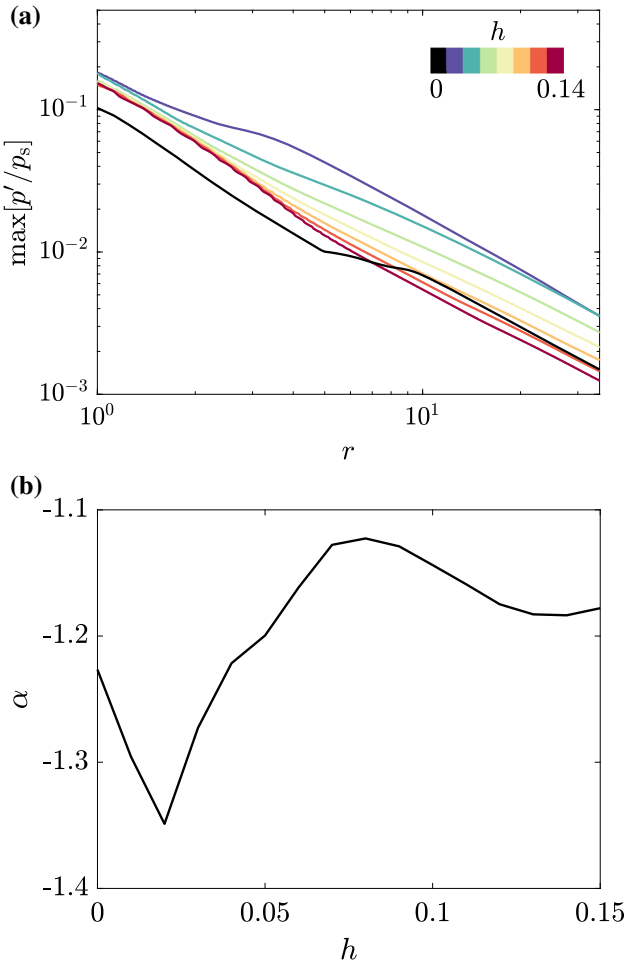

Fig. 12 **a** Evolution of the peak overpressure $\max(p')$ along the surface for the smooth and the rough surfaces. **b** Coefficient α of the fit $\max(p') \propto r^{\alpha}$ over the range $20 \leq r \leq 35$ as a function of roughness scale

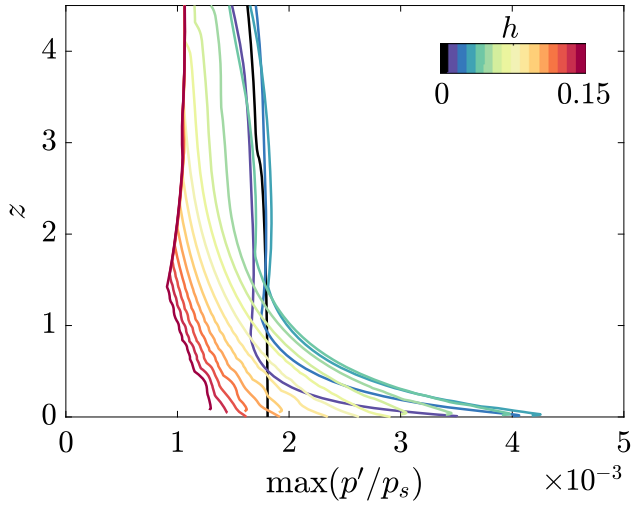

Fig. 13 Vertical profile of the peak overpressure at $r = 30$ for different surface conditions

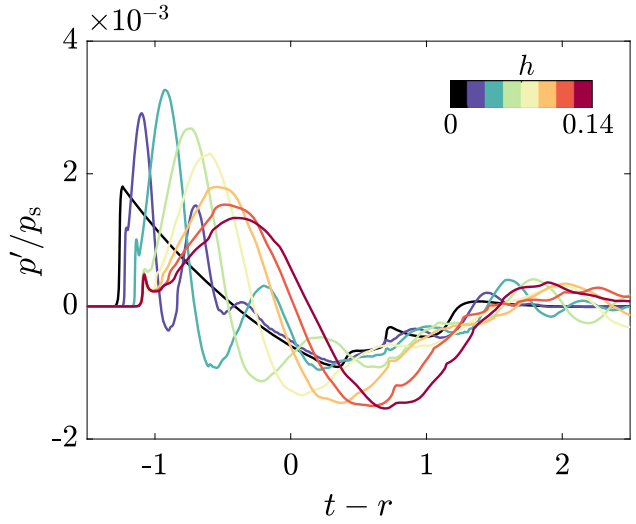

Fig. 14 Overpressure waveforms at $r = 30$ and $z = 0.2$ for different surface conditions

function of h. It is observed that the maximum overpressure first increases up to $h = 0.03$ before decreasing. At its maximum, the peak overpressure is one and a half times greater than for a smooth surface. The shock pressure jump reduces with h and becomes almost constant for $h > 0.07$. Compared to a smooth surface, it diminishes at most by a factor of 4. This could explain differences between experimental studies regarding the peak overpressure: In Dewey et al. [3] and Huber and McFarland [5], roughness was noticed to induce a reduction in peak overpressure, but, on the contrary, Karzova et al. [7] observed an increase in peak overpressure. While peak overpressure was determined directly from the waveforms in Karzova et al. [7], they were calculated from the shock speed in Dewey et al. [3] and Huber and McFar-

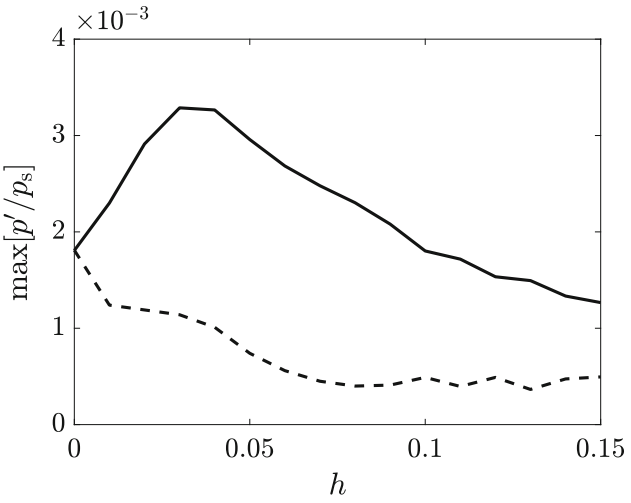

Fig. 15 (Solid) Peak overpressure and (dashed) shock pressure jump at $r = 30$ and $z = 0.2$ as a function of h

land [5]. This corresponds to the shock overpressure, which is actually smaller for rough surfaces than for a smooth surface.

4.2 Surface wave

The characteristics of the pressure near the surface at long range, namely the exponential decay of the amplitude with height and the presence of oscillations on the waveforms, evoke the presence of a surface wave. This section aims at confirming this point and at examining the variations of the surface wave with roughness scale and source amplitude.

4.2.1 Comparison in the linear regime

In order to confirm the oscillations observed on the waveforms are due to a surface wave, the numerical solution is compared with an analytical solution in the linear regime, in which the surface wave contribution is explicit.

In the linear regime ($p_s \ll 1$), the initial value problem becomes:

$$\frac{\partial^2 p'}{\partial t^2} - \Delta p' = 0, \tag{12}$$

$$p'(r, z, t = 0) = p_s \exp\left(-\log(2)\frac{r^2 + (z-1)^2}{B^2}\right), \tag{13}$$

$$\frac{\partial p'}{\partial t}(r, z, t = 0) = 0, \tag{14}$$

with the slip boundary condition at the rough surface:

$$\frac{\partial p'}{\partial n}(r, z = \sigma(r), t) = 0, \tag{15}$$

where $\partial/\partial n$ is the normal derivative.

Analytical solutions for this kind of initial value problem can be formulated based on the Green's function of the associated Helmholtz equation. Indeed, the initial conditions in (13)–(14) lead to the propagation of a pulse with a spherical symmetry, as if generated by a broadband point source. The spectrum of this equivalent point source can be shown to depend on the spatial Fourier transform of the pulse distribution [35]. For that, the Fourier transform of the overpressure:

$$p'(r, z, t) = \frac{1}{2\pi}\int_{-\infty}^{+\infty} \hat{p}(r, z, \omega)\mathrm{e}^{-\mathrm{i}\omega t}\mathrm{d}\omega, \tag{16}$$

is first introduced. In the above equation, ω denotes the angular frequency and is related to the frequency $f = \omega/(2\pi)$. It is recalled that the frequency, like the other variables, is dimensionless and that the frequency scale is c_0/z_s in accordance with the set of scales proposed in Sect. 2.2.1. The problem in (12)–(14) is then equivalent to:

$$\Delta\hat{p} + \omega^2\hat{p} = S(\omega)\frac{\delta(r)}{\pi r}\delta(z-1), \tag{17}$$

with the source spectrum:

$$S(\omega) = p_s \mathrm{i}\omega\pi^{3/2}B_s^3 \exp\left(-\frac{\omega^2 B_s^2}{4}\right). \tag{18}$$

Before going further, the smoothed boundary condition approach is introduced with the aim of formulating an analytical solution to the problem. It consists in replacing the slip boundary condition on the rough surface $z = \sigma(r)$ by an admittance boundary condition on the smoothed surface $z = 0$:

$$\frac{\partial\hat{p}}{\partial z}(r, z = 0, \omega) + \mathrm{i}\omega\beta\,\hat{p}(r, z = 0, \omega) = 0, \tag{19}$$

with an admittance β that depends on the frequency, the geometry, and the roughness characteristics. For a 1D rough surface made of the sinusoidal profile introduced in (1), the effective admittance is given by the boss model [9,36] at grazing incidence and at low frequencies ($\omega h \leq 1$) by:

$$\beta(\omega) = -\mathrm{i}\omega\alpha h, \tag{20}$$

with $\alpha \approx 0.2$. Details on the derivation are given in Appendix 2.

The analytical solution of (17) with the boundary condition in (19) can be written as a sum of three contributions: [37]

$$\hat{p}(r, z, \omega) = \hat{p}_{\mathrm{DW}}(r, z, \omega) + \hat{p}_{\mathrm{RW}}(r, z, \omega) + \hat{p}_{\mathrm{SW}}(r, z, \omega). \tag{21}$$

The first one is the direct wave:

$$\hat{p}_{\mathrm{DW}}(r,z,\omega) = -S(\omega)\frac{\exp(\mathrm{i}\omega R_1)}{4\pi R_1}, \tag{22}$$

with $R_1 = \sqrt{r^2+(z-1)^2}$ being the distance between the source and the receiver. The second contribution can be interpreted as the reflected wave and is given for $\mathrm{Im}(\beta) < 0$ by:

$$\hat{p}_{\mathrm{RW}}(r,z,\omega) = -S(\omega)\left[\frac{\exp(\mathrm{i}\omega R_2)}{4\pi R_2} -2\mathrm{i}\omega\beta\int_{-\infty}^{0}\exp(\mathrm{i}\omega\beta q)\frac{\exp(\mathrm{i}\omega R_q)}{4\pi R_q}\mathrm{d}q\right], \tag{23}$$

with $R_2 = \sqrt{r^2+(z+1)^2}$ being the distance between the image source and the receiver and $R_q = \sqrt{r^2+(z+1+q)^2}$. Finally, the third contribution is the surface wave:

$$\hat{p}_{\mathrm{SW}}(r,z,\omega) = S(\omega)\frac{\omega\beta}{2} \times \exp[-\mathrm{i}\omega\beta(z+1)]H_0^{(1)}\left(\sqrt{1-\beta^2}\omega r\right), \tag{24}$$

with $H_0^{(1)}$ being the Hankel function of the first kind and of zeroth order. It is noticed that the surface wave amplitude decays inversely as the square root of the propagation distance and exponentially with height, with a skin depth $1/|\omega\,\mathrm{Im}(\beta)|$. The analytical solution for each of the contributions in the time domain can then be calculated from the Fourier transform in (16).

Comparisons between the numerical and analytical solutions for a source amplitude $p_s = 0.01$ and for two rough surfaces with $h = 0.02$ and 0.05 at $r = 30$ and $z = 0.2$ are shown in Fig. 16. The contribution of the surface wave component is also represented. The agreement between the numerical and analytical solutions is satisfactory, especially for the smallest roughness. It is noted that the oscillations at the tail of the waveform for $h = 0.05$ are reproduced by the analytical solution, although they are of reduced amplitude and period. As expected, these are due to the surface wave component. In fact, the entire waveform for $h = 0.05$ is due almost exclusively to the surface wave. The discrepancies between the numerical and analytical solutions for $h = 0.05$ may be due to the low-frequency assumption for determining the effective admittance (i.e., $\omega h \leq 1$), which starts to be restrictive for this roughness scale: The period of oscillations for the surface wave component is thus about 0.6, corresponding to an angular frequency of $0.5/h$.

4.2.2 Effect of the roughness scale

The variation of the surface wave characteristics with the roughness scale is investigated. Information is first obtained

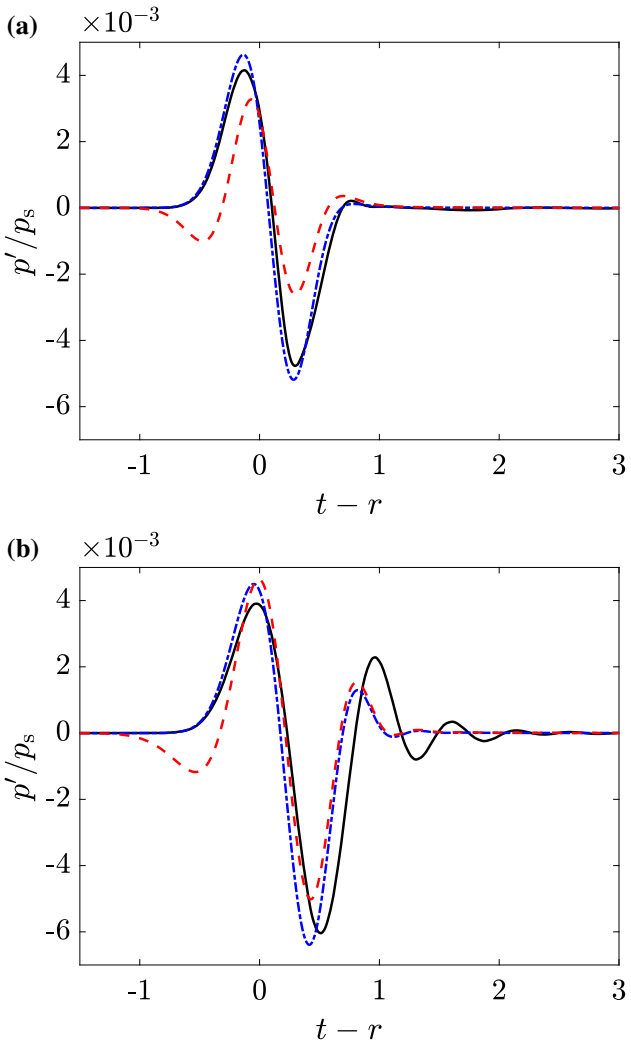

Fig. 16 Waveforms of the overpressure for $p_s = 0.01$ at $r = 30$ and $z = 0.2$ for two rough surfaces with **a** $h = 0.02$ and **b** $h = 0.05$: (solid) numerical solution, (dash-dotted) analytical solution, and (dashed) surface wave component

in the linear regime from the analytical expression in (24). In the frequency range of interest, $\omega h \ll 1$, one has $|\beta| \ll 1$ and $\sqrt{1-\beta^2} \approx 1$. Approximating $|H_0^{(1)}(u)| \approx \sqrt{2/(\pi u)}$, the modulus of the surface wave component is then expressed as:

$$|\hat{p}_{\mathrm{SW}}(r,z,\omega)| = p_s\,\omega^{5/2}\alpha h B_s^3\frac{\pi}{\sqrt{2r}} \times \exp\left[-\omega^2\left(\frac{B_s^2}{4}+\alpha h(z+1)\right)\right]. \tag{25}$$

The maximum of $|\hat{p}_{\mathrm{SW}}|$ is thus obtained at the frequency f_{SW}:

$$f_{\mathrm{SW}} = \frac{1}{2\pi}\left(\frac{5}{4\alpha h(z+1)+B_s^2}\right)^{1/2}. \tag{26}$$

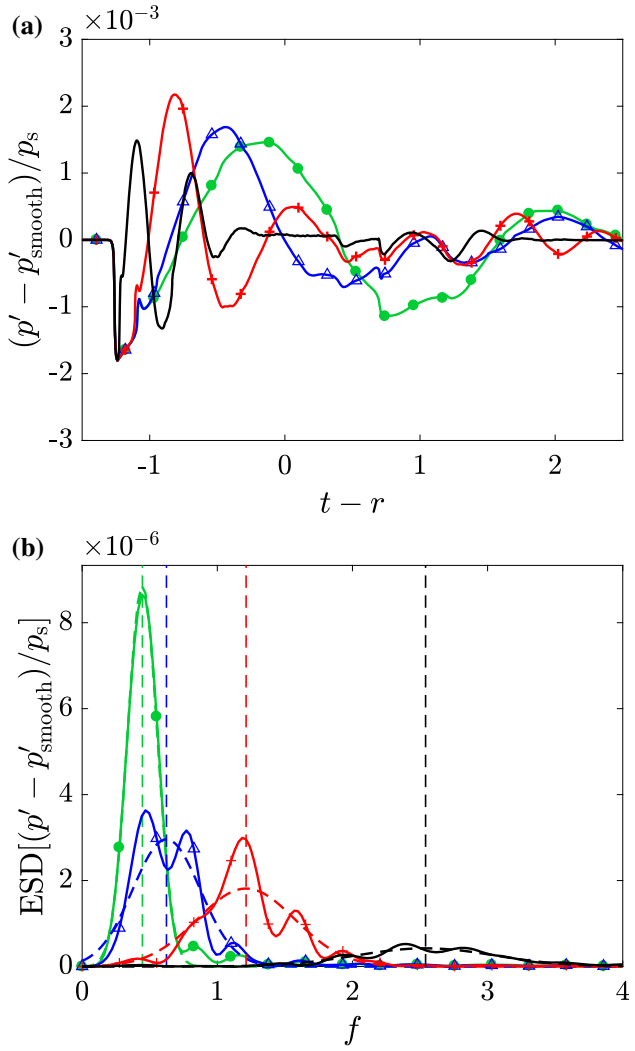

Fig. 17 **a** Signal obtained by subtracting the waveform for the smooth surface to the one for a rough surface at the same position $r = 30$ and $z = 0.2$ and **b** corresponding energy spectral densities: (solid) $h = 0.02$, (cross) $h = 0.05$, (triangle) $h = 0.1$, and (circle) $h = 0.15$. The vertical lines in (**b**) indicate the central frequency f_{SW} of the surface wave hump. The source amplitude is $p_{\mathrm{s}} = 7.5$

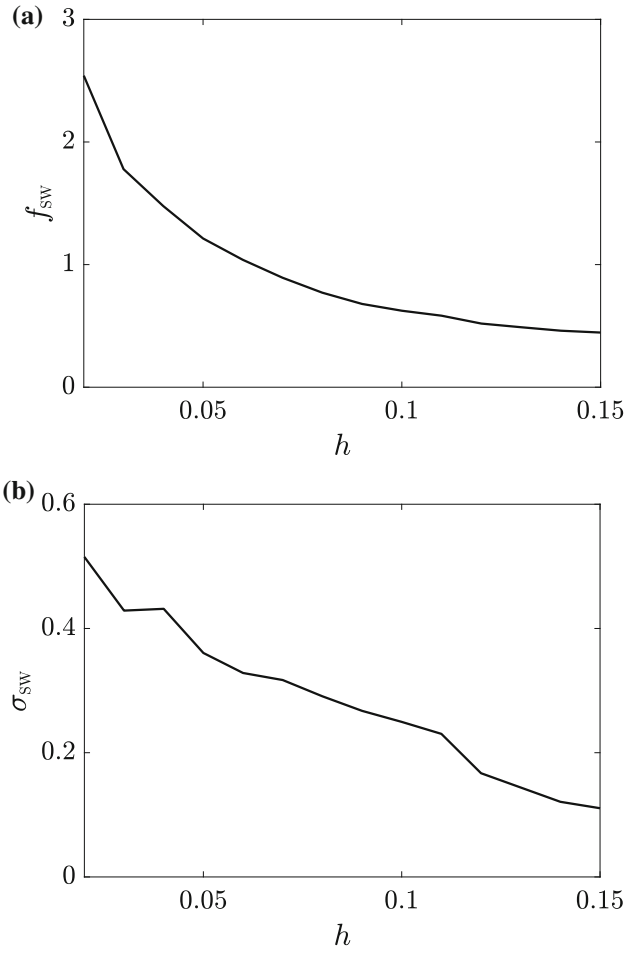

Fig. 18 Estimated **a** central frequency and **b** half-width of the surface wave spectrum as a function of the roughness scale h for $p_{\mathrm{s}} = 7.5$

It depends on the roughness scale and also on the frequency content of the pulse through the parameter B_{s}. As B_{s} is notably greater than h, f_{SW} is slightly dependent on h. For instance, it is equal to 1.08 for $h = 0.02$ and 0.96 for $h = 0.05$.

For higher values of p_{s}, information about the surface wave has to be extracted from the numerical solution. To do so, the oscillations due to the surface waves are separated from the rest of the waveform by examining the difference between the waveforms corresponding to the rough and smooth surfaces. An example of the resulting signal is shown in Fig. 17a for four values of h. While the shock discontinuities at the start of the signal are not eliminated by this procedure, the oscillations are clearly visible and they have most energy. The corresponding one-sided energy spectral densities ($\mathrm{ESD}[p](f) = 2|\hat{p}(f)|^2$) are depicted in Fig. 17b. They present a hump whose central frequency and bandwidth decrease with h. To quantitatively analyze this hump, the energy spectral densities are fitted by a Gaussian function:

$$A_{\mathrm{SW}} \exp\left[-\log(2) \frac{(f - f_{\mathrm{SW}})^2}{\sigma_{\mathrm{SW}}^2} \right], \tag{27}$$

where A_{SW} is the estimated amplitude of the surface wave hump, f_{SW} its central frequency, and σ_{SW} its spectral half-width.

The variations of f_{SW} and σ_{SW} with the roughness scale h are depicted in Fig. 18. As observed above, the central frequency decreases with h, approximately as $h^{-0.9}$, while in the linear regime it varies as $h^{-0.5}$ [see (26)]. The spectral half-width also tends to reduce with the roughness scale, almost linearly.

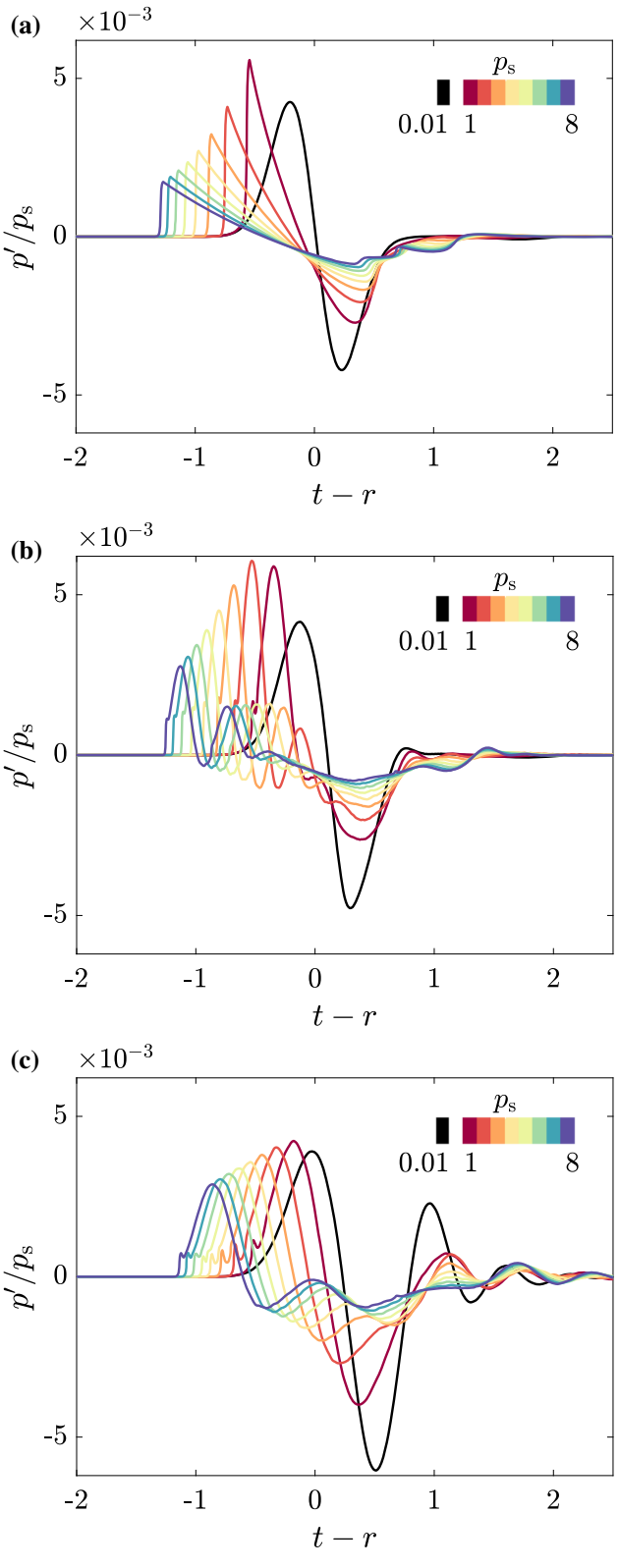

Fig. 19 Waveforms at $r = 30$ and $z = 0.2$ **a** for a smooth surface and for rough surfaces with **b** $h = 0.02$ and **c** $h = 0.05$ and for source amplitudes between 0.01 and 8

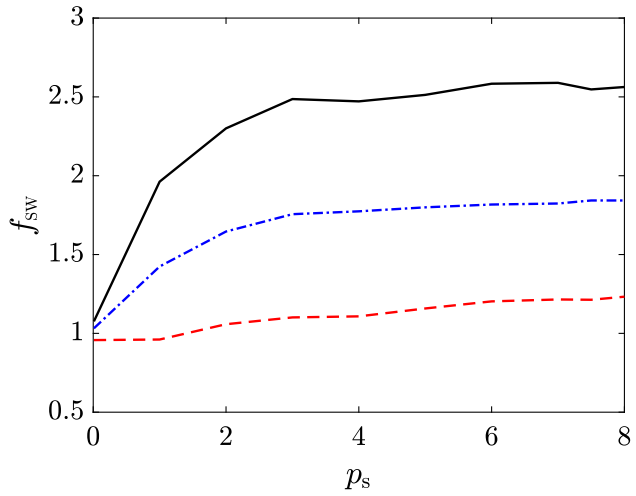

Fig. 20 Estimated central frequency of the surface wave spectrum as a function of the source amplitude for (solid) $h = 0.02$, (dash-dotted) $h = 0.03$, and (dashed) $h = 0.05$

4.2.3 Effect of the source characteristics

In this section, the evolution of the surface wave with the source characteristics, notably the source amplitude, is investigated.

The waveforms of overpressure are shown in Fig. 19 for several source amplitudes and for three surface conditions, namely a smooth surface and two rough surfaces with $h = 0.02$ and 0.05, at $r = 30$ and $z = 0.2$. For the smooth surface, the increase in source amplitude induces, first, the appearance of the shock discontinuity from $p_s = 1$ and then a lengthening of the waveform. Concerning the rough surfaces, for $h = 0.02$ and $p_s \geq 1$, the shock discontinuity is observed similarly and it is followed by the oscillations originating from the surface wave. The number of oscillations increases with p_s, and the period seems to decrease. As observed for the smooth surface, the signal lengthens with p_s. For $h = 0.05$, also note the presence of oscillations whose number tends to increase with p_s. Their period does not seem to vary with p_s. Finally, the oscillations at the tail of the waveform observed in the linear regime are still noticed for $p_s \geq 1$.

The procedure described in Sect. 4.2.2 to extract the characteristics of the surface waves is applied. The estimated central frequency of the surface wave is plotted as a function of the source amplitude in Fig. 20. Note that for $p_s = 0.01$, the value given by (26) has been used. The variations of the central frequency with source amplitude are significant mostly for $p_s \leq 3$. For $p_s \geq 3$, it slowly increases with the source amplitude in the three cases.

Besides, the waveforms were obtained for a particular source. In order to verify that this surface wave component is a general feature that should be expected for weak blast wave propagation above a rough surface, additional simulations

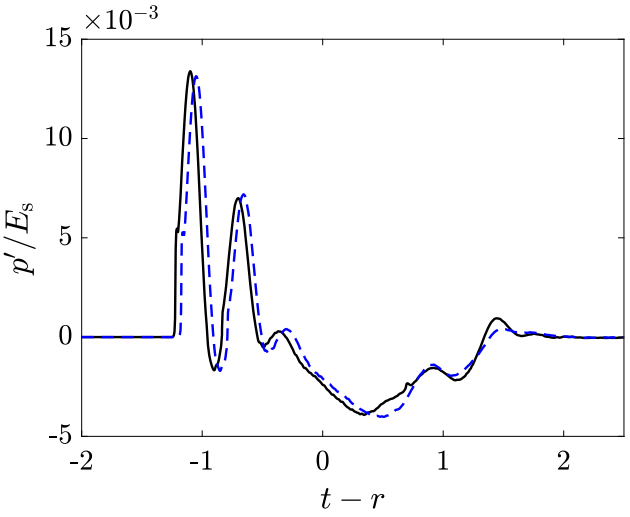

Fig. 21 Waveforms of the overpressure for $h = 0.02$ at $r = 30$ and $z = 0.2$ for two sources with the same energy (solid) $p_s = 7.5$ and $B = 0.25$ and (dashed) $p'_s = p_s/2$ and $B' = 2^{1/3}B$

have been conducted for a source with a reduced amplitude $p'_s = p_s/2$ and an increased half-width $B' = 2^{1/3}B$ (to keep the same source energy $E'_s = E_s$). Figure 21 shows an example of the waveforms for $h = 0.02$ at $r = 30$ and $z = 0.2$ obtained with the two sets of coefficients of the source. While the details of the waveforms differ, the oscillations related to the surface wave persist, which tends to confirm that surface waves are excited by weak blast waves over a rough surface.

5 Conclusions

The propagation of weak spherical blast waves above a rough periodic surface has been studied. To do so, numerical simulations of the Euler equations have been carried out. A detailed analysis of the reflection pattern has been performed. It has been shown that the waves diffracted by the rough surface combine to form an effective reflected shock that is first detached from the incident shock. For a sufficiently large source energy, it may interact with the incident shock and induce a Mach reflection pattern. Compared to a smooth surface, the appearance of the Mach stem is delayed and its height is reduced as if the source was of smaller amplitude and at a larger distance. For large roughness scales, the incident and reflected shocks remain detached. As weak blast waves degenerate to sound waves at long range, this behavior is expected to persist even for larger distances than those simulated. The variation of the peak overpressure with roughness scale has also been investigated. Near the surface, the peak pressure is larger for small roughness scales than for a smooth surface, but it is comparable or smaller far from the surface in all cases. The increase in peak pressure is related to oscillations that appear on the waveforms behind the shock. These properties have been associated with the presence of a surface wave that propagates along the rough surface. A comparison with an analytical solution in the linear regime has confirmed its existence. The evolution of the surface wave properties with the source amplitude has thus been examined, showing that an increase in source amplitude induces a shift toward higher frequencies.

There are several directions in which this work can be continued. This kind of simulations can be used to develop or extend empirical formula to account for roughness in predicting triple-point trajectory, as done recently by Xiao et al. [38] for a smooth and flat surface.

Furthermore, as axisymmetric roughness has been considered, an extension would be to perform simulations for a more realistic two-dimensional roughness. In addition, the roughness has been characterized by a single parameter, as, for simplicity, the roughness width was set to two times its height. Effect of these two parameters on the reflection of spherical weak blast waves could be investigated separately. Viscosity and thermal conduction have also been neglected. Nevertheless, in the experiments of Adachi et al. [20] for a plane shock wave impinging on a crenellated wedge (with a Mach number, however, larger than those considered in this work), schlieren pictures show the generation of vortices every time the plane shock wave passes above a roughness element. This should bring extra dissipation, not accounted for in the paper. This would also require to perform simulations with two-dimensional roughness to avoid generating unrealistic vortex rings and with a finer mesh near the walls to accurately capture the boundary layer.

Moreover, an effective boundary condition has been recently proposed for time-domain simulations in linear acoustics [39] to avoid the extra cost due to a fine mesh at a rough surface. It would thus be worthwhile to apply this boundary condition to spherical blast waves and investigate its range of validity in terms of Mach number.

Supplementary Information The online version contains supplementary material available at https://doi.org/10.1007/s00193-021-01024-8.

Acknowledgements This work was performed within the framework of the Labex CeLyA of the Université de Lyon, within the program "Investissements d'Avenir" (ANR-10-LABX-0060/ANR-16-IDEX-0005) operated by the French National Research Agency (ANR). It was also supported by LETMA (Laboratoire ETudes et Modélisation Acoustique), a Contractual Research Laboratory shared between CEA, CNRS, Ecole Centrale de Lyon, C-Innov, and Sorbonne Université. It was granted access to the HPC resources of PMCS2I (Pôle de Modélisation et de Calcul en Sciences de l'Ingénieur et de l'Information) of Ecole Centrale de Lyon, PSMN (Pôle Scientifique de Modélisation Numérique) of ENS de Lyon, and P2CHPD (Pôle de Calcul Hautes Performances Dédiés) of Université Lyon I, members of FLMSN (Fédération Lyonnaise de Modélisation et Sciences Numériques), partner of EQUIPEX EQUIP@MESO, and to the resources of IDRIS (Institut du Développement et des Ressources en Informatique Sci-

entifique) under the allocation 2019-02203 made by GENCI (Grand Equipement National de Calcul Intensif).

Appendix 1: Grid convergence

In this appendix, results of a grid convergence study are presented. A rough surface with $h = 0.01$ is considered. It corresponds to the smallest roughness scale investigated, with the least number of points per period. It is thus the most restrictive case. Simulations are performed for five grid sizes along the ξ-direction, ranging from $\Delta\xi = 1 \times 10^{-3}$ to 2×10^{-3}, with 1.5×10^{-3} being the reference grid size used in the paper. The number of points per period of the rough surface $2h/\Delta\xi$ is thus between 10 (for $\Delta\xi = 2 \times 10^{-3}$) and 20 (for $\Delta\xi = 1 \times 10^{-3}$). For all simulations, the grid size along the η-direction is 4×10^{-3} and the CFL number is set to 0.28.

The waveforms of the overpressure at $r = 30$ and $z = 0.2$ are plotted in Fig. 22 for the five grid sizes. Overall, an excellent agreement is obtained for the different grid sizes. In particular, the peak overpressure only fluctuates by 4% between the finest mesh and the coarsest mesh. The effect of the grid size on the waveforms can be noticed on the oscillations after the first peak, whose period is about 0.18. They appear smoothed for the coarsest mesh, and their peak-to-peak amplitude slightly increases with the reduction in the grid size.

The corresponding energy spectral densities are shown in Fig. 23. Here as well, the curves show only little dependence on the grid size. The main difference is observed on the amplitude of the hump near $f = 5.5$, which is related to the oscillations on the waveforms discussed on the previous paragraph.

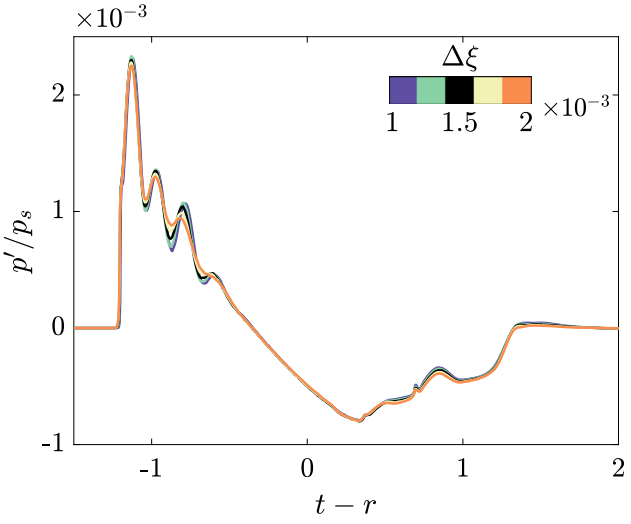

Fig. 22 Waveforms of the overpressure for $h = 0.01$ at $r = 30$ and $z = 0.2$ for several grid sizes

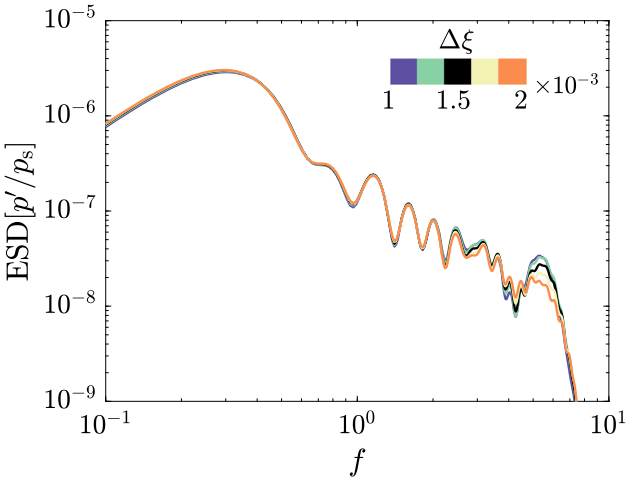

Fig. 23 Energy spectral density for $h = 0.01$ at $r = 30$ and $z = 0.2$ for several grid sizes

Additional convergence tests have been performed for roughness scales of $h = 0.02$ with the same grid sizes than for $h = 0.01$ and of $h = 0.15$ with grid sizes $\Delta\xi$ between 2×10^{-3} and 3×10^{-3}. Results are not shown for conciseness. The waveforms and the energy spectral densities present even smaller differences with the different grid sizes than for the case exemplified in Figs. 22 and 23.

In conclusion, the grid convergence study has shown that the results in terms of waveforms and spectra only marginally depend on the grid size. This demonstrates that grid convergence is obtained with the mesh used in the study.

Appendix 2: Effective admittance

Several methods have been proposed in the literature for deriving effective admittance of rough surfaces. Among

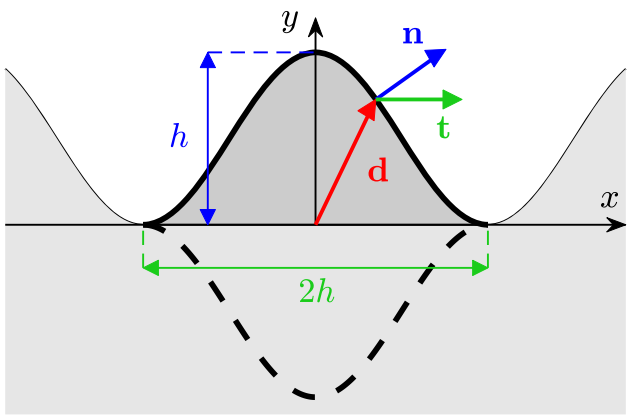

Fig. 24 Definition of the parameters to calculate I in the boss model

them, the boss model [9,36] is especially well suited for rough periodic surfaces. In this model, the rough surface is composed of identical roughness elements with a characteristic size h placed on an underlying smooth surface and spaced apart by a distance b.

For a 1D rough periodic surface at low frequencies ($\omega h < \omega b \leq 1$), the effective admittance can be written at grazing incidence as [9,36]:

$$\beta(\omega) = -\mathrm{i}\omega\epsilon, \tag{28}$$

where ϵ is related to the geometric properties of the rough surface via:

$$\epsilon = V\left(\frac{1+K}{\nu} - 1\right), \tag{29}$$

with ν given by:

$$\nu = 1 + \frac{\pi}{3} V \frac{1+K}{b}. \tag{30}$$

The parameter V is the cross-sectional area of the roughness elements above the smooth plane per unit length, and K is a hydrodynamic factor that depends on the shape of the roughness element. Following Tolstoy [36] and Lauriks et al. [40], it can be determined by the relation $K = I/(1-I)$ with:

$$I = \frac{1}{\pi}\int_L \frac{\mathbf{d}\cdot\mathbf{t}}{|\mathbf{d}|^2}\mathrm{d}\mathbf{L}\cdot\mathbf{t}, \tag{31}$$

where the integral is performed along the surface of the roughness element. In the above equation, $\mathbf{t}$ denotes the vector tangent to the smooth plane and $\mathbf{d}$ the vector between the centroid of the roughness element plus its image by the smooth plane and a point on the surface of the roughness element (Fig. 24). Setting $\mathbf{t} = (1,0)$ and using the parametrization $\mathbf{d} = (x(t), y(t))$ with $a \leq t \leq c$, one has $\mathrm{d}\mathbf{L} = (-y'(t), x'(t))\,\mathrm{d}t$, which yields:

$$I = -\frac{1}{\pi}\int_a^c \frac{x(t)\,y'(t)}{x^2(t)+y^2(t)}\,\mathrm{d}t. \tag{32}$$

The profile in (1) is modeled as a 1D rough surface with roughness elements of sinusoidal shape and of width $2h$ separated by a distance $2h$. This corresponds to $b = 2h$ and $V = h/2$. For determining K, the parametrization $x(t) = ht$ and $y(t) = h/2[1+\cos(\pi t)]$ for $-1 \leq t \leq 1$ is chosen. This gives:

$$I = \frac{1}{2}\int_{-1}^{1} \frac{t\sin(\pi t)}{t^2+\cos^4(\pi t/2)}\mathrm{d}t \approx 0.55. \tag{33}$$

Combining the values of the different parameters to determine ϵ in (29) finally leads to (20).

References

1. Kinney, G.F., Graham, K.J.: Explosive Shocks in Air, 2nd edn. Springer, New York (1985)
2. Ben-Dor, G.: Shock Wave Reflection Phenomena, 2nd edn. Springer, Berlin (2007)
3. Dewey, J.M., McMillin, D.J.: Photogrammetry of spherical shocks reflected from real and ideal surfaces. J. Fluid Mech. **81**(4), 701–717 (1977). https://doi.org/10.1017/S0022112077002304
4. Dewey, J.M., McMillin, D.J.: An analysis of the particle trajectories in spherical blast waves reflected from real and ideal surfaces. Can. J. Phys. **59**(10), 1380–1390 (1981). https://doi.org/10.1139/p81-182
5. Huber, P.W., McFarland, D.R.: Effect of surface roughness on characteristics of spherical shock waves. NASA Technical Report R-23, pp. 1–25 (1959)
6. Needham, C.E.: Blast Waves, 2nd edn. Springer, New York (2018)
7. Karzova, M.M., Lechat, T., Ollivier, S., Dragna, D., Yuldashev, P.V., Khokhlova, V.A., Blanc-Benon, P.: Effect of surface roughness on nonlinear reflection of weak shock waves. J. Acoust. Soc. Am. **146**(5), EL438-433 (2019). https://doi.org/10.1121/1.5133737
8. Qin, Q., Attenborough, K.: Characteristics and application of laser-generated acoustic shock waves in air. Appl. Acoust. **65**(4), 325–340 (2004). https://doi.org/10.1016/j.apacoust.2003.11.003
9. Attenborough, K., Li, K.M., Horoshenkov, K.: Predicting Outdoor Sound. Taylor & Francis, London (2007)
10. Boulanger, P., Attenborough, K.: Effective impedance spectra for rough sea effects on atmospheric impulsive sounds. J. Acoust. Soc. Am. **117**(2), 751–762 (2005). https://doi.org/10.1121/1.1847872
11. Donato, R.J.: Model experiments on surface waves. J. Acoust. Soc. Am. **63**(3), 700–703 (1978). https://doi.org/10.1121/1.381797
12. Daigle, G.A., Stinson, M.R., Havelock, D.I.: Experiments on surface waves over a model impedance plane using acoustical pulses. J. Acoust. Soc. Am. **99**(4), 1993–2005 (1996). https://doi.org/10.1121/1.415386
13. Bashir, I., Taherzadeh, S., Attenborough, K.: Surface waves over periodically-spaced rectangular strips. J. Acoust. Soc. Am. **134**(6), 4691–4697 (2013). https://doi.org/10.1121/1.4824846
14. Berry, D.L., Taherzadeh, S., Attenborough, K.: Acoustic surface wave generation over rigid cylinder arrays on a rigid plane. J. Acoust. Soc. Am. **146**(4), 2137–2144 (2019). https://doi.org/10.1121/1.5126856
15. Duff, R.E.: The interaction of plane shock waves and rough surfaces. J. Appl. Phys. **23**(12), 1373–1379 (1952). https://doi.org/10.1063/1.1702077
16. Takayama, K., Gotoh, J., Ben-Dor, G.: Influence of surface roughness on the shock transition in quasi-stationary and truly non-stationary flows. In: Treanor, C.E., Hall, J.G. (eds.) Shock Tubes and Waves, Proceedings of the 13th International Symposium on Shock Tubes and Waves, Niagara Falls, NY, pp. 326–334 (1981)
17. Takayama, K., Ben-Dor, G., Gotoh, J.: Regular to Mach reflection transition in truly nonstationary flows–influence of surface roughness. AIAA J. **19**(9), 1238–1240 (1981). https://doi.org/10.2514/3.7852
18. Ben-Dor, G., Mazor, G., Takayama, K., Igra, O.: Influence of surface roughness on the transition from regular to Mach reflection in pseudo-steady flows. J. Fluid Mech. **176**, 333–356 (1987). https://doi.org/10.1017/S0022112087000703
19. Reichenbach, H.: Roughness and heated layer effects on shock wave propagation and reflection—experimental results. Ernst-Mach-Institut, Rep. E25/85 (1985)
20. Adachi, T., Kobayashi, S., Suzuki, T.: An experimental analysis of oblique shock reflection over a two-dimensional multi-guttered wedge. Fluid Dyn. Res. **9**(5), 119–132 (1992). https://doi.org/10.1016/0169-5983(92)90062-2

21. Suzuki, T., Adachi, T., Kobayashi, S.: Experimental analysis of reflected shock behavior over a wedge with surface roughness. JSME Int. J. Ser. B Fluids Therm. Eng. **36**(1), 130–134 (1993). https://doi.org/10.1299/jsmeb.36.130
22. Gal-Chen, T., Sommerville, R.C.J.: On the use of a coordinate transformation for the solution of the Navier-Stokes equations. J. Comp. Phys. **17**, 209–228 (1975). https://doi.org/10.1016/0021-9991(75)90037-6
23. Salomons, E.M., Blumrich, R., Heimann, D.: Eulerian time-domain model for sound propagation over a finite-impedance ground surface. Comparison with frequency-domain models. Acta Acust. Acust. **88**(4), 483–492 (2002)
24. Bogey, C., Bailly, C.: Three-dimensional non-reflective boundary conditions for acoustic simulations: far field formulation and validation test cases. Acta Acust. Acust. **88**(4), 463–471 (2002)
25. Mohseni, K., Colonius, T.: Numerical treatment of polar coordinate singularities. J. Comput. Phys. **157**(2), 787–795 (2000). https://doi.org/10.1006/jcph.1999.6382
26. Bogey, C., Bailly, C.: A family of low dispersive and low dissipative explicit schemes for flow and noise computations. J. Comput. Phys. **194**(1), 194–214 (2004). https://doi.org/10.1016/j.jcp.2003.09.003
27. Bogey, C., de Cacqueray, N., Bailly, C.: A shock-capturing methodology based on adaptative spatial filtering for high-order non-linear computations. J. Comput. Phys. **228**(5), 1447–1465 (2009). https://doi.org/10.1016/j.jcp.2008.10.042
28. Berland, J., Bogey, C., Marsden, O., Bailly, C.: High-order, low dispersive and low dissipative explicit schemes for multiple-scale and boundary problems. J. Comput. Phys. **224**(2), 637–662 (2007). https://doi.org/10.1016/j.jcp.2006.10.017
29. Sabatini, R., Marsden, O., Bailly, C., Bogey, C.: A numerical study of nonlinear infrasound propagation in a windy atmosphere. J. Acoust. Soc. Am. **140**(1), 641–656 (2016). https://doi.org/10.1121/1.4958998
30. Berland, J., Bogey, C., Bailly, C.: Low-dissipation and low-dispersion fourth-order Runge-Kutta algorithm. Comput. Fluids **35**(10), 1459–1463 (2006). https://doi.org/10.1016/j.compfluid.2005.04.003
31. Karzova, M.M., Lechat, T., Ollivier, S., Dragna, D., Yuldashev, P.V., Khokhlova, V.A., Blanc-Benon, P.: Irregular reflection of spark-generated shock pulses from a rigid surface: Mach–Zehnder interferometry measurements in air. J. Acoust. Soc. Am. **145**(1), 26–35 (2019). https://doi.org/10.1121/1.5084266
32. Emmanuelli, A., Dragna, D., Ollivier, S., Blanc-Benon, P.: Characterization of topographic effects on sonic boom reflection by resolution of the Euler equations. J. Acoust. Soc. Am. **149**(4), 2437–2450 (2021). https://doi.org/10.1121/10.0003816
33. Boutillier, J., Ehrhardt, L., De Mezzo, S., Deck, C., Magnan, P., Naz, P., Willinger, R.: Evaluation of the existing triple point path models with new experimental data: proposal of an original empirical formulation. Shock Waves **28**, 243–252 (2018). https://doi.org/10.1007/s00193-017-0743-7
34. Reed, J.W.: Atmospheric attenuation of explosion waves. J. Acoust. Soc. Am. **61**(39), 39–47 (1977). https://doi.org/10.1121/1.381266
35. Dragna, D., Blanc-Benon, P., Poisson, F.: Time-domain solver in curvilinear coordinates for outdoor sound propagation over complex terrain. J. Acoust. Soc. Am. **133**(6), 3751–3763 (2013). https://doi.org/10.1121/1.4803863
36. Tolstoy, I.: Smoothed boundary conditions, coherent low-frequency scatter, and boundary modes. J. Acoust. Soc. Am. **75**(1), 1–22 (1984). https://doi.org/10.1063/1.1666645
37. Habault, D., Filippi, P.J.T.: Ground effect analysis: surface wave and layer potential representations. J. Sound Vib. **79**(4), 529–550 (1981). https://doi.org/10.1016/0022-460X(81)90464-8
38. Xiao, W., Andrae, M., Gebbeken, N.: Development of a new empirical formula for prediction of triple point path. Shock Waves **30**, 677–686 (2020). https://doi.org/10.1007/s00193-020-00968-7
39. Faure, O., Gauvreau, B., Junker, F., Lafon, P., Bourlier, C.: Modelling of random ground roughness by an effective impedance and application to time-domain methods. Appl. Acoust. **119**, 1–8 (2017). https://doi.org/10.1016/j.apacoust.2016.11.019
40. Lauriks, W., Kelders, L., Allard, J.F.: Surface waves above gratings having a triangular profile. Ultrasonics **36**(8), 865–871 (1998). https://doi.org/10.1016/S0041-624X(98)00009-2

JASA ARTICLE

Characterization of topographic effects on sonic boom reflection by resolution of the Euler equations

Ariane Emmanuelli,[a] Didier Dragna, Sébastien Ollivier, and Philippe Blanc-Benon
Ecole Centrale de Lyon, Institut National des Sciences Appliquées de Lyon, Centre National de la Recherche Scientifique, Laboratoire de Mécanique des Fluides et d'Acoustique, Université Claude Bernard Lyon I, Unité Mixte de Recherche 5509, 36 Avenue Guy de Collongue, F-69134, Ecully, France

ABSTRACT:
The influence of topography on sonic boom propagation is investigated. The full two-dimensional Euler equations in curvilinear coordinates are solved using high-order finite-difference time-domain techniques. Simple ground profiles, corresponding to a terrain depression, a hill, and a sinusoidal terrain, are examined for two sonic boom waves: a classical N-wave and a low-boom. Ground reflection of the sonic boom is affected by elevation variations: a concave ground profile induces compression, which tends to increase the peak pressure in particular, while the opposite is true for convex elevation variations, which lead to expansion and a reduction in peak pressure. The reflected boom is then strongly altered. Furthermore, a sufficiently concave topography can cause focal zones, which generate extra contributions at ground level in the form of U-waves in addition to the reflected wave. This mechanism has the largest effect on waveforms at ground level. The variations of standard metrics are of a few dBs compared to a flat ground for both sonic boom waves, and they are notably greater for the terrain depression than for the hill. Finally, in the case of a sinusoidal terrain, the pressure waveforms are composed of multiple arrivals due to successive focal zones.
 https://doi.org/10.1121/10.0003816
(Received 6 November 2020; revised 4 February 2021; accepted 1 March 2021; published online 8 April 2021)
[Editor: Lixi Huang] Pages: 2437–2450

I. INTRODUCTION

Several supersonic business jet projects are under development (Sun and Smith, 2017), with entry-into-service planned in the coming years. This should mark the beginning of a second era of commercial supersonic flight. However, due to the sonic boom, overland commercial supersonic flight remains banned in most countries. This has serious consequences on the possible demand for supersonic transport and on its commercial success (Liebhardt *et al.*, 2020). For public acceptance, it is thus important to reduce sonic boom annoyance by designing low-boom aircraft, but also to be able to accurately predict the sonic boom that will be generated at ground level by this new generation of supersonic aircraft.

To this end, meteorological and ground effects have to be taken into account. While several studies are devoted to the former, ground effects have not received much attention. It is thus common in prediction models to account for ground reflection by multiplying the sonic boom incident to the ground by a constant factor, usually equal to 1.9 [for instance, in recent papers Ueno *et al.* (2017) and Phillips and West (2019)]. However, for specific configurations such as focused booms and booms near the carpet cut-off, studies (Coulouvrat, 2002; Rendón and Coulouvrat, 2005) have shown that ground absorption significantly affects the sonic boom signature with a reduction of the peak overpressure and an increase in rise time. Similar effects have been observed for sea roughness (Boulanger and Attenborough, 2005). The influence of irregular terrain on sonic boom reflection has been studied little, even though the dependence of sonic boom at the ground level on the surrounding topography can be expected. In their comprehensive review, Maglieri *et al.* (2014) only refer to the work of Dini and Lazzeretti (1969) on this subject. Therefore, there is a need to investigate how a sonic boom is affected by the topography at ground level using modern prediction methods.

The prediction of the sonic boom remains mainly based on the analytical or numerical calculation of the flow field near the aircraft, coupled with efficient geometric acoustic methods to calculate the propagation through the atmosphere to the ground [see, e.g., Cleveland *et al.* (1996), Rallabhandi (2011), and Kanamori *et al.* (2018)]. Ray-tracing was thus the only method employed for far-field prediction in the second and third AIAA Sonic Boom Prediction Workshops (AIAA, 2017, 2020; Rallabhandi and Loubeau, 2019). One-way wave equation methods are favored when propagation in a turbulent medium is examined (Blanc-Benon *et al.*, 2002; Yuldashev *et al.*, 2017). State-of-the-art simulations (Luquet *et al.*, 2019; Stout and Sparrow, 2019) are now able to consider a three-dimensional geometry.

[a]Electronic mail: ariane.emmanuelli@ec-lyon.fr, ORCID: 0000-0003-3153-194X.

https://doi.org/10.1121/10.0003816

Recently, the first direct simulations of the entire flow field around a supersonic body were performed by Yamashita and Suzuki (2016) with the aim of computing the generation of the sonic boom and its propagation in the atmosphere in a single simulation. While appealing, this approach is computationally demanding, especially to capture the high-frequency characteristics of the sonic boom wave. A grid refinement strategy is thus required near the shocks, which is relevant for a steady sonic boom but seems to be hardly applicable as soon as atmospheric turbulence or irregular terrain are accounted for. Such simulations have been limited to a stratified atmosphere until now, and ground reflection was neglected.

Numerical simulations based on the fluid mechanics equations are, however, also attractive for sonic boom propagation in the planetary boundary layer. Compared to ray-tracing methods, they readily handle diffraction and do not suffer from the angular limitations of one-way wave equations. This is of particular importance for propagation over irregular terrain because shadow zones, caustics, and focal zones and backward diffraction are significant in this case.

The objectives of this study are to investigate the influence of irregular terrain on sonic boom reflection and to identify the physical mechanisms at play. With this aim, numerical simulations based on the Euler equations are carried out. For ease of analysis, simple ground profiles are considered. Two sonic boom signatures are examined: a classical N-wave, as generated by the former generation of civil supersonic aircraft, and a low-boom wave, which is expected for the next generation.

The paper is organized as follows. In Sec. II, the propagation model is detailed, including the equations, the boundary conditions, and the injection of the sonic boom wave. The configurations investigated are then described in terms of both input and computational parameters and a mesh convergence study is performed. The results for isolated terrain irregularities, namely, a terrain depression and a hill, are shown in Sec. III. The change in the sonic boom signature along the ground and in the corresponding metrics are discussed. Section IV focuses on a sinusoidal terrain and cumulative effects are examined. Concluding remarks are given in Sec. V.

II. SETUP OF NUMERICAL SIMULATIONS

A. Presentation of numerical methods

Sonic boom propagation above non-flat terrain is considered in a two-dimensional geometry, corresponding to the vertical plane through the axis of the aircraft (see Fig. 1). The Euler equations (Anderson, 1995) are solved using numerical simulation, hence neglecting viscous and thermal diffusion terms. A curvilinear coordinate transformation is applied to allow for variations of the ground profile, as illustrated in the computational domain representation in Fig. 2. In what follows, ρ denotes the density, p the pressure, ρe the energy density, u and v the horizontal and vertical components of velocity. Their mean values are

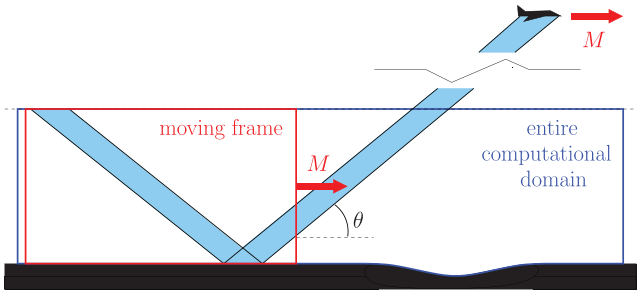

FIG. 1. (Color online) Sketch of the computational setup including the moving frame.

indicated by the subscript 0. After transformation from the Cartesian to curvilinear coordinate systems $(\vec{e}_x, \vec{e}_z)$ and $(\vec{e}_\xi, \vec{e}_\eta)$, the Euler equations in the conservative form are written as

$$\frac{\partial}{\partial t}\left(\frac{\mathbf{U}}{J}\right) + \frac{\partial}{\partial \xi}\left(\frac{\xi_x \mathbf{E} + \xi_z \mathbf{F}}{J}\right) + \frac{\partial}{\partial \eta}\left(\frac{\eta_x \mathbf{E} + \eta_z \mathbf{F}}{J}\right) = 0, \tag{1}$$

where t is time, $\mathbf{U} = [\rho\ \rho u\ \rho v\ \rho e]^T$ is the vector of unknowns, and $\mathbf{E}$ and $\mathbf{F}$ are the following vectors:

$$\mathbf{E} = \begin{bmatrix} \rho u \\ \rho u^2 + p \\ \rho uv \\ u(\rho e + p) \end{bmatrix}, \quad \mathbf{F} = \begin{bmatrix} \rho v \\ \rho uv \\ \rho v^2 + p \\ v(\rho e + p) \end{bmatrix}. \tag{2}$$

Finally, in Eq. (1), the Jacobian of the transformation is denoted by $J = (\xi_x \eta_z - \xi_z \eta_x)$, where the notation $i_j = \partial i / \partial j$ is used for the Jacobian terms. The equations are closed using the definition of energy density for a perfect gas,

$$\rho e = \frac{p}{\gamma - 1} + \frac{\rho}{2}(u^2 + v^2), \tag{3}$$

with γ the heat capacity ratio.

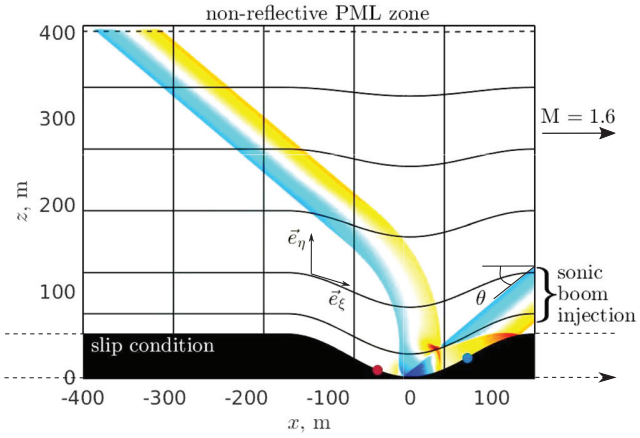

FIG. 2. (Color online) Illustration of the evolution of the mesh in curvilinear coordinates with an irregular ground profile and description of the boundary conditions of the moving frame domain.

https://doi.org/10.1121/10.0003816

The terrain-following transformation proposed by Gal-Chen and Sommerville (1975) is employed,

$$x(\xi,\eta) = \xi, \tag{4}$$

$$z(\xi,\eta) = h(\xi) + \frac{\eta}{z_{max}}[z_{\max} - h(\xi)], \tag{5}$$

where h is the ground profile and $z_{\max}$ is the maximal altitude of the computational domain. This formulation assumes the terrain is sufficiently smooth, without any slope discontinuity, so that topographies such as cliffs or buildings cannot be considered with this version of the code. The first line of the mesh follows the ground profile, as represented in Fig. 2. The following lines in the direction parallel to the ground then slowly adapt towards a horizontal line at the top of the domain. The mesh lines in the z-direction remain at constant axial positions, which leads to the simplification of Eq. (1) with $\xi_x = 1$ and $\xi_z = 0$.

High-order, optimized numerical schemes are used to accurately capture acoustic fluctuations. A fourth order Runge-Kutta scheme including six sub-steps is used in time (Berland *et al.*, 2006). The equations are discretized in space using fourth order finite difference schemes over 11 points (Bogey and Bailly, 2004; Berland *et al.*, 2006). Selective filters of sixth order for the interior points (Bogey *et al.*, 2009) and of second order for the boundary points (Berland *et al.*, 2006) are used. They aim at removing grid-to-grid oscillations that are not solved by the finite-difference schemes and can lead to numerical instabilities. A shock-capturing method (Bogey *et al.*, 2009; Sabatini *et al.*, 2016) is applied to handle shocks, that can be generated during sonic boom propagation. It consists in adding artificial viscosity only near the shocks. Note that as an explicit time-integration scheme is used, the time step and the grid size are related via the Courant-Friedrichs-Lewy (CFL) number.

The grid size in both directions $\mathrm{d}\xi$ and $\mathrm{d}\eta$ remains constant in Cartesian coordinates throughout the computational domain and is the same, i.e., $\mathrm{d}\xi = \mathrm{d}\eta$. While the mesh coordinates and Jacobian terms are computed over the whole domain, flow variables are only simulated in a moving frame, allowing one to reduce the computational cost significantly. As shown in Fig. 1, this moving frame corresponds to a smaller domain which advances in time along the ground profile and at the flight Mach number M, in order to follow the sonic boom wave emitted by the supersonic aircraft.

A rigid wall boundary condition is set at the bottom of the domain, with normal velocity equal to zero. While ground absorption is expected to attenuate the high frequency content of the reflected boom significantly, increasing the rise time and reducing the peak pressure, it is not taken into consideration in order to focus on topographic effects. Note that specific numerical methods suitable for high-order time-domain solvers have been developed to account for locally- or extended-reacting ground surfaces (Dragna *et al.*, 2015; Troian *et al.*, 2017). Modeling ground absorption on sonic boom reflection is thus readily feasible and is left for future work. As previously explained, the use of curvilinear coordinates allows this boundary to be curved to take into account variations of terrain elevation. The ground profile is read from a file, so that any curved complex terrain may be considered. A non-reflective boundary condition of convolutional PML (perfectly matched layer) type is applied at the top of the domain (Komatitsch and Martin, 2007). As illustrated in Fig. 2, it uses a sponge zone over which flow variables are attenuated increasingly with altitude, up to the top boundary where perturbations are zero. This damping is implemented by applying the following coefficient:

$$\sigma(z) = \frac{1}{\mathrm{d}t}\left(\frac{z - z_{\mathrm{PML}}}{d_{\mathrm{PML}}}\right)^2, \tag{6}$$

where $\mathrm{d}t$ is the time step of the simulation, z_{PML} is the altitude in the beginning of the PML zone, and d_{PML} its size. The attenuation is therefore zero at $z = z_{\mathrm{PML}}$ and it reaches a maximum of $1/\mathrm{d}t$ at the top boundary of the computational domain. Note that since the moving frame is attached to the aircraft, it advances at supersonic speed. Therefore, the acoustic fluctuations naturally leave the computational domain at its left boundary, without the need of a non-reflective condition. The sonic boom wave is injected through the right-hand side of the domain by interpolation. Linear interpolation is used, which proves sufficient, especially when the original sonic boom wave is much more discretized than the mesh. Usually, only the acoustic pressure waveform p' is available as an input, for instance, from ray-tracing simulations, which are typically used to propagate the wave from the aircraft near-field through the atmosphere and towards the ground. Thus, the relation between pressure and the other variables must be specified. Assuming isentropic perturbations without a mean flow (Thisse *et al.*, 2015), the boundary conditions on the right of the domain are written as

$$p = p_0 + p', \tag{7}$$

$$\rho = \rho_0\left(\frac{p}{p_0}\right)^{1/\gamma}, \tag{8}$$

$$\rho u = \frac{2\rho c_0}{\gamma - 1}\left[\left(\frac{p}{p_0}\right)^{(\gamma-1)/2\gamma} - 1\right]\sin\theta, \tag{9}$$

$$\rho v = -\frac{2\rho c_0}{\gamma - 1}\left[\left(\frac{p}{p_0}\right)^{(\gamma-1)/2\gamma} - 1\right]\cos\theta, \tag{10}$$

where $c_0 = \sqrt{\gamma p_0/\rho_0}$ is the sound speed and the wave is injected at an angle θ from the horizontal, equal to $\theta = \sin^{-1}(1/M)$ for a homogeneous atmosphere at rest. For sufficiently small values of p'/p_0, these relations become the classical plane wave relations between the acoustic pressure and the acoustic density and velocity. In particular, for the input waveforms considered thereafter, the differences between the nonlinear relations in Eqs. (8)–(10) and the

plane wave relations were found to be negligible. It is, however, recalled that the full Euler equations are solved with this method, rather than the linearized Euler equations to account for possible nonlinear effects during the propagation of the sonic boom, for example, in the case of focusing.

The flow variables are initialized with their ambient values. The sonic boom wave progressively develops from the right boundary and, after a transient period, extends over the entire moving frame. To reduce computation time, the simulations are performed in two steps. First, a simulation is run for a flat ground and is stopped once the transient period is over and a steady sonic boom wave is obtained. Second, the simulation with the irregular terrain is launched using the flow at the last iteration of the transient computation as the initial condition. This allows one to perform simulations for different ground profiles without having to compute the transient period each time. Note this is only the case if the grid size remains unchanged.

The code is parallelized using the OpenMP parallel-computing language (Mattson *et al.*, 2019) to reduce restitution times. The flow variables are obtained in the temporal domain, and the resulting signals are post-processed, notably to compute the perceived noise. To do so, two different metrics are used: PL (perceived level) (Stevens, 1972), which is well suited to various sonic boom signatures (Leatherwood *et al.*, 2002), and CSEL weighting, which gives emphasis to lower frequencies. Other metrics, namely, ASEL, BSEL, DSEL, ESEL, and ISBAP, were shown to be highly correlated to human perception (Loubeau *et al.*, 2015), like PL. For conciseness, they are not discussed hereafter. However, Appendix B shows these metrics vary with ground elevation in a similar way as PL and CSEL.

B. Case description

1. Input parameters

The configurations investigated are described in this section. Two sonic boom waves are considered. The first is an N-wave, which is the classical sonic boom wave expected from a conventional supersonic aircraft. The chosen wave has a rise time of 0.0011 s. The second is the low-boom C25D wave, that originates from the near-field signature of a notional configuration aiming at representing a sonic boom demonstrator class vehicle. It was in particular used in the 2nd AIAA Sonic Boom Workshop (AIAA, 2017; Rallabhandi and Loubeau, 2019). This near-field signature was then propagated down to the ground by ONERA using BANGV nonlinear ray tracing code in a stratified and absorbing atmosphere (Loubeau and Coulouvrat, 2009). The rise time of this low-boom wave is equal to 0.014 s which is much larger than that of the N-wave. Both waves are presented in Fig. 3(a). They are injected through the right boundary of the domain, as illustrated in Fig. 3(b) which shows the reflection of the N-wave in the baseline case of a flat terrain through a pressure fluctuation map.

Throughout this study, the atmosphere is kept homogeneous and at rest following the conditions in Table I, which allows one to focus on topographic effects. Note the code

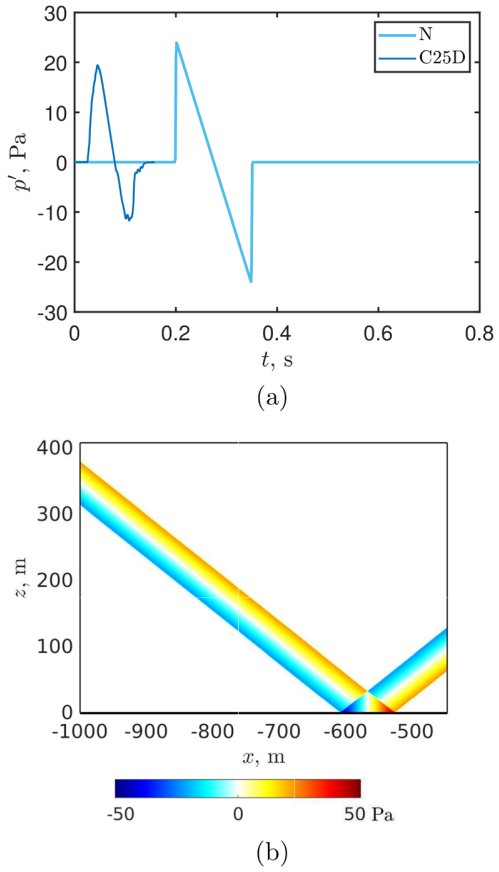

FIG. 3. (Color online) (a) Sonic boom time signals—classical N-wave and C25D low-boom wave. (b) Pressure fluctuation map of an N-wave reflected over flat terrain.

allows the use of varying atmospheric conditions, which will be taken into account in future studies. Furthermore, the flight Mach number is set to 1.6.

Simple ground profiles are investigated for easier identification of mechanisms associated with topographic effects on sonic boom reflection. A single terrain depression, a hill and a sinusoidal ground profile are chosen, and discussed in Secs. III and IV. A maximal elevation variation $H = 50$ m is chosen, associated with a terrain irregularity characteristic length $L = 300$ m, leading to a large slope and allowing to highlight topographic effects in these simplified configurations.

2. Computational domain parameters

For all simulations, the moving frame is shifted along the ξ-direction by one grid size every two time steps. The CFL number defined by $\mathrm{CFL} = c_0 \mathrm{d}t/\mathrm{d}\xi$ is thus equal to $\mathrm{CFL} = 1/(2M)$. This yields a CFL number of 0.3125, well below 1 throughout the domain in curvilinear coordinates.

TABLE I. Initial flow conditions: mean density ρ_0, speed of sound c_0, heat capacity ratio γ, and flight Mach number M.

ρ_0	c_0	γ	M
1.22 kg/m^3	340 m/s	1.4	1.6

https://doi.org/10.1121/10.0003816

TABLE II. Mesh convergence over flat terrain with both an N-wave and the low-boom C25D wave. Results are compared to those obtained with the wave initially injected into the domain with a reflection factor of 2, for which the absolute value of the peak pressure and perceived noise are given.

Wave	$d\xi$ (m)	p_{peak}	PL (dB)	CSEL (dB)
N	initial	47.8 Pa	98.2	103.2
N	0.25	−1.1 %	−4.0	−0.7
N	0.10	−0.05 %	−0.5	−0.1
N	0.06	+0.01 %	−0.01	+0.02
C25D	initial	38.8 Pa	83.2	97.2
C25D	0.25	−0.008 %	−1.3	−0.05
C25D	0.10	−0.003 %	−0.3	−0.002

A mesh convergence study is performed to choose a grid size leading to accurate sonic boom propagation. Table II gives the evolution of peak pressure and perceived noise with grid size for both N and C25D sonic boom waves reflected over a flat surface. Compared to the wave initially injected into the computational domain, the peak pressure variation appears negligible for all grid sizes, with only 1.1% variation at worst with the N-wave and a grid size $d\xi = 0.25$ m. Perceived noise levels prove more sensitive to grid size, and variations heavily depend on the type of metric considered. PL and CSEL metrics are chosen for this study, as explained in Sec. II A. Indeed, with the N-wave and the coarsest grid ($d\xi = 0.25$ m), the error compared to the initial wave reaches −4.0 PLdB and only −0.7 dBC. This is due to the nature of these metrics, as CSEL weighting takes into account the entire range of audible frequencies, including low frequencies, while PL gives much more weight to high frequencies than to low ones. These variations are greatly reduced with a grid size of $d\xi = 0.1$ m, although a difference of –0.5 PLdB persists, becoming negligible at $d\xi = 0.06$ m. The C25D wave has a lower frequency content, in particular, with a longer rise time than the sharp N-wave. This is reflected on the evolution of perceived noise with grid size, with a –1.3 PLdB difference compared to the initial C25D wave with the coarse grid and a negligible error with $d\xi = 0.1$ m, while the difference is negligible even with the coarsest grid using CSEL.

The spectra of these waves are represented in Figs. 4(a) and 4(d). They show the $d\xi = 0.1$ m mesh captures high frequencies well compared to the initial wave, as well as to the $d\xi = 0.06$ m mesh in the case of the N-wave. Also, note the vast improvement compared to the coarsest mesh. This confirms the good convergence with a grid size of $d\xi = 0.1$ m. The other plots presented in Fig. 4 show similar spectra, this time for reflection over irregular terrain: at $x = -40$ and 60 m, corresponding to positions in the downward and upward slopes of a terrain depression as illustrated in Fig. 2. Note the initial wave corresponds to a flat surface case and it is shown as reference only. Concentrating on the N-wave first, Figs. 4(b) and 4(c) display slightly degraded spectrum with $d\xi = 0.1$ m compared to $d\xi = 0.06$ m. This is due to the curvilinear transformation of the mesh, which, in the case of a terrain depression, leads to slightly larger grid sizes in the vicinity of the ground irregularity than with the Cartesian mesh. In the case of the C25D wave, the

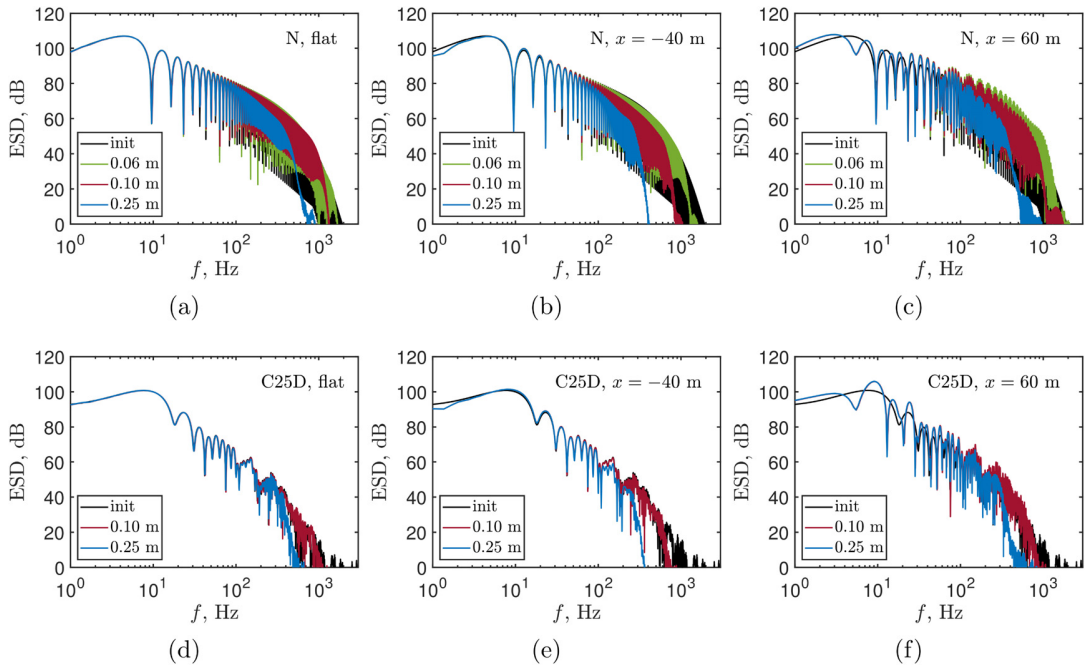

FIG. 4. (Color online) Energy spectral density (ESD) levels (reference 4×10^{-10} Pa^2/Hz^2) obtained with different grid sizes, and for (top) the N-wave and (bottom) the C25D wave with various terrain conditions: (left) flat surface and terrain depression (middle) on the downward slope, $x = -40$ m and (right) on the upward slope, $x = 60$ m. The case of the initial wave (init) is shown as reference. Note its pressure was multiplied by a factor of 2 to make the spectrum comparable with the spectra of the other waves, including ground reflection.

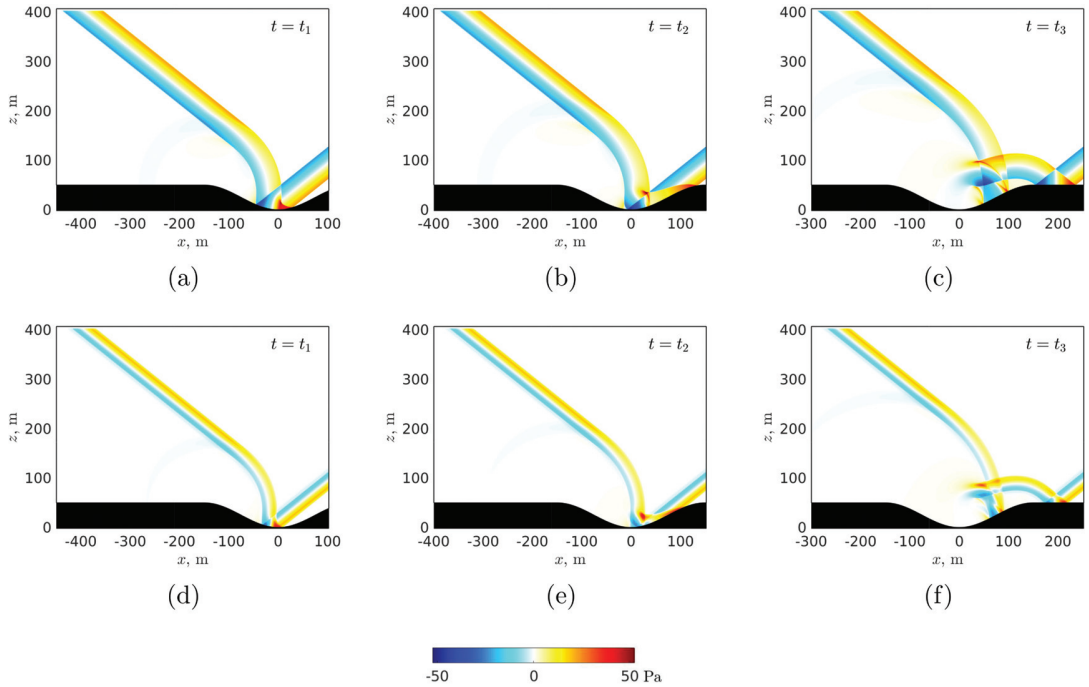

FIG. 5. Terrain depression-pressure fluctuation maps at different instants in time $t_1 < t_2 < t_3$ for the (top) N and (bottom) C25D waves.

$d\xi = 0.1$ m spectra frequency content appears satisfactory at both positions, as shown in Figs. 4(e) and 4(f). Note the initial wave does not account for topographic effects which explains spectrum shape differences. In view of this result and taking into account computational cost, a grid size of $d\xi = 0.1$ m is used for the C25D and sinusoidal cases. However, considering the sensitivity of PL noise level to high frequency content, a grid size of $d\xi = 0.06$ m is used for the N-wave terrain depression and hill cases in order to ensure good accuracy. See Appendix A for a discussion on the sensitivity of PL with the N-wave.

In the case of local terrain irregularities (terrain depression, hill), the moving frame domain size is set to 800×400 m, while with sinusoidal ground profiles which affect a larger region, it is 1000×400 m. The moving frame mesh sizes are thus for the local terrain irregularities of 32×10^6 and 90×10^6 points for grid sizes of $d\xi = 0.1$ m and $d\xi = 0.6$ m, respectively, and for the sinusoidal ground profile of 40×10^6 points.

The simulations were led with 32 processors. For the cases with locally irregular terrain, computational times $d\xi = 0.1$ m are about 1000 and 730 CPU hours for the transient period and the useful signal simulation over 1.6 km respectively, and 4400 and 3400 CPU hours $d\xi = 0.6$ m, while they are of 1200 and 2200 CPU hours in the case of a sinusoidal ground profile to obtain a signal over 4 km.

III. IMPACT OF ISOLATED TERRAIN IRREGULARITIES

The objective of this section is to characterize the sonic boom reflection mechanisms induced by topographic variations and their effect on the noise perceived at ground level in the case of simple local elevation variations, in order to isolate and explain topographic effects.

Mm. 1. Video showing the reflection of the N-wave along the terrain depression ground profile using pressure fluctuation maps($[-50; 50]$ Pa), a corresponding wavefront (blue) and wavefronts at other instants in time (dashed black), as well as caustic curves (red).

A. Terrain depression

A terrain depression is considered first. It is defined by the relation

$$h(x) = \begin{cases} \frac{H}{2}\left[1 - \cos\left(2\pi\frac{x}{L}\right)\right] & \text{if } x = [-L/2; L/2], \\ H & \text{otherwise}, \end{cases} \quad (11)$$

where $H = 50$ m and $L = 300$ m. The ground profile is visible on the pressure fluctuation maps shown in Fig. 5, which are represented at different iterations and for both the N and C25D waves. Their evolution along the full profile is available for the N-wave in Mm. 1. Focusing on the N-wave, first note the pressure map is heavily affected locally where the wave is reflected on the ground. As the ground profile slope reduces, expansion occurs, affecting the reflected sonic boom, in particular by the reduction of its peak pressure. This is visible in the latter part of the terrain irregularity in Fig. 5(b). The opposite is true in the case of an increasing slope such as in Fig. 5(a), where compression occurs and the peak pressure increases. Second, a strong variation of the

https://doi.org/10.1121/10.0003816

reflected wave can be observed, both in angle and amplitude, which is directly related to the change in elevation at ground level. Third, a focal zone is present in Fig. 5(c), leading to the most significant change in the pressure fluctuation field, with an additional high amplitude zone at the focal point, but also a component of the wave propagating back down towards the ground. This phenomenon can be explained by analyzing the wavefronts represented at different instants in time in Fig. 6(a). They are computed using a ray-tracing method (Candel, 1977; Gainville, 2008; Scott *et al.*, 2017). They are folded in the upward part of the terrain depression, at $x > 0$, which leads to the focal zone observed on the pressure map. The caustic curve (red) corresponding to this focal zone is also plotted. In this terrain depression case, it is reflected on the upward part of the profile at $x = 53$ m. In addition, a ray is plotted (green). After reflection ($x = -100$ m), it grazes the top of the terrain irregularity near $x = 150$ m. Subsequent rays will be reflected on the upward part of the depression, so that this ray delimits a shadow zone. Indeed, reflected rays cannot reach the zone below this ray, to the right of the terrain irregularity at ground level, for $x > 150$ m. Figure 6(b) shows the pressure fluctuation map presented in Fig. 5(c), on which the wavefronts and caustic curve are superposed. Note the pressure map and the wavefront corresponding to the same instant (full black line) are in good agreement. At this macroscopic level, the same mechanisms are found in the case of the low-boom C25D wave in Figs. 5(d)–5(f). Indeed, on these pressure maps, the local variations at ground level, the evolution of the reflected wave, and the focalization phenomenon are globally comparable with the N or C25D sonic boom waves.

Now, let us focus on how these phenomena affect the signals obtained at ground level. Waveforms simulated at different axial positions and resulting from the reflection of the N-wave are presented in Fig. 7. They are represented following a relative time $\tau = t - t_{\text{flat}}$, where t_{flat} is the time at the beginning of the waveform in the corresponding flat case. The signal that is the most affected compared to the smooth surface case was computed at position $x = 70$ m, just after the folding of the wavefront. This results in a U-wave, which is characteristic of focal zones and which originates from the additional contribution propagating back towards the ground. The resulting additional peaks are of larger amplitude and sharper than the first one. At position $x = 150$ m,

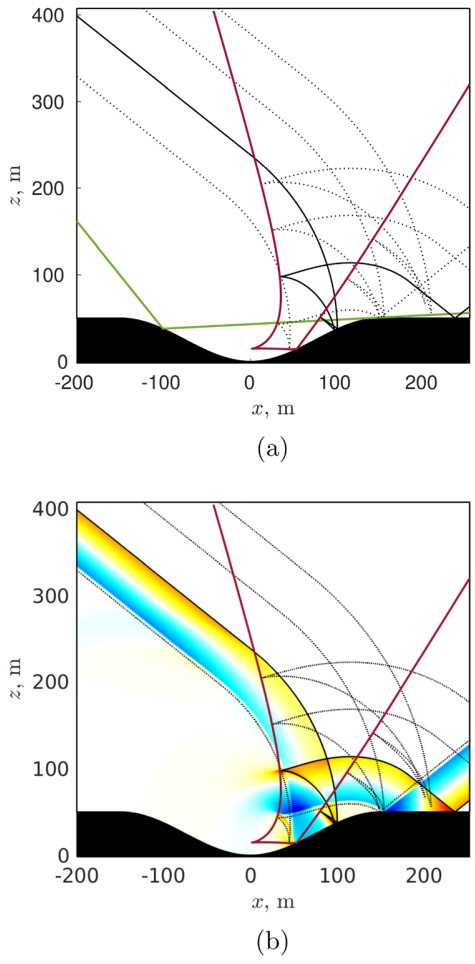

FIG. 6. (Color online) Terrain depression, N-wave (a) wavefronts at different instants in time (dotted black), and wavefront (full black line) corresponding to the pressure fluctuation map in Fig. 5(c), with the caustic curve (red) and the ray (green) delimiting the caustic shadow zone and (b) wavefronts overlaid on the pressure fluctuation map with the caustic curve.

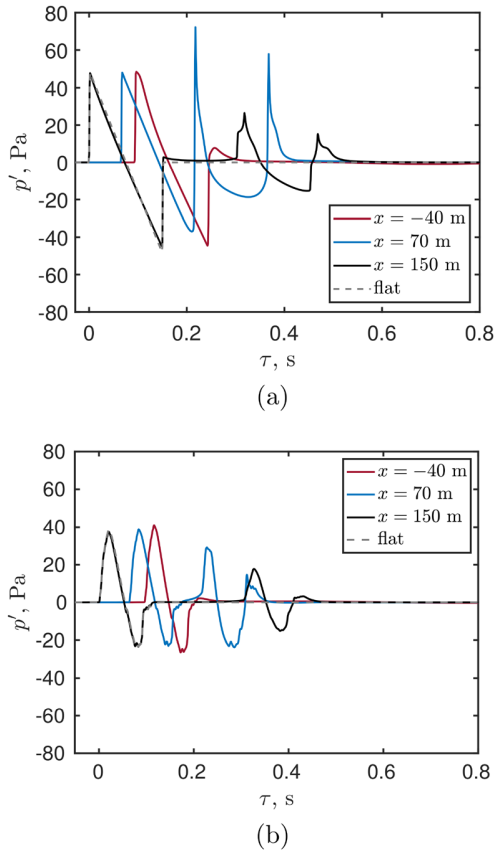

FIG. 7. (Color online) Terrain depression, (a) N and (b) C25D waves—time signals simulated at ground level, with τ the time relative to the beginning of the waveform in the flat case.

which corresponds to the end of the terrain depression, the U-wave is still present, but it has already been heavily attenuated. The rapidity of this attenuation can be explained by the presence of a shadow zone resulting from the elevation variation, as explained in the previous paragraph. Rays cannot reach this region and the energy of the signal is reduced. Finally, the signal at $x = -40$ m, before wavefront folding occurs, is much less affected, although a low amplitude secondary bump can be observed for $\tau = 0.25$ s. In addition, the N-wave peak appears more rounded at this position. In the same way as for the pressure fluctuation fields, the waveforms obtained with the C25D wave follow a similar trend as with the N-wave, although there are some differences. Indeed, the secondary peaks caused by wavefront folding have lower amplitudes than the first one. They also remain much more rounded with C25D than with the N-wave, corresponding to a lower frequency content of the original wave.

The signals discussed in the previous paragraphs are used to estimate the noise perceived at ground level with PL and CSEL metrics. It is normalized by the noise levels obtained with a flat terrain in each case, in order to highlight the influence of ground elevation. Its evolution over the ground profile is given in Fig. 8(a) in the N-wave case, along with the terrain slope $\mathrm{d}h/\mathrm{d}x$. In the first part of the terrain depression ($x = [-150; 0]$ m), both PL and CSEL variations due to topography remain negligible. After the minimum elevation point of the terrain depression, where the slope is zero and continues to rise ($x = [0; 75]$ m), both PL and CSEL are significantly amplified by ground elevation variations, by 5.5 PLdB and 4.9 dBC, respectively. This corresponds to the focal zone and the U-wave resulting from wavefront folding, as described previously. As the elevation gradient reduces again between the upward part of the terrain depression and the subsequent flat ground ($x = [75; 150]$ m), the perceived noise collapses back towards levels obtained over flat ground. This corresponds to the attenuation of the U-wave illustrated in Fig. 7(a).

A similar plot is shown for the C25D wave in Fig. 8(b). PL noise variations due to topography remain negligible in the downward part of the terrain depression, while CSEL variations are present, which is consistent with the lower frequency content of the C25D wave. Noise amplification reaches 1.1 dBC where the slope rises, towards the bottom of the terrain depression ($x = [-75; 0]$ m). This can be explained by the rise in signal energy caused by the superposition of the forming U-wave with the main waveform. This leads to an increase in wave amplitude in particular, as shown in Fig. 9 at position $x = -22$ m. The peak-to-peak amplitude reaches 72.3 Pa, that is 20% more than the initial C25D wave. The CSEL amplification due to topography then sharply reduces at the position $x = 24$ m, where the forming U-wave is superposed with the minimum of the original wave, cancelling out the negative peak. Once the U-wave has fully separated from the primary peak, noise spikes up before reducing back to the flat case levels at the end of the terrain depression, in a similar way as with the N-wave. The maximum perceived noise amplification reaches 4.6 PLdB and 3.5 dBC. This is lower than with the N-wave, by 0.9 PLdB and 1.4 dBC, respectively.

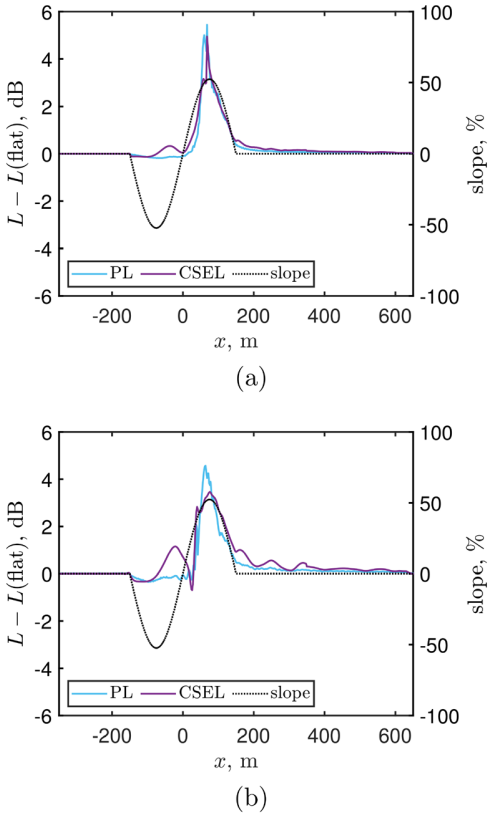

FIG. 8. (Color online) Terrain depression, (a) N and (b) C25D waves—perceived noise level L computed at ground level using PL and CSEL and normalized by the flat surface case, and ground profile slope.

B. Hill

This section is dedicated to sonic boom reflection over a hill. Similar to the ground profile discussed in the Sec. III A, it is defined by the relation

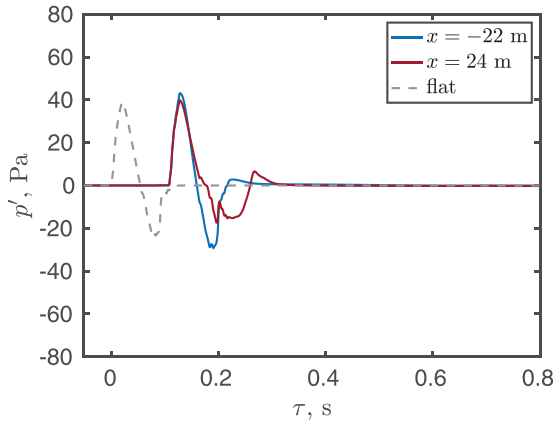

FIG. 9. (Color online) Terrain depression, C25D waves—time signals simulated at ground level at positions where the U-wave is formed, with τ the time relative to the beginning of the waveform in the flat case.

https://doi.org/10.1121/10.0003816

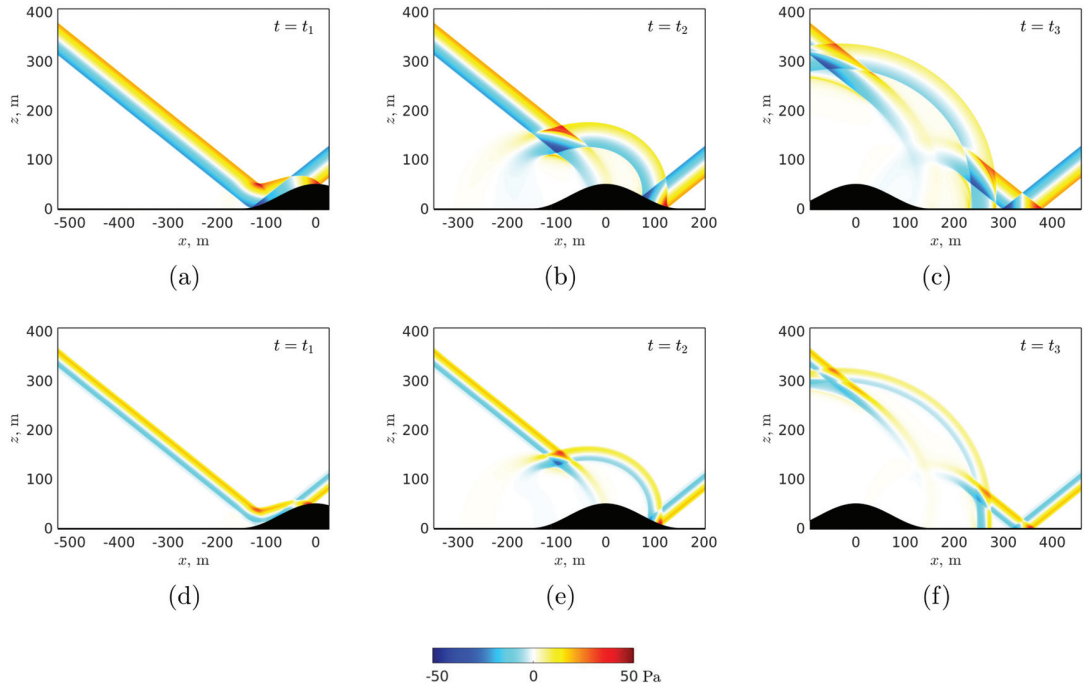

FIG. 10. Hill—pressure fluctuation maps at different instants in time $t_1 < t_2 < t_3$ for the (top) N and (bottom) C25D waves.

$$h(x) = \begin{cases} \dfrac{H}{2}\left[1 + \cos\left(2\pi\dfrac{x}{L}\right)\right] & \text{if } x = [-L/2; L/2], \\ 0 & \text{otherwise,} \end{cases} \quad (12)$$

where $H = 50$ m, $L = 300$ m. The ground profile is visible on the fluctuating pressure field maps presented in Fig. 10. They show both N and C25D waves are affected locally at the point of reflection on the ground and that their reflected component is strongly impacted, in a similar way as with the terrain depression. The evolution of the N-wave pressure fluctuation maps along the full profile is available in Mm. 2. Figures 10(c) and 10(f) show two focal zones are generated this time: the first is due to the transition between flat ground and the upward slope ($x = [-150; -75]$ m) and it results in a low amplitude additional contribution at ground level; the second, generated by the downhill part ($x = [75; 150]$ m) leads to stronger levels on the ground. Figure 11 depicts the same pressure map as Fig. 10(c), in the case of the N-wave, on which wavefronts and caustic curves are superposed. It shows wavefront folding over the upward part of the hill leads to the first focal zone, which moves upwards with time, while the second is generated as the wave moves from the downward part of the hill to the flat surface. This time, the focal zone moves towards the right and the caustic curve remains close to the ground. This explains why the additional contribution at ground level is of larger amplitude for the second focal zone, as the decay of a signal away from a caustic is related to the distance from the caustic [see, e.g., Salomons (1998)].

Mm. 2. Video showing the reflection of the N-wave along the hill ground profile using pressure fluctuation maps ([–50;50] Pa), a corresponding wavefront (blue) and wavefronts at other instants in time (dashed black), as well as caustic curves (red).

As for the terrain depression case, a U-wave is observed in Fig. 12 where focal zones are present, for both the C25D and N-waves. It is of low amplitude at $x = -30$ m, a position in the first half of the ground profile, where the additional contribution at ground level due to wavefront folding is weak. It is more significant at $x = 270$ m, where this contribution is stronger, but the secondary peak amplitude remains much smaller than in the terrain depression case (see Fig. 7), where the reflection of the caustic leads to increased amplitude. However, with the hill, this secondary peak is barely

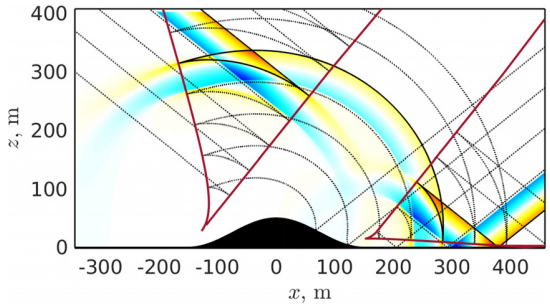

FIG. 11. (Color online) Hill, N-wave—pressure fluctuation map presented in Fig. 10(c), with corresponding wavefront (full black line), others at different instants in time (dotted black) and caustic curves (red).

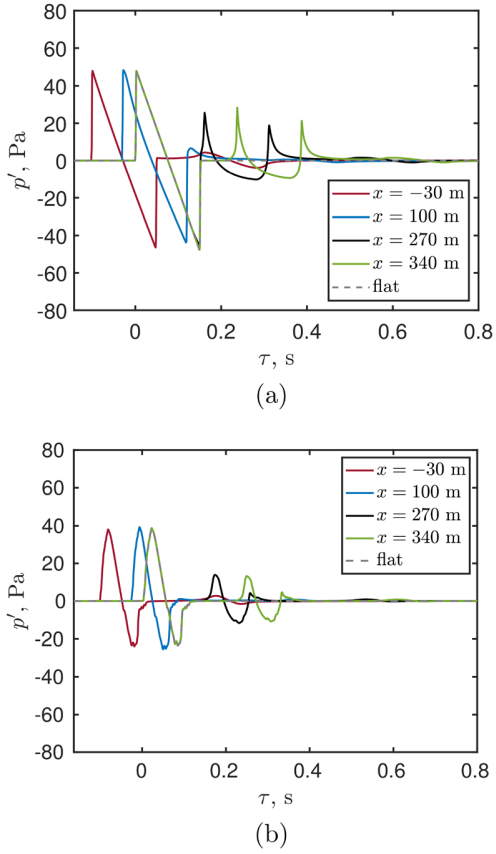

FIG. 12. (Color online) Hill, (a) N and (b) C25D waves—time signals simulated at ground level, with τ the time relative to the beginning of the waveform in the flat case. Note the main peak at $x = 340$ m coincides with the flat case curve for both wave types.

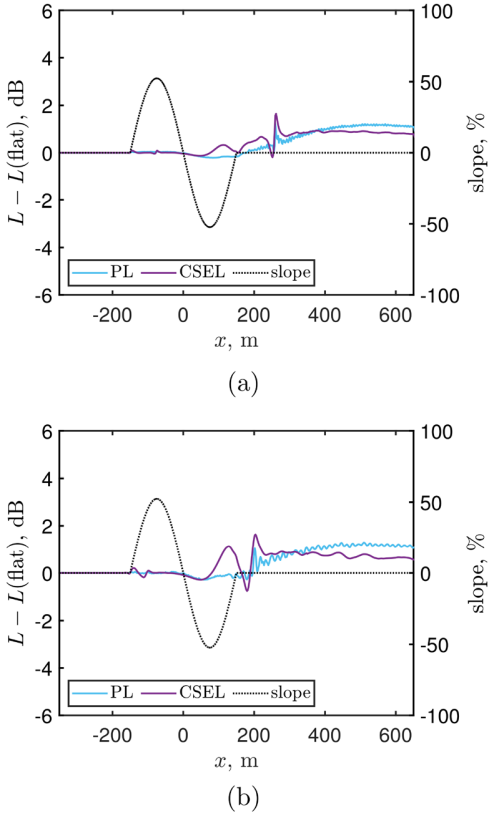

FIG. 13. (Color online) Hill, (a) N and (b) C25D waves—perceived noise level L computed at ground level using PL and CSEL and normalized by the flat surface case, and ground profile slope.

attenuated at positions further along the ground profile, and the signals at $x = 340$ m display similar secondary peak amplitudes as at $x = 270$ m. This is explained first by the absence of a shadow zone, which accelerates the decay in the case of the depression, and second by the proximity of the caustic curve with the ground after the hill, because of the relation between signal attenuation and distance from the caustic. As previously, a small secondary bump is observed at $x = 100$ m, just before wavefront folding occurs, and the main peak is blunter than the original N-wave.

The perceived noise levels computed from these waveforms, obtained at ground level in the N and C25D cases and normalized by the corresponding flat case, are plotted in Fig. 13, along with the elevation gradient. Variations with topography remain small up to the second and stronger wavefront folding, towards the end of the hill ($x > 150$ m). Then, as detailed in Sec. III A for the C25D wave, as the U-wave is formed and superposed to the original wave, CSEL increases before decreasing sharply as this superposition cancels out part of the signal. Finally, CSEL rises again as the U-wave detaches from the original wave. These CSEL variations are larger with C25D than with the N-wave, due to the C25D wave's thicker peak. In both cases, PL is much less affected by the superposition of the U-wave with the original wave, but it reaches similar amplification once the U-wave detaches, leading to additional peaks in the waveform. Unlike with the terrain depression, this focal zone leads to a plateau in the perceived noise plot in all cases. This is due to the slow attenuation of the U-wave along the caustic line, as explained in the previous paragraph. The maximum amplification due to topography along these plateaus are very close with the N and C25D waves, reaching 1.2 PLdB and 1.3 PLdB, respectively, and 0.9 dBC for both waves. These are significantly lower than in the case of a terrain depression (Fig. 8), which can be explained by the smaller slope variation between the hill's downward part and the flat terrain compared to the terrain depression.

IV. IMPACT OF SINUSOIDAL TERRAIN

While Sec. III was devoted to isolated terrain features, this section deals with sonic boom propagation above a sinusoidal terrain that can be considered as a succession of hills or, equivalently, of terrain depressions of the same size. The ground profile is given by

$$h(x) = \frac{H}{2}\left[1 - \cos\left(2\pi\frac{x}{L}\right)\right], \tag{13}$$

with the same values of H and L as those used in Sec. III.

https://doi.org/10.1121/10.0003816

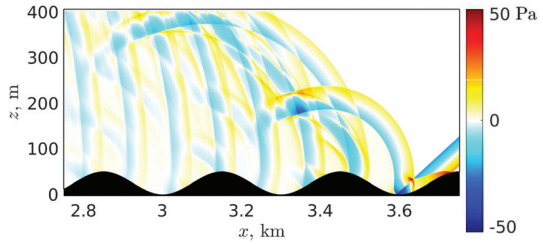

FIG. 14. Sinusoidal terrain, N-wave—pressure fluctuation map.

An example of a fluctuating pressure field map after propagation over more than ten terrain periods is presented in Fig. 14 for the N-wave. First, it can be observed that the wavefront structure of the incident and reflected boom waves near $x = 3.6$ km is similar to that for the terrain depression shown in Fig. 5(b). Second, after these two waves, a large number of wavefronts are observed. These are due to the generation of U-waves at each terrain irregularity and to their subsequent diffraction on the following irregularities.

Figure 15 shows a pressure waveform at the ground level in the case of both the N and C25D waves. In accordance with Fig. 14, it does not present a single contribution, as for a flat ground, or two main contributions as observed for isolated terrain irregularities, but many more. The two first contributions, considered separately, are very close to the waveform for the terrain depression at $x = 70$ m in Fig. 7 and they are the dominant ones. The additional contributions are however far from negligible: thus, for the N-wave, the peak-to-peak amplitude is of 23 Pa for the third contribution around $\tau = 0.6$ s, 15 Pa for the fourth one at $\tau = 0.9$ s and 11 Pa for the fifth one at $\tau = 1.2$ s. A similar order of magnitude is obtained for the C25D wave. Compared to the main U-wave, each successive additional contribution appears more and more rounded, and the sharp peaks of the U-wave are absent. Its duration seems to increase as well, which shows diffraction tends to cumulatively reduce the high-frequency content of the U-wave.

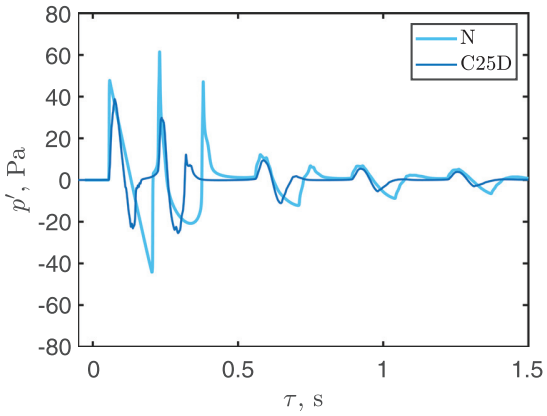

FIG. 15. (Color online) Sinusoidal terrain, N and C25D waves—time signals simulated at ground level, with τ the time relative to the beginning of the waveform in the flat case.

The evolution of the PL and CSEL metrics along the ground, relative to the flat ground case, is depicted in Fig. 16. It presents a periodic behavior, associated with the periodic variation of the ground profile. For comparison, the evolution of PL and CSEL along the isolated terrain depression (see Fig. 8) is also represented in Fig. 16. Interestingly, a close match is observed. This shows that the effects due the terrain depression prevail over those caused by the hill. This also indicates that, while having a large impact on the pressure waveforms, the cumulative effects related to the topography have little influence on the noise perceived, which is thus mostly governed by the local evolution of the ground profile, at least using the metrics employed in this work.

V. CONCLUSION

In this paper, a numerical method for the prediction of sonic boom reflection over irregular terrain based on the Euler equations is presented. The physical mechanisms associated with varying elevation are characterized using academic ground profiles (terrain depression, hill, periodic). The effect of slope variation is observed locally in the reflection zone, on the reflected wave, and on the wavefronts. Furthermore, wavefront folding is observed where slope variations are largest, leading to focal zones, caustics, and U-waves, which strongly affect the signals and lead to

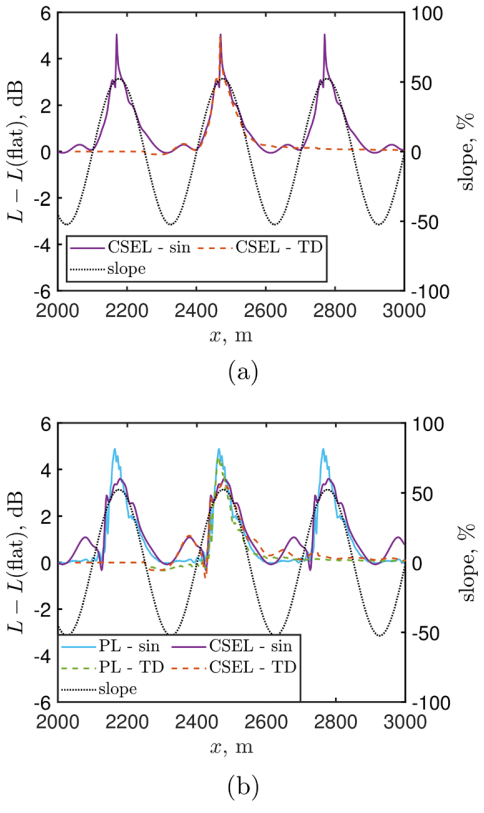

FIG. 16. (Color online) Sinusoidal terrain (sin), (a) N and (b) C25D waves—perceived noise level L computed at ground level using PL and CSEL and normalized by the flat surface case, and ground profile slope. Comparison with the isolated terrain depression (TD) case.

the most significant variations in perceived noise at ground level. Similar mechanisms were observed with the classical N-wave and the low-boom C25D wave, but the different natures of these waves lead to differences in how these mechanisms affect the waveforms and the perceived noise at ground level, depending on the chosen metrics.

Between the terrain depression and the hill ground profiles, the first was found to have the strongest effect, in particular, with stronger focalization at ground level, resulting in higher amplitude U-waves and larger levels of perceived noise. This terrain depression focalization was also found to be dominant in the case of a sinusoidal ground profile, which yielded similar perceived noise levels. Furthermore, the sinusoidal ground profile allowed us to highlight the presence of cumulative effects that affect the signal tail and could prove significant with real terrain.

In order to estimate the significance of the mechanisms highlighted in the present study, the investigation of topographic effects on sonic boom reflection using real ground profiles is under way. In addition, while this study focuses on topography, the tools used allow us to consider various atmospheric conditions, so that they can be used to investigate the combined impact of topographic and meteorological effects on sonic boom propagation in the future. This study has highlighted the influence of the topography based on a two-dimensional model. While similar effects are expected, the three-dimensionality of both the ground surface and of the sonic boom could affect the quantitative results that remain to be evaluated.

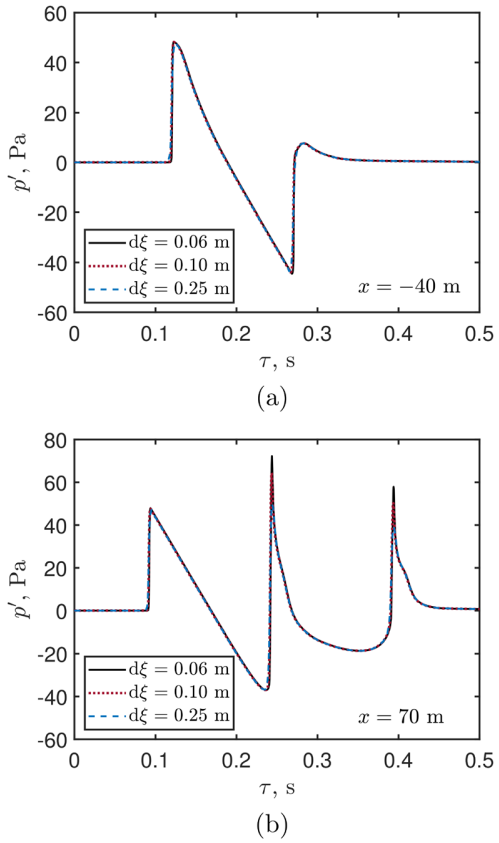

FIG. 17. (Color online) Terrain depression, N-wave—time signals obtained using different mesh sizes at positions (a) $x = -40$ m and (b) $x=70$ m along the terrain depression ground profile.

ACKNOWLEDGMENTS

This project has received funding from the European Union's Horizon 2020 research and innovation programme under Grant Agreement No. 769896 (RUMBLE, 2020). This publication reflects only the authors' view and the Innovation and Networks Executive Agency (INEA) is not responsible for any use that may be made of the information it contains. It was performed within the framework of the LABEX CeLyA (ANR-10-LABX-0060) of Université de Lyon, within the program "Investissements d'Avenir" (ANR-16-IDEX-0005) operated by the French National Research Agency (ANR). This work was granted access to the HPC resources of PMCS2I (Pôle de Modélisation et de Calcul en Sciences de l'Ingénieur et de l'Information) of Ecole Centrale de Lyon, PSMN (Pôle Scientifique de Modélisation Numérique) of ENS de Lyon and P2CHPD (Pôle de Calcul Hautes Performances Dédiés) of Université Lyon I, members of FLMSN (Fédération Lyonnaise de Modélisation et Sciences Numériques), partner of EQUIPEX EQUIP@MESO.

APPENDIX A

This appendix aims at completing the discussion on mesh convergence in Sec. II B 2 including the effect of elevation variations in the case of the N-wave reflecting over the terrain depression ground profile. Furthermore, this appendix primarily concentrates on PL variations with grid size, as this metric is particularly sensitive in the presence of the N-wave. This is due to PL's sensitivity to high frequencies, present in the N-wave due to its sharp peak and short rise time.

Figure 17 shows waveforms obtained using three different mesh sizes at positions $x = -40$ and 70 m along the terrain depression, i.e., on either side of the point of minimum elevation at $x = 0$ m. At $x = -40$ m, the three waveforms are very close, although one may notice peaks are slightly more rounded with the coarse grid size $d\xi = 0.25$ m. The waveform obtained at $x = 70$ m is the least favourable case, with particularly sharp secondary peaks. These secondary peaks are somewhat affected by the grid size. Using grid sizes of 0.25, 0.1, and 0.06 m, the second peak reaches 49.6, 64.3, and 72.2 Pa, respectively, and the third peak reaches 39.0, 50.5, and 57.9 Pa.

Overall, these waveforms are thus very close, especially with the two finer grid sizes. This explains why CSEL, which accounts for a wide range of frequencies, yields accurate results with both these meshes, as detailed in Sec. II B 2. Furthermore, the perceived noise variations along the terrain depression are plotted for different grid sizes using CSEL in Fig. 18(b), which shows levels obtained with these two meshes remain close even in the presence of ground

https://doi.org/10.1121/10.0003816

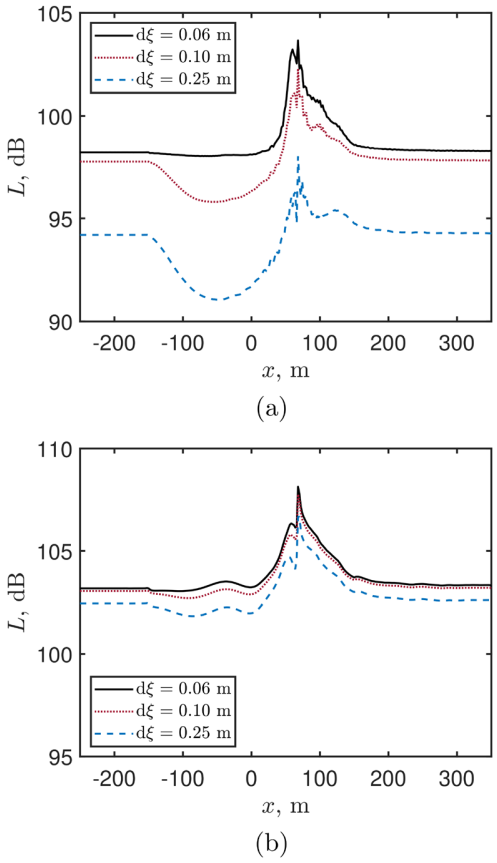

FIG. 18. (Color online) Terrain depression, N-wave—perceived noise variation along the terrain depression ground profile obtained using the (a) PL and (b) CSEL metrics with different mesh sizes.

elevation variations. On the contrary, PL is more sensitive to high frequencies than to low frequencies and consequently the convergence of the mesh with an N-wave is not so simple with this metric, as illustrated in Fig. 18(a). First notice the substantial improvement in accuracy between a grid size of 0.25 and 0.1 m, compared to $d\xi = 0.06$ m. The difference between the two finer meshes remains small over flat ground ($x < -150$ m and $x > 150$ m), as detailed in Table II, but some significant deviations appear with elevation variation, especially between $x = -122$ and 35 m. This corresponds to the downhill part of the ground profile, where as the curvilinear mesh adapts to the surface, some cells are larger than the nominal size. On the other hand, the uphill section, where wavefront folding occurs, is favourable in terms of mesh convergence, and some cells are smaller than the nominal size in this part of the mesh.

In view of this, a grid size of 0.06 m is used to simulate the propagation of the N-wave over both the terrain depression and hill cases. Our confidence in the accuracy of the results with this mesh is supported by the good accordance with the reference initial wave in the flat case (see Table II), as well as by the spectra in Fig. 4 which show this grid size allows to capture frequencies in the higher frequency range, including with non-flat ground. The downside of using the finer mesh is increased computational cost. While it remains reasonable over short ground profiles, it becomes a limiting factor when longer profiles or a large number of cases are considered. A grid size of 0.1 m is therefore chosen for all cases with the C25D wave, which has a lower frequency content than the N-wave (see Sec. II B 2). Furthermore, the discussion in Appendix B shows the major variations in perceived noise induced by topographic effects are captured by each of the metric types which have been tested, including CSEL. A grid size of 0.1 m will therefore also be used for the sinusoidal terrain case, as well as other long ground profiles which will be studied in the future. Then, CSEL is used to calculate the perceived noise in the case of the N-wave, while both PL and CSEL are used with the C25D wave.

APPENDIX B

The PL and CSEL metrics have been used in Secs. III and IV to evaluate the impact of terrain on perceived noise of sonic booms. This appendix presents corresponding results for five other metrics, that were shown to correlate highly with human perception (Loubeau *et al.*, 2015). These metrics are ASEL, BSEL, DSEL, ESEL, and ISBAP.

Figure 19 shows the evolution of the seven metrics along the terrain depression ground profile, normalized by their values for a flat terrain. Concerning the N-wave in Fig. 19(a),

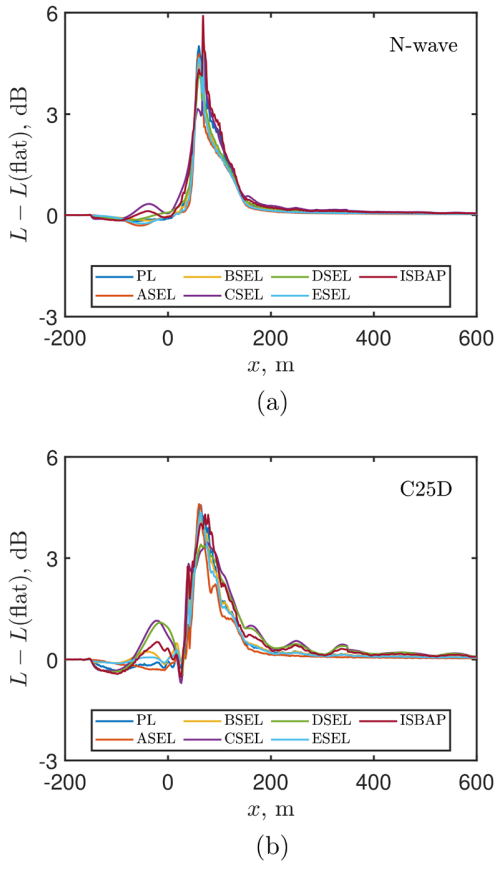

FIG. 19. (Color online) Terrain depression, (a) N and (b) C25D waves—perceived noise computed at ground level using seven metrics and normalized by the flat surface case.

ASEL, BSEL, DSEL, and ESEL have similar values and are closely related to PL. As explained in Sec. III A, CSEL follows a comparable trend, but its maximum is smaller by about 1 dB. For the C25D wave in Fig. 19(b), notice the curves for CSEL and DSEL are almost superimposed and that ASEL, BSEL and ESEL have a similar evolution to PL. For both boom waves, the ISBAP metric, which is composed of PL and CSEL, is located in between the PL and CSEL curves. Analogous results (not shown for conciseness) are obtained for the hill ground profile.

In conclusion, the seven metrics follow the same evolution along the two ground profiles. It is thus expected that the variations related to terrain elevation determined for one of these seven metrics would also be representative of those of the other ones.[1]

[1]See supplementary material at https://www.scitation.org/doi/suppl/10.1121/10.0003816 for videos of the reflection of the low-boom C25D wave along both the terrain depression and hill ground profiles using pressure fluctuation maps ([−50; 50] Pa).

AIAA (**2017**). 2nd AIAA Sonic Boom Prediction Workshop, Grapevine, TX, 7–8 January, http://lbpw.larc.nasa.gov/ (Last viewed November 4, 2020).

AIAA (**2020**). 3rd AIAA Sonic Boom Prediction Workshop, Orlando, FL, 4–5 January, http://lbpw.larc.nasa.gov/ (Last viewed November 4, 2020).

Anderson, J. D. (**1995**). *Computational Fluid Dynamics: The Basics with Applications* (McGraw-Hill, New York), Chap. 2.

Berland, J., Bogey, C., and Bailly, C. (**2006**). "Low-dissipation and low-dispersion fourth-order Runge–Kutta algorithm," Comput. Fluids **35**, 1459–1463.

Blanc-Benon, P., Lipkens, B., Dallois, L., Hamilton, M. F., and Blackstock, D. T. (**2002**). "Propagation of finite amplitude sound through turbulence: Modeling with geometrical acoustics and the parabolic approximation," J. Acoust. Soc. Am. **111**(1), 487–498.

Bogey, C., and Bailly, C. (**2004**). "A family of low dispersive and low dissipative explicit schemes for flow and noise computations," J. Comput. Phys. **194**, 194–214.

Bogey, C., de Cacqueray, N., and Bailly, C. (**2009**). "A shock-capturing methodology based on adaptative spatial filtering for high-order non-linear computations," J. Comput. Phys. **228**, 1447–1465.

Boulanger, P., and Attenborough, K. (**2005**). "Effective impedance spectra for predicting rough sea effects on atmospheric impulsive sounds," J. Acoust. Soc. Am. **117**(2), 751–762.

Candel, S. (**1977**). "Numerical solution of conservation equations arising in linear wave theory: Application to aeroacoustics," J. Fluid Mech. **83**(3), 465–493.

Cleveland, R. O., Chambers, J. P., Bass, H. E., Raspet, R., Blackstock, D. T., and Hamilton, M. F. (**1996**). "Comparison of computer codes for the propagation of sonic boom waveforms through isothermal atmospheres," J. Acoust. Soc. Am. **100**(5), 3017–3027.

Coulouvrat, F. (**2002**). "Sonic boom in the shadow zone: A geometrical theory of diffraction," J. Acoust. Soc. Am. **111**(1), 499–508.

Dini, D., and Lazzeretti, R. (**1969**). "Ground configuration effects on sonic boom," AGARD Conference Proceedings No. 42, Vol. 25, pp. 1–29.

Dragna, D., Pineau, P., and Blanc-Benon, P. (**2015**). "A generalized recursive convolution method for time-domain propagation in porous media," J. Acoust. Soc. Am. **138**(2), 1030–1042.

Gainville, O. (**2008**). "Modélisation de la propagation atmosphérique des ondes infrasonores par une méthode de tracé de rayons non linéaire" ("Numerical modelling of atmospheric infrasound propagation using a nonlinear ray-tracing method"), Ph.D. thesis No. 2008-07, Ecole Centrale de Lyon, Lyon, France.

Gal-Chen, T., and Sommerville, R. C. J. (**1975**). "On the use of a coordinate transformation for the solution of the Navier-Stokes equations," J. Comput. Phys. **17**, 209–228.

Kanamori, M., Takahashi, T., Makino, Y., Naka, Y., and Ishikawa, H. (**2018**). "Comparison of simulated sonic boom in stratified atmosphere with flight test measurements," AIAA J. **56**(7), 2743–2755.

Komatitsch, D., and Martin, R. (**2007**). "An unsplit convolutional perfectly matched layer improved at grazing incidence for the seismic wave equation," Geophysics **72**(5), SM155–SM167.

Leatherwood, J. D., Sullivan, B. M., Sheperd, K. P., McCurdy, D. A., and Brown, S. A. (**2002**). "Summary of recent NASA studies of human response to sonic booms," J. Acoust. Soc. Am. **111**(1), 586–598.

Liebhardt, B., Lütjens, K., Ueno, A., and Ishikawa, H. (**2020**). "JAXA's S4 supersonic low-boom airliner—A collaborative study on aircraft design, sonic boom simulation, and market prospects," AIAA Aviation Forum, June 15-19, Virtual event, AIAA-Paper 2020-2731, pp. 1–12.

Loubeau, A., and Coulouvrat, F. (**2009**). "Effects of meteorological variability on sonic boom propagation from hypersonic aircraft," AIAA J. **47**(11), 2632–2641.

Loubeau, A., Naka, Y., Cook, B., Sparrow, V., and Morgenstern, J. (**2015**). "A new evaluation of noise metrics for sonic booms using existing data," AIP Conf. Proc. **1685**, 0090015.

Luquet, D., Marchiano, R., and Coulouvrat, F. (**2019**). "Long range numerical simulation of acoustical shock waves in a 3D moving heterogeneous and absorbing medium," J. Comput. Phys. **379**, 237–261.

Maglieri, D., Bobbitt, P., Plotkin, K., Shepherd, K., Coen, P., and Richwine, D. (**2014**). "Sonic boom: Six decades of research," Technical Report No. NASA/SP-2014-622, L-20381, NF1676L-18333, NASA, Washington, DC, pp. 1–539.

Mattson, T. G., He, Y. H., and Koniges, A. E. (**2019**). *The OpenMP Common Core: Making OpenMP Simple Again* (MIT Press, Cambridge).

Phillips, B. D., and West, T. K. IV (**2019**). "Trim flight conditions for a low-boom aircraft design under uncertainty," J. Aircraft **56**(1), 53–67.

Rallabhandi, S. K. (**2011**). "Advanced sonic boom prediction using the augmented Burgers equation," J. Aircraft **48**(4), 1245–1253.

Rallabhandi, S. K., and Loubeau, A. (**2019**). "Summary of propagation cases of the second AIAA sonic boom prediction workshop," J. Aircraft **56**(3), 876–895.

Rendón, P. L., and Coulouvrat, F. (**2005**). "Reflection of caustics and focused sonic booms," Wave Motion **42**(3), 211–225.

RUMBLE (**2020**). EU-H2020-Project, EU Grant Agreement No. 769896, http://rumble-project.eu (Last viewed November 4, 2020).

Sabatini, R., Marsden, O., Bailly, C., and Bogey, C. (**2016**). "A numerical study of nonlinear infrasound propagation in a windy atmosphere," J. Acoust. Soc. Am. **140**(1), 641–656.

Salomons, E. M. (**1998**). "Caustic diffraction fields in a downward refracting atmosphere," J. Acoust. Soc. Am. **104**(6), 3259–3272.

Scott, J. F., Blanc-Benon, P., and Gainville, O. (**2017**). "Weakly nonlinear propagation of small-wavelength, impulsive acoustic waves in a general atmosphere," Wave Motion **72**, 41–61.

Stevens, S. S. (**1972**). "Perceived level of noise by Mark VII and decibels (E)," J. Acoust. Soc. Am. **51**(2), 575–601.

Stout, T. A., and Sparrow, V. W. (**2019**). "Three-dimensional simulation of shaped sonic boom signature loudness variations due to atmospheric turbulence," in *25th AIAA/CEAS Aeroacoustics Conference*, AIAA-Paper 2019-256, 20–23 May, Delft, The Netherlands, pp. 1–18.

Sun, Y., and Smith, H. (**2017**). "Review and prospect of supersonic business jet design," Prog. Aerosp. Sci. **90**, 12–38.

Thisse, J., Polacsek, C., Lewy, S., and Mayeur, J. (**2015**). "A numerical simulation method of shock-wave propagation in turbofan intakes," *InterNoise 2015*, 9–12 August, San Francisco, CA, pp. 1–12.

Troian, R., Dragna, D., Bailly, C., and Galland, M.-A. (**2017**). "Broadband liner impedance eduction for multimodal acoustic propagation in the presence of a mean flow," J. Sound Vib. **392**, 200–216.

Ueno, A., Kanamori, M., and Makino, Y. (**2017**). "Robust low-boom design based on near-field pressure signature in whole boom carpet," J. Aircraft **54**(3), 918–925.

Yamashita, R., and Suzuki, K. (**2016**). "Full-field sonic boom simulation in stratified atmosphere," AIAA J. **54**(10), 3223–3231.

Yuldashev, P. V., Ollivier, S., Karzova, M. M., Khokhlova, V. A., and Blanc-Benon, P. (**2017**). "Statistics of peak overpressure and shock steepness for linear and nonlinear N-wave propagation in a kinematic turbulence," J. Acoust. Soc. Am. **142**(6), 3402–3415.